CONTRACTOR REPORT

SAND88—7054
Unlimited Release
UC—814

Yucca Mountain Site Characterization Project

Processes, Mechanisms, Parameters, and Modeling Approaches for Partially Saturated Flow in Soil and Rock Media

J. S. Y. Wang, T. N. Narasimhan
Earth Sciences Division
Lawrence Berkeley Laboratory
University of California
Berkeley, CA 94720

Prepared by Sandia National Laboratories Albuquerque, New Mexico 87185 and Livermore, California 94550 for the United States Department of Energy under Contract DE-AC04-76DP00789

Printed June 1993

"Prepared by Yucca Mountain Site Characterization Project (YMSCP) participants as part of the Civilian Radioactive Waste Management Program (CRWM). The YMSCP is managed by the Yucca Mountain Project Office of the U.S. Department of Energy, DOE Field Office, Nevada (DOE/NV). YMSCP work is sponsored by the Office of Geologic Repositories (OGR) of the DOE Office of Civilian Radioactive Waste Management (OCRWM)."

Issued by Sandia National Laboratories, operated for the United States Department of Energy by Sandia Corporation.

Available to DOE and DOE contractors from
Office of Scientific and Technical Information
PO Box 62
Oak Ridge, TN 37831

Prices available from (615) 576-8401, FTS 626-8401

Available to the public from
National Technical Information Service
US Department of Commerce
5285 Port Royal Rd
Springfield, VA 22161

NTIS price codes
Printed copy: A13
Microfiche copy: A01

SAND88-7054
LBL-26224
Unlimited Release
Printed June 1993

Distribution
Category UC-814

PROCESSES, MECHANISMS, PARAMETERS, AND MODELING APPROACHES FOR PARTIALLY SATURATED FLOW IN SOIL AND ROCK MEDIA

by
J. S. Y. Wang and T. N. Narasimhan
Earth Sciences Division
Lawrence Berkeley Laboratory
University of California
Berkeley, CA 94720

Work performed for
Sandia National Laboratories
Albuquerque, NM 87185
Under Sandia Contract: 754347
P. G. Kaplan, System Performance Assessment Division

ABSTRACT

This report discusses conceptual models and mathematical equations, analyzes distributions and correlations among hydrological parameters of soils and tuff, introduces new path integration approaches, and outlines scaling procedures to model potential-driven fluid flow in heterogeneous media. To properly model the transition from fracture-dominated flow under saturated conditions to matrix-dominated flow under partially saturated conditions, characteristic curves and permeability functions for fractures and matrix need to be improved and validated. Couplings from two-phase flow, heat transfer, solute transport, and rock deformation to liquid flow are also important. For stochastic modeling of alternating units of welded and nonwelded tuff or formations bounded by fault zones, correlations and constraints on average values of saturated permeability and air entry scaling factor between different units need to be imposed to avoid unlikely combinations of parameters and predictions. Large-scale simulations require efficient and verifiable numerical algorithms. New path integration approaches based on postulates of minimum work and mass conservation to solve flow geometry and potential distribution simultaneously are introduced. This verifiable integral approach, together with fractal scaling procedures to generate statistical realizations with parameter distribution, correlation, and scaling taken into account, can be used to quantify uncertainties and generate the cumulative distribution function for groundwater travel times.

ACKNOWLEDGMENTS

We thank P. G. Kaplan and S. Sinnock of Sandia National Laboratories for stimulating discussions throughout this study. The critical technical reviews by R. J. Glass and B. M. Rutherford of Sandia National Laboratories and by K. Pruess and Y. W. Tsang of Lawrence Berkeley Laboratory helped considerably in improving the quality of the final version of this report. This work was supported by Sandia National Laboratories for the Yucca Mountain Site Characterization Project of the U.S. Department of Energy.

This report was prepared under the former Yucca Mountain Project WBS number 1.2.1.4.4.1; the current WBS number is 1.2.5.4.4. The information and data documented in this report were developed at a Quality Assurance Level III and the work activity was not subject to QA controls. The information in this report is not qualified and is not to be used for licensing.

TABLE OF CONTENTS

TABLE OF CONTENTS (continued)

LIST OF FIGURES

LIST OF FIGURES (continued)

LIST OF FIGURES (continued)

LIST OF FIGURES (continued)

LIST OF TABLES

LIST OF ABBREVIATIONS

Abbreviation	Expansion
BFw	Bullfrog welded tuff unit
CDF	cumulative distribution function
CFUn	Crater Flat upper nonwelded tuff unit
CHnv	Calico Hills nonwelded, vitric tuff unit
CHnz	Calico Hills nonwelded, zeolitic tuff unit
DOE	United States Department of Energy
DRI	Desert Research Institute
GDF	Ghost Dance Fault
GWTT	groundwater travel time
HLW	High Level Nuclear Wastes
MINC	multiple interacting continuum
NRC	United States Nuclear Regulatory Commission
NTS	Nevada Test Site
PPw	Prow Pass welded tuff unit
PTn	Paintbrush nonwelded tuff unit
REV	representative element volume
RIB	Reference Information Base
SC	Solitario Canyon
SCP	Site Characterization Plan
SNL	Sandia National Laboratories
TAC	Technical Advisory Committee
TCw	Tiva Canyon welded tuff unit
TSw	Topopah Spring welded tuff unit
USDA	United States Department of Agriculture
USGS	United States Geological Survey
YMP	Yucca Mountain Site Characterization Project

NOMENCLATURE

A	area	$[L^2]$
C	concentration	
$\overline{\overline{C}}$	elastic tensor of fourth rank	$[ML^{-1}t^{-2}]$
C_h	soil moisture capacity	$[L^{-1}]$
C_β	normalizing constant for Beta - distribution	
D	fractal dimension	
D_c	dispersion coefficient	$[L^2t^{-1}]$
D_{c0}	diffusion coefficient	$[L^2t^{-1}]$
D_f	fracture spacing	$[L]$
F	cumulative distribution function	
F_D	domain-dependent factor	
H	enthalpy	$[L^2t^{-2}]$
$\overline{\overline{I}}$	unit diagonal tensor	
K	hydraulic conductivity	$[Lt^{-1}]$
K_h	thermal conductivity	$[MLt^{-3}T^{-1}]$
L	length of a core	$[L]$
M	liquid mass density within volume V	$[ML^{-3}]$
M^h	heat density within volume V	$[ML^{-1}t^{-2}]$
N	number of data points	
P	pressure	$[ML^{-1}t^{-2}]$
P_c	capillary pressure	$[ML^{-1}t^{-2}]$
PD	probability distribution	
Q	volumetric flow rate	$[L^3t^{-1}]$
R	flow resistance	$[L^{-1}t^{-1}]$
S	saturation	
S_e	effective saturation or reduced moisture content	

NOMENCLATURE (continued)

T	temperature	$[T]$
U	internal energy	$[L^2t^{-2}]$
V	volume	$[L^3]$
W	sum of weights in statistical averaging	
W_t	total weight in statistical moment averaging	
X	mass fraction	
a	correlation range	$[L]$
b	aperture	$[L]$
c	specific heat	$[L^2t^{-2}T^{-1}]$
d	displacement	$[L]$
d_s	shear displacement or scaled correlation range	$[L]$
f	distribution function	$[L^{-1}]$
f_h	shape factor	
g	gravitational acceleration	$[Lt^{-2}]$
h	pressure head	$[L]$
k	permeability	$[L^2]$
k_{ct}	permeability of cylindrical tube	$[L^2]$
k_r	relative permeability	
k_{pp}	permeability of parallel plate channel	$[L^2]$
l	length along flow path	$[L]$
m	pore-size distribution parameter in van Genuchten's formula	
$\dot{m}$	mass source or sink	$[ML^{-3}t^{-1}]$
$\dot{m}^h$	heat source or sink	$[ML^{-1}t^{-3}]$
m_z	mean of parameter z	
n	pore-size distribution parameter in van Genuchten's formula	
$\vec{n}$	unit vector normal to surface A	
p_β	parameter in Beta - distribution	

NOMENCLATURE (continued)

q	mass flux	$[ML^{-2}t^{-1}]$
q^h	heat flux	$[Mt^{-3}]$
q_β	parameter in Beta - distribution	
r	radius	$[L]$
r_h	hydraulic radius	$[L]$
s_2	coefficient of variation	
s_3	coefficient of skewness	
s_4	coefficient of kurtosis	
t	time	$[t]$
v	velocity	$[Lt^{-1}]$
w	weight in statistical averaging	
x	coordinate of curvilinear axis along stream tube	$[L]$
z	elevation	$[L]$
Θ	contact angle	
Φ	fluid potential	$[L^2t^{-2}]$
Ω	potential functional	$[ML^2t^{-3}]$
α	air entry scaling factor	$[L^{-1}]$
β	gamma distribution parameter	$[L^{-1}]$
γ	variogram	
ε	volumetric strain	
$\overline{\overline{\varepsilon}}$	strain tensor	
θ	moisture content	
λ	pore-size distribution index in Brooks and Cory formula	
λ_D	dispersivity	$[L]$
μ	viscosity	$[ML^{-1}t^{-1}]$
ξ	exponent in dispersion coefficient	
ρ	mass density	$[ML^{-3}]$
σ	surface tension	$[Mt^{-2}]$

σ_z	standard deviation of parameter z	
$\bar{\bar{\sigma}}$	stress tensor	$[ML^{-1}t^{-2}]$
σ'	effective stress	$[ML^{-1}t^{-2}]$
σ_N	normal stress	
τ	phase constriction or tortuosity factor	
ϕ	porosity	
X	Bishop parameter	
ω	fraction of area of fracture-matrix flow	
ω_o	fraction of contact area	

Superscript

c	concentration
h	heat
κ	mass component (water w or air a)

Subscript

0	zero stress or zero saturation
R	rock
ae	air entry value
c	contact cutoff
d	drying
g	gas phase
i	index for stream tube or data point in statistical averaging
j	index for potential drop
l	liquid phase
p	pore
r	residual value
s	saturation or saturated value
w	wetting
β	phase

1.0 INTRODUCTION

The work described in this report was performed for Sandia National Laboratories (SNL) as a part of the Yucca Mountain Site Characterization Project (YMP). The YMP is administered by the Nevada Operations Office of the U.S. Department of Energy (DOE). The project is part of the DOE's program to dispose safely of commercial high-level nuclear wastes. The purpose of the project is to determine the feasibility of developing a mined repository for high-level nuclear waste in partially saturated tuff formations at Yucca Mountain, on and adjacent to the Nevada Test Site (NTS) in southern Nevada.

The objective of this work is to aid the performance assessment activities at SNL by reviewing and studying processes, mechanisms, and parameters governing partially saturated flows in geological media. Success of performance assessment for a spatial scale of kilometers and for a time scale of over thousands of years will depend on mathematical modeling procedures which are thoroughly verified and properly validated. Both conceptual and mathematical models need to account for physical processes, driving mechanisms, and parameter variations in the geological media surrounding the repository.

Our past efforts (Wang and Narasimhan, 1985, 1986, 1987) focused on conceptual models for fluid flow in partially saturated, fractured, porous tuff in different spatial and temporal scales. Scoping calculations with available tuff properties demonstrated the dominance of matrix flow over fracture flow under ambient conditions, the damping of transient infiltration pulses by near-surface units, and the near-vertical flow pattern within fault-bounded blocks with alternating welded and nonwelded units from ground surface to water table. Some of these findings are important for performance assessment of fluid flow and contaminant transport. Because modeling results depend on input parameters, the next logical step is to perform sensitivity analyses to either substantiate or refute the conclusions from preliminary scoping calculations. Meaningful sensitivity analyses require the specification of ranges and distributions of parameters that represent the geological media. This report mainly addresses parameter variabilities for tuff and other natural geological materials to better quantify the geologic media at the potential repository locale.

1.1 Literature Review

Because concerted efforts to study partially saturated tuff formations at Yucca Mountain were initiated only a few years ago, the data base for tuff properties is relatively small in comparison with data bases for other geological media, especially soils. We surveyed the soil physics and groundwater hydrology literature on characteristic curve data and partially saturated flows. Most of these survey results will be discussed in following relevant sections. Although the primary focus of our literature survey is on the variations of hydrological parameters of partially saturated flows, the basic concepts, potential driving mechanisms, flow processes, and governing equations in models for partially saturated systems have also been reviewed.

One of the early data bases on hydrological properties of partially saturated soils is the catalog by Mualem (1976a), in which 89 soils, from literature during the period from 1939 to 1971,

were classified according to basic soil textural classes. Tabulated data were given for $h(\theta)$, $K(h)$ and to a lesser extent $K(\theta)$ relationships between capillary head, h, water content, θ, and hydraulic conductivity, K. For some soils, several wetting and drying curves were tabulated to characterize capillary hysteresis phenomena. Experimental data up to 1982 in the literature were tabulated by Case et al. (1983) for an additional 76 soils. In this report from the Desert Research Institute (DRI), Nevada, the data were plotted and fitted with polynomials for *log(h) - S, log(K) - log(h), or log(K) - S* curves (*S* for saturation). Drawing upon data from many papers and reports, these catalogs present brief descriptions of original analyses, experimental methods, and other available parameters. A U.S. Department of Agriculture (USDA) study by Holtan et al. (1968) sampled approximately 200 Agricultural Research Service experimental watersheds. Five-foot-deep pits were dug to collect samples from different horizons for laboratory measurements of saturated conductivity and moisture retention. Panian (1987) of DRI plotted and fitted this moisture-retention data set of over 1300 soil samples with the van Genuchten (1980) model. Some of the recent studies carried out with these data sets, together with our analyses of soil parameter correlations, will be discussed in this report.

With regard to basic concepts, driving mechanisms, and governing equations, the following review articles in the literature form the basis for our further study of partially saturated media (also termed "unsaturated zone" or "vadose zone"). Nielsen et al. (1986) reviewed deterministic mathematical models and conceptual understanding of water flow and chemical transport in the unsaturated zone. They emphasized the need to have a unified and interdisciplinary approach that includes all pertinent physical, chemical, and biological processes operative in the unsaturated zone. van Genuchten and Jury (1987) summarized the progress in past 4 years in unsaturated flow and transport modeling. Flow through macropores (and fractures) and spatial and temporal variability in soil hydraulic properties are receiving more attention in the literature for better understanding of field-scale transport processes. The coupling of fluid processes with mechanical deformations was reviewed by Narasimhan (1982). The influence of negative pore pressure on soil deformation remains a difficult process to model. Pruess and Wang (1987) reviewed isothermal and nonisothermal modeling studies for partially saturated, fractured tuff. Fluid mobility in fractures may have drastic impact on the waste container environment and vapor movements may be very rapid both near the container and kilometers away from the repository.

1.2 Model Validation

Although soils are very different from fractured tuff, it is important for the YMP to use knowledge developed in soil literature to supplement site-specific tuff studies. Most of our basic understanding of unsaturated systems is based on studies in near-surface soils. We need to be aware of the assumptions and limitations of equations of moisture movement in soils, if we are to apply them to deep tuff formations. If we develop new approaches specific for the tuff medium, we need to check against credible soil phenomena to validate the models. Model validation is the key to defensible performance assessment.

One example of ongoing model validation efforts is a field experiment in loamy soils performed by New Mexico State University (Wierenga et al., 1986; Nicholson et al., 1987), and sponsored

by the U.S. Nuclear Regulatory Commission (NRC). A 6-m-deep trench was excavated to collect soil samples for spatial variability analyses and to observe vertical advancement and lateral spreading of the wetting front. Another example is a field study at a sandy hillslope by the New Mexico Institute of Mining and Technology (Stephens and Knowlton, 1986; McCord and Stephens, 1987), and sponsored by the U.S. Department of the Interior. Part of a small drainage basin was instrumented to estimate natural groundwater recharge and to characterize the influence of topography on the direction of vadose water flow paths beneath a hillslope. Both studies are relevant to partially saturated water movements in soils at semiarid sites.

At the Yucca Mountain site, thin soil layers do cover some of the ground surface. Top soils may control the amount of evaporation and transpiration and the net infiltration into underlying tuff formations. Within alternating layers of tuff, the physical characteristics of interbedded nonwelded materials may be intermediate between those of soils and hard rocks. If the porous Calico Hills nonwelded unit, below the repository candidate Topopah Spring welded unit, is considered to be the main barrier between repository and water table, we need to model this heterogeneous unit with spatially varying material properties. The need to understand processes in top soils and nonwelded units is another reason to digress into soil literature in the course of studying fractured, porous tuff formations.

The ultimate goal for performance assessment activities is to satisfy NRC's preemplacement and postemplacement performance criteria. Most of the review in this report will focus on issues related to the preemplacement, 1000-yr groundwater travel time (GWTT) criterion in 10 CFR 60.113(a)(2) (NRC, 1986). However, some review of nonisothermal and solute-dependent processes will also be important to other postemplacement criteria. An interpretation of the GWTT performance objective (Codell, 1986) treats the GWTT as a random variable to be quantified by a cumulative distribution function (CDF) of travel times for nonreactive, nondecaying, infinitesimal tracer particles from the disturbed zone to the accessible environment along macroscopic paths. This CDF will combine all spatial variability, temporal variability, and uncertainty of the GWTT into a single curve. Compliance with the 1000-yr objective will have been demonstrated if it can be shown that any tracer particle leaving the disturbed zone has a (100-x)% or greater probability of arriving at the accessible environment in a time greater than 1000 yr, where x is a small number. In addition to uncertainties associated with site data, Codell (1986) also recognizes that dispersion, molecular diffusion, matrix diffusion, and distributed source will affect the GWTT CDF, and distinguishes unsaturated media from saturated media considerations.

1.3 Uncertainties

Concurrent with our literature survey, SNL established a Technical Advisory Committee (TAC) with R. Allen Freeze, Jacob Bear, Milton E. Harr, R. William Nelson, and Benjamin Ross, to evaluate the uncertainties in GWTT calculations at Yucca Mountain. The TAC reviews models, modeling procedures, and sources of uncertainty in the estimation of GWTT, and recommends experimental and numerical approaches for reducing these uncertainties. The TAC classifies the uncertainties and estimates the likely relative influence of each uncertainty on the GWTT CDF.

Three classes of uncertainties have been defined by the TAC: *model uncertainty, parameter uncertainty, and calibration uncertainty.* Model uncertainty includes conceptual models and mathematical modeling procedures. Parameter uncertainty refers to coefficients and conditions for the solutions of a given model. Both classes of uncertainty address media-related considerations (fracture flow versus matrix flow, dead-end pores, spatial variability, etc.); fluid-related considerations (single-phase versus two-phase, isothermal versus nonisothermal conditions, etc.); initial and boundary conditions (infiltration, lateral boundary, water table, etc.); domain geometry (dimensionality, extent); and geological framework (welded and nonwelded layers, stratigraphic contacts, fault zones, etc.). The third class of uncertainty regards model calibration and validation. Uncertainties in measurements of state variables (pressures, saturations, fluxes, temperatures, concentrations, etc.) will affect estimation of model coefficients and confirmation of model structures. Indirect measures from geochemical interpretation and age dating are also considered in the calibration uncertainty.

Interactions with the TAC, facilitated by SNL, greatly benefit our review and research efforts. Of the uncertainties listed by TAC, those of greatest significance to preemplacement GWTT include fracture-flow/matrix-flow interactions, permeability and porosity of matrix and fractures, dead-end-pore effects, variability of medium properties, stratigraphic contacts, capillary barriers, perched zones, lateral flows, fault zone properties, infiltration distributions and rates, water table positions, two-phase nonisothermal flow effects, and geochemistry for age dating and recharge location interpretation. Some of major issues identified by the TAC were addressed in our past research in conceptual models and numerical calculations (Wang and Narasimhan, 1985, on fracture/matrix flows; Wang and Narasimhan, 1986, on infiltration effects; and Wang and Narasimhan, 1987, on lateral flows and parameter variabilities). In this report, we will review and discuss most of these major issues so that future modeling efforts can generate calibrated GWTT CDF for Yucca Mountain.

2.0 CONCEPTUAL MODELS

Conceptual models are important to the assessment of system behavior of complex geological formations. A good conceptual model must be both simple enough to facilitate understanding and complete enough to catch the essential features. If a conceptual model can explain the main trends in observations and experimental measurements, then deviations from calculated results can be treated as small perturbations. If there are large differences between model predictions and experimental results, a new or a modified conceptual model is required to explain and reduce the differences. In this section, we review the conceptual models used in studies of partially saturated media. In addition to the general description, we will briefly discuss the usefulness and potential limitations of the models for tuff studies.

The structure of the medium dictates the choice of conceptual models. If the medium is homogeneous and uniform, we can treat it as a porous medium. If the structure and texture of the formation changes discontinuously from depth to depth or from location to location, we may break the formation into porous layers or domains. For a formation with large holes or fractures coexisting with porous matrix, we need to take into account these "secondary" pores. Certainly the choice of conceptual models depends on the scale and the process of interest. In this section, we focus on the structural aspects of conceptual models. Once we adopt a conceptual model, we quantify it with mathematical equations for given processes based on physical and chemical laws and principles. We will defer the quantification of the conceptual models to the next section, and limit ourselves to qualitative description in this section.

2.1 Porous Medium

A porous medium is a macroscopic idealization to represent geological formations. In groundwater hydrology, the concept of representative element volume (REV) is sometimes used to define the macroscopic scale (Bear, 1988). We are mainly interested in the macroscopic transport of mass and energy through formations, and less interested in the detailed kinematics and dynamics in the pore- and particle-size scales. If the scale is less than the REV, macroscopic state variables (saturation, potential, temperature, concentration, fluxes, etc.) and properties (density, porosity, permeability, thermal conductivity, dispersivity, etc.) are ill-defined, and values fluctuate depending on microscopic structures. For example, density is defined and measured by the average of mass over volume. Certainly in the extreme limit with the volume in the subatomic scale, density value will fluctuate between a large value if the volume contains a nucleus and zero value if the volume contains vacuum. The amplitude of the fluctuation decreases as the volume increases. In the REV concept, we assume that variables and parameters will stablize to well-defined values which represent macroscopic averages integrated over microscopic structures.

For some of the variables and properties, such as temperature and density, REVs are well-defined and values are easily measurable and essentially scale-independent. However, some of the transport properties, such as permeability and dispersivity, depend on the scales of observation. For these properties, the transition from microscopic structure-induced fluctuation to macroscopic heterogeneity-induced scale dependence is not clearly defined. The values of

variables and properties are determined by measuring devices. When we obtain large variations in samples from the "same" formation in the laboratory, and values in the laboratory are orders of magnitude different from values determined in the field, it is very difficult to choose a representative value for permeability to model that formation. This is still a significant open issue in groundwater hydrology when modeling large-scale systems.

In the studies for tuff, we face the very same difficulty in using porous medium models to represent the tuff matrix. Permeability values of subcores from the same core can differ by two orders of magnitude, and values of cores from the same heterogeneous nonwelded stratigraphic unit can differ by six orders of magnitude. It remains to be determined if the large spatial variations in permeability will drastically influence the results based on porous medium models. In field-scale simulation, local variations in properties may be averaged out in determining the total flow through the system. Because of their simplicity, porous medium models should be useful in estimating average fluxes in large-scale studies. If fracture flows are not significant in partially saturated tuff and porous matrix controls the flow field, porous medium models can be used to determine the pressure distribution. A note of caution is pertinent here. The very variations that are smoothed out in the equivalent porous media averages, namely the fluxes, dictate the nature of dispersive chemical transport. Two media with identical average fluxes may give rise to widely different patterns of dispersive spreading.

When simple models are used to infer microscopic information from macroscopic results, we may run into difficulty. The travel time of fluid molecules through the pores requires the division of flux by the cross-sectional areas of the pores. We then need microscopic information about how the fluid flows through the pores. In a porous medium model, we define an effective porosity to represent the fraction of the pores through which the fluid moves and the remaining porosity for stagnant fluid. While total porosity is a well-defined macroscopic property, effective porosity cannot be easily determined. The effective porosity, together with the permeability, are the two important parameters in determining GWTT CDF, but are also two difficult parameters to quantify in porous medium models.

Porous medium models are used for both saturated and partially saturated flow. Under partially saturated conditions, the permeability is saturation-dependent. Even if the porous medium is homogeneous with a spatially uniform saturated permeability, the solution of a partially saturated flow field becomes a nonlinear problem. In calculating travel time, the flux is divided by the saturation in addition to the effective porosity. Except for this additional saturation division factor, the effective porosity remains as a saturation-independent parameter in most studies. The validity of this assumption needs to be assessed. An alternate way to find GWTT is to divide the saturated pore volume of a flow tube by the steady-state flux through the tube.

We treat multilayer systems and regional models with domains of different porous medium properties as generalizations of simple porous medium models. We can also have heterogeneous and anisotropic properties. So long as the medium is only characterized by "macroscopic" parameters and not by "microscopic" structure details, we classify the model as a porous medium model. Some of the models to be discussed below can be regarded as special cases or approximations of generalized porous medium models.

2.2 Capillary Tube

Although microscopic processes are not of direct interest, idealistic microscopic models are frequently used to represent macroscopic media or to deduce functional relationships among parameters and variables of such media. The capillary tube model is widely used in studies of partially saturated flow to derive the relationships between saturation and pressure head, and between permeability and saturation (Purcell, 1949; Burdine et al., 1950; Fatt and Dykstra, 1951). In conjunction with the capillary theory, the saturation-pressure relationship is used to infer the pore size distribution -- a microscopic structural characteristic.

The simplest capillary tube idealization is to represent the medium with a bundle of disconnected capillary tubes arranged parallel to a given flow direction. In this simple representation, the total flow is partitioned into components through individual tubes. Each tube determines independently the flow rate according to its hydraulic radius. The solution of the total flow rate through the bundle of tubes is mathematically similar to the solution of electric current through resistors in parallel: the total equivalent conductance (reciprocal of resistance) is the sum of individual conductances.

For more complex networks, we can have resistors in series and in parallel. The model that uses a bundle of parallel capillary tubes can be generalized by allowing the radius to vary along the tubes. The section with the smallest radius is the bottleneck that controls the flow through the tube. The sum of resistances along the tube is the equivalent resistance for that tube. Tubes with varying radii are also used in explaining hysteretic effects. Another generalization is to allow different sections of the tube to deviate from the average flow direction. This generalization effectively increases the total length of the tubes to account for the tortuous nature of flow path through the medium. Tortuosity factor is the ratio of the flow path length to the straight length from flow inlet to flow outlet. In addition to quasi one-dimensional models, multidimensional resistor networks can be used to represent porous media, either numerically in simulations or physically in laboratory analog models.

Simple microscopic models are very valuable to gain better fundamental understanding of flow through a medium. With simple geometry, solutions of fluid mechanical equations can be obtained. When more complex geometry of the flow field is taken into account, solutions become approximations and phenomenological factors, such as the tortuosity factor, are introduced. Striking a balance between maintaining simplicity of idealistic solutions and explaining complexity of realistic phenomena is the challenge in constructing conceptual models. The simple capillary model, together with its generalizations, will be discussed in detail in Section 5 for the partially saturated characteristic curves.

The adequacy and usefulness of capillary tube models for natural media with wide pore-size distributions and low permeability remains an active topic in the literature. For tuff matrix, like many consolidated media and some hard rock matrix, we have high porosity, large specific surface area, and low permeability. The pore-size distribution, based on interpretation of capillary tube model for the saturation-pressure relationship, accounts for only part of the pores which can be desaturated by suction pressure. Different fluids may be sensitive to different sizes of pores. The microscopic pore-size distribution information deduced using different fluids may be mutually inconsistent. Direct observations with the electron microscope may yield pore-size

distributions different from the distributions from saturation-pressure measurements. This is, however, a common difficulty in relating microscopic structure with macroscopic phenomena, and is not unique in tuff studies.

2.3 Fracture Network

For hard rock formations, fractures are the main conduits for liquid flow under saturated conditions. Because fracture orientations, spacings, and trace lengths can be measured in outcrops, tunnel walls, and, to a limited extent, in boreholes, geometric distribution parameters for the fracture network can be assembled. In statistical network models, measured or empirical distributions of fracture geometry are used to generate realizations of fracture network patterns (Long et al., 1982; Schwartz et al., 1983). The debate in the literature is whether it is meaningful to use the concept of REV in describing the flow and transport through the fracture network, and whether we can still use a macroscopic permeability tensor to model the fracture system.

In two-dimensional network simulations, fractures are represented by line segments. In three-dimensional network simulations, fractures are represented by disks, polygons, or other idealistic geometric shapes. Centers of fractures, lengths or areal extent, and orientations of fractures are randomly generated according to distributions for each geometric parameter. If fracture density is low and fractures are not connected to form a continuous network, fluid can not percolate through the network. Some of the network analyses focus on the system behavior near the percolation threshold associated with the onset of transition from insulator to conductor. For connected networks, simulations of flow also require the assignment of fracture aperture or fracture permeability to each segment of the network. The parallel plate model is frequently used to relate the fracture aperture to fracture permeability.

Among the geometric parameters in fracture network analyses, the aperture and permeability distribution is difficult to quantify. Fracture permeability depends on stress loading and loading history. Although the parallel-plate idealization is a good approximation for regions of large aperture and high flow rate (Witherspoon et al., 1980), the approximation begins to break down at high normal stress when the fracture walls are in contact (Engelder and Scholz, 1981; Pyrak-Nolte et al., 1987). In addition to normal stress dependence, shear displacement can change the fracture permeability (Makurat, 1985). Determination of fracture aperture based on flow experiments is also sensitive to sample size (Witherspoon et al., 1979). Permeability values from the field tests can be orders of magnitude larger than the values measured in the laboratory for the same rock type. In field experiments, the equivalent fracture aperture derived from flow experiments can be orders of magnitude smaller than that derived from tracer experiments (Abelin et al., 1985). Field observations also indicate that the flow is channelled through part of the fractures (Neretnieks, 1985). Aperture variations within the single fracture plane, in addition to distributions of apertures among different fractures in the network, need to be quantified to describe the nonuniform channel flow field (Tsang and Tsang, 1987).

Statistical fracture network models are mainly used in studies of saturated systems where fractures dominate the flow and transport. Idealistic network models with parallel fracture sets have been used in partially saturated studies (Evans and Huang, 1982). For welded tuff units

that are densely fractured with fractures well connected, the fracture network probably controls flow under saturated conditions. Under partially saturated conditions, the fracture network will be easily drained if the fractures have large apertures and good connectivity. Neglecting the porous matrix flows in network analyses limits the usefulness of fracture network models in studies of partially saturated flow. However, the fracture network is the main conduit for vapor flow which is also very important to the understanding of ambient and postemplacement conditions.

2.4 Fractured Porous Medium

Although the saturated permeability of rock matrix is much smaller than that of fractures, the matrix may control the flow if fractures are drained. The importance of porous matrix is recognized even in saturated flow studies. The porous matrix with large porosity contains the bulk of fluid and supplies or absorbs the mass to be transported by the fractures. The double porosity models (Barenblatt et al., 1960; Warren and Root, 1963; Duguid and Lee, 1977) and multiple interacting continuum (MINC) model (Pruess and Narasimhan, 1985) take into account the interaction between the porous matrix and the fracture network. The permeability of the fracture network determines the transport and the capacitance of the porous matrix controls the fluid storage. The flow field is described by two sets of thermodynamic variables, one set representing the fractures, one set representing the matrix. The coupling between fracture and matrix variables is determined by interface areas, block volumes, and material properties of the medium. The double porosity and MINC models are macroscopic models with fracture and matrix variables representing macroscopically averaged values. The coupling term depends in principle on the microscopic structure details of the fracture-matrix interfaces. The coupling coefficient is usually treated as an empirical parameter in applying these models in petroleum and groundwater simulations.

Under partially saturated conditions, the porous matrix not only provides the storage capacity but also may become the main flow domain. During desaturation, the effective permeability of fractures to liquid flow may decline as portions of fractures with large apertures no longer sustain the suction pressure which overcomes the capillary force holding the liquid to fracture walls. If the effective permeability of the drained fractures becomes smaller than that of the matrix, the flow along fractures will be less than the flow through the matrix. In densely fractured media, the porous matrix will be surrounded by fractures. Therefore, the matrix flow will tend to flow across fractures at asperity contacts from one matrix block to another. The flow lines may be expected to circumvent drained portions of the fractures. Figure 2-1 schematically illustrates the distribution of liquid water held in fine pores of the matrix and near fracture contacts. The flow lines bypass the drained portions of the fractures, going from one matrix block to another normal to the fracture planes. Figure 2-2 schematically shows the changes of liquid-phase configurations from continuous at high saturation (low suction) to discontinuous at low saturation (high suction) with liquid forming rings around contact areas (Wang and Narasimhan, 1985).

The change in the role played by the fractures, as active main conduits for flow in saturated conditions and becoming passive dry pores in unsaturated conditions, has not yet been substantiated in the tuff site. There are, however, a number of recent studies of the unsaturated

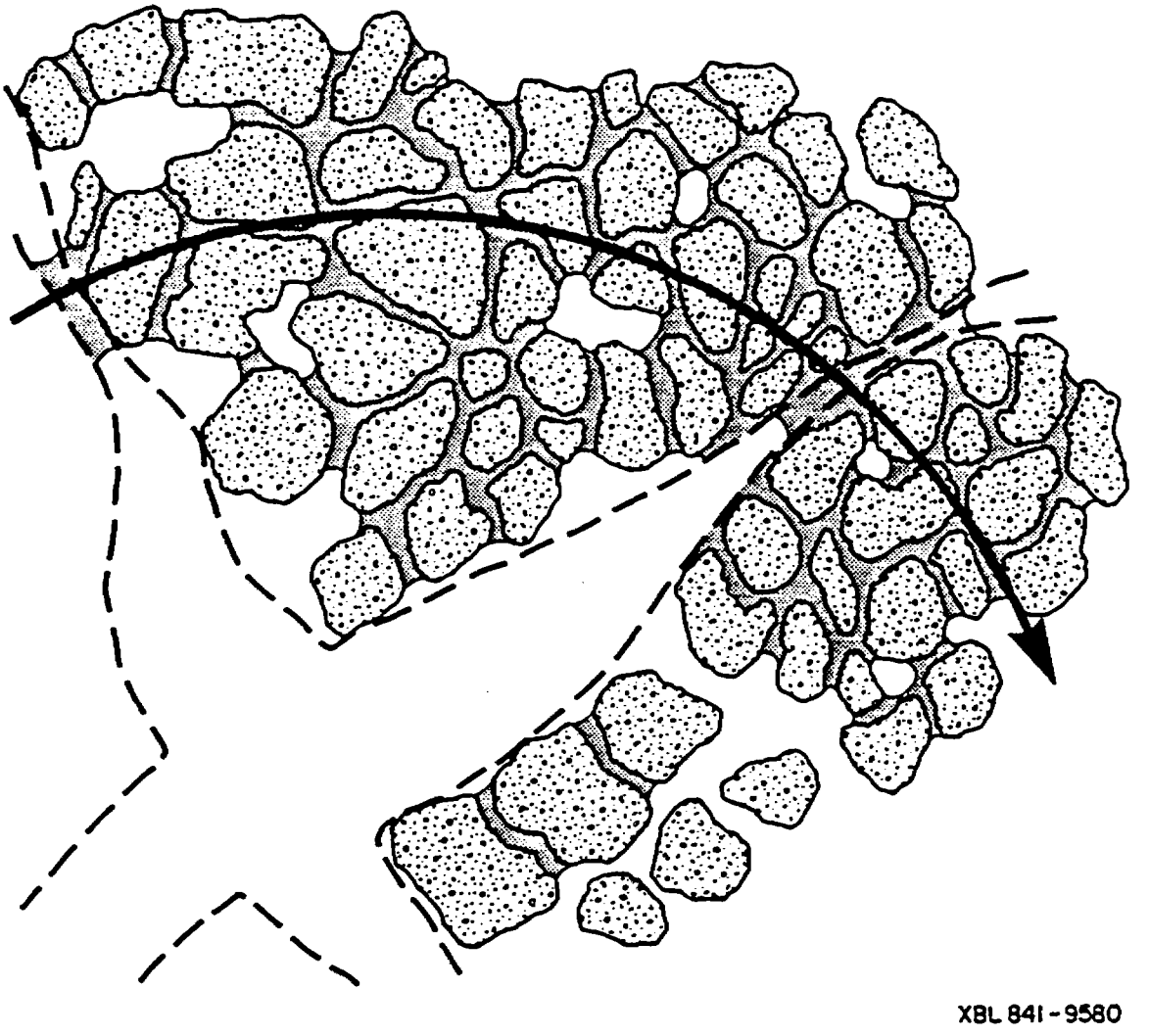

Figure 2-1. Conceptual Model of a Partially Saturated, Fractured, Porous Medium Schematically Showing Flow Lines Moving Around the Dry Portions of Fractures (Wang and Narasimhan, 1985).

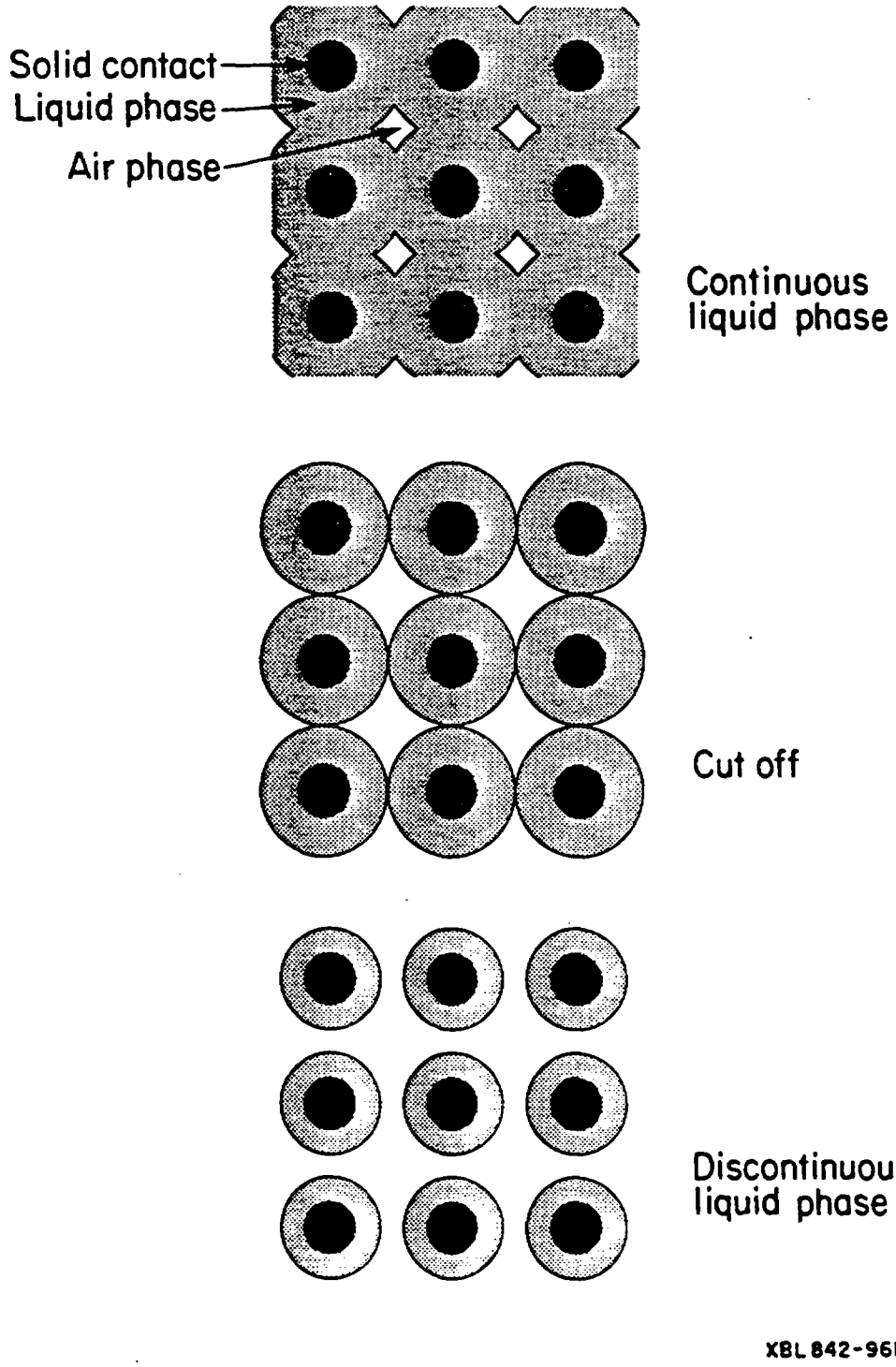

Figure 2-2. Desaturation of Fracture Surface Schematically Showing Changes in the Fracture Plane of Liquid-Phase (Shaded Areas) Configuration from Continuous Phase at High Saturation (Top) to Discontinuous Phase at Low Saturation (Bottom) with Liquid Forming Rings Around Contact Areas (Blackened Areas) (Wang and Narasimhan, 1985).

flow behavior of heterogeneous soils containing large root channels and worm holes. Although these macropores in shallow soil are very different from the fractures in deep tuff rock, the contrast between macropores and soil matrix is similar to the contrast between fractures and tuff matrix. The results of macropore models indicate that responses of heterogeneous soils to infiltration of rainfall depend on the magnitude of rainfall. If the rainfall arriving at a soil surface is low, all the water at the surface is absorbed by the micropores in the soil matrix. Vertical flow of water into large cracks or tubular channels occurs when rainfall exceeds the infiltration rate into the soil matrix (Beven and Germann, 1982). When tracers (dyes and anions) were used to study soil core samples containing macropores under both unsaturated and saturated flow conditions, the tracers distributed over small pores in the soil matrix under unsaturated conditions and stayed around macropores under saturated flow conditions (Scotter and Kanchanasut, 1981). Similar studies in fractured tuff should be valuable to validate the conceptual models of fractured, porous media.

3.0 MATHEMATICAL EQUATIONS

To quantify conceptual models and driving mechanisms, differential, integral, and algebraic equations are used to describe the processes and governing laws. Although some of the mathematical equations can be complicated with many symbols, indices, and variables from couplings among processes and from complexities of medium geometry, the basic laws governing the state variables are simple for the processes of interest for modeling the partially saturated flow field. We focus on the basic equation structures and point out changes needed to describe additional effects not accounted for by the simple equations. We try not to present too many of the complex equations needed to completely quantify a given mathematical model, but which are not necessary for the general review we intended for this section.

For the evaluation of GWTT CDF, liquid flow is the main process in determining flow velocities and travel times along flow paths. Under isothermal conditions with constant fluid density and stationary gaseous phase in nondeformable medium, the groundwater flow field can be determined without solving gas transport, heat transfer, solute migration, and rock deformation processes. We start with equations related to liquid and then discuss the coupling effects of other processes on groundwater flow.

For each process, we discuss the balance equations, flux laws, and constitutive relations. Some problem-related and medium-related considerations, such as initial and boundary conditions, fracture-matrix interactions, domain dimensionality, and zonations, will be discussed if relevant to the tuff site modeling studies. In this report, we discuss the equations but do not attempt to provide detailed review of the conventional numerical approaches used to solve the equations. However, we will introduce a new numerical approach on calculating GWTT CDF in the next section. Summaries of well-established finite difference, finite element, and integrated finite difference methods used by a number of single- and two-phase models for thermohydrological flow in fractured rock masses can be found in a review by Wang et al. (1983).

3.1 Liquid Flow

The liquid flow is governed by the mass balance law. In integral form, for an arbitrary flow domain of volume V bounded by surfaces A, the mass balance equation is

$$\frac{\partial}{\partial t}\int_V M\,dV = -\int_A \vec{q}\cdot\vec{n}\,dA + \int_V \dot{m}\,dV. \tag{3.1}$$

The rate of change of mass M within V is equal to the net mass flux $\vec{q}$ flowing into the bounding surfaces A and the source or sink $\dot{m}$ within V. In the limit of small volume, the surface integral can be converted to a volume integral with the Gauss divergence theorem in elementary calculus, and the integral equation for any given V is equivalent to the familiar differential form of mass continuity equation:

$$\frac{\partial}{\partial t} M = -\nabla \cdot \vec{q} + \dot{m}. \tag{3.2}$$

For numerical solutions with grid blocks of finite sizes, we can start with the integral form and bypass the differential limit. This is the viewpoint adopted by the integrated finite difference method and represents one practical way to handle the basic mass conservation law (Narasimhan and Witherspoon, 1976).

The mass accumulation term for the partially saturated state is

$$M = \phi S \rho \tag{3.3}$$

where ϕ is porosity, S is liquid saturation, and ρ is liquid density. All three quantities can be functions of pressure and other state variables. If we consider pressure changes only and ignore the dependences on other variables for the moment, the rate of change of mass accumulation can be expressed as three terms associated with differentiation of these three quantities. In a partially saturated state, the rate of change of saturation is usually much larger than the rates of change of porosity and liquid density and we have $\partial M/\partial t \approx \phi \rho \partial S/\partial t$. In the transition from a partially saturated state into a fully saturated state with constant $S=1$, the changes of porosity and density cannot be ignored and the compressible changes of porosity and density yield the fluid storage capacity that controls the transient groundwater flow.

The mass flux term can be expressed by the generalized Darcy-Buckingham flux law as

$$\vec{q} = -\bar{\bar{k}} \cdot \frac{k_r(S)}{\mu} \rho(\nabla P - \rho \vec{g}) \tag{3.4}$$

where $\bar{\bar{k}}$ is absolute permeability tensor, $k_r(S)$ is liquid relative permeability, μ is liquid viscosity, P is pressure, and $\vec{g}$ is the gravitational acceleration. In soil and groundwater hydrology literature, $k\,k_r(S)$ is expressed as $k(S)$ for a saturation-dependent permeability, and the hydraulic conductivity $K(S) = k\,k_r(S)\,\rho g/\mu$ is frequently used instead of permeability.

There is no *a priori* reason to express the mass flux law in differential form. We can also express Darcy's law in integral form just as Equation 3.1 is an integral expression of Equation 3.2. The integral form of the equation of motion is (Narasimhan, 1985)

$$Q = \frac{\Delta\Phi}{\frac{\mu}{\rho}\int \frac{dx}{k(x)A(x)}} \tag{3.5}$$

where Q is the magnitude of total volumetric flow rate (volume per unit time, q in Equation 3.4 is mass per unit area per unit time) for a stream tube with inlet-outlet difference in potential $\Delta\Phi$. The integral form accounts for the variable cross-sectional area $A(x)$ and spatial dependence of permeability $k(x)$ along the curvilinear x-axis following a flow stream tube.

The substitution of the differential Darcy's law (Equation 3.4) into the differential mass continuity equation (3.2) yields the classical Richards' equation for partially saturated flow. As mentioned earlier, the integral form of the mass balance equation (3.1) has been used in the formulation of integrated finite difference method to solve the Richards' equation. In section 4, the potential usage of the integral form of Darcy's law (Equation 3.5) to solve flow geometry will be discussed.

The potential Φ in Equation 3.5 has the unit of velocity square or energy per unit mass.

$$\Phi = gz + \int \frac{dP}{\rho}. \tag{3.6}$$

In addition to the pressure and gravitational potentials, thermal, solute, electrochemical, and other potentials can be included in Equation 3.6. We will discuss other potentials in the following subsections. By multiplying the potentials in Equation 3.6 by the density of water ρ, potential is sometimes expressed in terms of energy per unit volume, or equivalently force per unit area or pressure. If one divides both sides of Equation 3.6 by g, then, $\Phi/g = z + h$ is fluid potential expressed as energy per unit weight of water, a practice that is common in soil physics and groundwater hydrology. Here $z + h$ is often called potentiometric head or hydraulic head with units of length. The pressure potential is applied to both the saturated and unsaturated zones. In the literature on unsaturated flow, it is customary to express pressure with reference to atmospheric pressure. Under this convention, the gauge pressure, or the pressure difference between fluid pressure and atmospheric pressure, in the unsaturated zone is negative. Absolute value of gauge pressure is referred to variously as moisture suction, matric suction, moisture tension, or suction pressure.

In terms of the pressure head $h = \frac{1}{g}\int \frac{dP}{\rho} \approx \frac{P}{\rho g}$ for slightly compressible fluid, the Richards' equation (Richards, 1931) is

$$C_h(h)\frac{\partial h}{\partial t} = \nabla \cdot [K(h)\ \nabla(h + z)] + \frac{\dot{m}}{\rho} \tag{3.7}$$

where $C_h(h) = \phi \partial S/\partial h$ is the soil moisture capacity or the slope of the soil water retention curve, $\theta(h)$; θ is the water content ϕS and is frequently used in soil literature instead of saturation S. The effective hydraulic conductivity $K(h)$, or $K(S)$, or $K(\theta)$ is another soil characteristic curve which is either measured experimentally or related theoretically to the water retention characteristic curve $\theta(h)$ or $S(h)$ when measurements are not available. The Richards' equation (3.7) states that the unsaturated hydraulic conductivity and the soil water retention curve are two essential functions for predicting liquid flow in unsaturated medium. These two characteristic curves will be discussed in detail in Section 5.

The mass balance equation (3.1 or 3.2) arises from basic mass conservation consideration, while the equation of motion (3.4) is approximate. The empirical Darcy-Buckingham equation

describes the flux driven by pressure gradient and gravitational forces with the permeability or conductivity coefficient accounting for the resistance of the medium to the flow of viscous fluid. It is a good approximation only for slow laminar flow. For saturated flow, the permeability or conductivity is defined in terms of the ratio of volumetric liquid flux to the potential or head gradient. The permeability is in principle determined by the geometric structure of connected pores in the medium. For unsaturated flow with part of the flow channels occupied by gaseous phase, the reduction of liquid flux is described in terms of saturation-dependent relative permeability.

The dependence of absolute permeability on pore geometry can be demonstrated by solving equations of fluid motion within idealistic flow channels. The movement of an incompressible viscous fluid in a homogeneous medium is governed by the Navier-Stokes equation

$$\rho \frac{D\vec{v}}{Dt} = -\nabla P + \mu \nabla^2 \vec{v} \tag{3.8}$$

which is derived from Newton's Second Law for fluid movement driven by pressure gradient and the countering viscous friction force. The derivation of the Navier-Stokes equation can be found in standard fluid mechanics textbooks (e.g., Landau and Lifshitz, 1959). The time differentiation on the material coordinate system moving with the fluid is expressed by $D/Dt = \partial/\partial t + \vec{v}\cdot\nabla$. For steady laminar flow with velocity so slow that terms proportional to v^2 can be ignored, the left-hand side of Equation 3.8 is zero. Let us consider in some detail the solution of steady flow between two fixed parallel planes to represent an idealistic flow channel. We choose the x-axis in the direction of $\vec{v}$ and z-axis normal to the parallel planes which are located at $z = \pm\frac{b}{2}$ with b the geometric separation or aperture of the flow channel. Neglecting the inertial term, the Navier-Stokes equation gives

$$\frac{\partial^2 v}{\partial z^2} = \frac{1}{\mu}\frac{\partial P}{\partial x}; \qquad \frac{\partial P}{\partial z} = 0. \tag{3.9}$$

Because P is independent of z, the solution of the first equation in Equation 3.9 is simply

$$v(z) = \frac{1}{2\mu} \nabla P\left(z^2 - \frac{b^2}{4}\right). \tag{3.10}$$

We have applied a no-slip boundary condition that $v = 0$ at the walls of flow channel $z = \pm\frac{b}{2}$. The solution Equation 3.10 indicates that the velocity profile between the parallel planes is parabolic. The average velocity over the aperture is

$$\bar{v} = \frac{1}{b}\int_{-\frac{b}{2}}^{\frac{b}{2}} v(z)dz = -\frac{b^2}{12}\frac{1}{\mu}\nabla P. \tag{3.11}$$

By comparing Equation 3.11 with Equation 3.4, with $q = \rho\bar{v}$ and $k_r = 1$ for saturated flow, we can equate

$$k_{pp} = \frac{b^2}{12} \tag{3.12}$$

for the permeability of a parallel plate channel, which is frequently used as an idealistic geometric model for a fracture. We may obtain total flow rate by multiplying $\bar{v}$ by the channel width or fracture aperture b and see that total flux is proportional to the aperture cube b^3. This is the Boussinesq's cubic law for fracture flow.

Another idealistic model is to use a cylindrical tube to represent a flow channel. We can express the Navier-Stokes equation in cylindrical coordinates instead of Cartesian coordinates in Equation 3.9 and show that the velocity profile across the tube is also parabolic and the average flow rate along the tube can be expressed in the form of Darcy's law with an equivalent permeability

$$k_{ct} = \frac{r^2}{8} \tag{3.13}$$

for a cylindrical tube of radius r. The total flow over the cross-sectional area πr^2 is proportional to r^4. This is the Poiseuille's law for tube flow. The cylindrical tube model is frequently used to idealize porous media as a bundle of capillary tubes. Carman (1937) generalized Equations 3.12 and 3.13 and used a mean hydraulic radius to characterize the size of the cross-sectional area for flow through an irregular cross section.

$$k = \frac{r_h^2}{f_h}. \tag{3.14}$$

The constant, f_h, is a shape factor which should be between the values of 2 and 3 for porous media. The hydraulic radius r_h is the ratio of cross-sectional area to length of perimeter, $r_h = b/2$ for the parallel plate channel and $r_h = r/2$ for the cylindrical tube.

For the studies of tuff formations in which high-permeability fractures coexist with low-permeability tuff matrix, the validity of the flux law (Equation 3.4) needs to be assessed. On the one hand, the fracture flow may under extreme conditions lead to high velocity and make a transition from laminar flow to turbulent flow in near-saturated conditions. We then need to

solve the full Navier-Stokes equation with v^2 terms to account for the nonlinear inertial effects for the motion of viscous fluid within the fractures. On the other hand, the Darcy-Buckingham law may not be valid at extremely low flow rates within the tuff matrix. A threshold potential gradient may exist below which no flow may occur in fine-textured medium. When the liquid phase is discontinuous, net liquid flow cannot be sustained. Darcy's law was originally derived for saturated flow and was extended by Buckingham to unsaturated flow with the introduction of relative permeability or saturation-dependent hydraulic conductivity. It is important to measure the relative permeability in tight tuff matrix to check the validity of Darcy's law in partially saturated tuff matrix. If part of liquid water is immobile in the tuff matrix, then the GWTT will be determined only by the mobile portion of the liquid water.

Determination of the liquid flow field in the tuff formations will be influenced by complex upper boundary conditions at the ground surface. The precipitation in the semiarid climate is erratic with sudden rain storms. Vigorous evaporation-transpiration processes will return major portions of precipitation and snow melts back to the atmosphere, and runoffs from the mountain top to the surrounding wash valleys will redistribute the surface water. It is generally assumed that these highly transient and heterogeneous processes will be damped out on a large time scale by the near-surface units and that the net infiltration into the deep vadose zone is constant below some depth. With these assumptions, the ambient condition in the tuff formations is treated to be steady state in response to the net infiltration on the upper boundary. The lower boundary is the constant head water table in one-dimensional models. In two-dimensional models for a region bounded on the sides by faults and/or open hillsides, the side boundaries are treated either as no-flow boundaries for closed faults or as seepage boundaries in communication with atmosphere for open faults or hillsides. The effects of faults and topographic variations on the flow field within the tuff units remain to be determined. The possibilities that the ambient condition is not steady state but is a slow transient state in response to ancient geologic or meteoric events need to be assessed.

One key issue in determining the GWTT CDF is to evaluate the possible contribution of fast fracture flows through the fractured tuff units. One can solve the fluid mechanics equations for a few discrete fractures; however, the amount of data required to describe fracture parameters and characteristics, as well as finite computational capacity, makes it impractical to model all the fractures in the formation. Incomplete data require geostatistical treatment to account for uncertainties and spatial variabilities. We are not interested in individual fracture flows but the cumulative effects summing the details. In petroleum engineering and groundwater hydrology, double porosity models (Barenblatt et al., 1960; Warren and Root, 1963; Duguid and Lee, 1977) and multiple interacting continuum models (Pruess and Narasimhan, 1985) have been used to treat the average behavior of fractured porous media. For each point in space, two sets of state variables are defined, one representing average over the fractures and one over the porous matrix. For fluid production and injection studies, one assumes that the global flow is through the fracture networks and that the blocks of porous matrix act as mass or energy sources or sinks communicating with the fracture network through the fracture-matrix interfaces. Quasi-steady or transient treatments have been used to model the fracture-matrix interactions. These models have not been extended to a partially saturated flow field where the global flow is through the matrix. In a partially saturated state, the bulk of flow may not be through the fracture network and instead may cross from one matrix block to another matrix block (Wang and Narasimhan, 1985). Another simpler model has been proposed to model the fractured porous medium,

assuming local pressure equilibrium between fractures and matrix and ignoring the fracture-matrix interaction driven by pressure differences (Pruess et al., 1985; Peters and Klavetter, 1988). The fracture effects are taken into account by composite characteristic curves with the sum of both fracture and matrix contributions. The composite model has been used in most modeling studies for the partially saturated flow field through the alternating tuff units. This composite model and the generalized double porosity and multiple interacting continuum models must be further developed and validated before their usefulness for tuff studies can be assessed.

3.2 Two-phase Flow

The classical Richards' equation for unsaturated liquid flow assumes that the temperature is constant and the gaseous phase is at a pressure of one atmosphere. At ambient temperature, the gaseous phase contains mainly air and the fraction of water vapor is small. As the temperature increases, water molecules gain momentum to escape the liquid phase and the vaporization becomes vigorous at the boiling point. At elevated temperature, the gaseous pressure will be increased above the atmospheric pressure and the water vapor will purge most of the air out of the two-phase region.

Just as in the liquid flow equation (3.1), two-phase flow equations can also be derived from mass balance considerations. The mass balance equation for the water or air components is:

$$\frac{\partial}{\partial t}\int_V M^\kappa dV = -\int_A \vec{q}^\kappa \cdot \vec{n}\, dA + \int_V \dot{m}^\kappa dV \tag{3.15}$$

with the superscript $\kappa = w$ for water or $\kappa = a$ for air. The mass accumulation terms are

$$M^\kappa = \phi \sum_{\beta=l,g} S_\beta \rho_\beta X_\beta^\kappa \tag{3.16}$$

where phi is porosity, S_β is saturation of phase β (= liquid l, gas g), ρ_β is density of phase β, and X_β^κ is the mass fraction of component κ present in phase β. Equation 3.16 is a simple generalization of the liquid water equation (3.3) to a two-phase, two-component system.

Equations 3.15 and 3.16 are written for each component κ. One can also express the mass balance equations for each phase instead of for each component. In the phase-based equation, water vaporization is explicitly treated as a source for the gaseous equation and as a sink for the liquid equation; water condensation is treated vice versa.

The mass fluxes in Equation 3.15 are sum over phases

$$\vec{q}^{\kappa} = \sum_{\beta=l,g} \vec{q}_{\beta}^{\kappa} \tag{3.17}$$

where the generalized Darcy's equation for the flux in each phase is:

$$\vec{q}_{\beta}^{\kappa} = -\bar{\bar{k}} \cdot \frac{k_{r\beta}}{\mu_{\beta}} \rho_{\beta} X_{\beta}^{\kappa} (\nabla P_{\beta} - \rho_{\beta} \vec{g}) \tag{3.18}$$

where $\bar{\bar{k}}$ is absolute permeability tensor, $k_{r\beta}$ is relative permeability of phase β, μ_{β} is viscosity of phase β, P_{β} is pressure in phase β. The difference between liquid pressure and gas pressure is the capillary pressure $P_c = P_l - P_g$. The gas pressure can be written as a sum of air and vapor partial pressures,

$$p_g = \sum_{\kappa=w,a} P_g^{\kappa}. \tag{3.19}$$

Ideal or real gas law can be used to relate partial pressure with density and temperature. Henry's solubility law can be used to relate the dissolved mass fraction of air in liquid with the partial air pressure.

Darcy's law accounts for the overall gaseous movement driven by total gas pressure gradient and gravity but does not account for two additional effects driven by partial pressure gradients: binary diffusion and Knudsen diffusion. Consider that a container has two compartments separated by a porous plug with one side containing only air and the other side containing only vapor. The air will diffuse toward the vapor compartment and vapor toward the air compartment even if initially both sides have the same gas pressure and the net flux is zero. The binary diffusion is driven by partial pressure gradients and the diffusion constant is determined by air-vapor molecular collisions.

For macroscopic continuum equations such as the Navier-Stokes equation or Darcy's equation, we are not concerned with the microscopic molecular motions, and the mean free path between molecule collisions is much smaller than the characteristic pore dimension. When the partial gas pressure is low and the gas-gas collisions become infrequent, or in media with extremely small pores, the mean free path of individual molecular trajectories may become comparable with the pore dimension. This gives rise to the Knudsen effect which may be of concern for tight tuff matrix with small pores (Hadley, 1982). The Knudsen effect becomes important when the momentum transfer from gas-pore wall collisions cannot be ignored. With momentum transfer, the fluid velocity cannot be set to zero (no-slip) at the fluid-solid boundaries for solving the Navier-Stokes equation. The main phenomenon associated with this Knudsen effect, also known as the Klinkenberg effect or slip flow effect, is the increase of gas permeability at successively lower pressures for a given medium (Klinkenberg, 1941; Reda, 1987).

For the transport of moisture in soils, the diffusive mechanism is of primary concern to account for the relative movement of vapor and air. The Richards' equation has been extended to weakly nonisothermal systems to model molecular diffusion in soils below 50°C (Philip and de Vries, 1957; Sophocleous, 1979; Milly, 1982). At much higher temperatures near and above the boiling point, overall gaseous movement becomes important. Geothermal models focus on the proper treatment of phase transitions, movement of two-phase mixtures, and production of steam (Coats, 1977; Garg et al., 1977; Faust and Mercer, 1979; Pruess and Schroeder, 1980). The air component in the two-phase region and the capillary pressure difference between liquid and vapor are ignored in some of the models for permeable porous formations. Models for two-phase flows driven by heat released from high-level nuclear wastes generally take into account the relative movement of air and vapor, as well as capillary pressure effects in small pores (Eaton et al., 1983; Travis et al., 1984; Pruess and Wang, 1984; Bixler, 1985; Pollock, 1986; Pruess, 1987).

For a repository in a partially saturated formation, two-phase processes can control the near-field system behaviors. The purge of air from the two-phase region around a waste container will affect the rate of oxidation and corrosion of the container (Pruess and Wang, 1984). From detailed simulations with both discrete fractures and porous tuff matrix taken into account, the gaseous movement is shown to be mainly through the fractures (Pruess et al., 1985,1986). After waste emplacement, boiling becomes vigorous as temperatures approach 100°C. Most of the vapor generated in the rock matrix flows toward the fractures and then radially outward, where it soon condenses on the cooler fracture walls. Two completely different system behaviors may occur, depending critically upon the mobility of liquid flow along the fracture walls. If the condensed liquid is immobile in the fractures, the liquid is sucked back into the matrix, where it migrates down the saturation gradient toward the boiling region near the waste container. Because of the low matrix permeability, the inflow of liquid to the heated region is less than the outflow of vapor in the fractures, so that the vicinity of the waste containers will dry up and temperature in the dry region can be much higher than 100°C. The other possibility is that the liquid has a finite mobility along the fracture walls. In that case, the backflow of condensate toward the heat source takes place along the fracture walls and the outflow of vapor is balanced by the backflow of condensate. With mobile liquid along fracture walls, the vicinity of the waste container will not dry up, and temperature will remain constrained to near 100°C. During some of the heater experiments in G-tunnel at NTS, long periods of constant saturation temperature at ambient pressure were observed (Zimmerman and Blanford, 1986). Therefore, measurement of relative permeability or mobility of liquid in the fracture walls is an important aspect to be studied in order to determine the system behaviors of the heated two-phase region.

Heat-driven vapor movement can also be significant on the repository scale (Travis et al., 1984; Pollock, 1986; Tsang and Pruess, 1987). The buoyancy mechanism is driven by fluid density differences associated with thermal expansions. With hot low-density fluid moving upward and surrounding cold fluid moving down, convective cells can form around heat sources. The buoyancy flow is a concern for repositories in saturated formations (Wang et al., 1988). For unsaturated formations, the buoyancy mechanism can induce fast gaseous movement through fracture networks. Convective gas circulation could accelerate the movement of gaseous radionuclides, such as volatile iodine 137, carbon 14 dioxide, and tritiated water vapor from repository to biosphere. Monitoring the fast gas movement can be very informative for remote sensing of the potential thermal impacts after waste emplacement.

Although two-phase effects are mainly of interest at elevated temperature, there is growing concern that the vapor movements cannot be ignored at ambient temperatures. Montazer and Wilson (1984) postulated that air convection cells exist in the thick welded tuff units driven by geothermal gradient. Weeks (1987) observed warm air with high flow rates blowing out of boreholes in a crest bounded by a steep hillside above a canyon floor during winter months at Yucca Mountain. In the summer, frequent reversals in flow direction were observed with wells taking in hot dry air and exhausting cool humid air following barometric pressure fluctuations. It is important to determine if topographic, barometric, geothermal, or other mechanisms can induce large vapor movements deep into the partially saturated zone. If the ambient gaseous movement is not a mere near-surface phenomenon, we must take into account the coupling of gaseous movement with liquid infiltration and the drying effects associated with vapor transport to properly model the ambient saturation distributions and fluid movements through the unsaturated units.

3.3 Heat Transfer

In the previous subsection on two-phase flows, we have already discussed the influence of temperature on fluid movement. The temperature distribution and heat transfer are determined by conduction, convection, and thermal radiation mechanisms. Heat conduction, primarily through the solid matrix, is driven by temperature gradient. Convection is associated with the heat carried by the moving fluid. Both conduction and convection are important in determining the temperature field in the formations. Thermal radiation is also driven by temperature differences across vacuum space without solid and fluid carriers. It is an important mechanism in the heat transfer from the waste container across the air gap to the rock medium if the gap is not filled with crushed rocks or engineered backfills. Thermal radiation is also important in determining the effective heat transfer coefficient from tunnel walls to the ventilating air currents for regulating the repository working environment. However, we will discuss mainly the conduction and convection mechanisms within the fractured, porous medium and will not cover the thermal radiation in this subsection.

The heat transfer is governed by the energy conservation law. In notations similar to the mass balance equations (3.1) and (3.15), we have

$$\frac{\partial}{\partial t}\int_V M^h dV = \int_A \vec{q}^h \cdot \vec{n}\, dA + \int_V \dot{m}^h dV. \tag{3.20}$$

The heat accumulation term contains solid rock and fluid contributions

$$M^h = (1-\phi)\rho_R c_R T + \phi \sum_{\beta=l,g} S_\beta \rho_\beta U_\beta \tag{3.21}$$

where ρ_R is rock grain density, c_R is specific heat of the solid rock, T is temperature, and U_β is specific internal energy of phase β.

The heat flux contains conductive and convective components (Pruess, 1987)

$$\vec{q}^{\,h} = K_h \nabla T + \sum_{\beta=l,g} \sum_{\kappa=w,a} H_\beta^\kappa \vec{q}_\beta^{\,\kappa} \tag{3.22}$$

where K_h is the heat conductivity of the rock-fluid mixture, and H_β^κ is the specific enthalpy of fluid component κ in phase β. Enthalpy and internal energy are related by $H = U + P/\rho$. The pressure work and viscous dissipation contributions to the energy balance are neglected in the above heat transfer equations.

For a saturated medium, temperature T and pressure P are frequently the pair of state variables used in modeling hydrothermal processes. All other parameters in the governing equations are expressed in terms of functions of these primary variables by constitutive relationships. Under two-phase conditions, the vapor pressure and temperature are not independent and are related by the saturated vapor pressure relationship for water. Therefore the pair of pressure and temperature is replaced by pressure and saturation as the pair of independent variables in phase transitions. Some models known in the literature use other pairs, such as (pressure and enthalpy) or (density and internal energy) which remain independent of each other throughout the single- and two-phase regions. Differences in two-phase models are mainly in the choice and handling of the primary variables and in the algorithms used to calculate the constitutive relationships of other thermophysical parameters.

Heat capacity and thermal conductivity are two important parameters in the heat transfer equation. In comparison with thermal conductivity, the heat capacity is less sensitive to rock types and temperature changes for different rock media being considered for nuclear waste repositories (Wang et al., 1988). The thermal conductivity depends on the mineral compositions of the solid matrix, on the temperature, and on the fluid saturations. A nonwelded tuff with higher porosity and water content generally has a lower thermal conductivity than a welded tuff with less porosity and more dense and compacted structure (Moss and Haseman, 1984). For unconsolidated oil sands, the dependence of thermal conductivity on liquid saturation can be fitted with linear or square root saturation relationships (Somerton et al., 1973). A generalized geometric mean model for the rock-water-air mixture,

$$K_h = K_{h,rock}^{(1-\phi)} K_{h,water}^{\phi S} K_{h,air}^{\phi(1-S)} = K_{h,wet} \left[\frac{K_{h,air}}{K_{h,water}} \right]^{\phi(1-S)} \tag{3.23}$$

(Wang and Tsang, 1983; Touloukian and Ho, 1981), is an example of a model for effective thermal conductivity which can be used to represent the thermal conductivity/saturation relationship.

For a closed-flow system with no fluid mass crossing the boundaries, internal gas-liquid counter flows can be set up if the opposite boundaries are maintained at different temperatures. The gas generated by vaporization near the hot end flows toward the cold end by gas pressure gradient. The condensate near the cold end increases the liquid saturation and sets up a capillary pressure

gradient to push liquid toward the hot end. This heat pipe effect with cyclic evaporation-condensation and gas-liquid counter current can effectively increase the heat transfer efficiency drastically. This heat pipe mechanism maintains the two-phase region at nearly constant temperature and overwhelms the conduction mechanism through the rock matrix.

For open systems with liquid infiltration on the ground surface and vapor convection or upward flow in unsaturated zone, the couplings among liquid flow, vapor flow, and heat flow under gravity, capillary forces, and geothermal gradient can be complicated. The simple conceptual model with liquid infiltration moving downward from the balance between gravity and capillary forces in fractured tuff units remains to be checked against more complex models taking into account nonisothermal, multiphase, multicomponent, and multidimensional effects. Uncertainties in the magnitudes of these coupling effects will also contribute to the GWTT CDF.

3.4 Solute Transport

The dependence of fluid density on temperature can induce buoyancy flows and convection cells in hydrothermal systems. The dependence of fluid density on solute concentration can also induce fluid movements. The coupling between fluid flow and solute transport can be very important in unsaturated soils (Nielsen et al., 1986). We will briefly discuss the governing equations of solute transport and various solute-related coupled processes. Although the transport of traced radionuclides is the most important issue in postclosure performance assessment, we will not discuss the geochemical transport issues associated with adsorption, retardation, complexation, exchange, parent-daughter decay chains, kinetics, and chemical reactions of radionuclides with rock media and with other chemical species. We will focus mainly on solute transport in liquid flow. A brief discussion of vapor diffusion in binary gas mixtures has been given earlier (Section 3.2).

The solute transport is governed by the mass balance law for a given solute and is equivalent to the liquid flow equation (3.1).

$$\frac{\partial}{\partial t}\int_V M^c dV = -\int_A \vec{q}^c \cdot \vec{n}\, dA + \int_V \dot{m}^c dV. \tag{3.24}$$

The solute mass accumulation term in partially saturated liquid state is

$$M^c = \phi S \rho C \tag{3.25}$$

where C is concentration and ρ is liquid density of water-solute mixture.

The solute flux contains diffusive and convective components

$$\vec{q}^{c} = -\phi S \rho D_c \nabla C + \vec{q} C \tag{3.26}$$

where D_c is the dispersion coefficient.

Considerable concern in solute transport modeling exists on the proper treatment of the parameter D_c. It is an empirical parameter which includes all of the solute spreading mechanisms. When a solute is injected into a flow field, it is carried by the moving fluid with flux $\vec{q}$, as described by the convective term in Equation 3.26. The solute also spreads to smear the front movement. The parameter D_c is generally assumed to have a velocity-independent component and a velocity-dependent component

$$D_c = D_{c0} + \lambda_D |v_p|^{\xi} \tag{3.27}$$

where v_p is pore velocity $\frac{v}{\phi}$ or $\frac{q}{\rho\phi}$. For a homogeneous medium with the exponent ξ equal to unity, λ_D is referred to as the dispersivity. The velocity-independent component D_{c0} is the diffusion coefficient.

The dispersivity λ_D, with a dimension of length, is sensitive to the scale of the tracer experiments, with values in the millimeter range for laboratory samples and in the meter range from field measurements. The heterogeneity of the medium is believed to influence the dispersion processes and control the magnitude of the dispersivity coefficient. A natural medium is always heterogeneous in different scales with distributions of varying pore sizes and flow channels. With larger scale and wider distribution of different channels to carry the solute tracer, the degree of mixing and spreading is enhanced. Because dispersion is also governed by the time needed for mixing, the dispersivity parameter also has a time-dependence aspect.

For fractured, porous media, the solute in the fractures can enter the pores in the matrix. This "matrix diffusion" mechanism can significantly retard the transport of solute in saturated fracture flow. Under partially saturated conditions with flow predominantly in the matrix and small net convective flux, the diffusion in the matrix could be the most important transport mechanism. Even for nonabsorbing tracers, matrix diffusion can change the transport velocity and travel times.

Rock surfaces generally have a negative charge and affect the distributions of ions in the solution. Positively charged cations will be attracted by the surface charges and negatively charged anions will be repelled by the surface charges to form an electric double layer. The repulsion of anions from the rock surfaces may limit the diffusion of anions into the matrix. This electrochemical mechanism may also affect the relative transport of ions. Because the velocity in the middle of the fractures or channels is higher than the region near the rock surfaces, the anions may have higher transport velocity than the cations.

For water moving slowly in the matrix, the concentrations may be saturated or supersaturated for various solid components of the rock matrix. When the solution is transported to the fractures, the dissolved solid may be re-precipitated on the fracture surfaces. Materials that fill in the fractures may contain useful information concerning the movement of water. If the fracture surfaces are coated with secondary minerals, fluid transport may be responsible for the alterations. If the fracture surfaces are clean, one may infer that the fractures are dry. An understanding of the fracture mineralogy and rock alteration can provide information on flow path distributions in fractured, porous media.

3.5 Rock Deformation

The solid rock forms the skeleton of the porous matrix and bounding surfaces for the fracture flow channels. The conduction through solid rock is very important for heat transfer, and the compressibility of pores and fractures is very important for fluid flow. With enormous surface areas in formations with small pores, surface diffusion of solute chemicals can also be very important. In this section, we will summarize the effect of rock deformation on fluid flow and will not discuss thermal conduction/expansion effects and solid surface diffusion processes.

Because solids can sustain shear, we need to use tensor to describe the stress field for the force components normal and tangential to the solid surfaces. At a solid-fluid interface, the fluid pressure can counteract the normal component of the compressive stress. With fluid pressure subtracted from the normal stress component, the effective stress can be related to rock strain or deformation in the form of Hook's law (Biot, 1941):

$$\bar{\bar{\sigma}} - P\bar{\bar{I}} = \bar{\bar{\bar{C}}} : \bar{\bar{\varepsilon}}. \tag{3.28}$$

For isotropic elastic rock media, the components of the tensor $\bar{\bar{\bar{C}}}$ can be expressed in terms of two elastic constants, for example, Young's modulus and Poisson's ratio. For anisotropic, inelastic deformable fractures, normal and shear stiffness (change of stress per unit change of displacement) are frequently used to characterize the fracture behavior.

For porous media under small strains, the volumetric strain, $\varepsilon = \varepsilon_{xx} + \varepsilon_{yy} + \varepsilon_{zz}$ can be related to the porosity of the medium. The change of porosity with respect to pressure change determines the compressibility of the medium. The pore compressibility, together with fluid compressibility, determine the storage capacity of a saturated medium. For most porous media, the storage capacity can be reasonably treated as a constant that determines the transient behavior of fluid flow. For a fracture, the rock displacement changes the aperture. For an open fracture under low stress loading, the fracture aperture can be easily changed with high compliance. As the stress loading increases, the fracture becomes more and more difficult to close and becomes stiff. The nonlinear change of fracture stiffness is controlled by the fracture surface roughness and contact areas.

For a partially saturated medium, the effective stress in the right-hand side of Equation 3.28 needs to be modified. Bishop (1959) proposed to replace the fluid pressure P with a weighted

sum of liquid water pressure P_l and gaseous air pressure P_g so that the effective normal stress σ' is

$$\sigma' = \sigma - [\chi P_l + (1 - \chi)P_g] = \sigma - P_g + \chi(P_g - P_l). \tag{3.29}$$

The weighting parameter χ varies from zero to one. In general, the deformation and saturation in partially saturated media depend on both the $\sigma - P_g$ and the capillary pressure $P_c = P_l - P_g$ (Narasimhan, 1982).

If the stress field is unknown, we need to solve for the stress distribution. For quasi-static states, the stress field is determined by Newton's first law of static equilibrium which for an infinitesimal volume element is

$$\nabla \cdot \bar{\bar{\sigma}} + \rho \bar{g} = 0 \tag{3.30}$$

where ρ is bulk mass density and only gravity body force is assumed. The stress field will be determined by boundary conditions and elastic or inelastic mechanical properties. Structure stability is the main concern for rock mechanics. If the stress and strain exceed failure criteria, fracturing and instability occur and the fluid flow field will be changed.

In addition to static equilibrium studies, the dynamic responses of the rock medium to stress loading and failure are also of interest. In general, the vibration responses of the medium to the propagation of seismic (compressive and shear) waves will depend on the rock deformation properties and fluid saturation states. The fluid in the fractures and in the pores can affect the transmission and damping of seismic waves. The possibilities of monitoring seismic waves or of using induced seismicity to detect fractured zones and fluid saturation distributions can be useful to study partially saturated, fractured formations.

4.0 NEW NUMERICAL APPROACHES

Evaluation of GWTT CDF, required to justify licensing, is currently the focus of performance assessment of Yucca Mountain. To account for the complex physical processes and heterogeneous formation properties that control the hydrology of Yucca Mountain, computer codes will be used to evaluate the GWTT CDF. In this section, we examine the numerical approaches that are currently being used in regard to their ability to evaluate the GWTT CDF. We also discuss potential alternative approaches to be used if the conventional approaches are inadequate in regard to verification and efficiency for the purpose of generating credible GWTT CDF.

In the context of licensing, an important requirement is that the solutions generated by the models be *verifiable*. By the phrase, verification, we here signify the internal mathematical consistency of the solution with the equations that govern the problem. A verifiable mathematical model will be an invaluable asset during the licensing phase of the repository. Another important requirement is that the computer codes can be run efficiently. The Monte Carlo method may be a very useful approach, if not a preferred approach, to develop the GWTT CDF. The Monte Carlo approach essentially consists of using statistically generated input data in deterministic models and generating many outputs as a basis to quantify uncertainty. Because the Monte Carlo technique involves running the deterministic models many times, it is highly desirable that the computer codes used to carry out the deterministic calculations be efficient in storage requirement and in computational speed. Thus, we need to choose tools for computation that are both verifiable and efficient.

4.1 Modeling Problem

At Yucca Mountain, we are concerned with a partially saturated domain extending vertically from the rim of the disturbed zone to the water table below (Figure 4-1). For practical purposes, the edge of the disturbed zone as well as the water table may be assumed to be horizontal. Laterally, the flow domain can be conveniently assumed to be bounded by two flow lines, as shown in Figure 4-1. Within the domain the material properties are characterized by heterogeneity. The heterogeneity exists on two scales:

(1) The large, stratigraphic heterogeneity, dictated by the disposition of the Topopah Spring and Calico Hills units; and

(2) The smaller heterogeneity dictated by the variations in material property within each unit.

The reasonably well-defined large-scale heterogeneity exists on a scale of several tens of meters in vertical thickness. The smaller heterogeneity exists on the scale of a few meters or less. More details of these heterogeneities should be forthcoming in the future as a result of the proposed drilling program contemplated under the YMP.

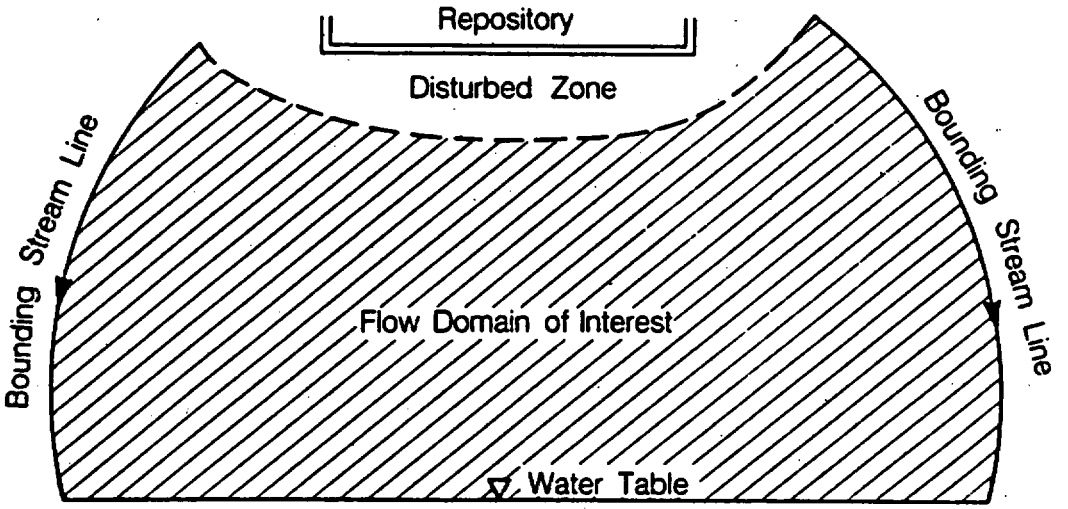

Figure 4-1. Flow Domain of Interest for Analysis of the Unsaturated Zone Hydrology.

As part of the preemplacement GWTT CDF problem, we consider steady laminar flow of water within the domain of interest, subject to prescribed potentials or fluxes at the upper boundary and prescribed potential at the water table below. The task is to find the GWTT CDF for this domain.

Perhaps the most direct method for finding the GWTT CDF is to follow the following procedure:

Step 1: Using an appropriate statistical technique, generate material property distributions and boundary conditions.

Step 2: Using an appropriate solution strategy, determine the disposition of an adequately large number of flow tubes.

Step 3: For each flow tube, find the total conductance (reciprocal resistance) from inlet to outlet, by progressively integrating conductivity and flow tube geometry. Also evaluate, by progressive integration, the water-saturated pore volume of each flow tube.

Step 4: Using end potentials, determine the flux through each flow tube.

Step 5: Obtain GWTT for each tube by dividing the saturated pore volume by the average flux. Thus,

$$t_i = \frac{V_{p,i}}{Q_i} \tag{4.1}$$

where t_i is the GWTT for the *i-th* flow tube, whose saturated pore volume is $V_{p,i}$ and the steady flux passing through it is Q_i.

Step 6: By arranging GWTTs for all tubes in sequence, generate the CDF. If GWTTs for all flow tubes are arranged in an ascending sequence, then the probability that the GWTT is equal to or smaller than a prescribed value may be expressed as

$$PD(t_{presc}) = \frac{\sum_{i=1}^{i=J} Q_i}{\sum_{i=1}^{i=M} Q_i} \tag{4.2}$$

where *PD* is the GWTT CDF for $t_J \leq t_{presc}$ and M is the total number of flow tubes.

Note that the CDF generated above pertains to one statistical realization of material property variations and boundary conditions used in Step 1. By repeating Steps 1 to 4 for many statistical realizations of material property distributions, one can incorporate uncertainty into the estimate of GWTT CDF.

4.2 Implementation by Current Models

In general, the methodology outlined above is applicable in three dimensions. However, available knowledge about the geology and hydrology of Yucca Mountain suggests that a fully three-dimensional simulation of Yucca Mountain is time-consuming and expensive. Therefore, from a practical point of view, we restrict the discussion to two-dimensional simulations.

At the present time, several computer algorithms (e.g., TRUST, SAGUARO, TOSPAC, UNSAT2) are available to solve steady-state unsaturated flow problems of interest. Despite differences in solution procedures, these programs have a common base: they all compute fluid potentials at preselected points (locations), given specifications of flow domain geometry, material property distributions, and boundary conditions. It is fairly easy to visualize how these programs may be used to calculate the GWTT CDF. Once fluid potentials are obtained at discrete locations, the next step is to generate lines (surfaces in three dimensions) of equal potential and derive flow lines. In systems containing only isotropic materials, flow lines will be perpendicular to lines of equal potential. Alternatively, one could also solve for flow functions directly. Once flow lines are obtained, Steps 3 to 6 above should lead to the determination of CDF.

4.2.1 *A Computational Difficulty*

Although the procedure outlined above is fairly straightforward, a practical computational difficulty needs to be recognized. The task of solving for potentials at preselected points requires that a set of simultaneous equations be solved. If small heterogeneities in our system are of the order of a meter in scale and if the flow region itself exists on a scale of a few hundred meters to a few kilometers, one needs to solve for potentials at a very large number of points, requiring the computational manipulation of very large matrices. The task is rendered more difficult by the need to use a repetitive iteration process when dealing with unsaturated flow conditions. For these reasons, it is doubtful, considering the heterogeneities, that it is computationally realistic to attempt a two-dimensional Monte Carlo simulation of the hydrology at Yucca Mountain.

4.2.2 *The Issue of Verification*

Model verification is an important issue related to licensing. Simply stated, how may one assert that model calculations on which the GWTT CDF is based, are mathematically consistent with the equations governing the problem? If we use an analytical method of solution, the mathematical accuracy can be easily verified. But when numerical methods are used because of the complexity of the problem of interest, then verification is a question that cannot be dispensed with easily. At the present time, the most widely used approach to verification of a numerical model is to test numerical solutions against available analytical solutions. However, the fact that a given numerical model has been able to match one or more analytical solutions to some simple problems is not a guarantee that the numerical solution generated by the model to a different, complex problem is necessarily correct. Because the scope of analytical solutions is limited to relatively simple problems, a real need exists to develop approaches that will help verify numerical solutions in their own right, without linking verification to the availability of analytical solutions.

Therefore, in seeking to generate the GWTT CDF using currently available numerical techniques, one is confronted with two basic problems:

- the need to solve very large matrices resulting from the consideration of heterogeneous, nonlinear material distributions; and
- the verification of the solutions.

4.3 Possible New Approaches

In an effort to overcome the difficulties associated with estimating GWTT CDF, we propose possible alternatives that would avoid the computational limitations arising out of direct solvers, and still make use of all available information on the physical nature of the system. The alternative approach and solution strategy could take advantage of the notion of parallel processing. The computing industry has made enormous progress in parallel processing and many innovative computational architectures are continuing to evolve in this direction. It would

be doubly beneficial if the new approach can also provide alternate means of solution verification that is different from the currently followed approach of verification against analytical solutions.

We will now describe the concept of an approach which we shall term "Path Integration" to solve the steady-state fluid flow problem. Path Integration, as conceived here, is the procedure by which resistances along a flow tube are integrated using available information on flow geometry and material heterogeneities, and the integrated resistances are related to the steady flux through the flow tube. Although the concept is generally valid for three dimensions, we will restrict our discussions to two-dimensional systems. The ideas presented here are still preliminary in nature and further conceptual work is necessary to establish the feasibility of this method as a practical tool of mathematical modeling.

Consider a flow region such as the one shown in Figure 4-2 through which water is flowing under steady-state conditions caused by spatial variations in the fluid potential. The *Maximum Principle* states that in steady-flow systems, the maximum potential and the minimum potential will occur only on the boundary of the flow domain. Thus, water enters the flow region across boundary segments where the fluid potentials are high and leaves the flow region across boundary segments where the fluid potentials are low. The mass of water that enters the flow domain at an appropriate rate brings energy into the system, because fluid potential, by definition, is energy per unit mass. As water moves through the system, it progressively loses energy as it loses fluid potential in the direction of flow. The energy so lost is in part irretrievably expended as frictional heat and in part is expended in performing other work such as keeping the pores open against external compressive forces.

In order to facilitate the movement of water within the system, the fluid potentials will have to suitably distribute themselves in space, bounded by maximum and minimum values on the boundary. If we restrict ourselves to macroscopic, laminar flow in a domain occupied by isotropic materials, we are aware from empirical knowledge that the lines of flow *(flow lines)* will be perpendicular to surfaces of equal potential *(isopotential surfaces)*.

Owing to the inherent tendency of a natural physical system to conform to certain well-established physical laws (e.g., law of least action), the steady-state flow system under consideration must adjust itself in some predictable manner to conditions existing on the boundary of the flow domain. As a consequence, the isopotential surfaces and the associated flow lines must form a unique pattern. The *mathematical problem* of steady-state fluid flow, then, is to quantify how the fluid flow system will adjust itself to a unique spatial configuration in response to (1) boundary conditions, and (2) natural physical laws.

In the following we shall attempt to formulate the appropriate physical-mathematical expressions on the basis of such physical postulates as minimum work and mass conservation.

4.4 Principle of Minimum Work

Consider the shaded region in Figure 4-2, identified by the indices i,j (denoting *j-th* segment of potential drop in the *i-th* flow tube). This shaded region is bounded by two isopotential surfaces $\Phi_{i,j,L}$ and $\Phi_{i,j,R}$ ($\Phi_{i,j,L} > \Phi_{i,j,R}$) and by two flow lines.

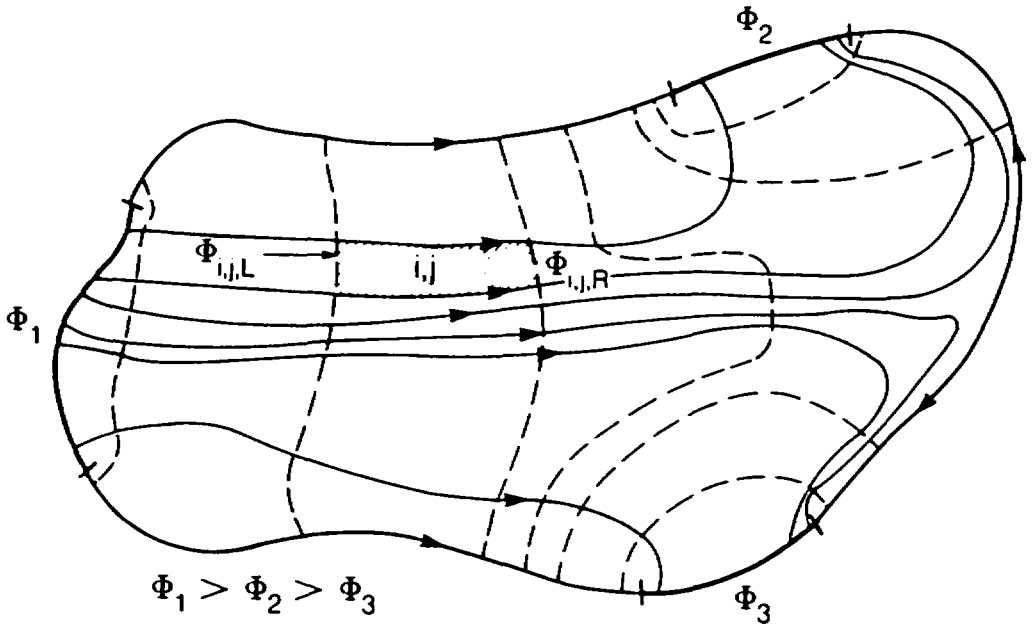

Figure 4-2. Flow Pattern in a Steady-State Flow Domain.

According to the equation of motion,

$$Q_{i,j} = \frac{1}{R_{i,j}}(\Phi_{i,j,L} - \Phi_{i,j,R}) \tag{4.3}$$

where $Q_{i,j}$ is the steady flux within the tube and $R_{i,j}$ is the resistance offered to fluid flow by the shaded area. Within this area, the energy lost by the water consequent to the drop in fluid potential is

$$\textit{Energy Lost} = Q_{i,j}\,(\Delta\Phi)_{i,j} \tag{4.4}$$

where $(\Delta\Phi)_{i,j}$ is the drop in potential over the shaded region. We now introduce the following postulate regarding the expected tendency of response of the flow system.

> **Postulate:** *In response to the boundary conditions, the flow system will adjust in such a way that the rate at which energy is dissipated over the entire flow domain, as a consequence of the drop in potential of the moving mass of fluid, is a minimum.*

Thus, the function Ω is a minimum where

$$\Omega = \sum_i \sum_j \rho \, Q_{ij} (\Delta\Phi)_{ij}. \tag{4.5}$$

The physical meaning of the above postulate may be described as follows. Suppose we arbitrarily choose a set of isopotential surfaces distributed over the flow domain and construct flow lines perpendicular to these surfaces. Further suppose that we compute Ω for this arbitrarily chosen configuration of flow as prescribed in Equation 4.5. Then, the postulate asserts that Ω will be larger than that value of Ω which corresponds to the flow configuration representing the true steady-state behavior of the system.

4.4.1 *Comparison with the Variational Principle*

It is of interest to compare this minimization postulate with the classical variational functional of the steady-state flow problem. The classical variational expression is sometimes known as Euler's equation.

As shown by Narasimhan (1985), for a flow tube of nonuniform cross-sectional area such as the shaded area in Figure 4-2, the fluid flux (see Figure 4-3) can be expressed by

$$Q_{ij} = \frac{(\Delta\Phi)_{ij}}{\dfrac{\mu}{\rho} \displaystyle\int_{\chi_{ij,L}}^{\chi_{ij,R}} \frac{dx}{k(x)A(x)}} \tag{4.6}$$

where, $\chi_{ij,L}$ and $\chi_{ij,R}$ the coordinates of intersection of $\Phi_{ij,L}$ and $\Phi_{ij,R}$ with an appropriately chosen curvilinear x-axis such that

$$V_{ij} = \int_{\chi_{ij,L}}^{\chi_{ij,R}} A(x)dx \tag{4.7}$$

in which V_{ij} is the volume of the shaded region i,j. Furthermore, in Equation 4.6, μ is the dynamic coefficient of viscosity of water, ρ is the density of the fluid, k is absolute permeability, and $A(x)$ is the area of the isopotential surface that intersects the x-axis at x. In general, Equation 4.7 is valid for a flow tube with variable material properties. For the sake of simplicity we shall ignore heterogeneities and consider a homogeneous flow domain. Therefore, in view of Equation 4.6,

$$\Omega = \sum_i \sum_j \rho \frac{k\rho}{\mu} \frac{(\Delta\Phi)_{ij} \, (\Delta\Phi)_{ij}}{\displaystyle\int_{\chi_{ij,L}}^{\chi_{ij,R}} \frac{dx}{A(x)}}. \tag{4.8}$$

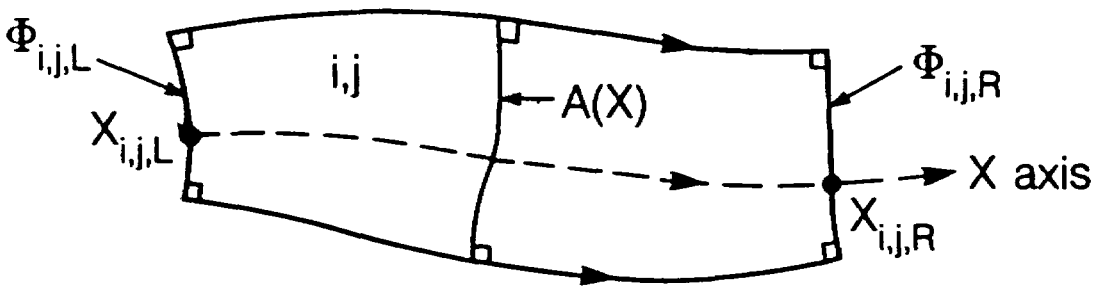

XBL 881-10003

Figure 4-3. Segment (i,j) of a Flow Tube.

If we make the spatial discretization arbitrarily fine, then the Δs and the integral in Equation 4.8 can be dispensed with and we shall have

$$\Omega = \sum_i \int_{X_{i,j,L}}^{X_{i,j,R}} \rho \frac{k\rho}{\mu} \left(\frac{d\Phi}{dx}\right)^2 A(x)dx. \tag{4.9}$$

But, noting that A(x)dx = dV, we get

$$\Omega = \sum_i \int_{V_i} \rho \frac{k\rho}{\mu} \left(\frac{d\Phi}{dx}\right)^2 dV_i. \tag{4.10}$$

Finally, because $\sum_i V_i = V$,

$$\Omega = \int_V \rho \frac{k\rho}{\mu} (\vec{V}\Phi)^2 dV, \tag{4.11}$$

which indeed is Euler's equation representing the variational functional for the steady-state fluid flow problem.

4.4.2 *Solution Approach*

The minimization postulate, in conjunction with Figure 4-2, suggests an approach for solving the steady-state fluid flow problem that is different from the conventional analytical or numerical approaches for solving the Laplace equation. The new approach consists of initially guessing a set of isopotential surfaces. This guessed configuration is then progressively refined through a systematic process of minimizing Ω until the correct configuration (solution) is obtained. At this juncture we do not address the issue of whether this approach is computationally efficient or advantageous. We merely explore whether an alternate solution strategy is possible.

Two features of this strategy are of interest. First, the task of verifying a solution generated this way consists of asserting that the minimization process indeed yields a global minimum for Ω. Second, the accuracy of the solution depends on how accurately the resistances, $R_{i,j}$, can be evaluated with the available information on flow geometry and heterogeneity, using the integral, $\int \frac{dx}{k(x)A(x)}$. Note that the entire process of solution and verification should be mathematically self-consistent and the process exists independently of the notion of a partial differential equation.

4.4.3 *Relation to Mass Conservation*

Suppose the particular configuration of isopotential surfaces and flow lines chosen does not correspond to a minimum for Ω. Then it stands to reason that along a given flow tube i in Figure 4-2, the fluxes will not be equal. That is, the values for $Q_{i,j}$'s will not be the same. This is because the flow geometry is incorrect and the resistances $R_{i,j}$ which depend on the flow geometry will not assure the equality of fluxes along the flow tube.

Note that the observation that fluxes are variable along a flow tube is exactly equivalent to stating that mass of water is not conserved along the flow tube. Because we know from simple empirical considerations that a steady-state fluid flow system cannot violate the principle of mass conservation, it follows that the flow configuration that corresponds to a global minimum for Ω must also assure mass conservation. In other words, the formulations of the problem of steady-state fluid flow using either the minimization principle or the conservation principle are exactly equivalent. Another way to assert this equivalence is to recognize that by perturbing the variational functional (Equation 4.11) with reference to Φ and minimizing it, one can obtain Laplace's equation which is merely an expression of mass conservation. This minimization logic is often used as a basis for deriving the finite element equations.

4.5 Mass Conservation and Continuity of Isopotential Surfaces

We shall now formulate the problem of steady-state fluid flow in a porous medium directly based on the principle of mass conservation. Figure 4-4 is a flow region in which we show a set of five guessed-at flow tubes. Because we define them to be flow tubes, fluid flow can occur only along them and fluid cannot cross the flow lines. If we invoke mass conservation law, the flux Q_i along the *i-th* flow tube must be a constant. Let $(\Delta\Phi)_i$ be the drop in potential between the inlet and the outlet of the *i-th* flow tube. Then, in view of Equation 4.6,

$$R_i = \frac{(\Delta\Phi)_i}{Q_i} \tag{4.12}$$

where R_i is the total resistance to flow offered by the *i-th* tube. Suppose we now wish to find the position of an isopotential surface within the flow tube *i* such that the drop in potential from the inlet to the desired isopotential surface is some fraction f of $(\Delta\Phi)_i$. In view of the fact that Q_i is a constant, it follows that the ratio of the resistance of the flow tube from the inlet to the desired isopotential surface to the total resistance of the flow tube, R_i, must be equal to f. Thus, for a given f we may find the position of the desired isopotential surface within flow tube *i* by progressively integrating resistance along the flow tube until a value of fR_i is attained. If we were to repeat this process for all the flow tubes in the system for a given f, the computed isopotential surfaces will not be continuous at the flow lines because the flow lines have been arbitrarily chosen. Figure 4-4 schematically shows the position of such isopotential surfaces for $f = 0.5$. However, it is clear that isopotential surfaces cannot be discontinuous at the flow lines. A discontinuity at the flow lines implies a potential variation across the flow line and this should cause fluid flow across the flow line. Such a cross flow is physically inconsistent with the definition of a flow line.

Suppose we now systematically adjust the geometric disposition of the flow lines in such a way that the isopotential surfaces are made to be continuous at the flow lines everywhere in the system. Such a configuration will satisfy mass conservation and at the same time will be consistent with the definition of a flow line. Therefore that flow configuration will constitute the desired solution to the steady-state fluid flow problem.

The task of verifying the solution in this case consists of asserting that all isopotential surfaces are continuous at flow lines over the entire domain of interest. The accuracy of the solution is dependent on the accuracy with which flow resistances are evaluated using flow geometry and material property variations. This approach based on mass conservation is also independent of the notion of a differential equation.

4.6 Relation to Conventional Techniques

It is instructive to compare the aforesaid approaches to conventional methods of analysis. First let us consider analytic solutions to the Laplace equation. Because differential equations are written in a specific coordinate system, analytic solutions are invariably obtained for specific flow geometries. If we consider a system with a specified flow geometry, then the shapes of

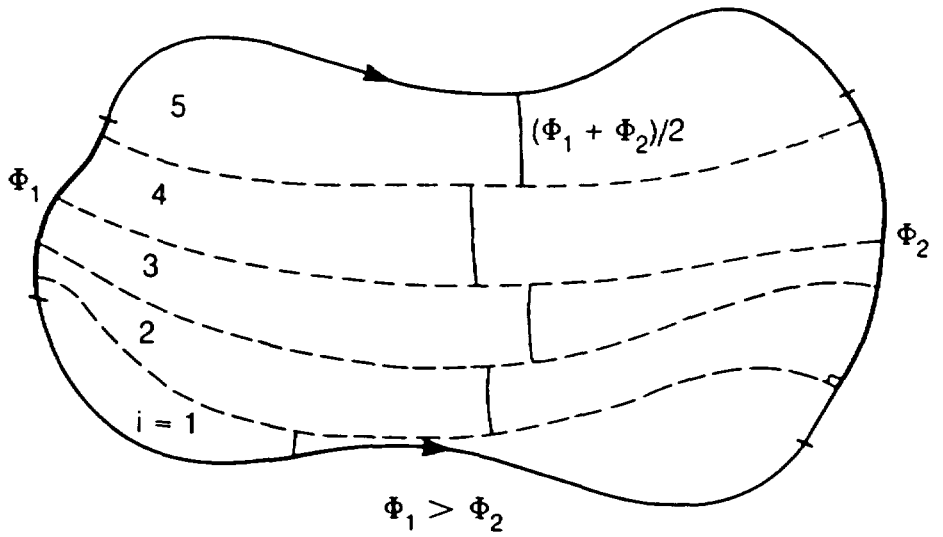

XBL 881-10005

Figure 4-4. Guessed Flow Lines and the Discontinuous Isopotential Surface $\Phi = 0.5\ (\Phi_1 + \Phi_2)$.

the isopotential surfaces and the flow lines are already known. The only unknown is the exact magnitude of potential of any chosen isopotential surface. Using the minimization technique one could solve for the magnitudes of isopotential surfaces by starting with a set of guesses and then progressively refining the guesses by minimizing the objective function Ω. Such a systematic minimization can be achieved, it appears, with the help of techniques of operational research. One could also solve the same problem using the mass conservation approach requiring continuity of isopotential surfaces. In this case, the ratio of the resistance up to any given isopotential surface to the total resistance along a flow tube directly provides the magnitude of potential drop up to that isopotential surface.

Let us now consider conventional numerical techniques that are often considered to be approximate solvers of partial differential equations. We restrict our consideration here to techniques collectively known as finite difference methods, integral finite difference methods, and finite element methods. Typically these methods consider a sufficiently large number of points within the flow domain (nodal points) and solve for the potentials at these points (in the present case, steady-state potentials) subject to constraints of mass conservation and boundary conditions. A primary feature of all these methods is that they use predetermined algebraic expressions to characterize the local spatial variation of potentials (e.g., linear, quadratic, polynomial). These expressions, then, determine the accuracy with which fluid fluxes are evaluated. Once the predetermined expressions are chosen, the solution for potentials at the nodal points is a single-step process of inverting a set of simultaneous equations. Accuracy of this procedure is obviously governed by the closeness with which the predetermined expressions match the local variations of potentials of the real system.

Note that in the two approaches developed earlier in the present work, the solution process consisted of adjusting simultaneously the fluid potential surfaces and the flow lines. In systems characterized by complex geometry and arbitrary heterogeneity, local variations in potentials will be governed by local material properties *as well as* by local flow geometry. Thus potential distribution and flow geometry are inherently intertwined. Thus, one has indeed to solve for two unknowns: potentials and flow geometry. It is not possible, therefore, to choose *a priori* a spatial operator that will accurately represent the potential variations throughout the flow domain.

Conventional wisdom dictates that local effects of flow geometry progressively decrease as the nodal points get infinitesimally close to each other, as is assumed in the derivation of the differential equation. Accordingly, a basic assumption in the use of conventional numerical methods is that accuracy will be improved by increasing the number of nodal points in the system.

However, we would like to suggest a new perspective that it is possible to improve the accuracy of numerical solutions without increasing the number of nodal points, or, equivalently, by refining mesh discretization. The interesting question, then, is how a numerical solution can be considered accurate independent of (or at least weakly dependent on) mesh discretization.

As we have already noted, local variations of potential are dependent on local flow geometry. In the absence of previous knowledge of local flow geometry, one must resort to an iterative approach by which flow geometry and fluid potential mutually help refine each other's estimate. Thus, for example, the predetermined expressions of the conventional methods may merely be trial functions to arrive at the first estimate of potential distribution. Then, by a process of contouring, the estimated flow geometry may be used to refine the trial functions for potential variations for the next iteration. The iterative process is stopped when the local flow geometry and the trial functions are mutually consistent.

This iterative logic asserts that (1) if the flow geometry is unknown, the steady-state problem cannot be solved accurately in a single step because the potentials as well as the flow geometry constitute the unknowns of the problem; and that (2) an iterative, feedback approach allows an accurate solution independent of fineness of mesh discretization.

4.7 Relevance to Network Models

The minimization approach is readily applicable to systems that comprise a network of resistors, a typical example of which is a fracture network. A special feature of such networks is that the notion of flow tubes is redundant; the flow paths are already known and the resistances of flow segments are also known *a priori*. As applied to such networks, the minimization postulate simply translates to

$$\Omega = \sum_{j}^{J} \rho \frac{(\Delta\Phi)_j^2}{R_j} \tag{4.13}$$

where J is the total number of resistors in the system. The minimization of Ω in (4.13) is subject to the constraint that the potential within any resistor within the system does not violate the maximum principle. Indeed, Equation 4.13 suggests the possibility of solving the fracture network problem by minimizing the objective function Ω using techniques of linear programming.

4.8 Concluding Remarks

In this section, we have attempted to formulate the problem of steady-state fluid flow in porous media in a self-consistent mathematical fashion that is different from the classical approach of partial differential equations. We have shown that viable formulations could be made drawing upon either a minimization of work postulate or a mass conservation postulate. These formulations use the integral equations instead of differential equations.

The minimization postulate requires that under steady conditions of fluid flow the flow system will adjust itself in such a fashion that the rate at which energy is dissipated over the system, as a consequence of the potential drop of moving fluid, is a minimum. This postulate is fully consistent with the classical variational functional for the steady-state problem, frequently referred to as Euler's equation.

A second approach for formulation is based on mass conservation, subject to the constraint that surfaces of equal potential be continuous at flow lines.

In principle, numerical algorithms for implementation on the digital computer could be developed from either of these formulations. The algorithms can be used to directly verify the self-consistency and accuracy of the solutions.

Despite its conceptual elegance, it is not clear whether the minimization approach will lead to an efficient algorithm except perhaps for problems of *a priori* prescribed flow geometries or for resistor network problems. It appears that the second approach based on mass conservation may provide a new possibility of developing algorithms that may be especially desirable to handle very large heterogeneous systems with material properties that may even vary with fluid potential. It should be of considerable practical interest to explore this possibility further. Moreover, once the flow system has been solved for by either of these techniques, one can interpolate exactly for potentials anywhere else in the flow domain. In this sense, the suggested integral approaches do in fact provide a *complete solution* to the steady-state fluid flow problem.

Philosophically, when one is concerned with heterogeneous systems with complex geometry, both the potential distribution and the flow geometry within the flow domain are unknown. Therefore, the task of solution consists of solving both these unknowns. Perhaps the greatest weakness of the conventional philosophy of approaching numerical methods is the failure to

recognize the importance of the inherent interrelationship between potential distribution and flow geometry. To overcome this weakness, the conventional approach is to use finer and finer mesh discretization. This, perhaps, is not the only way nor even the most desirable way of overcoming the weakness. The analyses presented above strongly argue that it is possible to develop powerful algorithms which can provide accurate verifiable solutions for large problems using relatively coarse spatial discretization.

5.0 HYDROLOGICAL PARAMETERS

To quantify the conceptual model for a fractured porous medium and to solve the mathematical equations for a fluid flow field with either conventional numerical codes or potentially more efficient and accurate path integration approaches, we need to specify the parameters characterizing the medium. We focus on the hydrological parameters which are used in saturated/unsaturated flow equations. The saturation characteristic curve and the relative permeability curve are two essential functions for predicting liquid water flow in an unsaturated medium. These two functions, together with saturated permeability and porosity, determine both the ambient partially saturated flow field and the transient changes associated with extreme flooding which may induce local saturated/unsaturated transitions.

In this section, we analyze the functional forms used in the literature for the saturation characteristic curve and the relative permeability curve. We are mainly interested in physical insights and the relationships of functional parameters to geometric properties of the porous medium. We recognize the limitations of using idealized geometric models to represent real media with complex pore structure and tortuous flow paths. Nevertheless, simple interpretations of parameters and direct relationships among parameters can assist us in rationally analyzing distributions and correlations of real data. One of the difficulties in studying processes in heterogeneous and complex geological formations is the uncertainties associated with limited data and samples. If data analyses are guided with simple physical models, we can put more confidence in modeling results obtained with parameters that have been accurately analyzed and properly constrained. If a modeling result does not make physical sense, we need to understand whether we have used improper parameters and equations. Before we analyze data in detail, as we shall do in the next section on the distributions and correlations among hydrological parameters, it is essential that we first understand the physical meaning of different parameters.

5.1 Saturation Characteristic Curves

The saturation characteristic curve, also known as the moisture retention curve or moisture characteristic, is the relationship of saturation, S, or moisture content, θ, to the capillary suction pressure head, h. Tabulated experimental data tables or analytic fitting functions for the characteristic curve can be used in mathematical models to determine saturated pore volumes, storage capacities, and relative permeabilities. In two-phase models using saturation as a state variable, we need the inverse relationship of capillary pressure as function of saturation. Although tabulated data can be used in numerical models, analytic functions provide two advantages. First, they can often be evaluated, differentiated, or inverted more accurately and easily. Second, some fitting parameters may be interpreted to represent meaningful physical or geometric characteristics of the medium.

5.1.1 *Physical Interpretation of Desaturation Parameters*

Various empirical analytic functions have been proposed in the literature to quantify saturation characteristics. The saturation can be a power, polynomial, algebraic, exponential, logarithmic,

or other special function of suction head. Different empirical functions have been shown by respective author(s) to adequately fit some measured data. Comparisons of different functions are available in the literature (e.g., Alexander, 1984; El-Kadi, 1985; van Genuchten and Nielsen, 1985). Two popular functions are the Brooks and Corey model (1964, 1966) and the van Genuchten model (1980). We briefly describe their functional forms and discuss interpretations of their respective parameters.

The Brooks and Corey model (1964, 1966) is the power function of the form

$$S_e(h) = \begin{cases} 1 & \text{if } |\alpha h| < 1 \\ |\alpha h|^{-\lambda} & \text{if } |\alpha h| \geq 1 \end{cases} \tag{5.1}$$

and S_e is the effective saturation (or reduced moisture content)

$$S_e = \frac{S - S_r}{S_s - S_r} = \frac{\theta - \theta_r}{\theta_s - \theta_r} \tag{5.2}$$

with the subscripts s and r indicating saturated and residual values, respectively. The value of α is positive and the variable h is negative for a partially saturated state. Many investigators in the literature deal with the absolute magnitude and redefine h as $|h|$. The inverse of the parameter α, $|h_{ae}| = \alpha^{-1}$, is frequently referred to as the air entry value or bubbling pressure in the soil literature. This is one interpretation for the parameter α or h_{ae}. When suction pressure head h overcomes the air entry pressure h_{ae} $\left(|h| \geq |h_{ae}|\right)$, air enters the pores and water flows out of the medium to initiate desaturation. This interpretation is based on the cutoff separating the saturated region, $S_e = 1$, from the desaturated region, $S_e = |\alpha h|^{-\lambda}$. Another interpretation for α is to treat it as a scaling parameter. The saturation depends on αh together and not on α and h separately. Characteristic curves of soils with different α, but same λ, can be scaled into one curve. Therefore, we refer to α as the *air entry scaling factor*. If flow channels are represented by capillary tubes, we can define air entry radius by the capillary equation

$$r_{ae} = -\frac{2\sigma\cos\Theta}{\rho g h_{ae}} = \frac{2\sigma\cos\Theta}{\rho g}\alpha. \tag{5.3}$$

In this report, we use surface tension $\sigma = 0.07183\ kg/s^2$, contact angle $\Theta = 0°$, water density $\rho = 1000\ kg/m^3$, and gravitational acceleration $g = 9.80665\ m/s^2$ in calculating r_{ae} from parameter h_{ae}, or α. The air entry radius r_{ae}, represents the largest pore radius in the medium that is most easily drained in a desaturation process. With σ, ρ, and g as constants, r_{ae} is proportional to α. We can treat the air entry radius r_{ae} as a parameter equivalent to the air entry scaling factor α.

The second parameter λ is an index for pore-size distribution. The value of λ must be positive in Equation 5.1 to represent the physical situation in which saturation decreases as suction increases (or pressure head becomes more negative). As suction overcomes the air entry cutoff and progressively desaturates the medium, pores with progressively smaller and smaller radii are being drained. If the index λ is large, the saturation will decrease rapidly over a narrow range of pressure head. This is equivalent to a narrow pore-size distribution. If the index λ is small, the pore-size distribution is broad. Scaled characteristic curves of effective saturation S_e versus dimensionless pressure head $|\alpha h|$ for different λ are plotted in Figure 5-1.

For soils with broad pore-size distributions, a sharp cutoff at an air entry value may not be well defined. Other empirical functions have been proposed to improve the description of a moisture retention curve near saturation with cutoff-free, continuously differentiable, smooth S-shaped features (King, 1965; Brutsaert, 1966; Visser, 1968; Laliberte, 1969; Su and Brooks, 1975; Gillham et al., 1976; van Genuchten, 1980; among others). The van Genuchten model (1980) has been popular in recent years. In its general form:

$$S_e = \left[1 + \left(|\alpha h|\right)^n\right]^{-m} \tag{5.4}$$

where α, n, and m are empirical parameters. We use the same symbol α in both Equations 5.1 and 5.4 to represent similar empirical scaling parameters. Even though the van Genuchten model does not have a cutoff at $h = -1/\alpha$, we will still use Equation 5.3 to define an equivalent air entry radius with the van Genuchten α parameter. For a given set of data points for a characteristic curve, the Brooks and Corey fitted α and the van Genuchten fitted α will be slightly different, as we shall discuss later.

In the range of large suction (large negative pressure head), Equation 5.4 asymptotically approaches a power function, and is approximately equivalent to Equation 5.1 with

$$\lambda = mn. \tag{5.5}$$

In a frequently used special case, van Genuchten (1980) reduces the number of empirical parameters by setting

$$m = 1 - \frac{1}{n}. \tag{5.6}$$

With Equation 5.6, Equation 5.5 becomes

$$\lambda = n - 1. \tag{5.7}$$

Like λ, we will also refer to $n - 1$ as a pore-size distribution index. However, we will retain the symbol n as proposed in the original paper. In tuff studies, n is sometimes referred to as

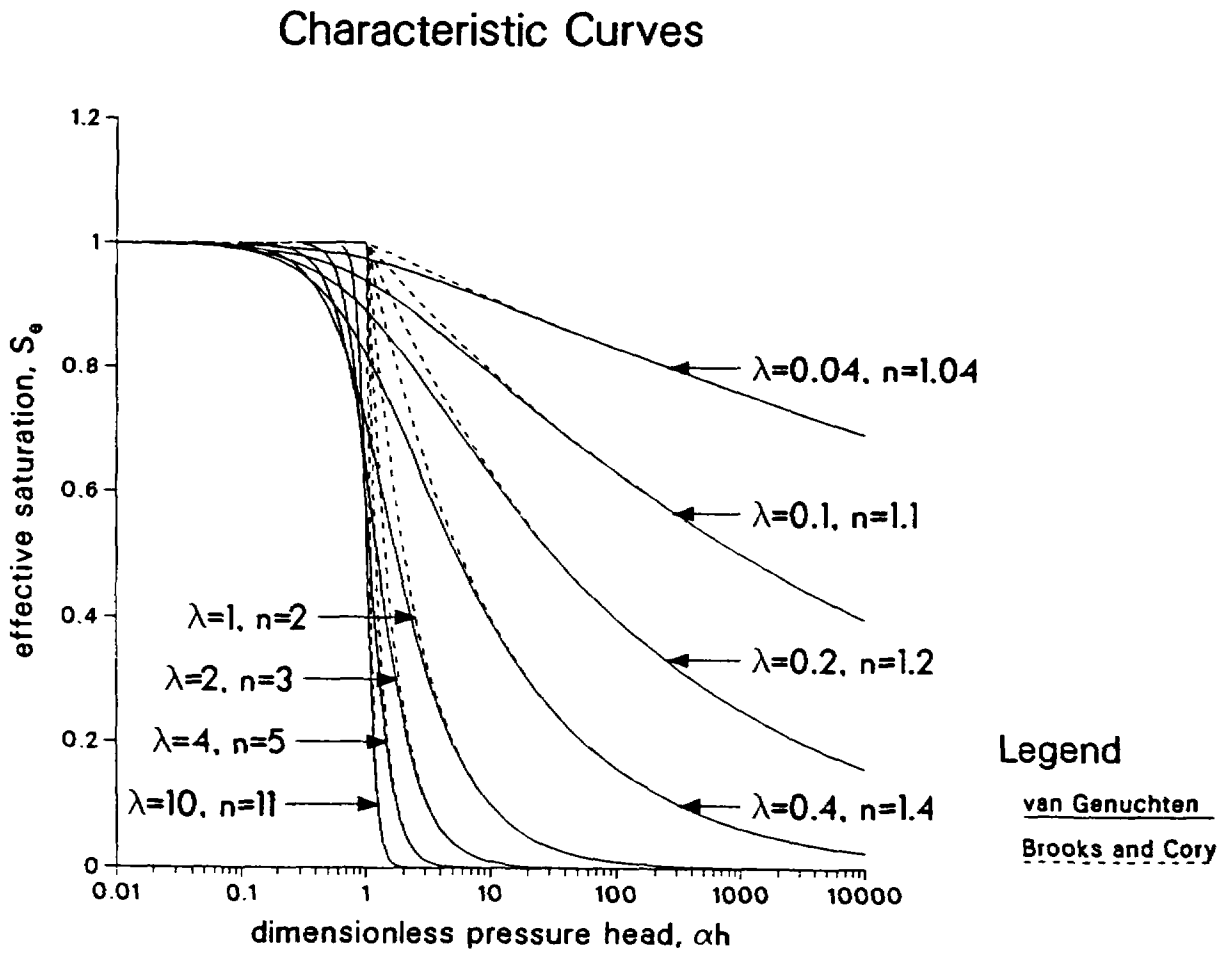

Figure 5-1. Scaled Characteristic Curves of van Genuchten Model and Brooks and Corey Model.

β (Peters et al., 1984; Klavetter and Peters, 1987). Scaled characteristic curves of Equation 5.4 with Equation 5.7 are shown in Figure 5-1 for different n values. For physical characteristic curves with $S_e \leq 1$, $n \geq 1$. Brooks and Corey curves and van Genuchten curves with equivalent pore-size distribution indices are different in the small suction region near saturation.

Several measured soil characteristic curves have been fitted with both the Brooks and Corey function and the van Genuchten function. Figure 5-2 for the pore-size distribution index and Figure 5-3 for the air entry scaling factor are based on parameters given by Brooks and Corey (1966), van Genuchten (1980), and van Genuchten and Nielsen (1985). For the same set of data, the fitted van Genuchten pore-size distribution index n - 1 is larger than the fitted Brooks and Corey index λ (Figure 5-2), and the fitted van Genuchten air entry scaling factor is slightly smaller than the fitted Brooks and Corey factor (Figure 5-3). In comparing different soils, the trends observed in both models are consistent with each other. If one soil has a higher van Genuchten index or factor than the other soil, the same soil will also have a higher index or factor if the Brooks and Corey model is used to fit the data. We will use results of both models in the literature to study the dependence of saturation characteristics on different geological media.

In addition to α representing pore size and λ (or n - 1) representing pore-size distribution, the other parameter S_r, or θ_r, in Equation 5.2 also has physical meaning. It represents the percentage of pore volume which cannot be desaturated by applying suction. Usually the soil characteristic curve is measured at ambient temperature and the suction pressure can overcome the capillary interphase forces holding the menisci between pore solid walls but may not overcome the adsorptive molecular forces holding thin films onto solid surfaces. Another possibility is that some pores are isolated or sealed from the bulk of pores. The isolated pore water cannot be drained unless the bottlenecks surrounding the isolated region are opened up by heating or by other mechanical forces rearranging the solid grain configurations. The residual saturation, S_r, represents the fraction of water in adsorbed films and in dead-end pores. In practice, determination of S_r, is often achieved by parameter-fitting procedures on analytic expressions. We see from Figure 5-4 that the fitted residual saturation with van Genuchten model is higher than that with Brooks and Corey model. Because experimental measurements are usually difficult at large negative suction and relatively fewer data points are in the extremely dry range, the determination of residual saturation by fitting may not be as reliable as those of α and λ (or n - 1). In some studies, S_r or θ_r in Equation 5.2 was assumed to be zero to reduce the number of parameters for fitting (e.g., Gardner et al., 1970; Campbell, 1974; Cosby et al., 1984).

One more parameter in Equation 5.2, S_s or θ_s, needs consideration. Most investigators set $S_s = 1$ and $\theta_s = \phi$, where ϕ is the total porosity. However, the full saturation S_s, or the saturated water content θ_s, can be considered as an empirical parameter (van Genuchten and Nielsen, 1985). For heterogeneous samples containing a few large pores, the large pores may desaturate easily with the application of a small suction before the bulk of pores desaturates. The measured curve may be fitted better with a $S_s < 1$ to represent the characteristics of bulk desaturation. It is also possible that entrapped air bubbles may take a long time to get out. Another more important reason is that the relative permeability prediction is sensitive to small changes in the fitted retention characteristic curve near saturation. By allowing one more

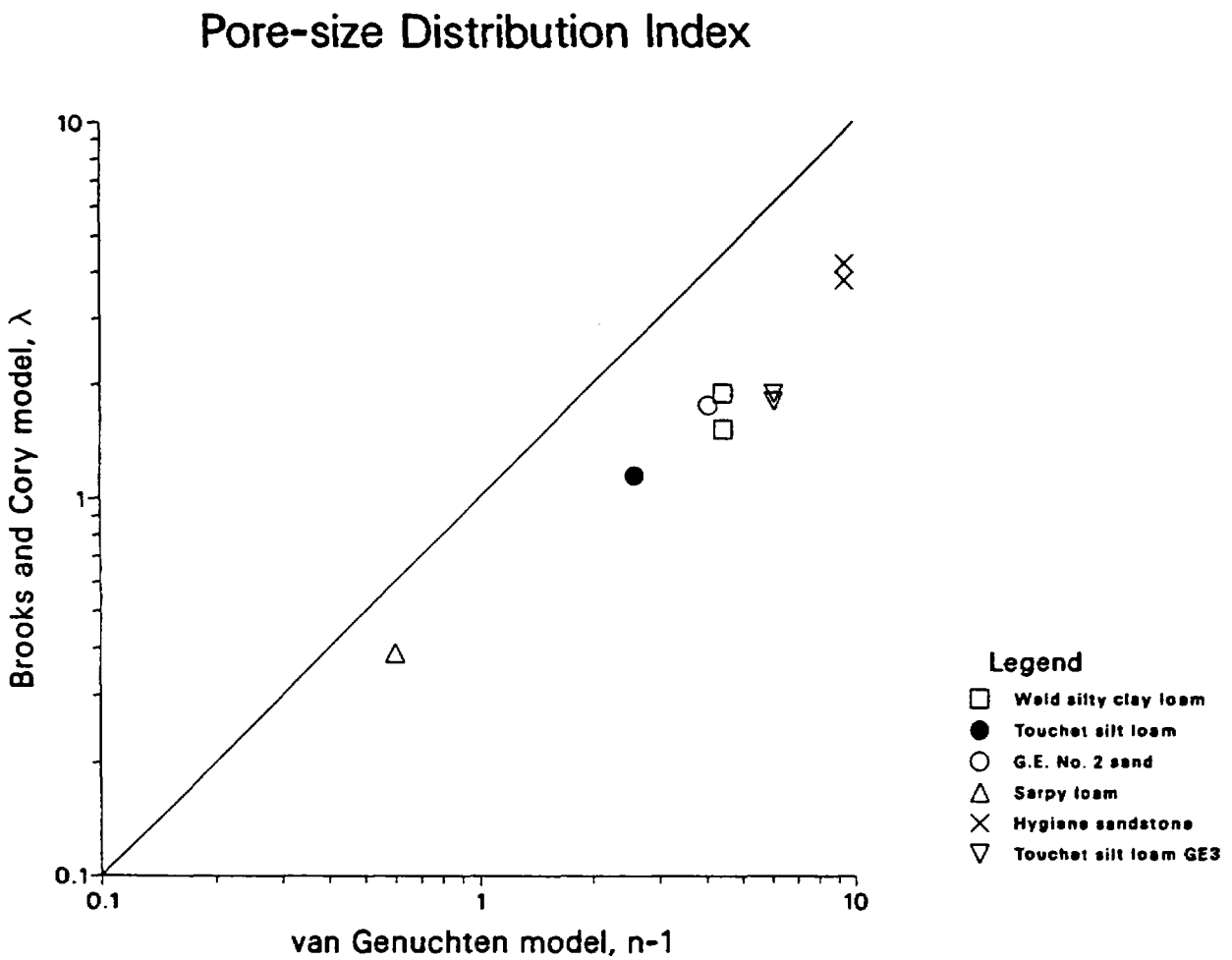

Figure 5-2. Soil Pore-Size Distribution Indices Using the van Genuchten and Brooks and Corey Models.

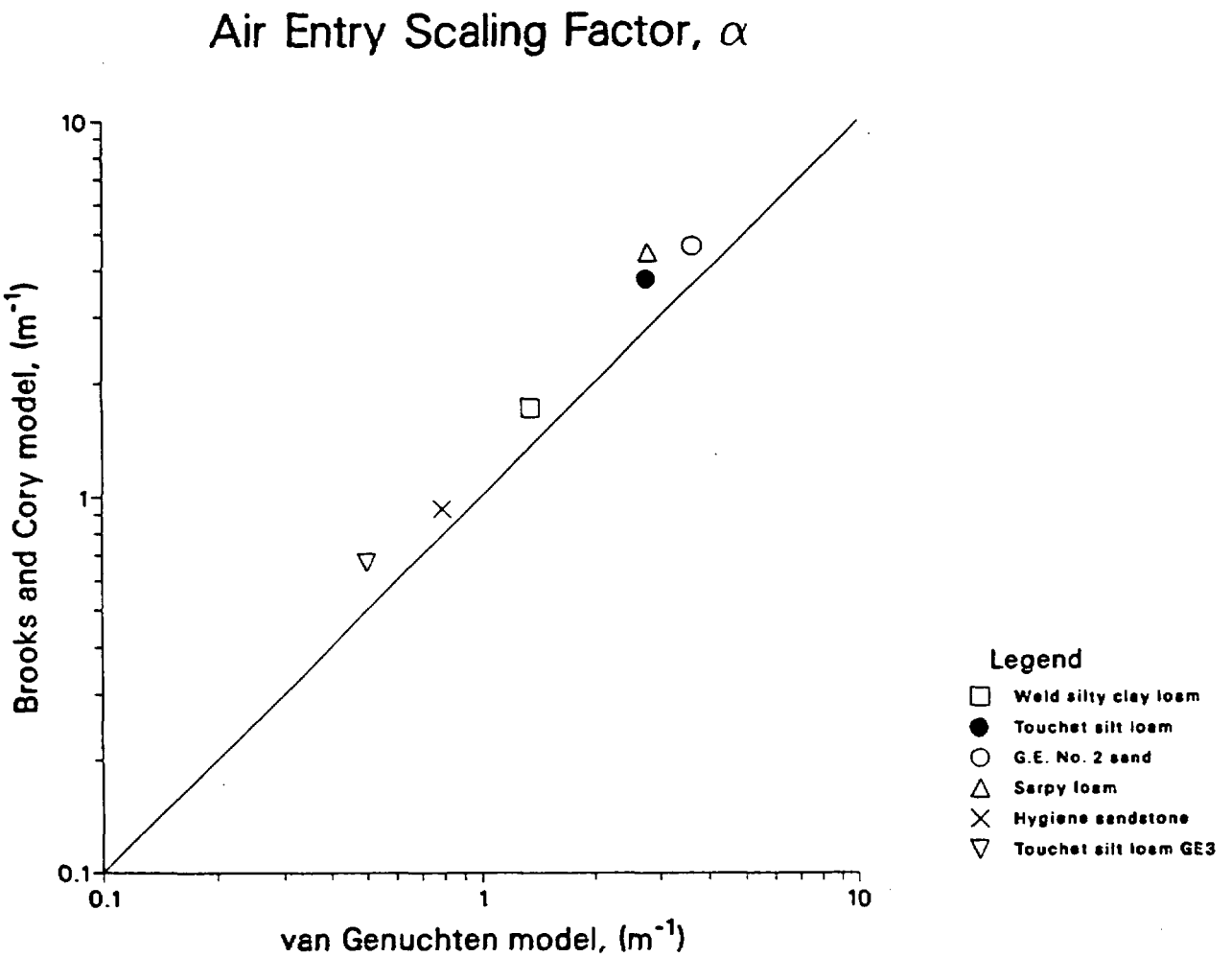

Figure 5-3. Soil Air Entry Scaling Factors Using the van Genuchten and Brooks and Corey Models.

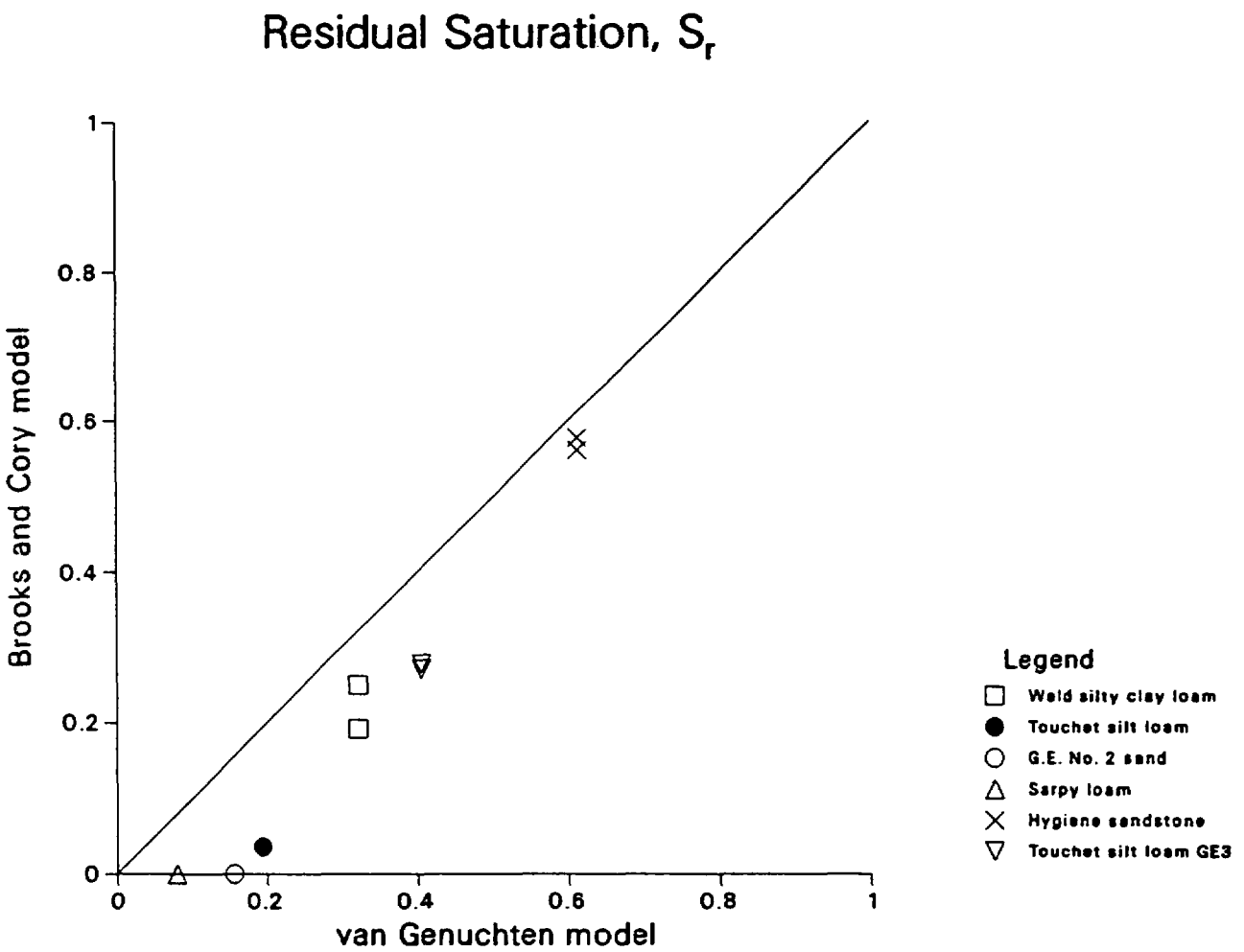

Figure 5-4. Soil Residual Saturations Using the van Genuchten and Brooks and Corey Models.

parameter to enhance the fitting near saturation, relative permeability predictions can be improved.

5.1.2 *Capillary Hysteresis Models*

The characteristic curve for the desaturation (drying or drainage) process is different from the curve for the resaturation (wetting or imbibition) process. The relationship between the saturation and capillary pressure head is a multi-valued, hysteretic function, depending on the history and nature of saturation changes. Starting with a fully saturated, air free sample and continuing the desaturation process until residual saturation is reached at a large enough negative suction h_r, we generate the "first drainage curve". If we resaturate the sample, the process follows the "main wetting curve" which, for the same capillary pressure head, has lower saturation value than the drainage curve. When the capillary pressure head returns to a reasonable minimum suction h_s, which is normally close to zero, the saturation value may not return to the original saturation value if some air-bubbles are trapped in the sample. When the sample is desaturated again, it follows the "main drying curve" which lies between the first two curves. The "main wetting curve" $S_w(h)$ and the "main drying curve" $S_d(h)$ form the boundary of a hysteresis loop. If saturation is a state variable, the hysteresis loop can be defined by the corresponding inverse functions $h_w(S)$ and $h_d(S)$. The curves of any subsequent reversal of capillary pressure head and any partial wetting or partial drying processes are contained within the loop. The higher order curves starting at reversal points are called the scanning curves (Figure 5-5).

The mechanisms for hysteresis include air-entrapment effect, the pore geometry with converging and diverging walls along flow paths (the ink-bottle effect), and the changes of contact angle (Θ is larger in an advancing meniscus toward a dry surface than in a receding meniscus). Many models have been developed to explain the hysteresis in terms of microscopic and macroscopic processes. Recent reviews of capillary hysteresis models have been given for example by Jaynes (1984) and Kool and Parker (1987). The domain theories for magnetism and other hysteresis phenomena (Everett, 1955; Enderby, 1955) have been generalized and applied to partially saturated porous media (Poulovassilis, 1962, 1970; Philip, 1964; Topp, 1969, 1971; Mualem, 1973, 1974, 1984). The domain theory assumes that the medium is a collection of pore domains with each pore has a characteristic wetting radius r_w and a drying radius r_d. The pore water distribution function $f(r_w, r_d)$ of these radii (or the corresponding distribution function $f(h_w, h_d)$ in terms of capillary pressure heads) determines the hysteresis curves. We briefly summarize the results of several models which predict the scanning curves from the main wetting and drying curves.

Parlange (1976) developed a model which used the curve and a derivative at one boundary of the hysteresis loop to extrapolate scanning curves. If the main wetting curve $S_w(h)$ is known, the primary drying scanning curve starting at a reversal point h_{1w} on the main wetting curve is

$$S(h_{1w},h) = S_w(h) - \left(h - h_{1w}\right)\left.\frac{dS_w}{dh}\right|_h . \qquad (5.8)$$

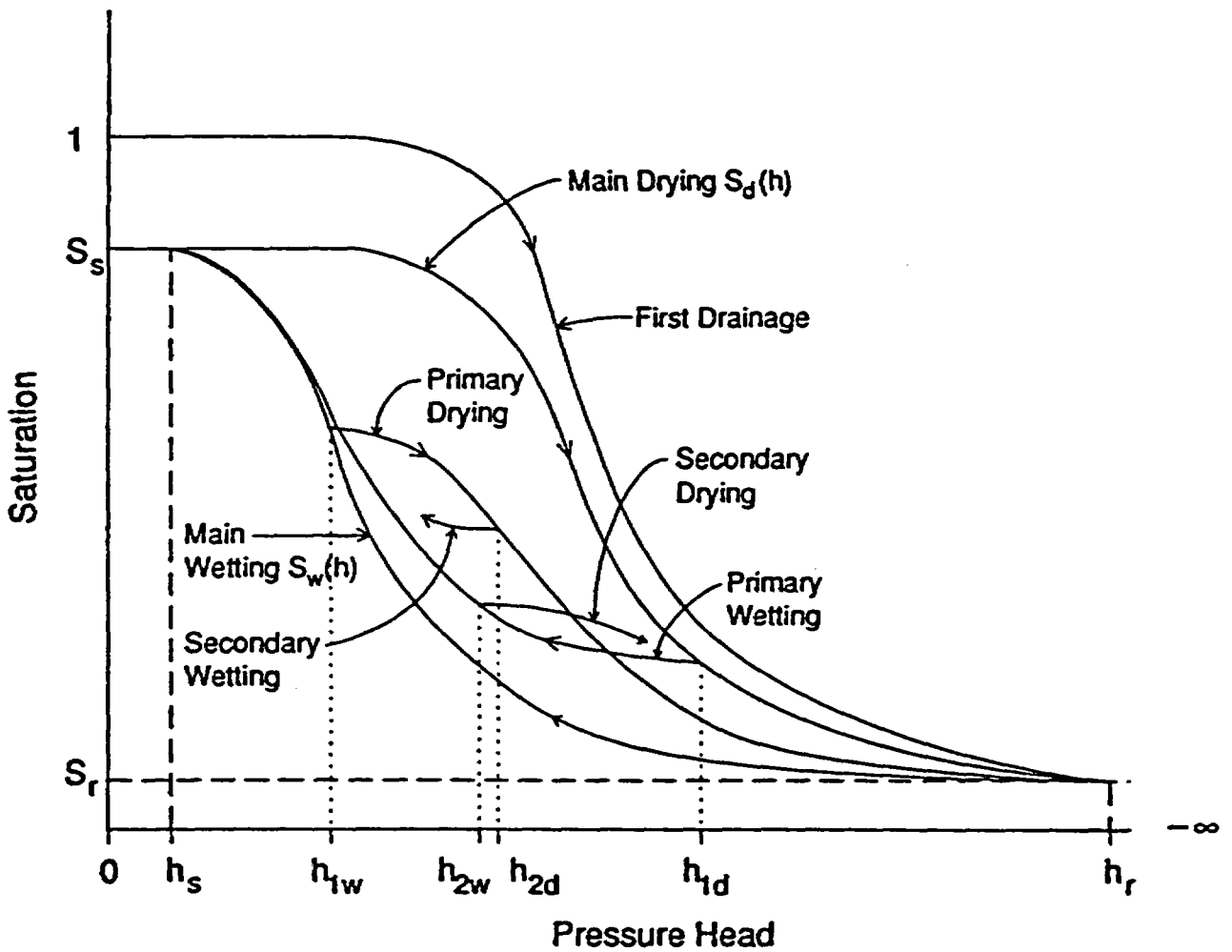

Figure 5-5. Capillary Hysteresis Curves.

The main drying curve corresponds to the limiting case with $h_{1w} = h_s$, the minimum suction for nearly saturated condition. The primary wetting scanning curve starting at a reversal point h_{1d} on the main drying curve is

$$S(h_{1d},h) = S_w(h) - \left(h - h_s\right)\left.\frac{dS_w}{dh}\right|_{h_{1d}}. \tag{5.9}$$

These equations were derived based on the assumption that the pore water distribution function $f(h_w,h_d)$ depends only on h_d and is independent of h_w. The model has been used to generate hysteresis curves by Haverkamp and Parlange (1986) in a study of mapping from soil texture to the saturation characteristic curve. According to Mualem and Morel-Seytoux (1978), this simple extrapolating model may distort the shapes of hysteresis curves.

If both boundaries of the hysteresis loop are known, the scanning curves can be interpolated from the main wetting and main drying curves. In the independent domain theory (Mualem, 1973, 1974), the pore water distribution function $f(h_w,h_d)$ is assumed to be a product of two functions, each depends on h_w and h_d, respectively:

$$f(h_w,h_d) = f_w(h_w)f_d(h_d). \tag{5.10}$$

The integrals of the independent distribution functions can be evaluated from the main wetting and main drying curves:

$$F_w(h) \equiv \int_{h_r}^{h} f_w(h')dh' = 1 - \exp\left[-\int_{h_r}^{h}\frac{dS_w(h')}{S_d(h') - S_w(h')}\right], \tag{5.11}$$

$$F_d(h) \equiv \int_{h_r}^{h} f_d(h')dh' = \frac{S_d(h) - S_w(h)}{1 - F_w(h)}. \tag{5.12}$$

The primary scanning curves for the same processes described in Equations 5.8 and 5.9 are:

$$S(h_{1w},h) = S_w(h) + [F_w(h_{1w}) - F_w(h)]F_d(h), \tag{5.13}$$

and

$$S(h_{1d},h) = S_w(h) + [1 - F_w(h)]F_d(h_{1d}), \tag{5.14}$$

respectively. Other higher order scanning curves after a series of alternating processes can be similarly expressed in terms of the cumulative distribution functions $F_w(h)$ and $F_d(h)$. If this model is further simplified by assuming $f_w(h) = f_d(h)$, based on the extension of a similarity hypothesis (Mualem, 1977), the cumulative distribution function can be expressed by a simple formula in terms of one branch of the hysteresis loop. The simplified model is shown to be good for sand with low air entry value but is not recommended for media which the effect of pore water blockage against air entry cannot be neglected.

The pore water blockage effect has been modeled by a domain dependent correction factor. In a modified domain model (Mualem, 1984), the factor is

$$F_D(S) = \frac{S_s - S}{[S_s - S_w(h^+)]^2}, \tag{5.15}$$

where h^+ is the pressure head at which $S_d(h^+) = S$. The primary drying scanning curve corresponding to Equation 5.8 or 5.13 is

$$S(h_{1w},h) = S_w(h_{1w}) - F_D(S)[S_s - S_w(h)][S_w(h_{1w}) - S_w(h)]. \tag{5.16}$$

This is an implicit equation since F_D in Equation 5.16 depends on the unknown saturation S. All higher order drying scanning curves are also implicit. On the other hand, all wetting scanning curves are explicit. For example, the primary wetting scanning curve corresponding to Equation 5.9 or 5.14 is

$$S(h_{1d},h) = S_d(h_{1d}) + F_D(S_d(h_{1d}))[S_s - S_w(h_{1d})][S_w(h) - S_w(h_{1d})]. \tag{5.17}$$

Niemi and Bodvarsson (1988) used the modified dependent domain model to demonstrate that the presence of capillary hysteresis in the matrix can enhance vertical fracture flow penetration. The modified dependent domain model has the desired feature that the scanning loops are closed; e.g., the secondary drying scanning curve passes through the point where the primary wetting scanning curve departs from the main drying curve. On the other hand, it fails to converge asymptotically to the correct residual or saturated saturation values for higher order scanning curves (Kool and Parker, 1987).

Other dependent domain models have been developed (e.g., Mualem and Dagan, 1975; Banerjee and Watson, 1984). These sophisticated models are more accurate than simpler models in predicting scanning curves but need the data of primary scanning curves, in addition to the main wetting and main drying curves, for calibration. The domain theories have also been used to predict permeability hysteresis (e.g., Mualem, 1976c). If permeability functions can be determined by the saturation characteristic curves, as discussed in the next section, different saturation hysteresis models will generate different predictions for the hysteresis of permeability functions. There are fewer experimental measurements of permeability hysteresis than saturation hysteresis. The existing data indicate that the hysteresis is significant in the $k(h)$ relationship but

minor in the $k(S)$ relationship. Pickens and Gilham (1980) suggested that $k(S)$ can be assumed to be non-hysteretic for all practical purposes.

5.2 Relative Permeability Curves

Relative permeability is the ratio of the effective permeability value under partial saturation to the value under saturated conditions. As a medium desaturates, the number of flow channels saturated with water decreases and the magnitude of flux and the corresponding effective permeability decreases. Because measurements of low flux are usually more difficult than measurements of moisture retention curves, especially for tight media, various models have been devised in the literature to predict the relative permeability curve from the saturation characteristic curve. We review some of these models in this section. We should emphasize that theoretical models cannot replace experimental measurements. The lack of measurements of relative permeabilities for both tuff matrix and tuff fractures is an important issue that merits full attention in modeling hydrological conditions at Yucca Mountain.

5.2.1 *Capillary Bundle Models*

In capillary bundle models, a medium is represented by a bundle of capillary tubes. If all the tubes have the same radius, denoted by r_{ae}, we shall have step functions for both the saturation characteristic curve and the relative permeability curve:

$$S(h) = \begin{cases} 1 & \text{if } |h| < |h_{ae}| \\ 0 & \text{if } |h| > |h_{ae}|, \end{cases} \tag{5.18}$$

and

$$k_r(h) = \begin{cases} 1 & \text{if } |h| < |h_{ae}| \\ 0 & \text{if } |h| > |h_{ae}|. \end{cases} \tag{5.19}$$

The air entry value h_{ae} is related to the radius r_{ae} by the capillary equation as in Equation 5.3.

The saturated permeability for each circular tube is $\frac{r_{ae}^2}{8}$ as in Equation 3.13 for Poiseuille flow. If there are N tubes in a core, the total flow rate through the tubes is

$$Q = N\frac{\pi r_{ae}^4 \Delta P}{8\mu l} \tag{5.20}$$

where ΔP is the pressure drop across the tube of length l. Because Darcy's law for saturated flow through a core is

$$Q = \frac{kA\ \Delta P}{\mu L} \tag{5.21}$$

for a core of permeability k, cross section area A, length L, and volume $V = AL$, the saturated permeability for the bundle of tubes is

$$k_{s,ct} = \frac{\phi}{\tau^2}\frac{r_{ae}^2}{8}. \tag{5.22}$$

The porosity ϕ is

$$\phi = \frac{N\pi r_{ae}^2 l}{AL} = \frac{V_p}{V}. \tag{5.23}$$

The porosity value depends on packing. The maximum porosity for the closest packing is $\frac{\pi}{2\sqrt{3}} = 0.907$. The tortuosity factor τ is

$$\tau = \frac{l}{L}. \tag{5.24}$$

In general, the length of a tortuous flow path l is longer than the length of core L. With $\phi < 1$ and $\tau \geq 1$, the maximum saturated permeability is

$$k_{s,\max} = \frac{r_{ae}^2}{8}. \tag{5.25}$$

We can easily generalize the uniform capillary tube model to a variable radius capillary tube model with discrete distribution $\sum_i N_i = N$:

$$Q = \sum_i \frac{N_i \pi r_i^4 \Delta P}{8\mu l_i}. \tag{5.26}$$

The saturated permeability is

$$k_{s,ct} = \frac{L}{A}\sum_i \frac{N_i \pi r_i^4}{8 l_i}. \tag{5.27}$$

If the maximum radius is denoted by r_{ae}, we can show that Equation 5.27 becomes

$$\begin{aligned} k_{s,ct} &= \frac{1}{8V}\sum_{r_i \le r_{ae}} \left[\frac{L}{l_i}\right]^2 N_i \pi r_i^4 l_i \le \frac{1}{8V}\sum_{r_i \le r_{ae}} N_i \pi r_i^4 l_i \\ &\le \frac{r_{ae}^2}{8V}\sum_{r_i \le r_{ae}} N_i \pi r_i^2 l_i = \phi\frac{r_{ae}^2}{8} < \frac{r_{ae}^2}{8} = k_{s,\max}. \end{aligned} \tag{5.28}$$

If we can determine r_{ae}, we can set an upper bound of Equation 5.25 for the saturated permeability.

Under partially saturated conditions, the fraction of tubes with radii greater than a capillary cutoff will be drained. The effective saturation and relative permeability are the ratios

$$S_e(h) = \frac{\sum_{r_i \le r_c} \pi r_i^2 l_i}{\sum_{r_i \le r_{ae}} \pi r_i^2 l_i} = \frac{\sum_{r_i \le r_c} \pi r_i^2 l_i}{\phi V} \tag{5.29}$$

and

$$k_r(h) = \frac{\sum_{r_i \le r_c} \frac{r_i^4}{l_i}}{\sum_{r_i \le r_{ae}} \frac{r_i^4}{l_i}} = \frac{\sum_{r_i \le r_c} \frac{r_i^2}{l_i^2} r_i^2 l_i}{\sum_{r_i \le r_{ae}} \frac{r_i^2}{l_i^2} r_i^2 l_i} \tag{5.30}$$

where the capillary radius is

$$r_c = -\frac{2\sigma\cos\Theta}{\rho g h} = -\frac{2\sigma\cos\Theta}{P_c}. \tag{5.31}$$

Equations 5.29 and 5.31 can be used to change the geometric variable of tube radius or pore size to saturation variable. The relative permeability function can be rewritten as

$$k_r(S_e) = \frac{\sum_{S_{e,i} \le S_e} \frac{S_{e,i}}{(h_i \tau_i)^2}}{\sum_{S_{e,i} \le 1} \frac{S_{e,i}}{(h_i \tau_i)^2}} = \frac{\int_0^{S_e} \frac{dS}{[h(S)\tau(S)]^2}}{\int_0^1 \frac{ds}{[h(S)\tau(S)]^2}}. \tag{5.32}$$

This is the form of relative permeability function in several models. Purcell (1949) treats τ as a constant. Fatt and Dykstra (1951) assume that τ is inversely proportional to the square root of r so that $[h(S)\tau(S)]^2$ in Equation 5.32 becomes $h(S)^3$. Burdine (1953) proposes that an effective tortuosity factor can be assumed for all flow channels so that the τ factor can be moved in front of the summations and integrals in Equation 5.32. The effective tortuosity factor is assumed to be inversely proportional to saturation S_e:

$$k_r(S_e) = \frac{S_e^2 \int_0^{S_e} \frac{dS}{h(S)^2}}{\int_0^1 \frac{dS}{h(S)^2}}. \tag{5.33}$$

Equation 5.33 is the integral representation of Burdine's capillary tube model. Another example is Alexander's model (1984) with the tortuosity factor proportional to $[r/S_e]^{1/2}$ so that

$$k_r(S_e) = \frac{S_e \int_0^{S_e} \frac{dS}{h(S)}}{\int_0^1 \frac{dS}{h(S)}}. \tag{5.34}$$

5.2.2 *Series-Parallel Models*

Extensions of simple capillary tube models have been proposed in the literature to account for variations of pore sizes not only in the plane normal to the direction of flow but also along the direction of flow. In series-parallel models, a core is also represented by a system of parallel tubes. A separation at any chosen plane normal to the length will exhibit two surfaces showing similar pore-size distributions. The medium is regarded as the random rejoining of these two surfaces. Let $f(r)$ be the pore size distribution function with $f(r)dr$ representing the fraction of total pore area which has radii in the interval $r \to r+dr$. The probability of pores of radii $r \to r_1+dr_1$ on surface 1 randomly encountering pores of radii $r_2 \to r_2+dr_2$ on surface 2 is $f(r_1)\,f(r_2)\,dr_1 dr_2$. With tube permeability proportional to radius squared, the relative permeability function is of the form

$$k_r(S_e = \frac{\int_0^{r_c}\int_0^{r_c} r^2 f(r_1)f(r_2)dr_1dr_2}{\tau_{ae}\tau_{ae}\int_0^{}\int_0^{} r^2 f(r_1)f(r_2)dr_1dr_2}. \quad (5.35)$$

Childs and Collis-George (1950) (see also Marshall, 1958; Brutsaert, 1967) assume that the effective resistance to flow in the sequence is confined to the smaller of the pores, with r in Equation 5.35 equal to $r_<$ ($r_< = r_1$ if $r_1 < r_2$, and $r_< = r_2$ if $r_2 < r_1$). Mualem (1976b) uses the total resistance of both tubes in series

$$\left[\frac{r^4}{L}\right]^{-1} = \left[\frac{r_1^4}{l_1}\right]^{-1} + \left[\frac{r_2^4}{l_2}\right]^{-1} \quad (5.36)$$

and assumes that the lengths are proportional to the tube radii (Fatt, 1956):

$$\frac{l_1}{l_2} = \frac{r_1}{r_2}. \quad (5.37)$$

Equations 5.36 and 5.37, together with the volume equality

$$r^2L = r_1^2l_1 + r_2^2l_2, \quad (5.38)$$

can be solved to obtain

$$r^2 = r_1r_2. \quad (5.39)$$

With Equation 5.39, the double integral in Equation 5.35 becomes the product of two single integrals. As in capillary tube models, we can also introduce tortuosity correction factors of the form S_e^i in front of Equation 5.35 to account empirically for the tortuosity effects. Millington and Quirk (1961) suggest that $i = \frac{4}{3}$ and Kunze et al. (1968) suggest that $i = 1$ to modify the Childs and Collis-George model (1950). Mualem (1976b) suggests that $i = \frac{1}{2}$ for his model from comparison with data of 45 soil materials. In terms of saturation, Mualem's series-parallel model is

$$k_r(S_e) = S_e^{1/2}\left[\frac{\int_0^{S_e}\frac{dS}{h(S)}}{\int_0^{1}\frac{dS}{h(S)}}\right]^2 . \qquad (5.40)$$

Mualem's model, together with Burdine's model, are frequently used in the literature.

5.2.3 *Comparison of Soil Permeability Models*

Although the predictive models described in the last section can be applied directly to measured saturation characteristic data to generate permeability functions in tabular form, we will focus on comparisons based on analytic expressions as applied to limited relative permeability data. Analytic expressions for the relative permeability functions can be derived (Brooks and Corey, 1966; van Genuchten, 1980) for the models of Burdine (1953, Equation 5.33) and Mualem (1976b, Equation 5.40), using the saturation characteristic equations of Brooks and Corey (1966, Equation 5.1) and van Genuchten (1980, Equation 5.4).

Brooks and Corey - Burdine:

$$k_r(h) = \begin{cases} 1 & \text{if } |\alpha h| < 1 \\ |\alpha h|^{-2-3\lambda} = S_e^{3+2/\lambda} & \text{if } |\alpha h| \geq 1 \end{cases} \qquad (5.41)$$

Brooks and Corey - Mualem:

$$k_r(h) = \begin{cases} 1 & \text{if } |\alpha h| < 1 \\ |\alpha h|^{-2-2.5\lambda} = S_e^{2.5+2/\lambda} & \text{if } |\alpha h| \geq 1 \end{cases} \qquad (5.42)$$

van Genuchten - Burdine:

$$k_r(h) = \frac{1 - |\alpha h|^{n-2}[1 + |\alpha h|^n]^{-m}}{[1 + |\alpha h|^n]^{2m}} = S_e^{2}[1 - (1 - S_e^{1/m})^m], \qquad (5.43)$$

with $m = 1 - 2/n$, $0 < m < 1$, and $n > 2$.

van Genuchten - Mualem:

$$k_r(h) = \frac{\{1 - |\alpha h|^{n-1}[1 + |\alpha h|^n]^{-m}\}^2}{[1 + |\alpha h|^n]^{m/2}} = S_e^{1/2}[1 - (1 - S_e^{1/m})^m]^2, \qquad (5.44)$$

with $m = 1 - 1/n$, $0 < m < 1$, and $n > 1$.

These four equations are compared in Figures 5-6 and 5-7 in dimensionless plots of relative permeability versus scaled pressure head $|\alpha h|$. The equations based on van Genuchten predict lower relative permeabilities than equations based on Brooks and Corey, especially in the small suction region around air entry point $|\alpha h| = 1$ near saturation. Asymptotically in the range of large suction with $|\alpha h| \gg 1$, Equation 5.43 approaches

$$m|\alpha h|^{-2-3nm} = \left(\frac{\lambda}{\lambda+2}\right)|\alpha h|^{-2-3\lambda} \qquad (5.45)$$

and Equation 5.44 approaches

$$m^2|\alpha h|^{-2-2.5nm} = \left(\frac{\lambda}{\lambda+1}\right)^2|\alpha h|^{-2-2.5\lambda}. \qquad (5.46)$$

Except for the multiplying factors $\left(\frac{\lambda}{\lambda+2}\right)$ and $\left(\frac{\lambda}{\lambda+1}\right)^2$, these asymptotic functional forms of van Genuchten-based equations are the same as Brooks and Corey-based equations (5.41 and 5.42). In media with wide pore-size distributions with $\lambda \ll 1$ for which the multiplying factors are small, van Genuchten's relative permeabilities can be orders of magnitude lower than Brooks and Corey's relative permeabilities.

Brooks and Corey (1966) measured the relative permeabilities of three sands, two soils, two sandstones, one glass bead pack, and one fragmented mixture of sand and clay; using a light hydrocarbon as the wetting fluid. The relative permeability measurements on some unconsolidated samples might have different degrees of soil compaction from saturation characteristics measurements. Measured slopes on log-log plots of relative permeability versus pressure head were compared with computed values of $2 + 3\lambda$, with λ's determined in saturation measurements. The Brooks and Corey-Burdine comparison is plotted in Figure 5-8. If we use Mualem's model with slope $2 + 2.5\lambda$ (Equation 5.42) or Alexander's model (1984) with slope $1 + 3\lambda$ (from Equations 5.1 and 5.34) instead of Burdine's model with slope $2 + 3\lambda$ so that computed slopes are lower, we will improve the agreements for some soil, sandstone, and fragmented mixture samples, and worsen the agreements for sands and other samples. The Brooks and Corey data cannot quite differentiate among the models as shown in Figure 5-8.

In terms of effective saturation S_e, Equations 5.41 and 5.42 are of the general form of $k_r(S_e) = S_e^i$. The exponent i has been proposed to have values 3, 3.5, and 4 by Irmay,

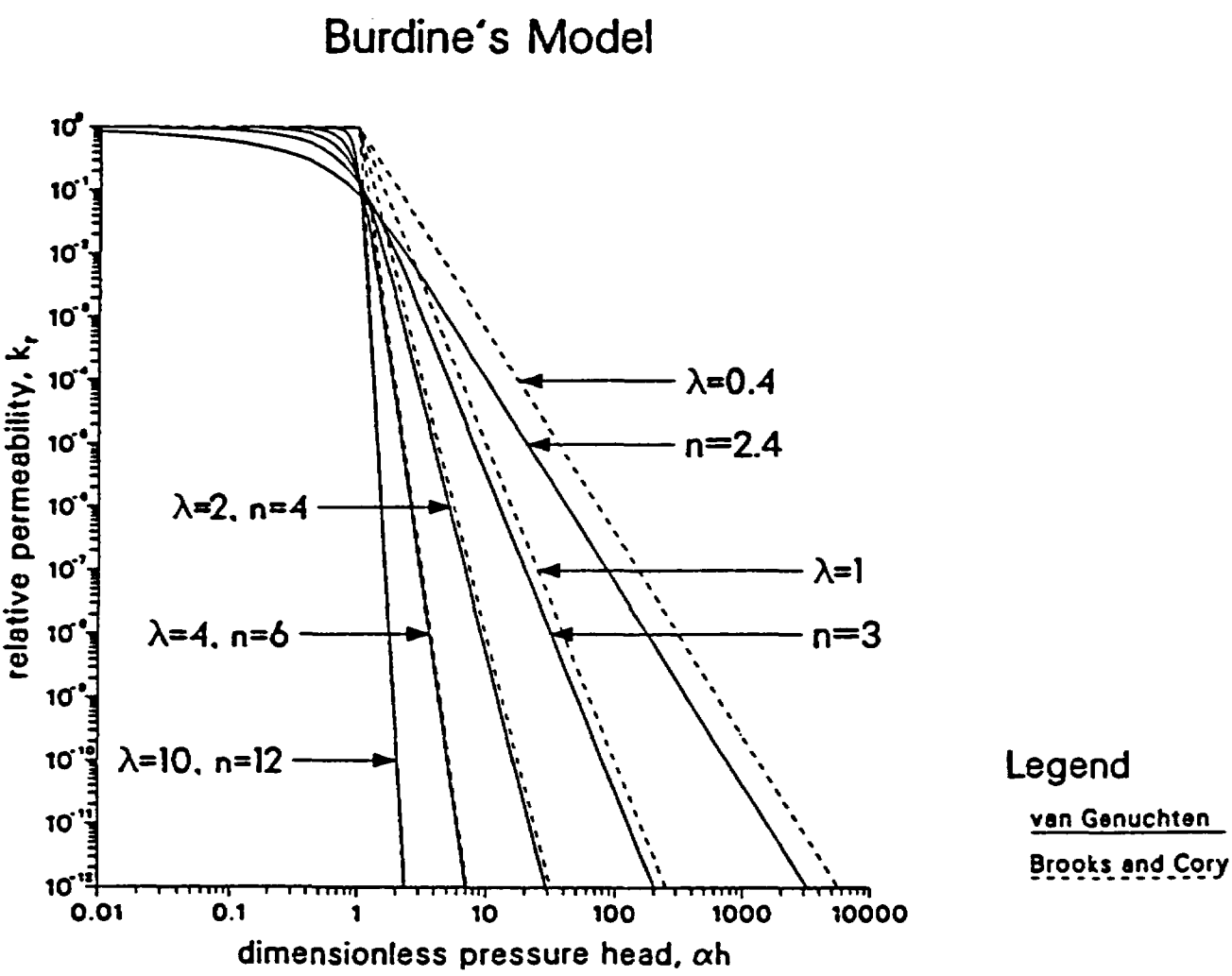

Figure 5-6. Scaled Relative Permeability Curves of the van Genuchten-Burdine and Brooks and Corey-Burdine Models.

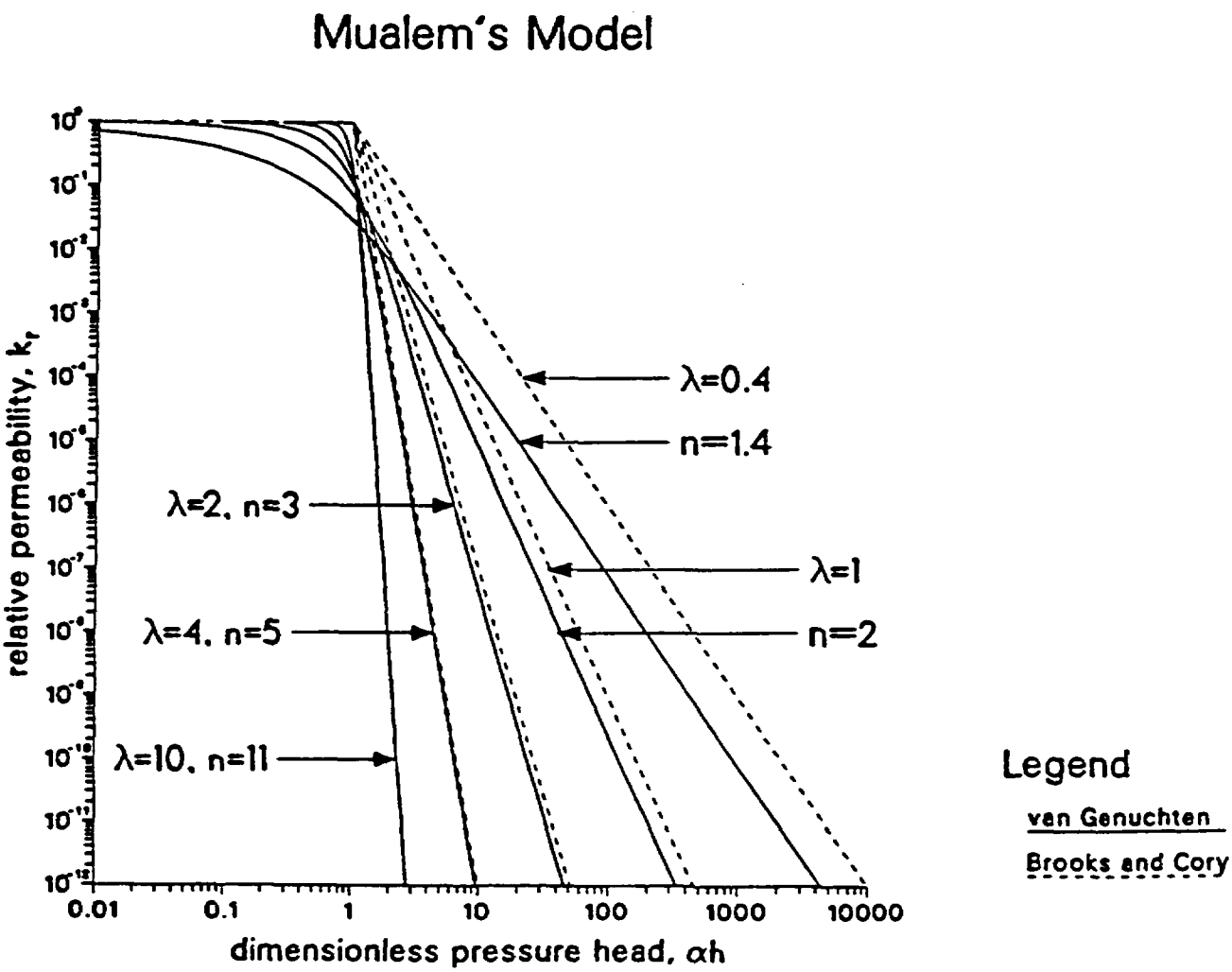

Figure 5-7. Scaled Relative Permeability Curves of the van Genuchten-Mualem and Brooks and Corey-Mualem Models.

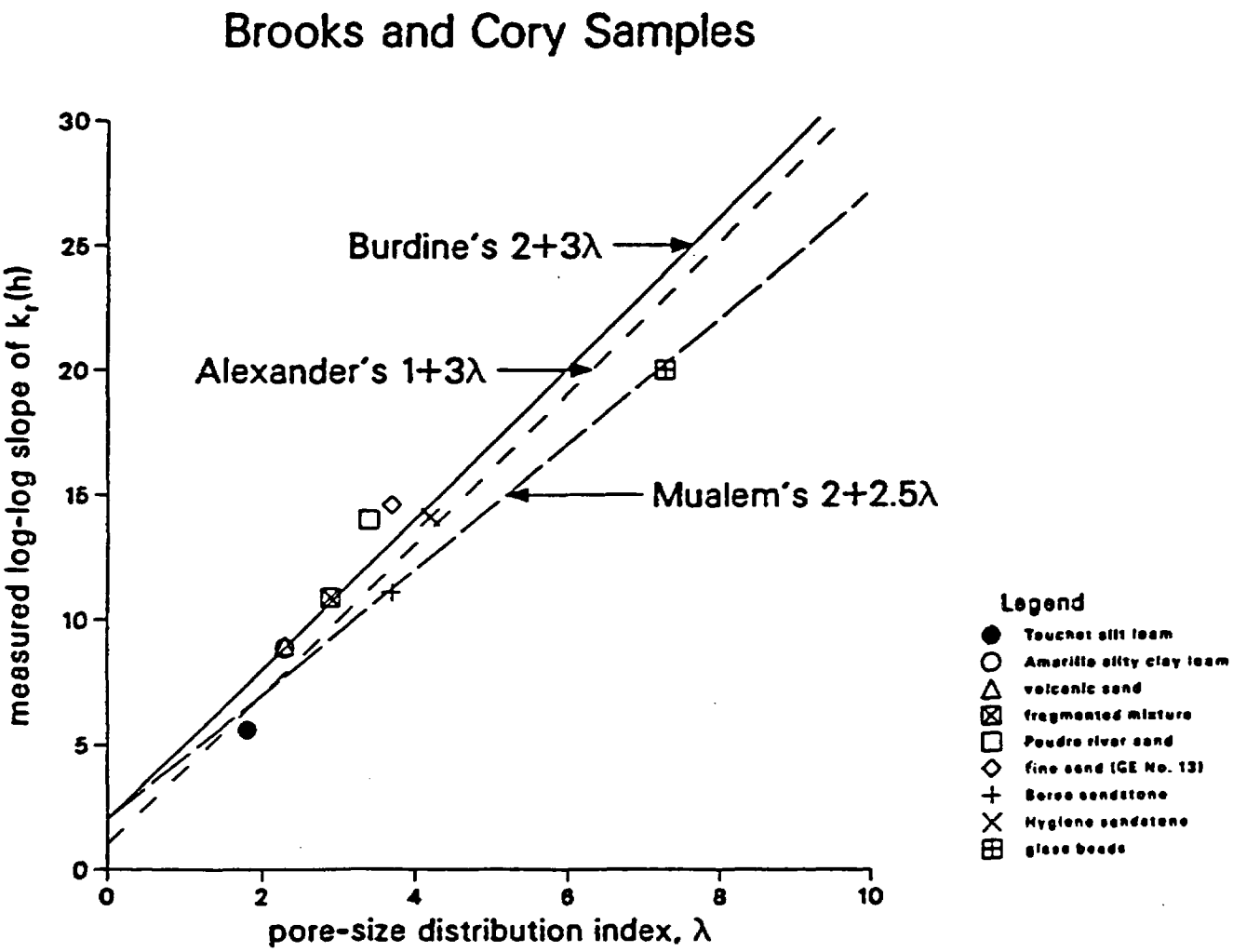

Figure 5-8. Comparison of Measured and Computed Values of Log-Log Slopes in Relative Permeability-Suction Pressure Plots.

Averjanov, and Corey, respectively, as quoted by Brooks and Corey (1966). Irmay's exponent 3 is for a uniform capillary tube model. Corey's exponent 4 is frequently used in petroleum literature. Brooks and Corey's exponents are $3 + 2/\lambda$ for Burdine's model (Equation 5.41) and $2.5 + 2/\lambda$ for Mualem's model (Equation 5.32). For soils with wide pore-size distributions with low λ values, the saturation exponent i can be large. According to El-Kadi (1985), $i = 9.33 \pm 7.8$, from 39 soil samples in Mualem's catalog (1976a). El-Kadi also determined $\lambda = 0.44 \pm 0.22$, from 448 soil samples of Rawls et al. (1981).

Equations 5.43 and 5.44 are based on van Genuchten's formula, using Burdine's model and Mualem's model, respectively. Because Burdine's model in Equation 5.43 requires $n > 2$ and Mualem's model in Equation 5.44 requires only $n > 1$, Mualem's model can be applied to a wider variety of soils than Burdine's model. Equation 5.44 was compared with experimental data for 5 soils by van Genuchten (1980). Only one soil (Beit Netofa clay) showed noticeable difference between measured relative permeability curve and that computed with Equation 5.44. In van Genuchten's equation (5.4), both m and n can be considered to be independent parameters instead of the unique relationship of $m = 1 - 2/n$ in Equation 5.43 and $m = 1 - 1/n$ in Equation 5.44. General solutions in terms of incomplete Beta function can be derived (van Genuchten and Nielsen, 1985). Similar solutions can be derived for the Su and Brooks equation (1975) which is originated from fitting the saturation characteristic curve to a Pearson type VIII distribution function. van Genuchten and Nielsen (1985) compared Equation 5.42, Equation 5.44, and the variable m,n incomplete Beta function solution with relative permeability data for two soils and diffusivity (permeability divided by water storage capacity) data of another soil. With one extra parameter for the variable m,n model, the match with experimental curves improved as expected. van Genuchten and Nielsen also emphasized the importance of good fitting near saturation and indicated that the saturated water content θ_s and saturated conductivity K_s should be treated as empirical fitting parameters in addition to α, n, m, and θ_r. The van Genuchten-Mualem model (Equation 5.44) has been used in tuff studies (Peters et al., 1984).

Alexander (1984) compared 14 different models for permeability predictions with data of 23 soil materials in the literature. The 14 models consist of 7 analytic expressions, 3 trapezoidal approximations, and 4 discrete approximations. The first 3 analytic expressions are based on Brooks and Corey (1966) equation (5.1) in 3 models: Burdine (1953), Mualem (1976b), and Alexander (1984). The next 3 analytic expressions are based on Campbell's equation (1974) in the same 3 models. Campbell's equation is same as Equation 5.1 with $S_r = 0$. The 7-th analytic expression is the van Genuchten-Mualem equation (5.44). The moisture-retention data, in tabulated form without fitting to analytic functions, can be used directly in these 3 models with trapezoidal approximation for the permeability integrals. The permeability predictions can also be expressed in discrete summations, instead of integrals, over pore classes as in the approximations of Marshall (1958), Millington and Quirk (1961), Kunze et al. (1968), and Sinclair (1981).

Judging from the graphical comparisons between predicted permeabilities and measured permeabilities presented by Alexander (1984) for these 14 models, errors over five orders of magnitude can be generated by some predictive models, especially for low permeability values in dry soils. The accuracy of the prediction by each model differs for different soil textures. The van Genuchten-Mualem model has low average relative errors for loamy soils. This model also tends to underpredict the permeability through the entire range of $k(h)$ for most of the soils

(see Figure 5-9 for loamy soils). By treating the saturated conductivity K_s as a fitting parameter, instead of a fixed parameter, the discrepancy between predicted and measured permeability can be substantially reduced (van Genuchten and Nielsen, 1985; Yates et al., 1989).

Since the permeability prediction is sensitive to the use of different models and different fitting parameters, as shown in the soil literature, we need to carefully examine the use of permeability prediction models in tuff studies. If unsaturated permeability is underestimated, we may underestimate the infiltration fluxes and overestimate the groundwater travel times.

In addition to models that predict relative permeability functions from saturation characteristic measurements, other models in the literature use soil texture or particle size analysis data to predict permeability functions. Based on percentages of sand, clay, and silt, soils can be catalogued according to USDA (1951) or other similar texture classification schemes. Clapp and Hornberger (1978), McCuen et al. (1981), and Cosby et al. (1984), among others, determined the average values of Campbell or Brooks and Corey parameters for each textural class from the watershed data of Holtan et al. (1968) and Rawls et al. (1976). The average model parameters for a given textural class could then be used for a soil in that class. Empirical relationships between model parameters and percentages of sand, clay, or silt can also be estimated (Ghosh, 1976; Cosby et al., 1984). In addition to soil texture classification, soil particle size distribution can be measured. Bloemem (1980) and Arya and Paris (1981) proposed empirical equations to describe pore space from particle size distributions. Alexander and Skaggs (1987) evaluated 14 different methods to predict unsaturated permeability from soil texture and/or particle size distribution data. Judging from the graphical comparisons presented in their paper, we may expect errors of several orders of magnitude in the predictions. The deviations of predicted values from the measured values can be even worse than the example shown earlier in Figure 5-9. Some models overestimate and some underestimate in different ranges of permeability values. Tuff may also be classified in accordance with degrees of welding, zeolization, and vitrification. If we wish to use these tuff texture data to supplement saturation and relative permeability measurements, we need to quantify and evaluate the uncertainties associated with the models.

5.3 Fracture Saturation and Fracture Permeability Models

For a fractured porous medium, we need fracture saturation characteristic curves and relative permeability curves in addition to the curves for the porous matrix. Relatively far fewer studies are available in the literature on desaturation processes and partially saturated flows in discrete fractures. Evans and Huang (1982) treated the fracture network as a collection of parallel plates with variable apertures. The aperture distribution for the parallel plates was assumed to be lognormal, as suggested by Snow (1970). Wang and Narasimhan (1985) treated discrete fractures with rough walls and finite contact areas and included flow through porous matrix. The aperture distribution function of a rough wall fracture was assumed to have the form of a one-parameter gamma distribution function (Tsang, 1984). Harrold et al. (1985) developed a fracture model with quasi periodic roughness structure. In this section, we summarize these fracture models.

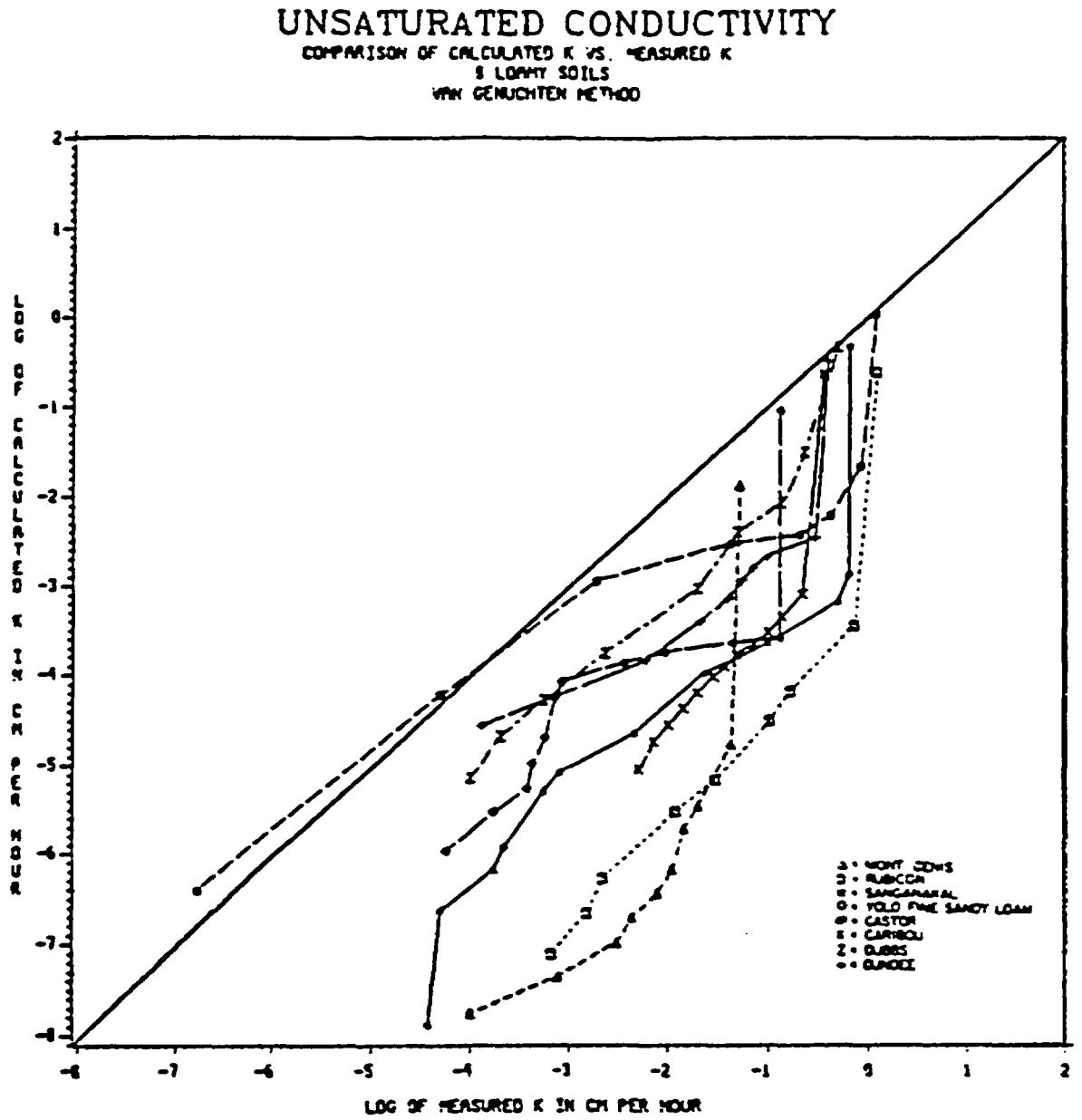

Figure 5-9. Predicted Permeability Using the van Genuchten-Mualem Model Versus Measured Permeability for Eight Loamy Soils (Alexander, 1984).

The distribution of "apparent apertures," measured on granite outcrops by photographing fractures treated with a fluorescent dye penetrant, was found to be very close to lognormal (Bianchi and Snow, 1969; Snow, 1970). Although the correlation between observed apparent aperture and effective hydraulic aperture may be poor (Gale, 1975), the hydraulic aperture in parallel plate models is frequently assumed in the literature to be lognormally distributed (Long et al., 1982; Evans and Huang, 1982). For the smaller scale within an individual discrete fracture with rough walls and variable apertures, the aperture distribution function can be measured by scanning the open fracture surfaces and tracing the roughness profiles. The mismatch between the roughness profiles between two surfaces yields the aperture distribution function $f_0(b_0)$, with subscript 0 denoting the condition of zero stress. Under zero stress, the fracture surfaces are in point contact and the contact area between the walls is zero. Analysis of natural granite fractures shows that $f_0(b_0)$ takes on a skewed shape, with long tails toward large apertures (Gentier, 1986). A one-parameter distribution, the gamma distribution, could fit the aperture measurements well (Tsang, 1984). Wang and Narasimhan (1985) used this form of distribution function to study the desaturation of discrete fractures. With gamma distribution, instead of the lognormal distribution, analytic expressions can be derived for the fracture saturation characteristic curve, the fracture relative permeability curve, and the effective fraction of area for fracture-matrix flow.

The gamma distribution is simply

$$f_0(b_0) = \beta^2 b_0 \exp(-\beta b_0) \tag{5.47}$$

and β is the distribution parameter. As we will show later for tuff studies, β can be determined by tuff fracture geometry and permeability data. For a given fracture surface plane which is divided into N equal area units, if there are n_i units having the apertures between b_i and b_{i+1}, then the aperture distribution is approximated by $f_i = n_i/N$. In the limit of large N, the histogram of f_i over aperture defines a continuous and normalized aperture distribution function. For the discrete histogram, an averaging with f_i is equivalent to counting the fraction n_i/N of the fracture plane with aperture between b_i and b_{i+1}. For a continuous and normalized aperture distribution function, the averaging over aperture is equivalent to normalized areal integration over the fracture plane.

For in situ fractures, the normal stress is greater than zero and the fracture surfaces will be in contact. The fraction of contact area, ω_o, of the total area of the fracture at any stress can be expressed as

$$\omega_o = \int_0^{b_c} f_0(b_0) db_0 = 1 - \exp(-\beta b_c)(1 + \beta b_c). \tag{5.48}$$

If ω_o is known, βb_c can be determined by the root of Equation 5.48. All the portions of fracture with initial aperture less than the contact aperture b_c will be in contact. The aperture under stress will be $b = b_0 - b_c$ in the open sections of the fracture. The aperture distribution of the fracture under stress will be denoted by $f(b)$, which is

$$f(b) = f_0(b + b_c) = \beta^2(b + b_c)\, exp[-\beta(b + b_c)]. \tag{5.49}$$

As the fracture desaturates under a negative pressure head, h, only the portions with aperture less than the saturation cutoff aperture b_s, or

$$b_s = -\frac{2\sigma\cos\Theta}{\rho g h}, \tag{5.50}$$

will be saturated. Flow from the matrix into the fracture and through the fracture into the next matrix block can occur only through the saturated portions and through the contact areas. The effective fraction of area for fracture-matrix flow, including the contact area, is

$$\omega(h) = \omega_o + \int_0^{b_2} f(b)db. \tag{5.51}$$

Because fracture volume is the product of aperture and area, and averaging of aperture distribution function over aperture is equivalent to areal integration over fracture surface, the fracture saturation is

$$S(h) = \frac{< b >_s}{< b >_1} \tag{5.52}$$

where the brackets $< >$ denote averaging:

$$< b >_s = \int_0^{b_s} bf(b)db. \tag{5.53}$$

Only the flow channels with aperture less than b_s can contribute to flow under partially saturated conditions. If flow channels are parallel to each other, the cube law can be generalized under partially saturated conditions by replacing the cube of the single value for the aperture by $< b^3 >_s$. The relative permeability for the fracture is therefore

$$k_r(h) = \tau(h)\frac{< b^3 >_s}{< b^3 >_1}. \tag{5.54}$$

The $\tau(h)$ factor accounts for modifications to the parallel-channel assumption. Equations 5.52 and 5.54 (with $\tau = 1$) are equivalent to Equations 5.29 and 5.30 of the capillary bundle models.

Equations 5.51, 5.52, and 5.54 can be used to determine effective fracture-matrix area ω, fracture saturation S, and relative permeability k_r for any given aperture distribution. Evans and Huang (1982) integrated Equations 5.52 and 5.54 (without the $\tau(h)$ factor) numerically over the lognormal distribution function for a parallel plate fracture network model. Wang and Narasimhan (1985) used the one-parameter gamma distribution Equation 5.49 to derive the following analytic expressions.

$$\omega(h) = 1 - exp(-\beta b_c - \beta b_s)(1 + \beta b_c + \beta b_s). \tag{5.55}$$

$$S(h) = \frac{1}{2+ \beta b_c}\Big\{[2 - exp(-\beta b_s)(2 + 2\beta b_s + \beta^2 b_s^2)] + \beta b_c[1 - exp(-B b_s)(1 + \beta b_s)]\Big\}. \tag{5.56}$$

$$k_r(h) = \tau(h)\frac{1}{6(4 + \beta b_c)}\Big\{[24 - exp(-\beta b_s)(24 + 24\beta b_s + 12\beta^2 b_s^2 + 4\beta^3 b_s^3 + \beta^4 b_s^4)] + \beta b_c[6 - exp(-\beta b_s)(6 + 6\beta b_s + 3\beta^2 b_s^2 + \beta^3 b_s^3)]\Big\}. \tag{5.57}$$

Figures 5-10, 5-11, and 5-12 illustrate these fracture characteristic curves and show that discrete fractures can be easily desaturated, effective fracture-matrix flow area reduced, and permeabilities decreased with small suctions in the range of -0.1 to -10 m. The parameters β and b_c in Equations 5.55, 5.56, and 5.57 are determined from tuff fracture properties. For each fracture set with spacing D_f, $\frac{< b^3 >_1}{12D_f}$ is assumed to contribute to the bulk continuum permeability under saturated condition. This is a conservative estimation with actual saturated permeability smaller than this parallel plate set model. If bulk permeability can be determined by well testing and if spacings of the fracture set can be determined from fracture frequency and orientation data, $< b^3 >_1$ can be determined for the vertical fracture sets and horizontal fracture set. The β parameter for each set can then be solved by

$$< b^3 >_1 = \frac{6(4 + \beta b_c)}{\beta^3} exp(-\beta b_c) \tag{5.58}$$

with βb_c determined by Equation 5.48. The fraction of in situ contact area ω_o in Equation 5.48 is assumed in our work to correspond to fraction of fracture coating, based on the assumption that hydrochemical alterations occur in contact areas which remain at continuous contact with water for a long time.

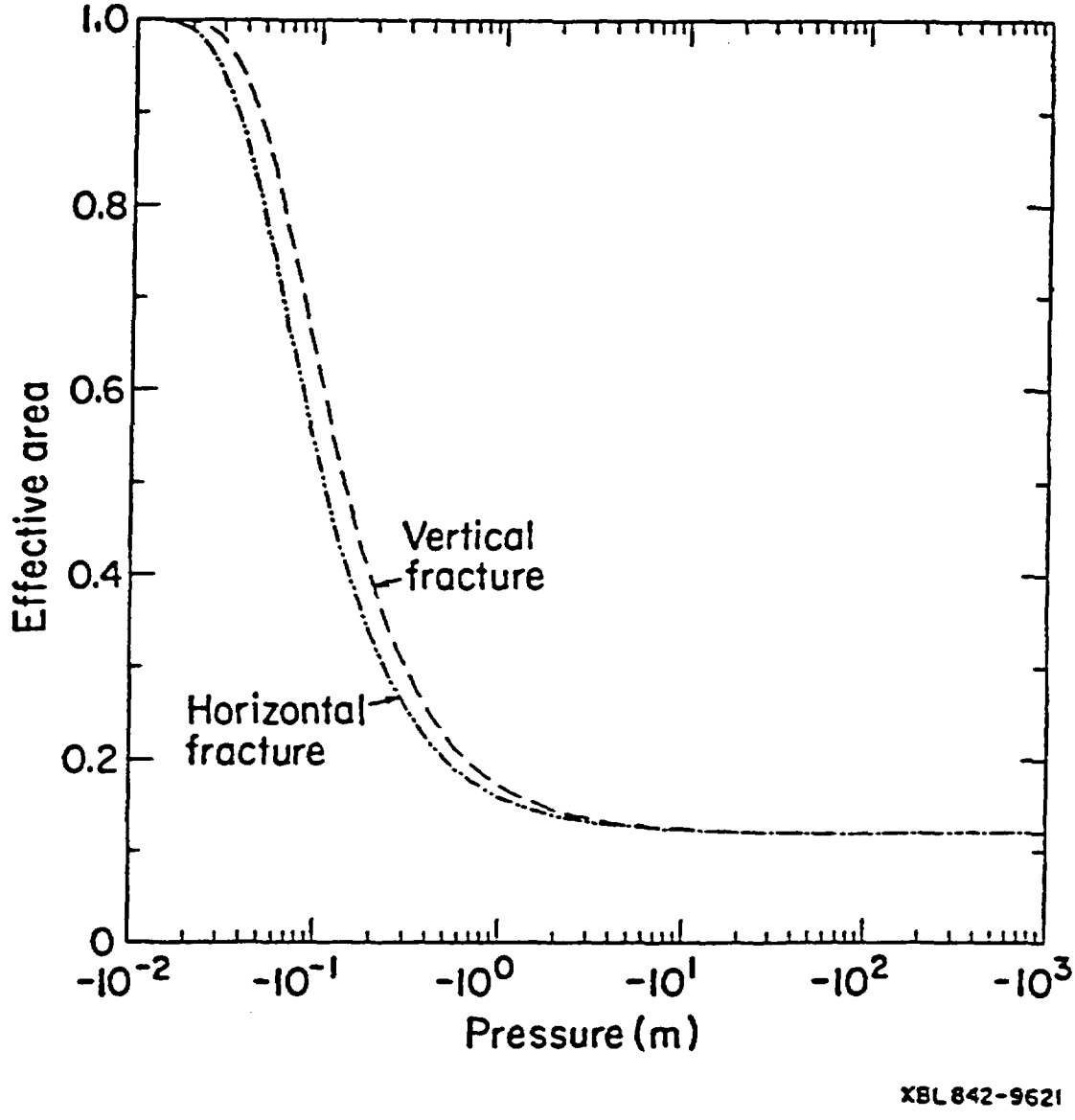

Figure 5-10. Effective Fracture-Matrix Flow Areas at Fracture-Matrix Interfaces.

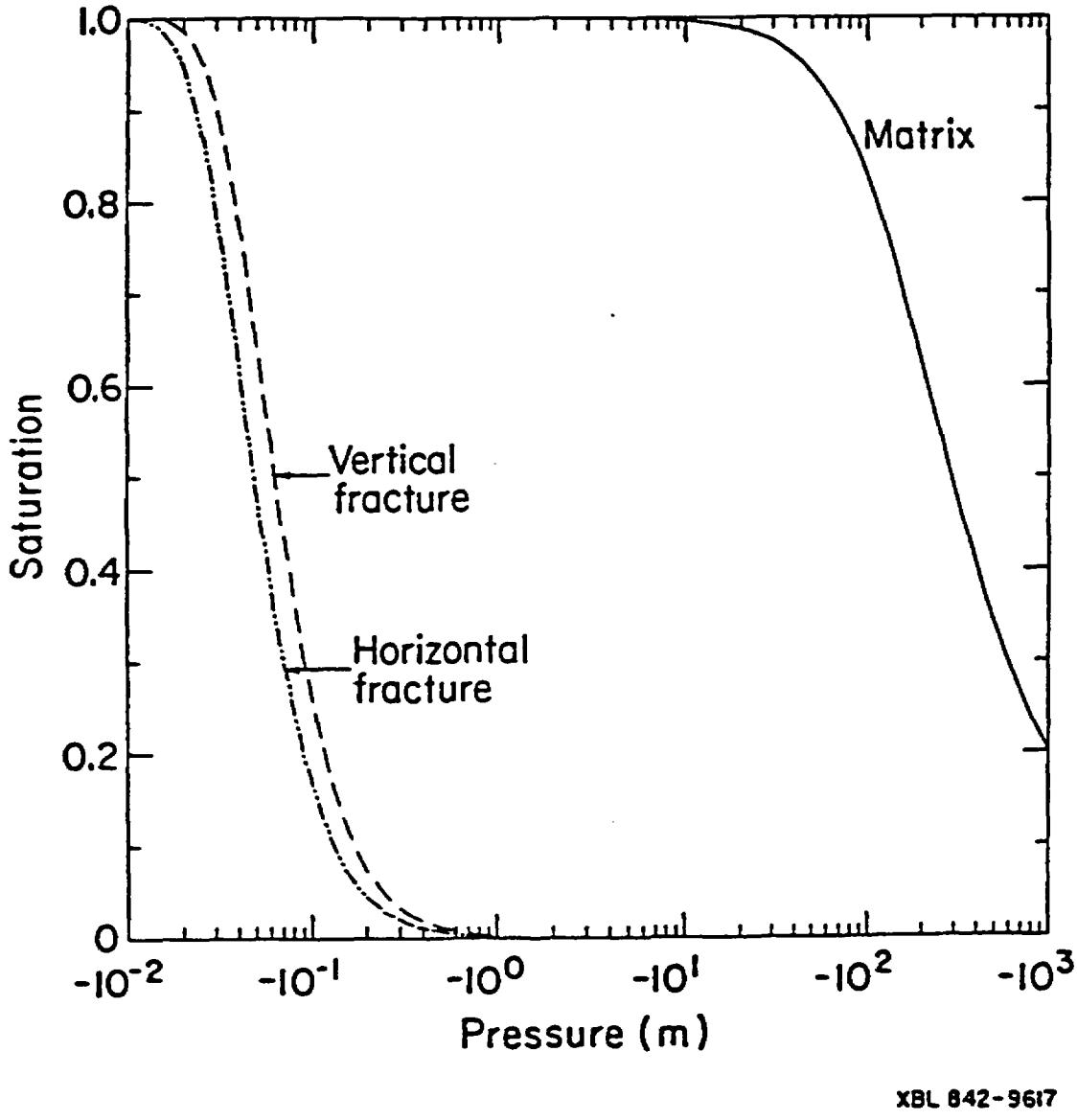

Figure 5-11. Characteristic Curves of Discrete Fractures and Tuff Matrix.

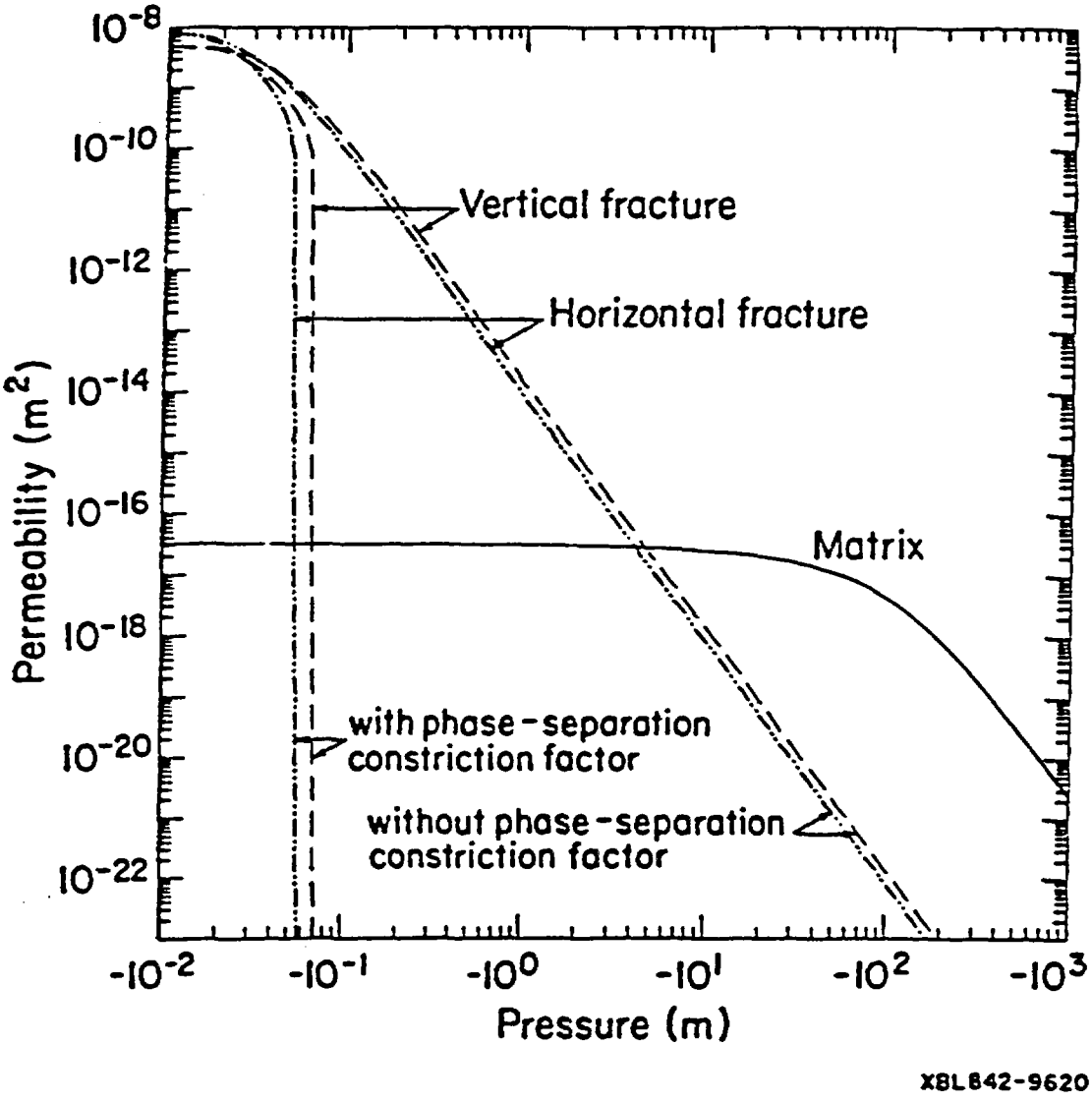

Figure 5-12. Permeabilities of Discrete Fractures and Tuff Matrix.

In the asymptotic limit of large negative pressure head or small b_s, Equation 5.56 approaches

$$S(h) \approx \frac{\beta b_c}{2(2 + \beta b_c)}(\beta b_s)^2. \tag{5.59}$$

If Equation 5.59 is compared with Brooks and Corey function (Equation 5.1) and van Genuchten function (Equation 5.4) with asymptotic dependence $|\alpha h|^{-\lambda}$, we can set the equivalent pore-size or aperture-size distribution index $\lambda = 2$ for this fracture model. We can also determine an equivalent air entry scaling factor α. From α, similar to Equation 5.3 and with Equation 5.50, we can define, for the gamma fracture model, the air entry aperture as

$$b_{ae} = \left[\beta\left[\frac{\beta b_c}{2(2 + \beta b_c)}\right]^{1/2}\right]^{-1}. \tag{5.60}$$

Equation 5.60 will be used in Section 6 to compare the air entry values between fractures and porous matrix.

For the relative permeability (Equation 5.57), the asymptotic behavior is

$$k_r(h) \approx \tau(h)\frac{\beta b_c}{24(4 + \beta b_c)}(\beta b_s)^4 \approx \tau(h)\frac{(2 + \beta b_c)^2}{6\beta b_c(4 + \beta b_c)}S(h)^2. \tag{5.61}$$

For the simple case with the factor $\tau = 1$ and with all the flow channels parallel to each other, Equation 5.61 shows that the relative permeability is proportional to S^i, with the exponent $i = 2$, in the asymptotic limit. From the earlier discussion on different parallel and parallel-series capillary tube models for soils, we note that both the tortuosity effect and the resistance-in-series effect can increase the magnitude of the exponent of saturation dependence, or equivalently, decrease the relative permeability in the dry range. Wang and Narasimhan (1985) recognized that the parallel-flow-channel assumption overestimated the relative permeability and introduced the $\tau(h)$ factor to modify the relative permeability function. Instead of tortuosity and resistance-in-series effects, Wang and Narasimhan focused on a phase constriction effect which might be more important for fracture flow within a plane. As a fracture desaturates, the liquid phase may change from continuous configuration to discontinuous configuration. If liquid phase is discontinuous with liquid islands surrounded by air, water cannot flow along the fracture surface and the relative permeability for liquid flow is zero. This phase separation effect to constrict and cut off flow may be stronger than tortuosity and resistance-in-series effects which only reduce the relative permeability but do not cut off the flow completely. Wang and Narasimhan (1985) used the idealized phase configuration changes illustrated earlier in Figure 2-2 to quantify the phase constriction factor $\tau(h)$. As illustrated in Figure 5-12, the fracture permeabilities can be very sensitive to whether this phase constriction factor is taken into account.

In a talk at an American Geophysical Union meeting, Harrold et al. (1985) summarized the statistical analyses of roughness profiles measured on volcanic tuff outcrops at Yucca Mountain. Fourier analyses indicated that a recurring periodicity occurred among fracture-wall asperities of various sizes in 55 roughness profiles. If periodicity were well-defined, a fracture model could be constructed with wavy surfaces composed of parallel features of hills and valleys along a given direction. If these two wavy surfaces were displaced laterally so that the hills on one surface were in contact with hills on the other surfaces, the unsaturated flow would be along the periodic contact strips. The fracture permeability would be high along the given direction and low perpendicular to it under partially saturated conditions. The anisotropic fracture permeability functions from this model were used in the simulation study by Rulon et al. (1986).

If the periodicity is large and the fracture surfaces are not displaced to the extent that hills are lined up, the unsaturated flow will be controlled mainly by smaller-scale roughness and will not be sensitive to large-scale periodicity. The periodic strip pattern is unusual when it is compared with other types of rock surfaces which are typically more irregular and less anisotropic. Brown and Scholz (1985) studied roughness profiles of different rock samples over six orders of spatial frequency scale. The Fourier power spectra have a nearly featureless nature and no obvious periodicity occurs, even for some surfaces with visually anisotropic textures. The rough surfaces can be described by scale-invariant fractal geometry (Mandelbrot, 1983). Wang et al. (1988b) constructed a fractal fracture model designed to lead to a more realistic representation of fracture aperture distribution to replace the schematic model in Figure 2-2.

5.4 Comparison of Fracture and Matrix Characteristics

The discrete fractures and porous matrix have very different characteristics in geometry, in saturation, and in permeability. The fracture apertures are larger than the pores in the matrix. Therefore, the fractures can be more easily desaturated with smaller suction pressure than the matrix, and the fracture permeabilities can drastically change from saturated values orders of magnitude larger than matrix values to unsaturated values much smaller than matrix values. In Figures 5-11 and 5-12, the saturation characteristics and permeability changes for discrete fractures and porous tuff matrix are compared. The fracture permeability curves, both with and without the phase-constriction effect taken into account, cross over the tuff matrix curve. With this crossover, we can separate the unsaturated state into two pressure ranges. For small suction pressure near full saturation condition, with fracture permeabilities greater than matrix permeability, fracture flow dominates. For large suction pressure with fracture permeabilities smaller than matrix permeability, matrix flow dominates. In the small suction pressure range, fracture saturation changes rapidly from 1 to 0 and matrix saturation remains near 1. When the matrix finally changes the saturation in the large suction pressure range, the fractures are dry and the fracture permeabilities are negligible in comparison with the matrix permeability.

The crossover between the fracture permeability curve and the matrix permeability is the key to sustaining the conceptual model that assumes that matrix flow dominates under ambient conditions with large suction pressure associated with a partially saturated state. If fracture permeabilities are larger than matrix permeability in the whole pressure range, the fractures will be the main conduits for water flows. In the larger spatial scale with tuff units bounded by faults, it is important to determine if the permeability of the fault material is always larger than

that of the tuff units in the formation or if the fault permeability crosses over the formation values. In the next section, we will analyze soil and tuff data to quantify and constrain the hydrological parameters of different porous media The determination of the dominant flow mechanism is crucial to performance assessment of fractured, porous tuff as a partially saturated formation for waste isolation.

From the above review, it is clear that both the fracture models and the soil models used for describing saturation characteristic curves and permeability curves are crude. We need data for aperture distribution functions to determine if fracture roughness is periodic or fractal; theoretical and experimental studies to quantify the phase constriction, tortuosity, and spatial distribution effects; and fracture saturation, permeability, and contact area measurements to check and improve models. Even in soils with some saturation and permeability measurements, capillary tube models with tortuosity and resistance-in-series effects taken into account do not always work. We need to go beyond idealized pore structures to construct more realistic models. An air bubble in the middle of a capillary tube with varying radius can shut off the flow completely. An even more basic limitation of capillary tube-based models is that flows are restricted to prescribed channel geometry. As pressure changes, the flow geometry will continuously change as the system optimizes its flow geometry under each capillary pressure. A segment of one flow channel at one given pressure may connect to a segment of a different channel as the pressure changes. It is not clear how the empirical parameters in saturation characteristic curves can adequately quantify the connectivity structure of pores and flow channels. It is a challenge to incorporate information beyond pore size distribution, such as pore connectivity and spatial correlation, into quantifiable models for relative permeabilities and other hydrological parameters. More realistic models can then lead us to better quantify the uncertainties associated with models, and to determine if the crossover from fracture-dominant to matrix-dominant flow is a realistic mechanism with a high degree of certainty.

6.0 STATISTICAL ANALYSES

To quantify uncertainties of groundwater travel times and radionuclide transport for performance assessment, we need to carry out statistical analyses on models and model parameters. Measurements in the laboratory and in the field will determine the values and distributions of parameters and conditions to be used in solving mathematical equations. If laboratory values are different from field values, spatial scale dependences and scaling properties need to be studied. Because many hydrological parameters are determined from microscopic pore structures, together with fluid properties and rock textures, correlations among different parameters may manifest themselves in the macroscopic laboratory scale and in the megascopic field scale. In the time domain, the reliability of long-term predictions will be assessed on the basis of sensitivity studies and stochastic models to take into account the ranges and distributions of parameters. Statistical analyses are also required to determine the probabilities of occurrence of extreme events and to assess the consequences of failure modes in repository designs.

With the majority of site characterization activities on the field scale in the planning or preliminary stages, most available data for Yucca Mountain are based on laboratory measurements of small samples from a few exploratory holes. Although much more data are expected in the future, difficulties will be encountered in data analyses to determine hydrological parameters in heterogeneous systems. Even in soil and groundwater studies with extensive testing data, the characterization of field-scale responses remains an active topic vigorously pursued by earth scientists (Dagan, 1986). In waste isolation studies, with the concern that extensive testing may compromise the integrity of formations as isolation barriers, data availability in the future may be limited. The task of performance assessment will thus have to depend even more on statistical analyses to predict the long-term behavior of the geological formations around the repository. In this section, we focus on the parameter distributions and correlations deduced from laboratory measurements on tuff and soil samples. We also briefly review the current thoughts on spatial scaling and stochastic modeling approaches.

6.1 Distribution Functions

Before we study the hydrological data for tuff and soils, we summarize standard statistical analyses used to quantify parameter distributions. When we have a number of data values for a given parameter, we can determine the mean, the standard deviation, and the higher moments by averaging. We can also represent the data population by histograms and by cumulative distributions and compare these with analytic density functions of different distributions.

For N data values of a variable z_i, $i = 1, \ldots, N$, the mean is simply

$$m_z = \frac{\sum_{i=1}^{N} w_i z_i}{W} \tag{6.1}$$

where w_i is a weight associated with z_i and W is the sum of the weights

$$W = \sum_{i=1}^{N} w_i. \tag{6.2}$$

The weighted standard deviation (second moment) is

$$\sigma_z = \left[\frac{\sum_{i=1}^{N} w_i (z_i - m_z)^2}{W_t} \right]^{1/2} \tag{6.3}$$

with

$$W_t = W - \frac{\sum_{i=1}^{N} w_i^2}{W}. \tag{6.4}$$

The corresponding skewness coefficient (third moment) is

$$s_3 = \frac{\sum_{i=1}^{N} w_i (z_i - m_z)^3}{W_t \, \sigma_z^3} \tag{6.5}$$

and the kurtosis coefficient (fourth moment) is

$$s_4 = \frac{\sum_{i=1}^{N} w_i (z_i - m_z)^4}{W_t \, \sigma_z^4}. \tag{6.6}$$

For data based on cores collected at different depths, some of the cores may have several subcores used in different measurements. We may assign different weights for the data points from these cores than the others. The coefficients calculated by Equations 6.1 to 6.6 depend on the weights chosen. In this report, we treat all data points with the same weight $w_i = 1$ and calculate the equal-weight population moments.

The distribution of data can be represented graphically by histograms and cumulative distribution plots. When a number of data are measured for a given parameter, we can divide the range between the maximum value and the minimum value into several intervals and tabulate the number of samples that fall within a given interval. The number of samples within an interval divided by the total number of samples is the relative frequency of that interval. The bar diagram of frequencies versus parameter range is the histogram of this parameter. The shape

of a histogram depends on the number of intervals chosen for the analyses. If we have too few intervals, we have coarse representation for the parameter distribution. If we have too many intervals, we have gaps with zero frequency sandwiched between intervals with high frequencies. We can also represent the distribution without interval specification. In a cumulative frequency plot, we start counting at the minimum value 1, and add one count at the next higher parameter value as we scan through the range. The cumulative count of number of samples below any data value, divided by the total number of samples, defines the cumulative distribution as a function of parameter value. Both histogram and cumulative distribution plots are used in our analyses.

The normalized histograms can be fitted with analytic density functions of different distributions. With a continuous density function, $f(z)$, the discrete sums in averaging as those in Equations 6.1 to 6.6 are replaced by integrals. The most commonly used function is the normal distribution with Gaussian density function:

$$f(z) = \frac{1}{\sigma_z \sqrt{2\pi}} \exp\left[-\frac{1}{2}\left[\frac{z - m_z}{\sigma_z}\right]^2\right]. \tag{6.7}$$

The integral of $f(z)$ from $-\infty$ to z is the cumulative distribution function. The normal distribution is a function of two parameters: mean m_z and standard deviation σ_z. The density function is bell-shaped and the cumulative distribution is S-shaped about the mean (Figure 6-1). With a normal distribution, if a sample is picked at random, there is more than two-thirds chance (68%) that the value will be within ± 1 standard deviation from the mean, a 95% chance that it will be within 2 standard deviations, and a 99.7% chance that it will be within 3 standard deviations. We can adapt the standard that $m_z \pm 3\sigma_z$ spans a practically certain range whatever the distribution of the statistics being estimated. In other words, the chances of a consistent sample estimate deviating from the true value by $3\sigma_z$ are treated as negligible (Hansen et al., 1953).

The normal distribution is symmetrical about the mean m_z. With a symmetrical distribution, all the odd moments about the mean, such as the third moment or the skewness coefficient,

$$s_3 = \frac{\int_{-\infty}^{+\infty} (z - m_z)^3 f(z)dz}{\sigma_z^3}, \tag{6.8}$$

are zero. For estimates from parameter data as calculated in Equation 6.5, a deviation of the skewness coefficient from zero measures the asymmetry of the distribution. A distribution with a long tail in the range larger than the mean has a large positive skewness coefficient. If s_3 is negative, the long tail is on the lower side.

For the normal distribution, all higher even moments about the mean can be expressed in terms of the standard deviation σ_z. The fourth moment about the mean or the kurtosis coefficient,

a

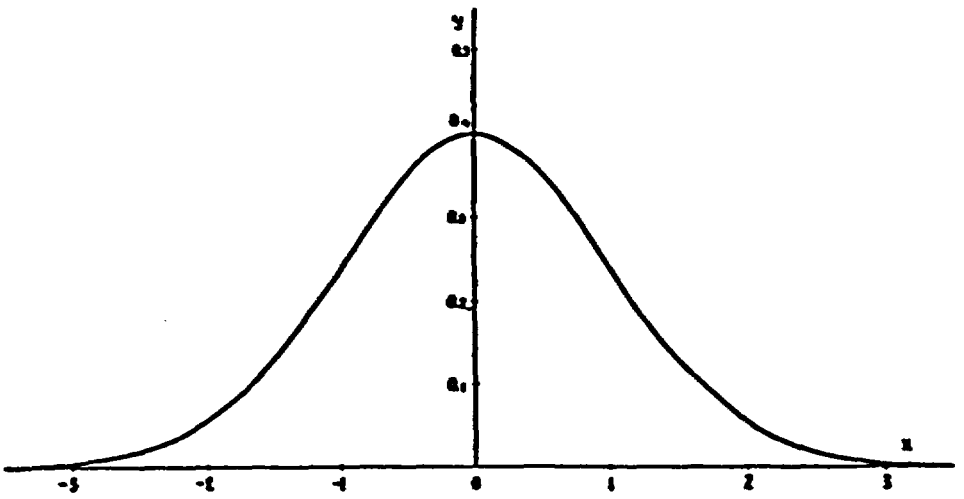

b

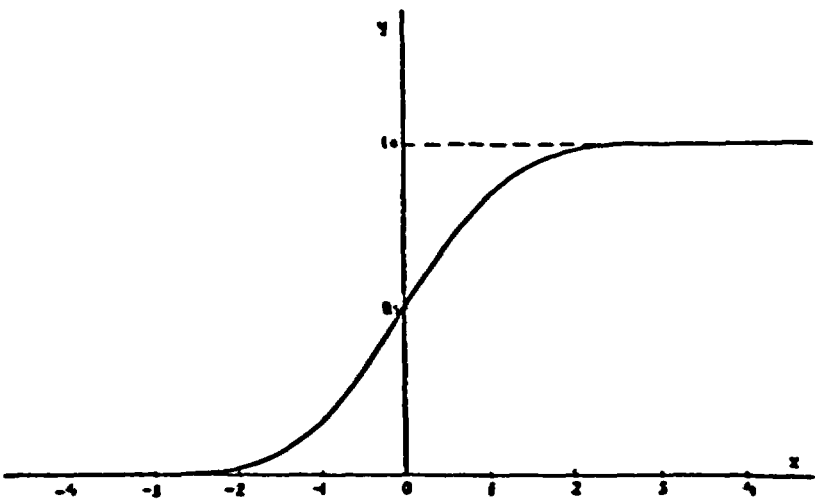

Figure 6-1. (a) Normal Distribution $y = \frac{1}{\sqrt{2\pi}} exp(-\frac{x^2}{2})$, (b) Normal Cumulative Distribution

$$y = \frac{1}{\sqrt{2\pi}} \int_{-\infty}^{X} exp(-\frac{x'^2}{2})dx'.$$

$$s_4 = \frac{\int_{-\infty}^{+\infty} (z - m_z)^4 f(z)dz}{\sigma_z^4}, \tag{6.9}$$

is equal to 3. The kurtosis coefficient can be used as a measure of the degree of flattening of a distribution curve near the mean. If the estimate from parameter values in Equation 6.6 is greater than 3, the distribution curve is more tall and slim than the bell shape of the normal distribution, and conversely for kurtosis coefficient less than 3. In some statistics textbooks, s_4 - 3 is defined as the kurtosis coefficient.

For some hydrological parameters, the data distributions are markedly skewed with long tails at high values. The data values do not follow a normal distribution; rather, their logarithms tend to be normally distributed. Only positive values are physically meaningful for porosity, permeability, residual saturation, air entry scaling parameter, and pore-size distribution index. If we use normal distribution for these parameters, we need to truncate the negative range. The logarithmic transformation expand the positive value range to the whole real axis. The lognormal density function is

$$f(z) = \frac{1}{z\,\sigma_{\log(z)}\sqrt{2\pi}} \exp\left[-\frac{1}{2}\left[\frac{\log(z) - m_{\log(z)}}{\sigma_{\log(z)}}\right]^2\right]. \tag{6.10}$$

For lognormal analyses, we use Equations 6.1 to 6.6 with the replacement of z by $log(z)$. With the mean and standard deviation of $log(z)$ calculated, we tabulate the results as $10^{m_{log\,(z)}}$ and $10^{m_{log\,(z)} \pm \sigma_{log\,(z)}}$.

In addition to normal and lognormal distributions, many other distributions are used in various studies (Cramer, 1946). For example, the discrete Poisson distribution and the binomial distribution are used in geostatistical ore reserve estimations (David, 1977). Various density functions related to the normal distribution have important statistical applications. Some examples are the χ^2-distribution, the Student's t-distribution, the Fisher's z-distribution, and the Beta-distribution. We also have the simple rectangular distribution with the variable uniformly distributed within a given range, various algebraic functions such as Cauchy's distribution and Pareto's distribution, and exponential functions such as Laplace distribution and gamma distribution. A majority of continuous distributions can be related to various types of Pearson's density functions which can be characterized by the first four moments. In tuff studies, the Beta-distribution, a Pearson Type I density function, has been used to analyze the pore-size distribution index and other hydrological parameters (Kaplan, 1989).

$$f(z) = C_\beta (z - z_{min})^{p_\beta - 1} (z_{max} - z)^{q_\beta - 1};$$
$$z_{min} < z < z_{max};\ p_\beta > 0,\ q_\beta > 0 \qquad (6.11)$$

with the normalizing constant C_β determined by the other four coefficients. The mean and the standard deviation are used to determine the distribution coefficients p_β and q_β. The density function can have various shapes, depending on the magnitudes of p_β and q_β. With the maximum and minimum values specified, the parameter distribution can be properly constrained (Kaplan, 1989).

Instead of standard deviation, the coefficient of variation is frequently used in the literature. The coefficient of variation is defined as a relative measure for the second moment

$$s_2 = \frac{\sigma_z}{m_z}. \qquad (6.12)$$

In this study, we did not present our results in terms of the coefficient of variation for the following reason. If a parameter is redefined by adding or subtracting a constant from the data values, the value of the mean will be changed but all higher moments, depending on the differences between data values and mean, will not be affected. For example, we can analyze van Genuchten's n parameter and determine that the mean m_n is 1.5 and the standard deviation σ_n is 0.5. The coefficient of variation for parameter n is 0.5/1.5 or 33%. If we analyze Brooks and Corey's pore-size distribution index λ, which is related to n by $\lambda = n - 1$, for the same data set, we have $m_\lambda = 1.5 - 1 = 0.5$ and $\sigma_\lambda = 0.5$, and the coefficient of variation for λ is 0.5/0.5 or 100%. If a distribution for n can be defined and characterized properly by a given number of samples, we expect that the distribution for λ can be defined equally well for the same number of data points.

From this example, we question the adequacy of sampling survey methods based on the magnitude of the coefficient of variation in determining the necessary sampling sizes. The coefficient of variation has been used to determine the number of samples necessary to obtain estimated mean within a specified precision. Both the coefficient of variation and the coefficient of kurtosis are used to determine the size of sample necessary to achieve specified precision in estimating the standard deviation (Hansen et al., 1953). The determination of sample sizes for establishing distribution coefficients is very important in statistical analyses when the number of samples is limited. The problem is nontrivial and iterative because good approximations are needed for higher moments to determine the necessary sample sizes for lower moments. In this study, we do not use sophisticated statistical sampling survey methods to judge if the sample sizes are sufficient to define meaningful distributions. Instead, we simply plot the dependence of distribution coefficients on sample sizes from population averaging calculations with Equations 6.1 to 6.6. For a given data set with N data points, we calculate a coefficient $N - 1$ times for subsets with 2, 3, ..., N points. If we had enough data points from a uniform population, the calculated results of this coefficient should converge. However, we frequently need to combine the data points from several different classes or units with similar hydrological properties into one set so that the set has enough data points for meaningful distribution analyses. In this study,

we systematically sampled the data points within a set to examine qualitatively if a hydrological parameter depended on texture or alternation which was used to classify the sub-populations within a set. These analyses illustrate the difficulty of establishing distribution coefficients and populations.

6.2 Parameter Distributions

In this section, we compare parameter distributions of watershed soils with the tuff matrix data. The distribution coefficients of these two very different media are used in the next section to study correlations of hydrological parameters between media with contrasting properties. The contrast in hydrological parameters between soil and tuff matrix may help us to understand the behavior of other heterogeneous systems (e.g., fractured rocks, stratigraphic units bounded by faults). The soil characteristic curves have been used for fractures. The lack of data in fractures and faults is one of the reasons we study the soil data. We are also interested in the variabilities of hydrological properties among soils with different texture and among tuffs with different degrees of alternation. The watershed soil data are from the USDA study by Holtan et al. (1968), fitted by Panian (1987) with the van Genuchten (1980) model. The tuff matrix data are from the SNL study by Peters et al. (1984) and Klavetter and Peters (1987), also fitted with the van Genuchten model. Before we discuss the parameter distributions, we summarize the methodology of data analyses of both data sets.

In the USDA watershed soil study (Holtan et al., 1968), approximately 200 Agricultural Research Service experimental plots at 34 locations in 23 states were sampled. Soil fragments in cohesive soils, core samples in noncohesive soils, and loose samples were collected from two to eight horizons in one or two 5-foot-deep pits at each experimental plot and sent to laboratories for measurements. Moisture retentions were determined under equilibrium at 0.1, 0.3, and 0.6 bar with a ceramic plate, and at 3 and 15 bars with a membrane. Bulk densities were determined in moist (0.3 bar) and oven-dry conditions. Weight-weight moisture retention data were converted to volume-volume measures and the total porosity of each horizon was computed by assuming specific gravities of the solids equal to 2.65 for all soils in both moist and oven-dry conditions. Saturated conductivities were determined for each horizon on two fist-sized fragments, trimmed roughly to cylindrical shape and 1-inch slices. Conductivity tests were carried out only on cohesive soils sampled by soil fragments, and tests were abandoned for field sample cores and laboratory-packed cores of noncohesive soils because of erratic results.

In the original data tables, the total porosity values for a few horizons were smaller than the percent volume values of moisture retention data at 0.1 bar. Panian (1987) used the 0.1 bar moisture retention values as total porosity (saturated moisture content) values in those horizons to convert the moisture retentions at higher suctions to percent saturations. In addition to data, Holtan et al. (1968) also provided descriptions of soil profiles by soil scientists in the field in accordance with the USDA Soil Survey Manual (USDA, 1951). Panian omitted the data from horizons containing shale, sandstone, limestone, schist, mica, or marl, and for soils containing excessive roots and worm holes and those with blocky, calcareous, mottled, or cemented structures. All data analyzed by Panian can be classified by soil texture with the USDA soil texture triangle (Figure 6-2).

a

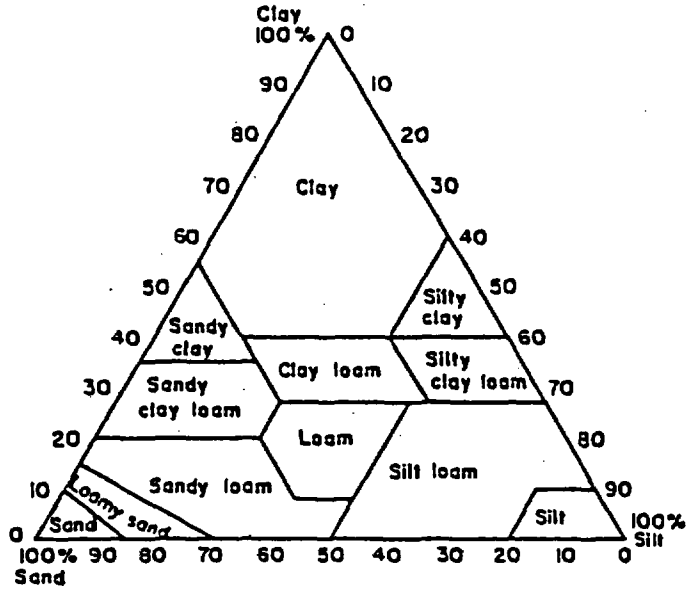

b

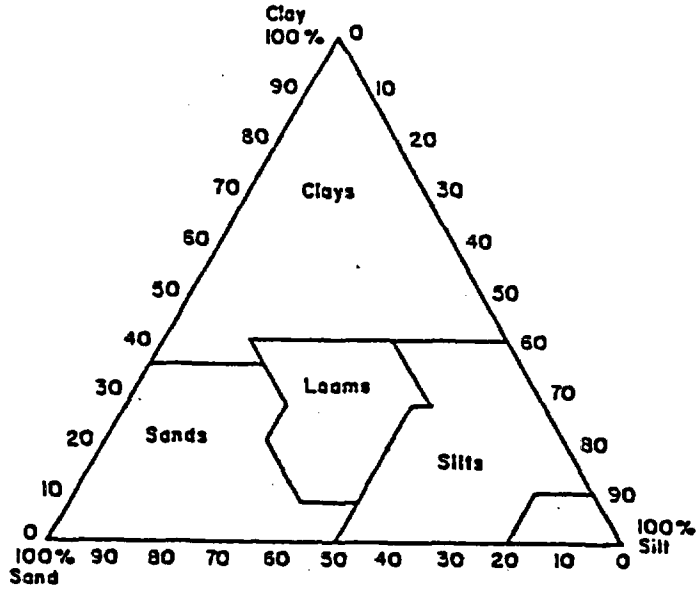

Figure 6-2. (a) USDA Soil Texture Triangle, (b) Reclassification of Texture Categories Into Four Broad Classes (Cosby et al., 1984).

We analyze this watershed soil data set in three ways: (1) separating the data into 11 categories according to the USDA texture triangle (Figure 6-2a); (2) grouping the data into four broad classes in accordance with the reclassification scheme of Cosby et al. (1984, Figure 6-2b); and (3) combining all data as one set. The figures for the detailed analyses in (1) and (2) will be presented in Appendix A. In this section, we summarize the detailed analyses in tables and present figures of combined analyses (3) together with the tuff matrix analyses.

In contrast to the watershed soil data set containing many data points (over 1300 horizons) from shallow depths (less than 5 feet) and with low resolution (5 retention values for each characteristic curve), the tuff matrix data set (Peters et al., 1984; Klavetter and Peters, 1987) has fewer data points (less than 70) from greater depths (up to 2100 feet) and with higher resolution (over 10 retention values for most characteristic curves). In the SNL tuff matrix study, core samples were collected from three deep boreholes at Yucca Mountain: USW G-1, USW G-4, and USW GU-3. Moisture retention tests were run on cylinders 1.4 cm in diameter by 1.2 cm in length that were subcored from the original core samples. Moisture content was determined gravimetrically, and the water potential was determined from the measured humidity with a thermocouple psychrometer. Microwave drying was used to desaturate the samples in a stepwise fashion. Saturated conductivities were determined for each core sample on one to three small subcores used in the moisture retention tests, and also on one wafer 6 cm in diameter by 2 cm in thickness from some core samples.

We analyze the tuff matrix data set in two ways: (1) separating the data into thirteen units according to the hydrological stratigraphy of Ortiz et al. (1984); and (2) grouping the data into two broad classes: nonwelded tuff versus welded or zeolitized tuff. Yucca Mountain consists of alternating units of welded and nonwelded tuff units. From top downward, these are: Tiva Canyon welded unit (TCw), Paintbrush nonwelded unit (PTn), Topopah Spring welded unit (TSw), Calico Hills nonwelded unit (CHn), Prow Pass welded unit (PPw), Crater Flat Upper nonwelded unit (CFUn), and Bullfrog welded unit (BFw). Some of the units are further divided into subunits. The lower portion of CHn is zeolitized and the hydrological characteristics of this nonwelded unit are closer to welded tuff. The interface between the vitric Calico Hills (CHnv) and zeolitized Calico Hills (CHnz) is approximately parallel to the water table. The interfaces between other stratigraphic units generally tilt eastward at 5° to 7° (Scott and Bonk, 1984) and some of the lower units are below the water table in eastern Yucca Mountain.

The characteristics of nonwelded tuffs are very different from those of the welded or zeolitized tuff. Although data are meager, especially for nonwelded tuffs, we analyze the nonwelded tuff data separately from the welded/zeolitized tuff data. In contrast, different watershed soils have relatively similar characteristics, showing only some dependence on soil texture as discussed in Appendix A. We compare the combined soil results with the welded/zeolitized tuff results and the nonwelded tuff results in this section, focusing on the differences among these three sets.

If we had more tuff data, it will be useful to develop a tuff texture or tuff alternation triangle similar to the soil texture triangle in Figure 6-2. In place of sand, silt, and clay percentages, the the variables are degree of welding, zeolitization, and vitrification. Cosby et al. (1984) analyzed the watershed data of Holtan et al. (1968) and Rawls et al. (1976) to determine the dependences of hydraulic parameters on sand, silt, and clay percentages. Similar functional dependences of tuff parameters on degrees of welding, zeolitization, and vitrification can convert

qualitative geologic descriptions of rock textures into quantitative equations directly useful for modeling.

The parameter distributions of the combined watershed soil data set, the welded/zeolitized tuff set, and the nonwelded tuff set are analyzed by the same procedure. We first determine if the distribution of a given parameter for each set is closer to normal distribution or closer to lognormal distribution. We then analyze the dependences of distribution coefficients on the number of data points. Each data set contains several sub-populations (11 texture classes in the watershed soil set, 9 stratigraphic units in the welded/zeolitized tuff set, and 4 stratigraphic units in the nonwelded tuff set). For example, in the calculations of distribution coefficients for the welded/zeolitized tuff set with 6 data points in TCw, 5 data points in TSwl, etc. (see e.g., Table 6-2), we first used 2, ..., 6 data points from TCw only and then continued with 7, ..., 11 data points with 6 from TCw and 1, ..., 5 points from TSwl. We continued the subset analyses with inclusion of more data points from deeper units until the data points from all 9 units were included in the calculations. With this systematic inclusion of data points, we examined qualitatively any dependence of hydrological parameters on degree of alternations (welding, zeolitization, vitrification) for the tuff matrix sets and the dependence on texture classes for the watershed soil set.

As an example of the first step of determining if the distribution is closer to normal or closer to lognormal, we analyze the pore-size distribution index, λ or n - 1, of the combined soil set with and without the logarithmic transformation. The distribution histogram and cumulative distribution in linear scale are shown in Figures 6-3a and 6-3b. The distribution histogram does not have the symmetric bell shape and the cumulative distribution does not have the S shape of a normal distribution. If we calculate the distribution coefficients -- the mean, standard deviation, skewness, and kurtosis -- we get nonconverging results as shown in Figures 6-3c and 6-3d. The mean λ or n - 1 value is small and the mean minus one standard deviation value can be less than the physical lower limit of $\lambda = n - 1 = 0$. We also have a skewness coefficient having high values and a kurtosis coefficient fluctuating as a function of number of data points, as shown in Figure 6-3d.

We plotted the same data in log scale as shown in Figures 6-4a and 6-4b. The histogram is closer to bell-shaped and cumulative distribution closer to S-shaped. Once we determine that the lognormal distribution represents the pore-size index λ or n - 1 better than the normal distribution, we calculate other distribution coefficients. As shown in Figure 6-4c, the mean and standard deviation values converge with a few hundred data points. There is a gentle trend of decreasing mean as we include more and more clay-rich data points. The skewness and kurtosis coefficients in Figure 6-4d are better defined, at least in comparison with the linear analyses in Figure 6-3d. Similar comparisons were used for some other parameters to determine the normality or lognormality. Only the results but not the details would be discussed. In this study, we did not examine if distributions other than normal and lognormal could fit the data better.

The distributions of welded/zeolitized tuff log pore-size distribution index are plotted in Figure 6-5. With fewer data points, the tuff histogram and cumulative distribution are less smooth than the combined soil plots. Although there are only a few data points, we note that the pore-size distribution indices of the upper two welded units, TCw and TSw, are different

a

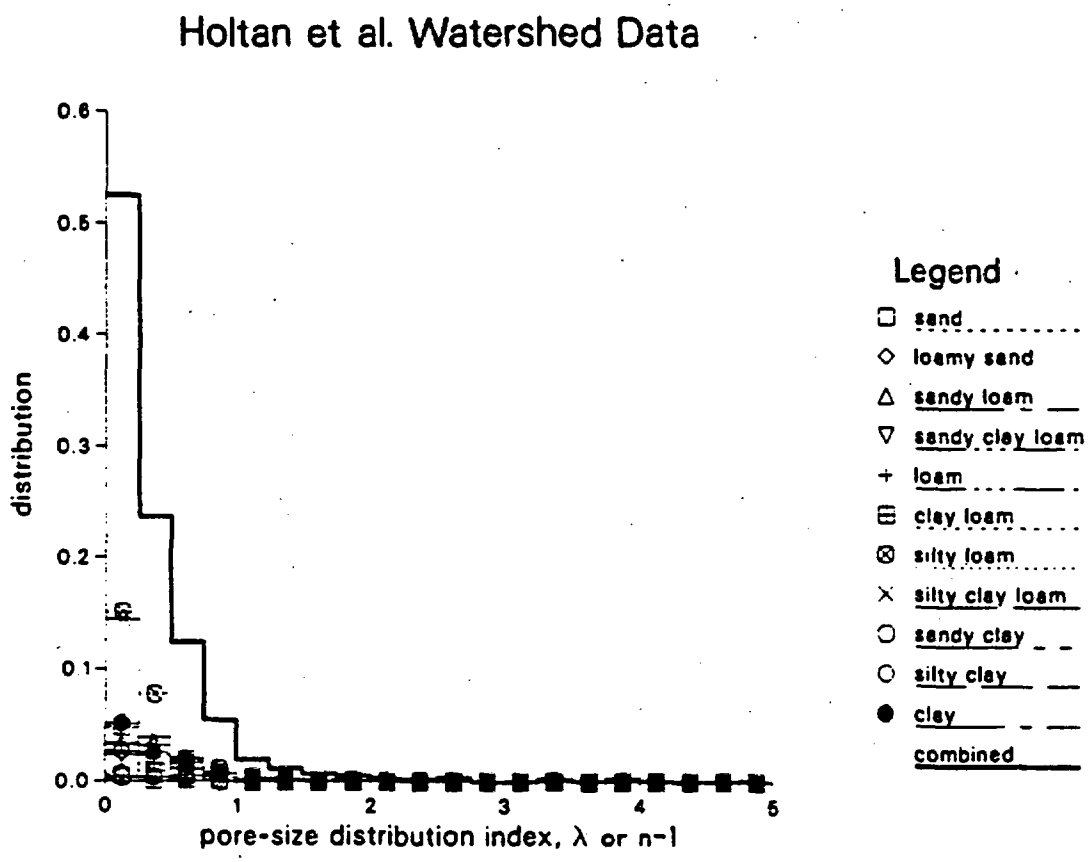

b

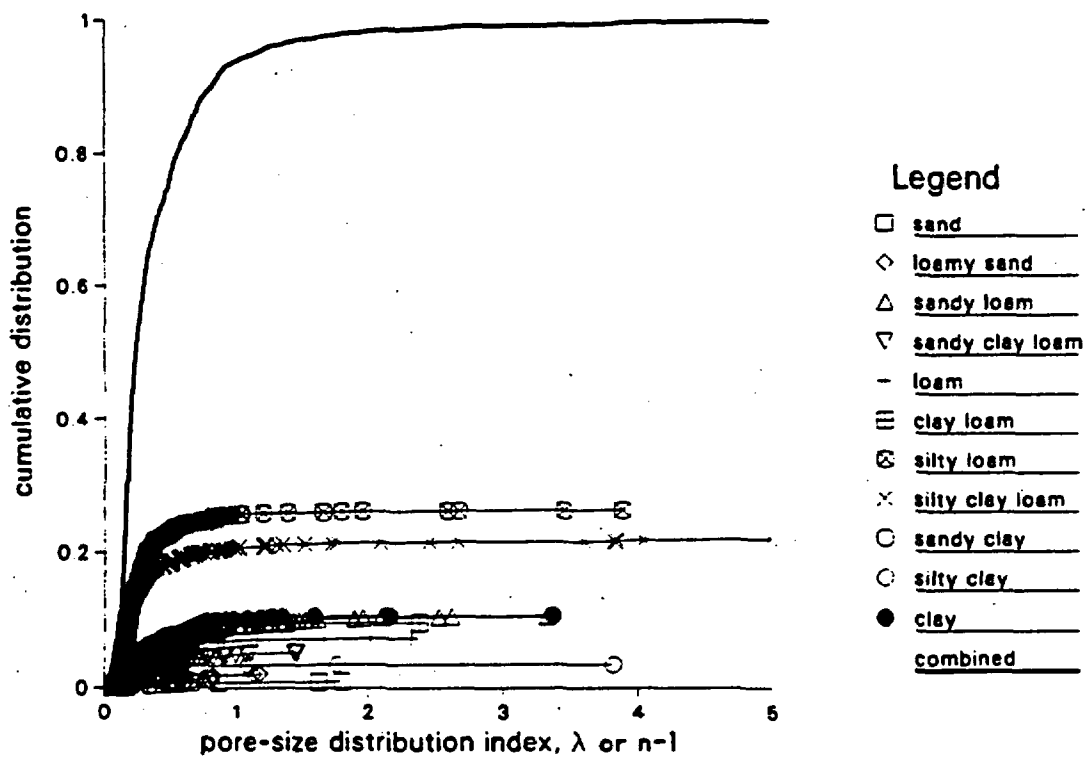

Figure 6-3. Distributions of Watershed Soil Pore-Size Distribution Index.

c

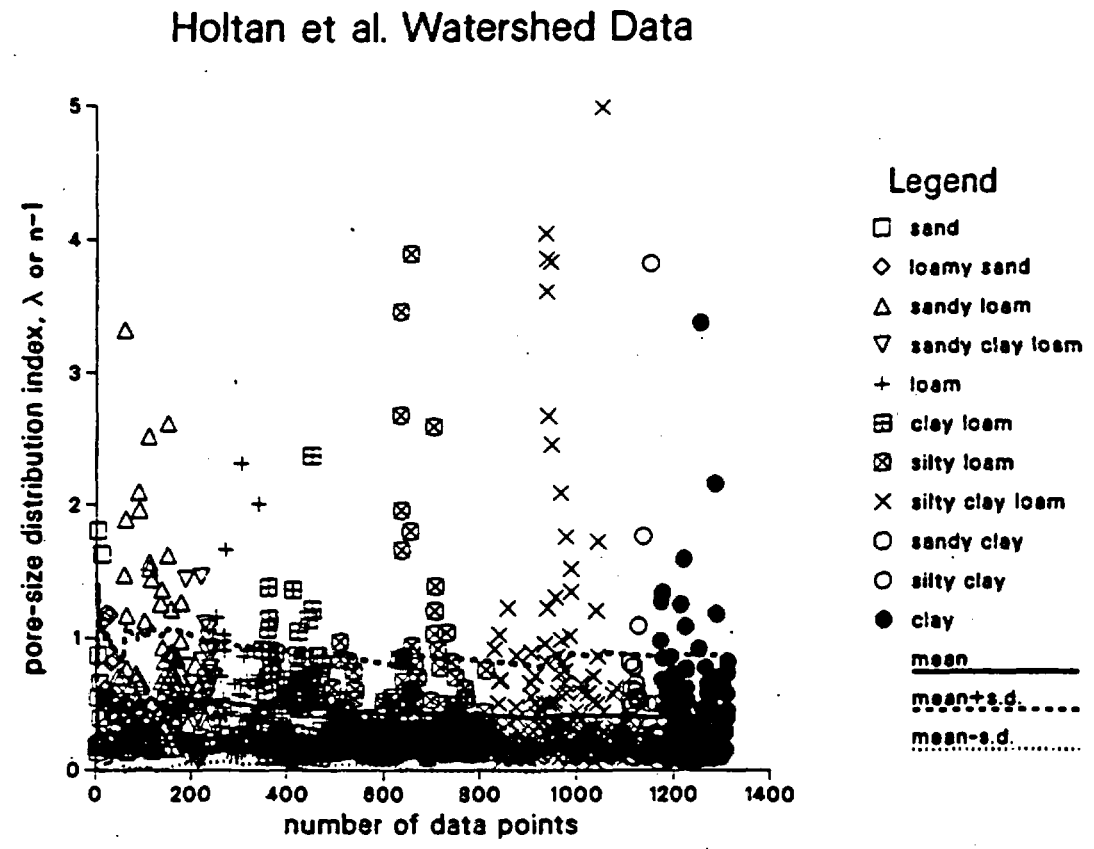

d

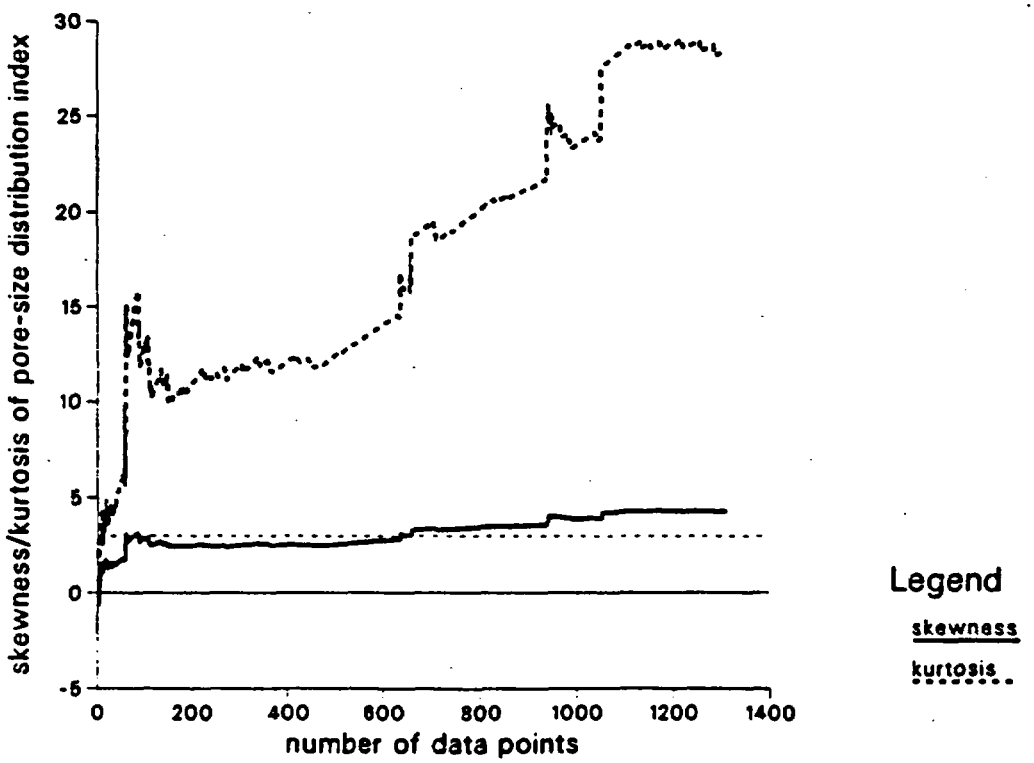

Figure 6-3. Distributions of Watershed Soil Pore-Size Distribution Index (concluded).

a

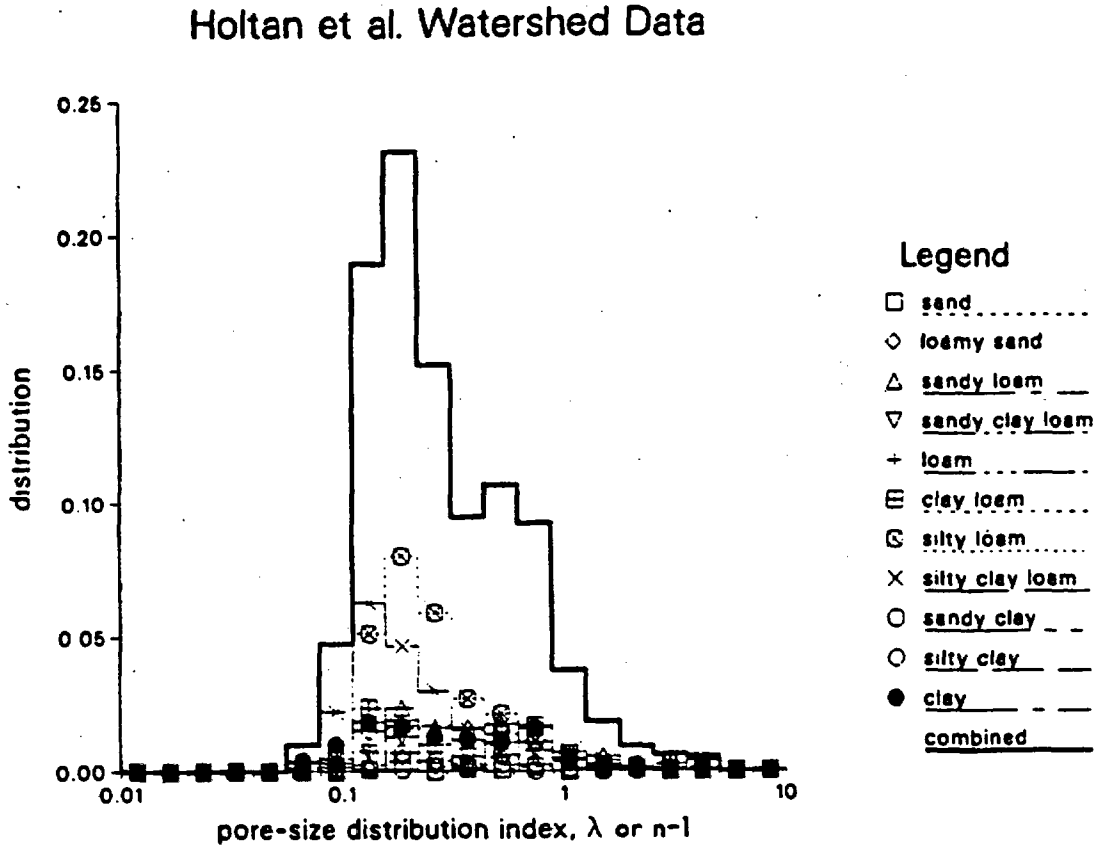

b

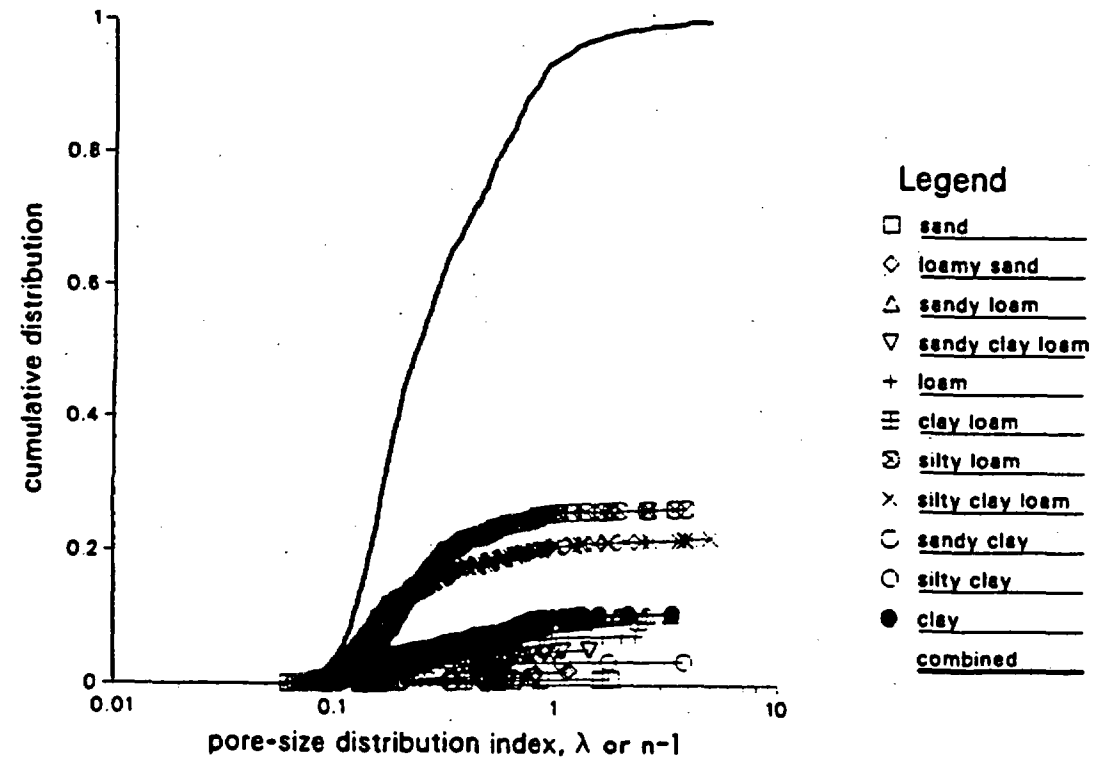

Figure 6-4. Distributions of Watershed Soil Log Pore-Size Distribution Index.

c

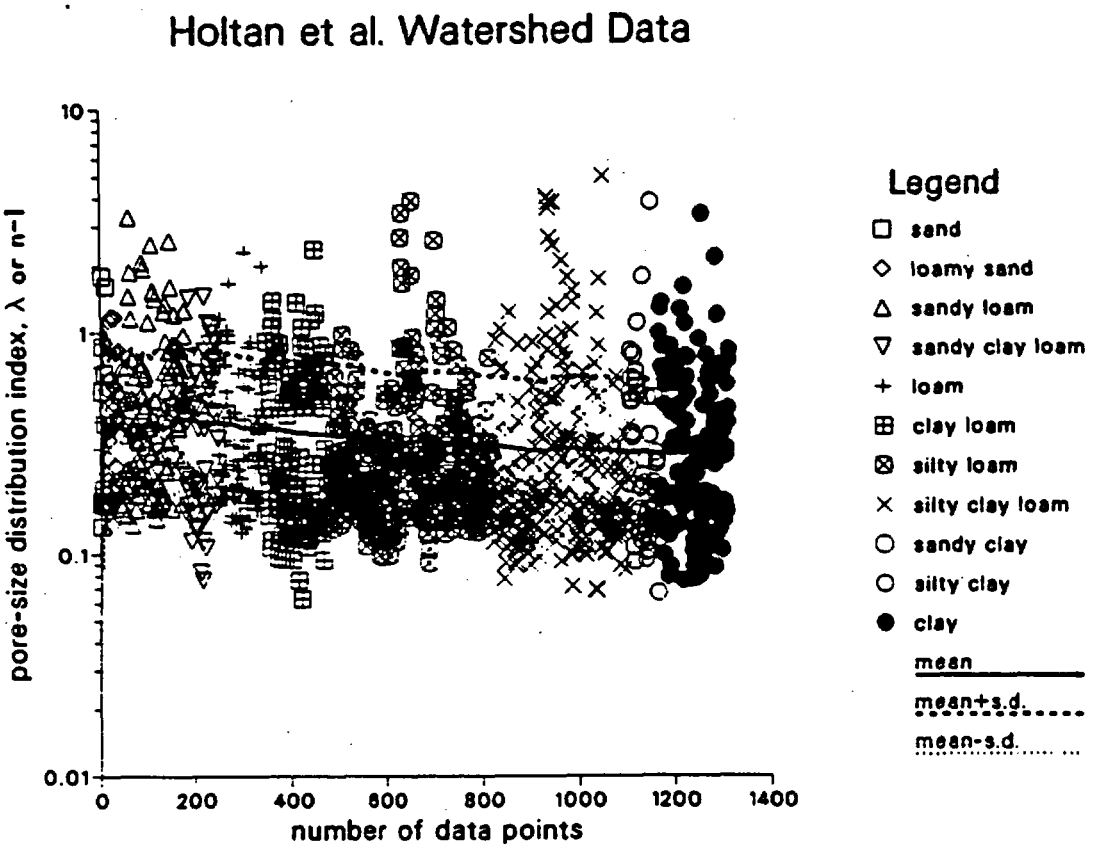

d

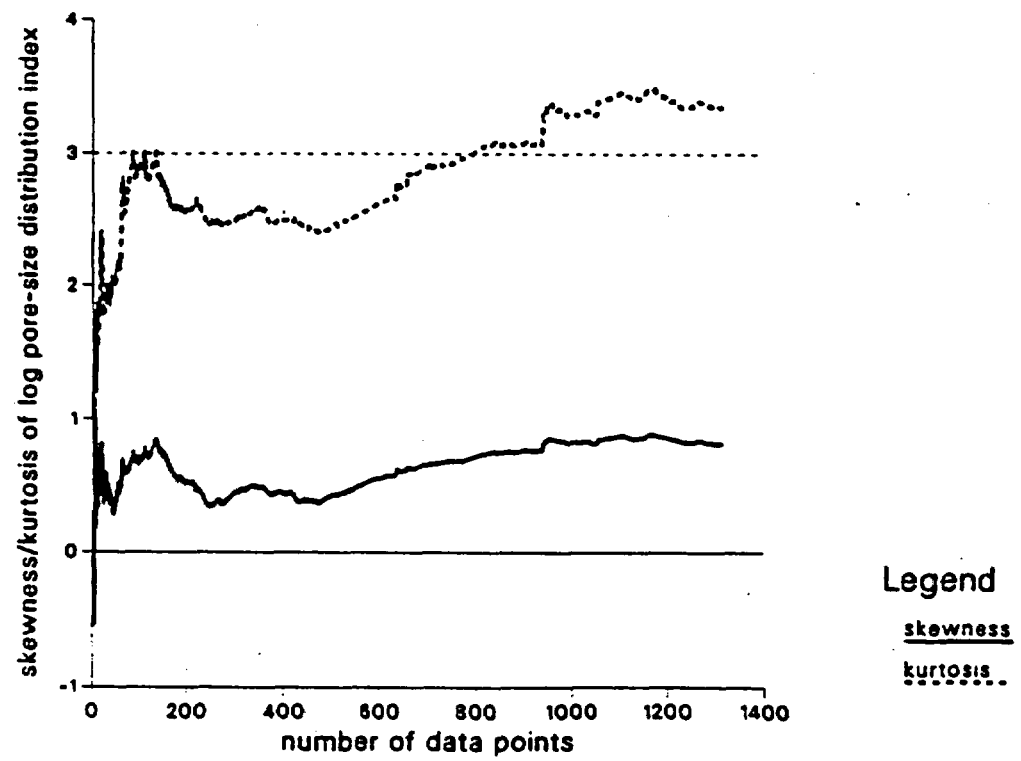

Figure 6-4. Distributions of Watershed Soil Log Pore-Size Distribution Index (concluded).

a

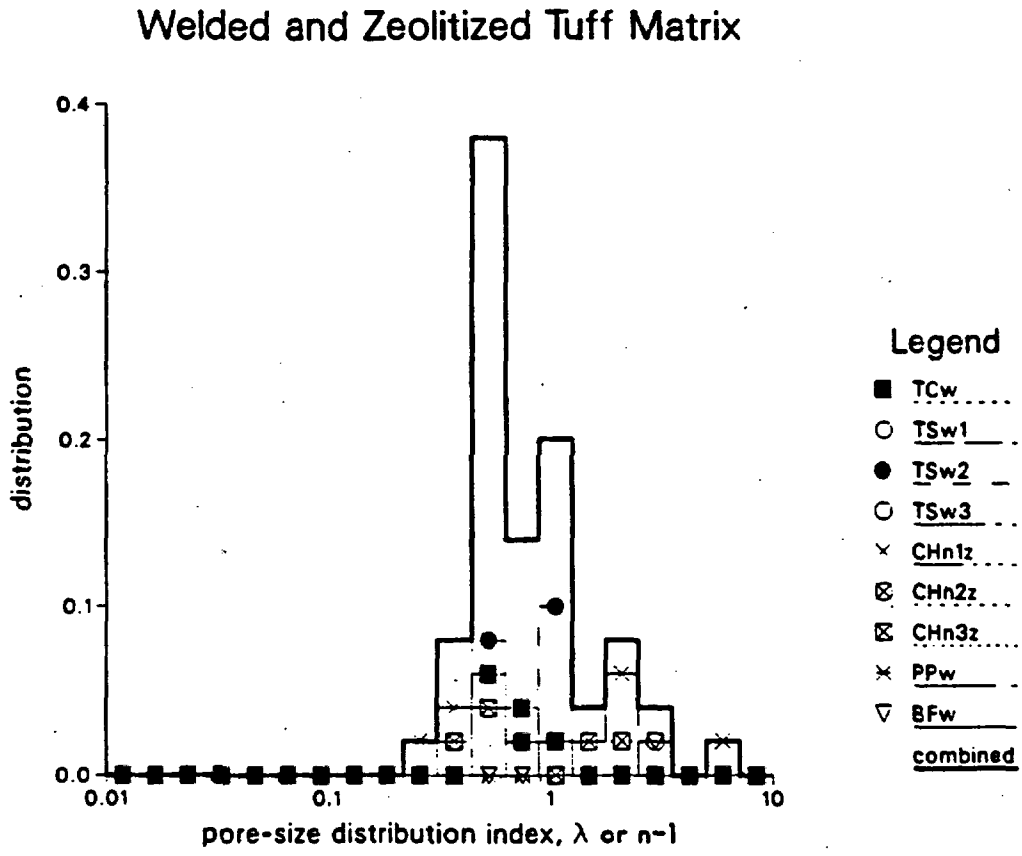

b

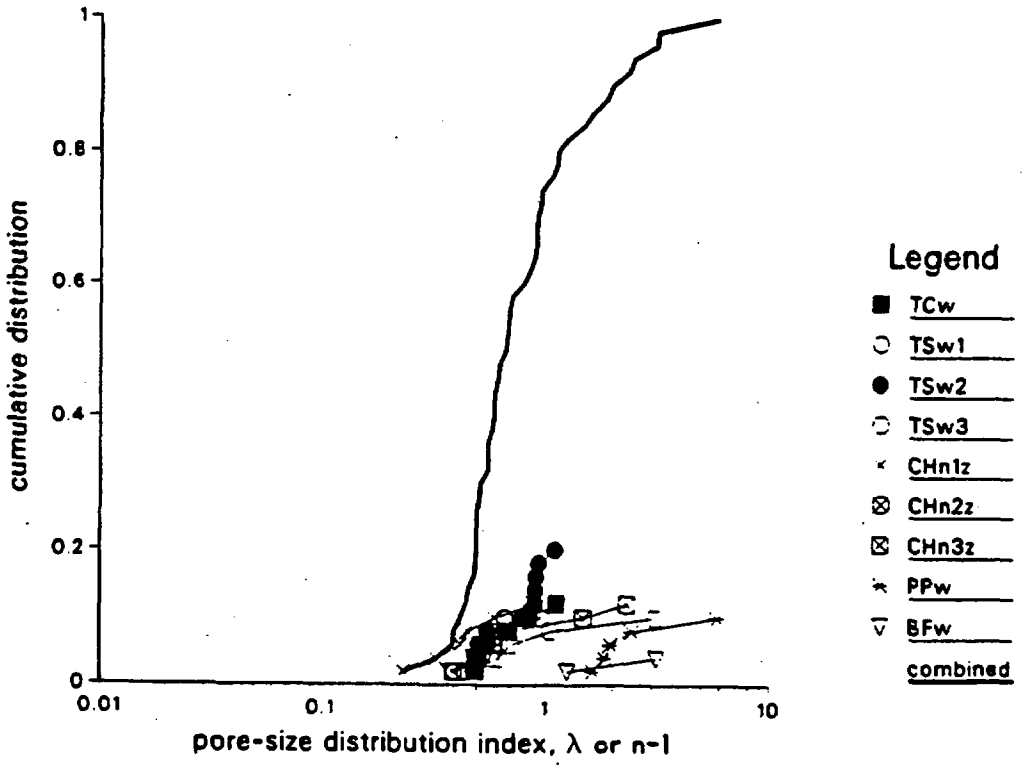

Figure 6-5. Distributions of Welded/Zeolitized Tuff Log Pore-Size Distribution Index.

c

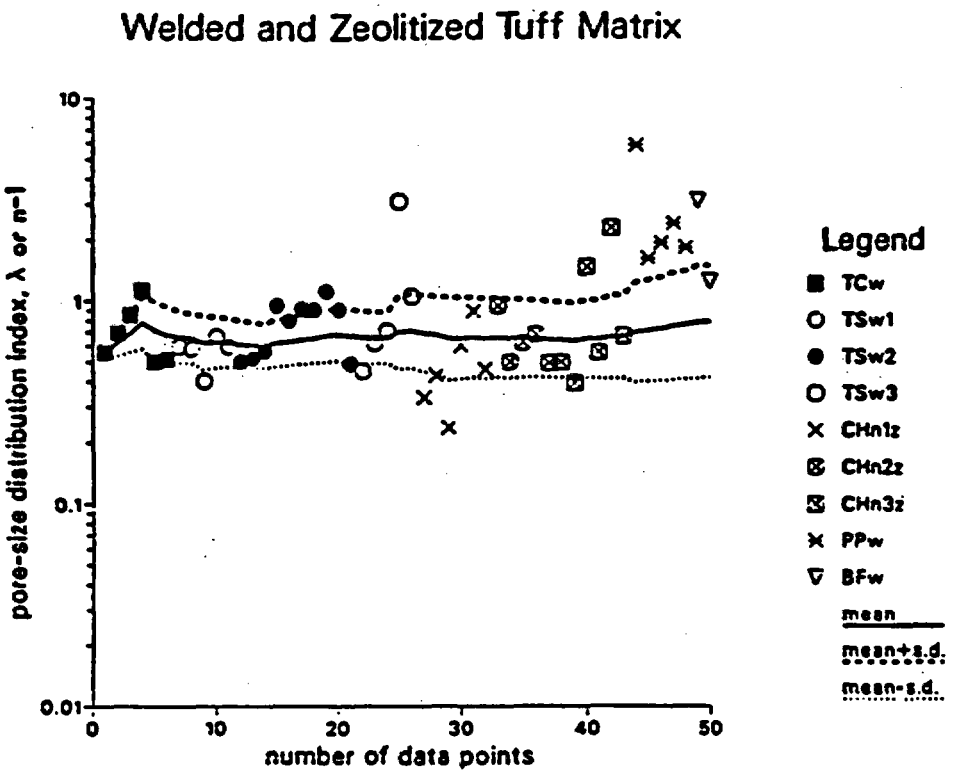

d

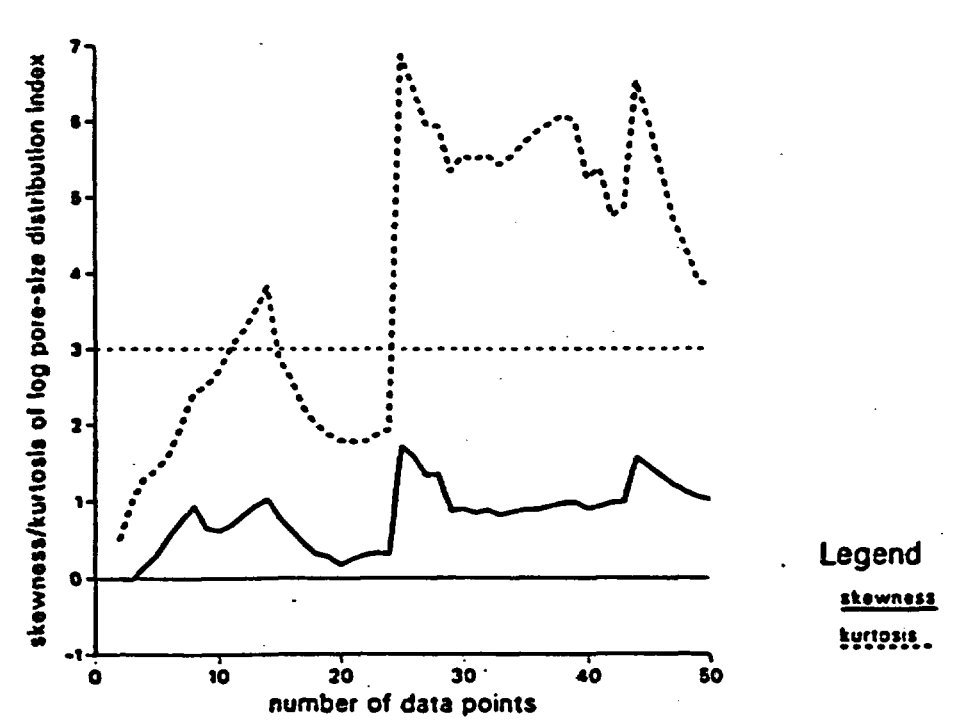

Figure 6-5. Distributions of Welded/Zeolitized Tuff Log Pore-Size Distribution Index (concluded).

from the indices of the lower zeolitized and welded units. There is a small increase in the index value as we add more data from deeper units when we examine the data from the top CHnz subunit downward to include deeper zeolitized subunits and welded units (Figure 6-5c). As one moves deeper toward the water table, one may expect to have more influence from the water to increase the pore-size distribution index, which is equivalent to making the pore-size distribution more narrow or more uniform. On average, the pore-size distribution index for tuff is slightly higher than for soils.

The nonwelded tuff analyses are given in Figure 6-6. With even fewer data points, the distributions are scattered. The pore-size distribution indices of some PTn samples and the data point of one CHn2v unit are much larger than the values of other samples (see Figures 6-6b and 6-6c). We include the figures of nonwelded tuff analyses for completeness and for comparisons with welded/zeolitized tuff analyses and with watershed soil analyses. If the few subcore samples in Figure 6-6 are representative of the nonwelded tuff, the pore-size distribution indices for nonwelded tuff are higher than welded/zeolitized tuffs and watershed soils.

In addition to pore-size distribution index, we analyze the data for the other four parameters: log air entry scaling factor (Figures 6-7, 6-8, 6-9), residual saturation (Figures 6-10, 6-11, 6-12), log saturated permeability (Figures 6-13, 6-14, 6-15), and porosity (Figures 6-16, 6-17, 6-18). For each parameter, the watershed soil results are presented first, followed by the welded/zeolitized tuffs, and then the nonwelded tuffs. Each figure includes a distribution histogram and a cumulative distribution as function of parameter value in linear or log scale, and mean, mean ± 1 standard deviation, skewness, and kurtosis as function of number of data points. The distribution subplots a and b also include the results of detailed analyses for different soil texture categories or for different stratigraphic tuff units. The actual data values are also included in subplot c with different symbols representing different categories and units. The results of the detailed analyses and broad grouping analyses are also summarized for the five parameters in Tables 6-1 to 6-10. For each table, the number of data points and the range of data values (maximum and minimum) are presented together with the distribution coefficients (mean, mean ± 1 standard deviation, skewness, and kurtosis). Because the results of distribution coefficients, especially the higher moment skewness and kurtosis coefficients, are very sensitive to the number of data points, the adequacy of the tabulated values must be carefully judged by examining the corresponding plots. One motivation for the distribution analyses is to evaluate if the number of data points is sufficient to determine the parameter distributions and to examine if the higher moment coefficients can be useful to improve the specification of distributions. The results indicate that in general the tuff data sets, especially for nonwelded tuff, do not have enough data points. The higher moment coefficients, especially the kurtosis, do not approach stable values as a function of number of data points for some of the parameters, even when the number of data points is fairly large.

The distributions of log air entry scaling factor (Figures 6-7, 6-8, 6-9, Tables 6-3, 6-4) are fairly well-defined. The most important observation is that the average air entry scaling factor for watershed soils is two to three orders of magnitude larger than both the welded tuff and nonwelded tuff. Because air entry radius is proportional to air entry scaling factor (Equation 5.3), the order of magnitude differences simply indicate that the soils have much larger pores that can be easily desaturated, and the tuff matrix has smaller pores that are more difficult to desaturate. There is little difference among different welded and nonwelded tuffs.

a

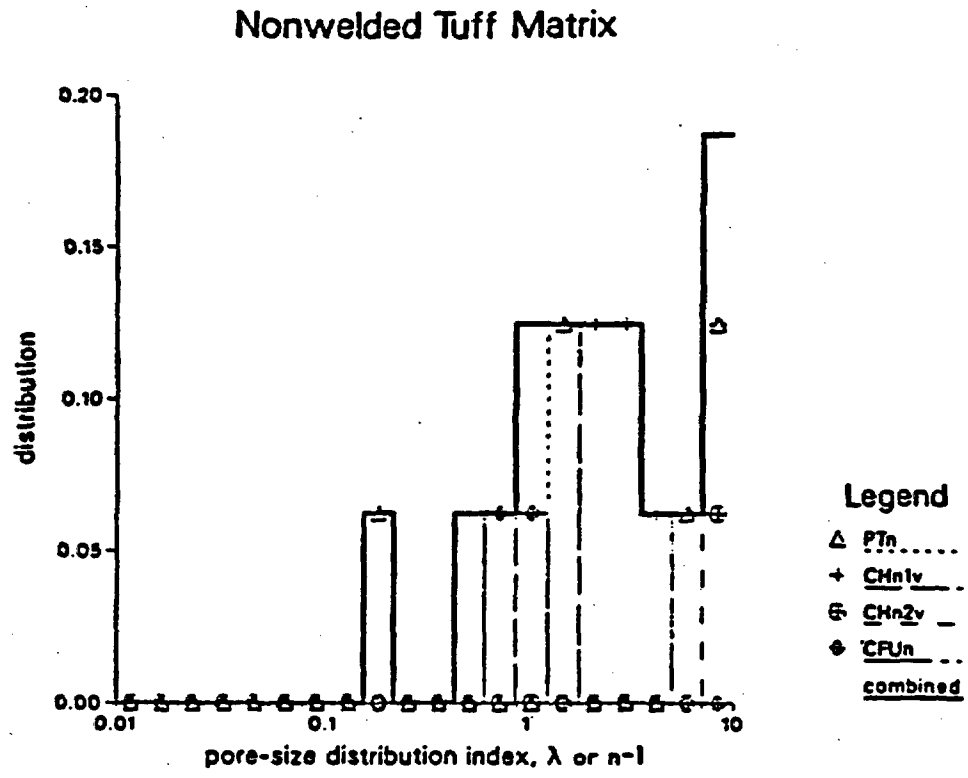

b

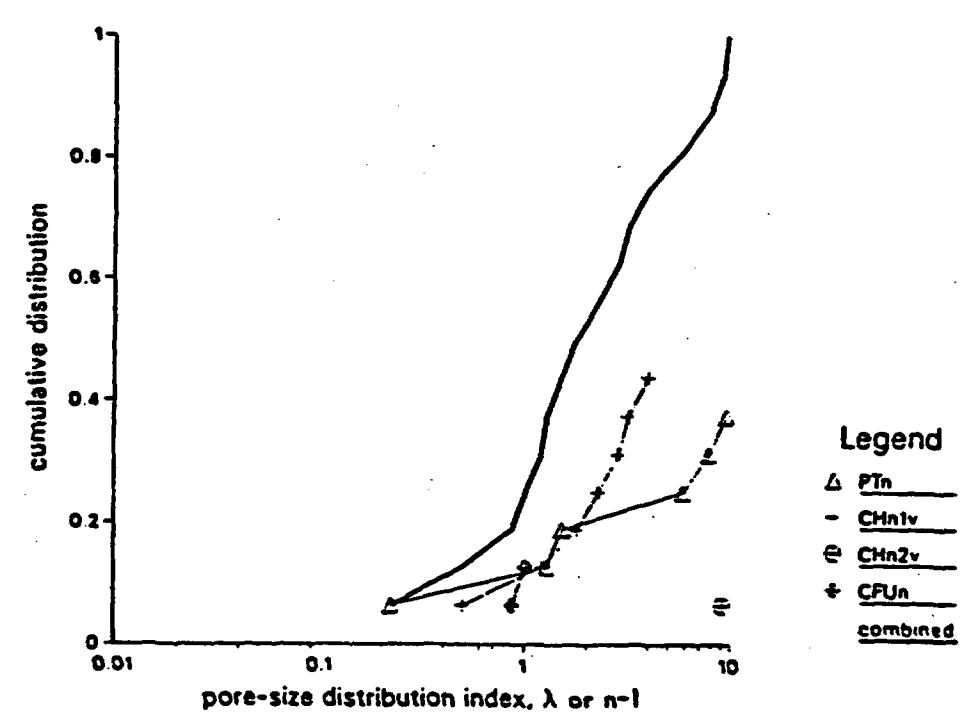

Figure 6-6. Distributions of Nonwelded Tuff Log Pore-Size Distribution Index.

c

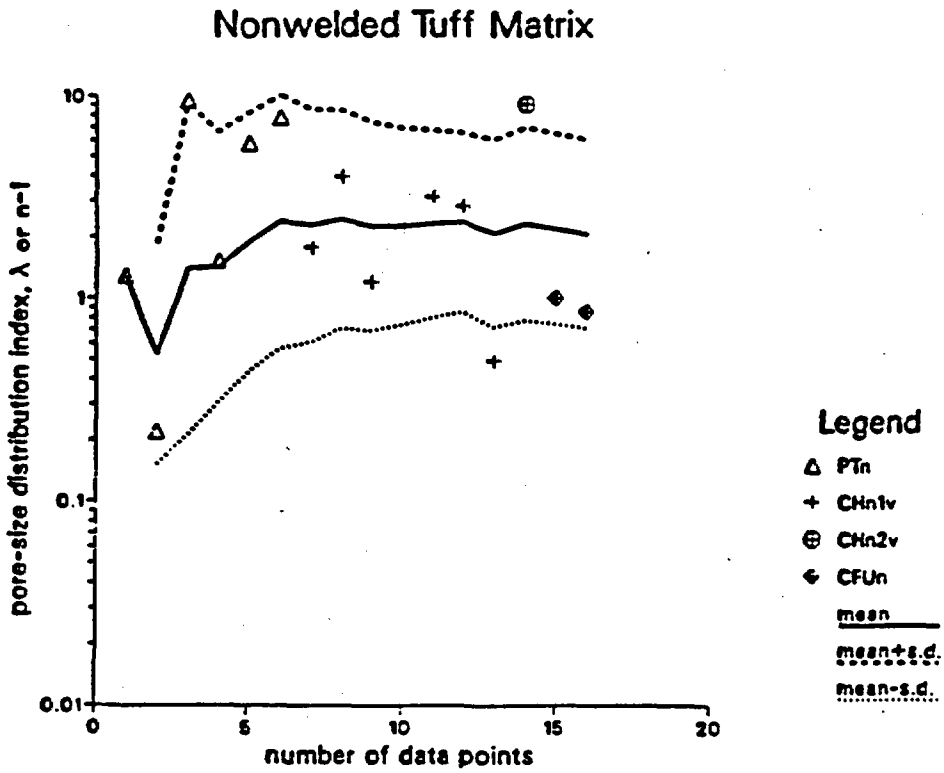

d

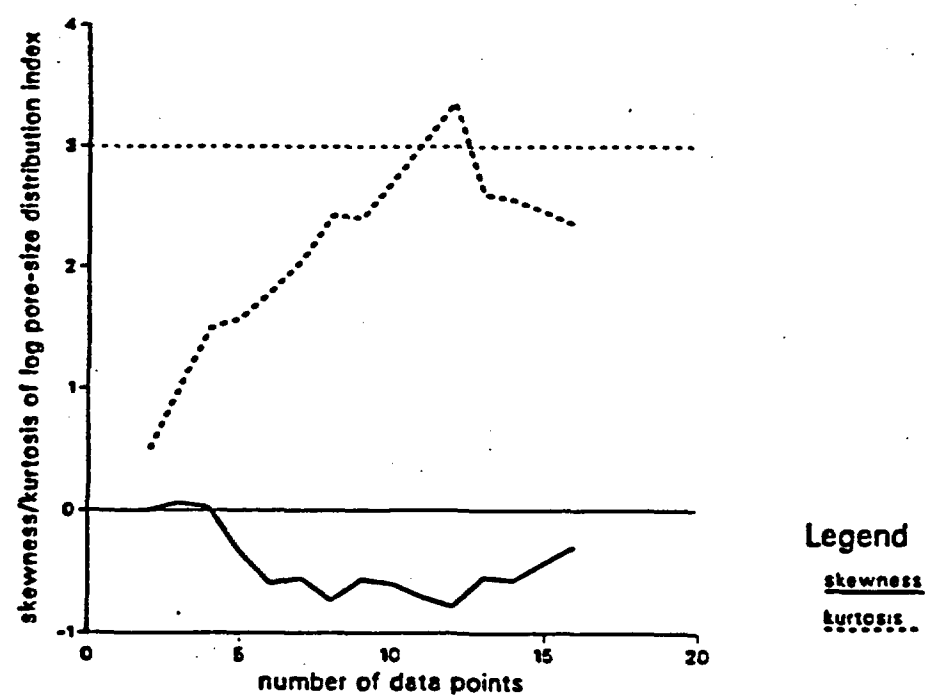

Figure 6-6. Distributions of Nonwelded Tuff Log Pore-Size Distribution Index (concluded).

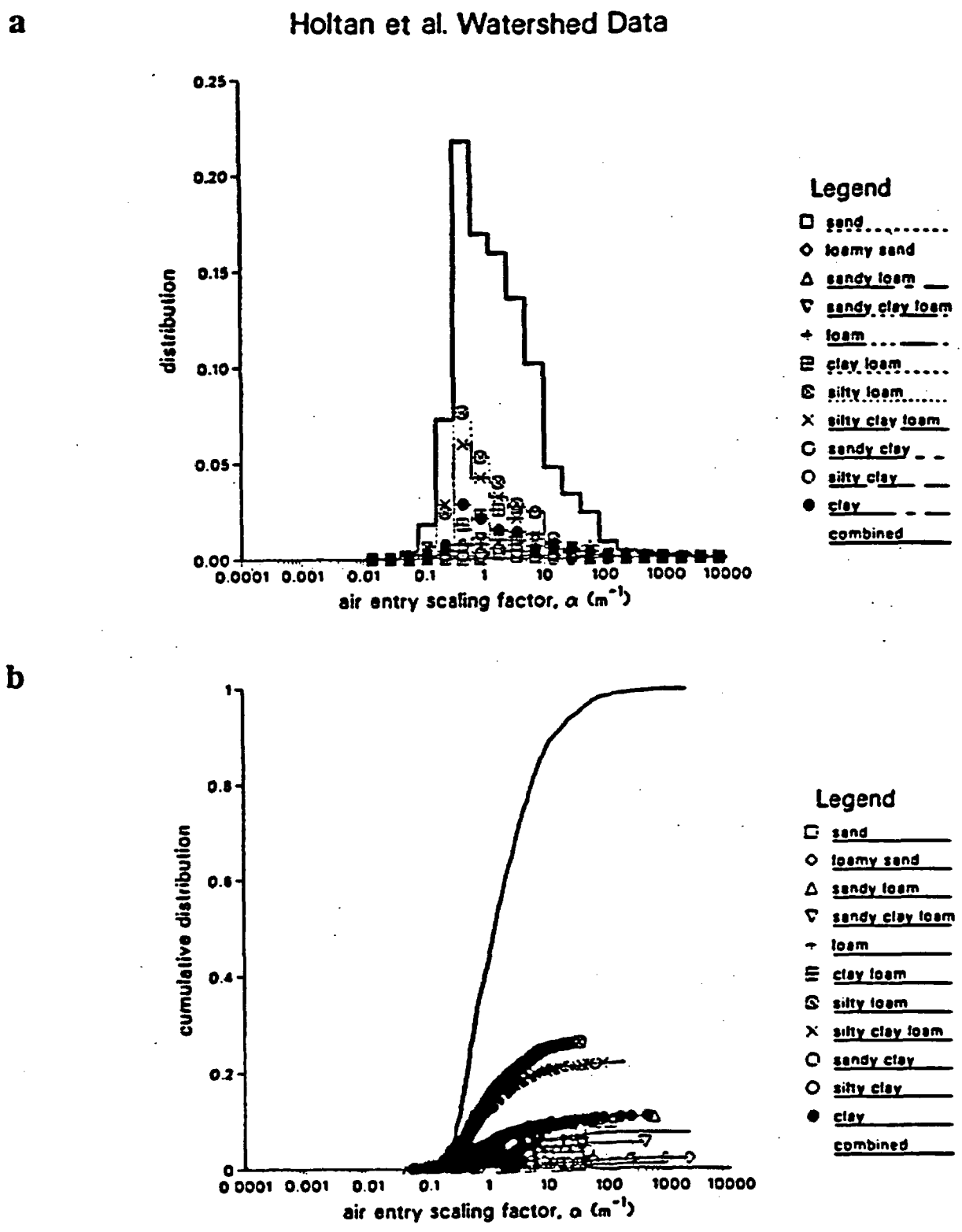

Figure 6-7. Distributions of Watershed Soil Log Air Entry Scaling Factor.

c

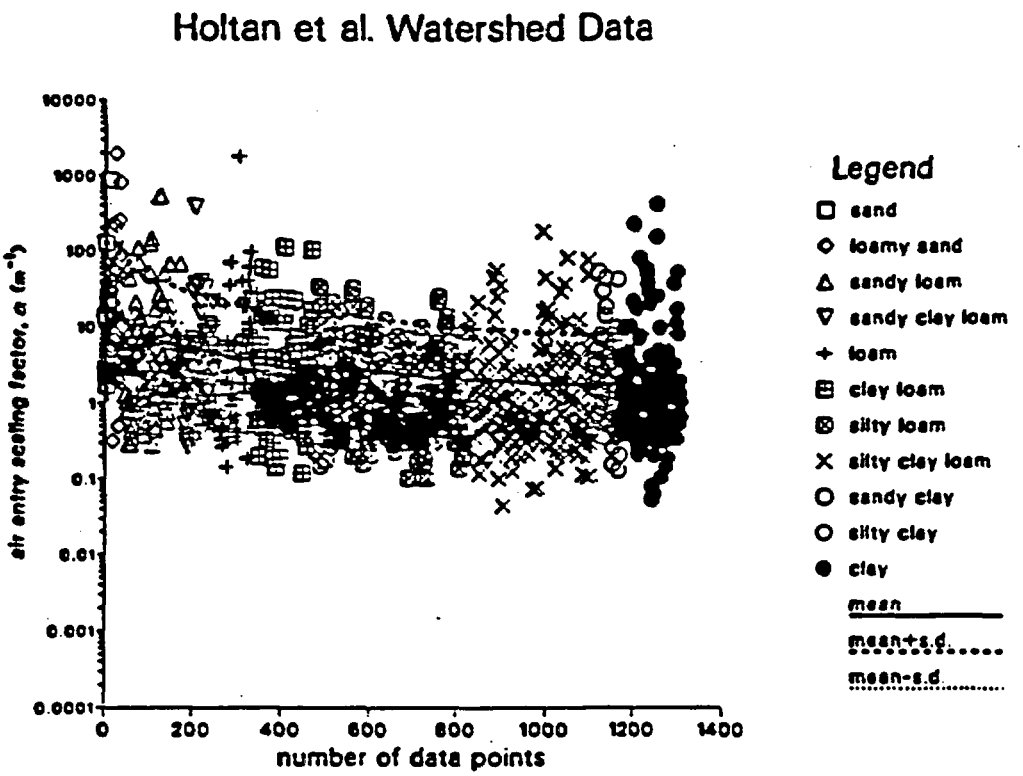

d

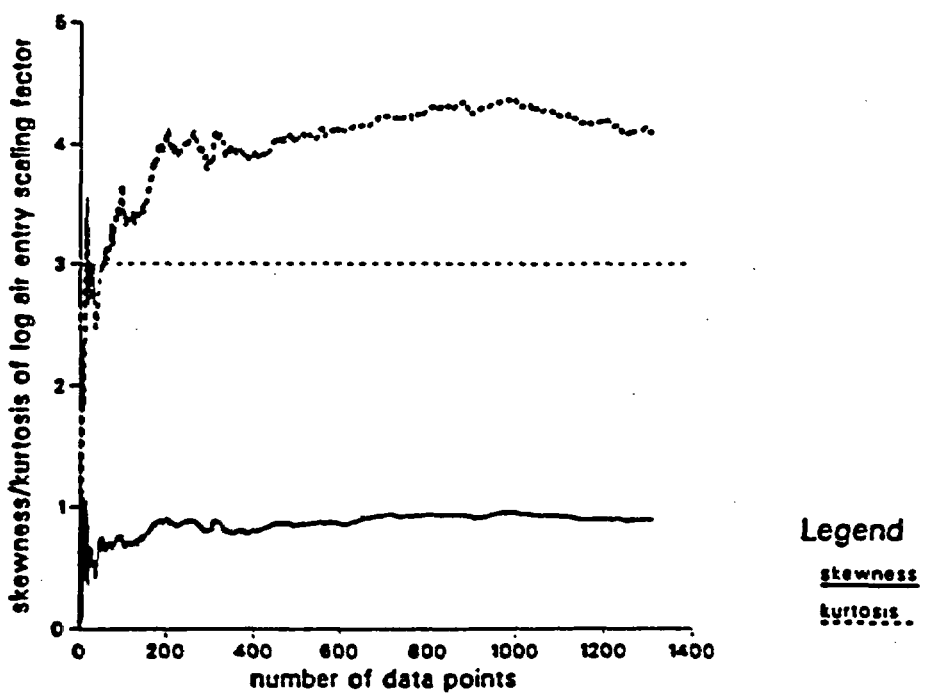

Figure 6-7. Distributions of Watershed Soil Log Air Entry Scaling Factor (concluded).

a

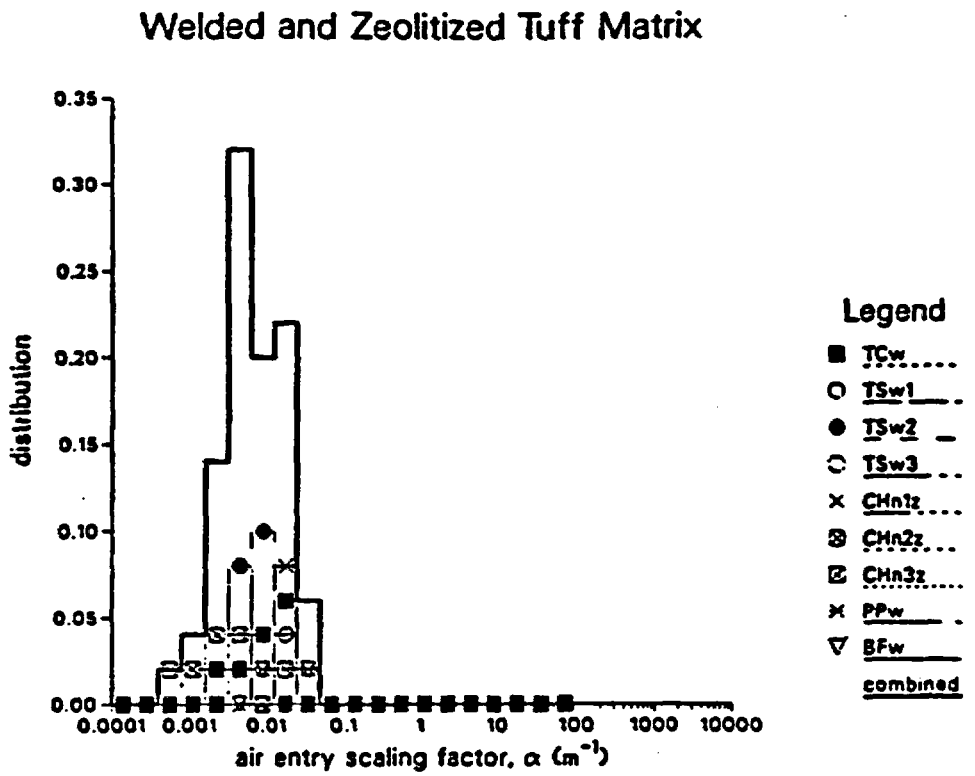

b

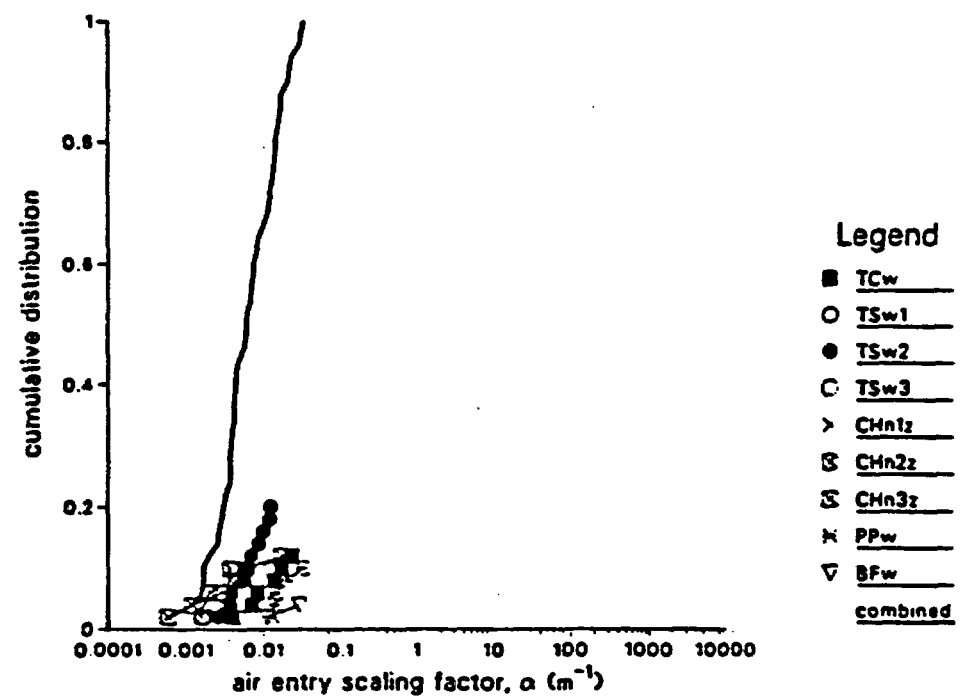

Figure 6-8. Distributions of Welded/Zeolitized Tuff Log Air Entry Scaling Factor.

c

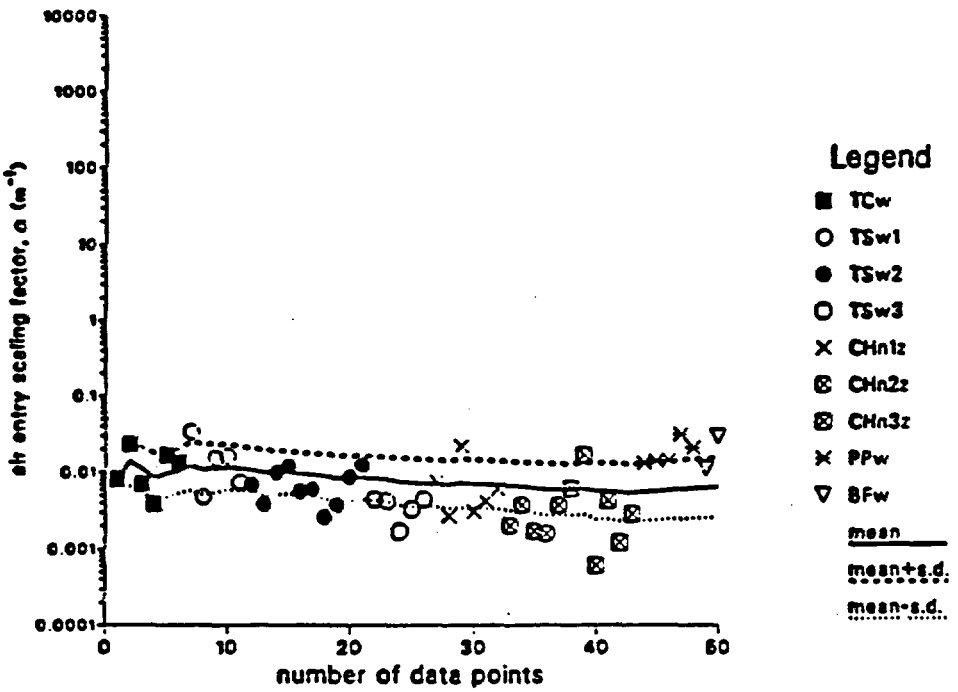

d

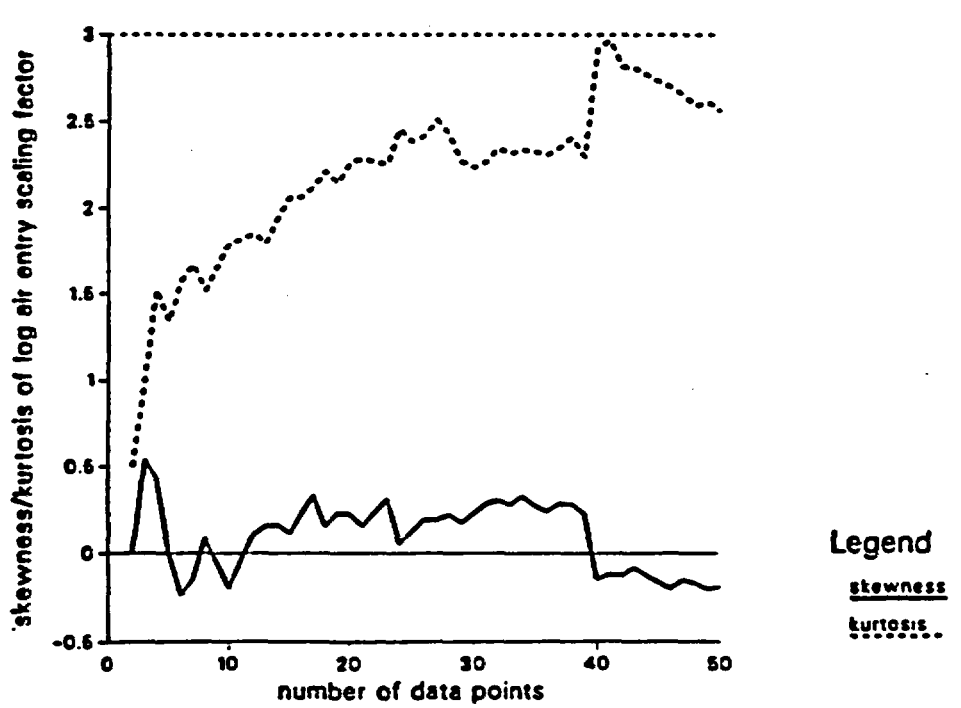

Figure 6-8. Distributions of Welded/Zeolitized Tuff Log Air Entry Scaling Factor (concluded).

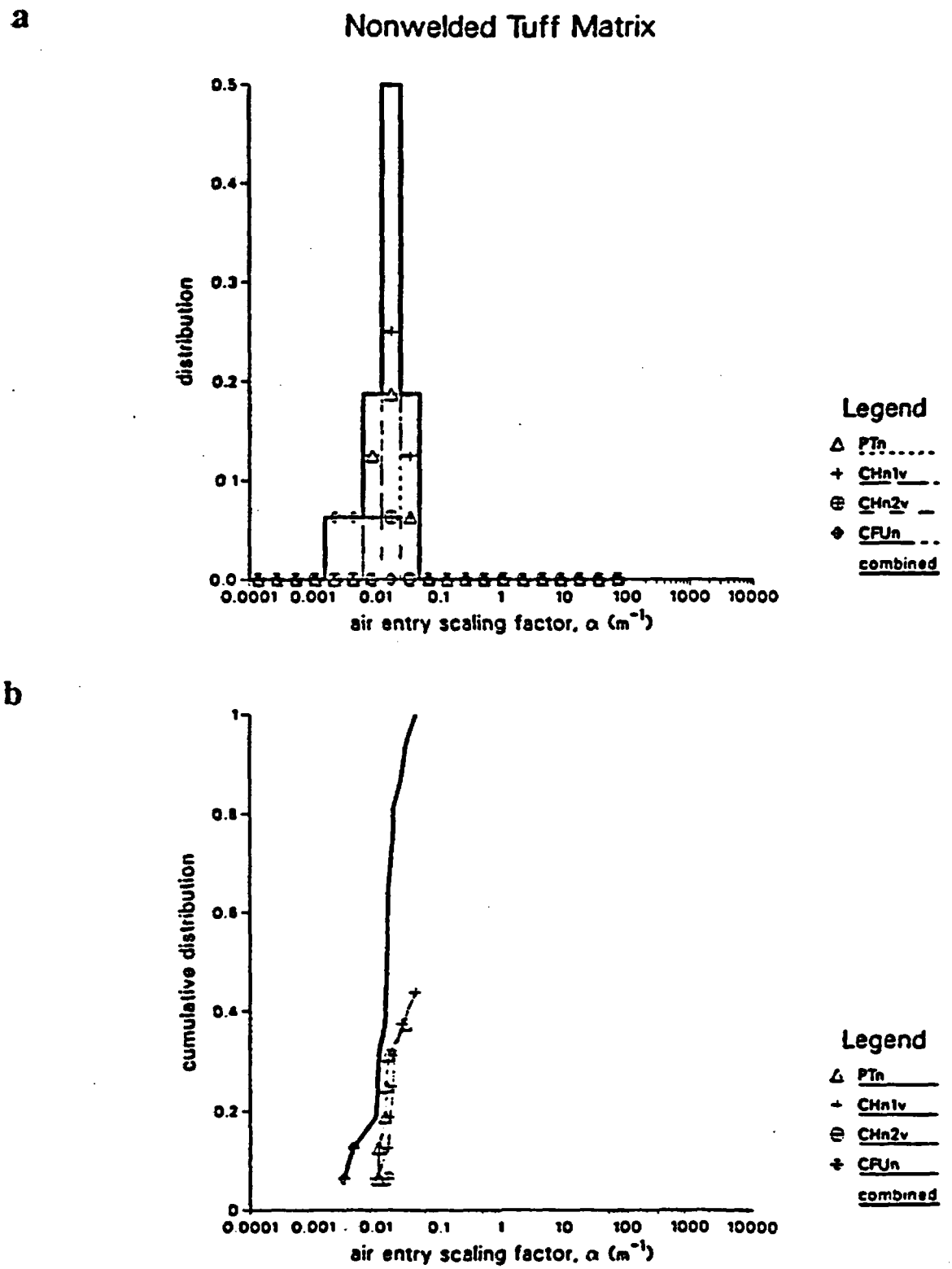

Figure 6-9. Distributions of Nonwelded Tuff Log Air Entry Scaling Factor.

c

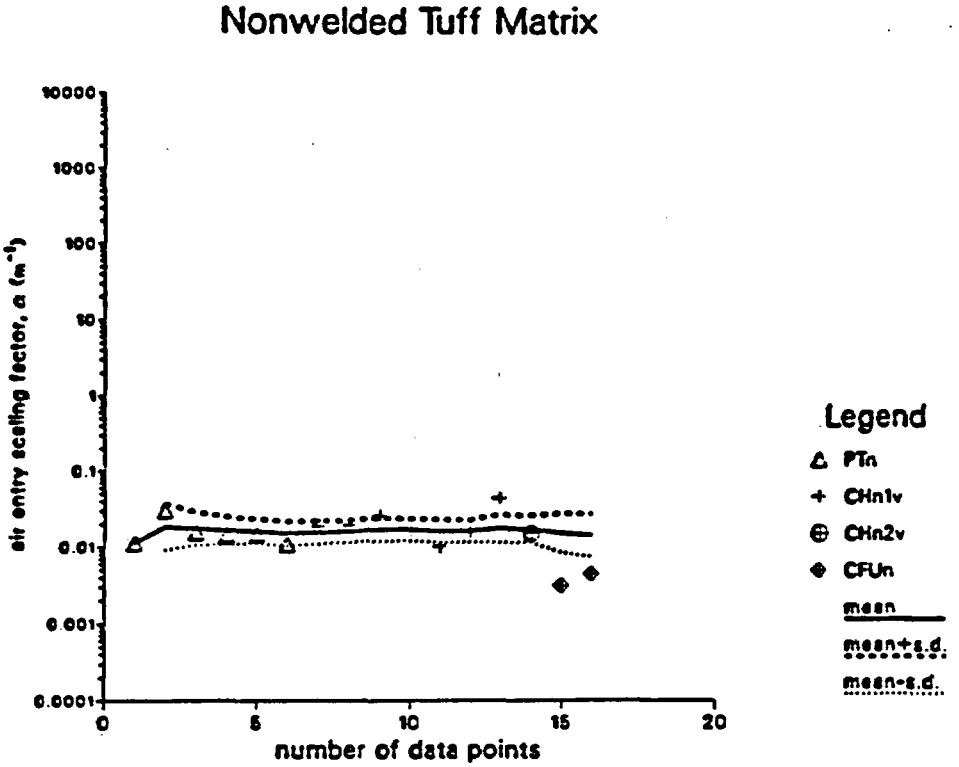

d

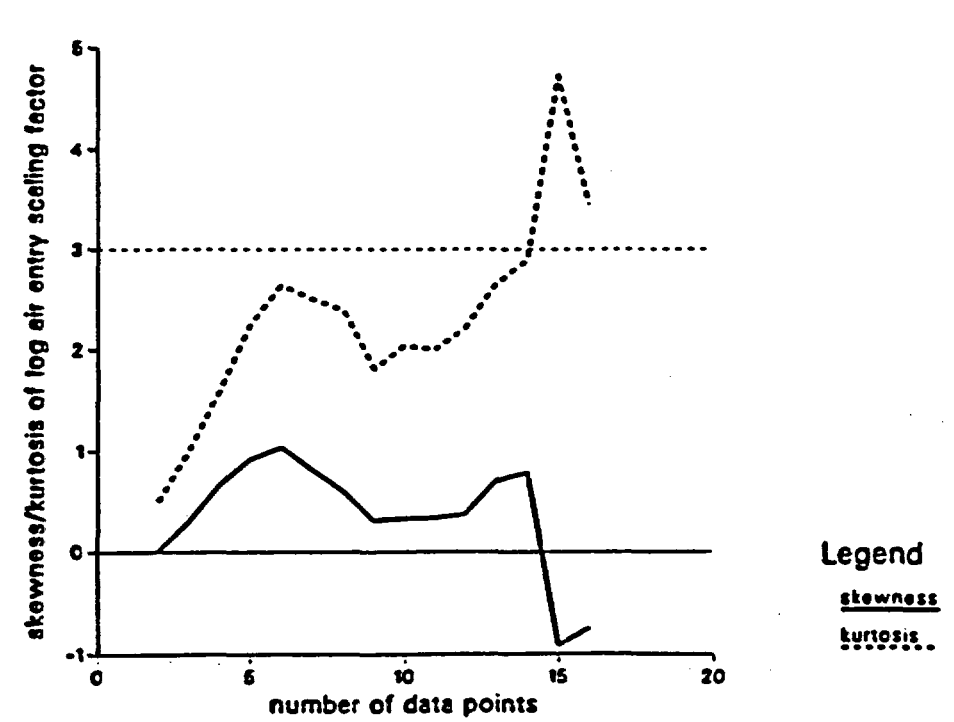

Figure 6-9. Distributions of Nonwelded Tuff Log Air Entry Scaling Factor (concluded).

a

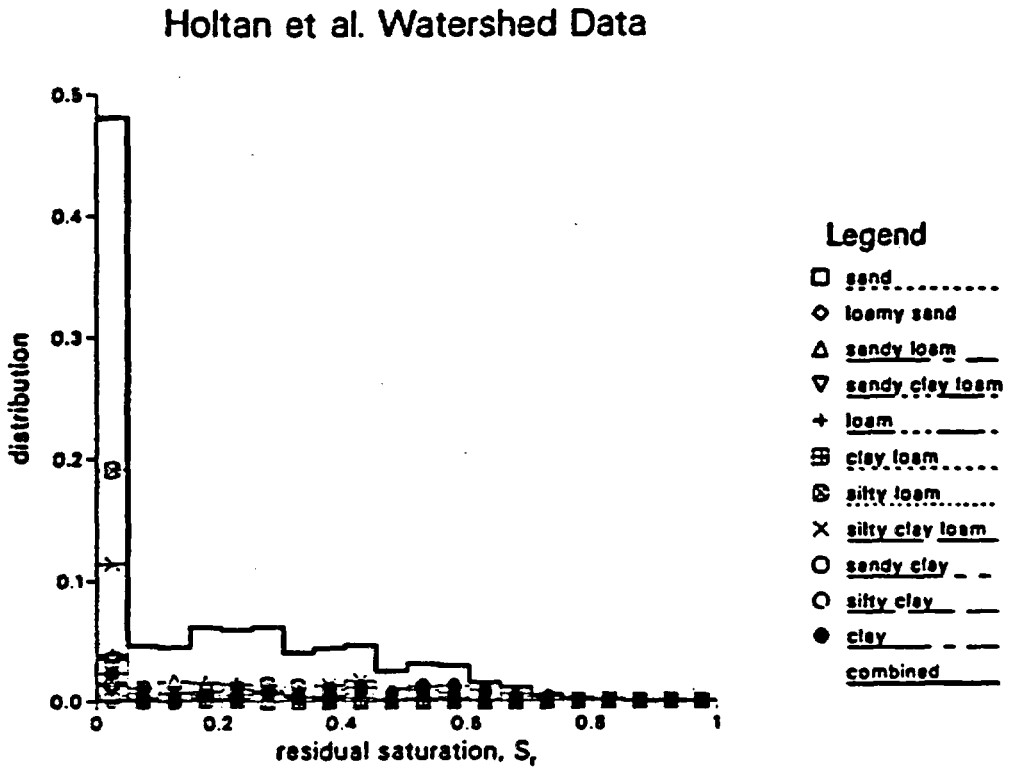

b

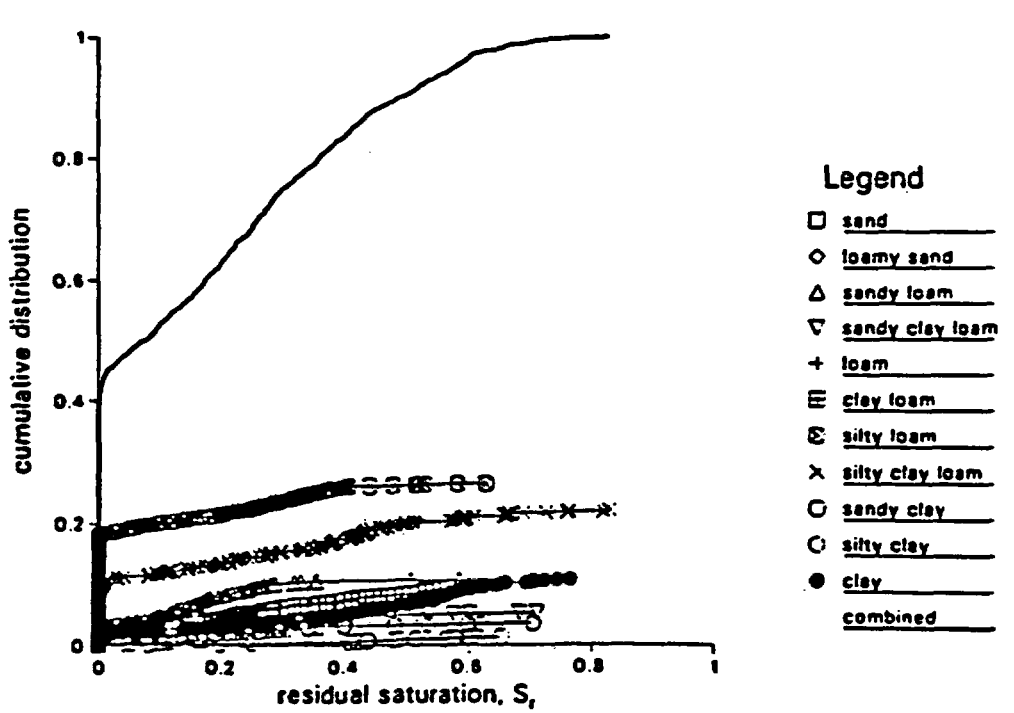

Figure 6-10. Distributions of Watershed Soil Residual Saturation.

c

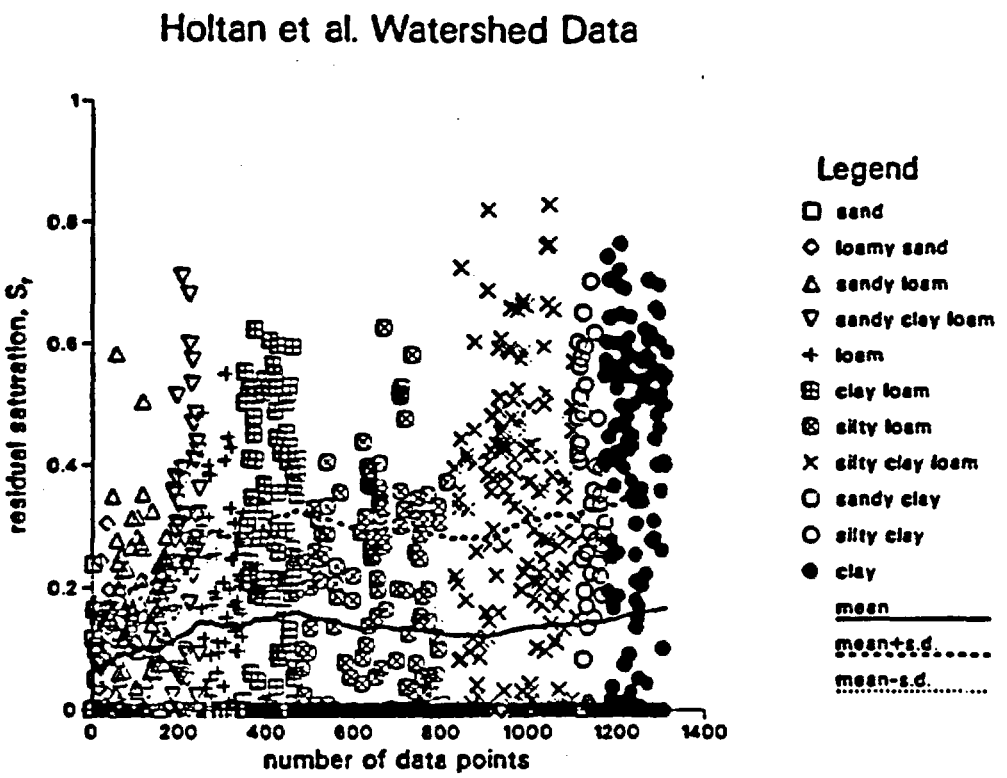

d

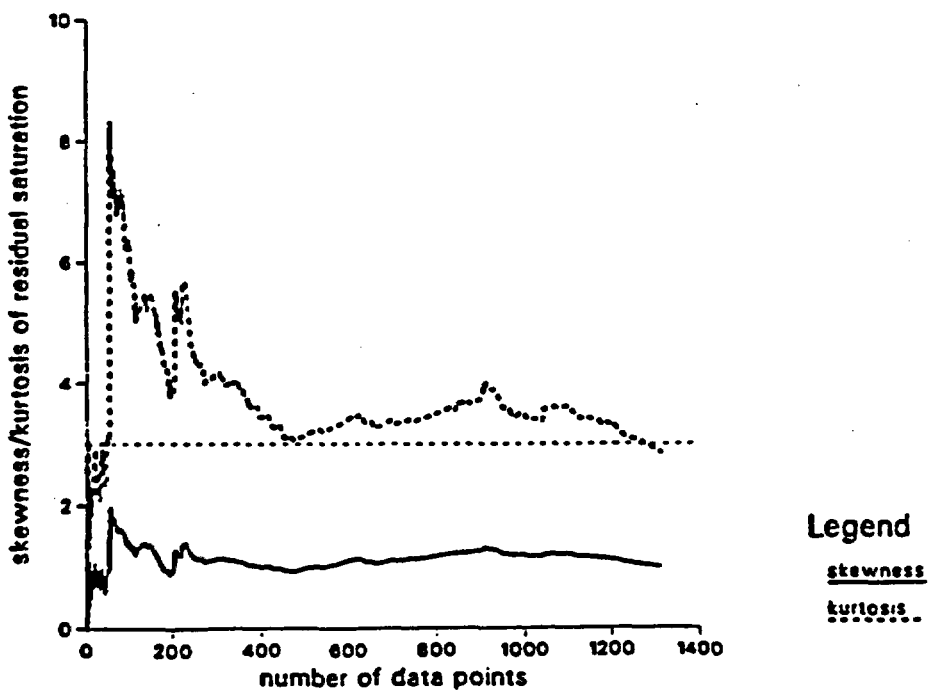

Figure 6-10. Distributions of Watershed Soil Residual Saturation (concluded).

a

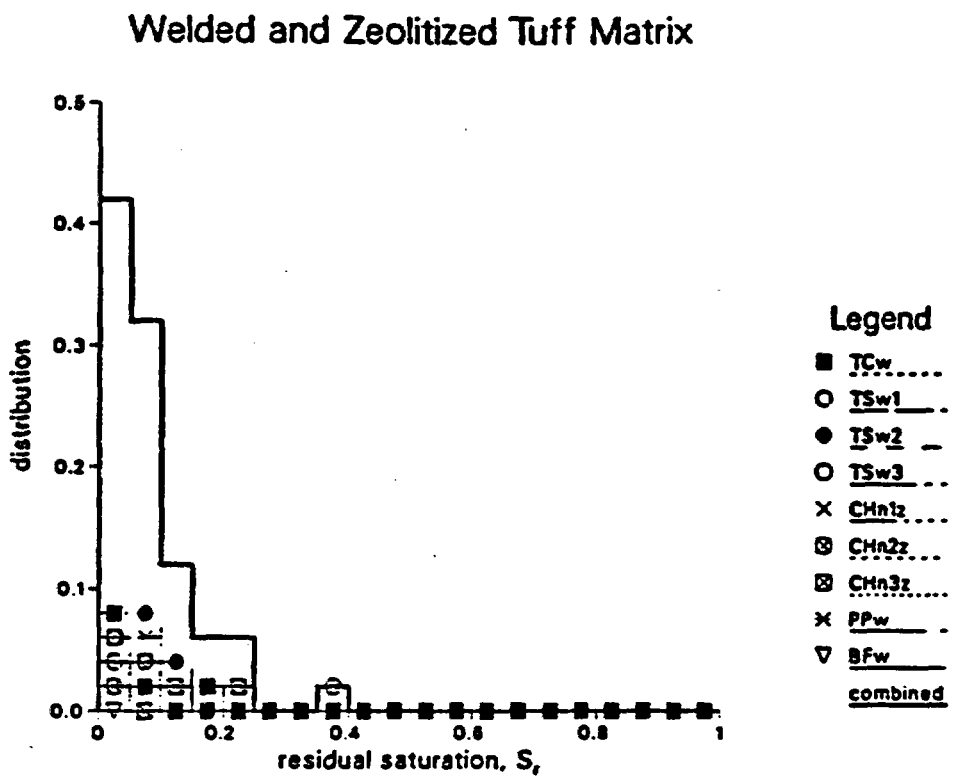

b

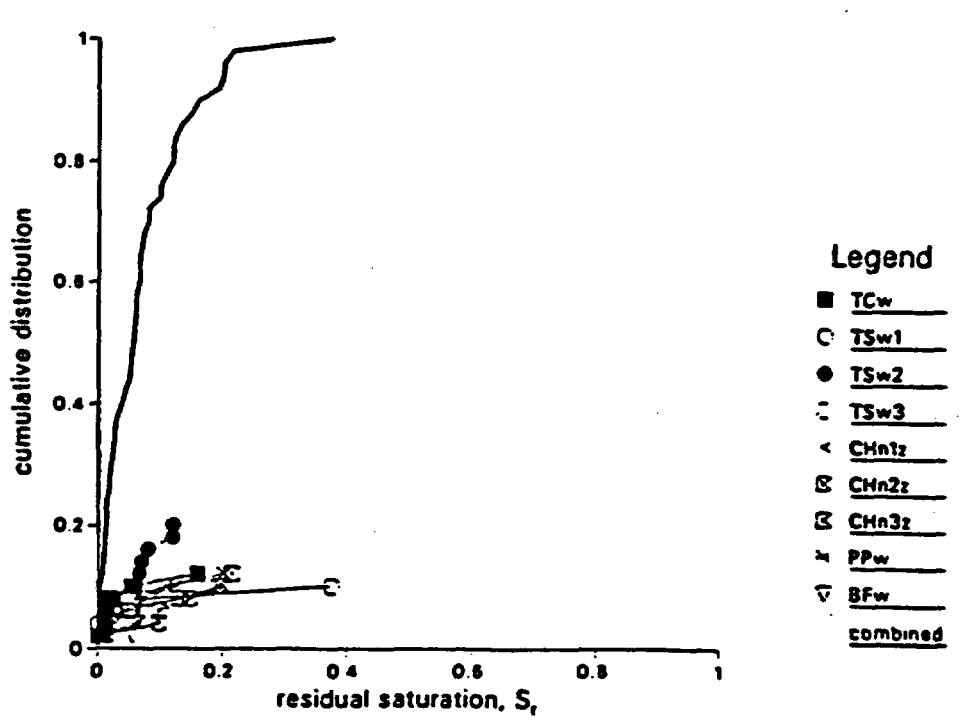

Figure 6-11. Distributions of Welded/Zeolitized Tuff Residual Saturation.

c

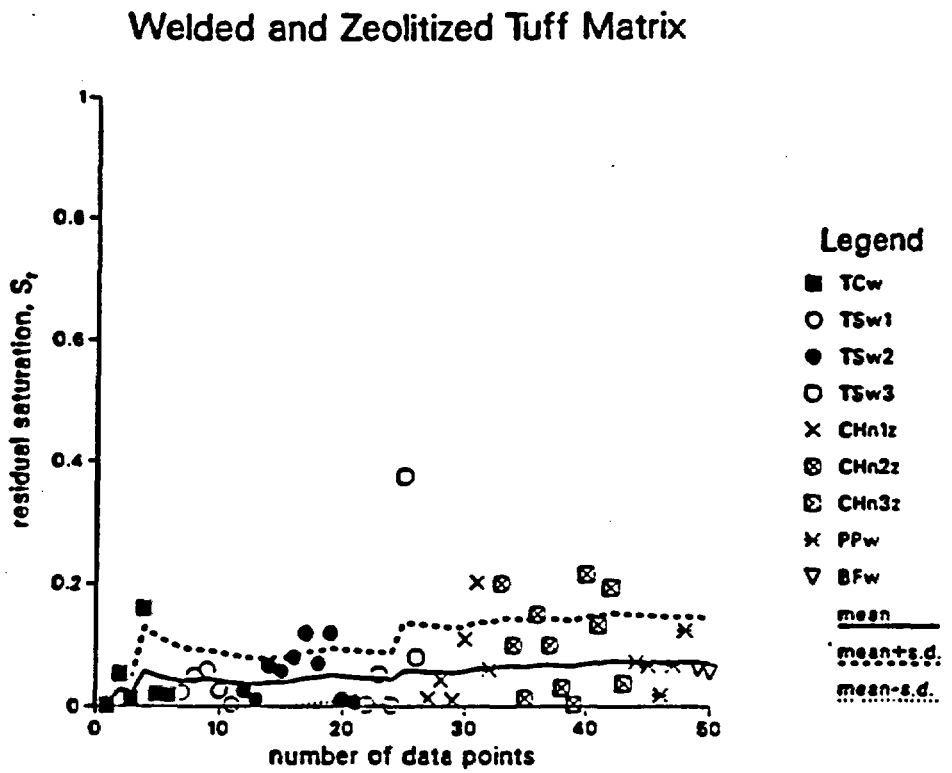

d

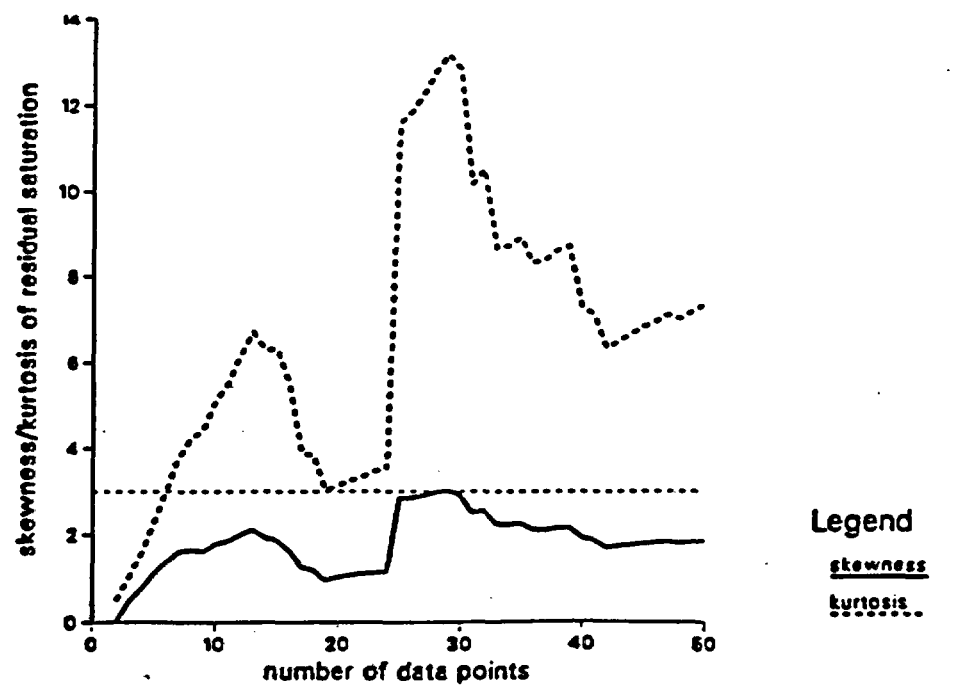

Figure 6-11. Distributions of Welded/Zeolitized Tuff Residual Saturation (concluded).

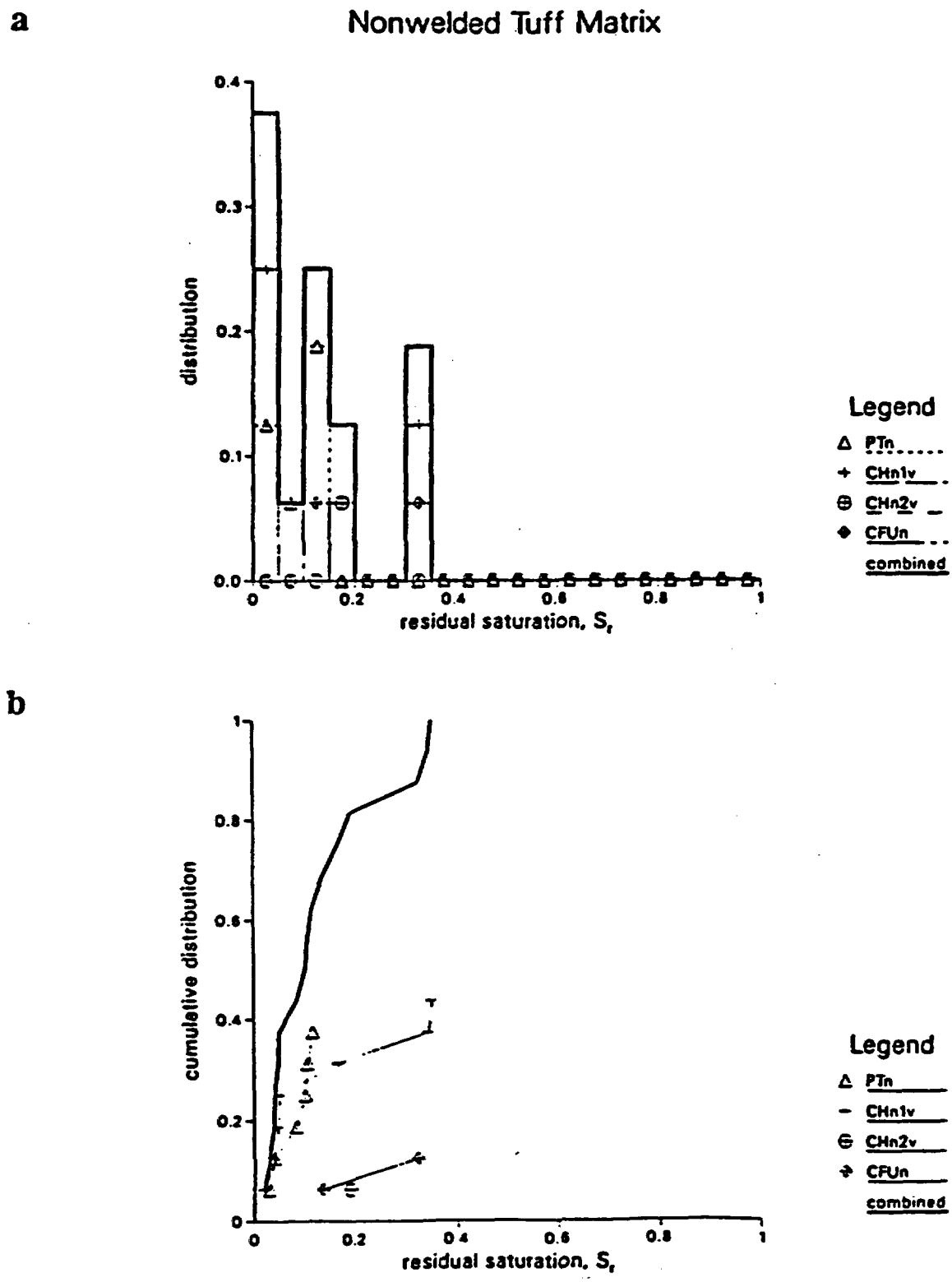

Figure 6-12. Distributions of Nonwelded Tuff Residual Saturation.

c

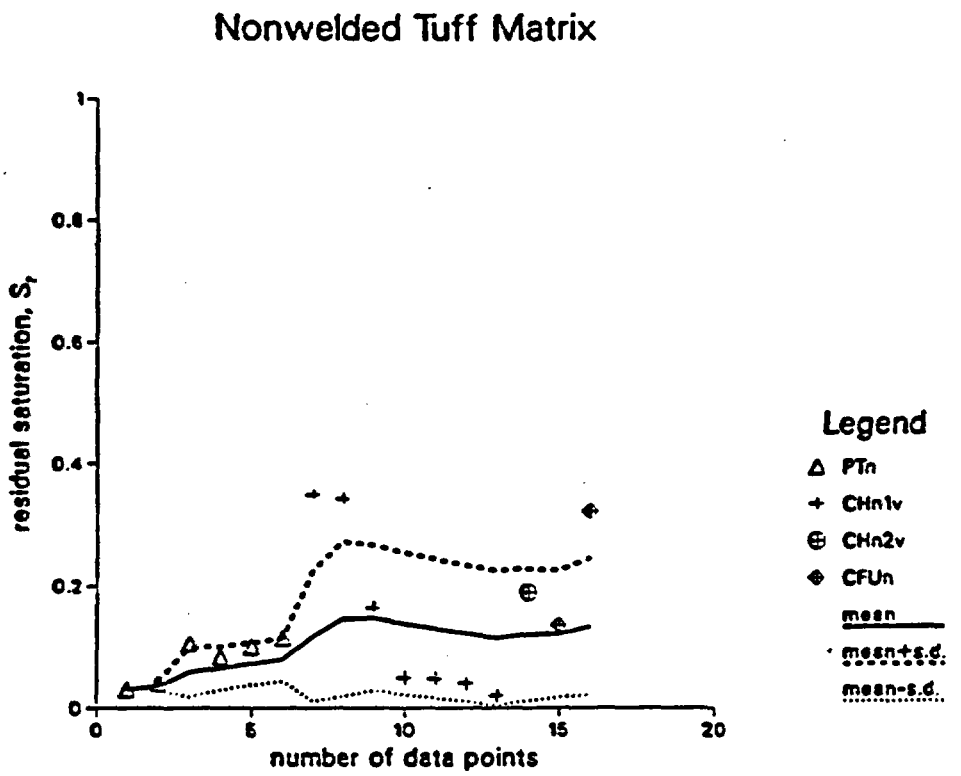

d

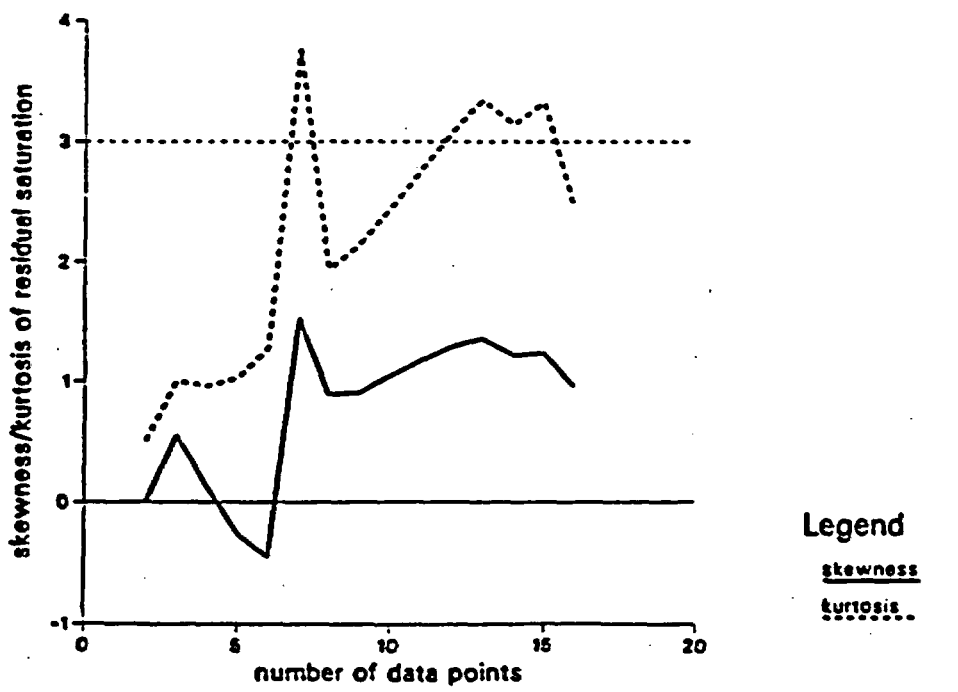

Figure 6-12. Distributions of Nonwelded Tuff Residual Saturation (concluded).

a

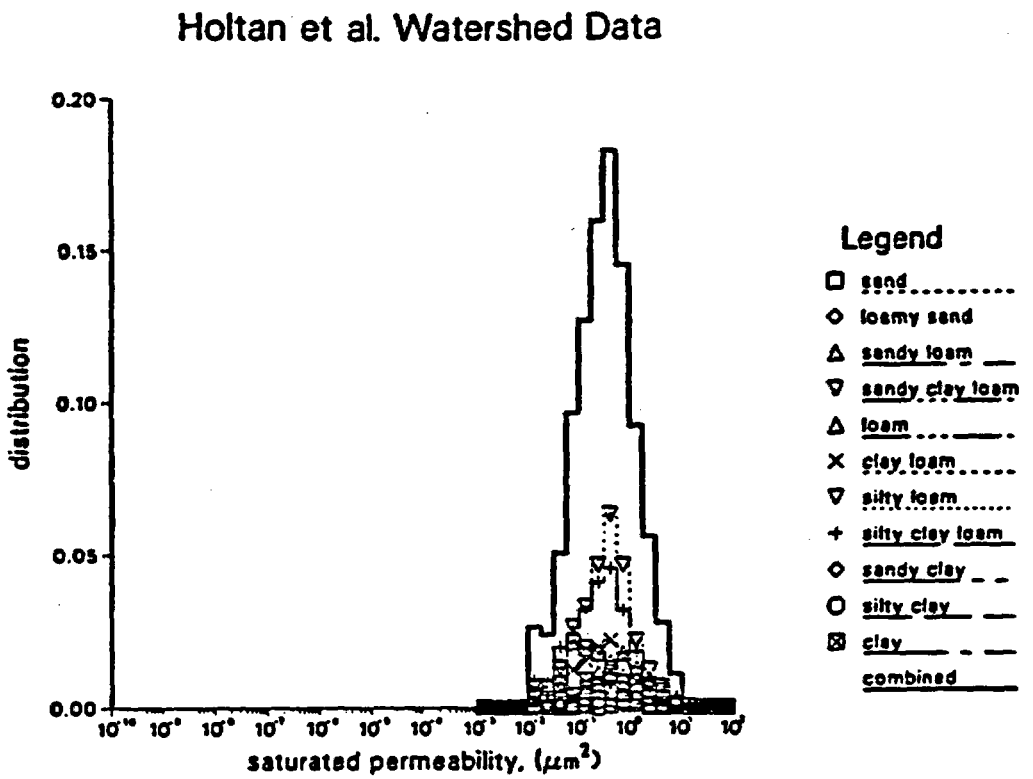

b

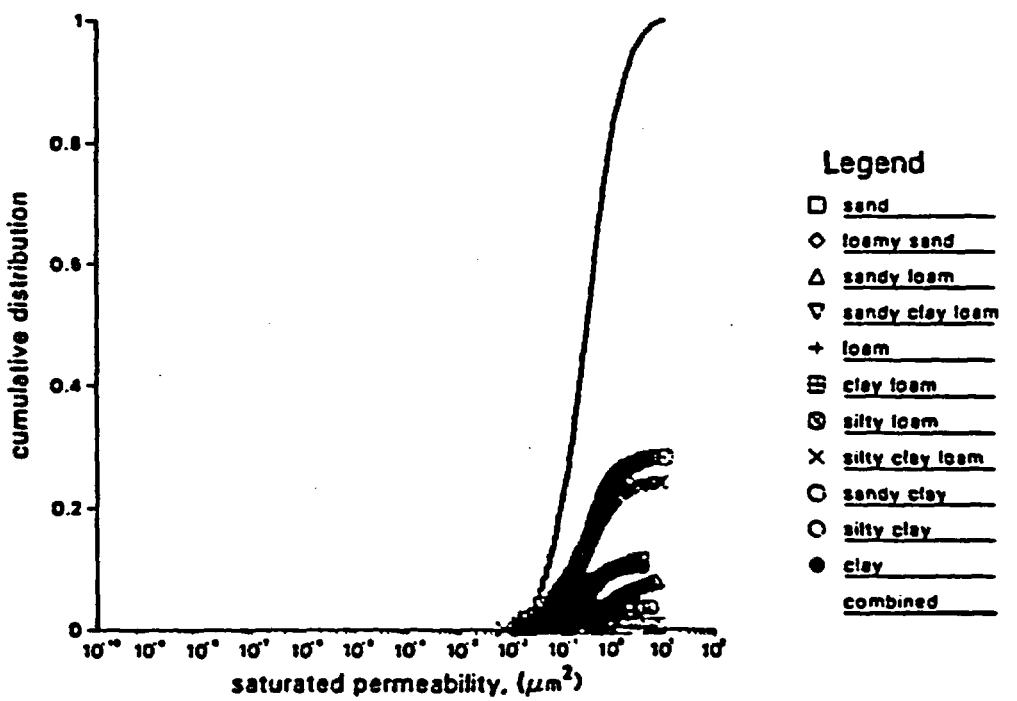

Figure 6-13. Distributions of Watershed Soil Log Saturated Permeability.

c

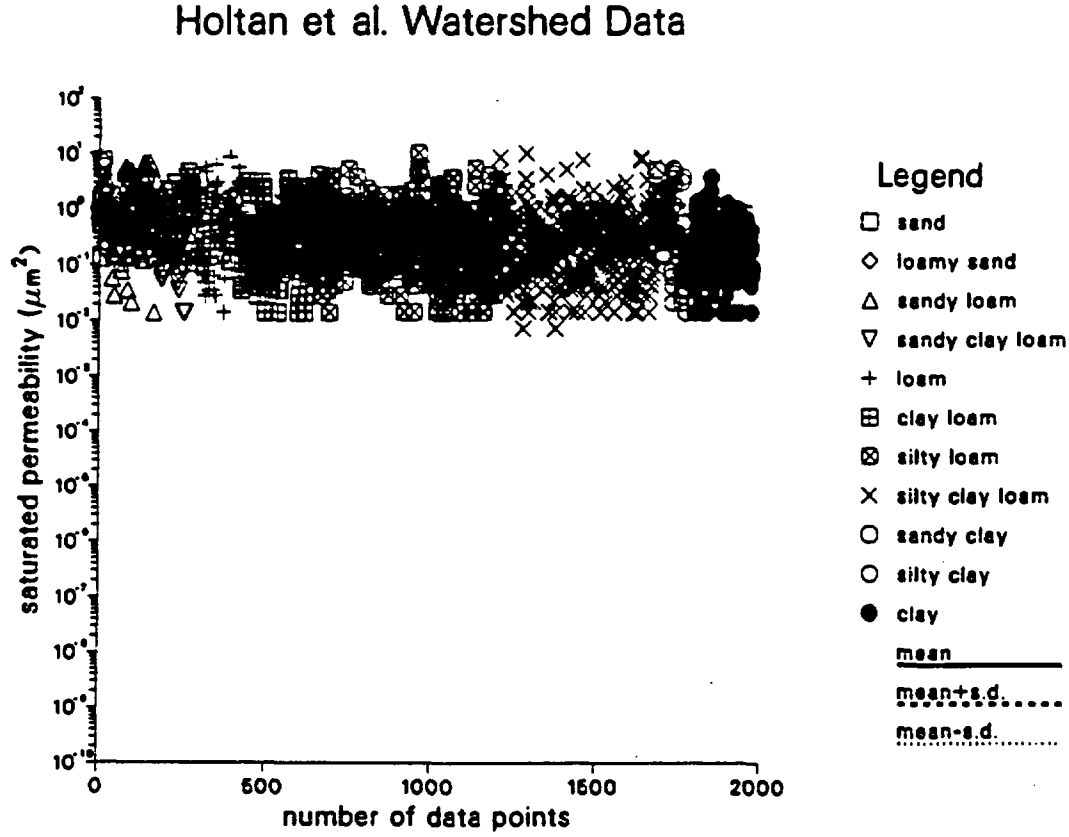

d

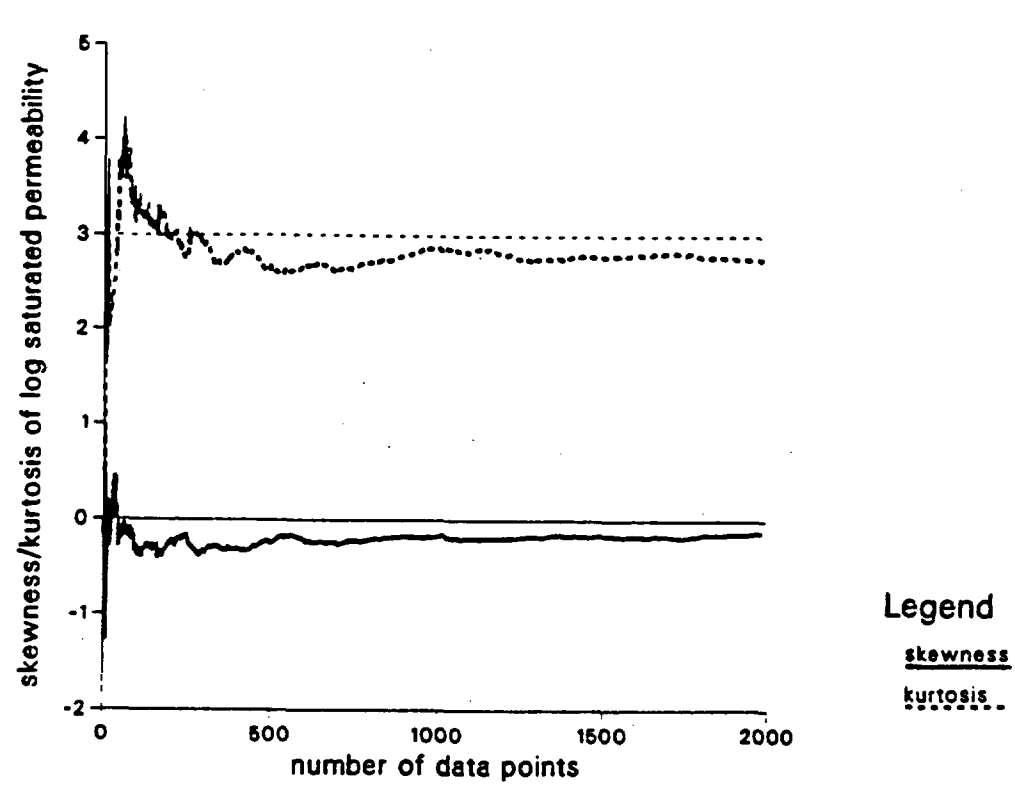

Figure 6-13. Distributions of Watershed Soil Log Saturated Permeability (concluded).

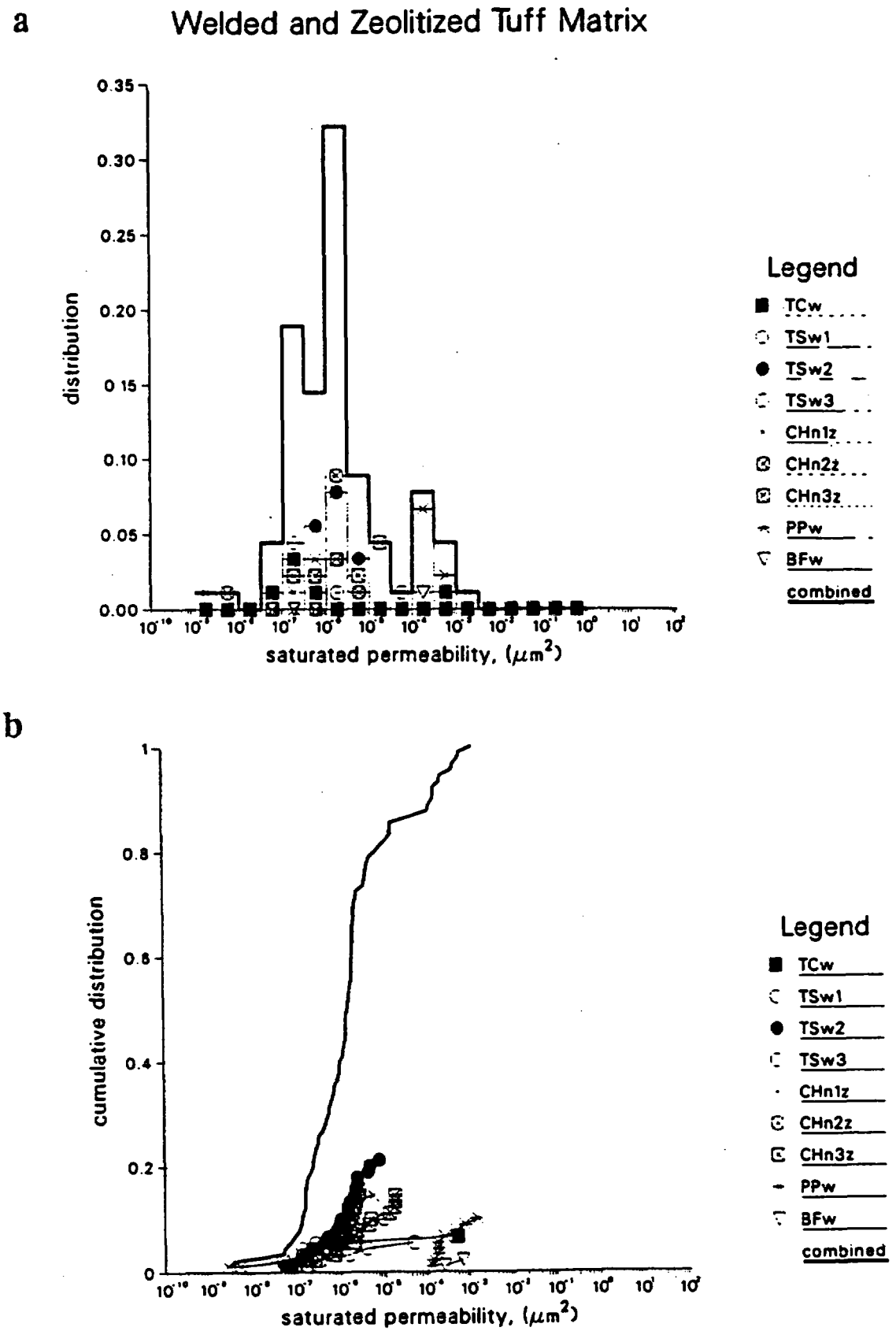

Figure 6-14. Distributions of Welded/Zeolitized Tuff Log Saturated Permeability.

c

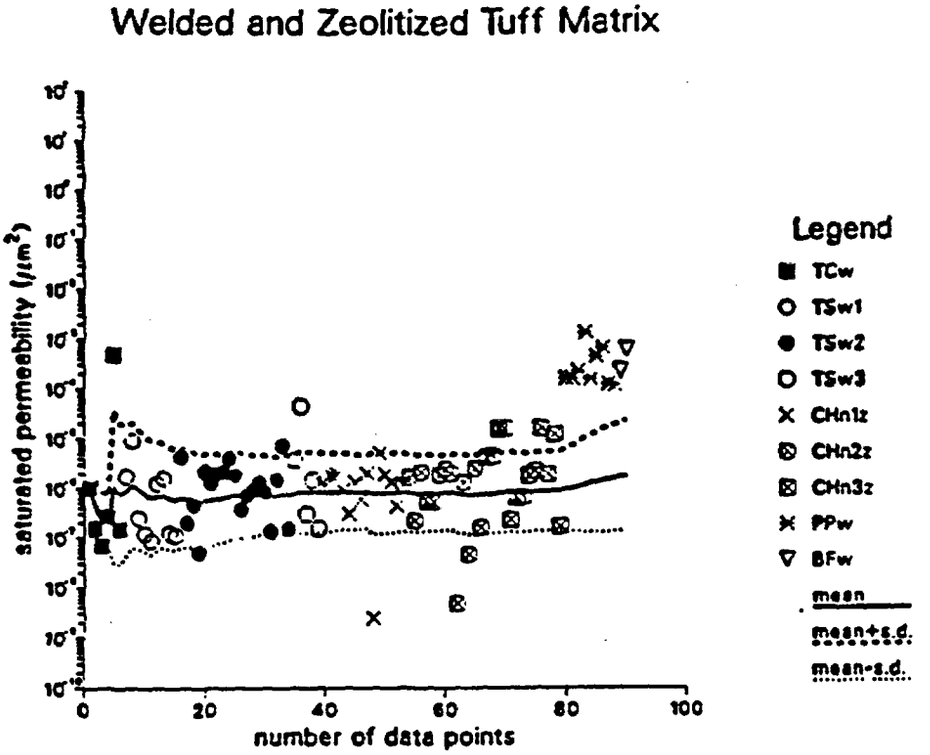

d

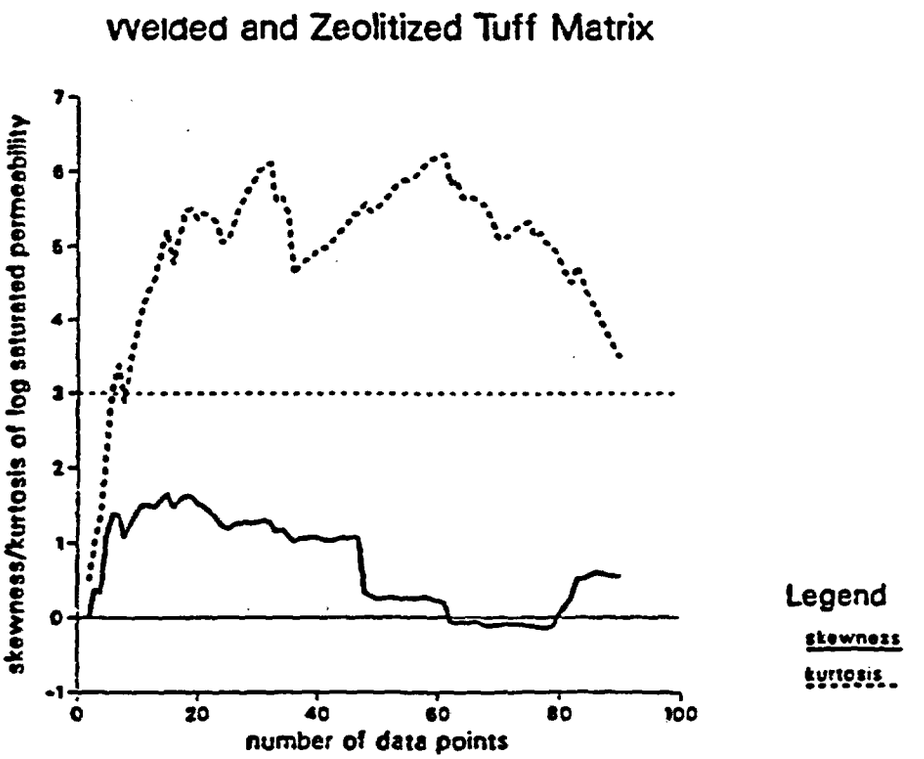

Figure 6-14. Distributions of Welded/Zeolitized Tuff Log Saturated Permeability (concluded).

a

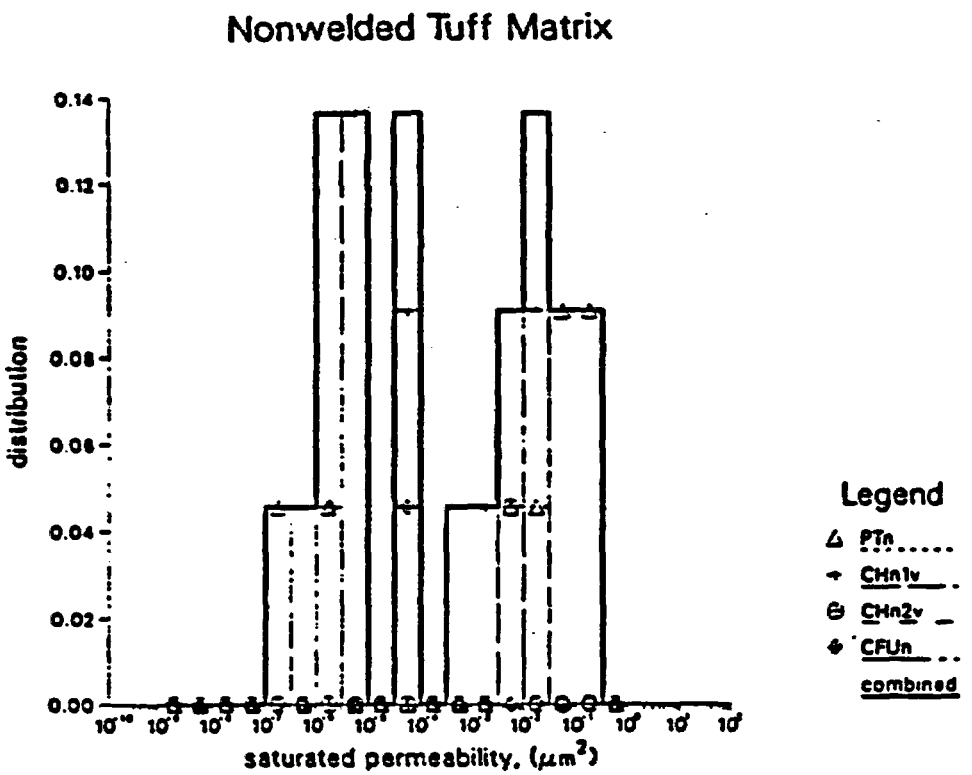

b

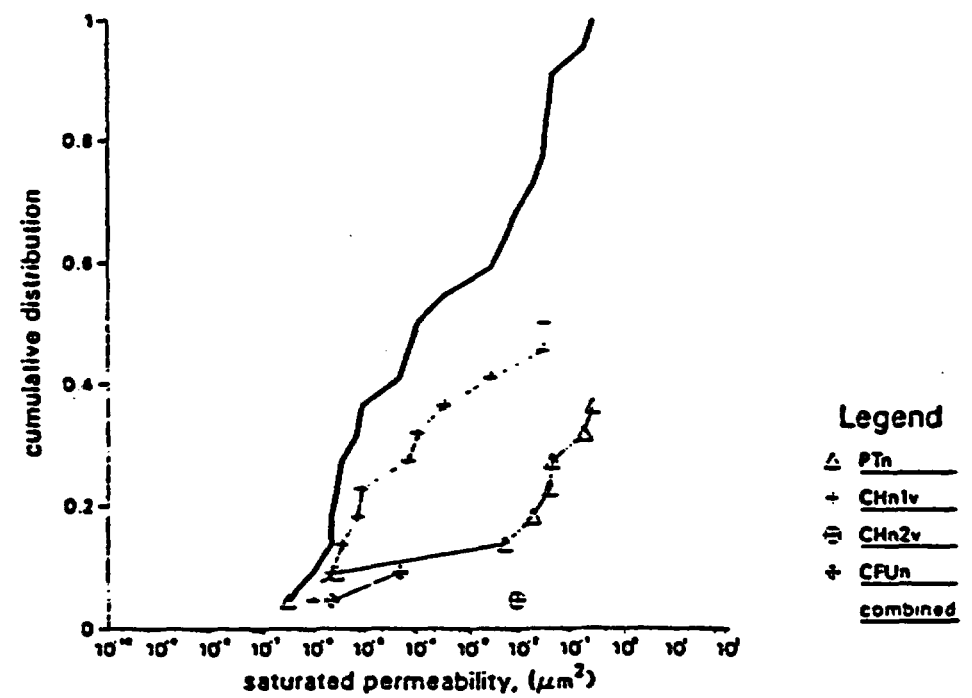

Figure 6-15. Distributions of Nonwelded Tuff Log Saturated Permeability.

c

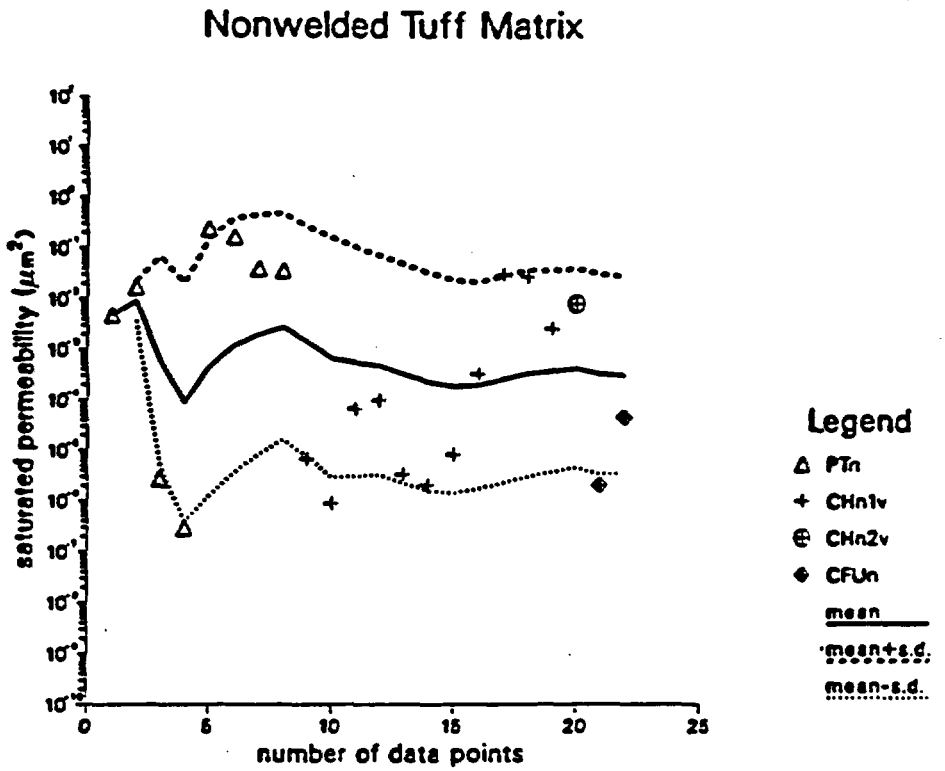

d

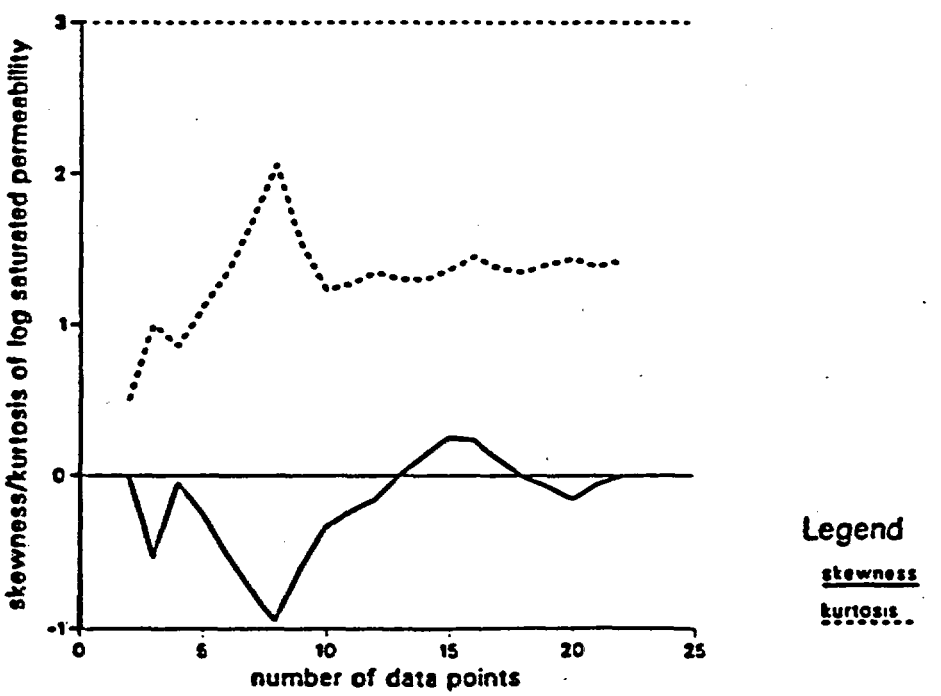

Figure 6-15. Distributions of Nonwelded Tuff Log Saturated Permeability (concluded).

a

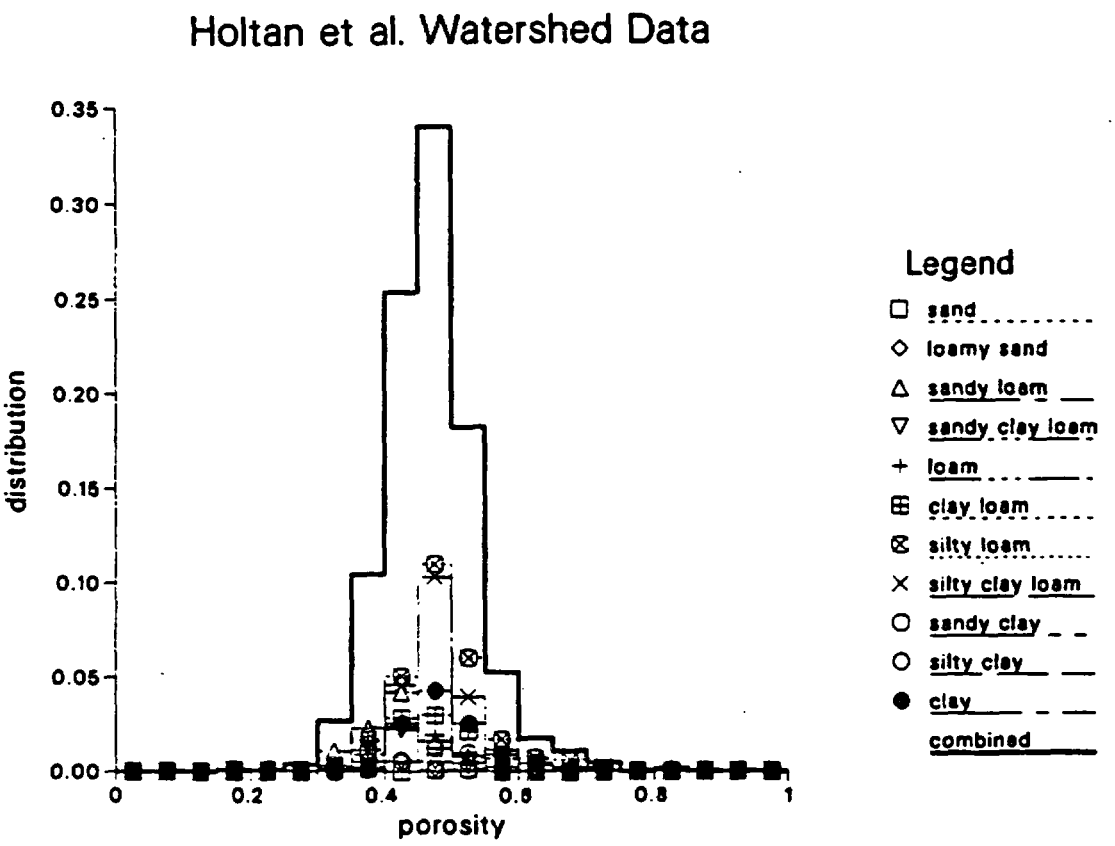

b

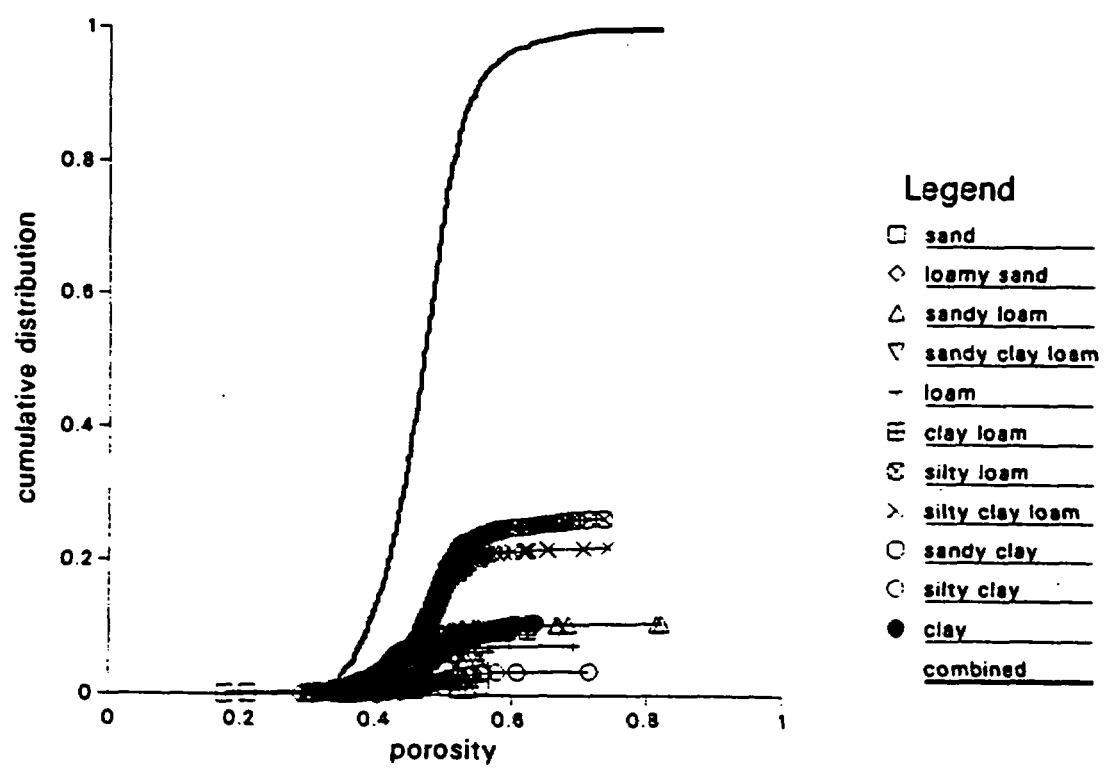

Figure 6-16. Distributions of Watershed Soil Porosity.

c

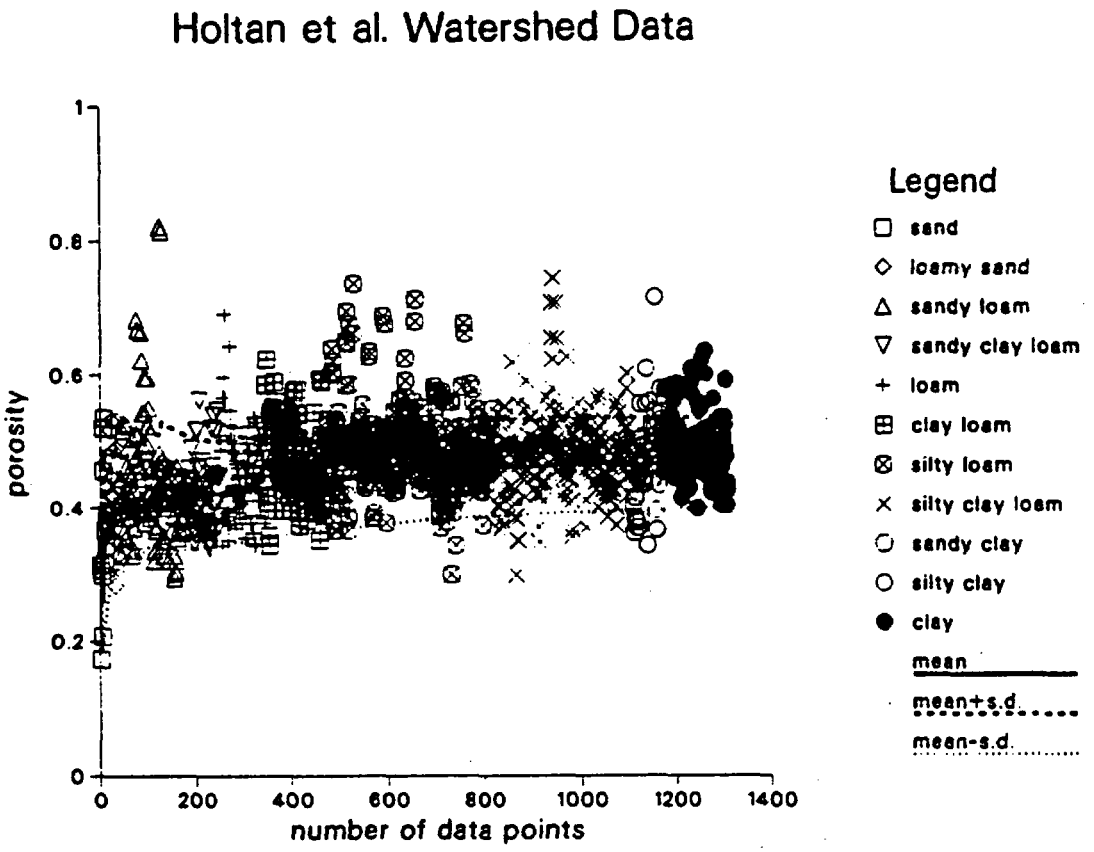

d

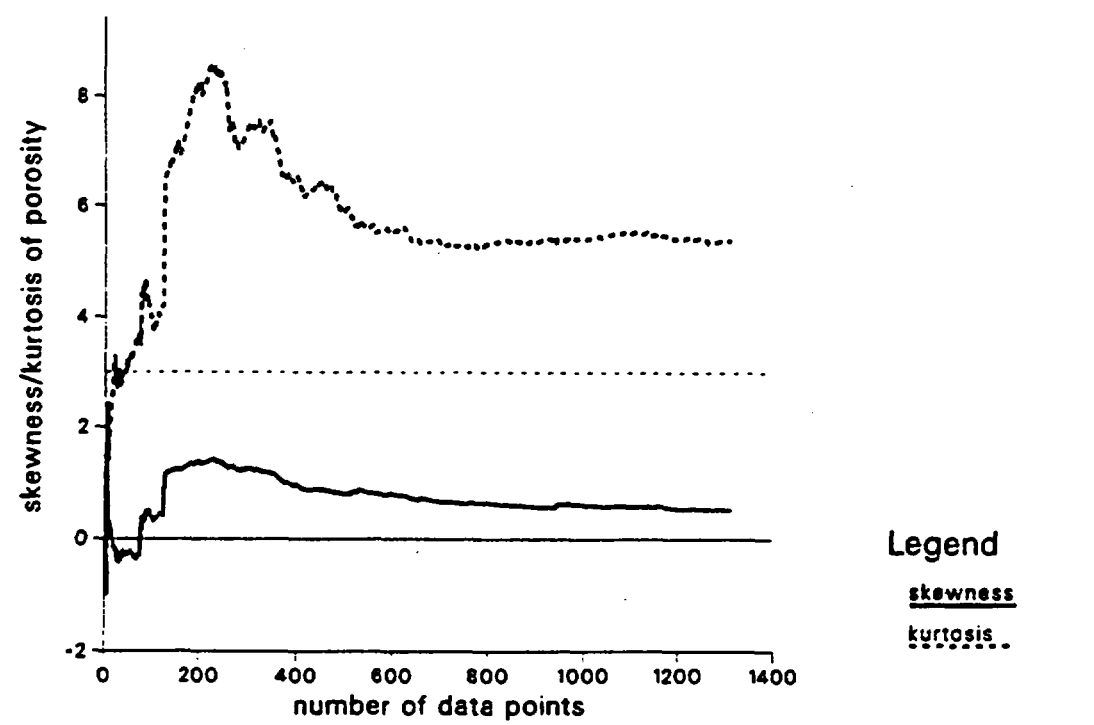

Figure 6-16. Distributions of Watershed Soil Porosity (concluded).

a

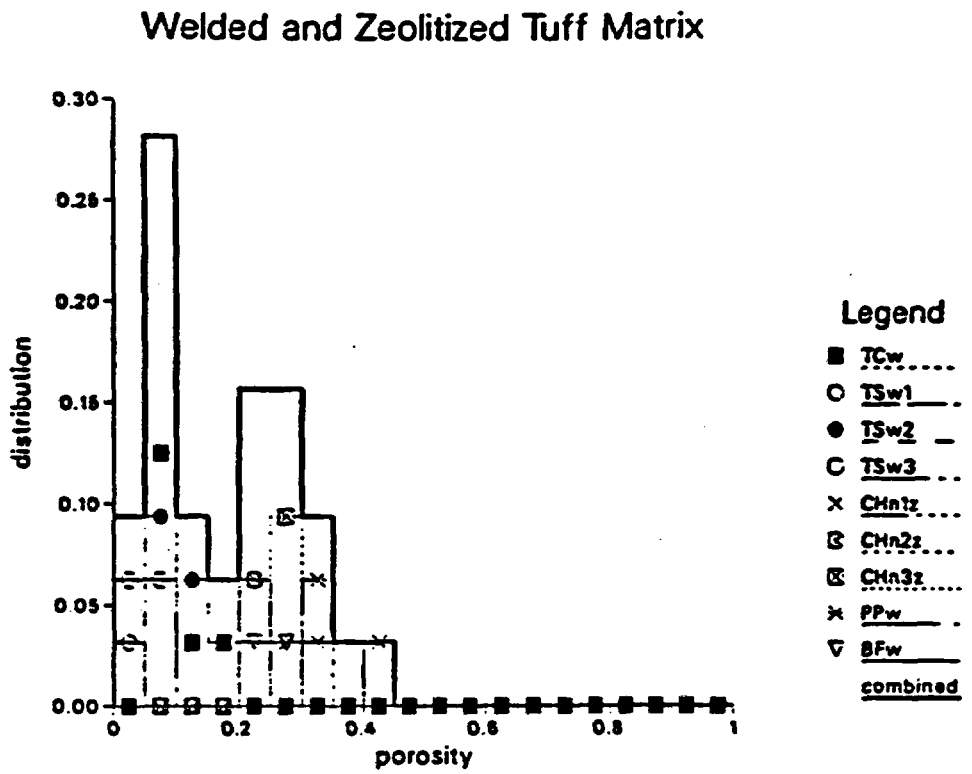

b

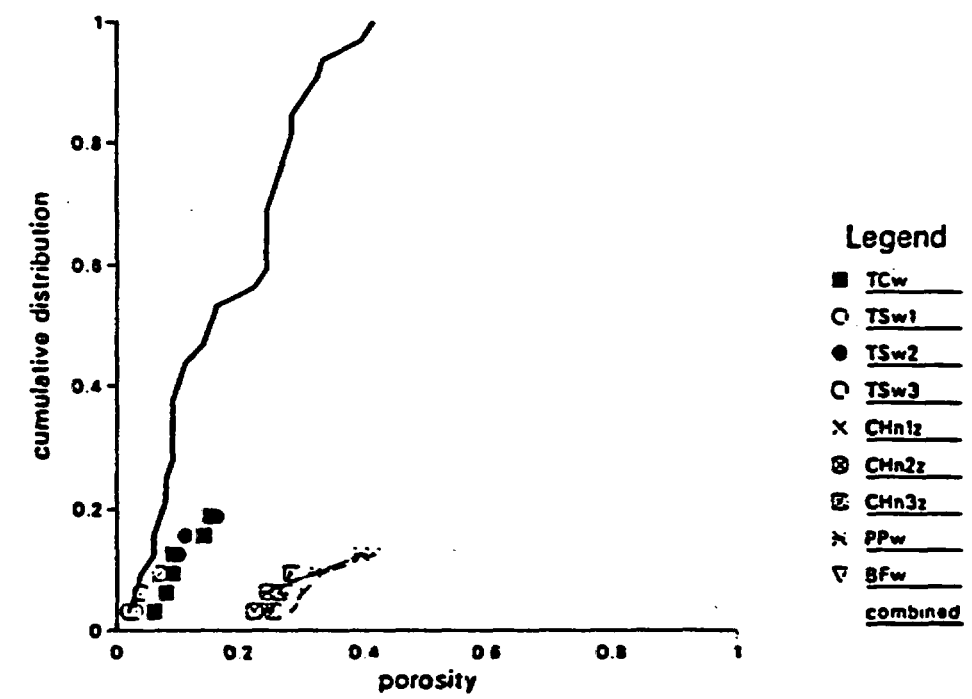

Figure 6-17. Distributions of Welded/Zeolitized Tuff Porosity.

c

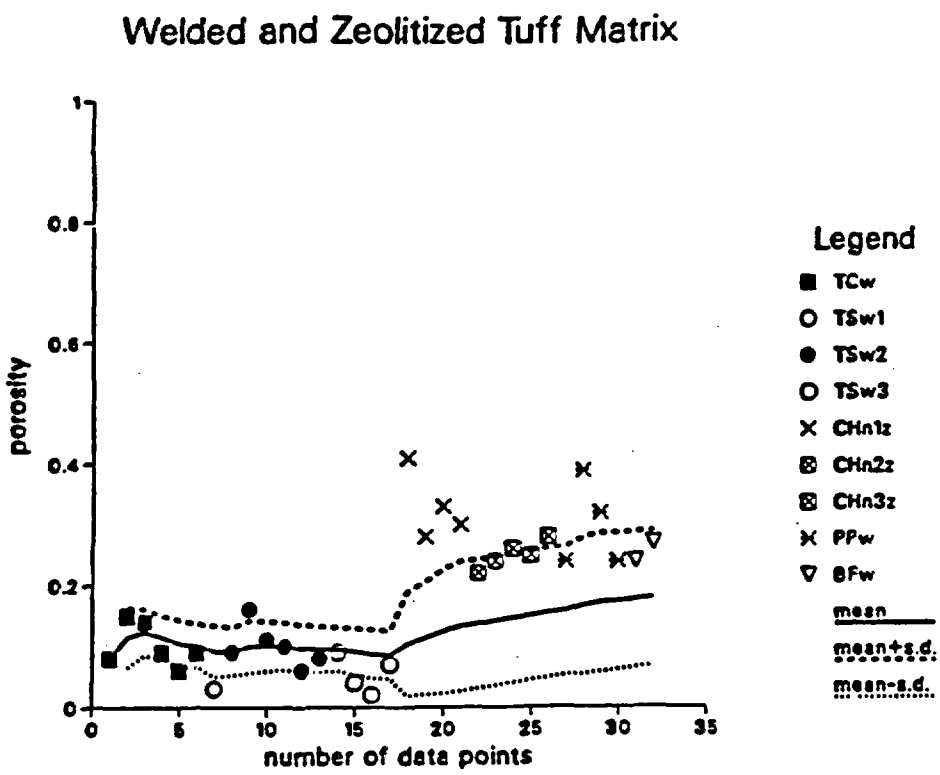

d

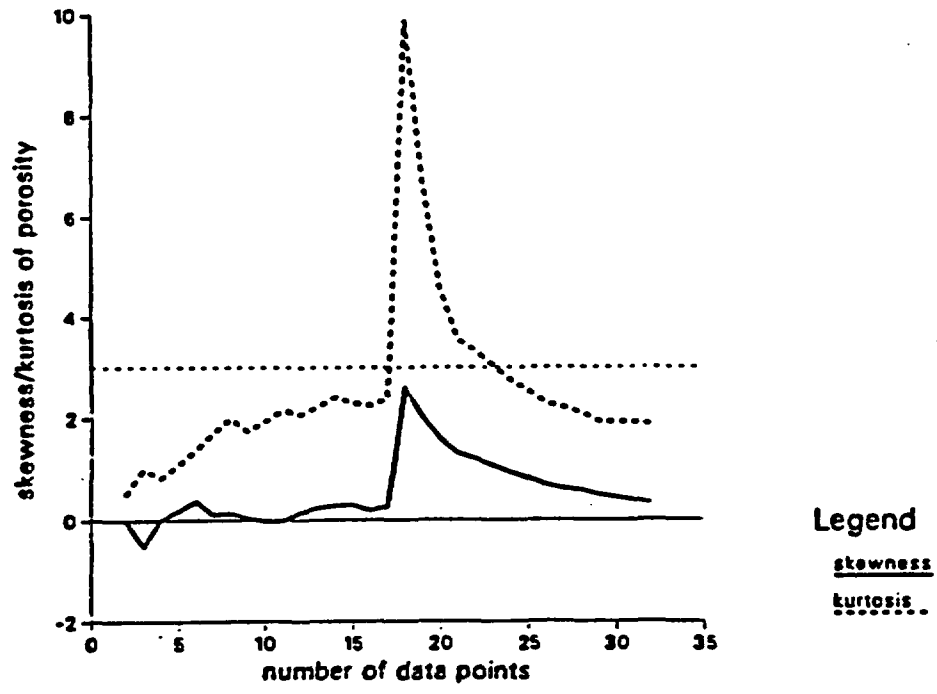

Figure 6-17. Distributions of Welded/Zeolitized Tuff Porosity (concluded).

a

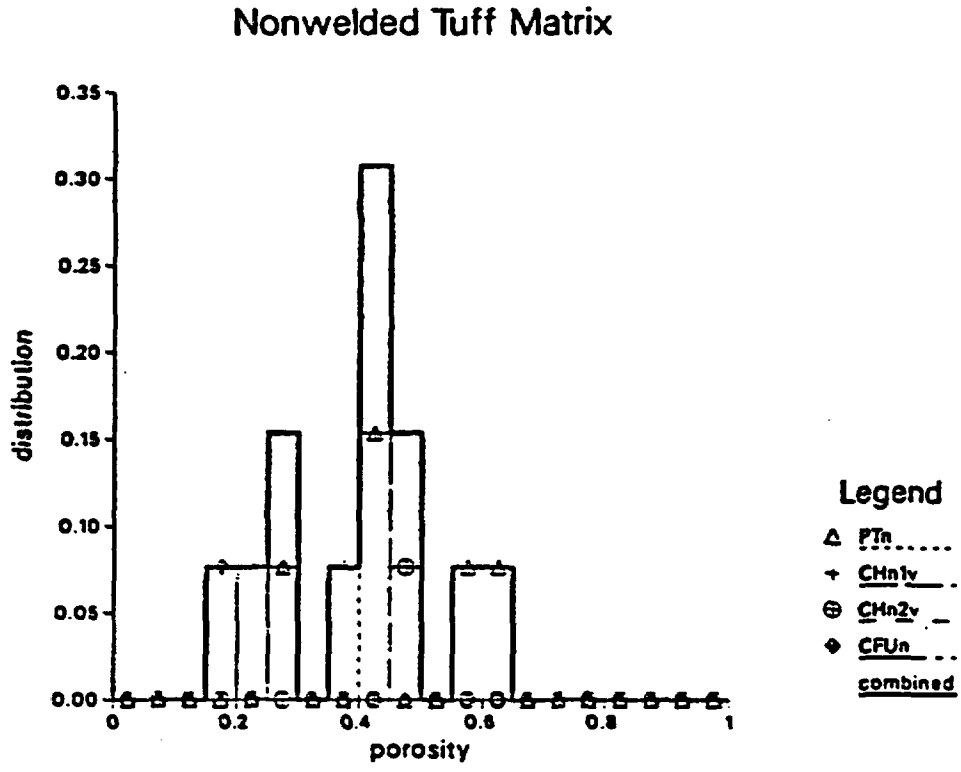

b

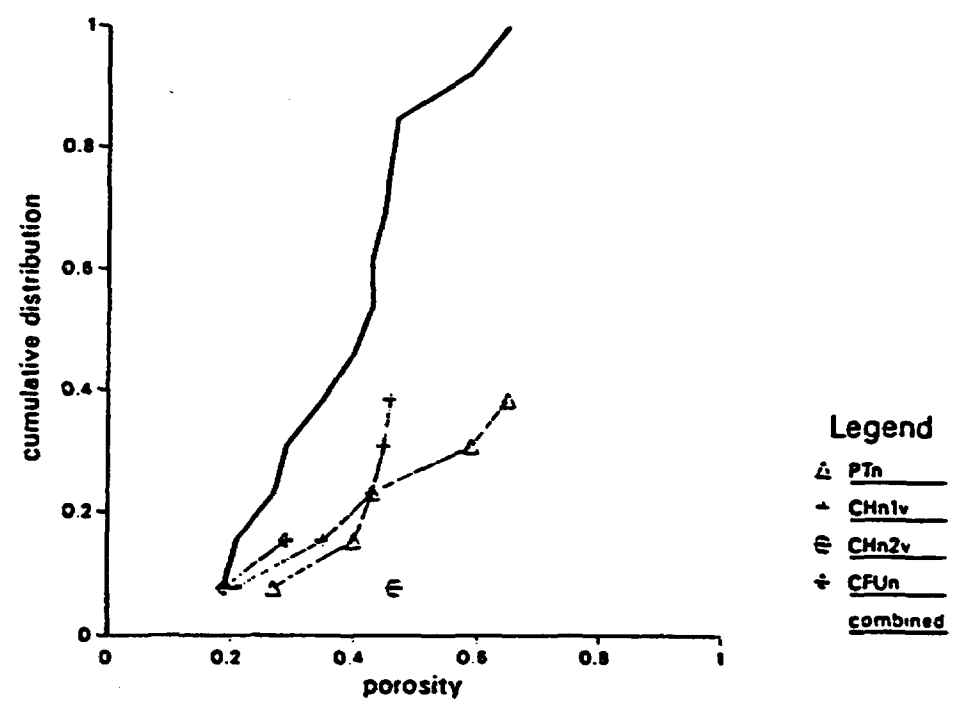

Figure 6-18. Distributions of Nonwelded Tuff Porosity.

c

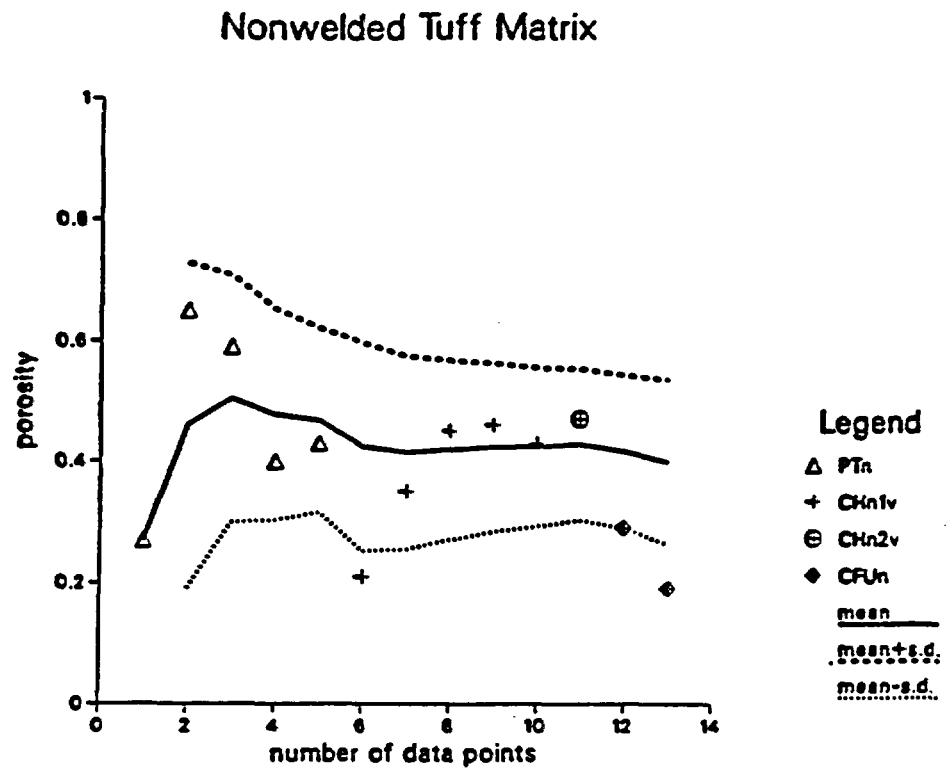

d

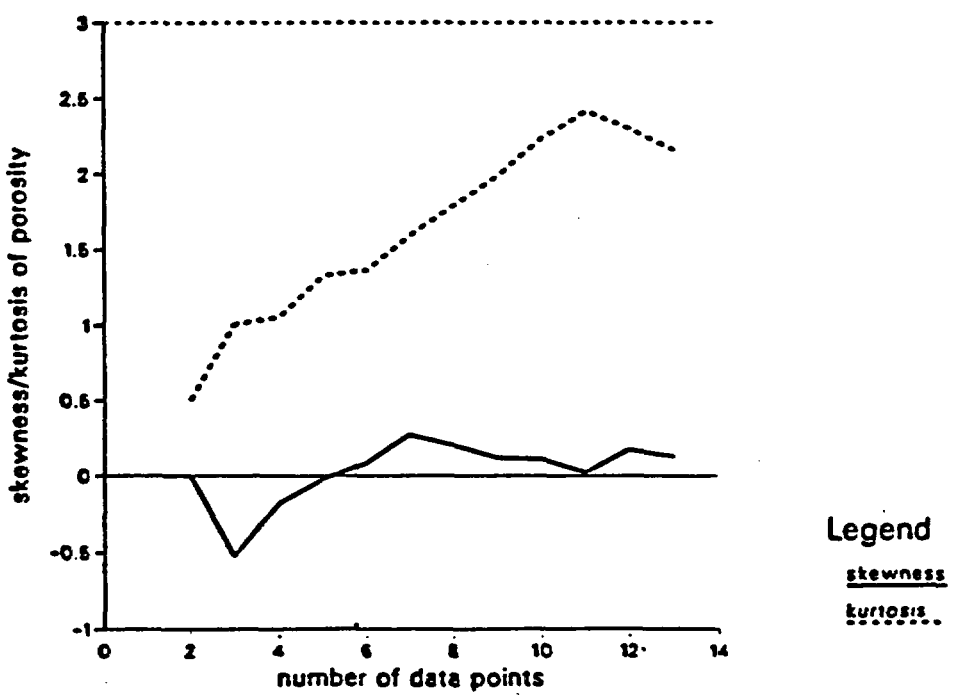

Figure 6-18. Distributions of Nonwelded Tuff Porosity (concluded).

Table 6-1
Distribution Parameters of Watershed Soil
Log Pore-Size Distribution Index, λ or n - 1

SOIL TEXTURE CLASS	NUMBER OF DATA POINTS	MEAN VALUE	MEAN + STANDARD DEVIATION	MEAN - STANDARD DEVIATION	MAXIMUM DATA VALUE	MINIMUM DATA VALUE	SKEWNESS	KURTOSIS
Sand	12	0.376e00	0.965e00	0.146e00	0.181e01	0.134e00	0.483e00	0.163e01
Loamy Sand	27	0.390e00	0.745e00	0.204e00	0.119e01	0.137e00	0.172e00	0.182e01
Sandy Loam	140	0.419e00	0.868e00	0.202e00	0.333e01	0.136e00	0.587e00	0.267e01
Sandy Clay Loam	69	0.341e00	0.727e00	0.160e00	0.146e01	0.764e-01	-0.140e-01	0.184e01
Sandy Soil Combined	248	0.391e00	0.819e00	0.186e00	0.333e01	0.764e-01	0.353e00	0.247e01
Loam	97	0.316e00	0.607e00	0.165e00	0.231e01	0.125e00	0.865e00	0.320e01
Clay Loam	127	0.296e00	0.671e00	0.131e00	0.237e01	0.630e-01	0.277e00	0.184e01
Loamy Soil Combined	224	0.305e00	0.645e00	0.144e00	0.237e01	0.630e-01	0.421e00	0.229e01
Silty Loam	347	0.256e00	0.475e00	0.138e00	0.389e01	0.909e-01	0.141e01	0.561e01
Silty Clay Loam	289	0.233e00	0.521e00	0.104e00	0.499e01	0.683e-01	0.142e01	0.499e01
Silty Soil Combined	636	0.245e00	0.499e00	0.120e00	0.499e01	0.683e-01	0.140e01	0.537e01
Sandy Clay	17	0.387e00	0.757e00	0.198e00	0.813e00	0.929e-01	-0.101e01	0.263e01
Silty Clay	46	0.196e00	0.419e00	0.913e-01	0.382e01	0.667e-01	0.206e01	0.761e01
Clay	141	0.282e00	0.648e00	0.123e00	0.338e01	0.758e-01	0.352e00	0.234e01
Clayey Soil Combined	204	0.267e00	0.607e00	0.117e00	0.382e01	0.667e-01	0.568e00	0.272e01

Table 6-2
Distribution Parameters of Tuff Matrix
Log Pore-Size Distribution Index, λ or n - 1

STRATI-GRAPHIC UNIT	NUMBER OF DATA POINTS	MEAN VALUE	MEAN + STANDARD DEVIATION	MEAN - STANDARD DEVIATION	MAXIMUM DATA VALUE	MINIMUM DATA VALUE	SKEWNESS	KURTOSIS
TCw	6	0.676e00	0.934e00	0.489e00	0.113e01	0.500e00	0.549e00	0.162e01
TSw1	5	0.558e00	0.678e00	0.460e00	0.665e00	0.400e00	-0.107e01	0.235e01
TSw2	10	0.733e00	0.100e01	0.535e00	0.112e01	0.488e00	-0.227e00	0.125e01
TSw3	5	0.919e00	0.194e01	0.434e00	0.312e01	0.450e00	0.827e-00	0.200e01
CHnlz	6	0.450e00	0.714e00	0.284e00	0.894e00	0.236e00	0.102e00	0.181e01
CHn2z	5	0.633e00	0.828e00	0.483e00	0.954e00	0.496e00	0.541e00	0.167e01
CHn3z	6	0.798e00	0.159e01	0.400e00	0.232e01	0.396e00	0.583e00	0.154e01
PPw	5	0.244e01	0.408e01	0.145e01	0.591e01	0.164e01	0.110e01	0.229e01
BFw	2	0.199e01	0.381e01	0.104e01	0.315e01	0.126e01	0.000e00	0.500e00
Welded/ Zeolitized Combined	50	0.796e00	0.151e01	0.419e00	0.591e01	0.236e00	0.102e01	0.384e01
PTn	6	0.240e01	0.102e02	0.567e00	0.956e01	0.220e00	-0.597e00	0.180e01
CHn1v	7	0.191e01	0.389e01	0.936e00	0.402e01	0.496e00	-0.881e00	0.243e01
CHn2v	1	0.914e01	0.914e01	0.914e01	0.914e01	0.914e01	0.000e-00	0.000e00
CFUn	2	0.943e00	0.105e01	0.844e00	0.102e01	0.872e00	0.000e00	0.500e00
Nonwelded Tuff Combined	16	0.210e01	0.611e01	0.722e00	0.956e01	0.220e00	-0.297e00	0.234e01

Table 6-3
Distribution Parameters of Watershed Soil
Log Air Entry Scaling Factor, α (m^{-1})

SOIL TEXTURE CLASS	NUMBER OF DATA POINTS	MEAN VALUE	MEAN + STANDARD DEVIATION	MEAN - STANDARD DEVIATION	MAXIMUM DATA VALUE	MINIMUM DATA VALUE	SKEWNESS	KURTOSIS
Sand	12	0.118e02	0.795e02	0.175e01	0.872e03	0.170e01	0.935e00	0.284e01
Loamy Sand	27	0.171e02	0.149e03	0.197e01	0.196e04	0.320e00	0.260e00	0.244e01
Sandy Loam	140	0.423e01	0.180e02	0.994e00	0.542e03	0.284e00	0.724e00	0.395e01
Sandy Clay Loam	69	0.295e01	0.123e02	0.711e00	0.388e03	0.270e00	0.727e00	0.361e01
Sandy Soil Combined	248	0.468e01	0.241e02	0.910e00	0.196e04	0.270e00	0.879e00	0.403e01
Loam	97	0.273e01	0.151e02	0.492e00	0.180e04	0.143e00	0.709e00	0.373e01
Clay Loam	127	0.159e01	0.592e01	0.426e00	0.112e03	0.121e00	0.970e00	0.410e01
Loamy Soil Combined	224	0.201e01	0.918e01	0.439e00	0.180e04	0.121e00	0.927e00	0.421e01
Silty Loam	347	0.116e01	0.390e01	0.345e00	0.337e02	0.101e00	0.596e00	0.276e01
Silty Clay Loam	289	0.106e01	0.426e01	0.262e00	0.181e03	0.440e-01	0.922e00	0.388e01
Silty Soil Combined	636	0.111e01	0.407e01	0.303e00	0.181e03	0.440e-01	0.768e00	0.345e01
Sandy Clay	17	0.249e01	0.765e01	0.810e00	0.546e00	0.563e00	0.944e00	0.423e01
Silty Clay	46	0.205e01	0.873e01	0.480e00	0.454e02	0.130e00	0.156e00	0.244e01
Clay	141	0.156e01	0.840e01	0.291e00	0.421e03	0.538e-01	0.951e00	0.375e01
Clayey Soil Combined	204	0.173e01	0.850e01	0.351e00	0.421e03	0.538e-01	0.765e00	0.354e01

Table 6-4
Distribution Parameters of Tuff Matrix
Log Air Entry Scaling Factor, α (m^{-1})

STRATI-GRAPHIC UNIT	NUMBER OF DATA POINTS	MEAN VALUE	MEAN + STANDARD DEVIATION	MEAN - STANDARD DEVIATION	MAXIMUM DATA VALUE	MINIMUM DATA VALUE	SKEWNESS	KURTOSIS
TCw	6	0.103e-01	0.197e-01	0.537e-02	0.231e-01	0.389e-02	-0.233e00	0.157e01
TSw1	5	0.124e-01	0.265e-01	0.583e-02	0.339e-01	0.480e-02	0.208e-01	0.146e01
TSw2	10	0.636e-02	0.108e-01	0.376e-02	0.123e-01	0.258e-02	-0.284e00	0.174e01
TSw3	5	0.339e-02	0.511e-02	0.226e-02	0.441e-02	0.169e-02	-0.108e01	0.222e01
CHnlz	6	0.568e-02	0.123e-01	0.263e-02	0.220e-01	0.267e-02	0.795e00	0.220e01
CHn2z	5	0.236e-02	0.359e-02	0.155e-02	0.370e-02	0.158e-02	0.258e00	0.976e00
CHn3z	6	0.312e-02	0.102e-01	0.952e-03	0.170e-01	0.605e-03	-0.659e-02	0.167e01
PPw	5	0.178e-01	0.257e-01	0.123e-01	0.314e-01	0.131e-01	0.704e00	0.162e01
BFw	2	0.181e-01	0.358e-01	0.918e-02	0.293e-01	0.112e-01	0.000e00	0.500e00
Welded/ Zeolitized Combined	50	0.641e-02	0.159e-01	0.259e-02	0.339e-01	0.605e-03	-0.191e00	0.256e01
PTn	6	0.153e-01	0.222e-01	0.106e-01	0.305e-01	0.110e-01	0.104e01	0.264e01
CHnlv	7	0.199e-01	0.312e-01	0.127e-01	0.440e-01	0.103e-01	0.403e00	0.241e01
CHn2v	1	0.155e-01	0.155e-01	0.155e-01	0.155e-01	0.155e-01	0.000e00	0.000e00 .sp
CFUn	2	0.376e-02	0.482e-02	0.294e-02	0.448e-02	0.316e-02	0.000e00	0.500e00
Nonwelded Tuff Combined	16	0.144e-01	0.276e-01	0.754e-02	0.440e-01	0.316e-02	-0.751e00	0.346e01

Table 6-5
Distribution Parameters of Watershed Soil Residual Saturation, S_r

SOIL TEXTURE CLASS	NUMBER OF DATA POINTS	MEAN VALUE	MEAN + STANDARD DEVIATION	MEAN - STANDARD DEVIATION	MAXIMUM DATA VALUE	MINIMUM DATA VALUE	SKEWNESS	KURTOSIS
Sand	12	0.783e-01	0.160e00	-0.370e-02	0.238e00	0.000e00	0.506e00	0.191e01
Loamy Sand	27	0.781e-01	0.167e00	-0.104e-01	0.305e00	0.000e00	0.822e00	0.265e01
Sandy Loam	140	0.120e00	0.232e00	0.669e-02	0.584e00	0.000e00	0.918e00	0.425e01
Sandy Clay Loam	69	0.228e00	0.416e00	0.395e-01	0.710e00	0.000e00	0.459e00	0.244e01
Sandy Soil Combined	248	0.143e00	0.288e00	-0.192e-02	0.710e00	0.000e00	0.116e01	0.439e01
Loam	97	0.127e00	0.271e00	-0.161e-01	0.551e00	0.000e00	0.896e00	0.280e01
Clay Loam	127	0.220e00	0.423e00	0.178e-01	0.624e00	0.000e00	0.341e00	0.174e01
Loamy Soil Combined	224	0.180e00	0.365e00	-0.477e-02	0.624e00	0.000e00	0.651e00	0.219e01
Silty Loam	347	0.725e-01	0.205e00	-0.603e-01	0.627e00	0.000e00	0.176e01	0.512e01
Silty Clay Loam	289	0.182e00	0.404e00	-0.407e-01	0.829e00	0.000e00	0.896e00	0.258e01
Silty Soil Combined	636	0.122e00	0.309e00	-0.650e-01	0.829e00	0.000e00	0.142e01	0.406e01
Sandy Clay	17	0.393e00	0.605e00	0.182e00	0.652e00	0.000e00	-0.752e00	0.218e01
Silty Clay	46	0.188e00	0.387e00	-0.105e-01	0.704e00	0.000e00	0.730e00	0.263e01
Clay	141	0.360e00	0.597e00	0.122e00	0.765e00	0.000e00	-0.327e00	0.172e01
Clayey Soil Combined	204	0.324e00	0.562e00	0.859e-01	0.765e00	0.000e00	-0.108e00	0.162e01

Table 6-6
Distribution Parameters of Tuff Matrix Residual Saturation, S_r

STRATI-GRAPHIC UNIT	NUMBER OF DATA POINTS	MEAN VALUE	MEAN + STANDARD DEVIATION	MEAN - STANDARD DEVIATION	MAXIMUM DATA VALUE	MINIMUM DATA VALUE	SKEWNESS	KURTOSIS
TCw	6	0.446e-01	0.104e00	-0.145e-01	0.160e00	0.200e-02	0.136e01	0.299e01
TSw1	5	0.324e-01	0.551e-01	0.970e-02	0.600e-01	0.300e-02	-0.331e-02	0.134e01
TSw2	10	0.571e-01	0.996e-01	0.146e-01	0.120e00	0.750e-02	0.245e00	0.160e01
TSw3	5	0.103e00	0.259e00	-0.536e-01	0.376e00	0.260e-02	0.119e01	0.242e01
CHnlz	6	0.729e-01	0.146e00	0.766e-04	0.202e00	0.100e-01	0.880e00	0.218e01
CHn2z	5	0.113e00	0.182e00	0.433e-01	0.200e00	0.135e-01	-0.190e00	0.170e01
CHn3z	6	0.102e00	0.193e00	0.110e-01	0.215e00	0.300e-02	0.169e00	0.110e01
PPw	5	0.694e-01	0.107e00	0.318e-01	0.124e00	0.180e-01	0.126e00	0.199e01
BFw	2	0.583e-01	0.618e-01	0.549e-01	0.608e-01	0.559e-01	0.000e00	0.500e00
Welded/ Zeolitized Combined	50	0.718e-01	0.145e00	-0.100e-02	0.376e00	0.200e-02	-0.185e01	0.735e01
PTn	6	0.790e-01	0.114e00	0.436e-01	0.114e00	0.307e-01	-0.450e00	0.127e01
CHn1v	7	0.145e00	0.289e00	-0.101e-03	0.349e00	0.200e-01	0.624e00	0.143e01
CHn2v	1	0.189e00	0.189e00	0.189e00	0.189e00	0.189e00	0.000e00	0.000e00
CFUn	2	0.228e00	0.360e00	0.959e-01	0.322e00	0.135e00	0.000e00	0.500e00
Nonwelded Tuff Combined	16	0.133e00	0.246e00	0.210e-01	0.349e00	0.200e-01	0.963e00	0.246e01

Table 6-7
Distribution Parameters of Watershed Soil
Log Saturated Permeability, k_s (10^{-12} m^2)

SOIL TEXTURE CLASS	NUMBER OF DATA POINTS	MEAN VALUE	MEAN + STANDARD DEVIATION	MEAN - STANDARD DEVIATION	MAXIMUM DATA VALUE	MINIMUM DATA VALUE	SKEWNESS	KURTOSIS
Sand	10	0.111e01	0.358e01	0.344e00	0.766e01	0.130e00	0.769e-01	0.253e01
Loamy Sand	6	0.104e01	0.447e01	0.240e00	0.728e01	0.194e00	0.133e00	0.131e01
Sandy Loam	155	0.733e00	0.248e01	0.216e00	0.709e01	0.144e-01	-0.411e00	0.323e01
Sandy Clay Loam	112	0.490e00	0.171e01	0.140e00	0.489e01	0.144e-01	-0.418e00	0.262e01
Sandy Soil Combined	283	0.639e00	0.223e01	0.183e00	0.766e01	0.144e-01	-0.381e00	0.299e01
Loam	140	0.470e00	0.172e01	0.129e00	0.895e01	0.144e-01	-0.204e00	0.256e01
Clay Loam	222	0.290e00	0.993e00	0.849e-01	0.368e01	0.144e-01	-0.122e00	0.258e01
Loamy Soil Combined	362	0.350e00	0.125e01	0.977e-01	0.895e01	0.144e-01	-0.120e00	0.258e01
Silty Loam	560	0.308e00	0.105e01	0.898e-01	0.105e02	0.144e-01	-0.211e00	0.296e01
Silty Clay Loam	480	0.238e00	0.904e00	0.627e-01	0.102e02	0.719e-02	-0.536e-01	0.289e01
Silty Soil Combined	1040	0.273e00	0.988e00	0.756e-01	0.105e02	0.719e-02	-0.151e00	0.292e01
Sandy Clay	32	0.765e00	0.177e01	0.331e00	0.535e01	0.151e00	0.970e-01	0.246e01
Silty Clay	68	0.302e00	0.145e01	0.630e-01	0.563e01	0.144e-01	0.964e-01	0.220e01
Clay	199	0.156e00	0.502e00	0.487e-01	0.383e01	0.144e-01	0.107e00	0.297e01
Clayey Soil Combined	299	0.215e00	0.823e00	0.563e-01	0.563e01	0.144e-01	0.159e00	0.269e01

Table 6-8
Distribution Parameters of Tuff Matrix
Log Saturated Permeability, k_s (10^{-12} m^2)

STRATI-GRAPHIC UNIT	NUMBER OF DATA POINTS	MEAN VALUE	MEAN + STANDARD DEVIATION	MEAN - STANDARD DEVIATION	MAXIMUM DATA VALUE	MINIMUM DATA VALUE	SKEWNESS	KURTOSIS
TCw	6	0.777e-06	0.206e-04	0.293e-07	0.493e-03	0.714e-07	0.139e01	0.308e01
TSw1	9	0.477e-06	0.250e-05	0.910e-07	0.931e-05	0.877e-07	0.499e00	0.172e01
TSw2	19	0.905e-06	0.335e-05	0.244e-06	0.731e-05	0.514e-07	-0.530e00	0.243e01
TSw3	5	0.165e-05	0.155e-04	0.175e-06	0.456e-04	0.155e-06	0.425e00	0.159e01
CHnlz	13	0.761e-06	0.499e-05	0.116e-06	0.516e-05	0.242e-08	-0.227e01	0.743e01
CHn2z	14	0.561e-06	0.346e-05	0.908e-07	0.253e-05	0.478e-08	-0.141e01	0.404e01
CHn3z	13	0.252e-05	0.123e-04	0.518e-06	0.164e-04	0.171e-06	-0.283e00	0.177e01
PPw	9	0.270e-03	0.634e-03	0.115e-03	0.141e-02	0.120e-03	0.853e00	0.216e01
BFw	2	0.388e-03	0.785e-03	0.192e-03	0.638e-03	0.236e-03	0.000e00	0.500e00
Welded/ Zeolitized Combined	90	0.184e-05	0.243e-04	0.140e-06	0.141e-02	0.242e-08	0.572e00	0.350e01
PTn	8	0.278e-02	0.481e00	0.161e-04	0.240e00	0.292e-06	-0.945e00	0.206e01
CHnlv	11	0.841e-04	0.346e-02	0.204e-05	0.298e-01	0.895e-06	0.450e00	0.170e01
CHn2v	1	0.806e-02	0.806e-02	0.806e-02	0.806e-02	0.806e-02	0.000e00	0.000e00
CFUn	2	0.959e-05	0.839e-04	0.110e-05	0.445e-04	0.207e-05	0.000e00	0.500e00
Nonwelded Tuff Combined	22	0.303e-03	0.267e-01	0.345e-05	0.240e00	0.292e-06	-0.960e-03	0.142e01

Table 6-9
Distribution Parameters of Watershed Soil
Porosity, ϕ

SOIL TEXTURE CLASS	NUMBER OF DATA POINTS	MEAN VALUE	MEAN + STANDARD DEVIATION	MEAN - STANDARD DEVIATION	MAXIMUM DATA VALUE	MINIMUM DATA VALUE	SKEWNESS	KURTOSIS
Sand	12	0.352e00	0.462e00	0.241e00	0.563e00	0.174e00	0.222e00	0.215e01
Loamy Sand	27	0.414e00	0.482e00	0.347e00	0.532e00	0.283e00	0.245e00	0.235e01
Sandy Loam	140	0.432e00	0.516e00	0.347e00	0.823e00	0.294e00	0.188e01	0.868e01
Sandy Clay Loam	69	0.418e00	0.471e00	0.366e00	0.562e00	0.340e00	0.790e00	0.312e01
Sandy Soil Combined	248	0.422e00	0.500e00	0.344e00	0.823e00	0.174e00	0.137e01	0.843e01
Loam	97	0.447e00	0.511e00	0.382e00	0.691e00	0.343e00	0.909e00	0.446e01
Clay Loam	127	0.470e00	0.525e00	0.414e00	0.623e00	0.343e00	0.309e00	0.275e01
Loamy Soil Combined	224	0.460e00	0.520e00	0.399e00	0.691e00	0.343e00	0.526e00	0.348e01
Silty Loam	347	0.488e00	0.549e00	0.427e00	0.736e00	0.300e00	0.957e00	0.539e01
Silty Clay Loam	289	0.478e00	0.535e00	0.422e00	0.742e00	0.298e00	0.788e00	0.646e01
Silty Soil Combined	636	0.484e00	0.543e00	0.425e00	0.742e00	0.298e00	0.904e00	0.586e01
Sandy Clay	17	0.420e00	0.472e00	0.368e00	0.555e00	0.362e00	0.105e01	0.346e01
Silty Clay	46	0.486e00	0.552e00	0.419e00	0.715e00	0.343e00	0.413e00	0.503e01
Clay	141	0.490e00	0.540e00	0.440e00	0.634e00	0.399e00	0.706e00	0.338e01
Clayey Soil Combined	204	0.483e00	0.540e00	0.426e00	0.715e00	0.343e00	0.424e00	0.412e01

Table 6-10
Distribution Parameters of Tuff Matrix Porosity, ϕ

STRATI-GRAPHIC UNIT	NUMBER OF DATA POINTS	MEAN VALUE	MEAN + STANDARD DEVIATION	MEAN - STANDARD DEVIATION	MAXIMUM DATA VALUE	MINIMUM DATA VALUE	SKEWNESS	KURTOSIS
TCw	6	0.102e00	0.137e00	0.662e-01	0.150e00	0.600e-01	0.375e00	0.138e01
TSw1	1	0.300e-01	0.300e-01	0.300e-01	0.300e-01	0.300e-01	0.000e00	0.000e00
TSw2	6	0.100e00	0.134e00	0.659e-01	0.160e00	0.600e-01	0.729e00	0.233e01
TSw3	4	0.550e-01	0.861e-01	0.239e-01	0.900e-01	0.200e-01	0.000e00	0.111e01
CHnlz	4	0.330e00	0.387e00	0.273e00	0.410e00	0.280e00	0.643e00	0.150e01
CHn2z	2	0.230e00	0.244e00	0.216e00	0.240e00	0.220e00	0.000e00	0.500e00
CHn3z	3	0.263e00	0.279e00	0.248e00	0.280e00	0.250e00	0.312e00	0.100e01
PPw	4	0.298e00	0.370e00	0.225e00	0.390e00	0.240e00	0.373e00	0.116e01
BFw	2	0.255e00	0.276e00	0.234e00	0.270e00	0.240e00	0.000e00	0.500e00
Welded/ Zeolitized Combined	32	0.179e00	0.290e00	0.678e-01	0.410e00	0.200e-01	0.327e00	0.187e01
PTn	5	0.468e00	0.621e00	0.315e00	0.650e00	0.270e00	-0.202e-01	0.132e01
CHnlv	5	0.380e00	0.484e00	0.276e00	0.460e00	0.210e00	-0.870e00	0.191e01
CHn2v	1	0.470e00	0.470e00	0.470e00	0.470e00	0.470e00	0.000e00	0.000e00
CFUn	2	0.240e00	0.311e00	0.169e00	0.290e00	0.190e00	0.000e00	0.500e00
Nonwelded Tuff Combined	13	0.399e00	0.536e00	0.263e00	0.650e00	0.190e00	0.130e00	0.216e01

For residual saturation, we use the linear scale in the distribution analyses even though the distributions are highly skewed. More than 40% of the fitted results in Panian (1987) for watershed data have zero residual saturation values. With zero value, we cannot use log scale to plot the data. For the fitted results of Peters et al. (1984) and Klavetter and Peters (1987) for the tuffs, the residual saturation values are nonzero. If we use log scale, the normality of distributions may be improved. We use the linear scales in Figures 6-10, 6-11, and 6-12 for consistent comparisons among watershed soils, welded/zeolitized tuffs, and nonwelded tuffs. In subplot c of the figures, negative, unphysical values of mean minus standard deviation are not plotted.

The distributions of log saturated permeability (Figures 6-13, 6-14, 6-15, Tables 6-7, 6-8) are well-defined for the watershed soils and welded/zeolitized tuffs. There are more data points for saturated permeability because more than one measurement was made for each soil horizon and for each tuff core sample. The scatter of measured values from subcores of the same sample is essentially as large as the scatter between different cores. For the watershed soils, the skewness is essentially 0 and the kurtosis is essentially 3. for nearly (log)normal distributions. The average saturated permeability for watershed soils is five to seven orders of magnitude larger than those for welded/zeolitized tuffs. Among the welded/zeolitized tuffs, the lower PPw and BFw units have higher saturated permeabilities than the other units. The nonwelded tuffs have very scattered values for the saturated permeability, covering six orders of magnitude for the data of PTn.

For completeness, we also analyze the porosity distributions. For the watershed soils, we have a nearly normal distribution, slightly skewed. When we compare Figure 6-16d with the corresponding Figure 6-13d, we note that more data points are needed to get meaningful skewness and kurtosis coefficients for porosity than for saturated permeability. The porosity distribution in Figure 6-17 for welded/zeolitized tuff has two peaks, with the lower CHnz, PPw, and BFw units having larger porosity than the upper TCw, TSw units. In general, the welded tuff units have lower porosity values than the nonwelded tuff units and the watershed soils.

The results of distribution analyses in this section on watershed soils, welded/zeolitized tuffs, and nonwelded tuffs are used in the next section in parameter correlation analyses. We have noted many differences and similarities between soils and tuffs. When we have more tuff data in the future, we can be more certain about the parameter variations controlling the hydrology of Yucca Mountain.

6.3 Parameter Correlations

In this section, we analyze the correlations in unsaturated and saturated hydrological parameters. The parameters are the pore-size distribution index, the air entry scaling factor, the residual saturation, the saturated permeability, and the porosity. To illustrate the existence or absence of parameter correlations, we cross-plot pairs of parameters for different geological media. In general, a correlation relationship between parameter x and parameter y is manifested in a cross plot with data points lining up monotonically with a slope which is not zero (parallel to the x-axis) and is also not infinite (parallel to the y-axis). If the data points line up vertically or

horizontally parallel to one of the parameter axes, there is no correlation between these two parameters. If the data points are scattered in a cross plot, there is also no correlation.

Each correlation pair between two parameters is first studied using the results from detailed distribution analyses of watershed soils, welded/zeolitized tuff matrix, and nonwelded tuff matrix. Specifically, we plot the mean values for the five parameters in Tables 6-1 to 6-10 and then plot the data values for watershed soils, welded/zeolitized tuff matrix, and nonwelded tuff matrix separately. Following these detailed data plots, we review the results in the literature to either substantiate or refute the correlation results based on watershed soil and tuff matrix analyses. The data and analyses by Brooks and Corey (1966), Mualem (1976b), Case et al. (1983), and Cosby et al. (1984) are reviewed for this purpose. The first three correlation pairs involve unsaturated parameters and the last two correlation pairs involve saturated permeability. The correlation between saturated permeability and air entry scaling factor was observed earlier in tuff data by Wang and Narasimhan (1987). In this report, we examine this correlation and other correlation relationships more thoroughly.

Figure 6-19 examines the correlation between air entry scaling factor and pore-size distribution index. If these two parameters are related, we can eliminate one parameter in the unsaturated characteristic curves. In comparison to tuffs, watershed soils have higher air entry scaling factor values, representing larger pores, and smaller pore-size distribution indices, representing broader pore distributions. Figure 6-19 is based on the average values of parameters between very different media. The subsequent figures are for the data points of each medium separately. The correlation of high air entry scaling factor with small pore-size distribution index is evident for the loamy sand data (Figure 6-20), less clear for all watershed soil data (Figure 6-21), not evident for welded/zeolitized tuff matrix data (Figure 6-22), and absent in nonwelded tuff data (Figure 6-23). The data of Brooks and Corey (1966, Figure 6-24) and the analyses based on the data of the Case et al. catalog (1983, Figure 6-25) also do not support the presence of this correlation in different media.

Because we will again use the data of Brooks and Corey (1966) and Case et al. (1983), we briefly summarize these two data sets, together with the Mualem (1976b) study. Brooks and Corey used a light hydrocarbon (Soltrol "C") to study the wetting and nonwetting characteristic curves for three unconsolidated sands, three soils, one glass bead pack, one fragmented mixture of sand and clay, and two consolidated sandstone cores. The data were fitted with their model (see Equation 5.1) to determine the model parameters. The Brooks and Corey study is one of the most frequently quoted early studies of characteristic curves. Mualem (1976a) tabulated the data of many studies from 1939 to 1971, including the Brooks and Corey data and other data using water as the wetting fluid. Mualem (1976b) also used the Brooks and Corey model in the range of high suction (large negative metric potential) to extrapolate the residual saturation values. Case et al. (1983) have reviewed the literature up to 1982 and tabulated and plotted the characteristic curve data from many studies. They also fitted the curves with polynomials. Because the polynomial fittings hold within the range of data points but may yield biased results in extrapolation, we have used the fitting results in the following procedure to estimate the characteristic parameters. We are mainly interested in the air entry scaling factor and the pore-size distribution index. Therefore, we omitted all results without data points above saturation $S = 0.9$, and omitted all polynomials which do not yield monotonic characteristic curves. With these two criteria, we eliminated nearly half of the curves, including all the clay results. We

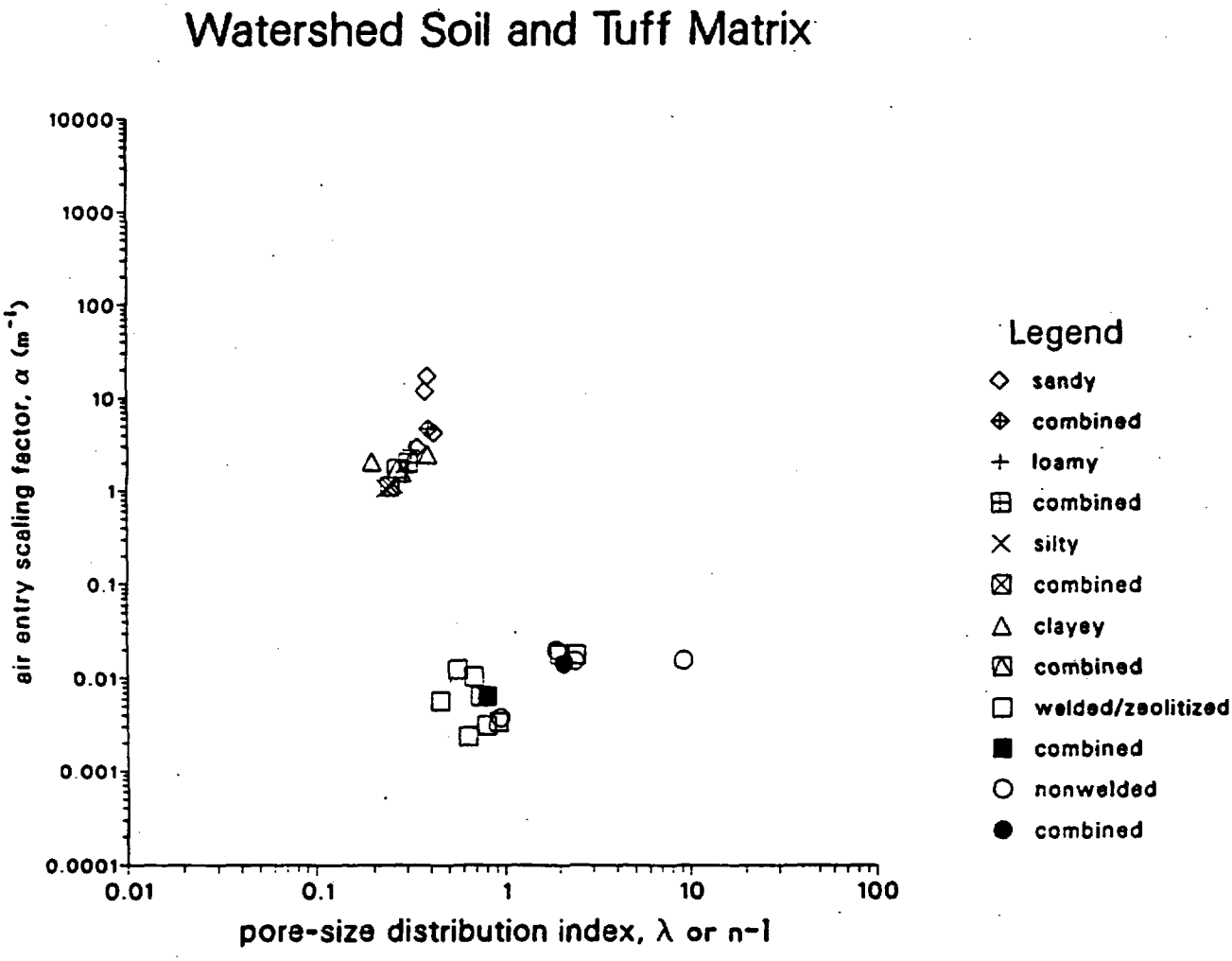

Figure 6-19. Correlation Between Air Entry Scaling Factor and Pore-Size Distribution Index for Watershed Soil and Tuff Matrix.

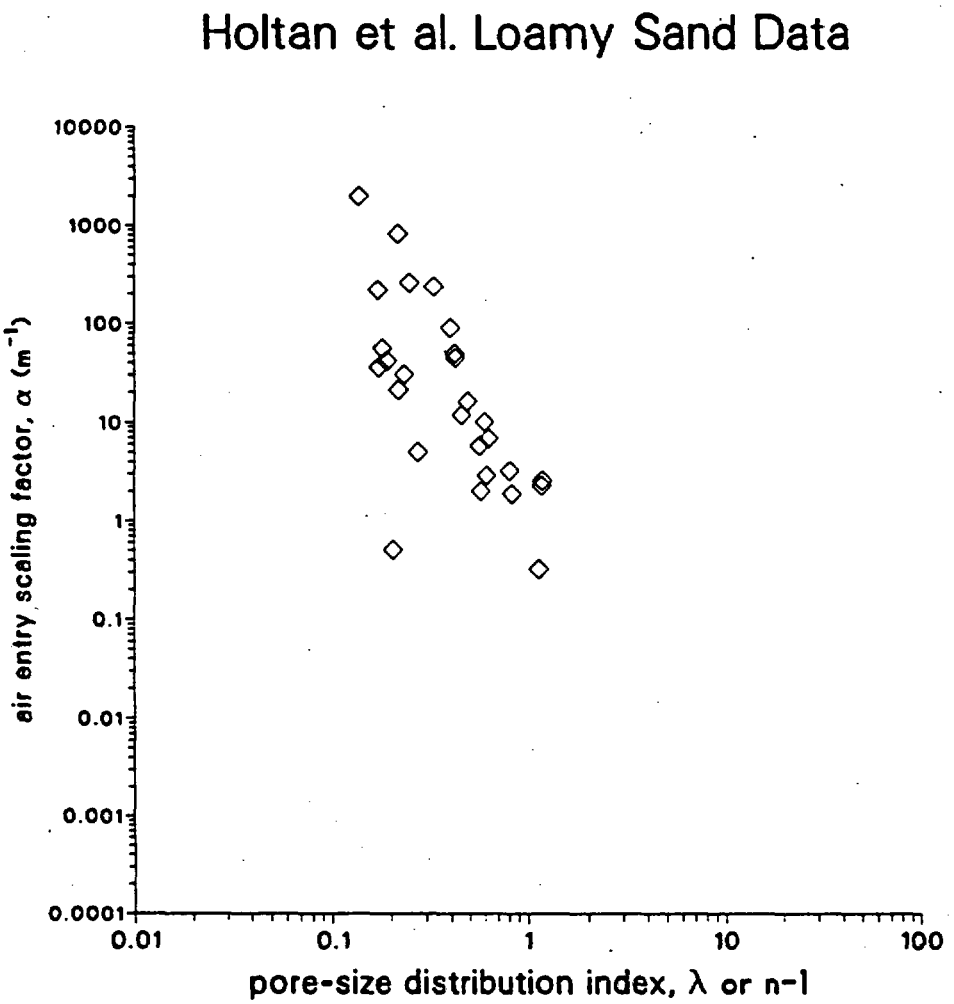

Figure 6-20. Correlation Between Air Entry Scaling Factor and Pore-Size Distribution Index for Loamy Sand.

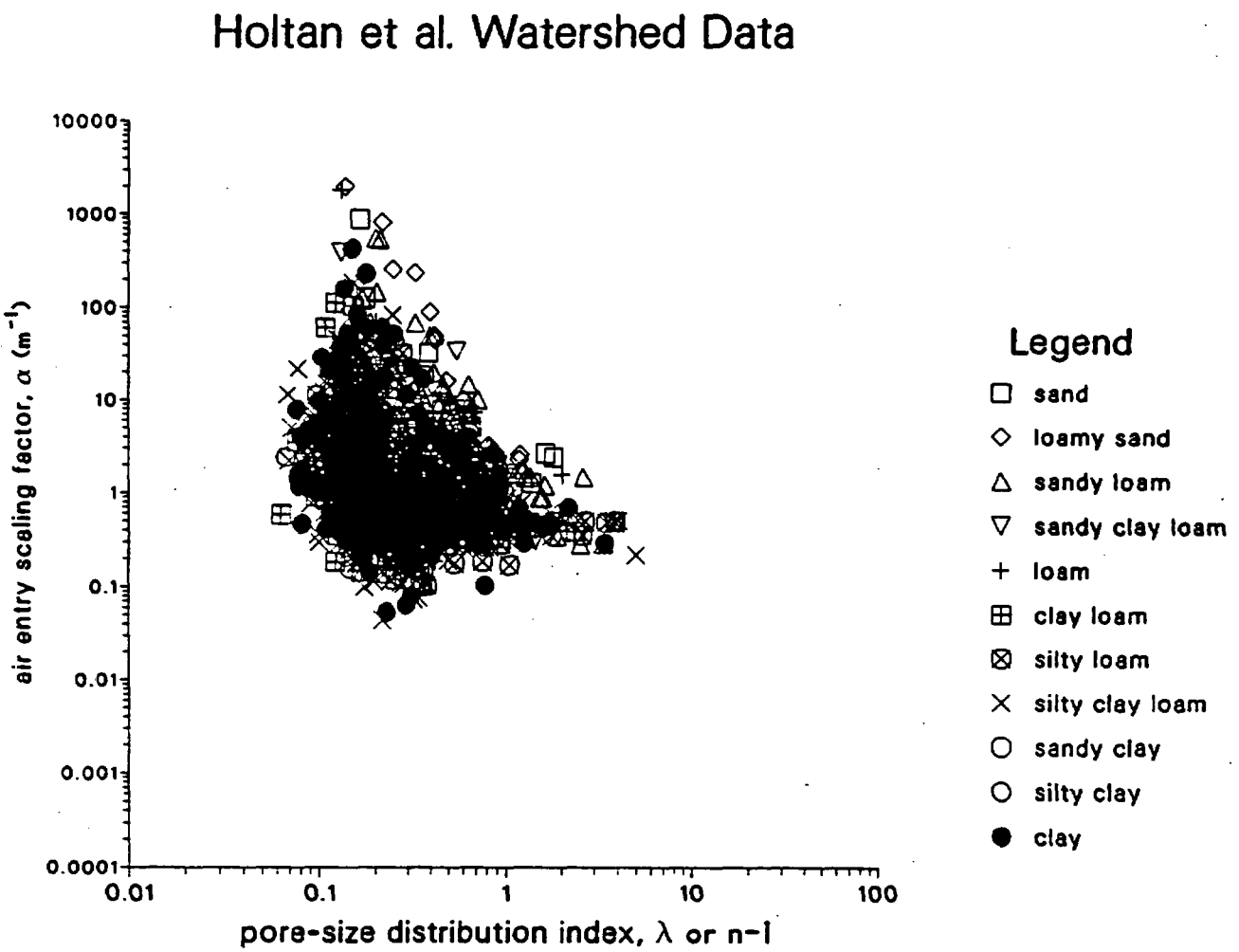

Figure 6-21. Correlation Between Air Entry Scaling Factor and Pore-Size Distribution Index for Watershed Soil.

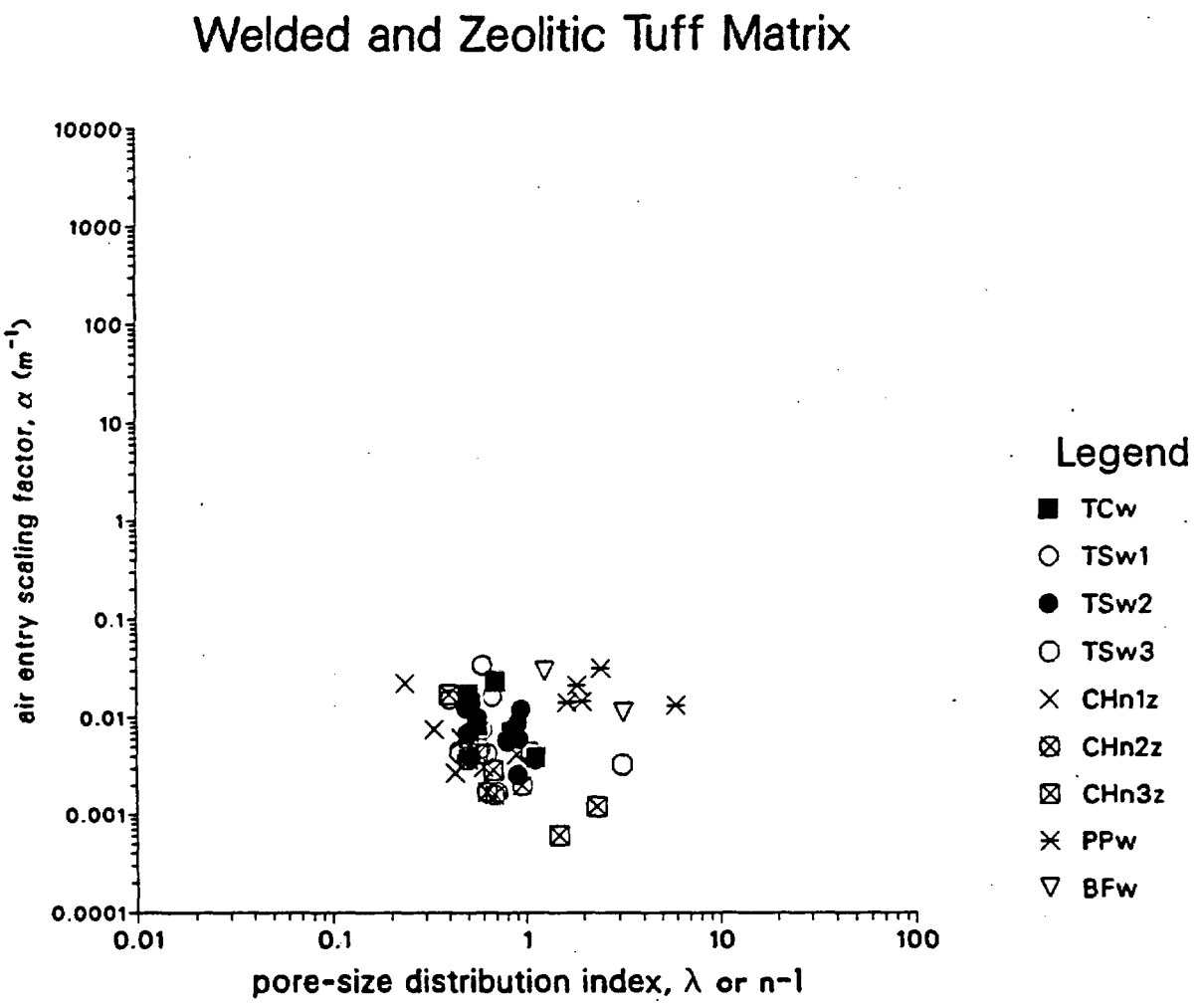

Figure 6-22. Correlation Between Air Entry Scaling Factor and Pore-Size Distribution Index for Welded and Zeolitized Tuff Matrix.

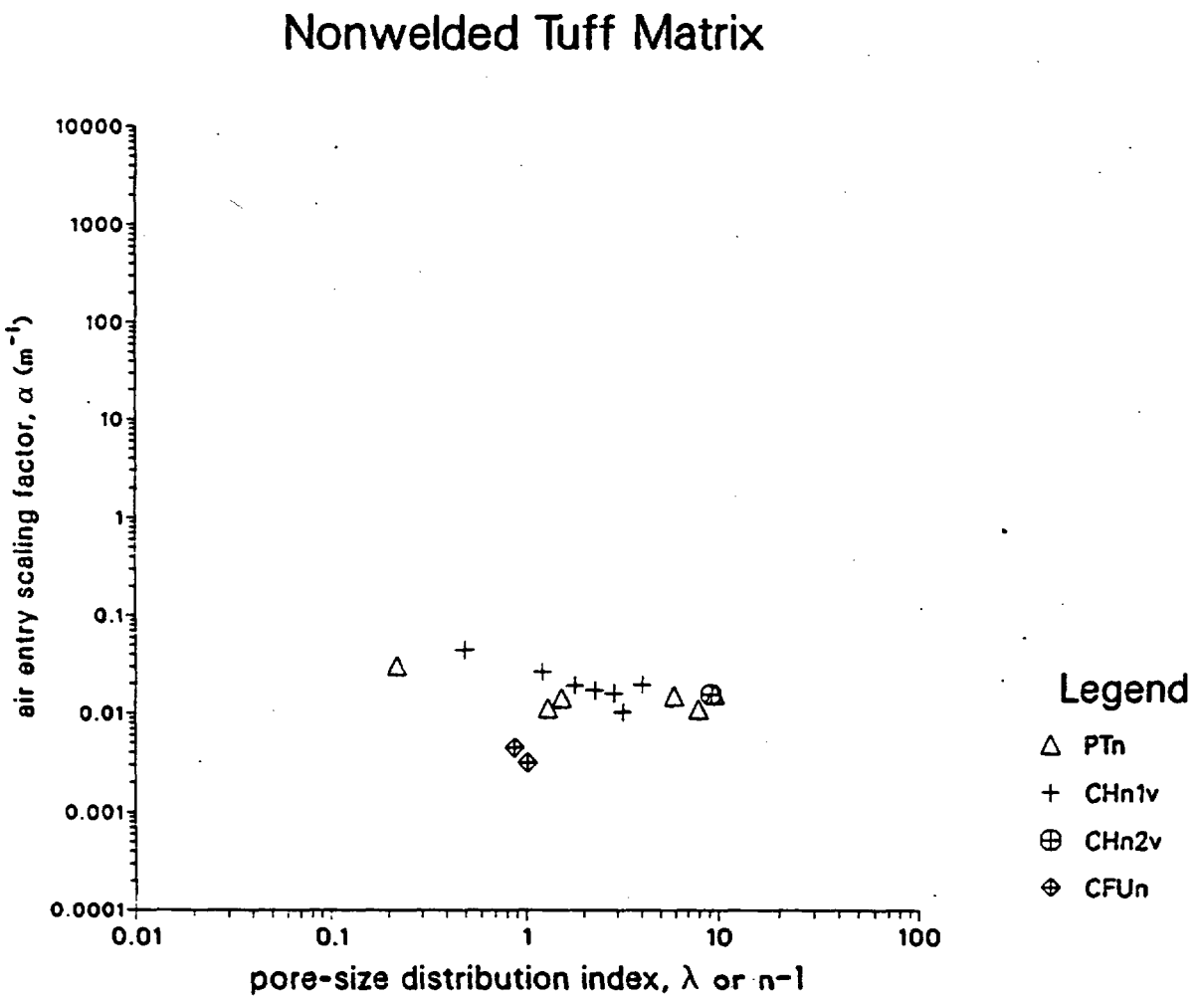

Figure 6-23. Correlation Between Air Entry Scaling Factor and Pore-Size Distribution Index for Nonwelded Tuff Matrix.

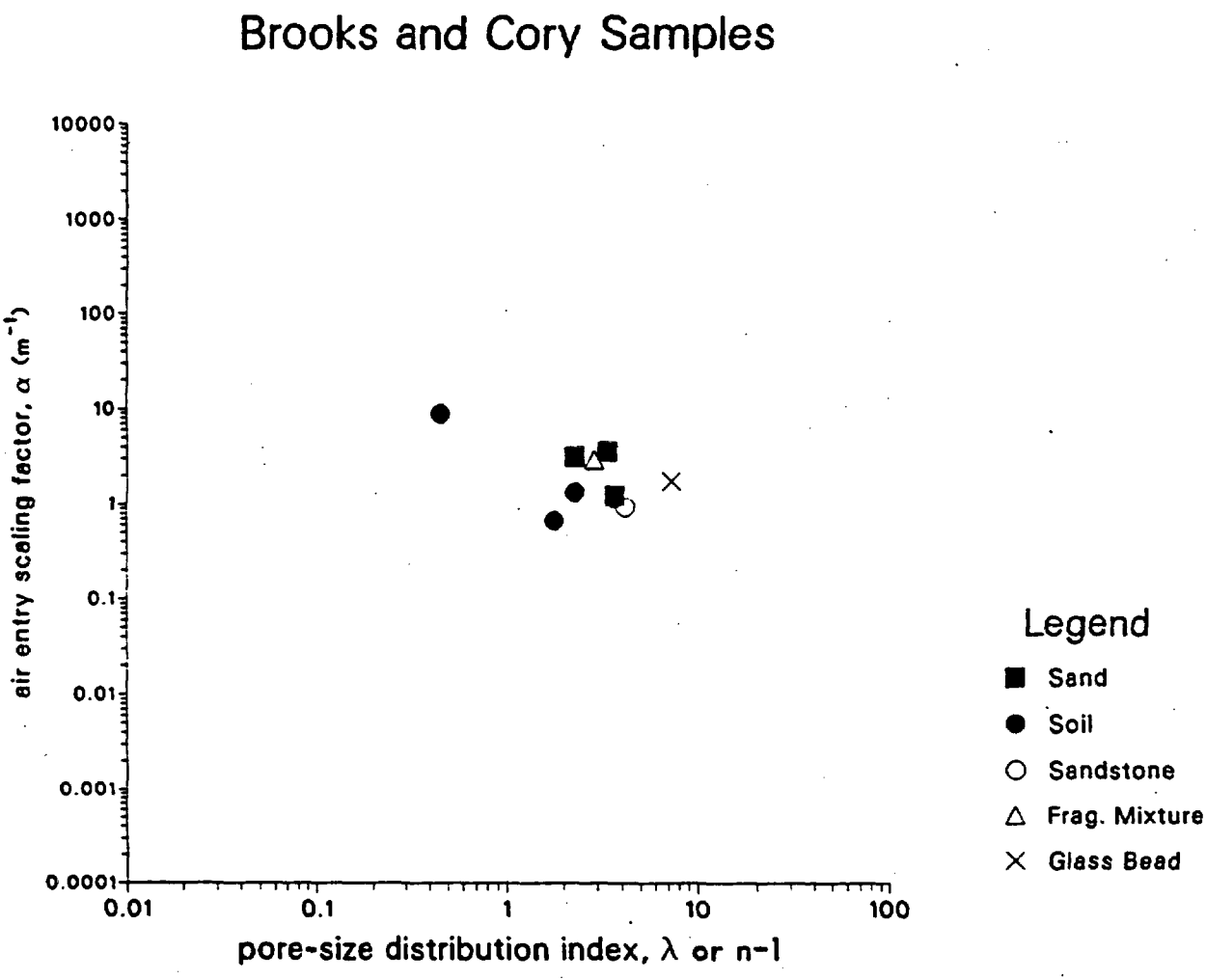

Figure 6-24. Correlation Between Air Entry Scaling Factor and Pore-Size Distribution Index for Data of Brooks and Corey (1966).

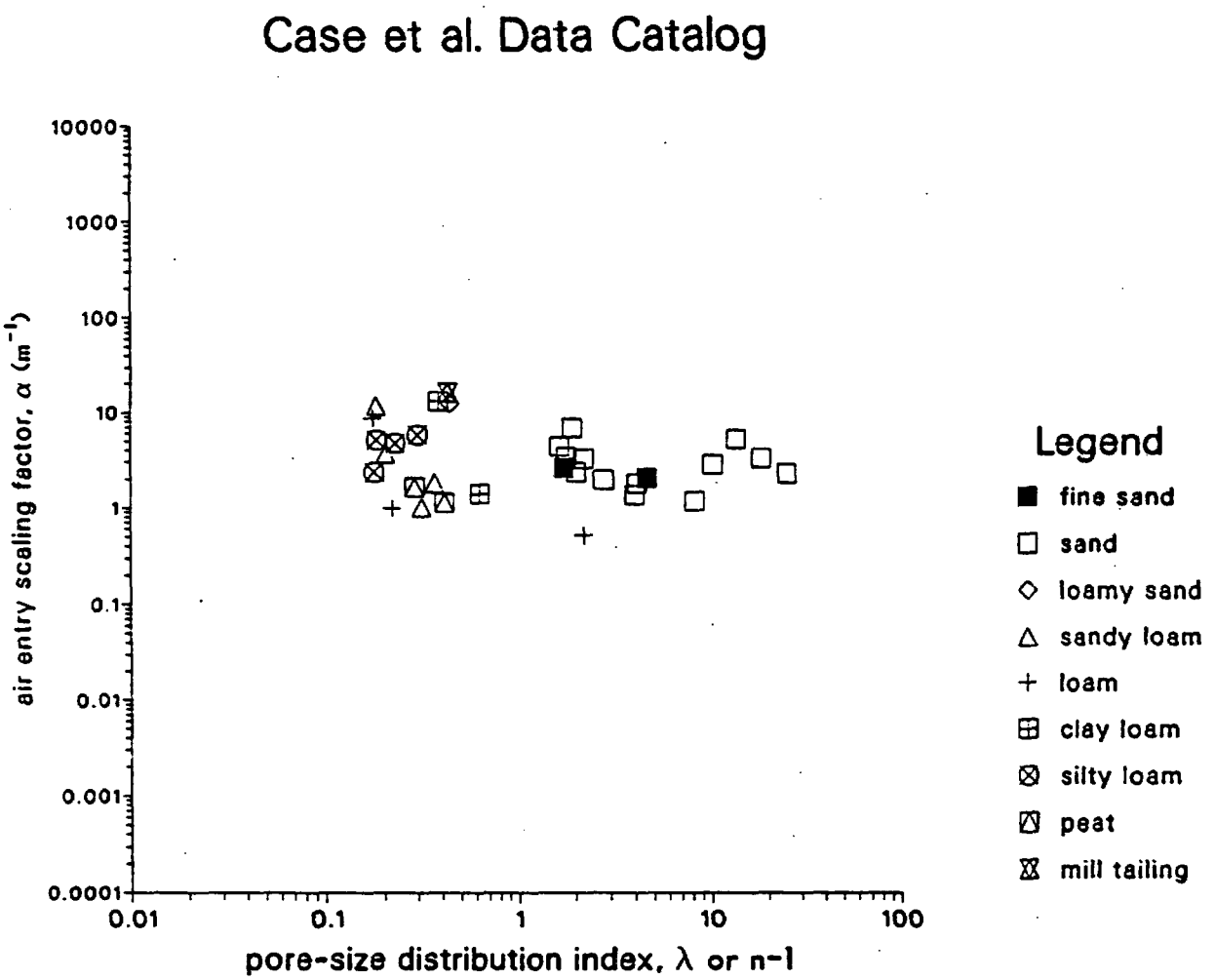

Figure 6-25. Correlation Between Air Entry Scaling Factor and Pore-Size Distribution Index for Data in Case et al. (1983) Catalog.

then used the van Genuchten (1980) procedure to estimate the characteristic parameters from the matric potential values and characteristic curve slopes at $S = 0.5$. We assumed the residual saturation to be zero to convert Case et al. (1983) polynomial coefficients into van Genuchten's parameters. The procedure outlined above is fairly crude. The results from this analysis should be evaluated with these approximations in mind.

The second correlation relationship analyzed is between residual saturation and pore-size distribution index (Figures 6-26 to 6-32). There are conflicting indications for this correlation relationship and no clear evidence that this correlation exists. Between two different media, the mean values of soils have higher residual saturation and smaller pore-size distribution index than the mean values of tuff matrix, i.e., the residual saturation decreases with pore-size distribution index (Figure 6-26). Within a medium, we note the opposite trend that the residual saturation increases with pore-size distribution index in sandy clay loam data (Figure 6-27), in all watershed soil data (Figure 6-28), and in welded/zeolitized tuff matrix data (Figure 6-29). This is also the case with Brooks and Corey data (Figure 6-31, without the glass bead result). The nonwelded tuff matrix data (Figure 6-30), and the analyses by Mualem (Figure 6-32) are too scattered to deduce any trend correlating these two parameters. There is no obvious physical argument to support this correlation within a medium or between different media.

Some of the consolidated media have high residual saturation (e.g., Figure 6-31). Residual saturation is an important parameter for partially saturated flow and transport studies. A high residual saturation value indicates the presence of stagnant water not actively participated in convective transport, but which influences transport by diffusive dilution. If the residual saturation value is low, then most of the water in the medium can be displaced relatively easily. The ambient saturation in Yucca Mountain tuff matrix is estimated to be 60% to 90%. We do not know if a significant fraction of the ambient saturation is residual saturation held tightly within the tuff matrix or if all the ambient water is mobile.

To better understand the residual saturation in geological media, we also examine the correlation between residual saturation and porosity (Figures 6-33 to 6-38). If residual saturation increases with porosity, the residual saturation may reside mainly on the rock grain surfaces held by adsorptive forces because pore surface area may be related to pore volume. The cross plots of data do not support this correlation. In addition to porosity, the residual saturation may also depend on other structural parameters of the pore geometry. Some of the residual saturation may be in dead-end pores. The watershed soils have narrow distribution of porosity and wide distribution of residual saturation (Figure 6-34). In general, the welded/zeolitized tuff matrix has low residual saturation and low porosity (Figure 6-35) and the nonwelded tuff matrix has low residual saturation and a wide range in porosity distribution (Figure 6-36).

Porosity is the ratio of void space to total volume of a porous medium. The void space includes both dead-end pores and connected flow channels. If there is no dead-end space, the total porosity may be related to the saturated permeability which measures the resistance from the drag of solid pore walls on flowing fluid. The permeability-porosity relationship has been extensively studied. Many theoretical models can be found in the literature on the dependence of permeability on flow channel dimensions which can be related to porosity. Two simple textbook examples for laminar flow of viscous fluid are the Poiseuille's solution through a circular tube with radius r, and the Boussinesq's solution between two parallel plates with

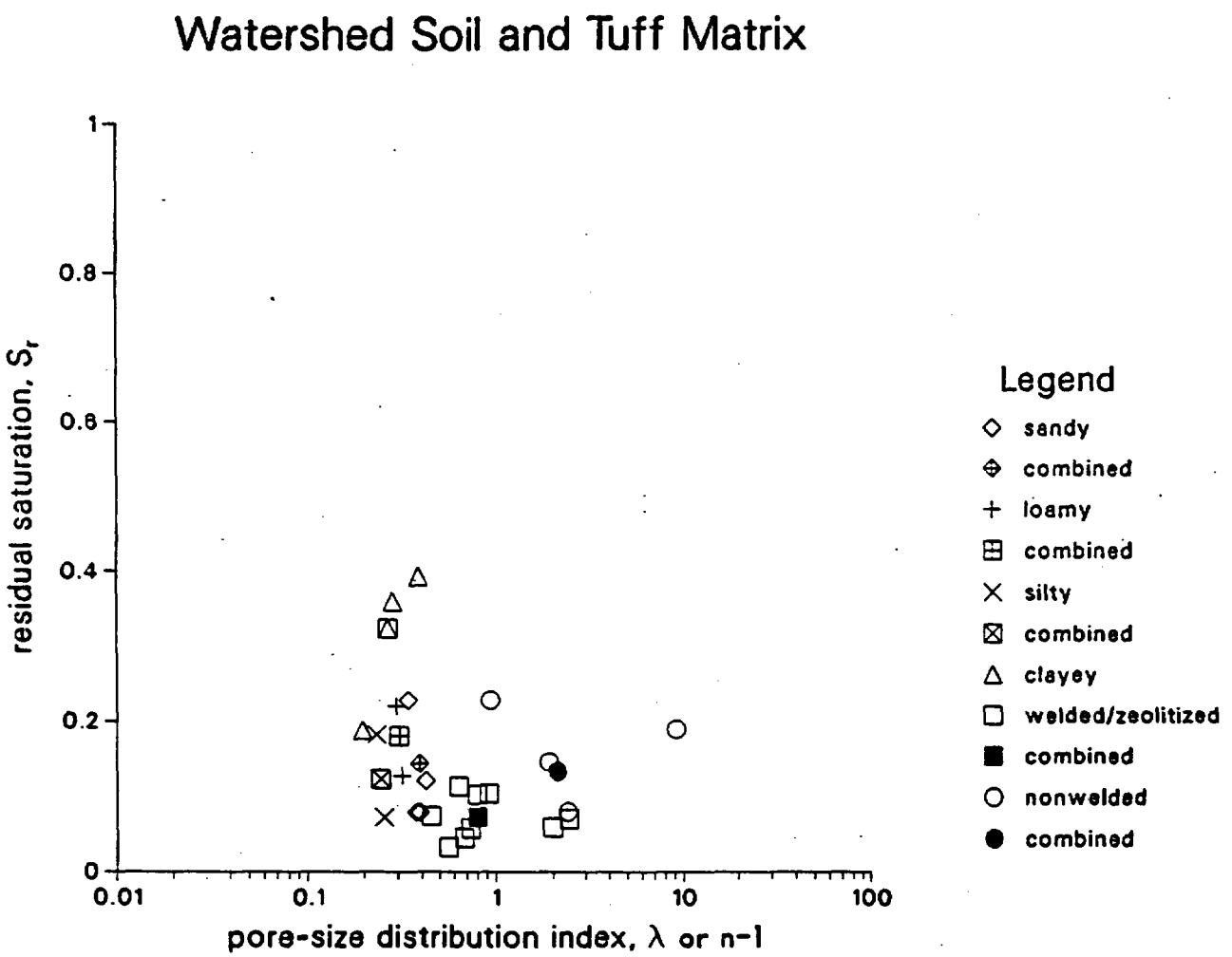

Figure 6-26. Correlation Between Residual Saturation and Pore-Size Distribution Index for Watershed Soil and Tuff Matrix.

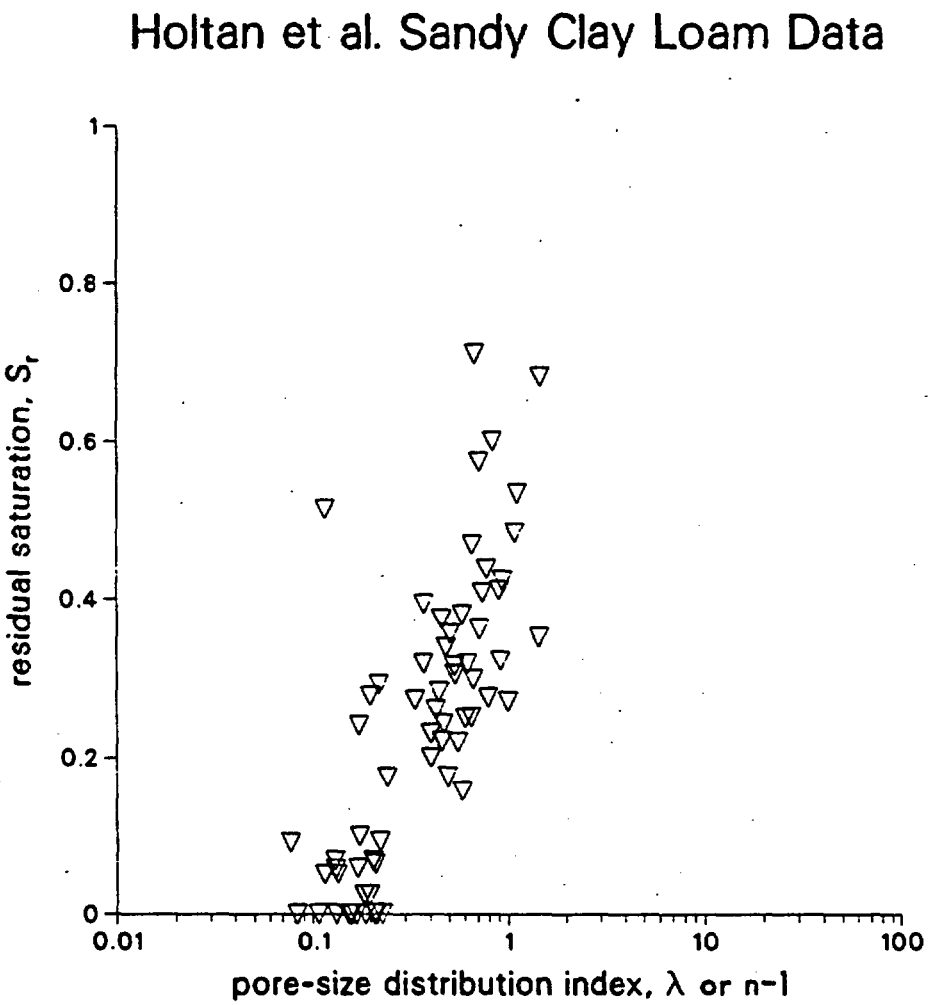

Figure 6-27. Correlation Between Residual Saturation and Pore-Size Distribution Index for Sandy Clay Loam.

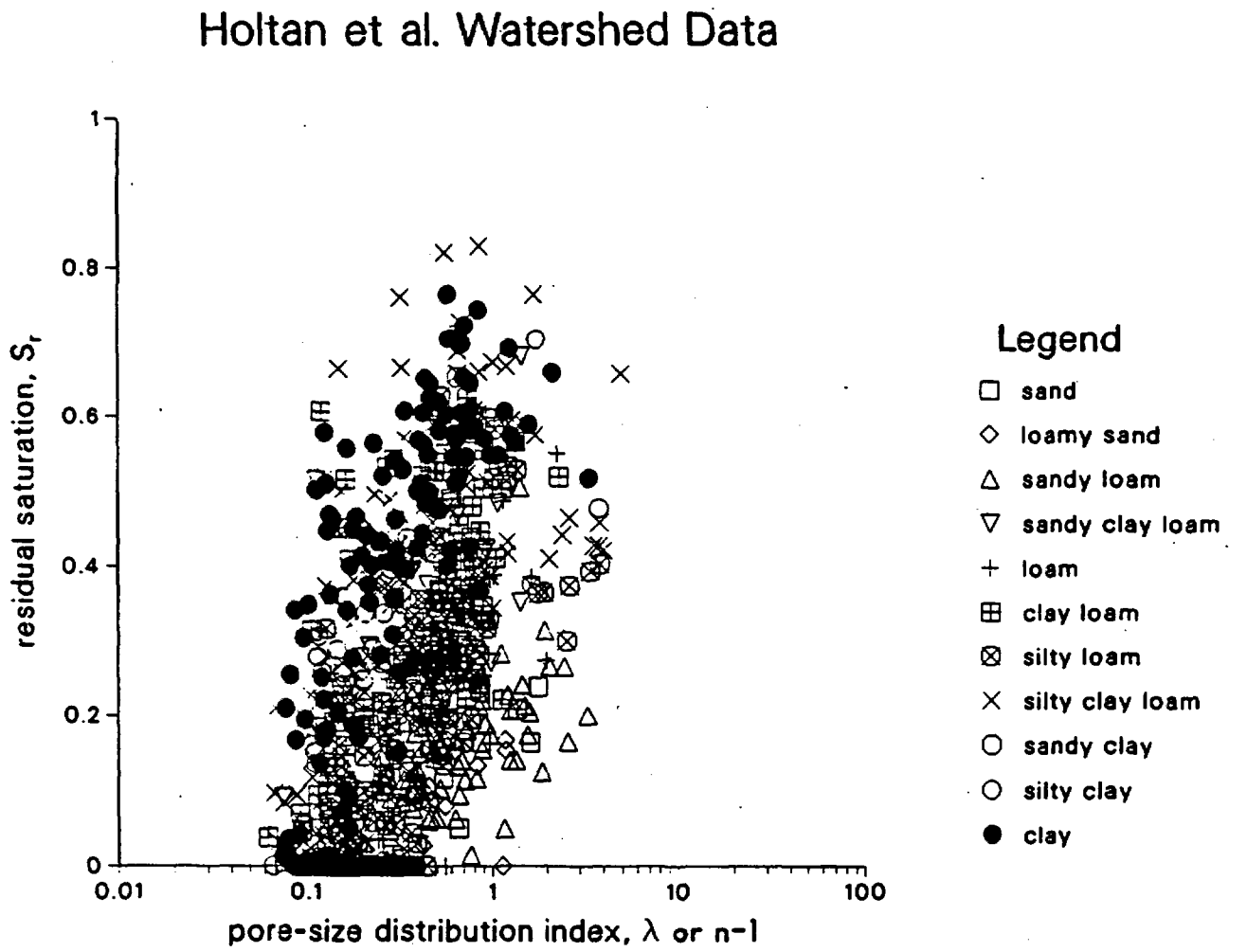

Figure 6-28. Correlation Between Residual Saturation and Pore-Size Distribution Index for Watershed Soil.

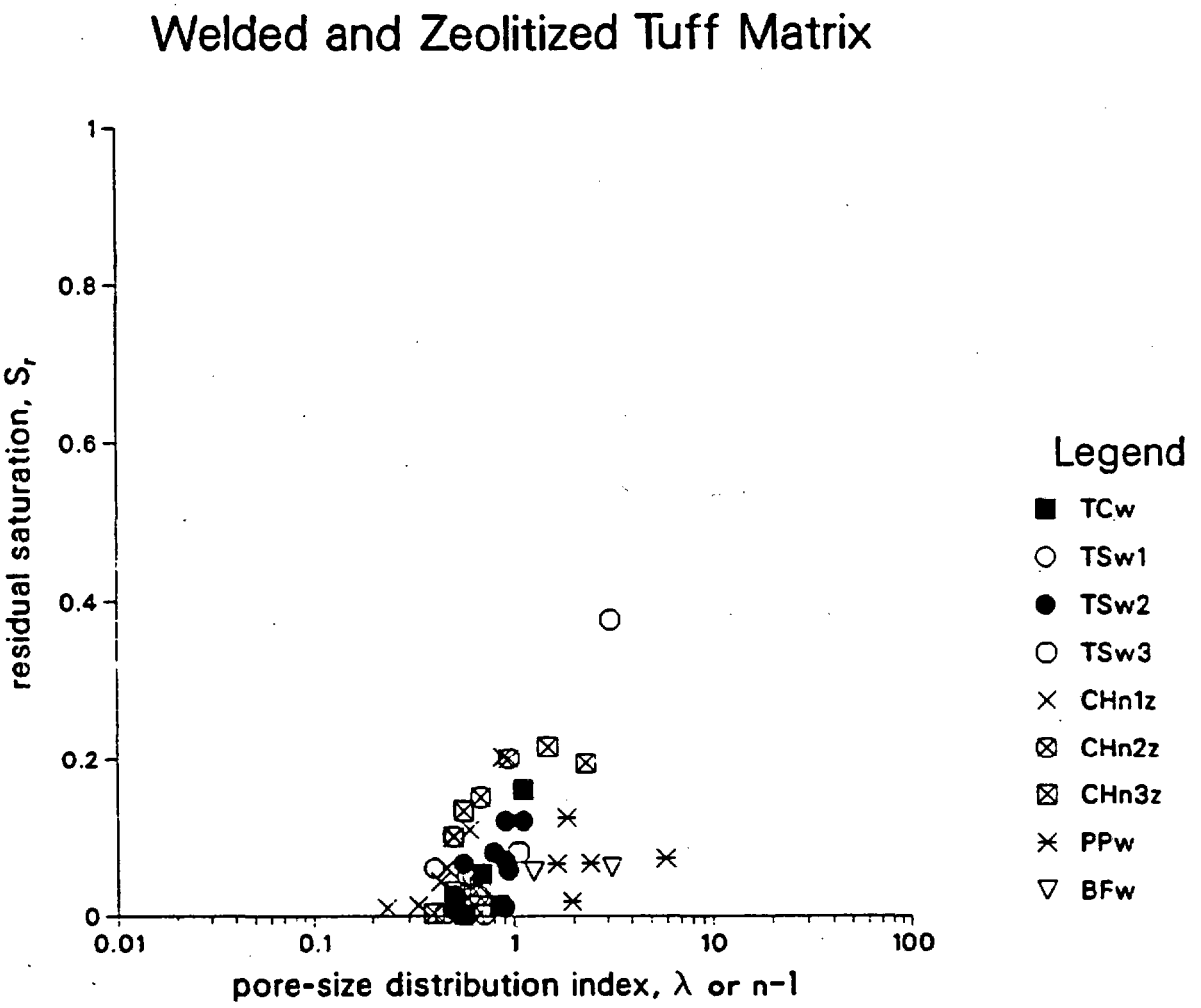

Figure 6-29. Correlation Between Residual Saturation and Pore-Size Distribution Index for Welded and Zeolitized Tuff Matrix.

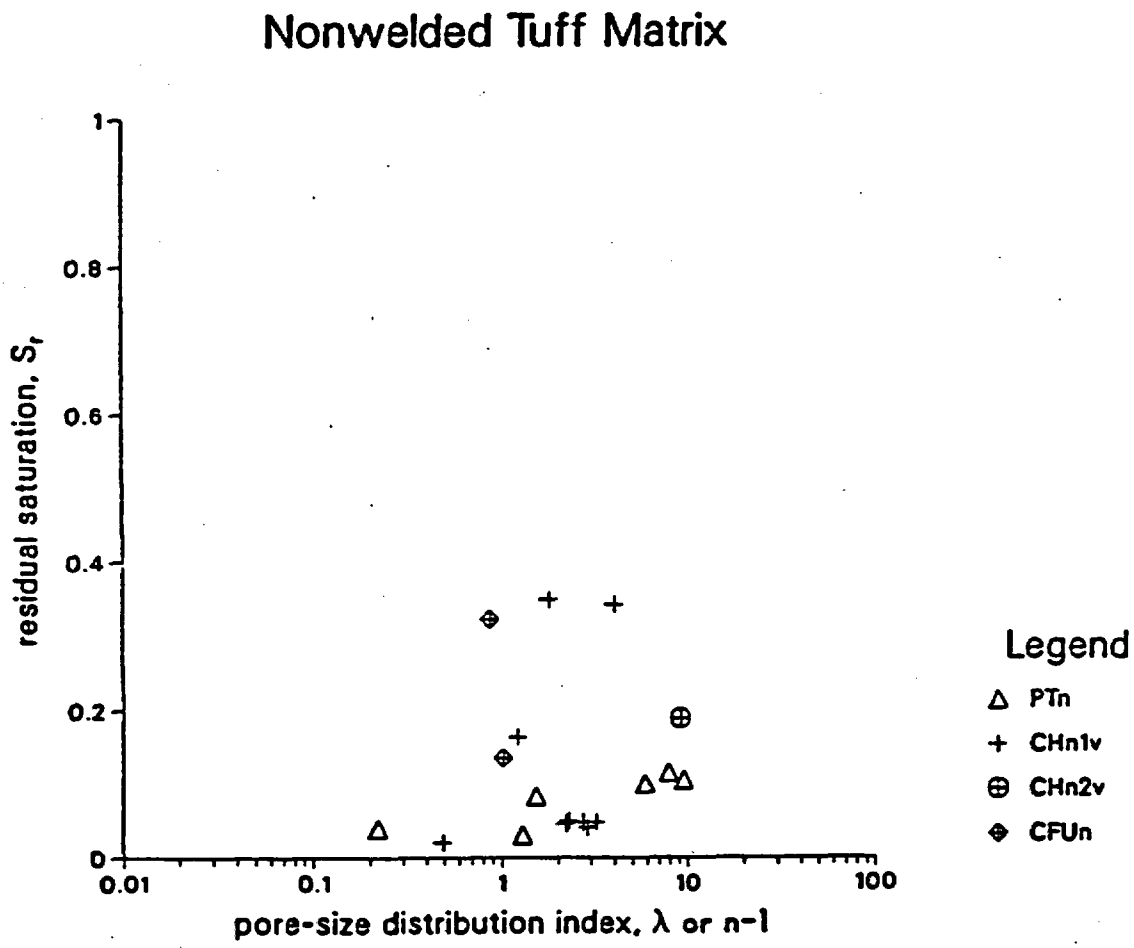

Figure 6-30. Correlation Between Residual Saturation and Pore-Size Distribution Index for Nonwelded Tuff Matrix.

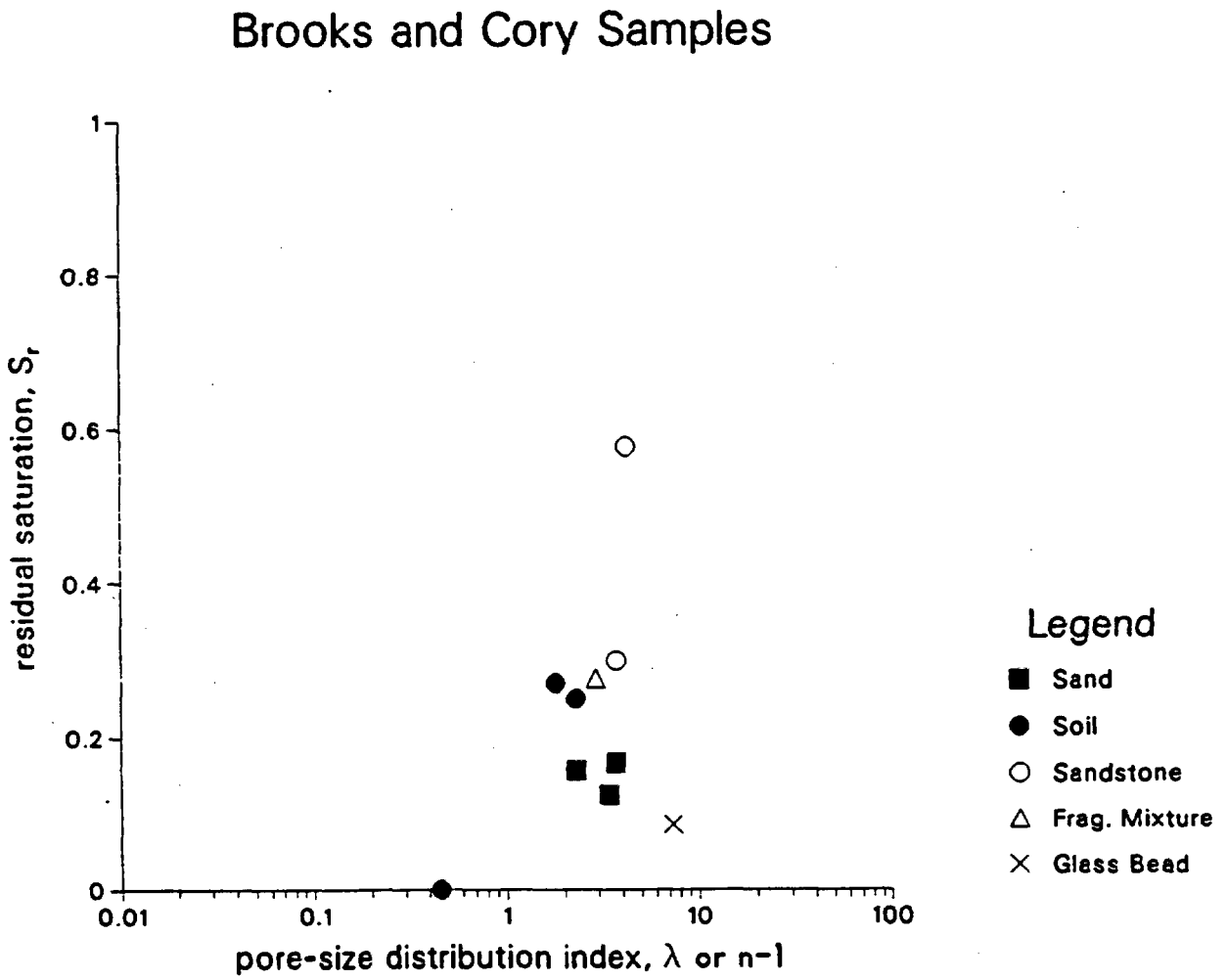

Figure 6-31. Correlation Between Residual Saturation and Pore-Size Distribution Index for Data of Brooks and Corey (1966).

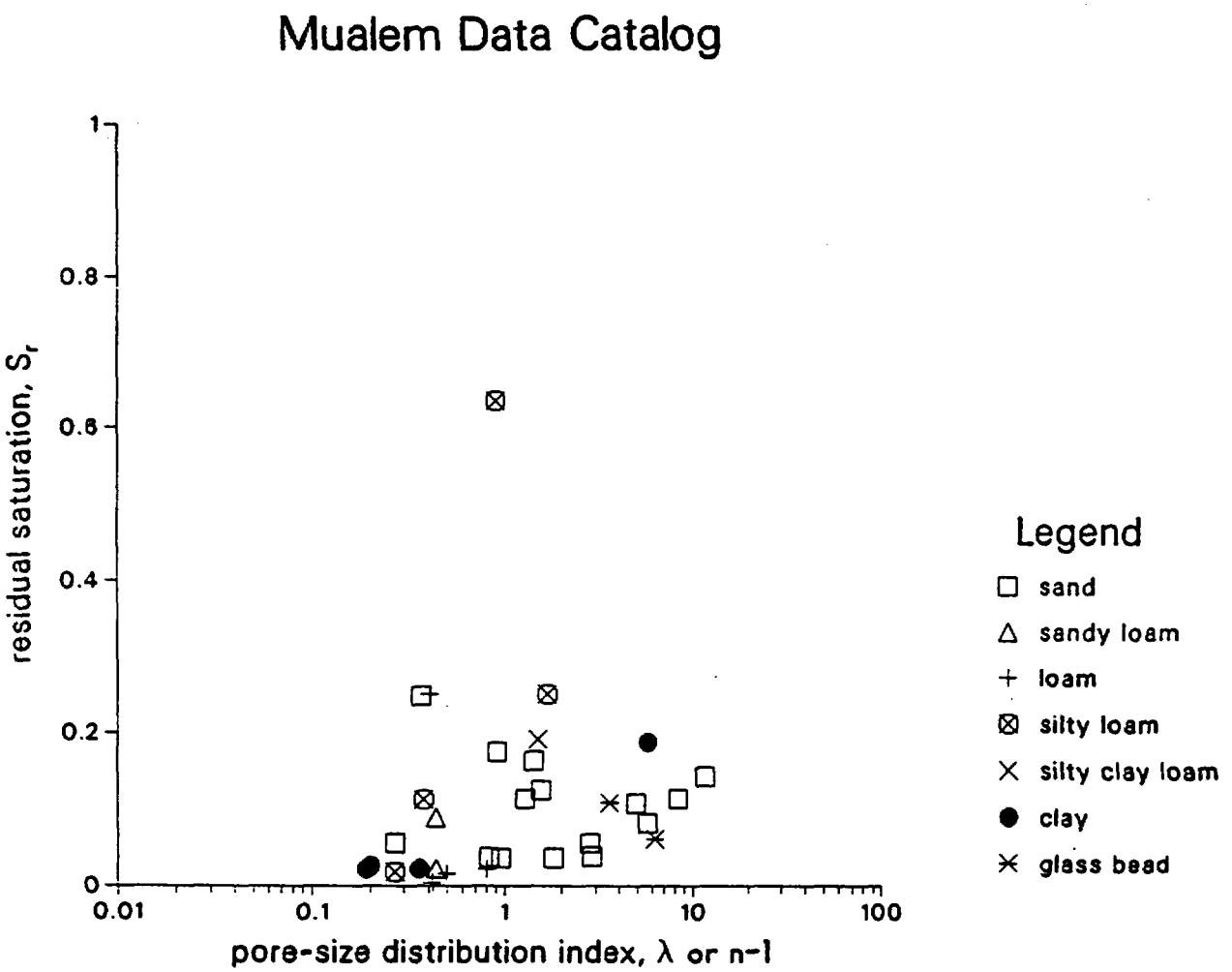

Figure 6-32. Correlation Between Residual Saturation and Pore-Size Distribution Index for Data of Mualem (1976b).

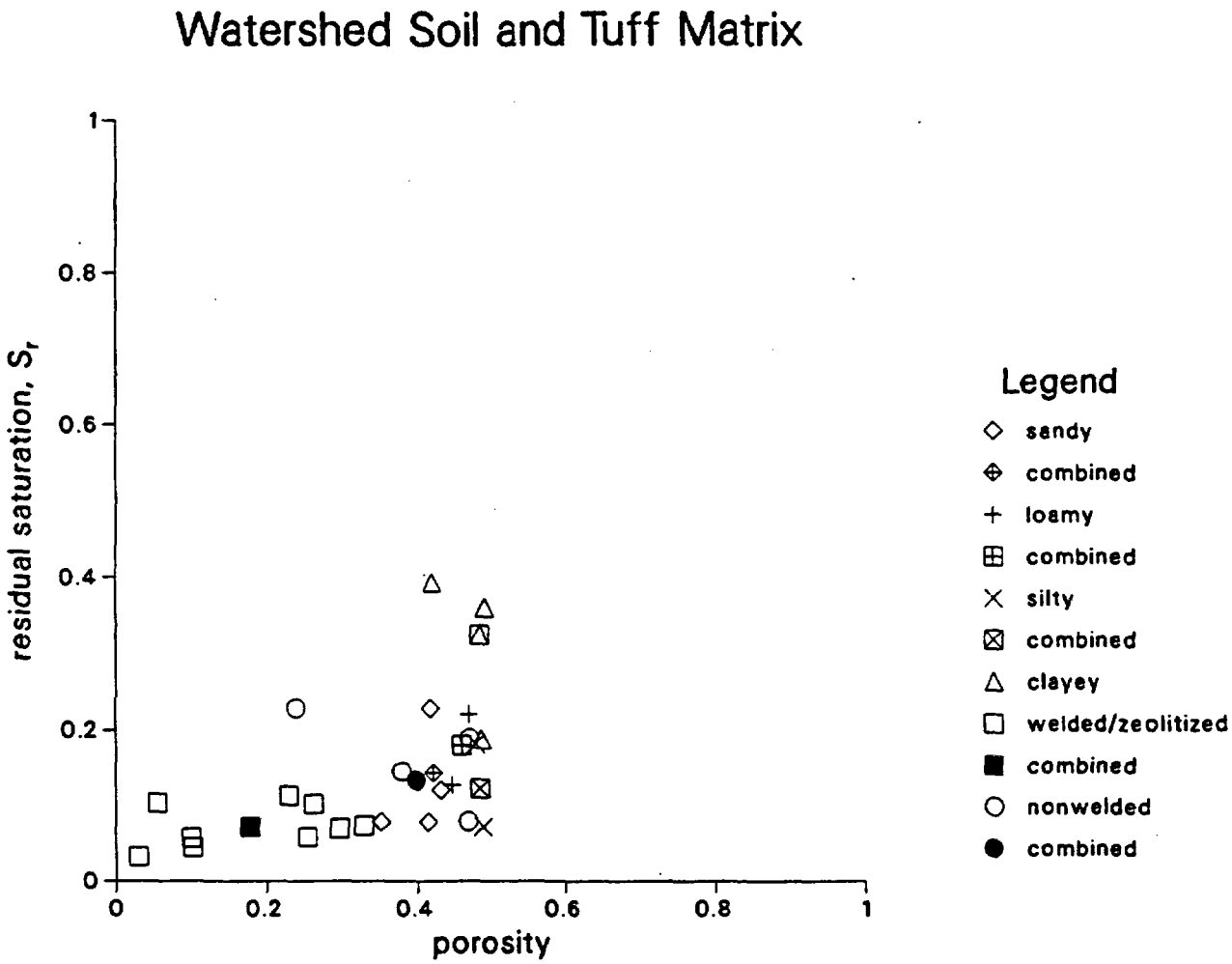

Figure 6-33. Correlation Between Residual Saturation and Porosity for Watershed Soil and Tuff Matrix.

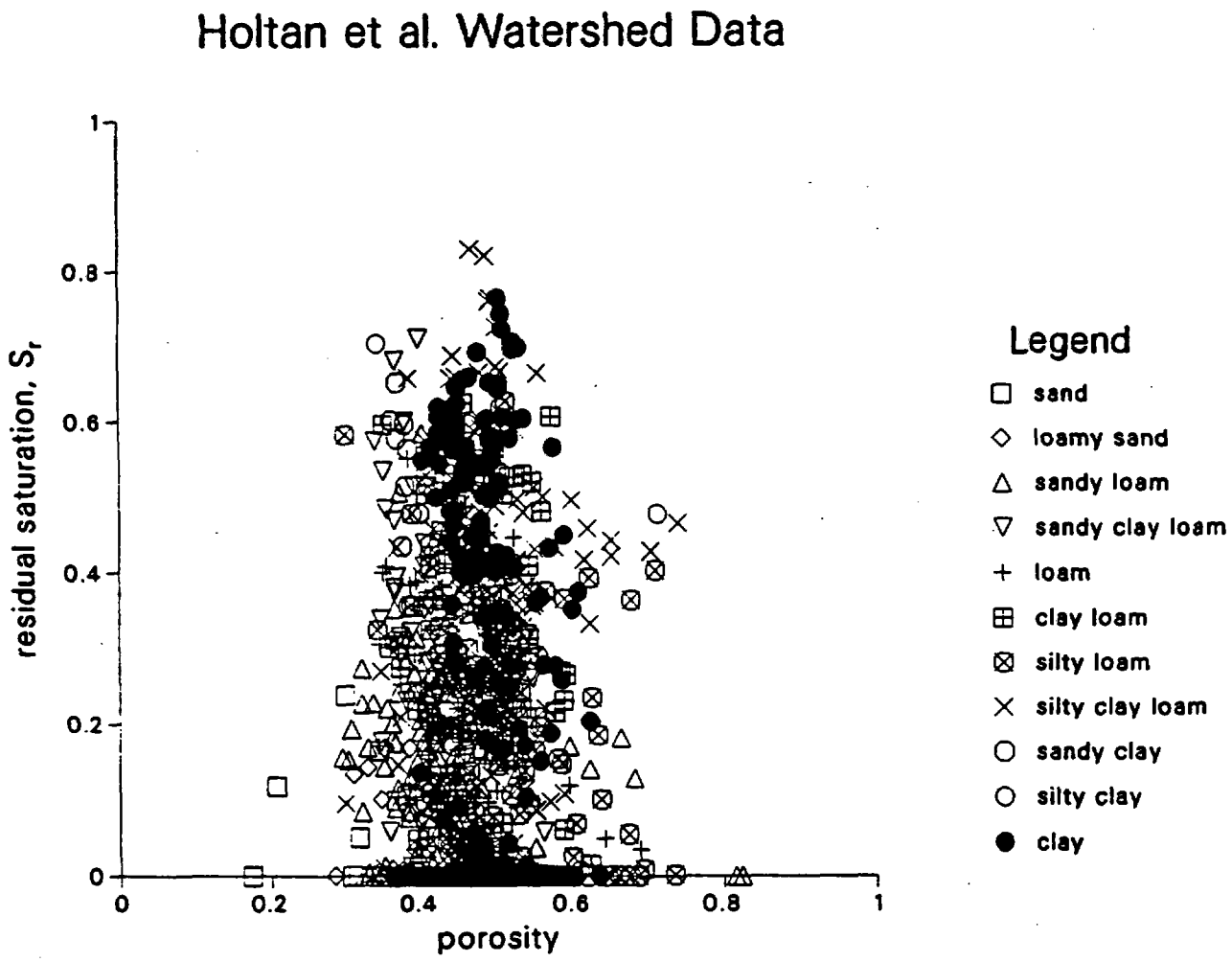

Figure 6-34. Correlation Between Residual Saturation and Porosity for Watershed Soil.

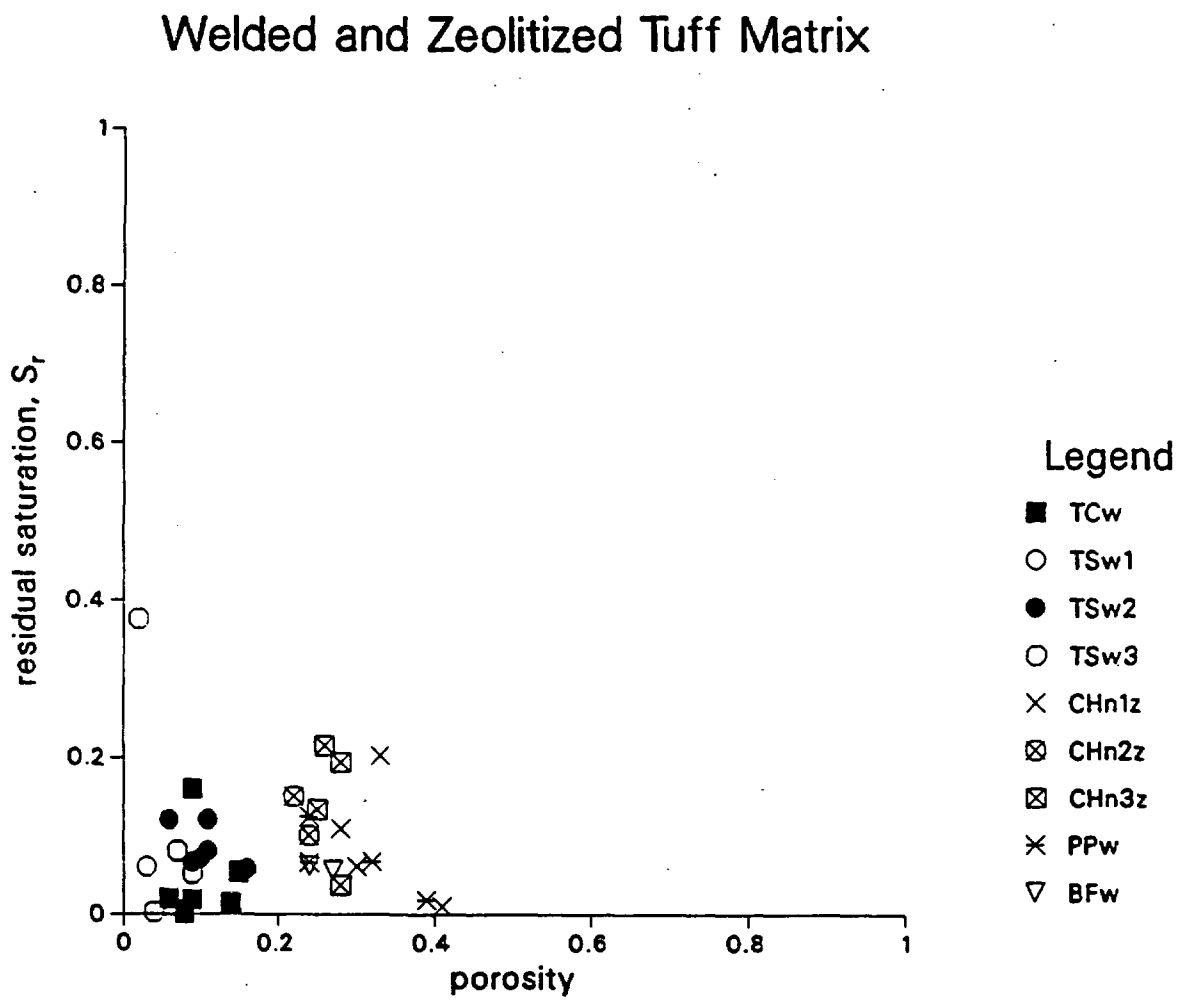

Figure 6-35. Correlation Between Residual Saturation and Porosity for Welded and Zeolitized Tuff Matrix.

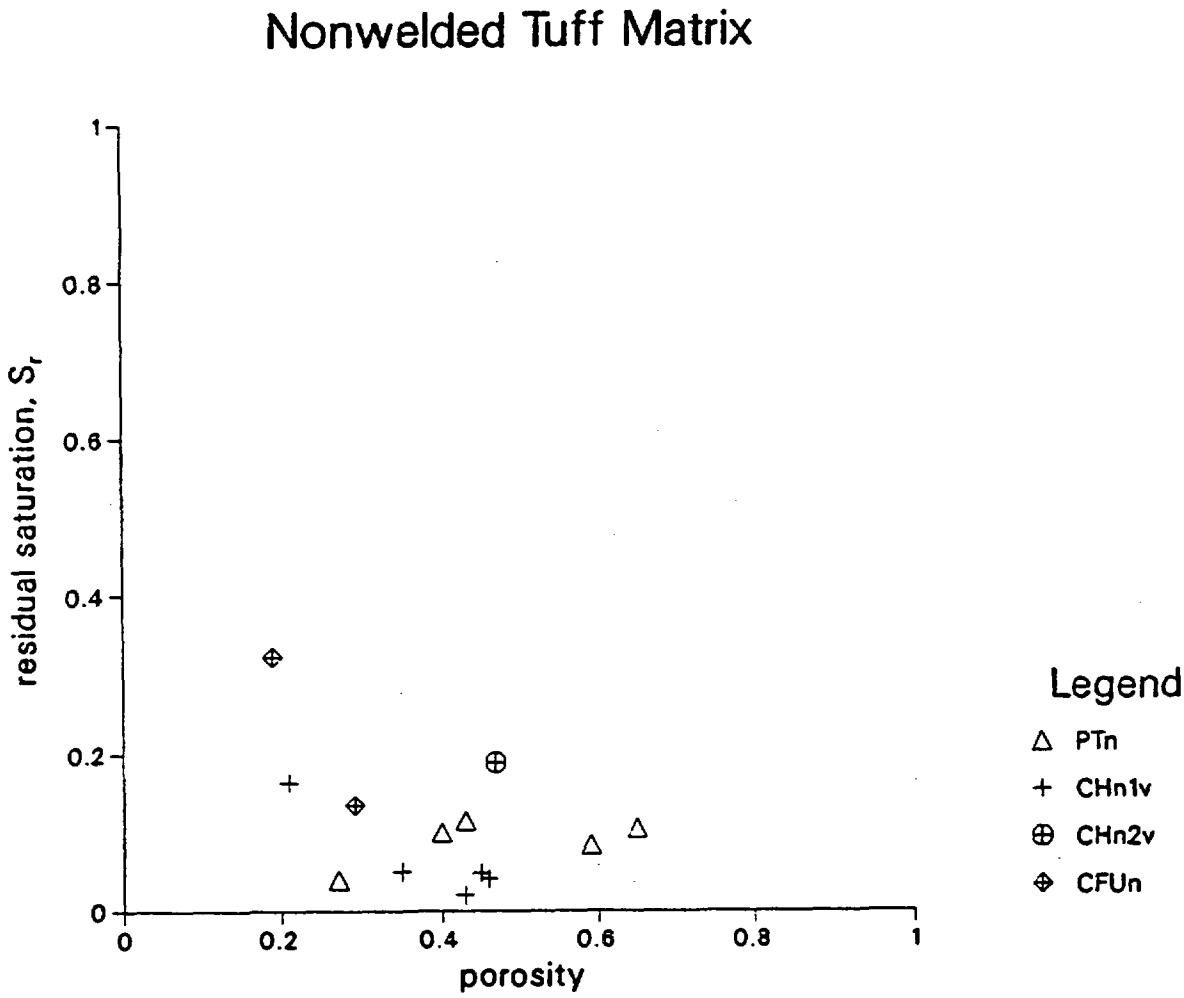

Figure 6-36. Correlation Between Residual Saturation and Porosity for Nonwelded Tuff Matrix.

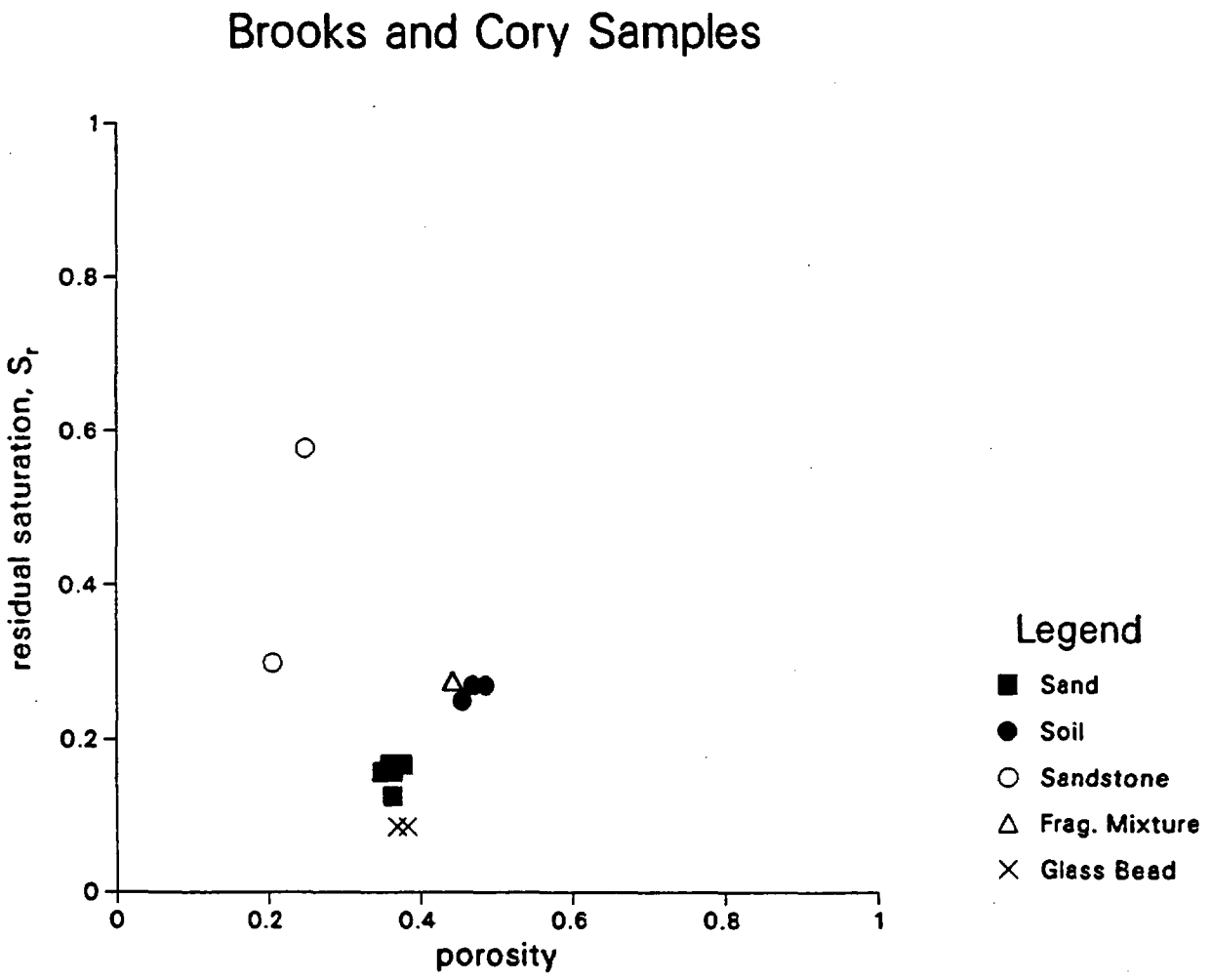

Figure 6-37. Correlation Between Residual Saturation and Porosity for Data of Brooks and Corey (1966).

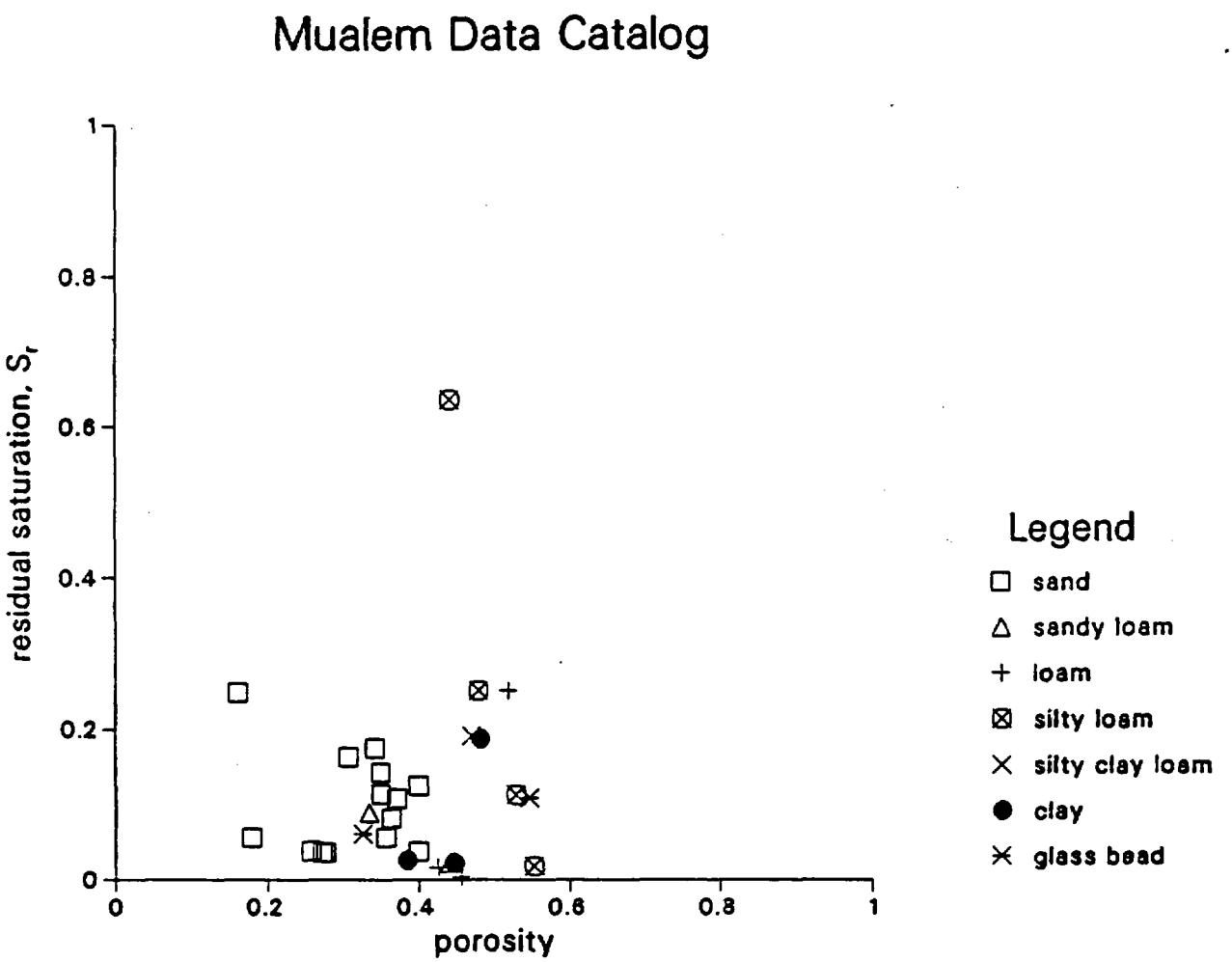

Figure 6-38. Correlation Between Residual Saturation and Porosity for Data of Mualem (1976b).

aperture b. The permeability through a circular tube (ct) is proportional to radius squared and the permeability between two parallel plates (pp) is proportional to aperture squared.

$$k_{ct} = \frac{r^2}{8} \tag{6.13}$$

and

$$k_{pp} = \frac{b^2}{12}. \tag{6.14}$$

Permeabilities of laminar flow through straight tubes of other cross-sectional shapes are also proportional to the square of mean hydraulic radius with the proportional constants depending on cross-sectional shapes (Carman, 1937). If pore volume is proportional to mean hydraulic radius, permeability is proportional to porosity squared.

Many empirical power functions or other functional forms can be found in the literature to fit permeability and porosity data with mixed success. One argument against the existence of permeability-porosity relationship is that the narrow segments of the flow channel (pore throats) control the permeability while the wide segments of the flow channel (pore bodies) correspond to the bulk of porosity (Verma and Pruess, 1987). Tortuosity of flow channels may also complicate the dependence of permeability on geometry. If dead-end pores are significant in total porosity, the correlation between permeability and porosity may be obscured by those dead-end pores not directly participated in fluid flow.

The watershed soil data and tuff matrix data support the general trend of positive correlation of large saturated permeability with large porosity (Figure 6-39). However, the watershed soil data set (Figure 6-40) and the welded/zeolitized tuff matrix data set (Figure 6-41) are too scattered to support convincingly the existence of this correlation. The nonwelded tuff matrix data set (Figure 6-42) shows good correlation, while the data of Brooks and Corey (1966, Figure 6-43) and the data of Mualem (1976b, Figure 6-44) show marginal, but not convincing, support of this correlation.

Similar support and ambiguity apply to the substantiation of the correlation relationship between saturated permeability and air entry radius. The air entry radius, r_{ae}, is defined in terms of the air entry scaling factor, α, in Equation 5.3. For constant surface tension and water density, r_{ae} is proportional to α. Two interpretations can be made for the air entry radius: (1) it represents the largest radius in the medium which is most easily drained; or (2) it represents the characteristic radius which scales the desaturation behavior of different media with similar pore-size distributions. If the medium is represented by uniform circular tubes with radius r_{ae}, the maximum permeability of this air entry tube model (Section 5.2.1 and Equation 5.15) is

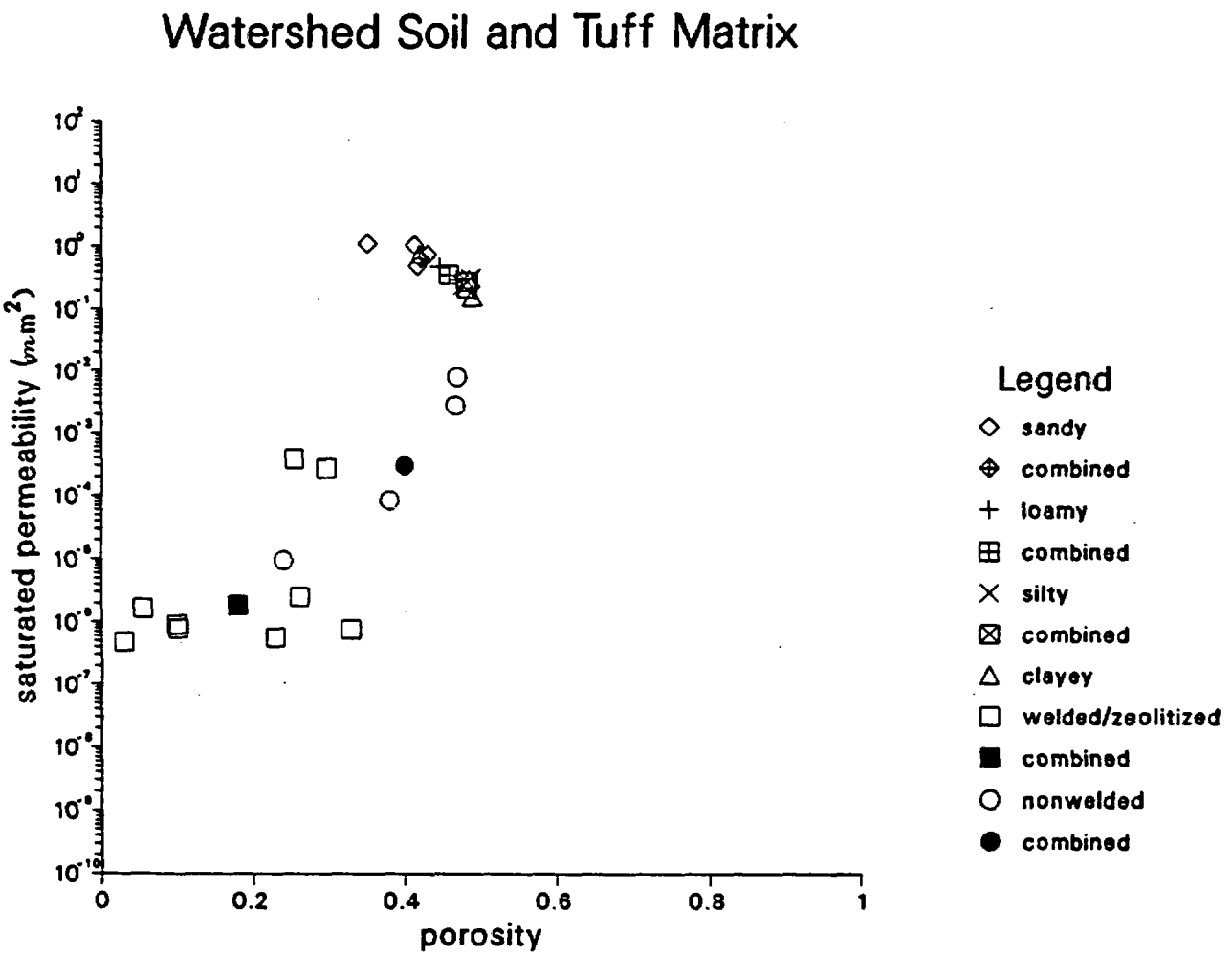

Figure 6-39. Correlation Between Saturated Permeability and Porosity for Watershed Soil and Tuff Matrix.

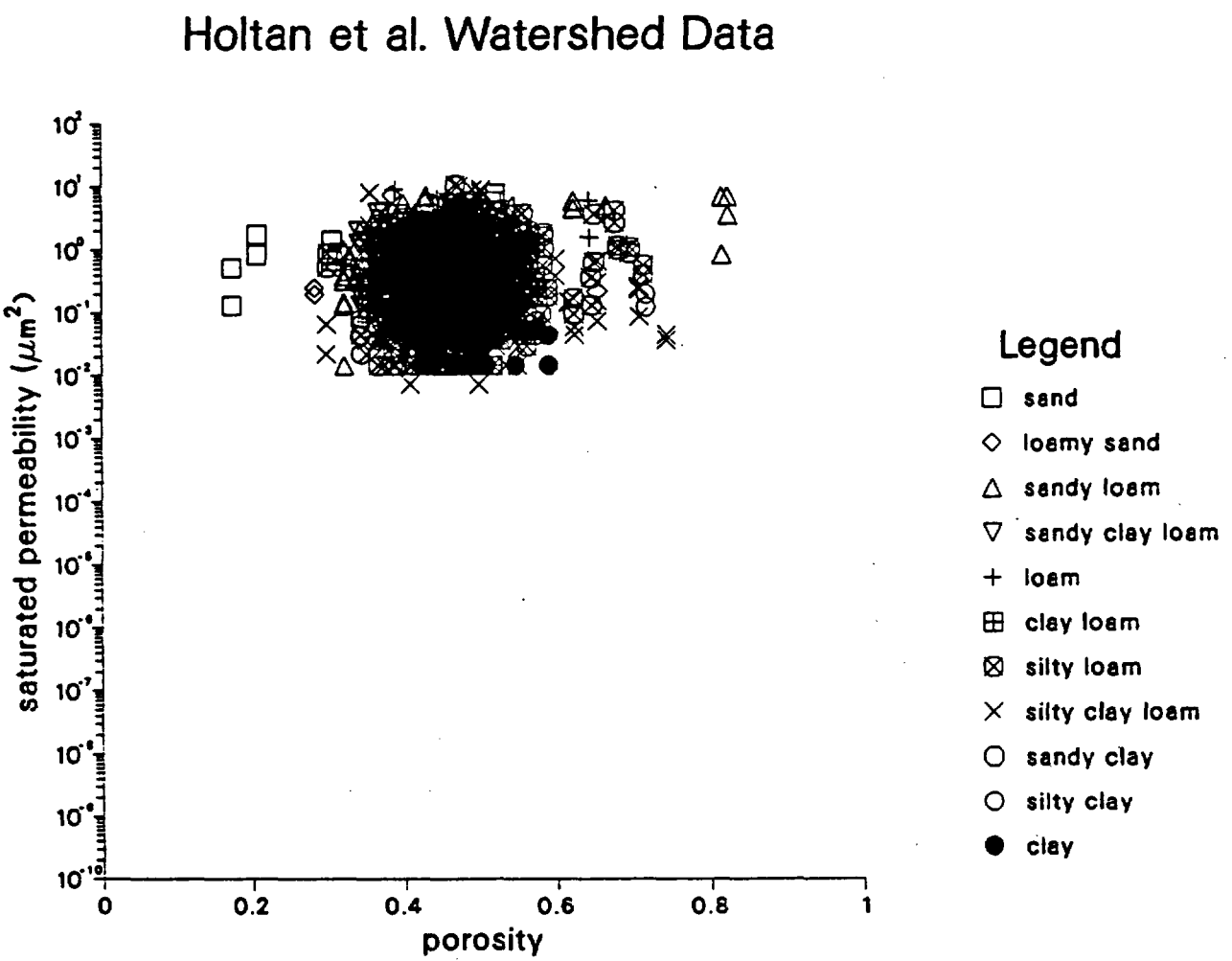

Figure 6-40. Correlation Between Saturated Permeability and Porosity for Watershed Soil.

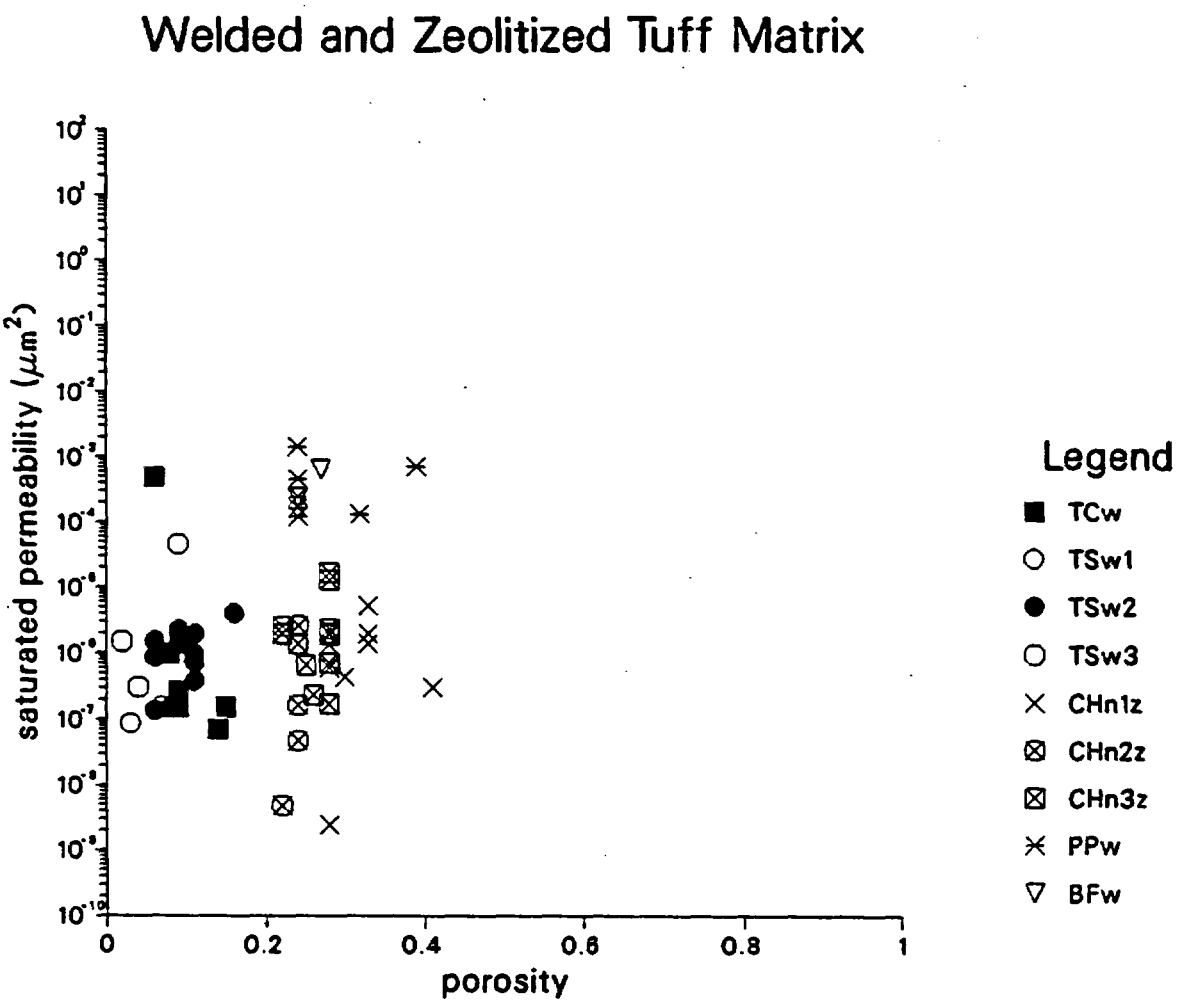

Figure 6-41. Correlation Between Saturated Permeability and Porosity for Welded and Zeolitized Tuff Matrix.

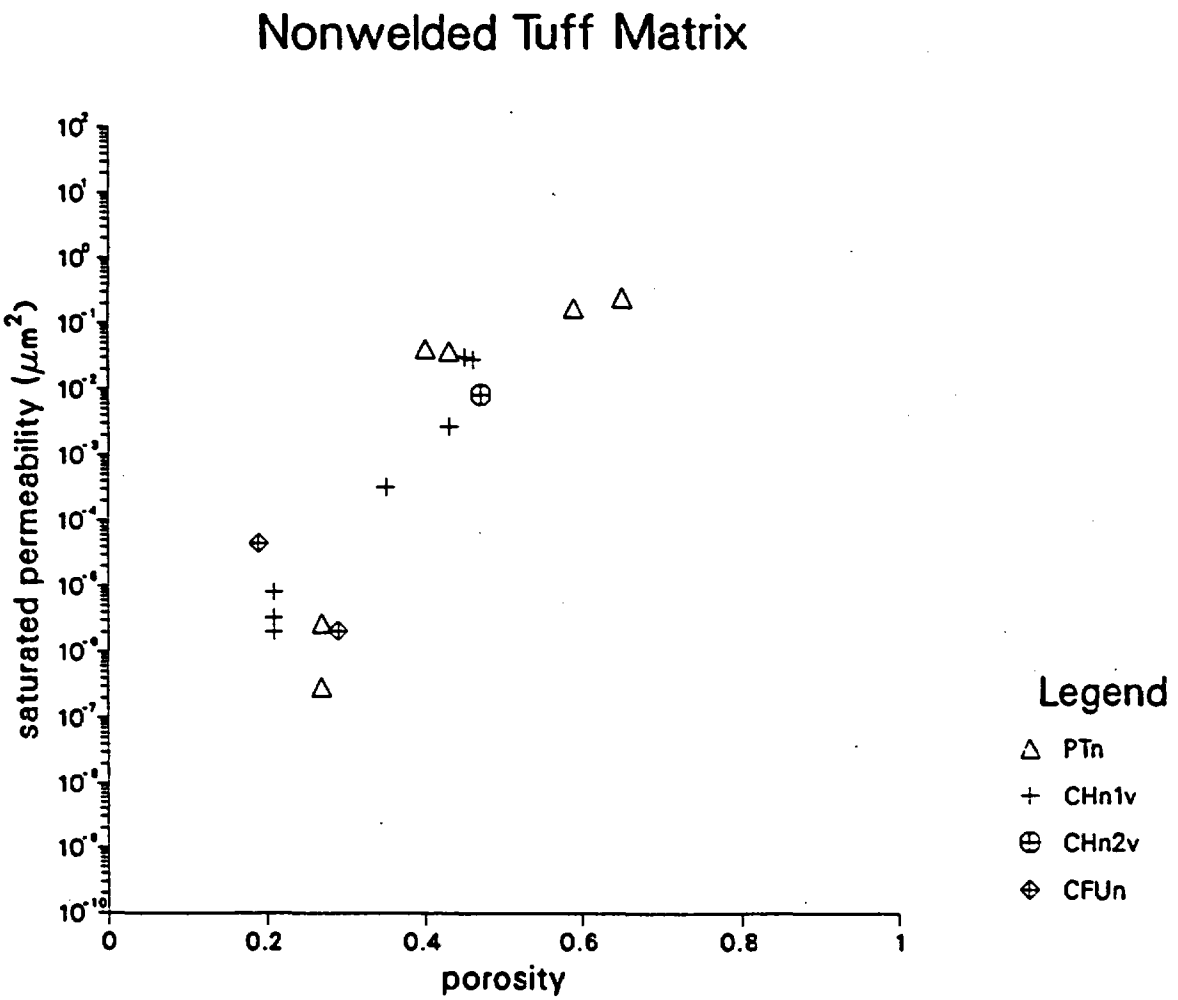

Figure 6-42. Correlation Between Saturated Permeability and Porosity for Nonwelded Tuff Matrix.

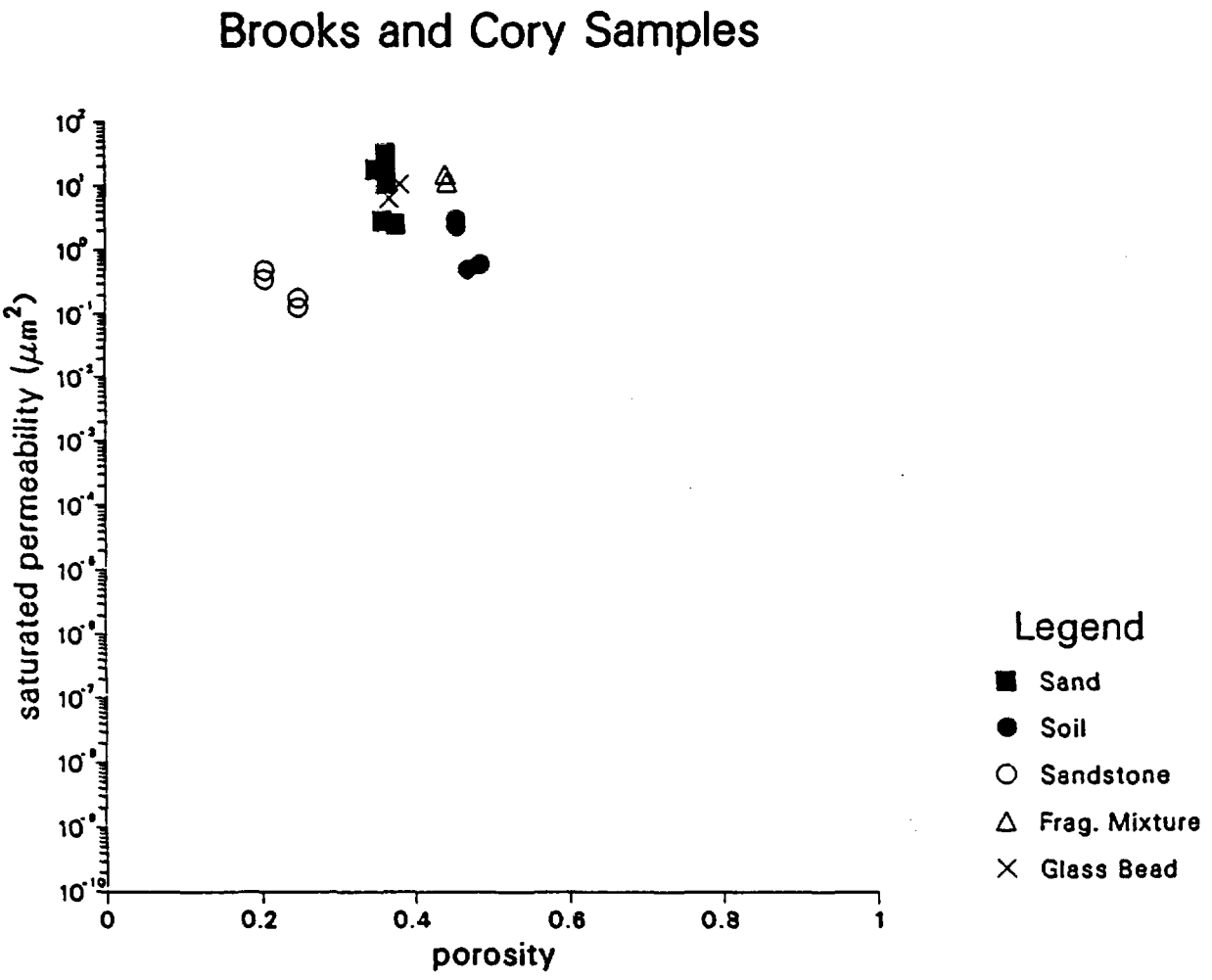

Figure 6-43. Correlation Between Saturated Permeability and Porosity for Data of Brooks and Corey (1966).

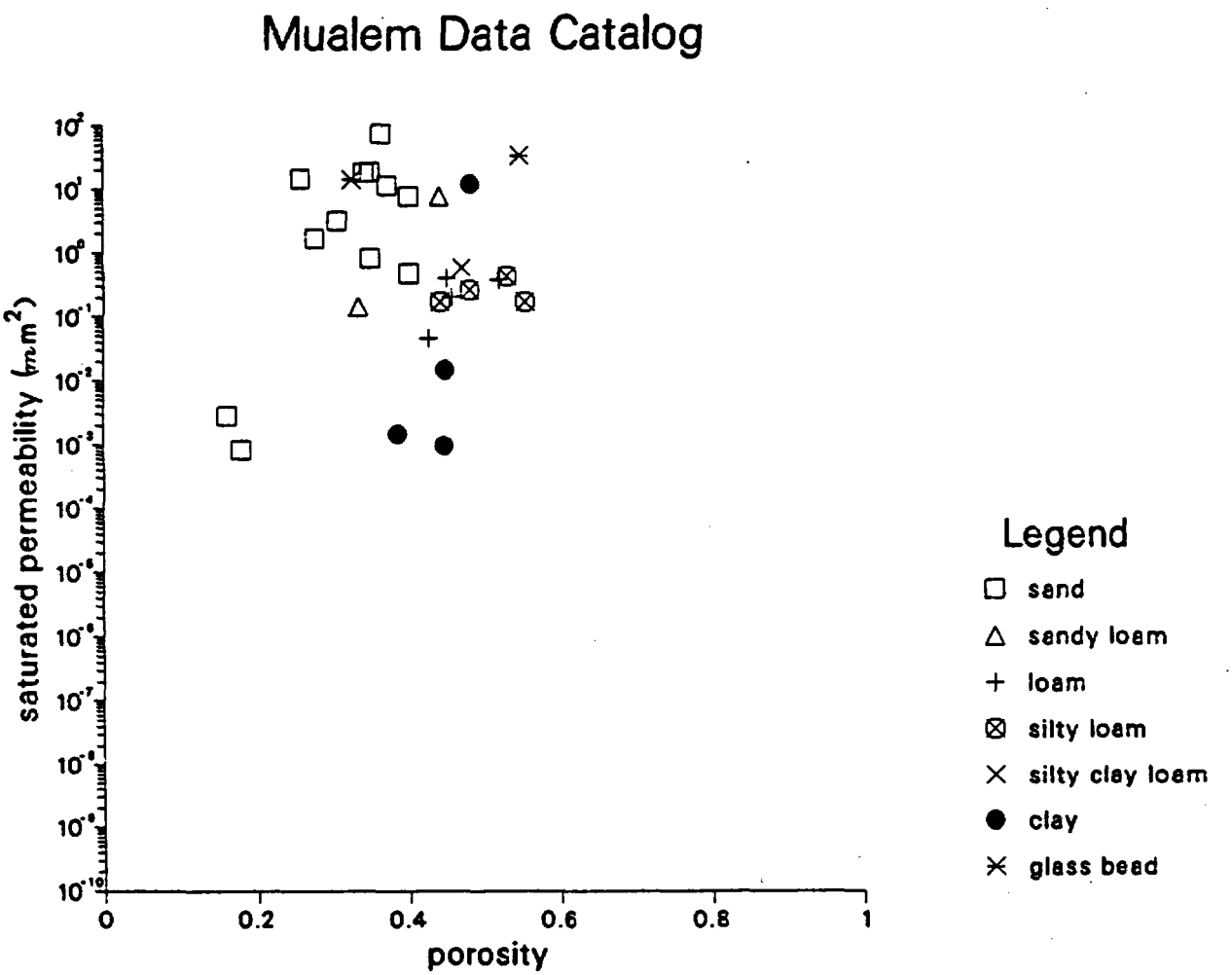

Figure 6-44. Correlation Between Saturated Permeability and Porosity for Data of Mualem (1976b).

$$k_{ae} = \frac{r_{ae}^2}{8}, \tag{6.15}$$

We note earlier two obvious differences between watershed soil parameters and welded/zeolitized tuff matrix parameters: (1) air entry scaling factor α is two to three orders of magnitude larger for soils than for welded tuff matrix (Figures 6-7c and 6-8c); and (2) saturated permeability k_s is approximately four to six orders of magnitude larger for soils than for welded tuff matrix (Figures 6-13c and 6-14c). The cross plot between saturated permeability and air entry radius based on mean values of these parameters for different soil texture categories and different tuff stratigraphic units is plotted in Figure 6-45. The scatter of watershed soil data is shown in Figure 6-46 and the scatter of welded/zeolitized tuff matrix data is shown in Figure 6-47. The nonwelded tuff matrix data in Figure 6-48 have narrow distribution in air entry radius and wide distribution in saturated permeability and do not support the correlation between these two parameters. Figure 6-49 shows the results of the Cosby et al. (1984) analyses, based on mean values of Holtan et al. (1968) and Rawls et al. (1976) watershed data with the Campbell (1974) model (Brooks and Corey model with $S_r = 0$). Figure 6-50 is based on the results of analyses with some of the data in the Case et al. (1983) catalog. Figure 6-51 is based on the results of Brooks and Corey (1966) and shows good correlation between saturated permeability and air entry radius. The data points in Figure 6-51 also are approximately lined up parallel to the log-log straight line of Equation 6.15.

To evaluate the correlation relationships involving saturated permeability, it is important to note that the saturated permeability values have large intrinsic variability for natural geological media. The watershed soil data from the same horizon and the tuff matrix data from the same core sample can differ by three orders of magnitude. The differences in experimental methods and resolutions also may obscure the data scattering and range. The resolution of the watershed soil data, based on significant figures in the tabulated conductivity values, is 0.01 *in/hr*, or equivalent to $7.2 \times 10^{-3} \mu m^2$. The resolution of the tuff matrix data (Peters et al., 1984) is 1.31×10^{-11} *m/s*, or equivalent to $1.32 \times 10^{-6} \mu m^2$. From the above variability and resolution considerations, we can deduce meaningful correlations involving saturated permeability only if the data range spans more than four orders of magnitude. The cross plots in Figures 6-49 to 6-51 from the data with permeable geological media do not span enough range to conclusively substantiate or refute the correlation between saturated permeability and air entry radius. The strongest support for this correlation is Figure 6-45, showing the large differences of four to six orders of magnitude in saturated permeability and two to three orders of magnitude in air entry radius between soils and welded/zeolitized tuff matrix. The scattering of data over smaller ranges is expected from considerations of data variability and differences in experimental procedures, resolutions, and analyses.

If the saturated permeability does correlate with other hydrological parameters, it probably correlates better with air entry radius than with porosity and other parameters. Physically, this correlation makes more sense with air entry radius than with porosity. The saturated permeability measures the flow through connected channels in a medium. The air entry radius measures the desaturation of fluid from the interior of a medium through connected channels to the outside. Neither parameter depends on dead-end pores with stagnant fluid isolated from the connected channels. The porosity measures the volume of both connected channels and dead-end

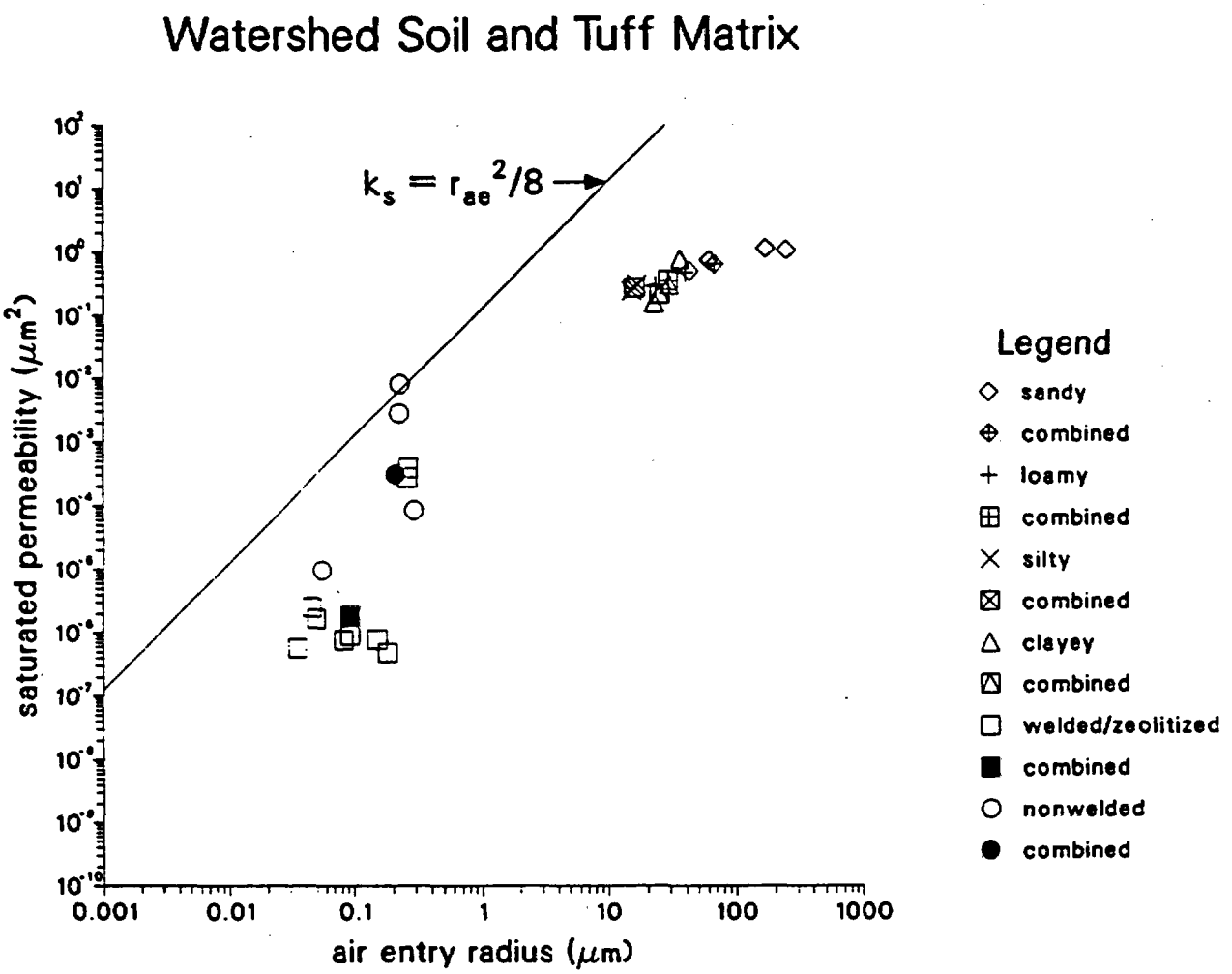

Figure 6-45. Correlation Between Saturated Permeability and Air Entry Radius for Watershed Soil and Tuff Matrix.

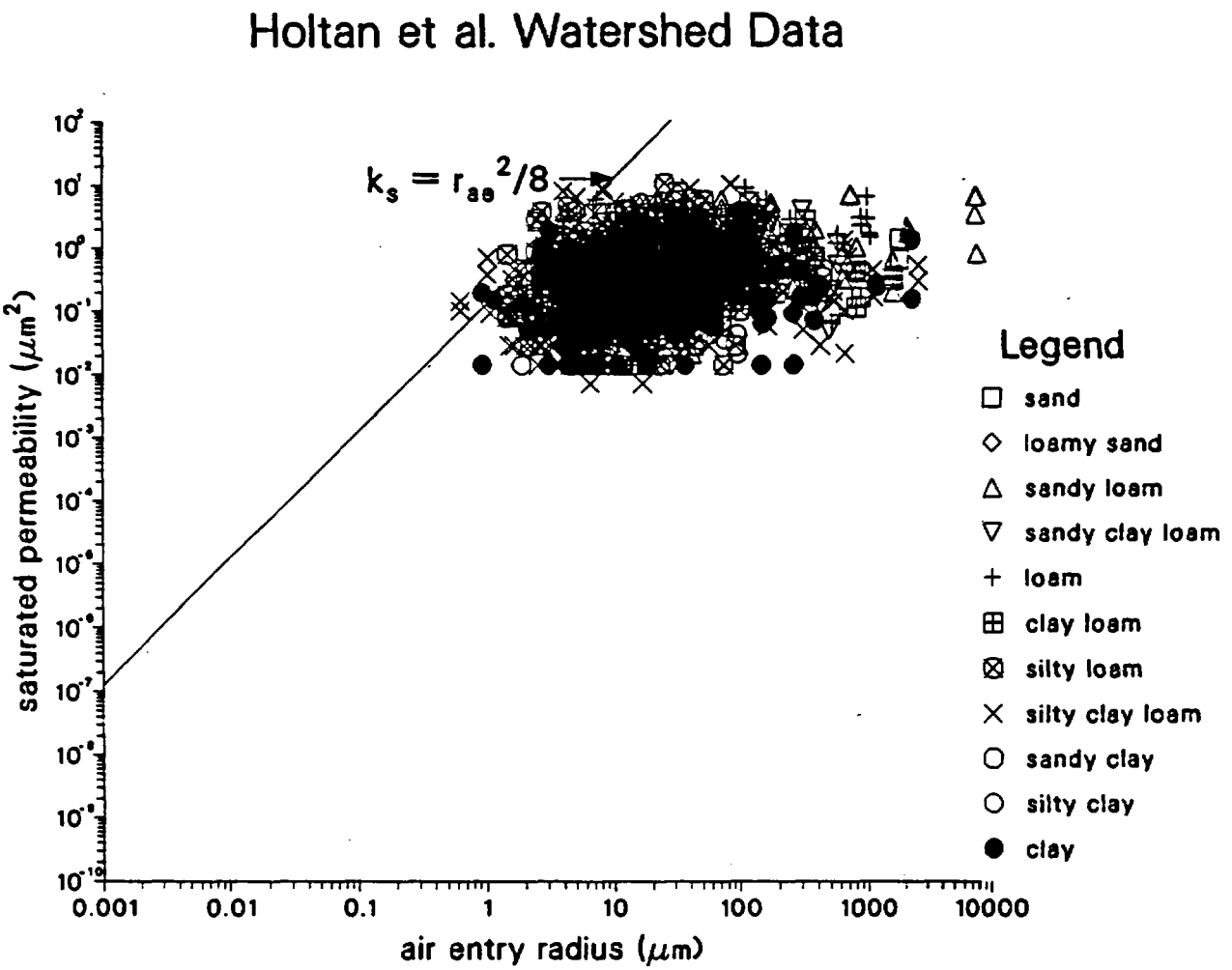

Figure 6-46. Correlation Between Saturated Permeability and Air Entry Radius for Watershed Soil.

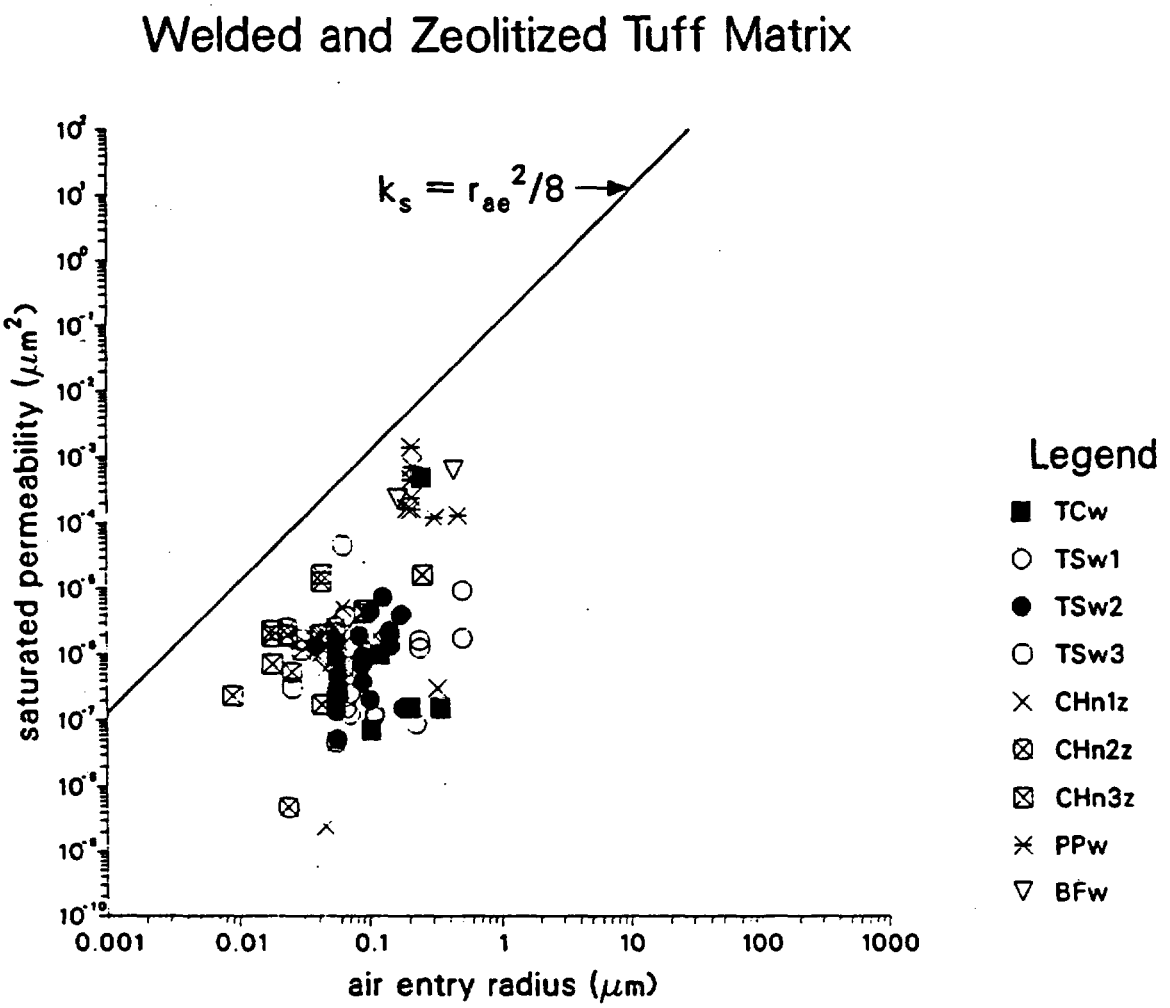

Figure 6-47. Correlation Between Saturated Permeability and Air Entry Radius for Welded and Zeolitized Tuff Matrix.

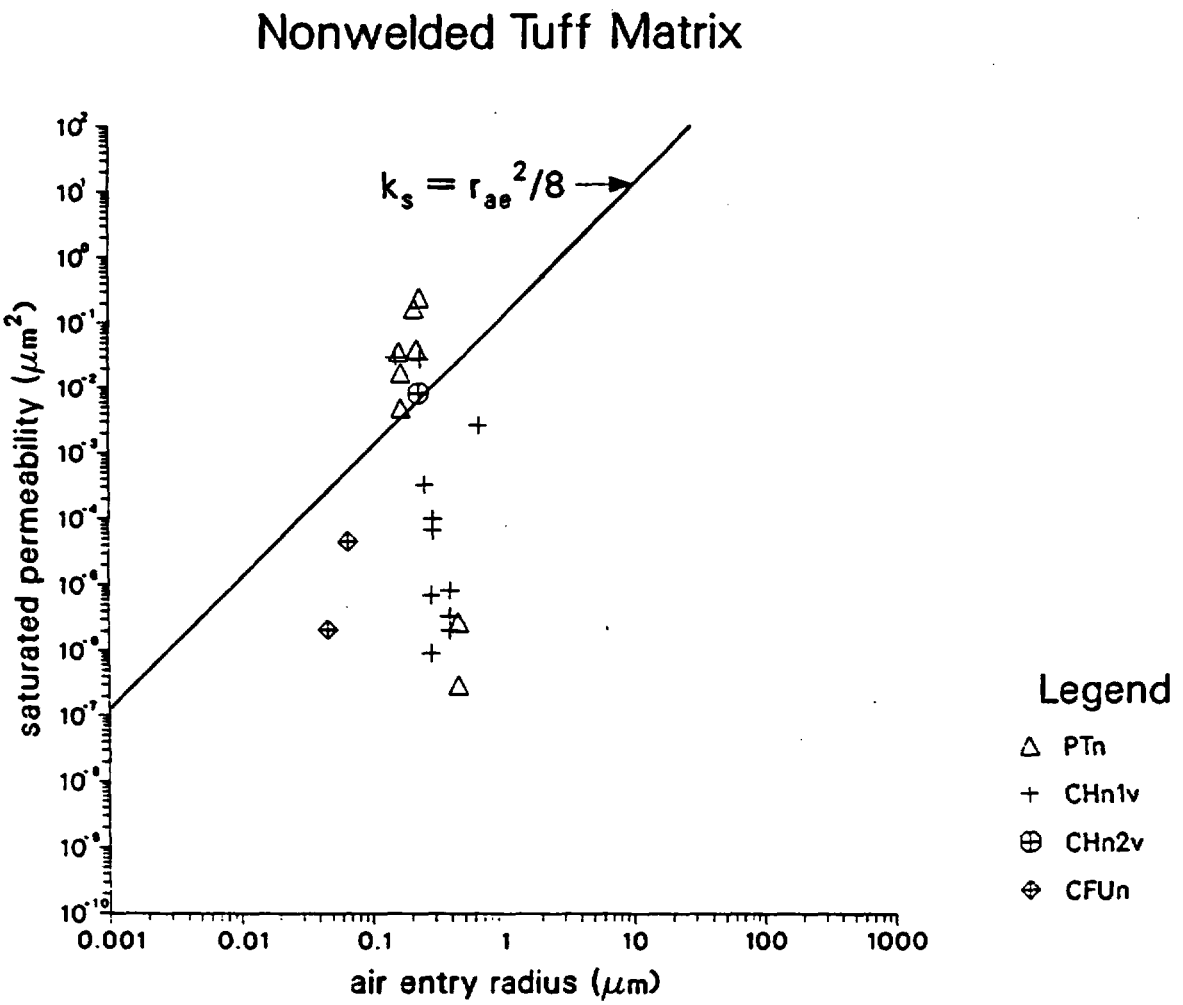

Figure 6-48. Correlation Between Saturated Permeability and Air Entry Radius for Nonwelded Tuff Matrix.

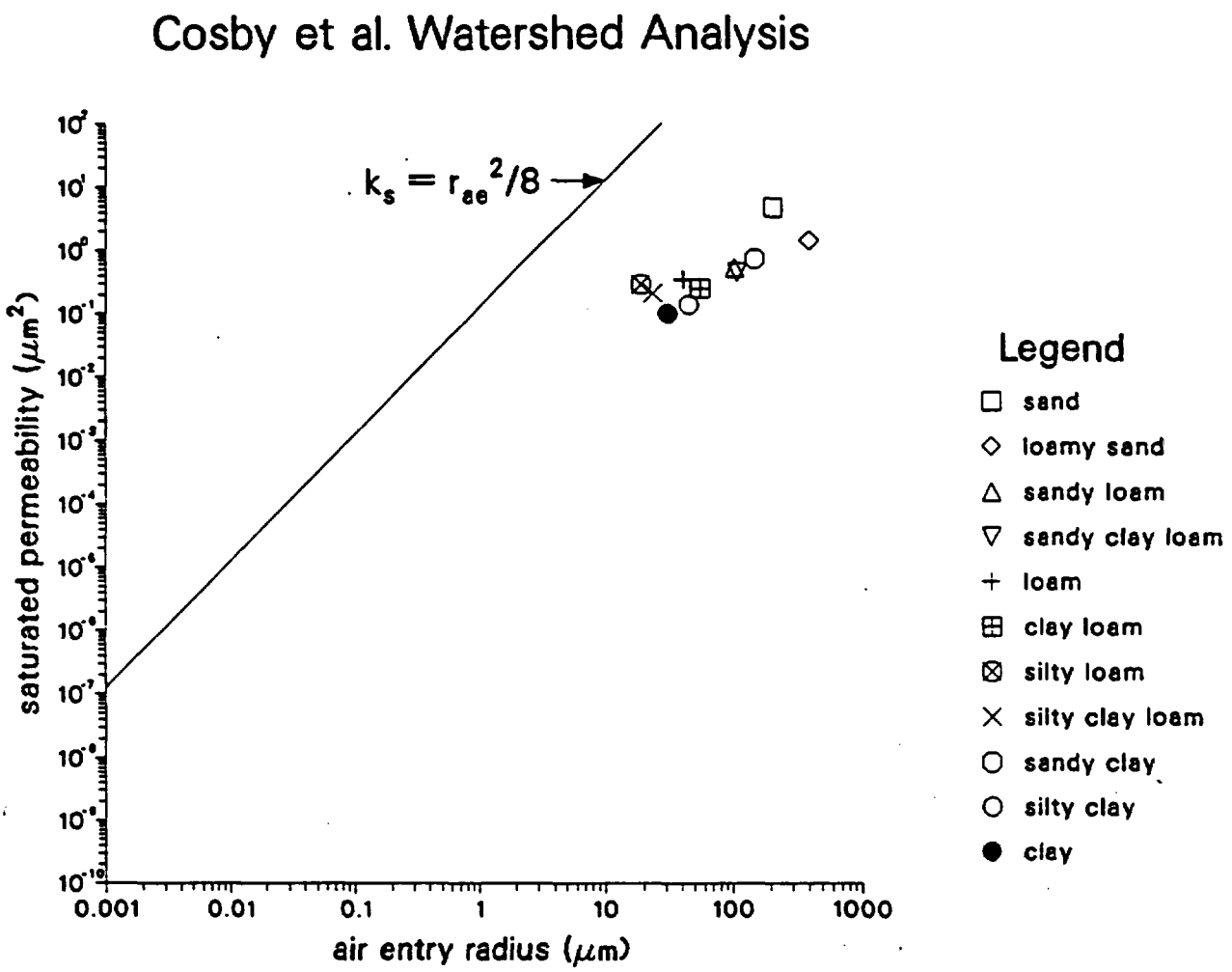

Figure 6-49. Correlation Between Saturated Permeability and Air Entry Radius for Watershed Soil Analyzed by Cosby et al. (1984).

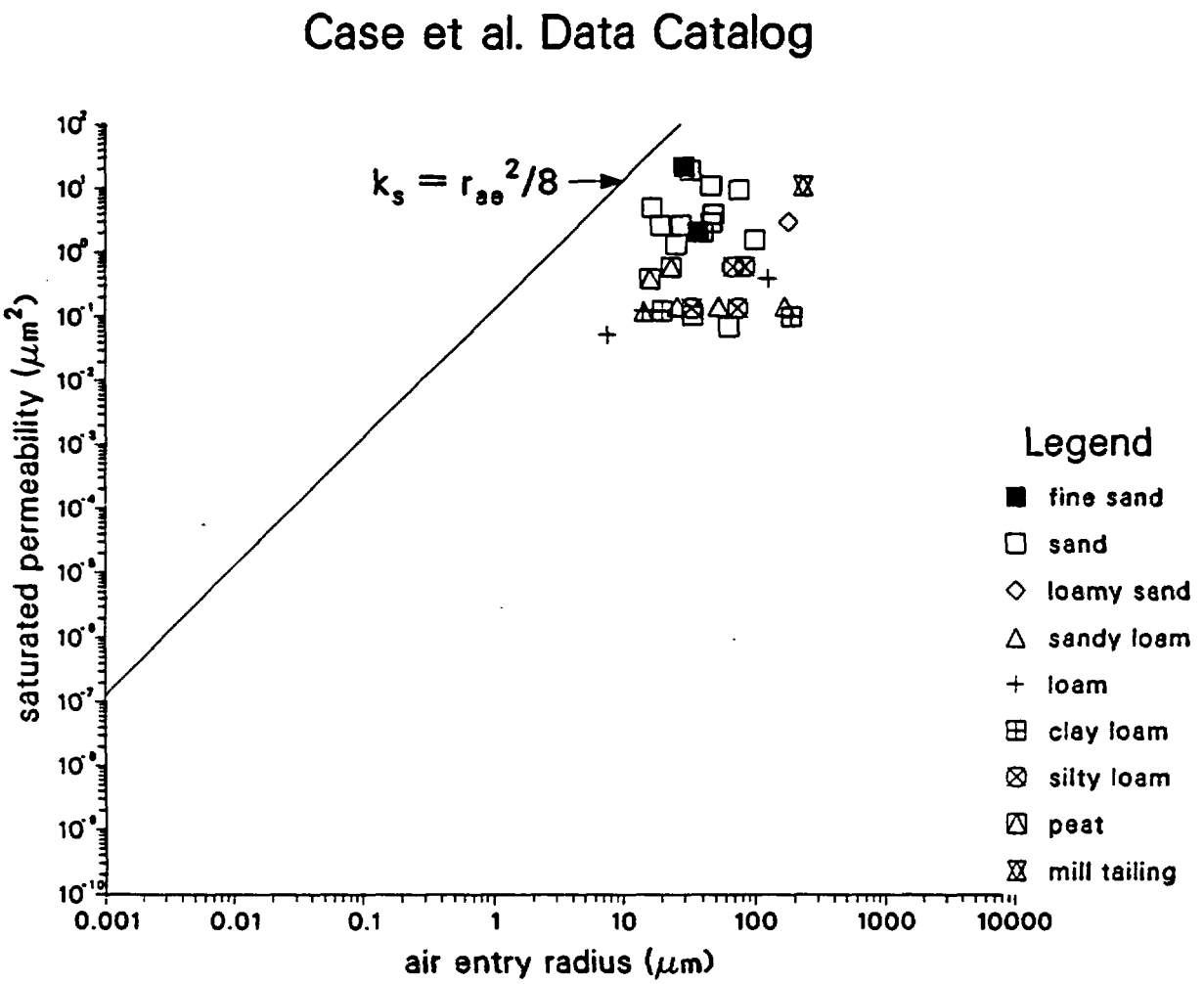

Figure 6-50. Correlation Between Saturated Permeability and Air Entry Radius for Data in Case et al. (1973) Catalog.

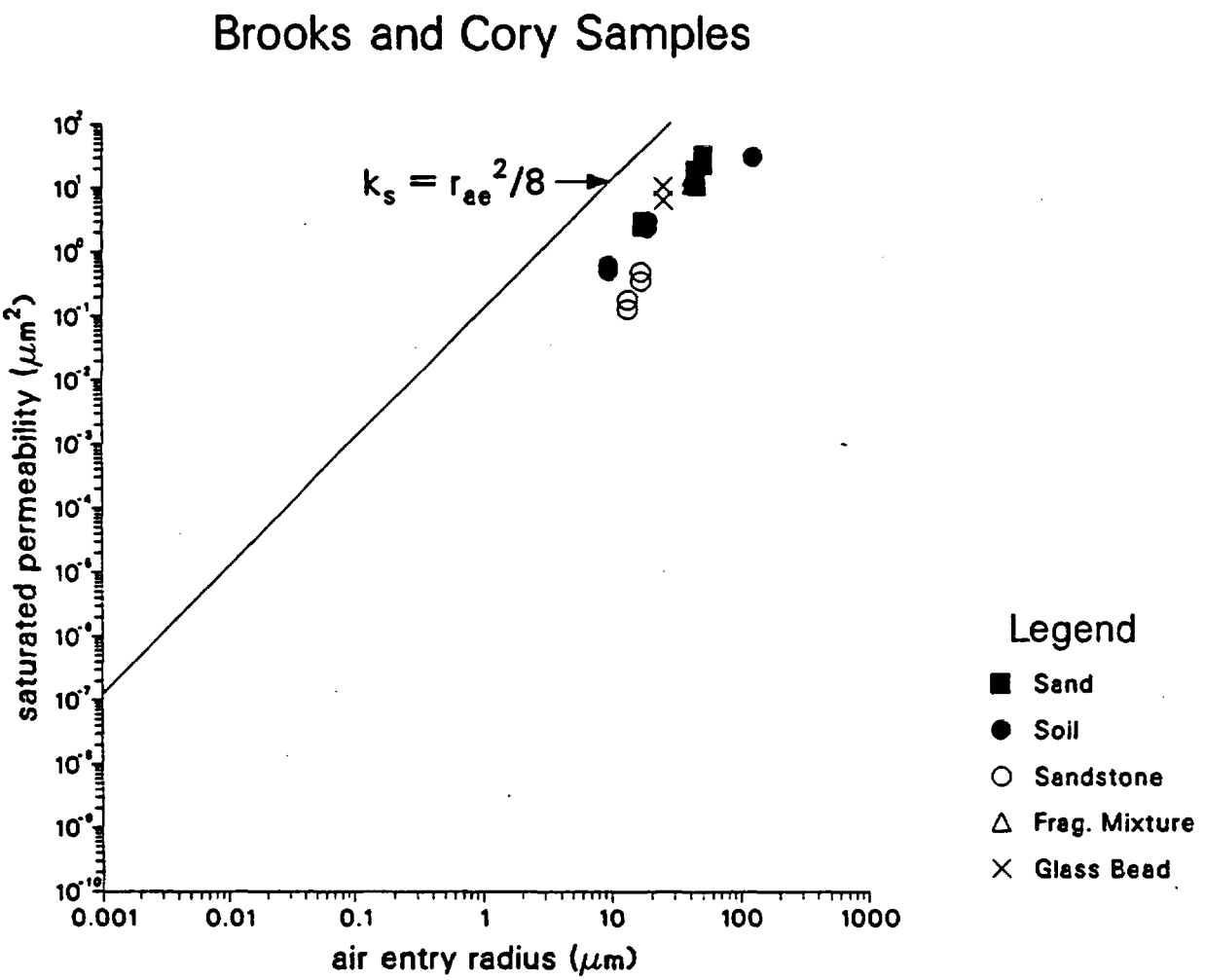

Figure 6-51. Correlation Between Saturated Permeability and Air Entry Radius for Data of Brooks and Corey (1966).

pores. Considerable interest exists in the literature on the permeability-porosity relationship. The correlation between permeability and air entry radius, observed in soil and tuff matrix data, also deserves attention in natural geological medium studies. Practically, this correlation of saturated permeability can be more easily demonstrated with air entry radius than with porosity. The air entry radius, or equivalently the air entry scaling factor, varies over several orders of magnitude among different geological media. The porosity varies over a much narrower range among different geological media. With wider variations, the air entry radius may correlate better with saturated permeability, which has the widest range of variation among all hydrological parameters.

The set of nonwelded tuff matrix data has very peculiar characteristics. It has narrow distribution in air entry scaling factor (Figure 6-9a) and wide distribution in saturated permeability (Figure 6-15a). Recent laboratory wetting experiments and scanning electron microscopic studies of PTn samples indicate that some nonwelded tuff has multimodal pore structure (Peters et al., 1987). From lithological descriptions of geological logs, the CHn unit can be divided into 11 hydrostratigraphic subunits (Kaplan, 1989). The heterogeneities in the pore scales and in functional subunit scales may explain the nonwelded tuff characteristics. We need more data for the nonwelded units and finer classification schemes to understand better the parameter distributions and correlations of these tuff units.

An even more urgent data need is for fracture and fault properties. Only a few measurements have been made on saturated permeability of fractured cores (Peters et al., 1984) and none have been made on unsaturated characteristic curves of fractures. Only theoretical models have been derived or assumed to represent the fracture and fault characteristic curves. For examples, Wang and Narasimhan (1985) derived the fracture curves in terms of measurable bulk conductivity, fracture orientations and spacings, and fractions of fracture coatings. Peters et al. (1984) assumed the fractures behave like permeable sand. Rulon et al. (1986) used a parallel channel model (Harrold et al., 1985) to derive anisotropic fracture and fault characteristic curves. Figure 6-52 compares the model parameters in the correlation cross plot of saturated permeability and air entry radius. Clearly the model parameters are very scattered and some of the models have saturated permeability greater than the maximum capillary tube value $r_{ae}^2/8$ (Equations 5.15 and 5.18). Even though theoretical models can be derived for fractures and faults, we need to have experimental measurements to validate the theoretical models. The contrast of hydrological parameters between fractures and tuff matrix in meter scale determines if the fluid flow is fast through fractures or slow through matrix under ambient partially saturated conditions. The contrast of hydrological parameters between stratigraphic units and bounding faults in kilometer scale determines if the net infiltration is dispersed through the unsaturated tuff formations or concentrated through a few major faults from ground surface to water table. The lack of data in fractures and faults is one of the reasons we survey the soil data and study the parameter variations and correlations among different natural geological media. If constraints and correlations can be shown to exist among different geological media, we can evaluate whether the theoretical model parameters are reasonable and establish better confidence in our calculation results.

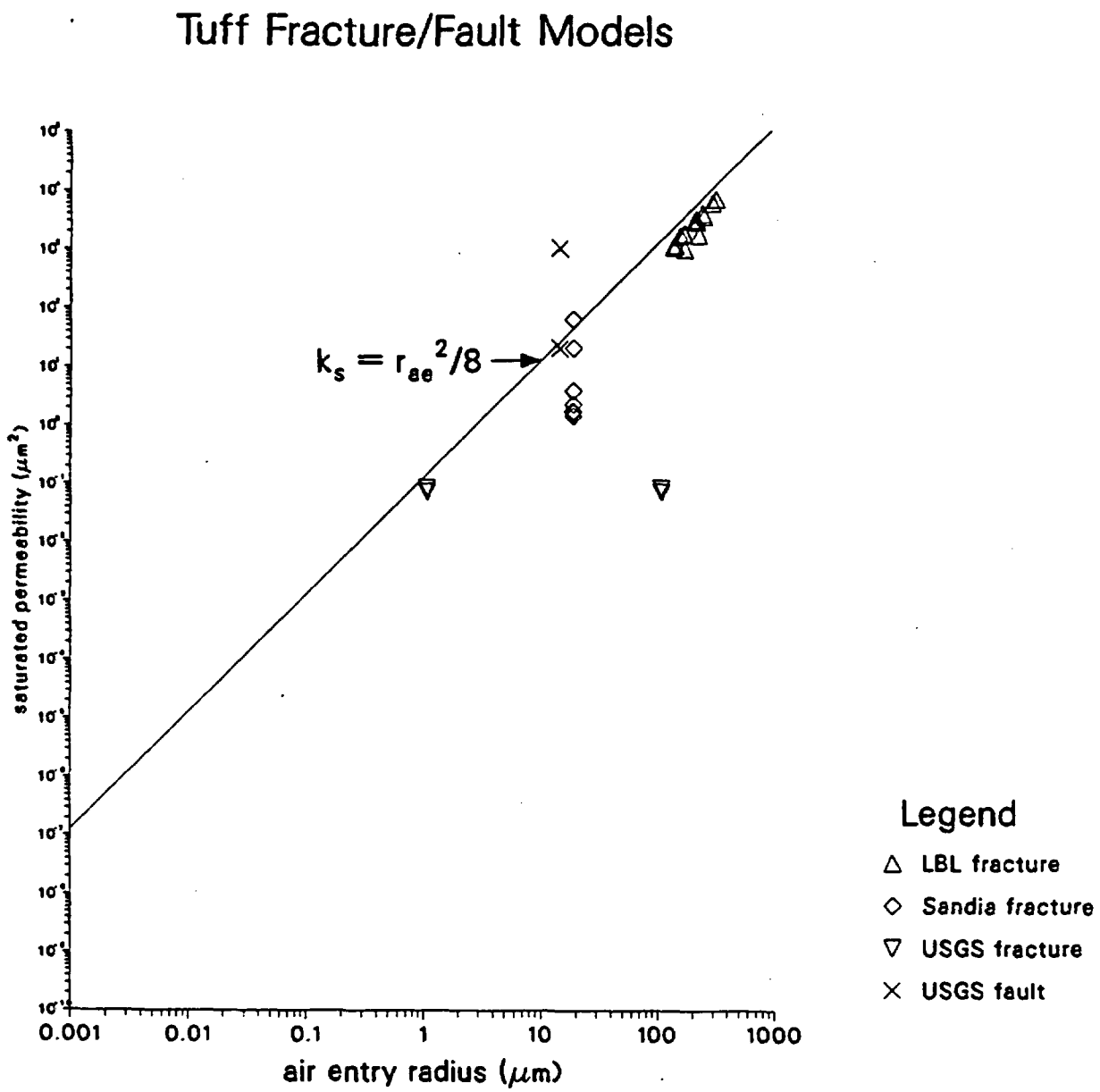

Figure 6-52. Correlation Between Saturated Permeability and Air Entry Radius for Tuff Fracture and Fault Models.

6.4 Spatial Correlation, Fractal Scaling, and Stochastic Modeling

With parameter distributions and correlations determined from laboratory measurements, we need additional information on spatial correlation and scale dependence to properly model field-scale hydrological processes. The spatial correlation structure determines the grid block sizes to represent a heterogeneous formation and the scaling law relates the laboratory measurements to field experiments. In this section, we review the use of the variogram for characterizing spatial correlation, summarize some on-going studies on spatial distributions of tuff and soil properties, discuss scale dependence and scale-invariant fractal geometry, relate the notion of fractal to the notion of variogram, and outline a stochastic modeling approach that accounts for fractal scaling.

Consider two points in the formation at coordinates $\vec{r}$ and $\vec{r} + \vec{d}$. If the distance of separation $d = |\vec{d}|$ is small, the parameter values at these two points will be very close to each other. If d is large, the parameter values at these two points may not be correlated. The variogram or semivariance is defined in terms of the average of squared difference of the parameter values.

$$\gamma_z(\vec{d}) = \frac{1}{2}<[z(\vec{r} + \vec{d}) - z(\vec{r})]^2>_{\vec{r}} = \frac{1}{2V}\int_V [z(\vec{r} + \vec{d}) - z(\vec{r})]^2 \, d\vec{r}. \qquad (6.16)$$

If data values are measured along a line, in an areal lattice, or in a three-dimensional grid, the volume integral in Equation 6.16 is replaced by a corresponding discrete sum. For example, if we have N samples collected at equal spacings along a line,

$$\gamma_z(I) = \frac{1}{2(N - I)} \sum_{i=1}^{N-I} [z(i) - z(i + I)]^2. \qquad (6.17)$$

The number of samples in the averaging is $N - I$ for distance of I intervals. For a finite number of measurements, the variogram is determined more accurately for a small distance with more data points included in the averaging, and less accurately for large distance approaching the data domain.

Most of the deterministic models assume that a formation or a stratigraphic unit is uniform with constant material properties. With this assumption, $\gamma_z = 0$ because the parameter z is independent of the spatial location. In this idealized limit with the parameter z fully correlated spatially, the size of grid blocks for the formation will not be limited by the spatial variability of this parameter. However, we know that the parameter has spatial variability because its distribution is not a delta function and its standard deviation is not zero. We can generalize the notion of uniformity to the notion of statistical stationarity which assumes that the mean value of the parameter, instead of parameter itself, is independent of the spatial coordinate. With stationary parameters,

$$
\begin{aligned}
\gamma_z(\vec{d}) &= \frac{1}{2}\langle [z(\vec{r}+\vec{d}) - m_z - z(\vec{r}) + m_z]^2 \rangle_{\vec{r}} \\
&= \frac{1}{2}\langle [z(\vec{r}+\vec{d}) - m_z]^2 \rangle_{\vec{r}} + \frac{1}{2}\langle [z(\vec{r}) - m_z]^2 \rangle \\
&\quad - \langle [z(\vec{r}+\vec{d}) - m_z][z(\vec{r}) - m_z] \rangle_{\vec{r}} \\
&= \sigma_z^2 - \langle [z(\vec{r}+\vec{d}) - m_z][z(\vec{r}) - m_z] \rangle_{\vec{r}}.
\end{aligned}
\tag{6.18}
$$

If the separation is larger than a correlation length so that data values are essentially uncorrelated, the cross-term average in Equation 6.18 is zero and γ_z approaches σ_z^2 asymptotically. In a simple Monte Carlo simulation with randomly distributed parameters, the correlation length a defines the block size. The value of a parameter for a given grid block is selected randomly with a specified distribution function and is independent of the values of the neighboring blocks. This is equivalent to the assumption that $\gamma_z(d) = 0$ for $d \leq a$ and $\gamma_z(d) = \sigma_z^2$ for $d > a$. This simple step change model can be replaced by more smooth and continuous variogram models.

The variogram models can be empirical or theoretical, based on geometrical or physical considerations. We first summarize the well-known models before we discuss and compare these models with a model based on fractal geometry. The linear model

$$
\gamma_z(d) = \begin{cases} \sigma_z^2 \dfrac{d}{a} & \text{if } d \leq a \\ \sigma_z^2 & \text{if } d > a \end{cases},
\tag{6.19}
$$

and the exponential model

$$
\gamma_z(d) = \sigma_z^2 \left[1 - exp\left(-\frac{d}{a}\right) \right],
\tag{6.20}
$$

are two empirical models used to fit measured values. The spherical model

$$\gamma_z(d) = \begin{cases} \sigma_z^2\left[\frac{3d}{2a} - \frac{1d^3}{2a^3}\right] & \text{if } d \le a \\ \sigma_z^2 & \text{if } d > a \end{cases} \tag{6.21}$$

is based on simple geometrical consideration. The volume of the intersection of two spheres of diameter a, volume V, the centers of which are d apart, is

$$V\left[1 - \frac{3d}{2a} + \frac{1d^3}{2a^3}\right] \tag{6.22}$$

if $d < a$ and 0 otherwise. The spherical model is widely used in geostatistical analyses, especially for ore deposits where grades become independent of each other once the range, a, is reached (David, 1977). From consideration of the area of the intersection of two circles of diameter a, the centers of which are d apart, we have a circular model

$$\gamma_z(d) = \begin{cases} \sigma_z^2\left[\frac{2}{\pi}\frac{d}{a}\left[1 - \left[\frac{d}{a}\right]^2\right]^{1/2} + \frac{2}{\pi}\sin^{-1}\left[\frac{d}{a}\right]\right] & \text{if } d \le a \\ \sigma_z^2 & \text{if } d > a \end{cases} \tag{6.23}$$

In Figure 6-53, we compare these variogram models. The distance of separation d is normalized to a d_s so that the leading d terms all have the same coefficient [$d_s = a$ for linear and exponential models, $d_s = (2/3)a$ for spherical model, and $d_s = (\pi/4)a$ for circular model]. All four models are proportional to d near $d = 0$:

$$\gamma_z(d) \approx \sigma_z^2\left[\frac{d}{d_s}\right]. \tag{6.24}$$

A more general class of models, based on consideration of fractal geometry (Mandelbrot, 1983), have the following limiting behavior (Berry and Lewis, 1980; Wang et al., 1988b):

$$\gamma_z(d) \approx \sigma_z^2\left[\frac{d}{d_s}\right]^{6 - 2D} \tag{6.25}$$

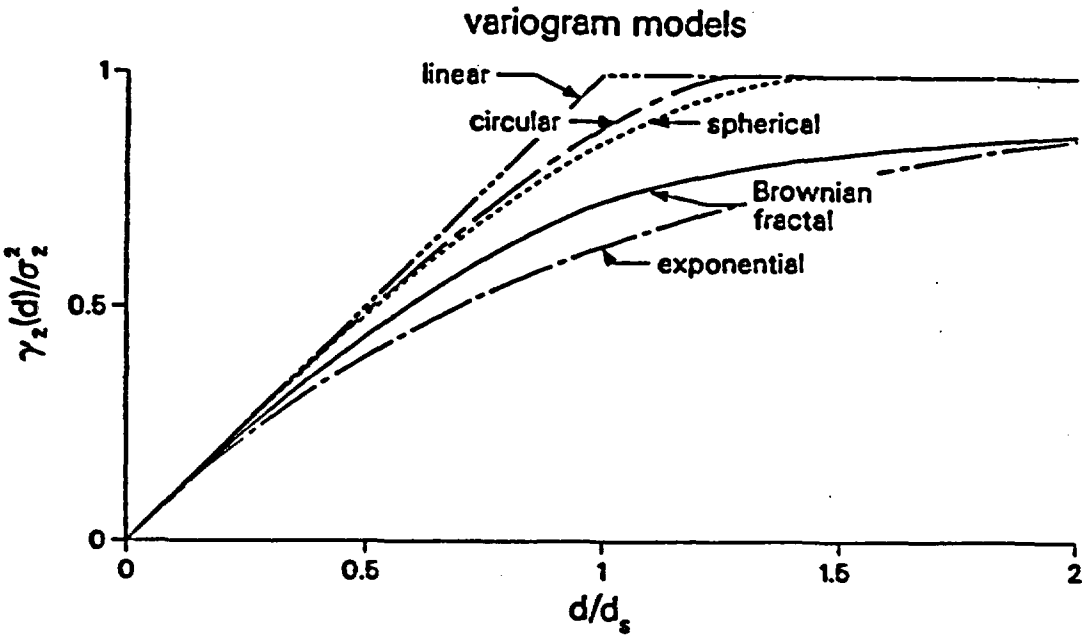

Figure 6-53. Comparison of Empirical and Simple Geometrical Variogram Models with Brownian Fractal (D = 2.5) Variogram.

in the vicinity of $d = 0$. D is a fractal dimension parameter. Wang et al. (1988b) derived a closed form variogram function for the aperture with a fractal fracture model:

$$\gamma_z(d) = \sigma_z^2 \left[1 + \left[\frac{d}{d_s} \right]^{6-2D} - \left[\frac{d_>}{d_s} \right]^{6-2D} F\left[D-3, D-3, 1; \frac{d_<^2}{d_>^2} \right] \right] \qquad (6.26)$$

where $d_< = d$ and $d_> = d_s$ if $d < d_s$; $d_< = d_s$ and $d_> = d$ if $d > d_s$. The hypergeometric function, F, can be easily evaluated by its series representation (Gradshteyn and Ryzhik, 1965). In the fractal fracture model, d_s is the shear displacement between two mirror-image fractal surfaces. A rough surface is characterized by the fractal dimension D between 2 and 3, with lower D for smoother surfaces and higher D for rougher surfaces. The mismatch caused by shear displacement determines the fracture aperture distribution. The aperture variograms Equation 6.26 of the fractal fracture model are illustrated in Figure 6-54. For a fractal fracture with low D close to 2, the fracture surfaces are smooth, and the aperture is nearly constant spatially. The variogram, a measure of the average aperture difference between neighboring points, is nearly zero over a range much larger than the shear displacement. For a fractal fracture with higher D, the aperture variation is more pronounced, and the neighboring apertures are less correlated. In the case with D close to 3, the surfaces are rough and the aperture at a given point in the fracture is almost completely uncorrelated with its neighboring points. Figure 6-54 shows that the variogram curves are concave for smooth fractures with $D < 2.5$ and are convex for rough fractures with $D > 2.5$. The Brownian fractal curve with $D = 2.5$ is the special case with $6 - 2D = 1$ and is compared with other empirical and simple geometry models in Figure 6-53. Wang et al. (1988b) proposed the use of log-log type curve analyses to deduce fractal dimension from variogram data. The limiting behavior of Equation 6.25 is equivalent to

$$\left[\frac{\partial \log \gamma_z(d)}{\partial \log (d)} \right]_{d \to 0} = 6 - 2D. \qquad (6.27)$$

In log-log plots, the fractal dimension can be determined even if we do not know the magnitudes of both the shear displacement d_s and the aperture variance σ_z^2. Different values of these two normalization constants will only shift the position of a variogram curve and will not change its slope. The log-log plot, Figure 6-55, can be used in a type curve fitting procedure with the theoretical plot overlaying on the experimental log-log variogram plot at the same scale, keeping the axes of both plots parallel, to determine the slope. The log-log variogram analyses highlight the small separation range. As we have discussed in Equation 6.17, the variogram value for large separation may have a large error associated with it when the number of data points is finite and only a few pair values are used in the variogram calculations for spatial separation approaching the data domain. In log-log plots, we will emphasize the range of small spatial separations where more pair values are used in determining the variogram values. Therefore log-log variogram plots should be added to supplement the linear plots frequently used in geostatisical analyses so that the spatial correlation and fractal structures of geological media can be elucidated.

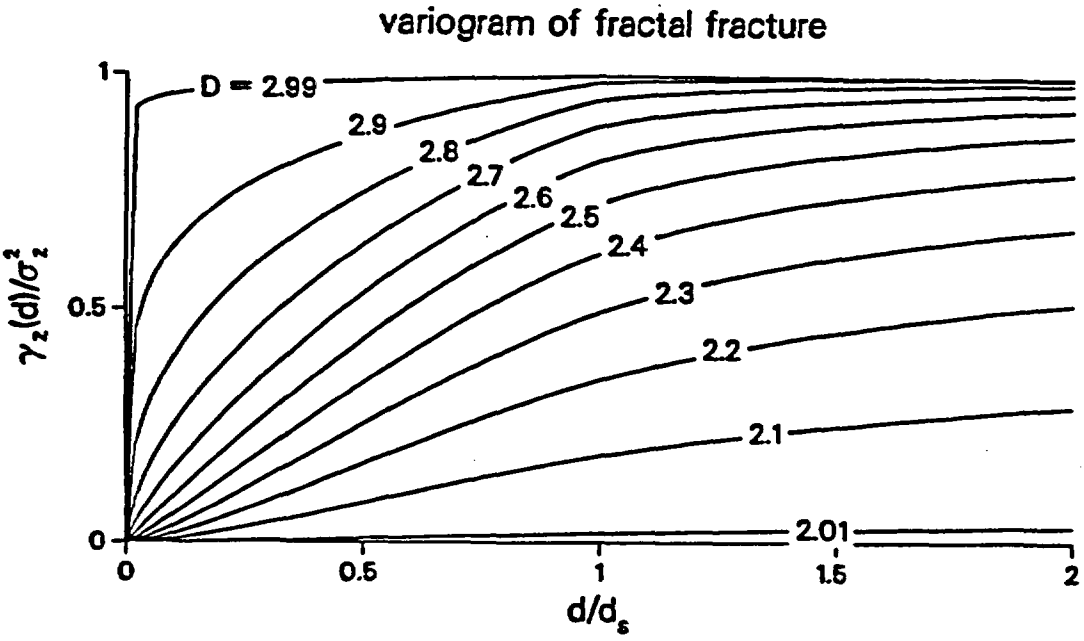

Figure 6-54. Aperture Variograms of Fractal Fracture Model.

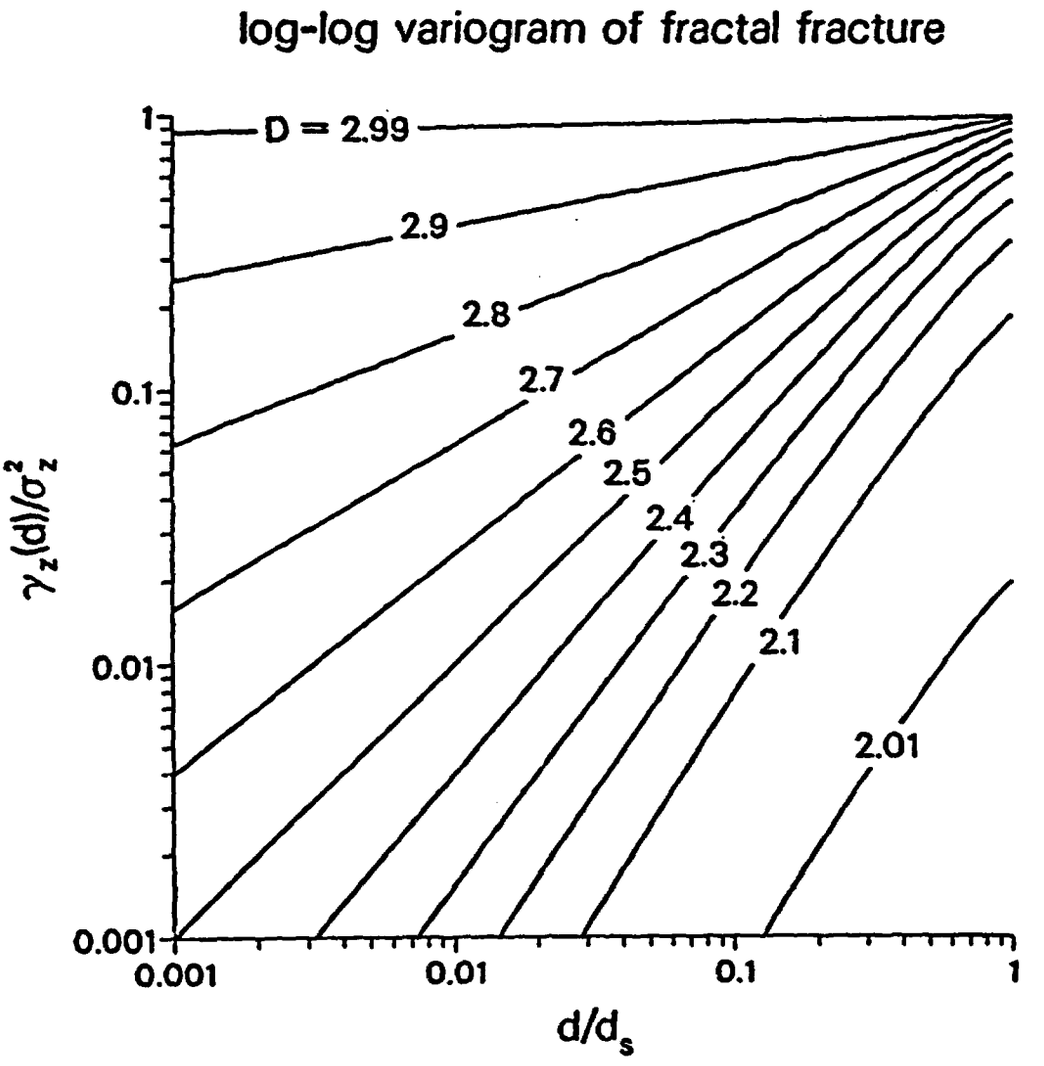

Figure 6-55. Log-log Type Curves of Fractal Fracture Variograms.

The spherical model has been used by Rautman (1987) to analyze porosity and air permeability data for tuff units. The horizontal correlation length from field samples collected along the outcrop of a stratigraphic unit was estimated to be a few thousand feet. The vertical correlation length from core samples within a unit was estimated to be one order of magnitude shorter. Similar anisotropy in correlation length was observed in a field study in a shallow trench in unsaturated soil (Nicholson et al., 1987; Wierenga et al., 1986). The horizontal and vertical correlation lengths were determined to be 2 *m* and 0.2 *m*, respectively. The exponential variogram was used to fit the ln K_s data which were obtained by Guelph permeameter measurements on a 15-*m*-wide, 6-*m*-deep trench face. It is not clear whether the difference in the magnitude of correlation lengths between the large tuff field sampling and the small soil field study originated from the difference in heterogeneity of the media or from the difference in scale of the studies. For the watershed data sets and the tuff matrix data set presented in the previous sections, we tried to calculate the variograms for the unsaturated and saturated properties and found out that these data sets did not have enough spatial resolution to yield meaningful results.

A very useful and interesting aspect of the fractal is its scaling behavior. A rough profile measured with a low-resolution measuring device over a large distance may be geometrically similar to the profile measured with a high-resolution device over a much smaller scale on the same rock sample. If this scaling property can indeed be demonstrated, we can deduce structural information at small scales by measurements at large scales, and vice versa. The fractal dimension *D* can be regarded as a scaling parameter. Figure 6-56 illustrates the steps in a recursive subdivision algorithm (Fournier et al., 1982; Brown, 1987) to generate a fractal surface. The procedure starts with a 3 by 3 mesh with zero *z* values on the mesh points to define a reference flat surface. In the second level with a 5 by 5 mesh, the *z* value of a new point is computed by a Gaussian random variable function, with the expected value determined by its four known neighbors (two on the boundaries) of the 3 by 3 mesh, and the standard deviation scaled by the fractal dimension *D* and distance to the neighbors. We can continue the generation procedure level by level to finer mesh. The standard deviation for a surface with low *D* will scale down faster than one with a high *D* as one proceeds from one level to another level to fill the mesh. Figure 6-57 compares the roughness surfaces generated with different *D* in scaling following the same sequence of random variables.

We can use a similar procedure to generate representations of heterogeneous media with spatially varying and correlated parameters. We simply replace the elevations by the property values and the Gaussian distribution by the parameter distribution. If data values are known at a given number of locations, we can start with these locations as the first-level mesh points and generate refinements in accordance to the parameter distribution and spatial correlation structure. The heterogeneous field generated by this procedure will take into account the spatial correlation because the mean value at a mesh point is determined by the values of its neighbors. Because the generation of each subdomain uses the same procedure as that used for the larger domain, domains of different sizes are sealed. We can have a low-level or low-resolution mesh to first model the field approximately and continue upgrading the results with meshes of higher-level refinements.

If a heterogeneous field is generated with parameter distribution, correlation, and scaling properly taken into account, we can then solve flow equations to obtain the distributions of pressure, flux, and velocity fields. In addition to the conceptually simple, computationally

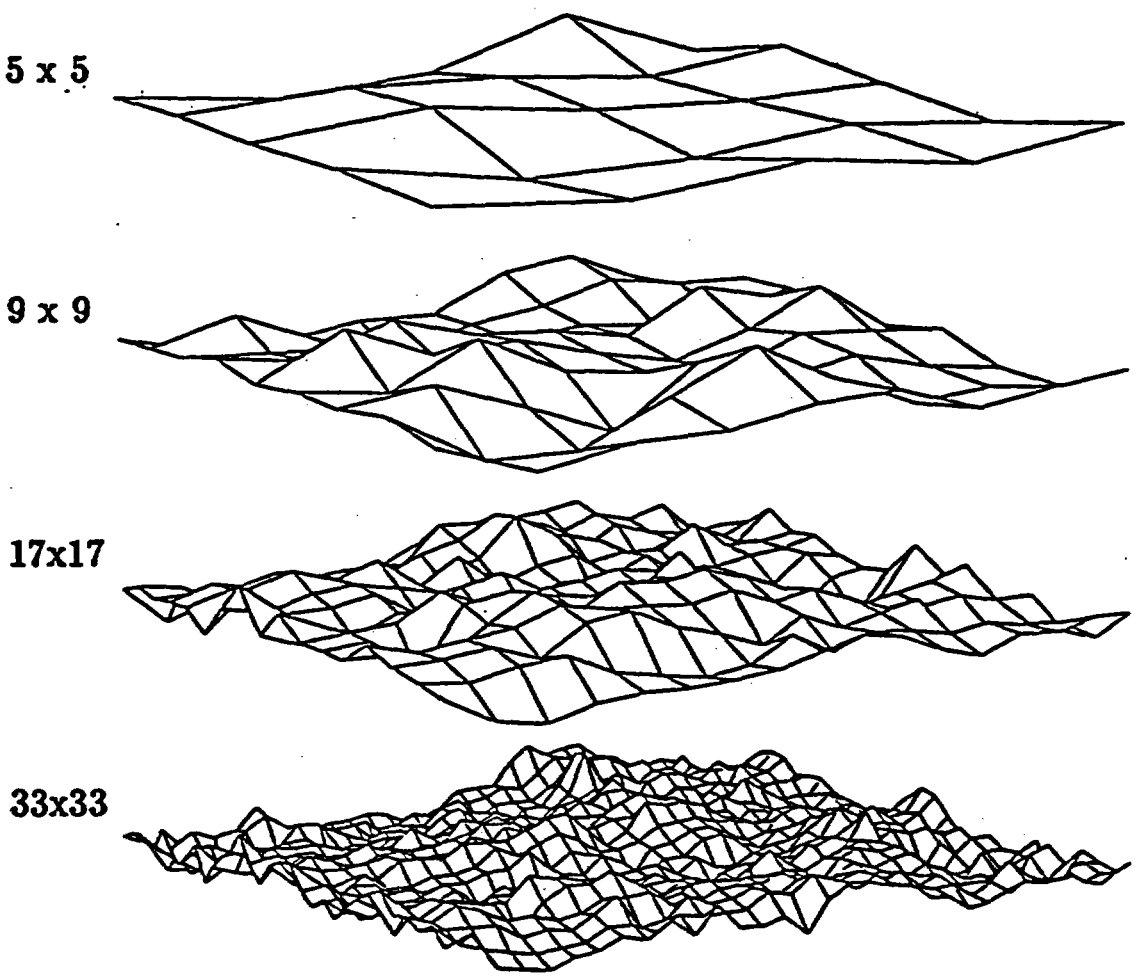

Figure 6-56. Generation of a Fractal Surface with Recursive Subdivision and Scaled Displacement Algorithm.

Fractal Surface to Represent Fracture Surface

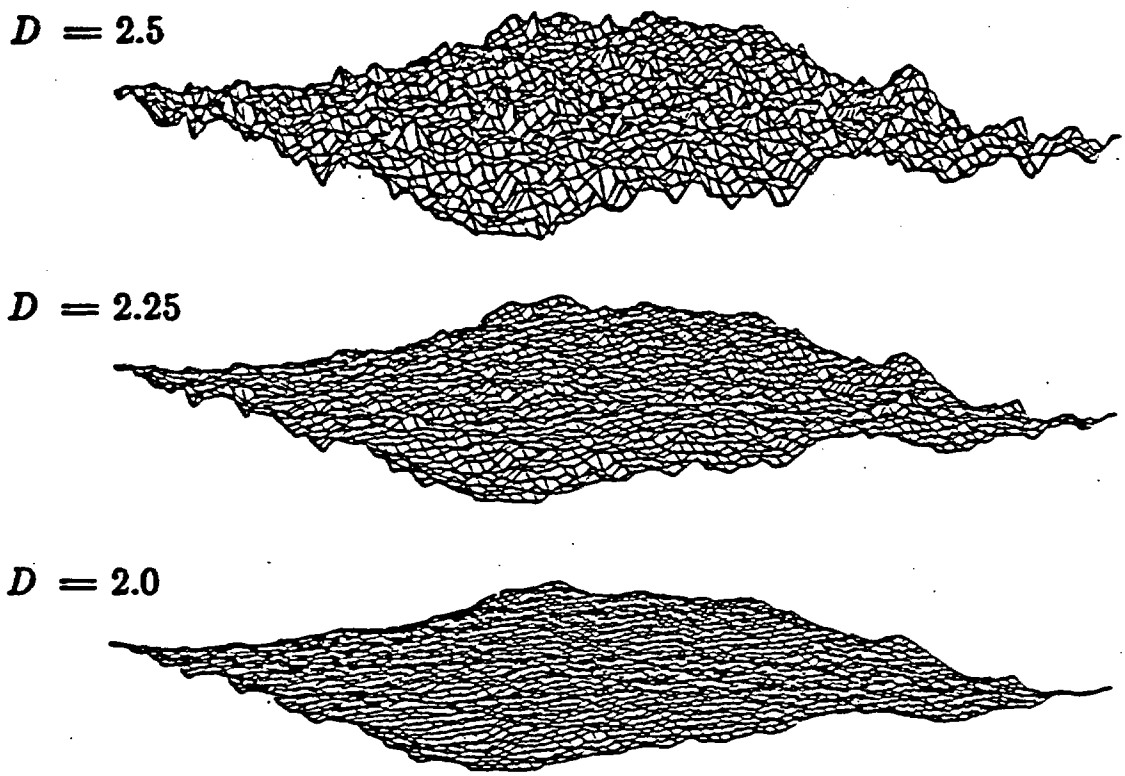

Figure 6-57. Comparison of Fractal Surfaces with Different Fractal Dimensions.

intensive, Monte Carlo simulation approach, various stochastic modeling approaches are being developed to relate the distributions in flow variables to the distributions in input parameters. Gelhar (1986) and Dagan (1986) reviewed the stochastic approaches to determine the statistical moments of space-averaged variables, given the statistical structure of spatially variable properties. The stochastic modeling predictions are being tested in field experiments. For example, the field experiment of NRC and New Mexico State University (Nicholson et al., 1987; Wierenga et al., 1986) is aimed to test if enhancement of lateral spreading, as predicted by spectral perturbation theory, is observed in the infiltration front advancement. In layered systems with pronounced parameter variability in the vertical direction and long correlation length in the horizontal direction, effective conductivity in the horizontal direction may be larger than in the vertical direction. However, the gravity driving force in the infiltration process is vertical. The preliminary results in the infiltration experiment showed the observed shape of the infiltration front did not have the degree of lateral enhancement predicted by stochastic theory. Some of these discrepancies between theory and experiment will undoubtedly induce more intensive research in stochastic modeling and statistical analyses so that models can be properly validated for performance assessment of flow processes in heterogeneous formations.

7.0 SUMMARY

To quantify flow and transport processes and to evaluate groundwater and solute travel times through heterogeneous formations, we need to understand the driving mechanisms, develop accurate and efficient computational models, and determine the distribution and correlation of material parameters. This report discusses the conceptual models and mathematical equations and analyzes the distributions and correlations among hydrological parameters of tuff and soils. We also introduce a new path integration approach and outline a fractal scaling procedure to model heterogeneous media.

7.1 Conceptual Models

The usefulness and potential limitations of porous medium, capillary tube, fracture network, and fractured, porous medium models in partially saturated studies are discussed:

- Porous medium models are simple and useful if macroscopic averages are well-defined for variables and parameters. Permeability values may vary over six orders of magnitude in cores from the same stratigraphic unit. Effective porosity cannot be easily determined and its dependence on saturation needs to be assessed.

- Capillary tube models are useful for deducing functional relationships among parameters and variables, such as the saturation-pressure and permeability-pressure relationships. Simple parallel capillary bundle models need to be modified to account for variable-radius, resistor-in-series and flow path tortuosity effects. The adequacy and usefulness of pore-size distribution information deduced from the saturation-pressure relationship needs further study, especially for tuff matrix and other consolidated media with low permeability and high porosity.

- Fracture network analyses are important for saturated flow studies. Under partially saturated conditions, the fracture network will be easily drained if the fractures have large apertures and good connectivity. Fracture aperture determinations are difficult since the contacts between fracture walls under stress, the scale dependence, and the nonuniform channel flow field, among other factors, all can change the fracture flow significantly.

- Fractured, porous medium models can account for the transition from fracture-dominated flow under saturated conditions to matrix-dominated flow under partially saturated conditions. Traditional double porosity models, with fractures controlling transport and matrix controlling storage, need to be modified to allow flow from one matrix block, across the fracture asperity contact areas, to the next matrix block. The change of the role played by fractures, as active main conduits for flow in saturated conditions to become passive dry pores in unsaturated conditions, needs to be substantiated in tuff studies. Similar observations in soils with macropores are interesting and encouraging.

7.2 Mathematical Equations

Basic equation structure for liquid flow, two-phase flow, heat transfer, solute transport, and rock deformation processes are reviewed:

- Liquid flow is governed by mass balance law, together with Darcy's flow law with saturation-dependent permeability. Instead of traditional partial differential equations, we can use integral equations for the mass balance and flux laws which are more natural for describing macroscopic processes in finite domains. The integral representation of the equation of motion along a flow stream tube forms the basis of a potentially more efficient and accurate path integration approach to solve for a heterogeneous flow field.

- Two-phase flow with convective and diffusive gas movements is important around hot waste containers and at ground surface with vigorous evaporation-transpiration processes. Depending on whether finite liquid mobility can be maintained along fracture walls, the container environment can either be maintained at two-phase conditions with temperature constrained near 100°C or will dry up with temperature reaching much higher values. Fast gas movements driven by repository heat, geothermal gradient, topographic relief, barometric pumping, and other mechanisms are also important for volatile radionuclide transport, remote sensing, and determination of saturation distributions and fluid movements through the unsaturated units.

- Heat transfer driven by conductive and convective mechanisms is governed by energy conservation law. Fluid flow and heat transfer can be strongly coupled through convection, phase change, and thermal conductivity-saturation dependence. The heat pipe effect with cyclic evaporation-condensation and gas-liquid counter current can enhance the heat transfer efficiency and change the flow field.

- Solute transport and its coupling to fluid flow are important in unsaturated soils. The solute dispersion coefficient depends on the flow velocity and is greatly influenced by the scale and heterogeneity of the medium. Under partially saturated conditions, diffusion into the matrix and filtration of ions because of electrochemical mechanisms may be important. Fracture infill materials may contain useful information concerning the movement of water, with clean surfaces inferring dry conditions and secondary mineral coatings indicating fluid transport.

- Rock deformation is governed by force balance law and elastic or inelastic stress and strain relationships. For a partially saturated medium, the effective stress depends on both the difference between total stress and gas pressure and the capillary pressure between liquid and gas phases. In addition to static equilibrium studies, dynamic propagation of seismic waves may be useful to detect fractured zones and fluid saturation distributions.

7.3 New Numerical Approaches

Potentially more efficient and verifiable path integration approaches are introduced and compared with traditional numerical methods:

- Path integration approaches are based on physical postulates of minimum work and mass conservation to solve flow geometry and potential distribution simultaneously. Traditional numerical methods focus on spatial resolution of potential distribution and derive flux and flow geometry after the partial differential equation is solved.

- The postulate of minimum work is based on consideration of energy dissipation and is shown to be equivalent to the variational principle for a steady-state flow problem in homogeneous domains. Global minimization of energy lost can be used as a self-consistent criterion for verifying the solutions with coarse meshes and not relying on comparisons with analytic solutions.

- With the minimum work postulate, isopotential configuration is progressively refined through systematic minimization procedure, using the integral form of the equation of motion to relate flux with potential drops. For systems with prescribed flow geometry, such as fracture network analyses, this minimization procedure can be easily implemented.

- The principle of mass conservation can also be used in an alternative path integration approach. Flow tube configuration is progressively adjusted to make the isopotential surfaces from different tubes continuous. Integration of the equation of motion along flow tubes can accurately take into account local material variations without global mesh refinements.

- Parallel processing, systematic minimization procedures from operation research, and contouring with equations of motion, in addition to linear programming, are some of the computational techniques expected to be useful to implement the path integration approaches and increase the efficiency. With efficient algorithms, Monte Carlo simulations can then be carried out for a large number of statistical realizations of a heterogeneous field.

7.4 Hydrological Parameters

Models of saturation characteristic curves and relative permeability functions for soils and fractures are summarized and compared:

- Models of Brooks and Corey and of van Genuchten for saturation characteristic curves are different in the small suction region near saturation and asymptotically approach the same power function at large suction. The air entry scaling factor, the pore-size distribution index, and the residual saturation parameter from these two models are consistent with each other. An air entry pore radius can be defined from the air entry

scaling factor using the capillary equation to represent the largest radius in a medium that is most easily drained in a desaturation process.

- Parallel capillary bundle models were modified by Burdine, Mualem, Alexander, and others to account for tortuosity and resistance-in-series effects. Limited relative permeability data do not differentiate among the models. Alexander showed that errors over five orders of magnitude could be generated by some predictive models, especially for low permeability values in dry soils.

- In addition to saturation and relative permeability, a characteristic curve for the effective fracture-matrix flow area is needed to model the transition from saturated flow along fractures to unsaturated flow through matrix blocks separated by dry fractures. A phase constriction factor is also needed for fracture permeability to take into account the change of liquid phase from continuous configuration to discontinuous configuration during fracture desaturation (Wang and Narasimhan, 1985).

- Most fracture models predict that fracture permeability will change from high saturated values to low unsaturated values which are less than the matrix values. This crossover between fracture permeability and matrix permeability is the key to sustain the conceptual model that assumes that matrix flow dominates under ambient conditions with large suction pressure associated with partially saturated state. We need data for fracture aperture distributions to check if fracture roughness is fractal or periodic; theoretical and experimental studies to quantify phase constriction, tortuosity, and spatial distribution effects; and fracture characteristic measurements to check and improve models.

7.5 Statistical Analyses

Distributions and correlations among hydrological parameters of soils and tuff matrix are analyzed and spatial correlation and scaling are discussed:

- Average air entry scaling factor is two to three orders of magnitude larger for watershed soils than for the tuff matrix. Average saturated permeability is five to seven orders of magnitude larger for watershed soils than for the welded/zeolitized tuff matrix. From this observation on the large differences between soil and tuff, we propose that the saturated permeability is proportional to the square of air entry radius, similar to Poiseuille's law for the circular tube and Boussinesq's law for the parallel plate. This correlation between a saturated parameter and an unsaturated parameter is substantiated by the Brooks and Corey data, but not by the nonwelded tuff matrix data.

- The tuff matrix data set from highly heterogeneous nonwelded units has narrow distribution in air entry radius and wide distribution in saturated permeability. Some of the saturated permeability values of nonwelded tuff are larger than the Poiseuille's permeability with air entry radius. The Poiseuille' permeability with air entry radius can be shown to be the maximum limit from capillary tube model derivations. Some

of the model parameters for saturated permeability used to represent faults in regional models are also greater than the maximum limit.

- For stochastic modelings of alternating units of welded and nonwelded tuff or formation blocks bounded by fault zones, we propose to impose correlations and constraints on average values of saturated permeability and air entry scaling factor between highly different units to avoid unlikely combinations of parameters and predictions. Within a given stratigraphic unit, this physically meaningful correlation is likely to be masked by data variability and uncorrelated parameters with wide distributions may be acceptable.

- Correlations between air entry scaling factor and pore-size distribution index, between residual saturation and pore-size distribution index, and between residual saturation and porosity are in general less well established among different media or not evident at all from available data. The frequently studied correlation between saturated permeability and porosity is marginally supported by the data from different media The scatter of saturated permeability data and the relatively narrow range of porosity values among different geological media make the substantiation of this correlation difficult.

- From the watershed soil data and tuff matrix data analyses, air entry scaling factor, pore-size distribution index, and saturated permeability are closer to lognormal distribution than normal distribution. Porosity has a slightly skewed normal distribution. Deviations from the lognormal or normal distributions can be quantified by the higher moment coefficients: skewness and kurtosis. More data points are needed to get meaningful skewness and kurtosis coefficients for porosity than for log saturated permeability.

- Available tuff data sets, especially for nonwelded tuff, do not have enough data points to determine the higher moment skewness and kurtosis coefficients for unsaturated and saturated parameters. More data are needed to determine these coefficients so that four parameter distribution functions, such as the beta distribution, can be used to specify the parameter distributions.

- USDA watershed soil data and SNL tuff matrix data analyzed in this report do not have enough spatial resolutions to yield meaningful variogram analyses for spatial correlation. Other soil field experiment and tuff field sampling indicated that the horizontal correlation length was longer than the vertical correlation length. The enhancement of lateral spreading of the infiltration front from this anisotropic spatial correlation structure was not clearly demonstrated by the field experiments.

- Scaling of geometrical and hydrological parameters from laboratory scale to field scale can be handled by fractal analyses. Fractal variogram models are more general than empirical and simple geometrical variogram models. Log-log type curve analyses can be used to elucidate spatial correlation and fractal structures of geological media. We can generalize a recursive subdivision algorithm with fractal dimension as a scaling parameter to generate statistical realizations for a heterogeneous field, taking into

account parameter distribution, correlation, and scaling properties. Monte Carlo simulations, with a fractal scaled field, and with an efficient path integration approach, can be used to quantify uncertainties and generate the cumulative distribution function for groundwater travel times.

8.0 REFERENCES

Abelin, H., I. Neretnieks, S. Tunbrant, and L. Moreno, "Final Report of the Migration in a Single Fracture - Experimental Results and Evaluation", Stripa Project Technical Report 85-3, Swedish Nuclear Fuel and Waste Management Co., Stockholm, Sweden, 162 pp., 1985. (NNA.890524.0180)

Alexander, L., "Predicting Steady Upward Flux from the Water Table", MS Thesis, Dept. Biological and Agricultural Eng., North Carolina State Univ., Raleigh, NC, 208 pp., 1984. (NNA.900720.0040)

Alexander, L., and R. W. Skaggs, "Predicting Unsaturated Hydraulic Conductivity from Soil Texture", *J. Irrigation and Drainage Eng., Am. Soc. Civ. Eng.*, 113(2), pp. 184-197, 1987. (NNA.890522.0224)

Arya, L. M., and J. F. Paris, "A Physicoempirical Model to Predict the Soil Moisture Characteristic from Particle-Size Distribution and Bulk Density Data", *Soil Sci. Soc. Am. J.*, 45(6), pp. 1023-1030, 1981. (NNA.890522.0258)

Banerjee, M., and K. K. Watson, "Numerical Analysis of Soil Water Movement Under Conditions of Rapid Intermittency of Water Application", *Water Resour. Res.*, 20(1), pp. 119-125, 1984. (NNA.910108.0002)

Barenblatt, G. I., I. P. Zheltov, and I. N. Kochina, "Basic Concepts in the Theory of Seepage of Homogeneous Liquids in Fissured Rocks (Strata)", English Translation, *J. Applied Mathematics and Mechanics*, 24(5), pp. 852-864, 1960. (NNA.870728.0027)

Bear, J., *Dynamics of Fluids in Porous Media*, Dover Publications, Inc., New York, NY, 1988. (NNA.890713.0163)

Berry, M. V., and Z. V. Lewis, "On the Weierstrass-Mandelbrot Fractal Function", *Proc. Royal Soc. London*, A 370, pp. 459-484, 1980. (NNA.891109.0124)

Beven, K., and P. Germann, "Macropores and Water Flow in Soils", *Water Resour. Res.*, 18(5), pp. 1311-1325, 1982. (NNA.890327.0050)

Bianchi, L., and D. T. Snow, "Permeability of Crystalline Rock Interpreted from Measured Orientations and Apertures of Fractures", *Annals of Arid Zone*, 8, pp. 231-245, 1969. (NNA.891106.0196)

Biot, M. A., "General Theory of Three-Dimensional Consolidation", *J. Appl. Phys.*, 12, pp. 155-164, 1941. (NNA.911021.0033)

Bishop, A. W., "The Principle of Effective Stress", *Teknik, Ukelbad*, Norway, 39, pp. 859-863, 1959. (NNA.900720.0061)

Bixler, N. E., "NORIA-A Finite Element Computer Program for Analyzing Water, Vapor, Air, and Energy Transport in Porous Media", SAND84-2057, Sandia National Laboratories, Albuquerque, NM, 1985. (NNA.870721.0002)

Bloemen, G. W., "Calculation of Hydraulic Conductivities of Soils from Texture and Organic Matter Content", *Z. Pflanzenernaehr, Bodenkd.*, 143, pp. 581-605, 1980. (NNA.890522.0277)

Brooks, R. H., and A. T. Corey, "Hydraulic Properties of Porous Media", Hydrol. Paper 3, Civ. Eng. Dept., Colorado State Univ., Fort Collins, CO, 27 pp., 1964. (HQS.880517.1737)

Brooks, R. H., and A. T. Corey, "Properties of Porous Media Affecting Fluid Flow", *J. Irrigation and Drainage Div., Proc. Am. Soc. Civ. Eng.*, 92, IR2, pp. 61-88, 1966. (NNA.870407.0356)

Brown, S. R., "Fluid Flow Through Rock Joints: the Effect of Surface Roughness", *J. Geophys. Res.*, 92, pp. 1337-1347, 1987. (NNA.891106.0181)

Brown, S. R., and C. H. Scholz, "Broad Bandwidth Study of the Topography of Natural Rock Surfaces", *J. Geophys. Res.*, 90, pp. 12575-12582, 1985. (NNA.891106.0182)

Brutsaert, W., "Probability Laws for Pore-Size Distributions", *Soil Science*, 101(2), pp. 85-92, 1966. (NNA.890522.0227)

Brutsaert, W., "Some Methods of Calculating Unsaturated Permeability", *Trans. Am. Soc. Agric. Eng.*, 10(3), pp. 400-404, 1967. (NNA.890522.0279)

Burdine, N. T., "Relative Permeability Calculations from Pore Size Distribution Data", *Pet. Trans., Am. Inst. Min. Eng.*, 198, pp. 71-78, 1953. (NNA.890522.0241)

Burdine, N. T., L. S. Gournay, and P. P. Reichertz, "Pore Size Distribution of Petroleum Reservoir Rocks", T. P. 2893, *Pet. Trans., Am. Inst. Min. Eng.*, 189, pp. 195-204, 1950. (NNA.890522.0242)

Campbell, G. S., "A Simple Method for Determining Unsaturated Hydraulic Conductivity from Moisture Retention Data", *Soil Science*, 117(6), pp. 311-314, 1974. (NNA.890522.0243)

Carman, P. C., "Fluid Flow Through Granular Beds", *Trans. Institution of Chem. Eng.*, London, England, 15, pp. 150-166, 1937. (NNA.890522.0280)

Case, C., M. Kautsky, P. Kearl, R. Goldfarb, S. Leatham, and L. Metcalf, "Unsaturated Flow Properties Data Catalog, Volume I", DOE/NV/10162-12, Desert Research Institute, University of Nevada, Reno, NV, 457 pp., 1983. (NNA.890327.0065)

Childs, E. C, and N. Collis-George, "The Permeability of Porous Materials", *Proc. Roy. Soc. London*, Ser. A, 201, pp. 392-405, 1950. (NNA.890522.0244)

Clapp, R. B., and G. M. Hornberger, "Empirical Equations for Some Soil Hydraulic Properties", *Water Resour. Res.*, 14, pp. 601-604, 1978. (NNA.890327.0048)

Coats, K. H., "Geothermal Reservoir Modelling", SPE 6892, presented at 52nd Annual Fall Technical Conference and Exhibition, *Soc. Pet. Eng., Am. Inst. Min. Eng.*, Denver, CO, 33 pp., Oct., 1977. (NNA.890327.0068)

Codell, R., "Draft Generic Technical Position on Ground Water Travel Time (GWTT)", U.S. Nuclear Regulatory Commission, Washington, DC, 30 pp., 1986. (NNA.870409.0282)

Cosby, B. J., G. M. Hornberger, R. B. Clapp, and T. R. Ginn, "A Statistical Exploration of the Relationships of Soil Moisture Characteristics to the Physical Properties of Soils", *Water Resour. Res.*, 20(6), pp. 682-690, 1984. (NNA.890522.0259)

Cramer, H., *Mathematical Methods of Statistics*, Princeton Univ. Press, Princeton, NJ, 575 pp., 1946. (NNA.891106.0199)

Dagan, G., "Statistical Theory of Groundwater Flow and Transport: Pore to Laboratory, Laboratory to Formation, and Formation to Regional Scale", *Water Resour. Res.*, 22(9), pp. 120S-134S, 1986. (NNA.891107.0098)

David, M., *Geostatistical Ore Reserve Estimation*, Elsevier Scientific Publishing Co., New York, NY, 364 pp., 1977. (NNA.891222.0026)

Duguid, J. Q., and P. C. Y. Lee, "Flow in Fractured Porous Media", *Water Resour. Res.*, 13(3), pp. 558-566, 1977. (NNA.890522.0262)

Eaton, R. R, D. K. Gartling, and D. E. Larson, "SAGUARO-A Finite Element Computer Program for Partially Saturated Porous Flow Problems", SAND82-2772, Sandia National Laboratories, Albuquerque, NM, 1983. (NN1.881007.0040)

El-Kadi, A. I, "On Estimating the Hydraulic Properties of Soil, Part 1. Comparison Between Forms to Estimate the Soil-Water Characteristic Function", *Adv. Water Resour.*, 8, pp. 136-147, 1985. (NNA.890327.0039)

Enderby, J. A., "The Domain Model of Hysteresis, Part 1.-Independent Domains", *Trans. Faraday Soc.*, 51, pp. 835-848, 1955. (NNA.911024.0078)

Engelder, T., and C. H. Scholz, "Fluid Flow Along Very Smooth Joints at Effective Pressures Up to 200 Megapascals", in *Mechanical Behavior of Crustal Rocks*, edited by N. L. Carter, M. Friedman, J. M. Logan, and D. W. Stearns, Am. Geophys. Union Monograph 24, pp. 147-152, 1981. (NNA.911108.0002)

Evans, D. D., and C. H. Huang, "Role of Desaturation on Transport Through Fractured Rock", in *Role of the Unsaturated Zone in Radioactive and Hazardous Waste Disposal*, edited by J. Mercer, P. S. Rao, and I. W. Marine, Ann Arbor Science Publisher, Ann Arbor, MI, pp. 165-178, 1982. (NNA.890523.0058)

Everett, D. H., "A General Approach to Hysteresis, Part 4. An Alternative Formulation of the Domain Model", *Trans. Faraday Soc.*, 51, pp. 1551-1557,1955. (NNA.911024.0079)

Fatt, I., "The Network Model of Porous Media, 1, 2, 3", *Trans. Am. Inst. Min. Eng.*, 207, pp. 144-181, 1956. (NNA.890707.0060)

Fatt, I., and H. Dykstra, "Relative Permeability Studies", *Pet. Trans., Am. Inst. Min. Eng.*, 192, pp. 249-256, 1951. (NNA.890522.0245)

Faust, C. R., and J. W. Mercer, "Geothermal Reservoir Simulation, 2. Numerical Solution Techniques for Liquid- and Vapor-Dominated Hydrothermal Systems", *Water Resour. Res.*, 15(1), pp. 31-46, 1979. (NNA.890327.0049)

Fournier, A., D. Fussell, and L. Carpenter, "Computer Rendering of Stochastic Models", *Comm. Asso. Computing Machinery*, 25, pp. 371-384, 1982. (NNA.891109.0129)

Gale, J. E., "A Numerical, Field and Laboratory Study of Flow in Rocks with Deformable Fractures", Ph.D. Thesis, Dept. Civil Eng., Geotechnical Eng. Group, Univ. California, Berkeley, CA, 255 pp., 1975. (NNA.900403.0025)

Gardner, W. R., D. Hillel, and Y. Benyamini, "Post-Irrigation Movement of Soil Water, I. Redistribution", *Water Resour. Res.*, 6(3), pp. 851-861, 1970. (NNA.890522.0246)

Garg, S. K., J. W. Pritchett, M. H. Rice, and T. D. Riney, "U.S. Gulf Coast Geopressured Geothermal Reservoir Simulation", SSS-R-77-3147, Systems, Science and Software, La Jolla, CA, 116 pp., 1977. (NNA.890315.0005)

Gelhar, L. W., "Stochastic Subsurface Hydrology from Theory to Applications", *Water Resour. Res.*, 22(9), pp. 135S-145S, 1986. (NNA.890523.0133)

Gentier, S., "Morphologie et Comportment Hydromecanique d'une Fracture Naturalle dans un Granite Sours Contrainte Normale", Doctoral Thesis, Univ. d'Orl'eans, France, 1986. (NNA.900919.0187)

Ghosh, R. K., "Model of the Soil-Moisture Characteristic", *J. Indian Soc. Soil Sci.*, 24, pp. 353-355, 1976. (NNA.890522.0281)

Gillham, R. W., A. Klute, and D. F. Heermann, "Hydraulic Properties of a Porous Medium: Measurement and Empirical Representation", *Soil Sci. Soc. Am. J.*, 40(2), pp. 203-207, 1976. (NNA.890522.0231)

Gradshteyn, I. S., and I. M. Ryzhik, *Table of Integrals, Series, and Products*, Academic Press, New York, 1086 pp., 1980. (NNA.910522.0047)

Hadley, G. R., "Theoretical Treatment of Evaporation Front Drying", *Int. J. Heat Mass Transfer*, 25(10), pp. 1511-1522, 1982. (NNA.890315.0016)

Hansen, M. H., W. N. Hurwitz, and W. G. Madow, *Sample Survey Methods and Theory, Volume I, Methods and Applications*, John Wiley & Sons, Inc., New York, NY, 638 pp., 1953. (NNA.890327.0072)

Harrold, P., C. C. Barton, and P. Montazer, "Statistical Analysis of Fracture Roughness Profiles in Volcanic Tuffs", Yucca Mountain, Nevada, *EOS*, 66(46), p. 883, 1985. (NNA.890315.0015)

Haverkamp, R., and J.-Y. Parlange, "Predicting the Water-Retension Curve from Particle-Size Distribution: 1. Sandy Soils Without Organic Matter", *Soil Science*, 142(6), pp. 325-339, 1986. (NNA.900122.0013)

Holtan, H. N., C. B. England, G. P. Lawless, and G. A. Schumaker, "Moisture-Tension Data for Selected Soils on Experimental Watersheds", ARS 41-144, Agricultural Research Service, U.S. Department of Agriculture, Beltsville, MD, 609 pp., 1968. (NNA.901128.0167)

Jaynes, D. B., "Comparison of Soil-Water Hysteresis Models", *J. Hydrology*, 75, pp. 287-299, 1984. (NNA.910108.0003)

Kaplan, P. G., "Modeling the Uncertainties in the Parameter Values of a Layered Variably Saturated Column of Volcanic Tuff Using the Beta Probability Distribution", in Proceedings of the Fourth International Conference of Solving Ground Water Problems with Models, National Water Well Association, Dublin, OH, pp. 111-128, 1989. (NNA.890324.0118)

King, L. G., "Description of Soil Characteristics for Partially Saturated Flow", *Soil Sci. Soc. Am. Proc.*, 29, pp. 359-362, 1966. (NNA.890713.0166)

Klavetter, E. A., and R. R. Peters, "An Evaluation of the Use of Mercury Porosimetry in Calculating Hydrologic Properties of Tuffs from Yucca Mountain, Nevada", SAND86-0286, Sandia National Laboratories, Albuquerque, NM, 1987. (NNA.890327.0056)

Klinkenberg, L. J., "The Permeability of Porous Media to Liquids and Gases", *Drilling and Production Practice*, pp. 200-213, 1941. (HQS.880517.1787)

Kool, J. B., and J. C. Parker, "Development and Evaluation of Closed-Form Expressions for Hysteretic Soil Hydraulic Properties", *Water Resour. Res.*, 23(1), pp. 105-114, 1987. (NNA.910108.0005)

Kunze, R. J., G. Uehara, and K. Graham, "Factors Important in the Calculation of Hydraulic Conductivity", *Soil Sci. Soc. Am. Proc.*, 32, pp. 760-765, 1968. (NNA.890522.0263)

Laliberte, G. E., "A Mathematical Function for Describing Capillary Pressure-Desaturation Data", *Bull. Int. Asso. Sci. Hydrol.*, 14(2), pp. 131-149, 1969. (NNA.890522.0264)

Landau, L. D., and E. M. Lifshitz, *Fluid Mechanics*, Pergamon Press, New York, NY, 536 pp., 1959. (NNA.900919.0190)

Long, J. C. S., J. S. Remer, C. R. Wilson, and P. A. Witherspoon, "Porous Media Equivalents for Networks of Discontinuous Fractures", *Water Resour. Res.*, 18(3), pp. 645-658, 1982. (NNA.870908.0026)

Makurat, A., "The Effect of Shear Displacement on the Permeability of Natural Rough Joints", Proc. Hydrogeology of Rocks of Low Permeability, Memoires 17, Int. Asso. Hydrogeologists, pp. 99-106, 1985. (NNA.911007.0050)

Mandelbrot, B. B., *The Fractal Geometry of Nature*, Wilt Freeman and Company, San Francisco, CA, 468 pp., 1983. (NNA.900123.0062)

Marshall, T. J., "A Relation Between Permeability and Size Distribution of Pores", *J. Soil Sci.*, 9(1), pp. 1-8, 1958. (NNA.890522.0265)

McCord, J. T., and D. B. Stephens, "Lateral Moisture Flow Beneath a Sandy Hillslope Without an Apparent Impeding Layer", *Hydrological Processes*, John Wiley & Sons, New York, NY, 1, pp. 225-238, 1987. (NNA.890522.0215)

McCuen, R. H., W. J. Rawls, and D. L. Brakensiek, "Statistical Analysis of the Brooks-Corey and the Green-Ampt Parameters Across Soil Textures", *Water Resour. Res.*, 17(4), pp. 1005-1013, 1981. (NNA.891109.0117)

Millington, R. J., and J. P. Quirk, "Permeability of Porous Solids", *Trans. Faraday Soc.*, 57, pp. 1200-1207, 1961. (NNA.890522.0233)

Milly, P. C. D., "Moisture and Heat Transport in Hysteretic, Inhomogeneous Porous Media: A Matric Head-Based Formulation and a Numerical Model", *Water Resour. Res.*, 18(3), pp. 489-498, 1982. (NNA.890327.0060)

Montazer, P., and W. E. Wilson, "Conceptual Hydrologic Model of Flow in the Unsaturated Zone, Yucca Mountain, Nevada", WRIR-84-4345, U.S. Geological Survey, Lakewood, CO, 55 pp., 1984. (NNA.890327.0051)

Moss, M., and G. M. Haseman, "A Proposed Model for the Thermal Conductivity of Dry and Water-Saturated Tuff", Proc. Scientific Basis for Nuclear Waste Management VII, Mat. Res. Soc. Sym. Proc., 26, pp. 967-974, 1984. (NNA.890327.0055)

Mualem, Y., "Modified Approach to Capillary Hysteresis Based on a Similarity Hypothesis", *Water Resour. Res.*, 9(5), pp. 1324-1331, 1973. (NNA.930423.0200)

Mualem, Y., "A Conceptual Model of Hysteresis," *Water Resour. Res.*, 10(3), pp. 514-520, 1974. (NNA.910506.0138)

Mualem, Y., "A Catalogue of the Hydraulic Properties of Unsaturated Soils," Research Project 442 Report, Hydrodynamics and Hydraulic Laboratory, Technion Isreal Institute of Technology, Haifa, Isreal, 100 pp., 1976a. (NNA.900702.0035)

Mualem, Y., "A New Model for Predicting the Hydraulic Conductivity of Unsaturated Porous Media", *Water Resour. Res.*, 12(3), pp. 513-522, 1976b. (NNA.890522.0250)

Mualem, Y., "Hysteretical Models for Prediction of the Hydraulic Conductivity of Unsaturated Porous Media", *Water Resour. Res.*, 12(6), pp. 1248-1254,1976c. (NNA.910506.0139)

Mualem, Y., "Extension of the Similarity Hypothesis Used for Modeling the Soil Water Characteristics", *Water Resour. Res.*, 13(4), pp. 773-780, 1977. (NNA.910506.0140)

Mualem, Y., "A Modified Dependent-Domain Theory of Hysteresis", *Soil Science*, 137(5), pp. 283-291, 1984. (NNA.910506.0141)

Mualem, Y., and G. Dagan, "A Dependent Domain Model of Capillary Hysteresis", *Water Resour. Res.*, 11(3), pp. 452-460, 1975. (NNA.910506.0142)

Mualem, Y., and H. J. Morel-Seytoux, "Analysis of a Capillary Hysteresis Model Based on a One-Variable Distribution Function", *Water Resour. Res.*, 14(4), pp. 605-610, 1978. (NNA.911021.0039)

Narasimhan, T. N., "Simulation of Consolidation in Partially Saturated Soil Materials", in Proc. Symp. Unsaturated Flow and Transport Modeling, NUREG/CP-0030, PNL-SA-10325, edited by E. M. Arnold, G. W. Gee, and R. W. Nelson, U.S. Nuclear Regulatory Commission, Washington, DC, pp. 115-158, 1982. (NNA.890818.0249)

Narasimhan, T. N., "Geometry-Imbedded Darcy's Law and Transient Subsurface Flow", *Water Resour. Res.*, 21(8), pp. 1285-1292, 1985. (NNA.890315.0008)

Narasimhan, T. N., and P. A. Witherspoon, "An Integrated Finite Difference Method for Analyzing Fluid Flow in Porous Media", *Water Resour. Res.*, 12(1), pp. 57-64, 1976. (NNA.890522.0253)

Neretnieks, I., "Transport in Fractured Rocks", Proc. Hydrogeology of Rocks of Low Permeability, Memoires 17, Int. Asso. Hydrogeologists, pp. 301-318, 1985. (NNA.900720.0078)

Nicholson, T. J., P. J. Wierenga, G. W. Gee, E. A. Jacobson, D. J. Polmann, D. B. McLaughlin, and L. W. Gelhar, "Validation of Stochastic Flow and Transport Models for Unsaturated Soils: a Comprehensive Field Study", presented at DOE/AECL '87 Conference on Geostatistical, Sensitivity and Uncertainty Methods for Ground-Water Flow and Radionuclide Transport Modeling, San Francisco, CA, 23 pp., 1987. (NNA.890327.0081)

Nielsen, D. R., M. Th. van Genuchten, and J. W. Biggar, "Water Flow and Solute Transport Processes in the Unsaturated Zone", *Water Resour. Res.*, 22(9), pp. 89S-108S, 1986. (NNA.890327.0059)

Niemi, A., and G. S. Bodvarsson, "Preliminary Capillary Hysteresis Simulations in Fractured Rocks, Yucca Mountain, Nevada", *J. Contaminant Hydrology*, 3, pp. 277-291, 1988. (NNA.911031.0013)

NRC (U.S. Nuclear Regulatory Commission), "Disposal of High-Level Radioactive Wastes in Geologic Repositories", *Code of Federal Regulations, Energy*, Title 10, Part 60, Washington, DC, 1986. (NNA.910315.0133)

Ortiz, T. S., R. L. Williams, F. B. Nimick, B. C. Whittet, and D. L. South, "A Three-Dimensional Model of Reference Thermal/Mechanical and Hydrological Stratigraphy at Yucca Mountain, Southern Nevada", SAND84-1076, Sandia National Laboratories, Albuquerque, NM, 1985. (NNA.890315.0013)

Panian, T. F., "Unsaturated Flow Properties Data Catalog, Volume II", DOE/NV/10384-20, Desert Research Institute, University of Nevada, Reno, NV, 493 pp., 1987. (NNA.890327.0061)

Parlange, J.-Y., "Capillary Hysteresis and the Relationship Between Drying and Wetting Curves", *Water Resour. Res.*, 12(3), pp. 224-228, 1976. (NNA.911021.0034)

Peters, R. R., and E. A. Klavetter, "A Continuum Model for Water Movement in an Unsaturated Fractured Rock Mass", *Water Resour. Res.*, 24(3), pp. 416-430, 1988. (NNA.890523.0139)

Peters, R. R., E. A. Klavetter, I. J. Hall, S. C. Blair, P. R. Heller, and G. W. Gee, "Fracture and Matrix Hydrologic Characteristics of Tuffaceous Materials from Yucca Mountain, Nye County, Nevada", SAND84-1471, Sandia National Laboratories, Albuquerque, NM, 188 pp., 1984. (NNA.870407.0036)

Peters, R. R., E. A. Klavetter, J. T. George, and J. H. Gauthier, "Measuring and Modeling Water Imbibition into Tuff", Proc. Symp. Flow and Transport through Unsaturated Fractured Rock, Geophysical Monograph 42, edited by D. D. Evans and T. J. Nicholson, Am. Geophys. Union, Washington, DC, pp. 99-106, 1987. (NNA.900308.0324)

Philip, J. R., "Similarity Hypothesis for Capillary Hysteresis in Porous Materials", *J. Geophys. Res.*, 69, pp. 1533-1562, 1964. (NNA.911021.0040)

Philip, J. R., and D. A. de Vries, "Moisture Movement in Porous Materials under Temperature Gradients", *EOS, Trans. Am. Geophys. Union*, 38(2), pp. 222-232, 1957. (NNA.890713.0173)

Pickens, J. F., and R. W. Gilham, "Finite Element Analysis of Solute Transport Under Hysteretic Unsaturated Flow Conditions", *Water Resour. Res.*, 16(6), pp. 1071-1078, 1980. (NNA.910506.0144)

Pollock, D. W., "Simulation of Fluid Flow and Energy Transport Processes Associated with High-Level Radioactive Waste Disposal in Unsaturated Alluvium", *Water Resour. Res.*, 22(5), pp. 765-775, 1986. (NNA.890315.0009)

Poulovassilis, A., "Hysteresis of Pore Water, an Application of the Concept of Independent Domains", *Soil Science*, 93, pp. 405-415, 1962. (NNA.910506.0145)

Poulovassilis, A., "Hysteresis of Pore Water in Granular Porous Bodies", *Soil Science*, 109, pp. 5-12, 1970. (NNA.911111.0001)

Pruess, K., "TOUGH User's Guide", NUREG/CR-4645, U.S. Nuclear Regulatory Commission, Washington, DC, SAND86-7104, Sandia National Laboratories, Albuquerque, NM, LBL-20700, Lawrence Berkeley Laboratory, Berkeley, CA, 78 pp., 1987. (NNA.890315.0010)

Pruess, K., and T. N. Narasimhan, "A Practical Method for Modeling Fluid and Heat Flow in Fractured Porous Media", *Soc. Pet. Eng. J.*, 25(1), pp. 14-26, 1985. (NNA.890522.0235)

Pruess, K., and R. C. Schroeder, "SHAFT79, User's Manual", LBL-10861, Lawrence Berkeley Laboratory, Berkeley, CA, 47 pp., 1980. (NNA.890327.0076)

Pruess, K., Y. W. Tsang, and J. S. Y. Wang, "Modeling of Strongly Heat-Driven Flow in Partially Saturated Fractured Porous Media", Proc. Hydrogeology of Rocks of Low Permeability, Memoires 17, Int. Asso. Hydrogeologists, pp. 486-497, 1985. (NNA.890522.0270)

Pruess, K., and J. S. Y. Wang, "TOUGH-A Numerical Model for Nonisothermal Unsaturated Flow to Study Waste Canister Heating Effects", Proc. Scientific Basis for Nuclear Waste Management VII, Mat. Res. Soc. Sym. Proc., Elsevier Science Publishing Co., New York, NY, 26, pp. 1031-1038, 1984. (NNA.890522.0234)

Pruess, K., and J. S. Y. Wang, "Numerical Modeling of Isothermal and Non-Isothermal Flow in Unsaturated Fractured Rock-A Review", Proc. Symp. Flow and Transport through Unsaturated Fractured Rock, Geophysical Monograph 42, edited by D. D. Evans and T. J. Nicholson, Am. Geophys. Union, Washington, DC, pp. 11-21, 1987. (NNA.900702.0037)

Pruess, K., J. S. Y. Wang, and Y. W. Tsang, "Effective Continuum Approximation for Modeling Fluid and Heat Flow in Fractured Porous Tuff", SAND86-7000, Sandia National Laboratories, Albuquerque, NM, LBL-20778, Lawrence Berkeley Laboratory, Berkeley, CA, 70 pp., 1986. (NNA.891019.0272)

Purcell, W. R., "Capillary Pressures-Their Measurement Using Mercury and the Calculation of Permeability Therefrom", T. P. 2544, *Pet. Trans., Am. Inst. Min. Eng.*, 186, pp. 39-48, 1949. (NNA.890522.0236)

Pyrak-Nolte, L. J., L. R. Myer, N. G. W. Cook, and P. A. Witherspoon, "Hydraulic and Mechanical Properties of Natural Fractures in Low Permeability Rock", Proc. 6th Int. Congress on Rock Mechanics, Montreal, Canada, 1, pp. 225-231, 1987. (NNA.900727.0306)

Rautman, C. A., "Application of Geostatistical Techniques to Modeling of Spatial Variability at the Proposed Yucca Mountain Repository Site, Nevada", in *EOS, Field Approaches and Techniques for Quantifying Spatial Variability in Porous Media II*, Abstracts for the American Geophysical Union Spring Meeting, May 18-22, Baltimore, MD, 1987. (NNA.911031.0014)

Rawls, W. J., D. L. Brakensiek, and K. E. Saxton, "Soil Water Characteristics", Winter Meeting of Am. Soc. Agric. Eng., Chicago, IL, 1981. (NNA.890327.0077)

Rawls, W., P. Yates, and L. Asmussen, "Calibration of Selected Infiltration Equations for the Georgia Coastal Plain", ARS-S-113, Agricultural Research Service, U.S. Department of Agriculture, Beltsville, MD, 110 pp., 1976. (NNA.911204.0004)

Reda, D. C., "Slip-Flow Experiments in Welded Tuff: the Knudsen Diffusion Problem", in *Coupled Processes Associated with Nuclear Waste Repositories*, edited by C. F. Tsang, Academic Press, pp. 485-493, 1987. (HQS.880517.1825)

Richards, L. A., "Capillary Conduction of Liquids Through Porous Mediums", *Physics*, 1, pp. 318-333, 1931. (NNA.890522.0282)

Rulon, J., G. S. Bodvarsson, and P. Montazer, "Preliminary Numerical Simulations of Groundwater Flow in the Unsaturated Zone, Yucca Mountain, Nevada", LBL-20553, Lawrence Berkeley Laboratory, Berkeley, CA, 91 pp., 1986. (NNA.870908.0027)

Schwartz, F. W., L. Smith, and A. S. Crowe, "A Stochastic Analysis of Macroscopic Dispersion in Fractured Media", *Water Resour. Res.*, 19, pp. 1253-1265, 1983. (NNA.890315.0011)

Scott, R. B., and J. Bonk, "Preliminary Geologic Map of Yucca Mountain, Nye County, Nevada with Geologic Sections", USGS-OFR-84-494, U.S. Geological Survey, Denver, CO, 1984. (HQS.880517.1443)

Scotter, D. R., and P. Kanchanasut, "Anion Movement in a Soil under Pasture", *Aust. J. Soil Sci.*, 19, pp. 299-307, 1981. (NNA.890522.0284)

Sinclair, L. R., "Improved Conductivities from Desorption Data", Summer Meeting of Am. Soc. Agric. Eng., Orlando, FL, paper 81-2027, 1981. (NNA.900720.0042)

Snow, D. T., "The Frequency and Apertures of Fractures in Rock", *Int. J. Rock Mech. Min. Sci.*, 7, pp. 23-40, 1970. (NNA.891222.0003)

Somerton, W. H., J. A. Keese, and S. L. Chu, "Thermal Behavior of Unconsolidated Oil Sands", SPE 4506, presented at the 48th Annual Fall Meeting, Soc. Pet. Eng., Am. Inst. Min. Eng., Las Vegas, NV, 1973. (NNA.890522.0271)

Sophocleous, M., "Analysis of Water and Heat Flow in Unsaturated-Saturated Porous Media", *Water Resour. Res.*, 15(5), pp. 1195-1206, 1979. (NNA.890522.0237)

Stephens, D. B., and R. Knowlton, Jr., "Soil Water Movement and Recharge Through Sand at a Semiarid Site in New Mexico", *Water Resour. Res.*, 22(6), pp. 881-889, 1986. (NNA.890522.0238)

Su, C., and R. H. Brooks, "Soil Hydraulic Properties from Infiltration Tests", Proc. Watershed Management, Irrigation and Drainage Div., Am. Soc. Civ. Eng., Logan, UT, pp. 516-542, 1975. (NNA.890522.0272)

Topp, G. C., "Soil-Water Hysteresis Measured in a Sandy Loam and Compared with the Hysteretic Domain Model", *Soil Sci. Soc. Am. Proc.*, 33, pp. 645-651, 1969. (NNA.910506.0149)

Topp, G. C., "Soil-Water Hysteresis: the Domain Theory Extended to Pore Interaction Conditions", *Soil Sci. Soc. Am. Proc.*, 35, 219-225, 1971. (NNA.911111.0002)

Touloukian, Y. S., and C. Y. Ho, *CINDAS Data Series on Material Properties, Vol. II-2, Physical Properties of Rocks and Minerals*, McGraw-Hill, New York, NY, 1981. (NNA.900919.0189)

Travis, B. J., S. W. Hodson, H. E. Nuttall, T. L. Cook, and R. S. Rundberg, "Numerical Simulation of Flow and Transport in Fractured Tuff", Proc. Scientific Basis for Nuclear Waste Management VII, Mat. Res. Soc. Sym. Proc., 26, pp. 1039-1046, 1984. (NNA.890522.0239)

Tsang, Y. W., and K. Pruess, "A Study of Thermally Induced Convection Near a High-Level Nuclear Waste Repository in Partially Saturated Fractured Tuff", *Water Resour. Res.*, 23(10), pp. 1958-1966, 1987. (NNA.890522.0273)

Tsang, Y. W., and C. F. Tsang, "Channel Model of Flow Through Fractured Media", *Water Resour. Res.*, 23(3), pp. 467-479, 1987. (NNA.900711.0085)

USDA (U.S. Department of Agriculture), *Soil Survey Manual, USDA Agric. Handbook,* 18,503 pp., 1951. (NNA.891222.0028)

van Genuchten, M. Th., "A Closed-Form Equation for Predicting the Hydraulic Conductivity of Unsaturated Soils", *Soil Sci. Soc. Am. J.*, 44, pp. 892-898, 1980. (NNA.890522.0287)

van Genuchten, M. Th., and W. A. Jury, "Progress in Unsaturated Flow and Transport Modeling", *Rev. Geophys.*, 25(2), pp. 135-140, 1987. (NNA.890522.0240)

van Genuchten, M. Th., and D. R. Nielsen, "On Describing and Predicting the Hydraulic Properties of Unsaturated Soils", *Ann. Geophys.*, 3(5), pp. 615-628, 1985. (NNA.890315.0017)

Verma, A., and K. Pruess, "Thermohydrological Conditions and Silica Redistribution Near High-Level Nuclear Wastes Emplaced in Saturated Geological Formations", LBL-21613, Lawrence Berkeley Laboratory, Berkeley, CA, 63 pp., 1987. (NNA.891222.0004)

Visser, W. C., "An Empirical Expression for the Desorption Curve", Proc. Wageningen Symp., Water in the Unsaturated Zone, edited by P. E. Rijtema and H. Wassink, IASH/AIHS, Unesco, Paris, I, pp. 329-335, 1968. (NNA.890713.0172)

Wang, J. S. Y., and T. N. Narasimhan, "Hydrologic Mechanisms Governing Fluid Flow in a Partially Saturated, Fractured, Porous Medium", *Water Resour. Res.*, 21(12), pp. 1861-1874, 1985. (NNA.870407.0209)

Wang, J. S. Y., and T. N. Narasimhan, "Hydrologic Mechanisms Governing Partially Saturated Fluid Flow in Fractured Welded Units and Porous Nonwelded Units at Yucca Mountain", SAND85-7114, Sandia National Laboratories, Albuquerque, NM, LBL-21022, Lawrence Berkeley Laboratory, Berkeley, CA, 126 pp., 1986. (NNA.870806.0063)

Wang, J. S. Y., and T. N. Narasimhan, "Hydrologic Modeling of Vertical and Lateral Movement of Partially Saturated Fluid Flow Near a Fault Zone at Yucca Mountain", SAND87-7070, Sandia National Laboratories, Albuquerque, NM, LBL-23510, Lawrence Berkeley Laboratory, Berkeley, CA, 122 pp., 1987. (NNA.871109.0057)

Wang, J. S. Y., and C. F. Tsang, "Thermal Calculations for Radioactive Waste Repositories in Alluvium and Tuff", in H. A. Wollenberg, J. S. Y. Wang, and G. Korbin, "An Appraisal of Nuclear Waste Isolation in the Vadose Zone in Arid and Semiarid Regions (with Emphasis on the Nevada Test Site)", LBL-15010, Lawrence Berkeley Laboratory, Berkeley, CA, pp. 95-126, 1983. (NNA.890522.0222)

Wang, J. S. Y., C. F. Tsang, and R. A. Sterbentz, "The State of the Art of Numerical Modeling of Thermohydrologic Flow in Fractured Rock Masses", *Environ. Geol.*, 4, pp. 133-199, 1983. (NNA.890522.0274)

Wang, J. S. Y., D. C. Mangold, and C. F. Tsang, "Thermal Impact of Waste Emplacement and Surface Cooling Associated with Geologic Disposal of High-Level Nuclear Waste", *Environ. Geol. Water Sci.*, 11(2), pp. 183-239, 1988a. (NNA.890522.0275)

Wang, J. S. Y., T. N. Narasimhan, and C. H. Scholz, "Aperture Correlation of a Fractal Fracture", J. *Geophys. Res.*, 93(B3), pp. 2216-2224, 1988b. (NNA.891222.0005)

Warren, J. E., and P. J. Root, "The Behavior of Naturally Fractured Reservoirs", *Soc. Pet. Eng. J.*, 3(5), pp. 245-255, 1963. (NNA.890522.0276)

Weeks, E. P., "Effect of Topography on Gas Flow in Unsaturated Fractured Rock: Concepts and Observations", Proc. Symp. Flow and Transport Through Unsaturated Fractured Rock, Geophysical Monograph 42, edited by D. D. Evans and T. J. Nicholson, Am. Geophys. Union, Washington, DC, pp. 165-170, 1987. (NNA.870908.0028)

Wierenga, P. J., L. W. Gelhar, C. S. Simmons, G. W. Gee, and T. J. Nicholson, "Validation of Stochastic Flow and Transport Models for Unsaturated Soils: A Comprehensive Field Study", NUREG/CR-4622, PNL 5875, U.S. Nuclear Regulatory Commission, Washington, DC, 1986. (NNA.890327.0081)

Witherspoon, P. A., C. H. Amick, J. E. Gale, and K. Iwai, "Observations of a Potential Size Effect in Experimental Determination of the Hydraulic Properties of Fractures", *Water Resour. Res.*, 15(5), pp. 1142-1146, 1979. (NNA.911021.0041)

Witherspoon, P. A., J. S. Y. Wang, K. Iwai, and J. E. Gale, "Validity of Cubic Law for Fluid Flow in a Deformable Rock Fracture", *Water Resour. Res.*, 16(6), pp. 1016-1024, 1980. (NNA.891109.0039)

Yates, S. R., M. Th. van Genuchten, and F. J. Leij, "Analysis of Predicted Hydraulic Conductivities Using RETC", presented at the International Workshop on Indirect Methods for Estimating the Hydraulic Properties of Unsaturated Soils, Riverside, CA, October 11-13, Program, p. 70, 1989. (NNA.911007.0049)

Zimmerman, R. M., and M. L. Blanford, "Expected Thermal and Hydrothermal Environments for Waste Emplacement Holes Based on G-Tunnel Heater Experiments", Proc. 27th U.S. Symp. on Rock Mechanics, Univ. Alabama, Tuscaloosa, AL, 1986. (NNA.891212.0018)

APPENDIX A
DISTRIBUTION AND CORRELATION OF WATERSHED SOIL CHARACTERISTIC PARAMETERS

In this appendix, we analyze the watershed soil data collected by Holtan et al. (1968) and fitted by Panian (1987) with the van Genuchten (1980) model. The data were grouped into 11 soil classes according to the texture descriptions. We analyze the data of the 11 texture classes separately as well as grouping them into 4 broader categories: sandy, loamy, silty, and clayey soils (Cosby et al., 1984). In each figure in this appendix, we compare the results of individual texture classes with the results of the combined data set.

The distributions of five parameters are plotted. Figures A-1 to A-4 are for the pore-size distribution index λ in the Brooks and Corey (1966) model or n -1 in the van Genuchten (1980) model. Figures A-5 to A-8 are for the air entry scaling factor, α. Both parameters are analyzed in logarithmic scales. Figures A-9 to A-12 are for the residual saturation, S_r, in linear scale. Figures A-13 to A-16 are for the log saturated permeability and Figures A-17 to A-20 are for the porosity. There are four plots in each distribution figure: (a) distribution histogram and (b) cumulative distribution versus parameter values; (c) mean value, mean ± 1 standard deviation and (d) skewness, kurtosis versus the number of data points.

Figures A-21 to A-24 are for the parameter correlation between air entry scaling factor and pore-size distribution index. Figures A-25 to A-28 are for the correlation between pore-size distribution index and residual saturation. Figures A-29 to A-32 are for the correlation between residual saturation and porosity. Figures A-33 to A-36 are for the correlation between saturated permeability and porosity. We also plot in Figures A-37 to A-40 the saturated permeability versus air entry radius, which is proportional to the air entry scaling factor. There are four figures for each correlation relationship for the four categories: (a) sandy, (b) loamy, (c) silty, and (d) clayey soil. The data points for individual texture classes are labelled with different symbols.

From the distribution plots in Figures A-1 to A-20, we can determine if normal or log normal distributions are good approximations for the soil data, if the number of data points is sufficient to define distribution parameters, and if different texture classes can be grouped into broader categories. From cross plots in Figures A-21 to A-40, we can analyze whether there are significant correlations among unsaturated and saturated flow parameters. General conclusions and comparisons of soil data with tuff matrix data are discussed in the main text. Some specific observations from distribution and correlation plots among different soil texture classes are summarized below.

- The pore-size distribution indices of sandy, loamy, and clayey watershed soils have two peaks: one in the 0.1-0.2 range, and one in the 0.5-1.0 range (Figures A-1a, A-2a, A-4a). The large index range, representing narrow pore-size distribution, is associated with clayey, and to a less extent, with loamy components in the soil. The silty watershed soil has one peak in the small index range with a tail extending into the large index range (Figure A-3a).

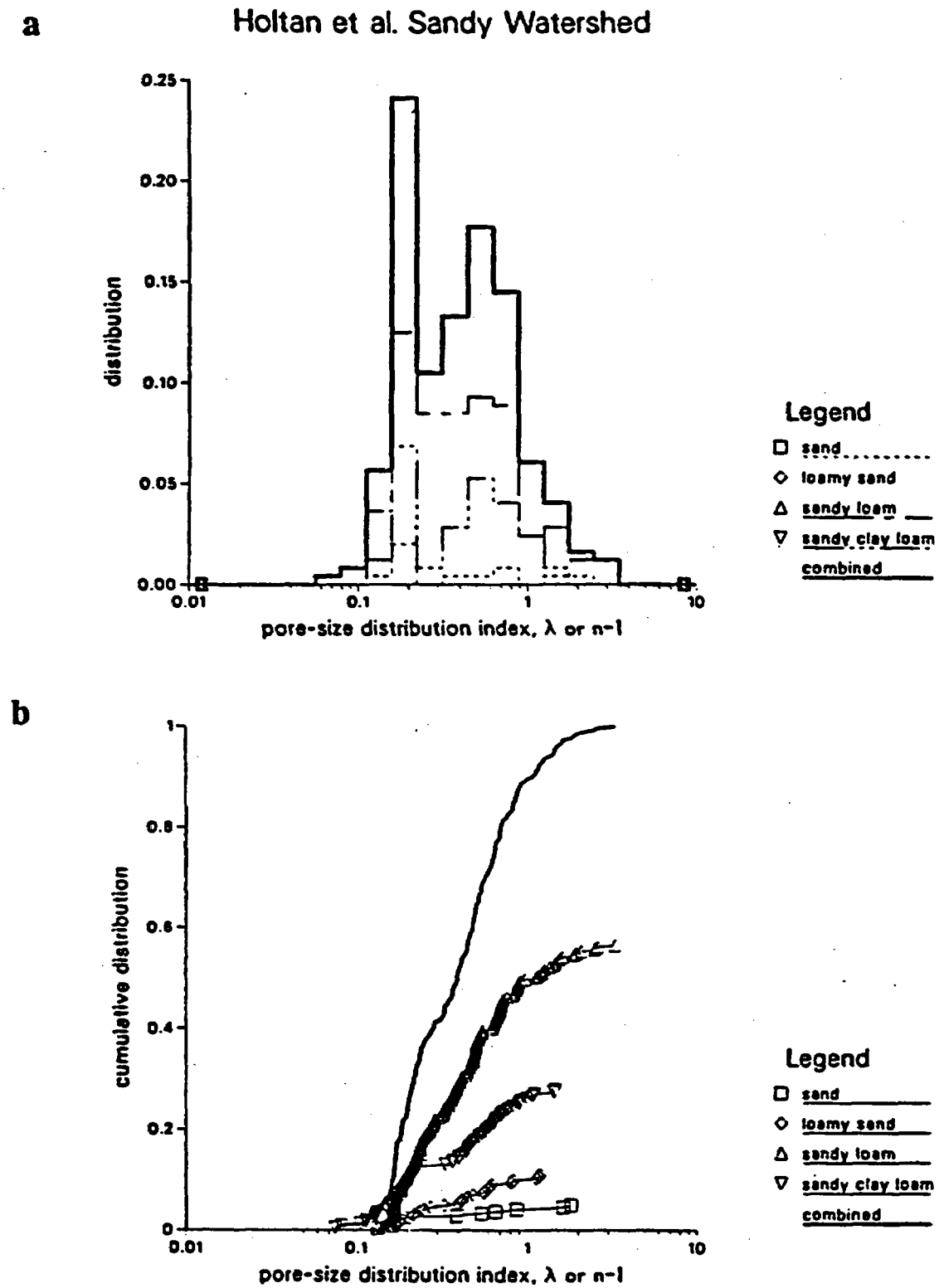

Figure A-1. Distributions of Sandy Watershed Soil Log Pore-Size Distribution Index.

c

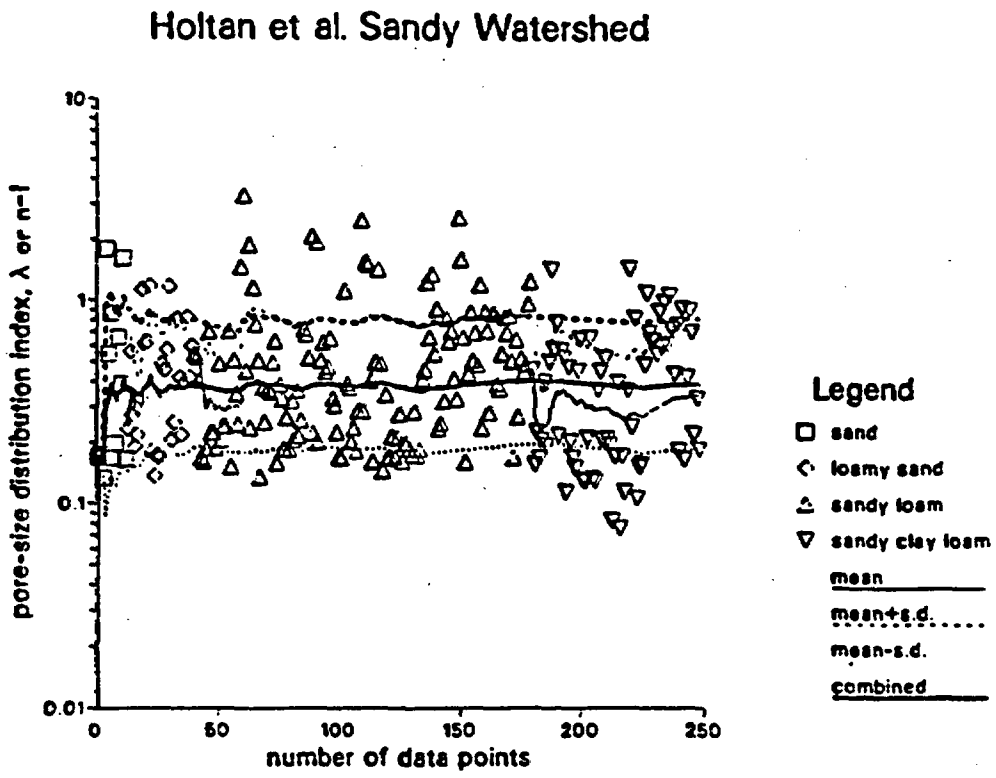

d

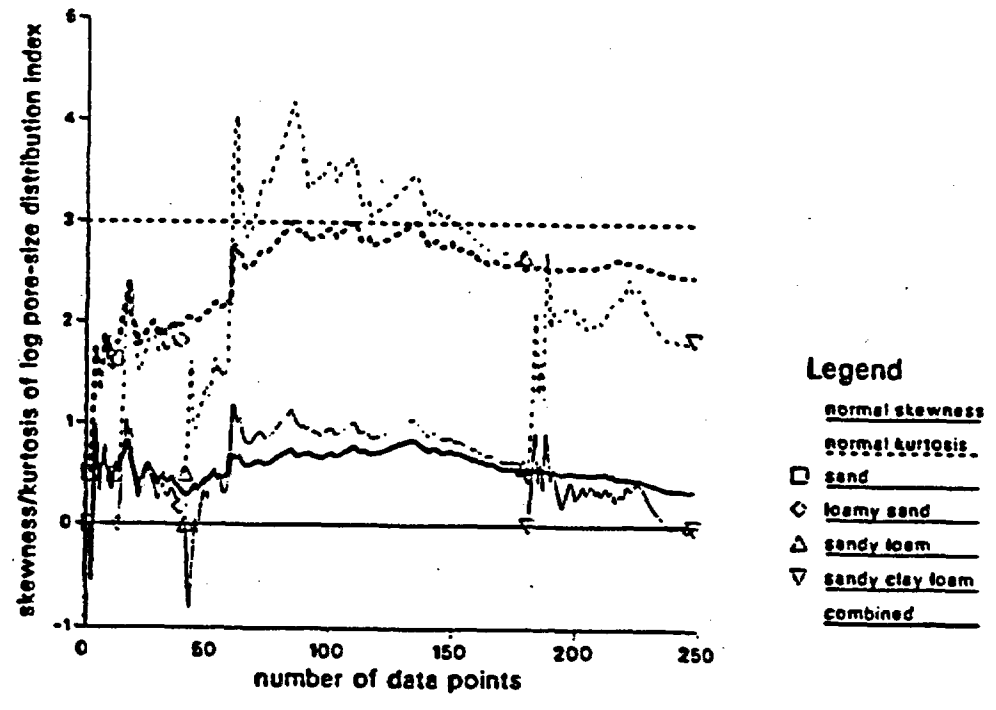

Figure A-1. Distributions of Sandy Watershed Soil Log Pore-Size Distribution Index (concluded).

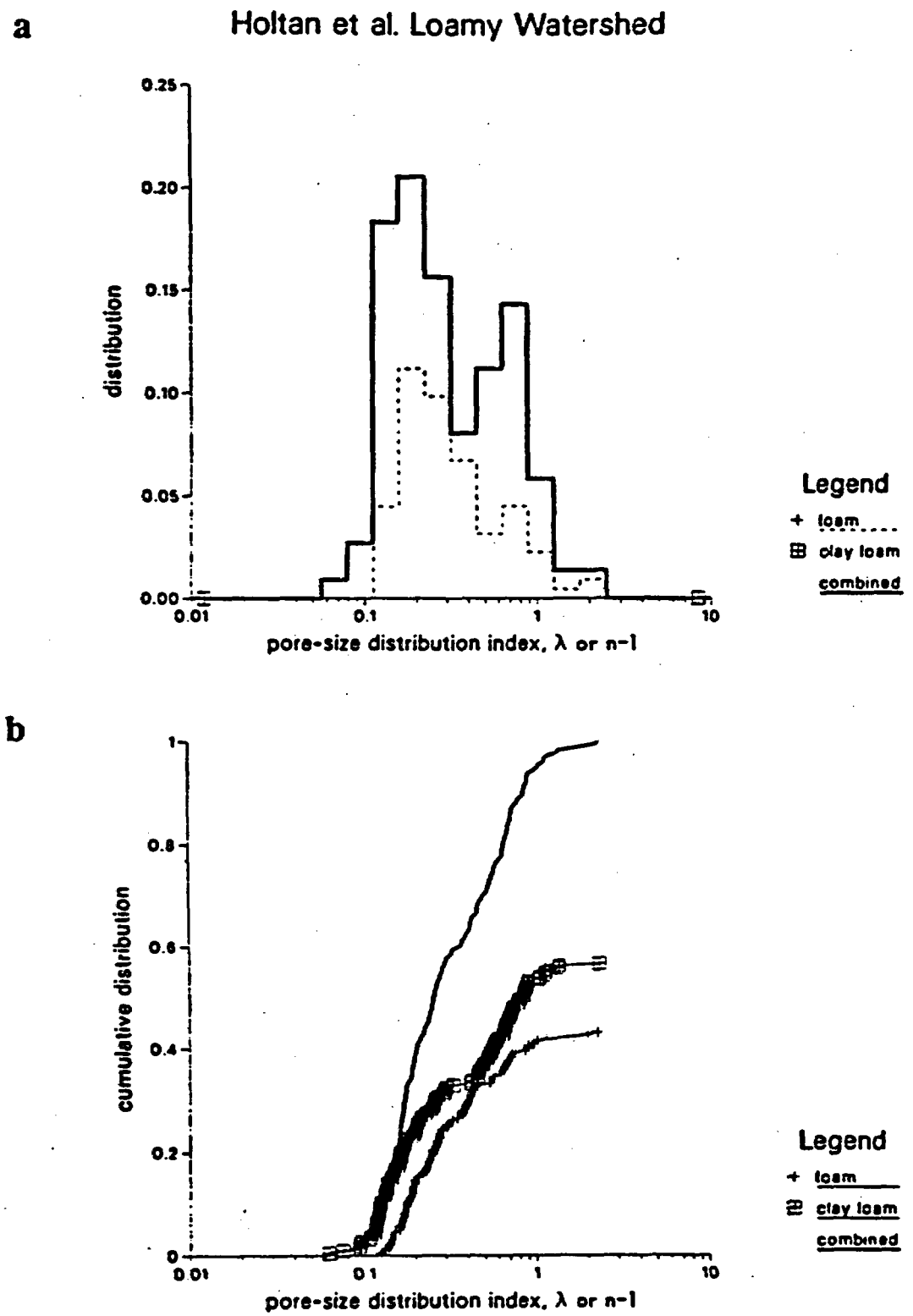

Figure A-2. Distributions of Loamy Watershed Soil Log Pore-Size Distribution Index.

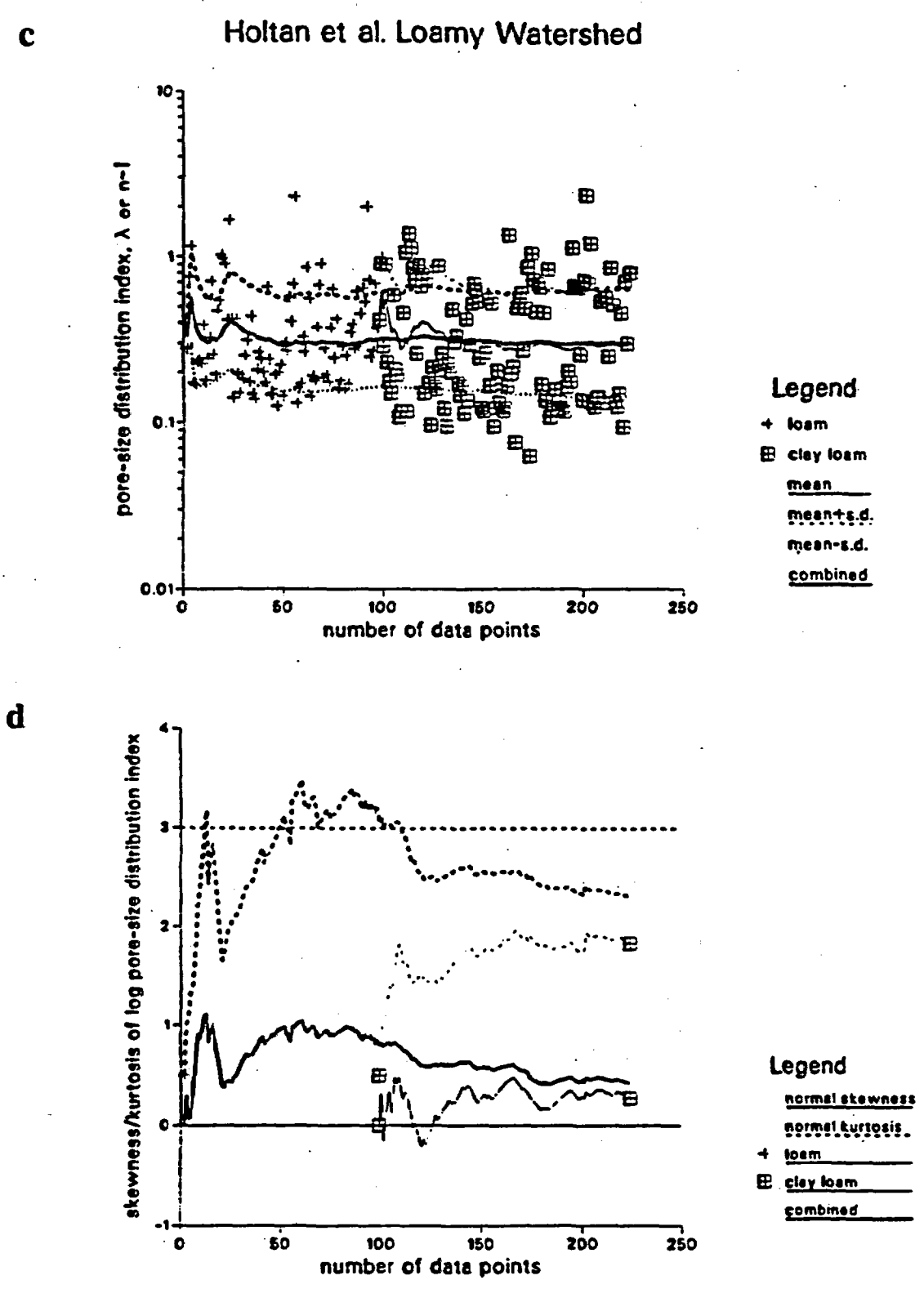

Figure A-2. Distributions of Loamy Watershed Soil Log Pore-Size Distribution Index (concluded).

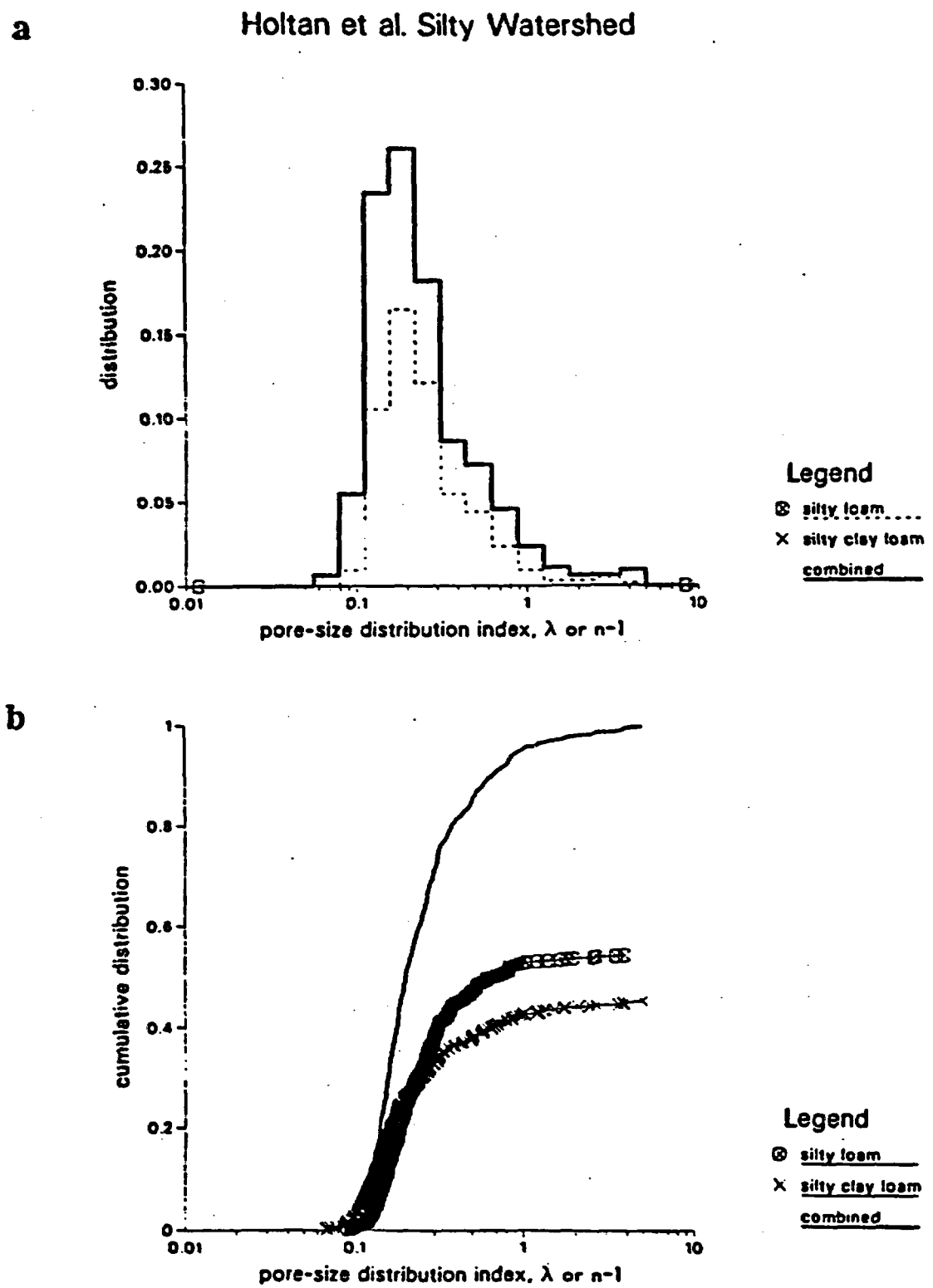

Figure A-3. Distributions of Silty Watershed Soil Log Pore-Size Distribution Index.

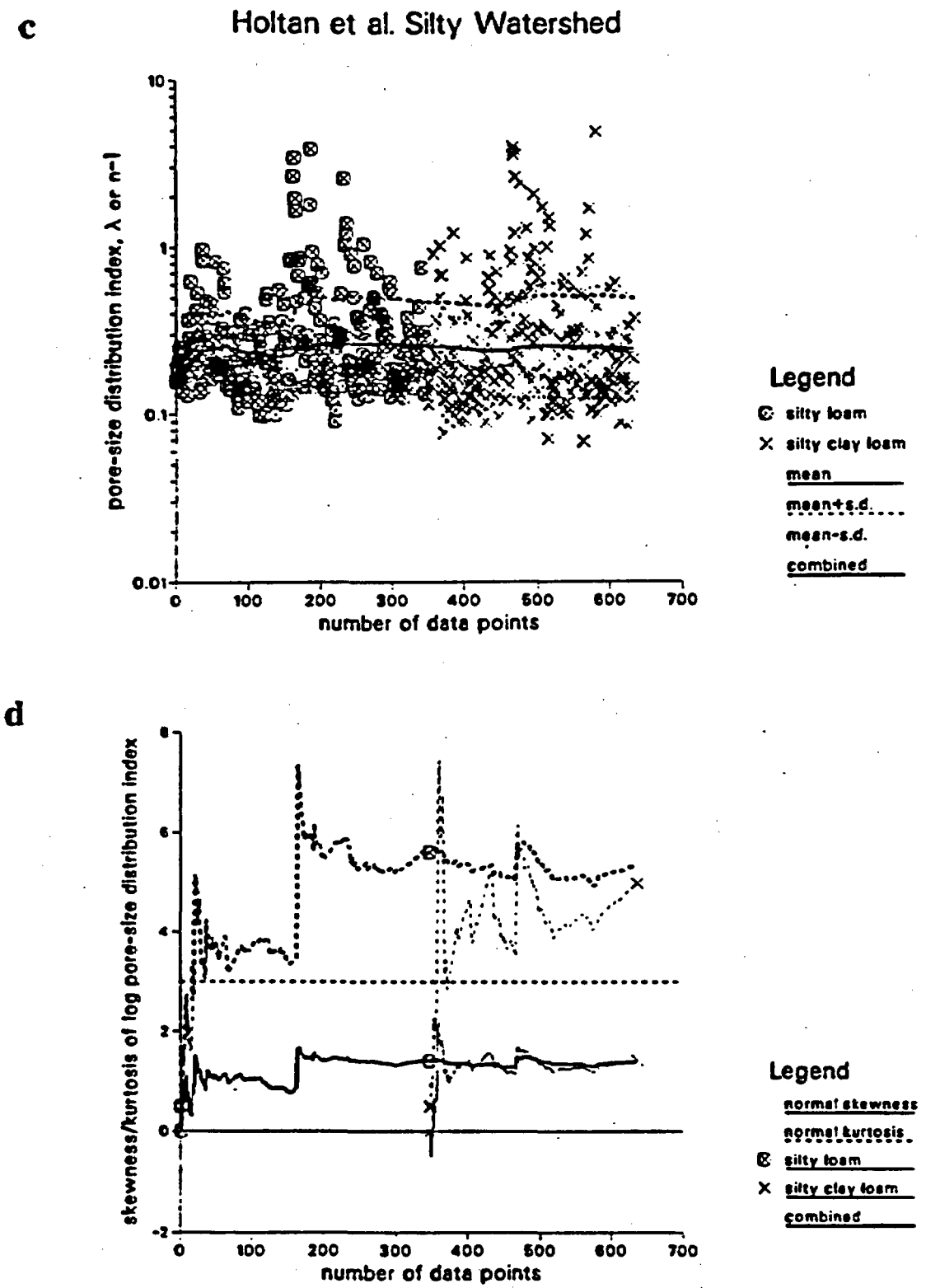

Figure A-3. Distributions of Silty Watershed Soil Log Pore-Size Distribution Index (concluded).

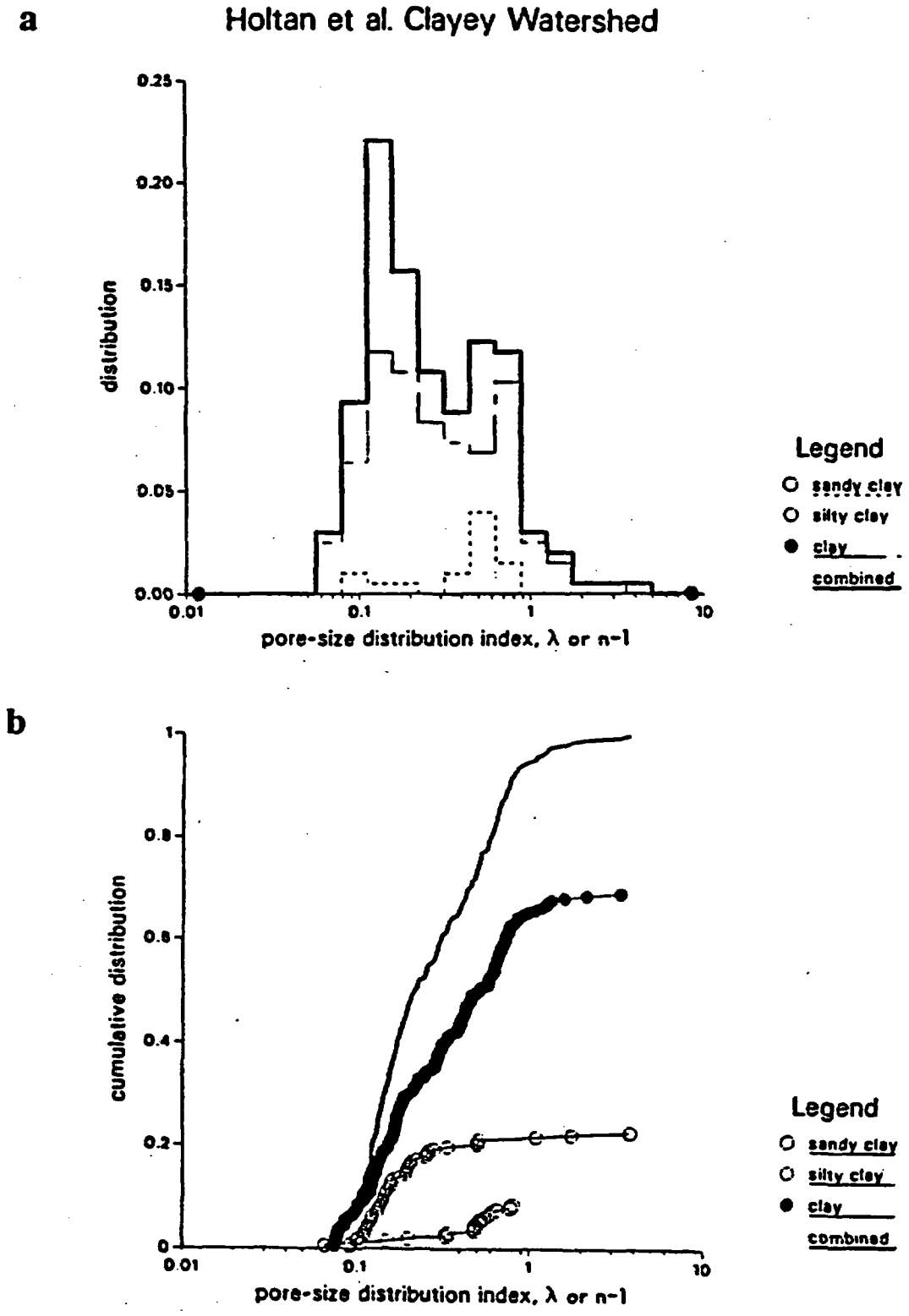

Figure A-4. Distributions of Clayey Watershed Soil Log Pore-Size Distribution Index.

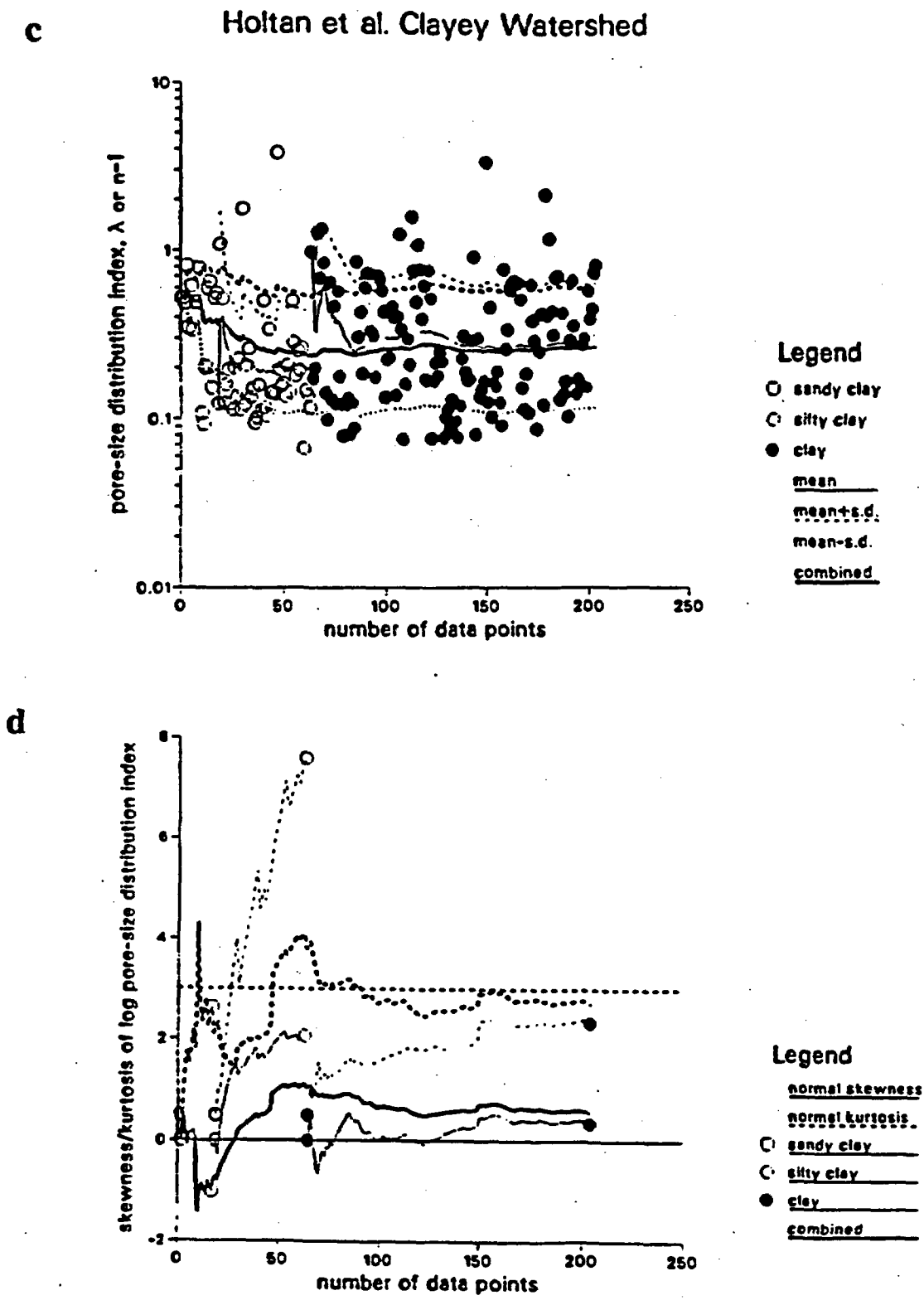

Figure A-4. Distributions of Clayey Watershed Soil Log Pore-Size Distribution Index (concluded).

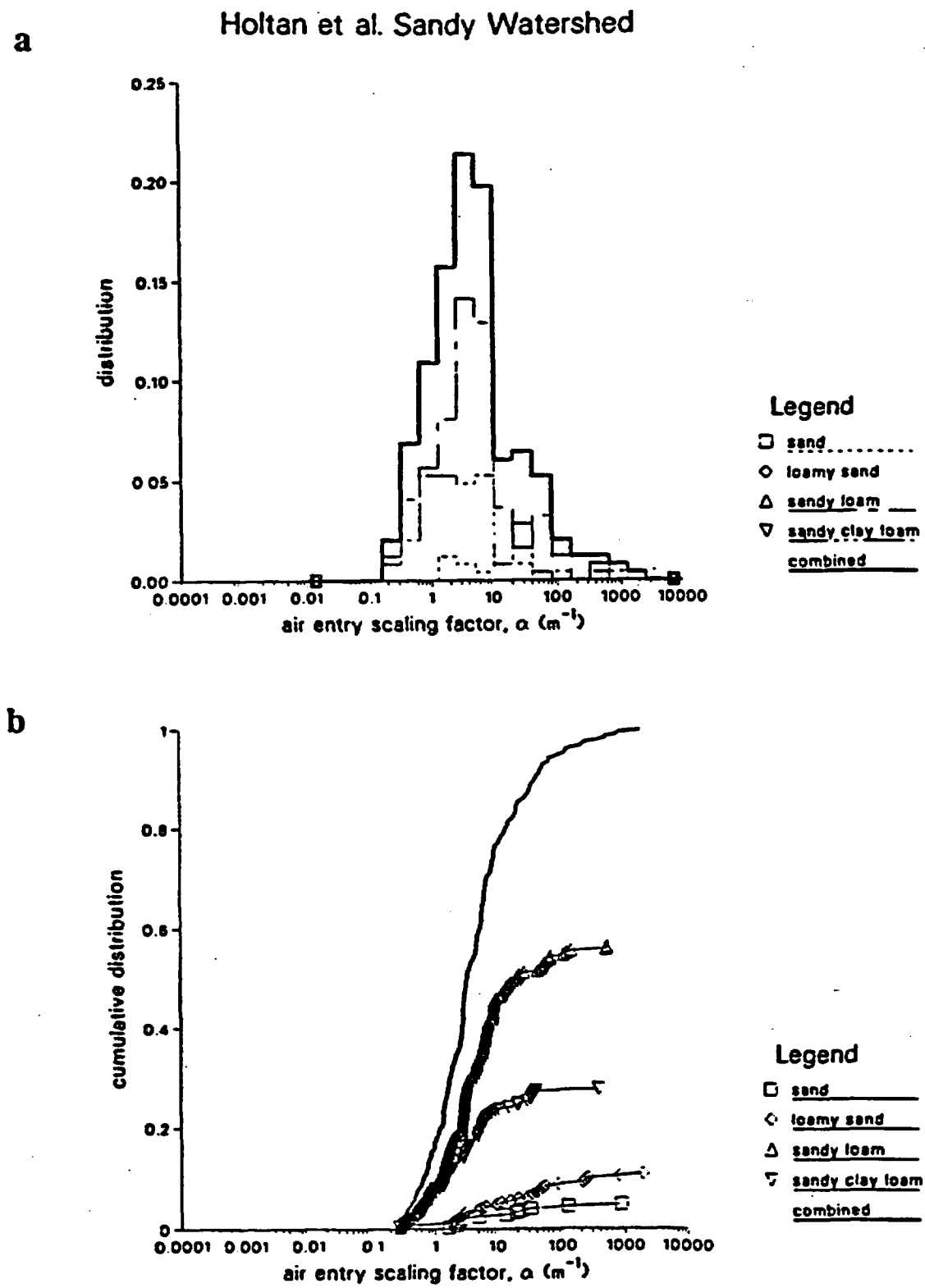

Figure A-5. Distributions of Sandy Watershed Soil Log Air Entry Scaling Factor.

c

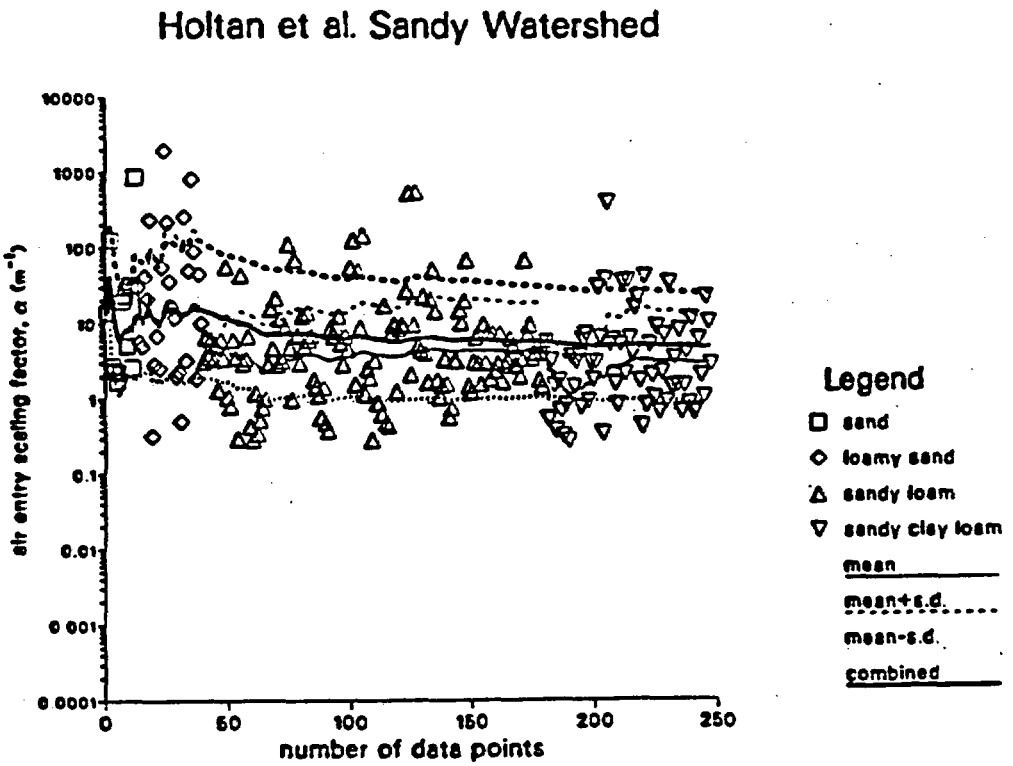

d

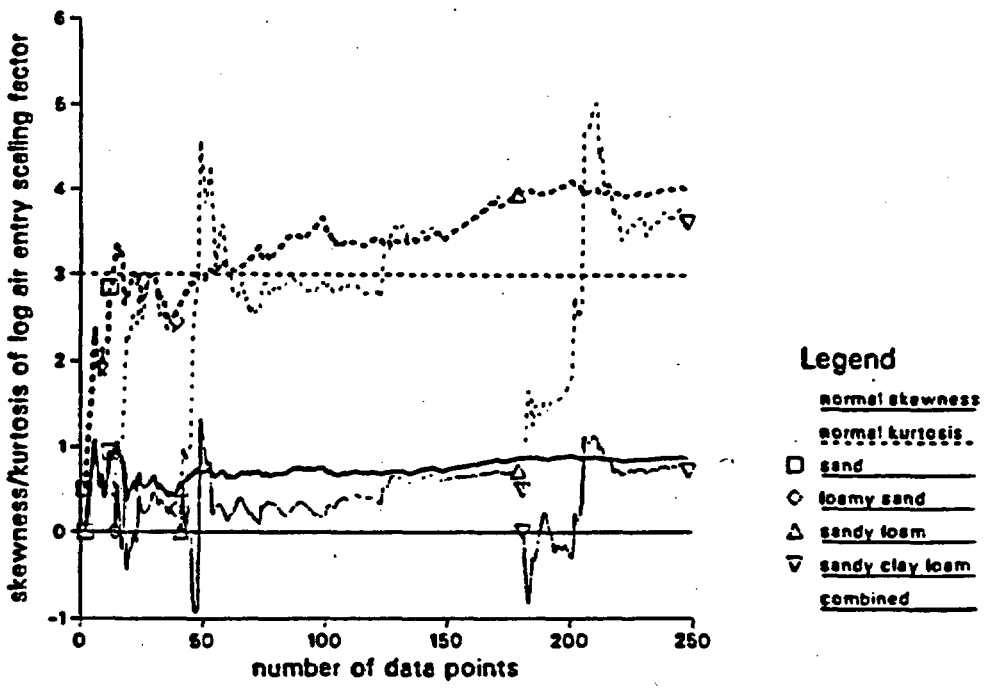

Figure A-5. Distributions of Sandy Watershed Soil Log Air Entry Scaling Factor (concluded).

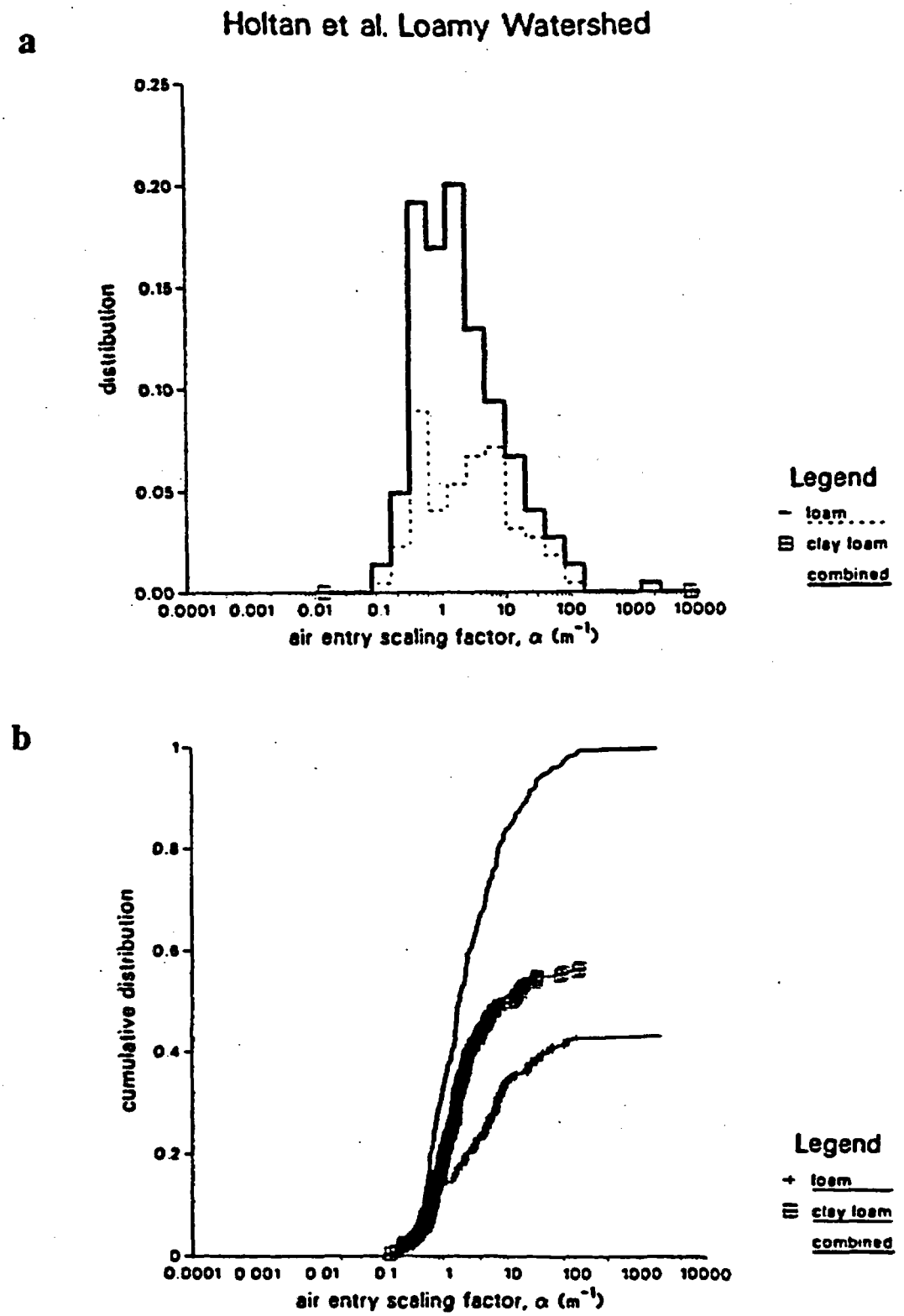

Figure A-6. Distributions of Loamy Watershed Soil Log Air Entry Scaling Factor.

c

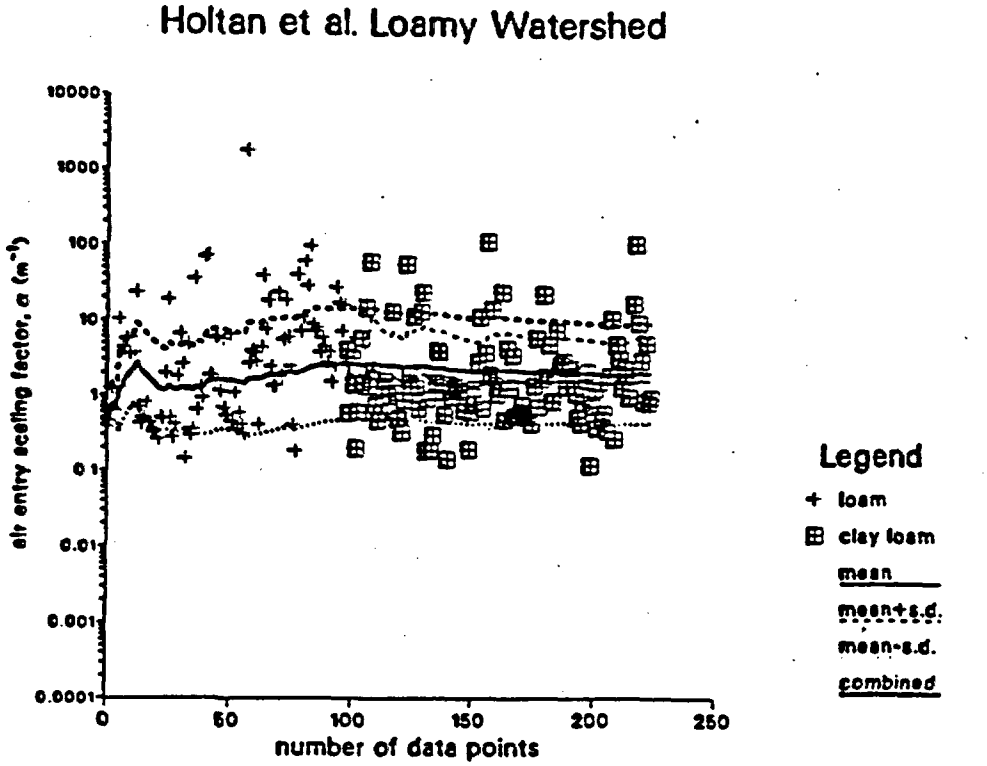

d

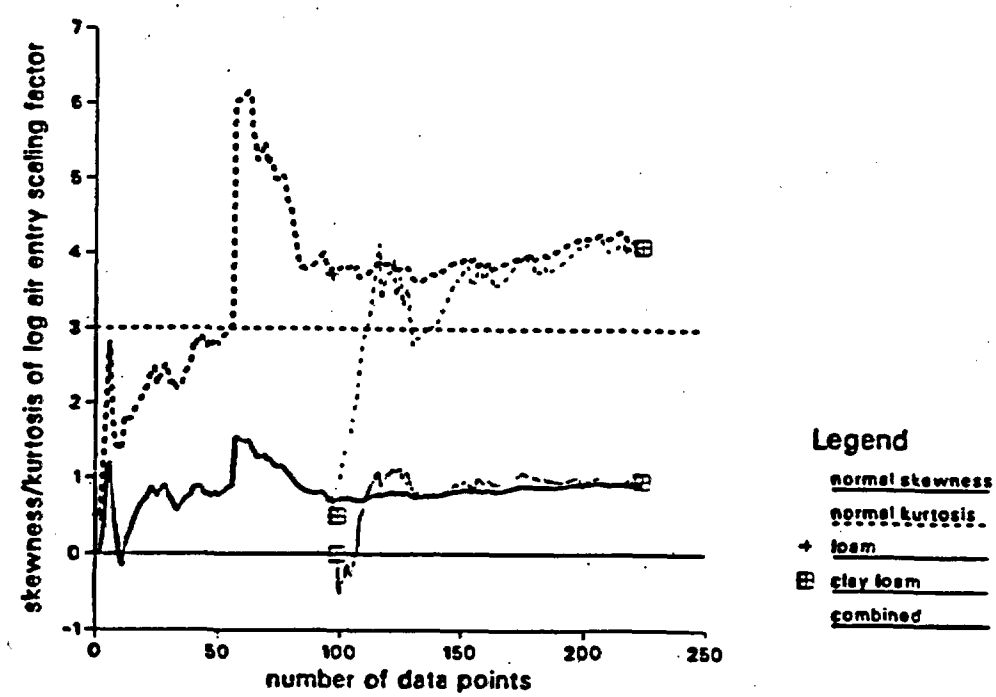

Figure A-6. Distributions of Loamy Watershed Soil Log Air Entry Scaling Factor (concluded).

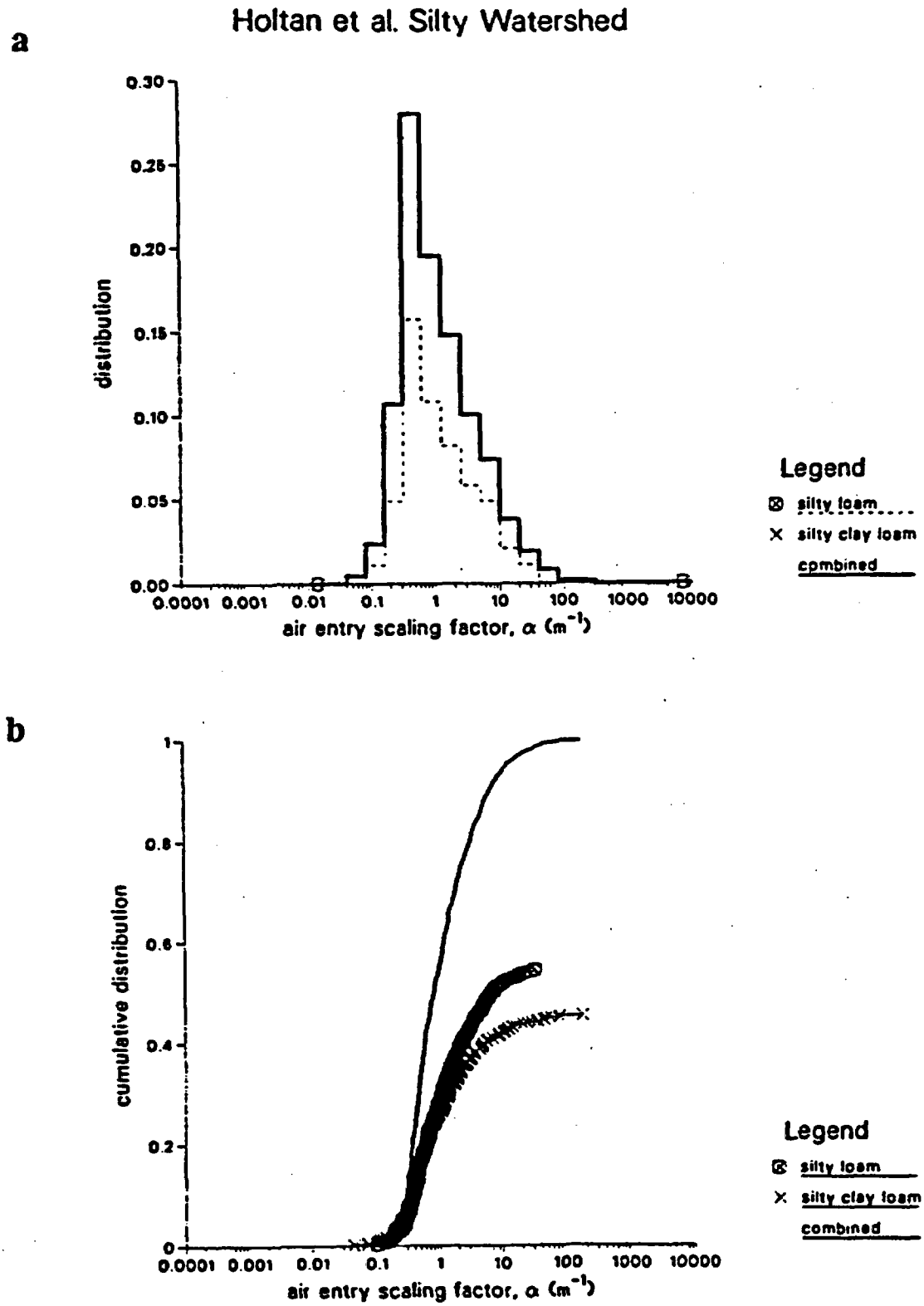

Figure A-7. Distributions of Silty Watershed Soil Log Air Entry Scaling Factor.

c

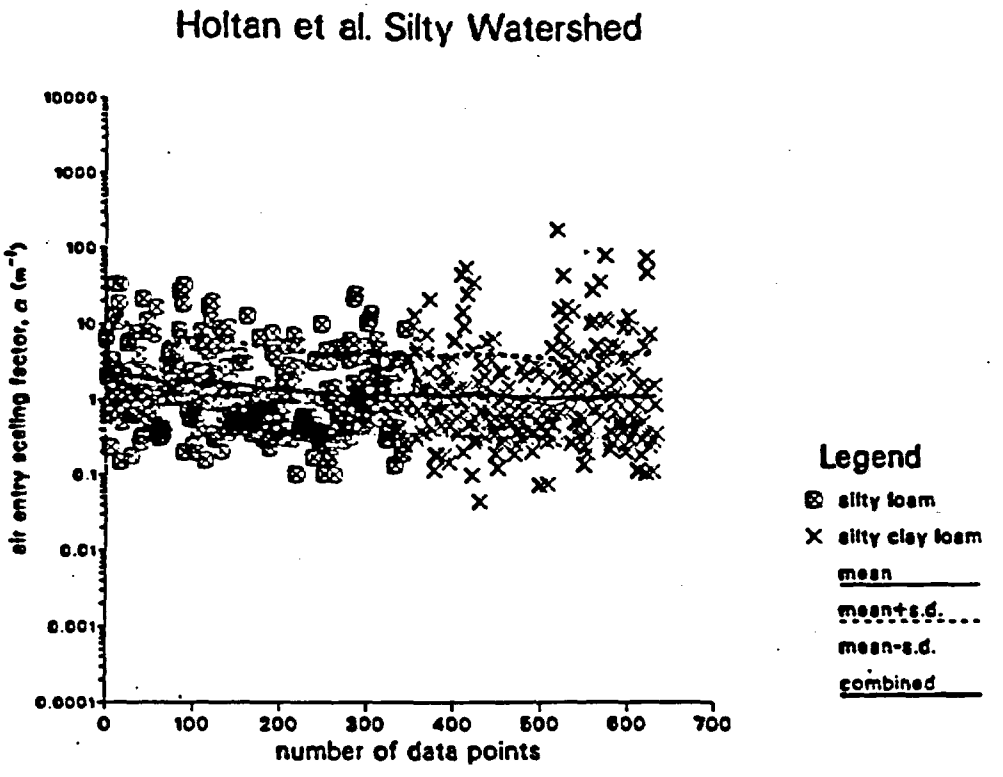

d

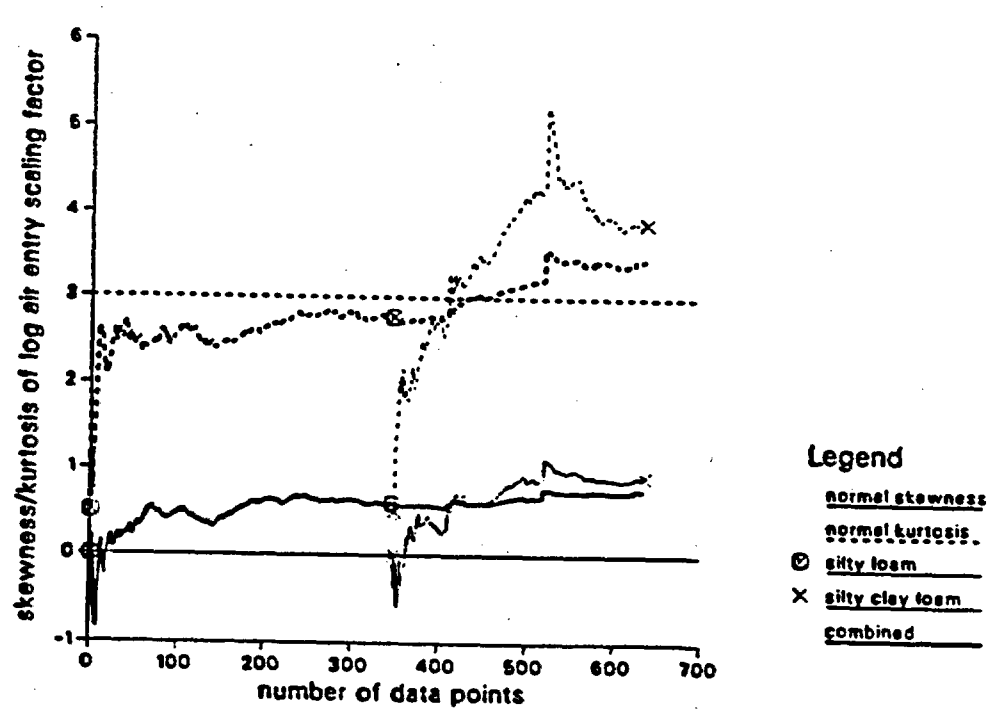

Figure A-7. Distributions of Silty Watershed Soil Log Air Entry Scaling Factor (concluded).

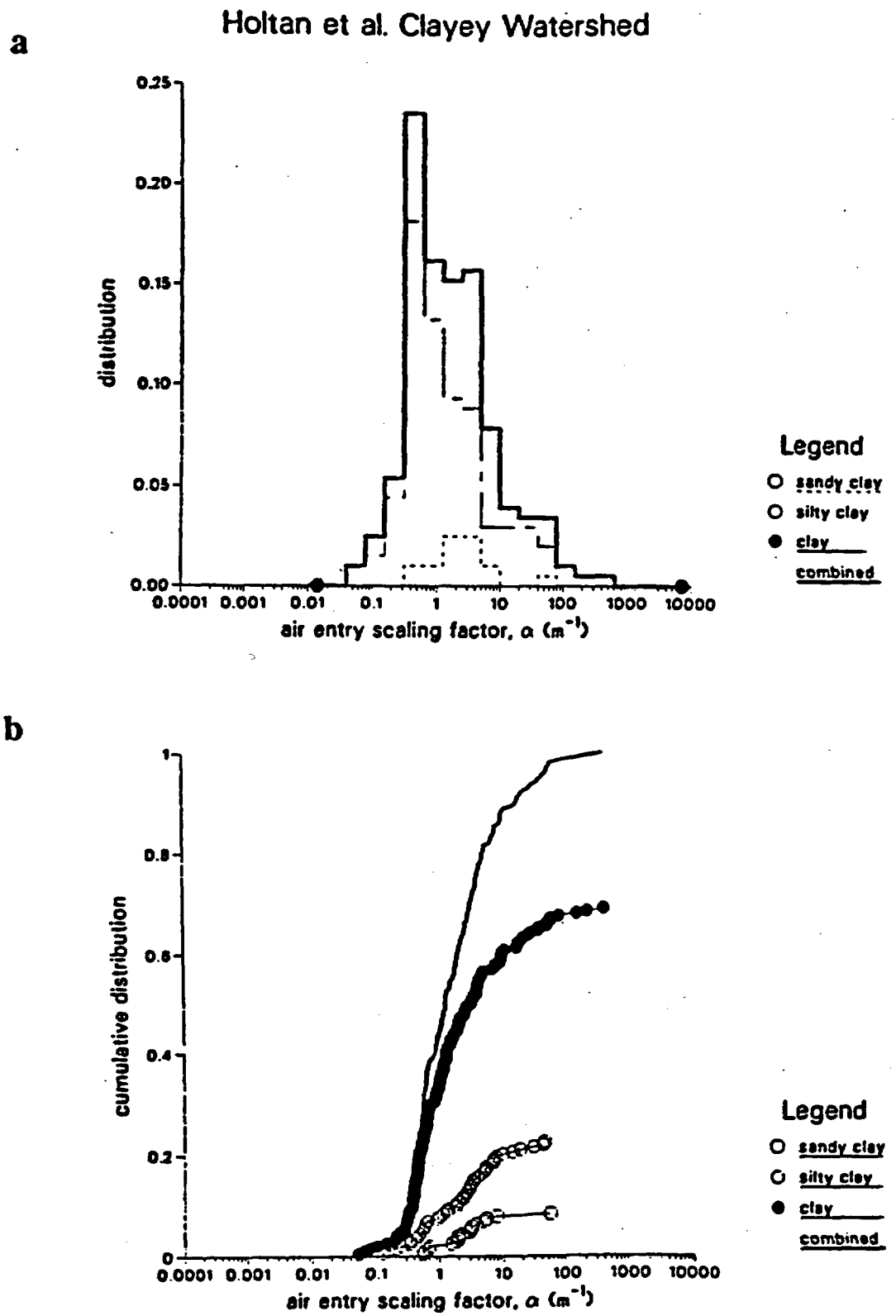

Figure A-8. Distributions of Clayey Watershed Soil Air Entry Scaling Factor.

c

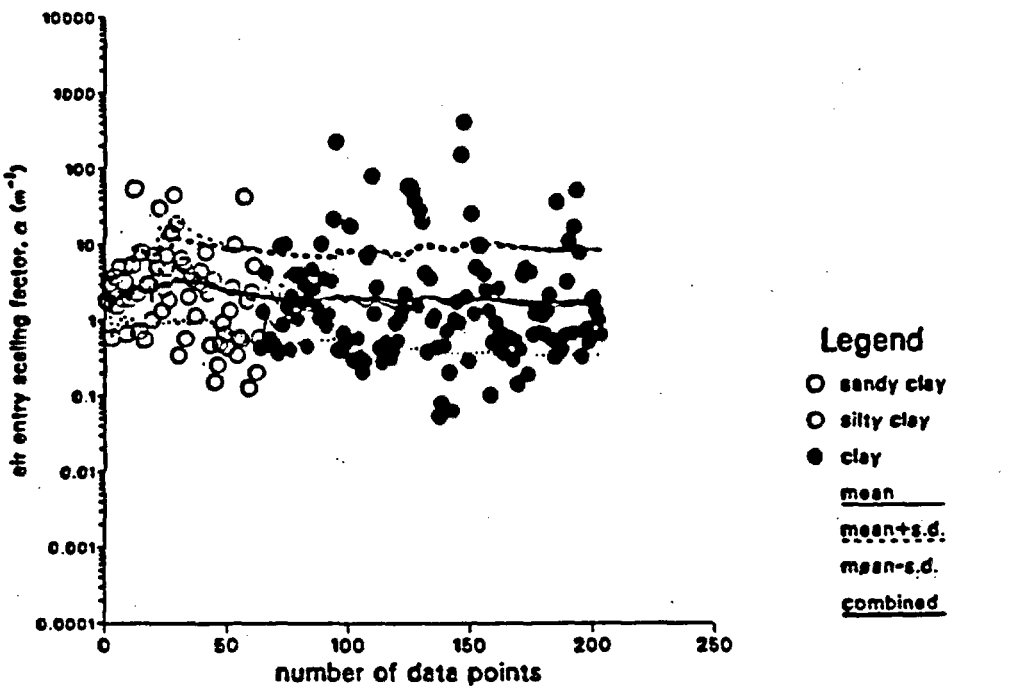

d

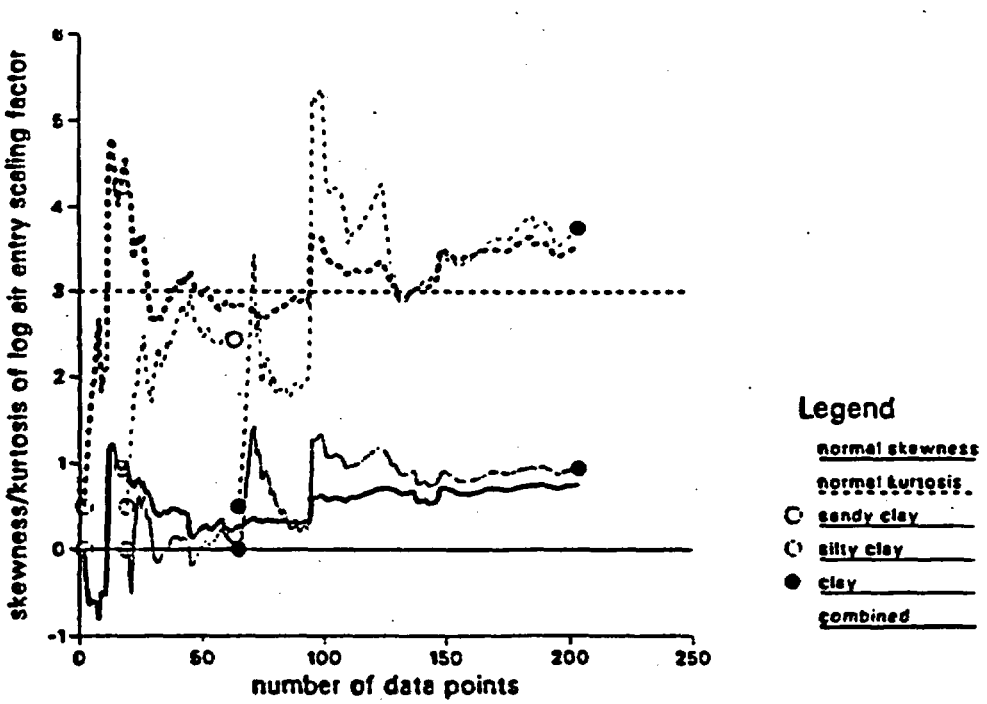

Figure A-8. Distributions of Clayey Watershed Soil Air Entry Scaling Factor (concluded).

a

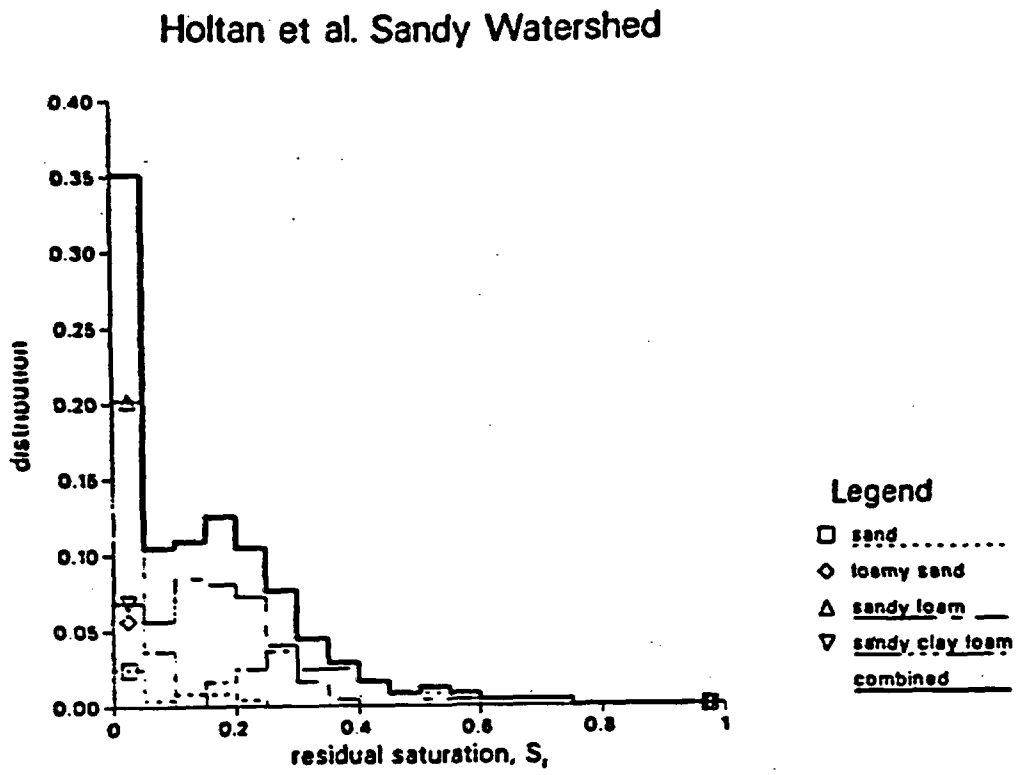

b

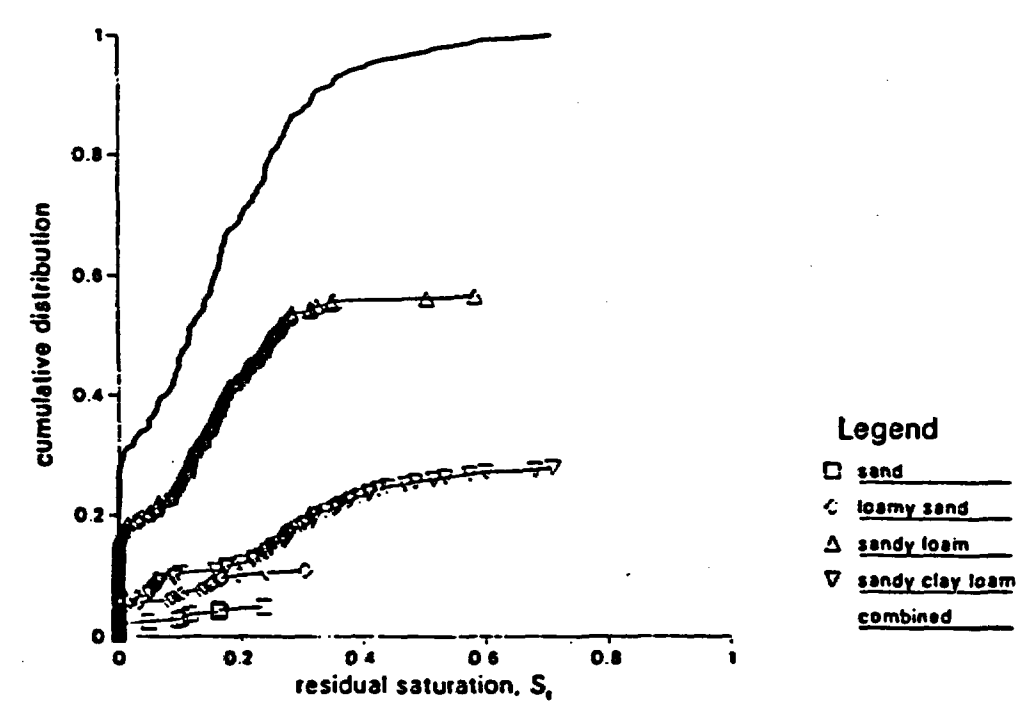

Figure A-9. Distributions of Sandy Watershed Soil Residual Saturation.

c

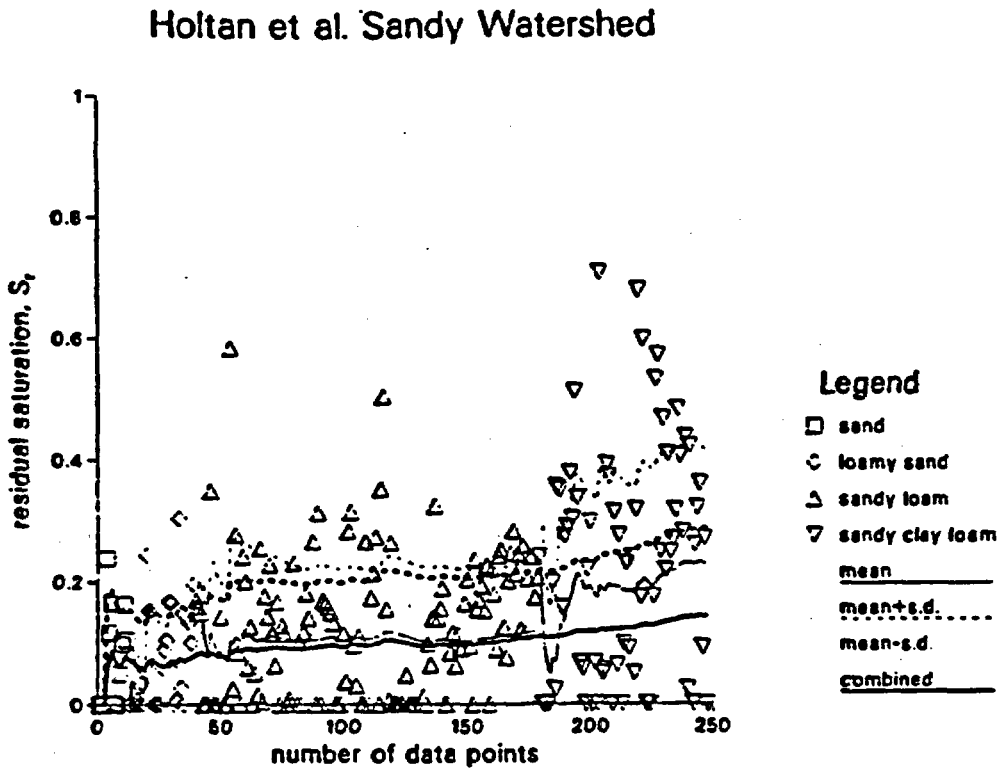

d

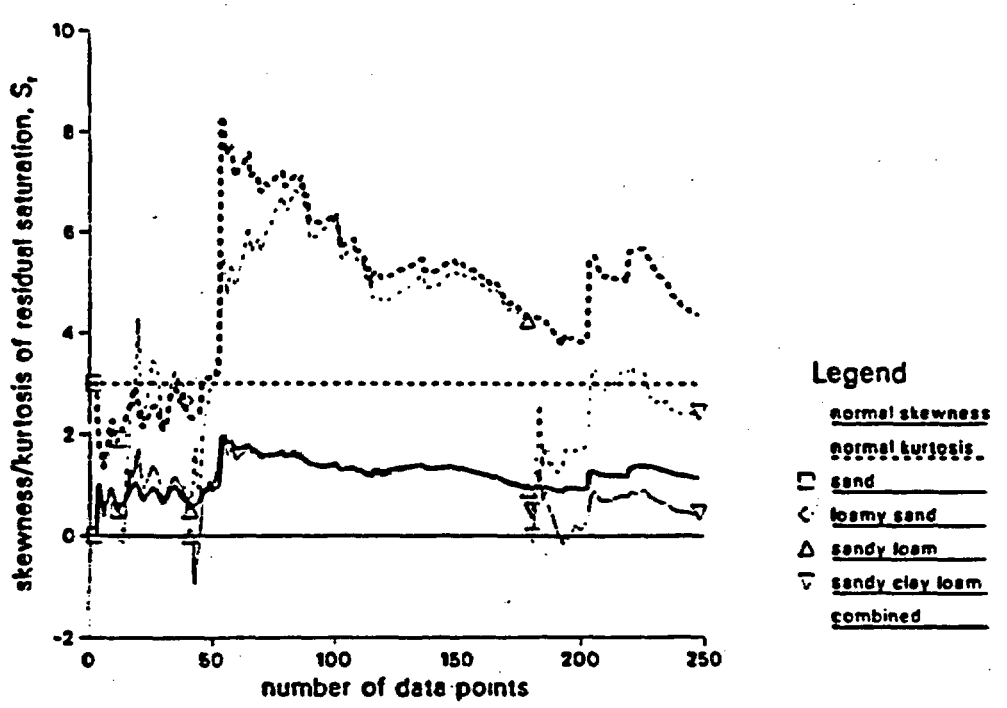

Figure A-9. Distributions of Sandy Watershed Soil Residual Saturation (concluded).

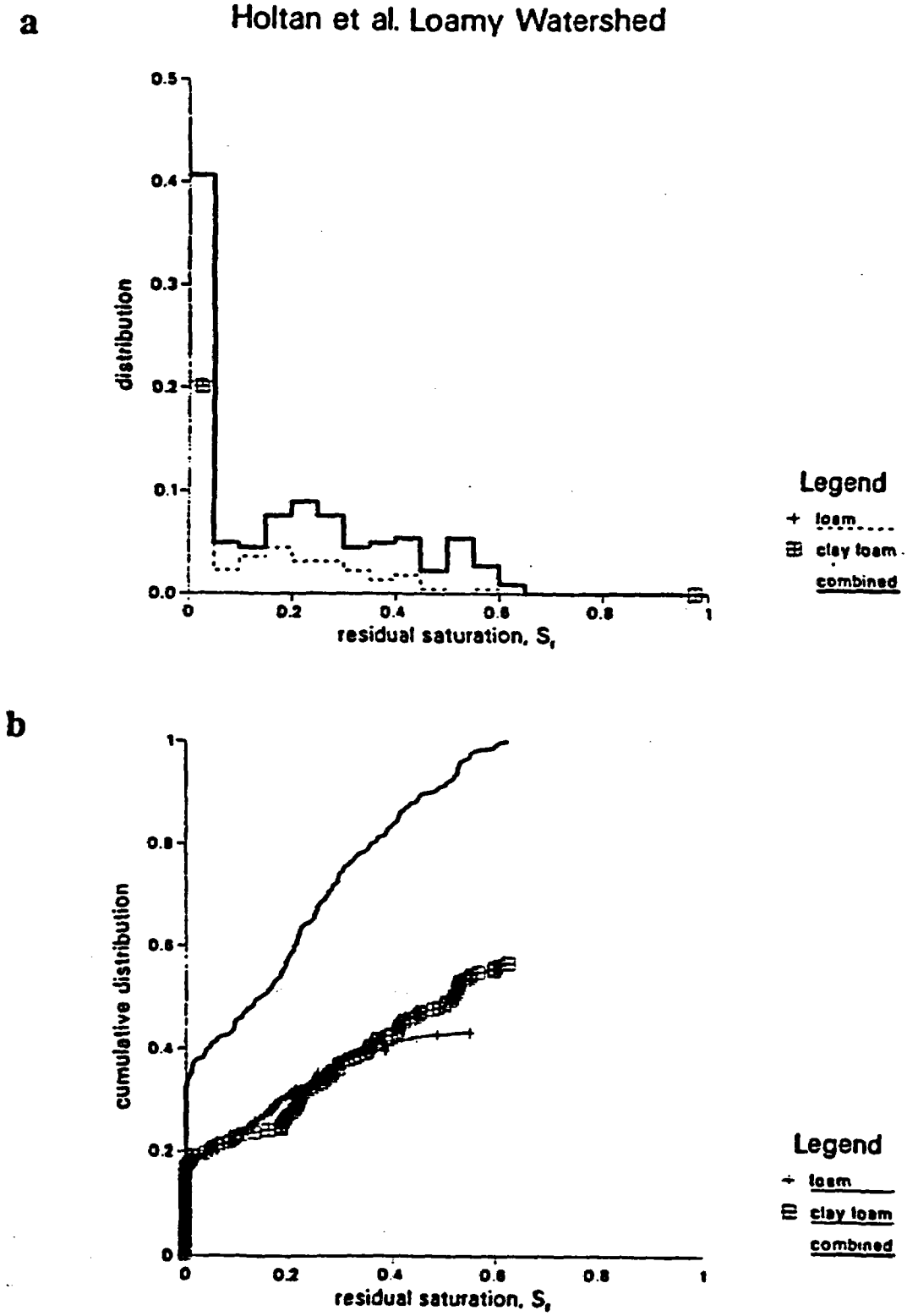

Figure A-10. Distributions of Loamy Watershed Soil Residual Saturation.

c

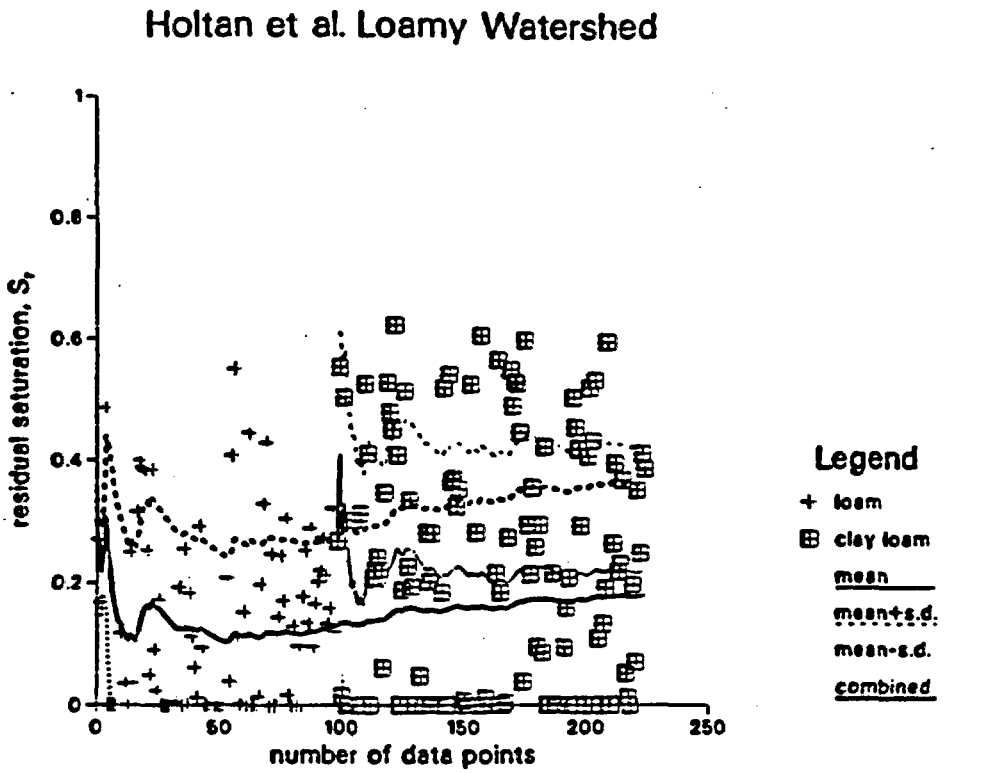

d

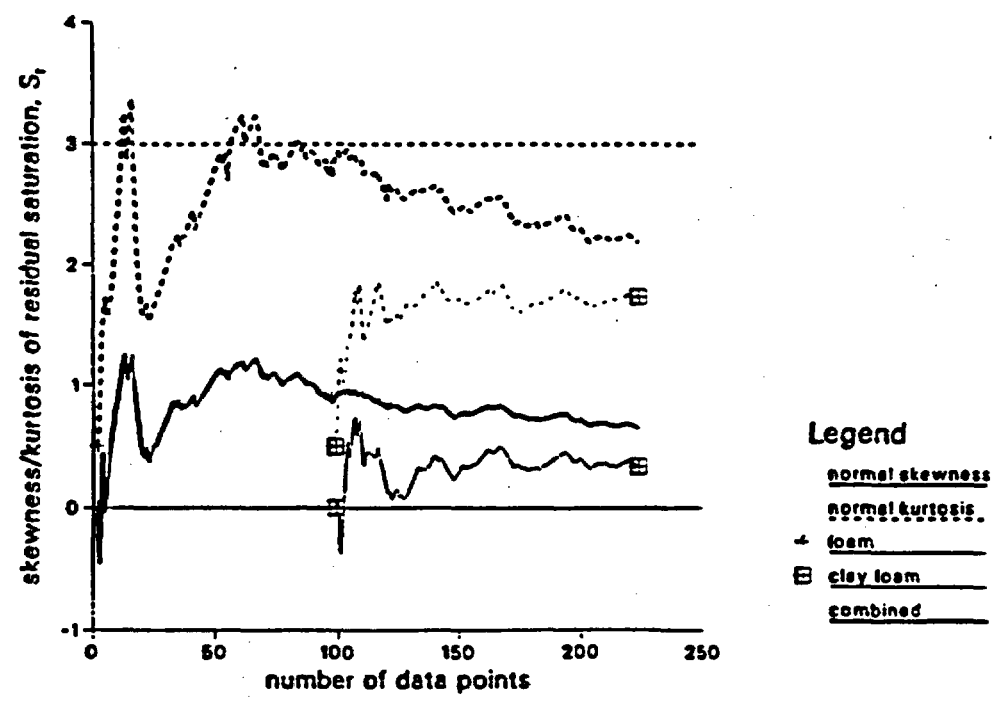

Figure A-10. Distributions of Loamy Watershed Soil Residual Saturation (concluded).

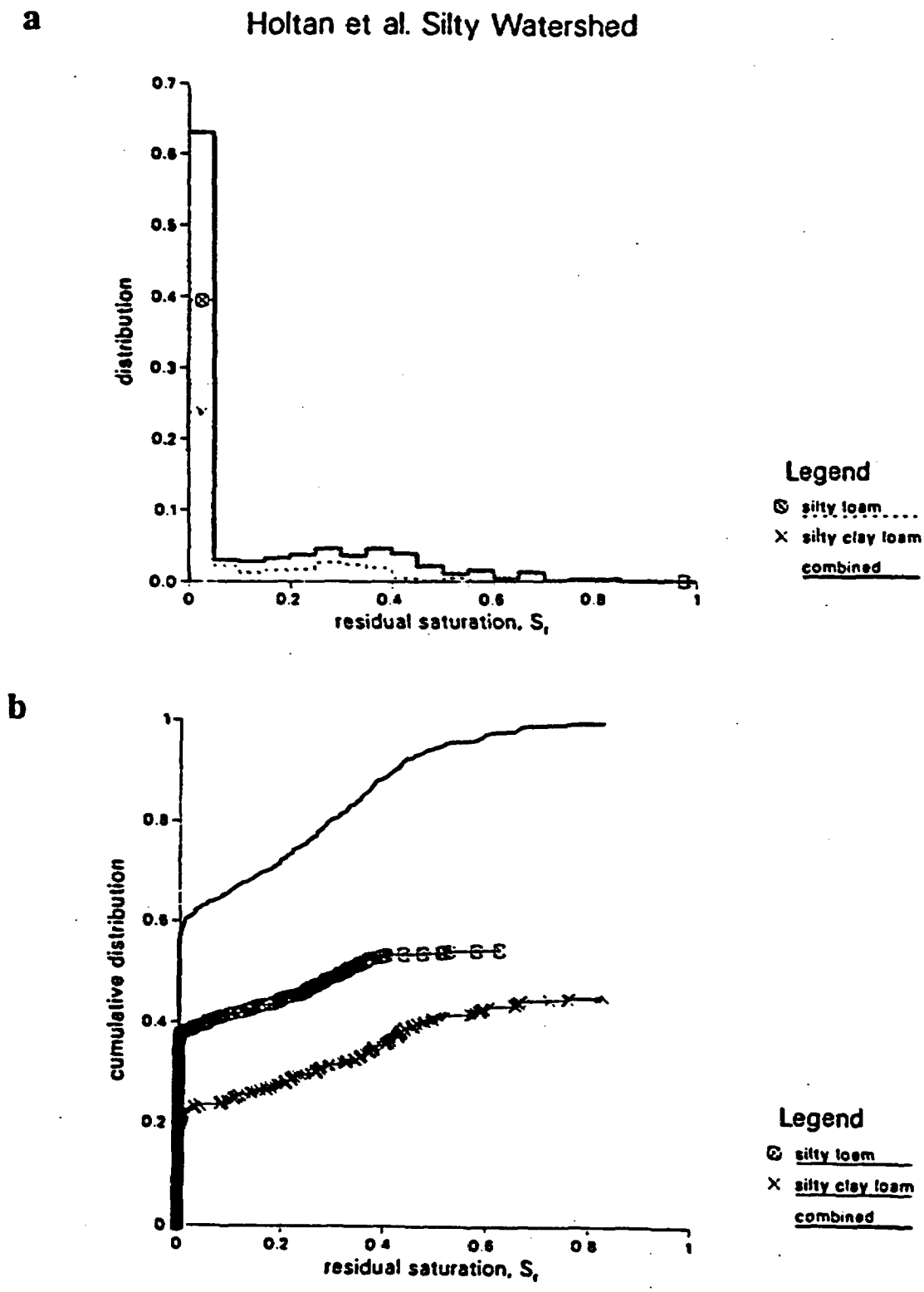

Figure A-11. Distributions of Silty Watershed Soil Residual Saturation.

c

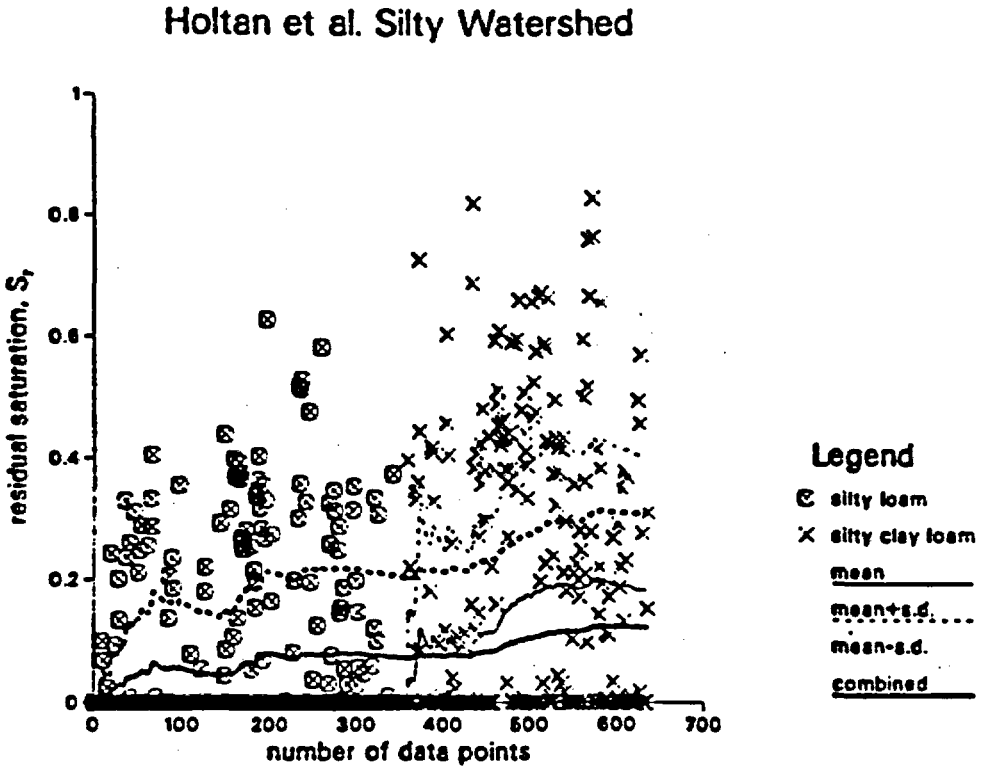

d

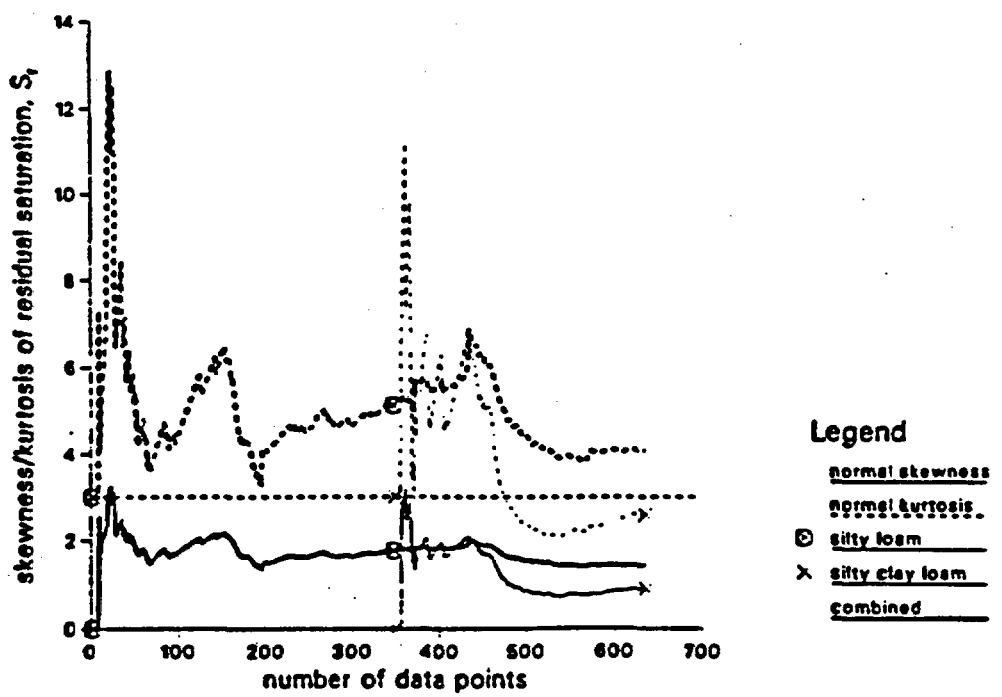

Figure A-11. Distributions of Silty Watershed Soil Residual Saturation (concluded).

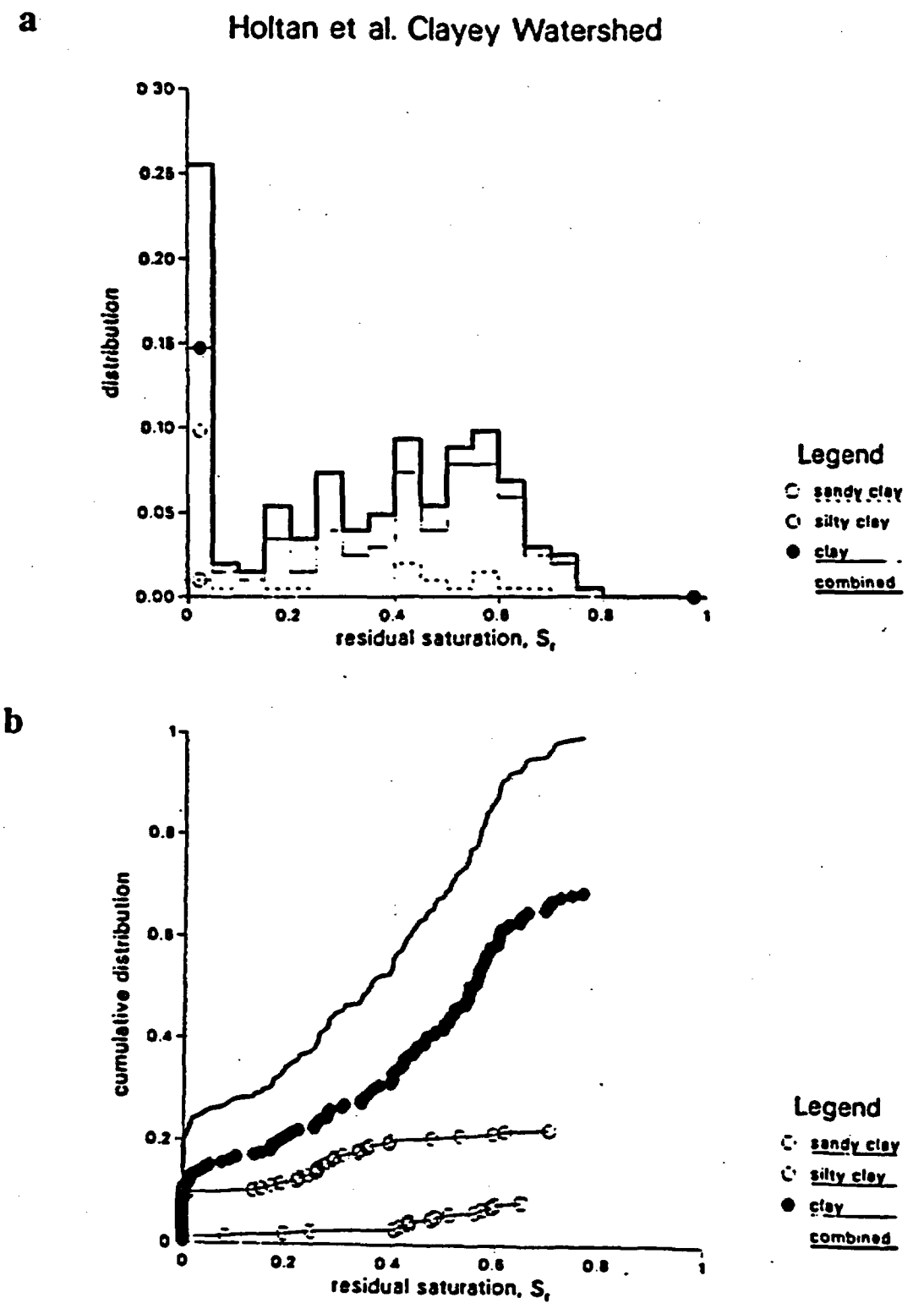

Figure A-12. Distributions of Clayey Watershed Soil Residual Saturation.

c

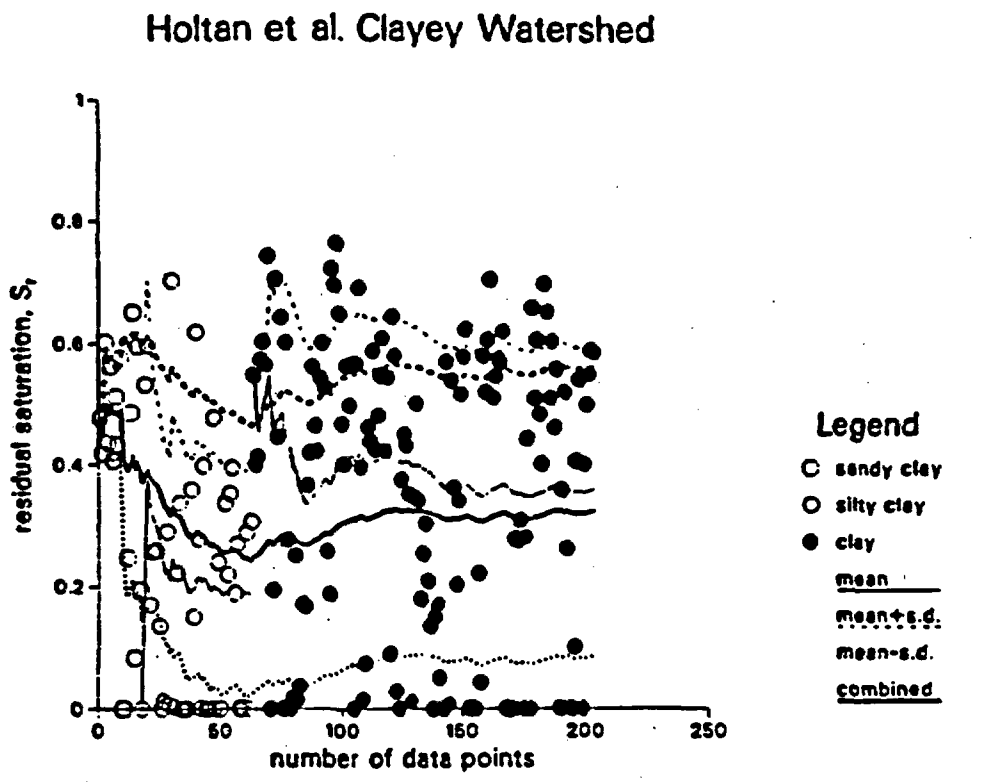

d

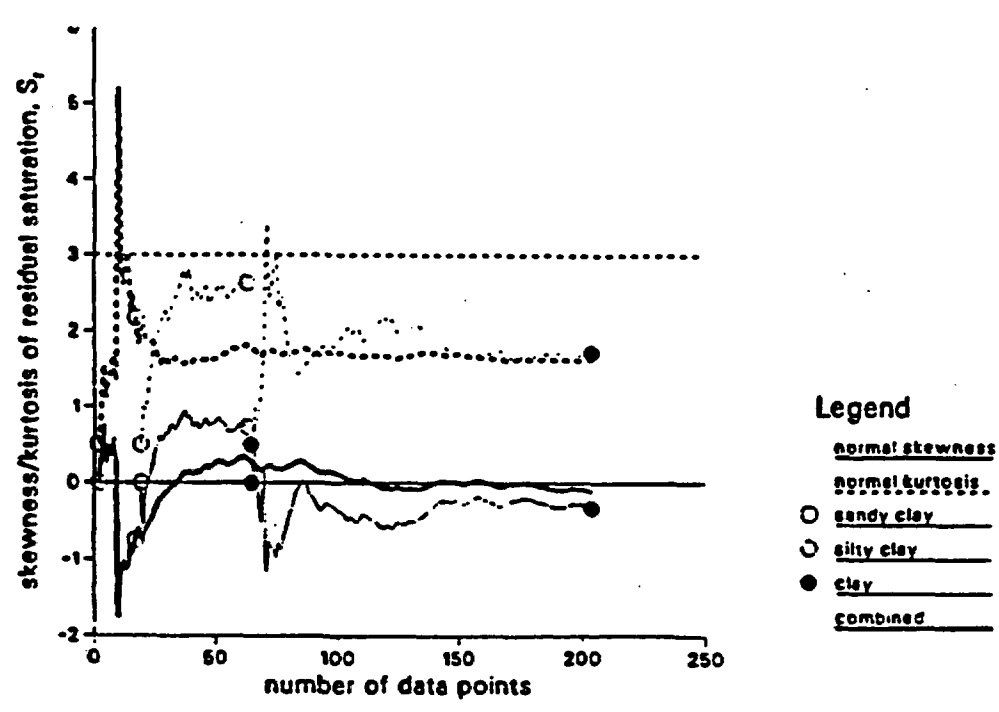

Figure A-12. Distributions of Clayey Watershed Soil Residual Saturation (concluded).

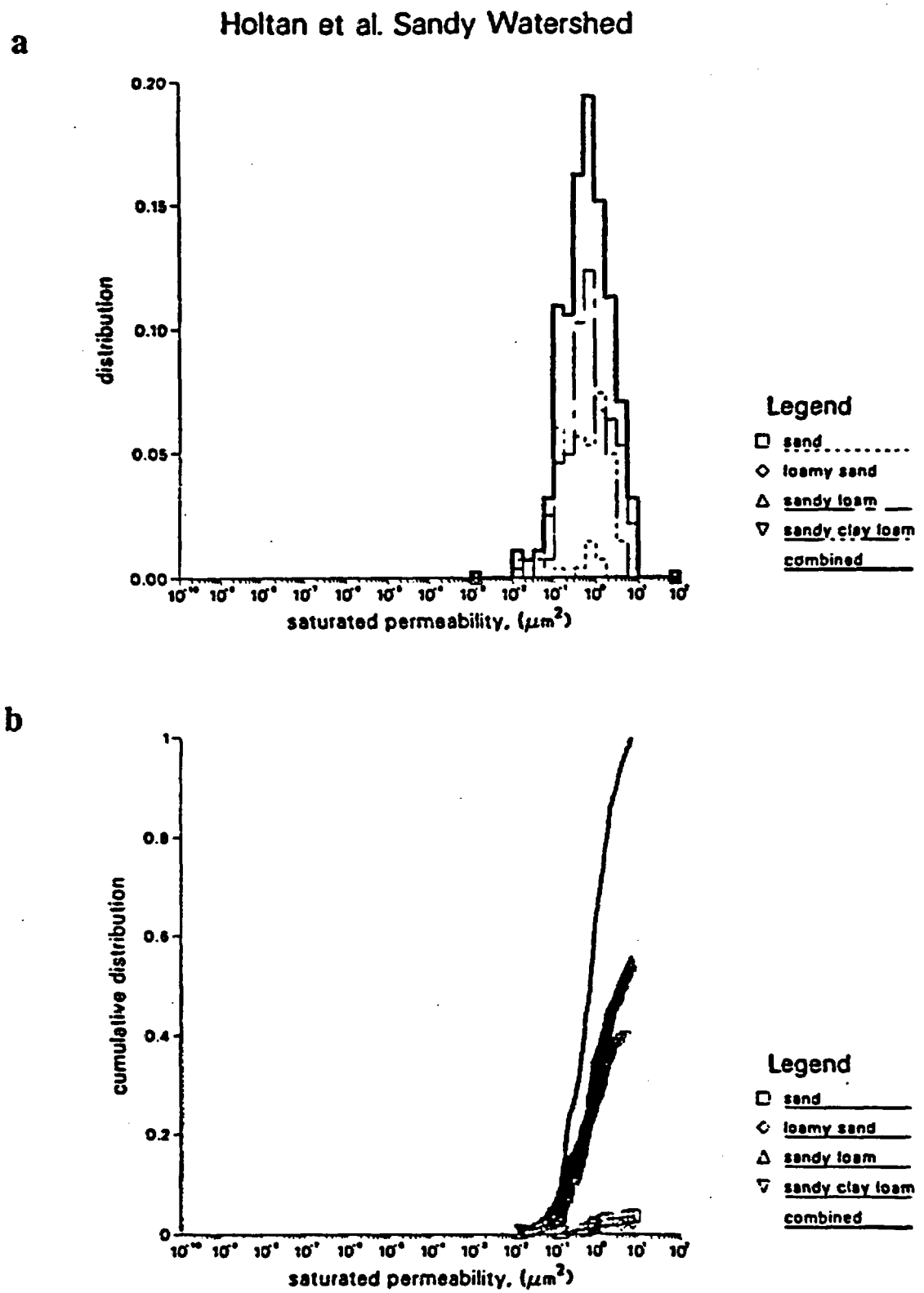

Figure A-13. Distributions of Sandy Watershed Soil Log Saturated Permeability.

c

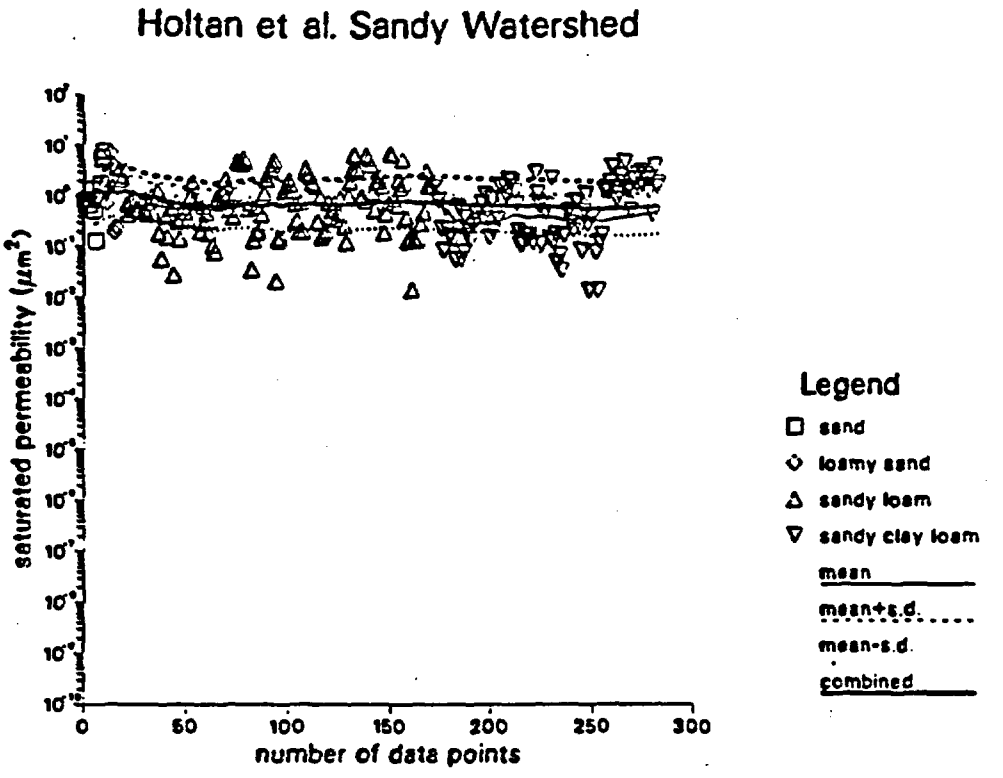

d

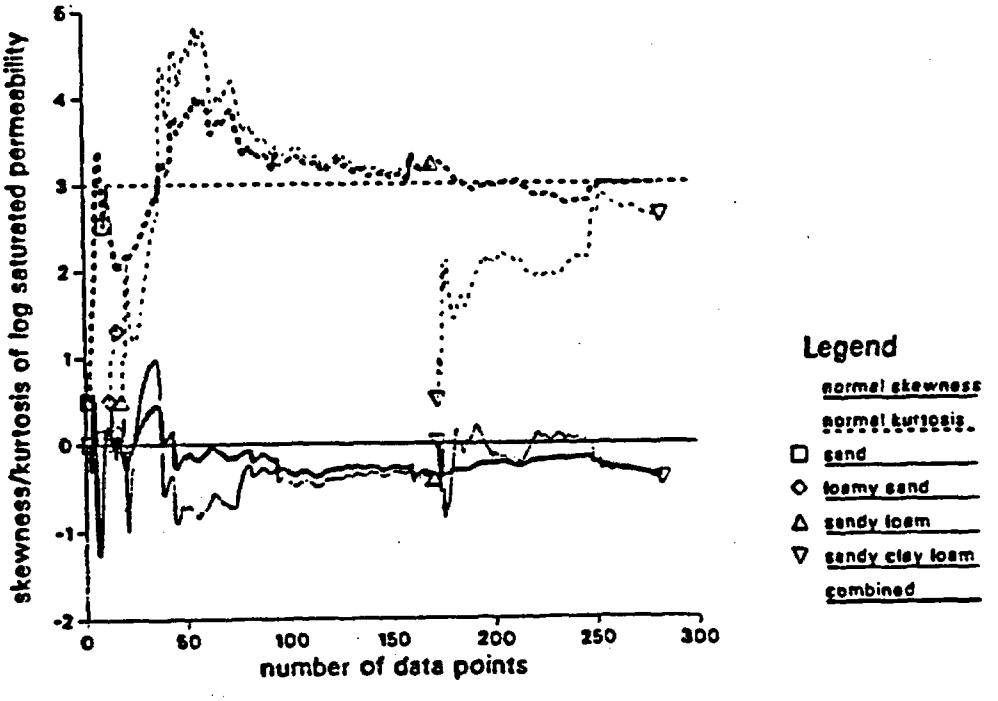

Figure A-13. Distributions of Sandy Watershed Soil Log Saturated Permeability (concluded).

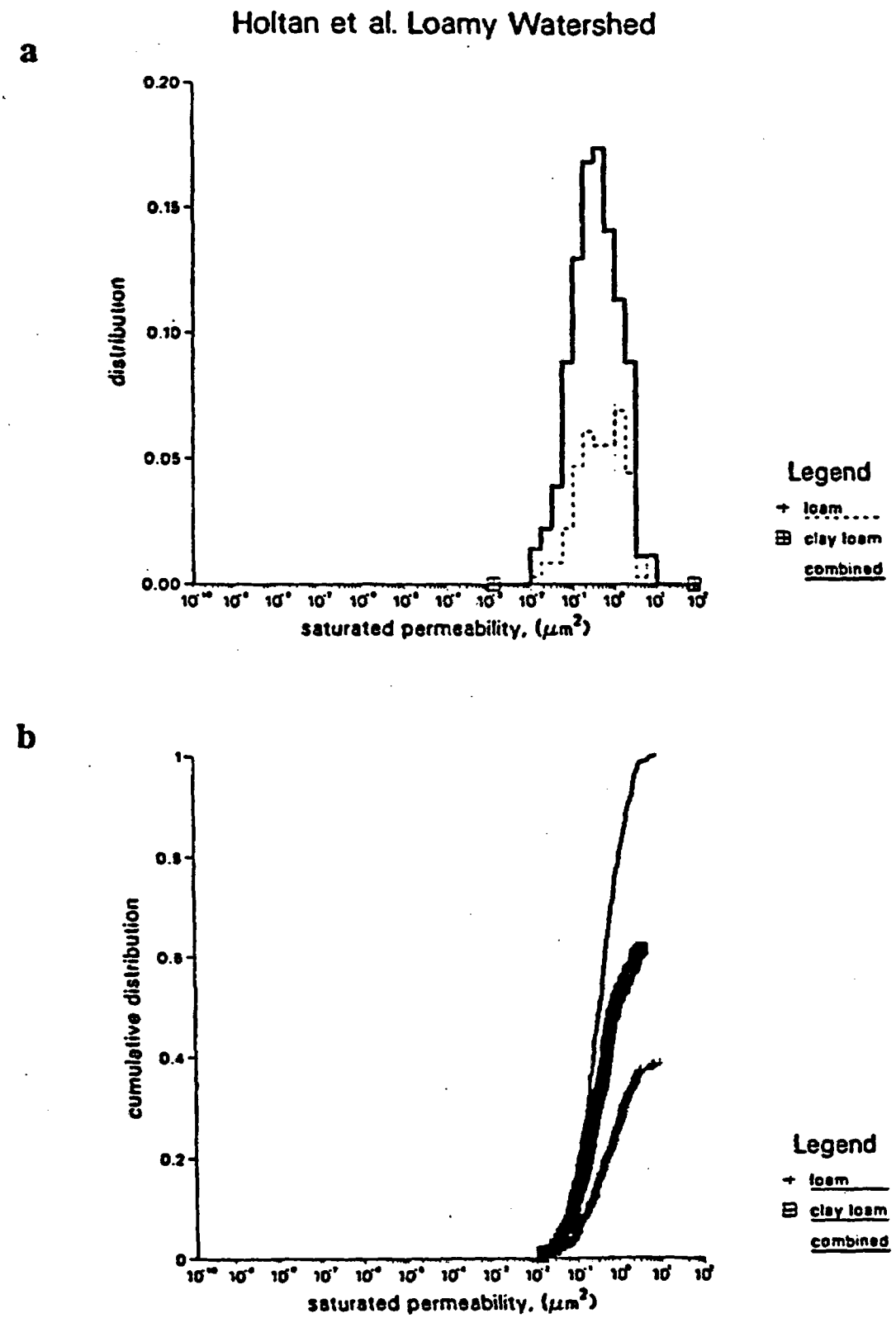

Figure A-14. Distributions of Loamy Watershed Soil Log Saturated Permeability.

c

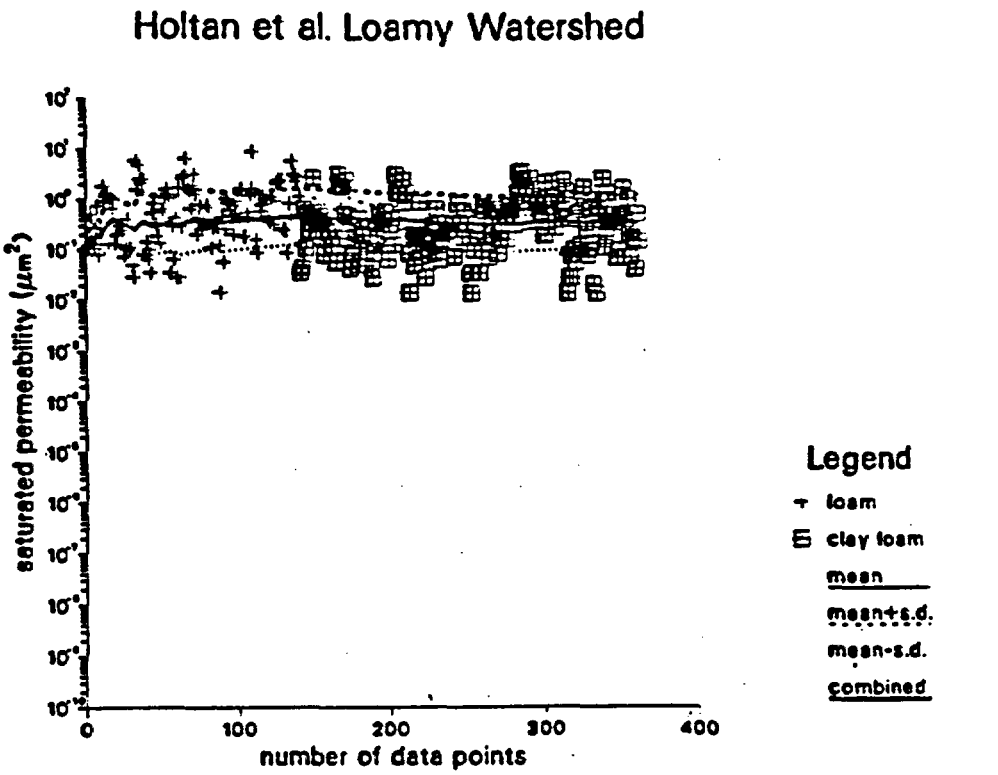

d

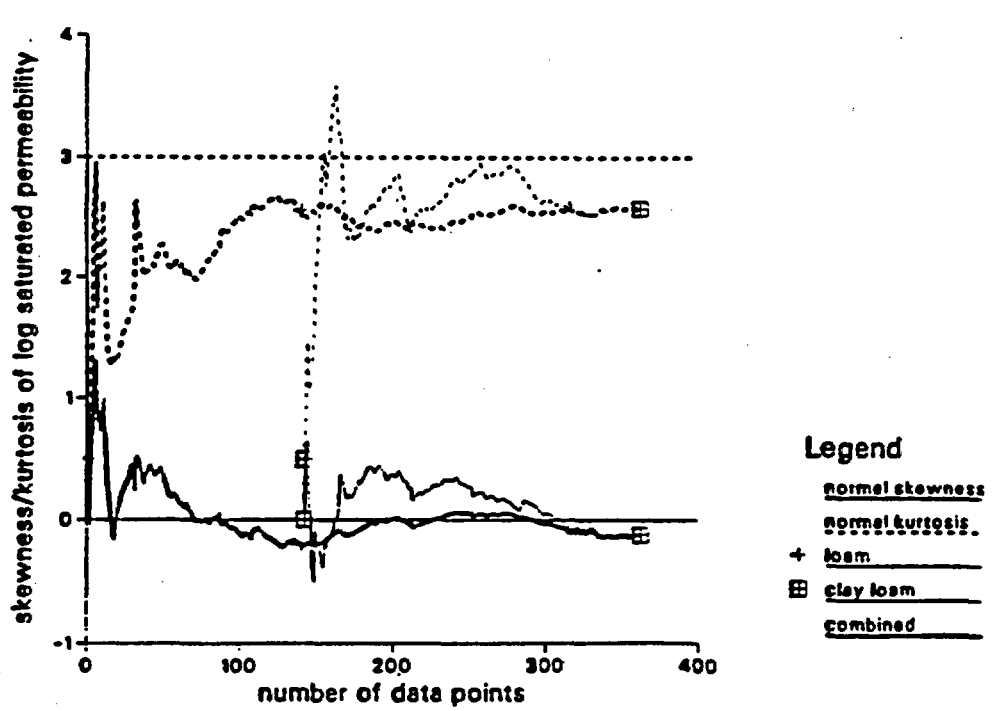

Figure A-14. Distributions of Loamy Watershed Soil Log Saturated Permeability (concluded).

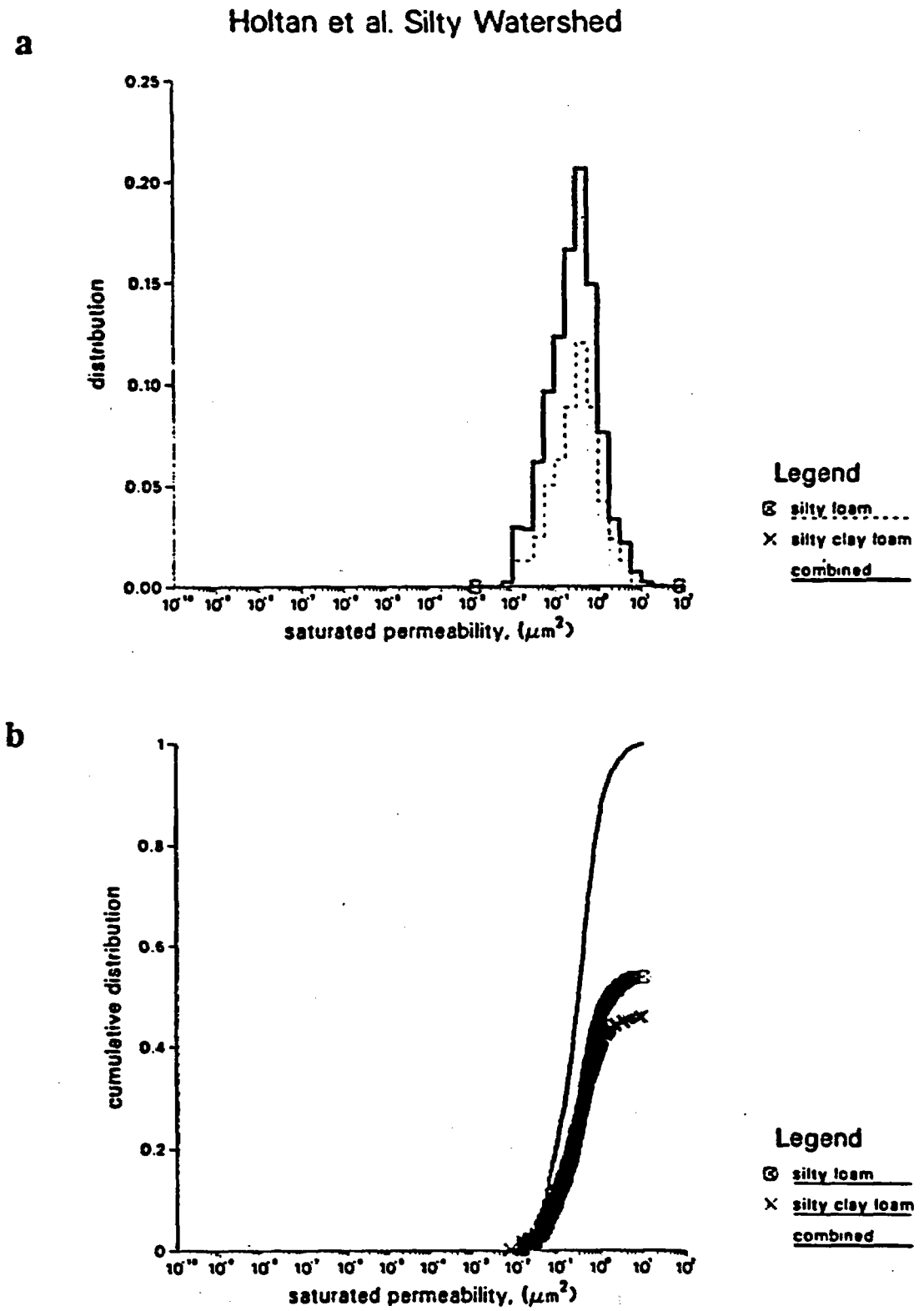

Figure A-15. Distributions of Silty Watershed Soil Log Saturated Permeability.

c

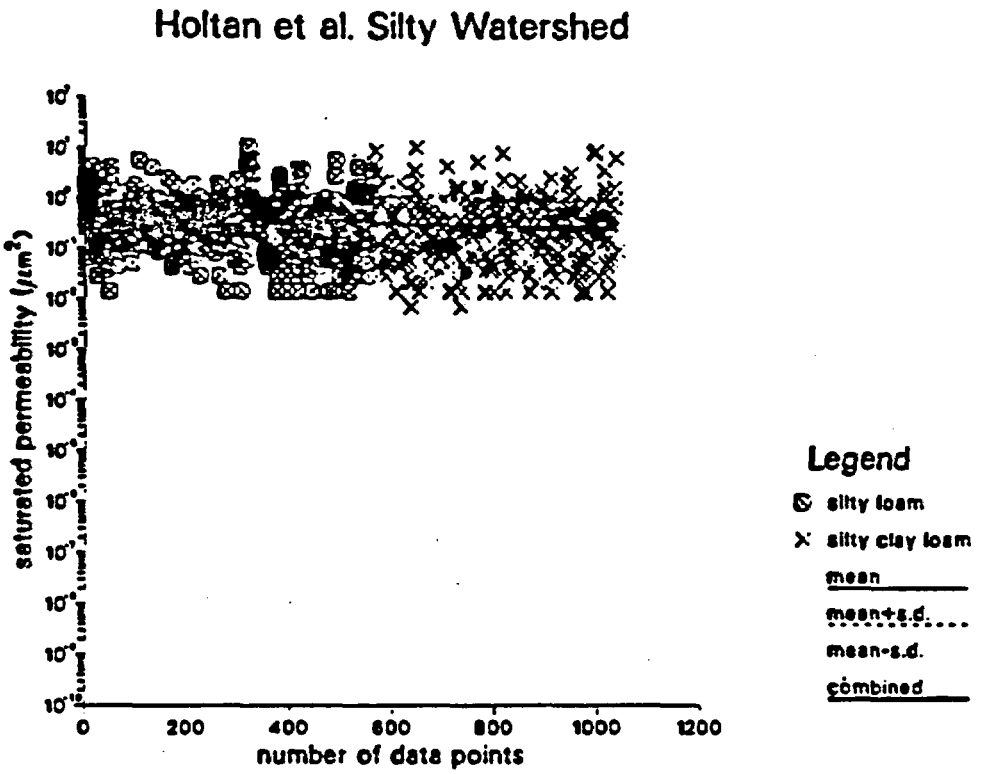

d

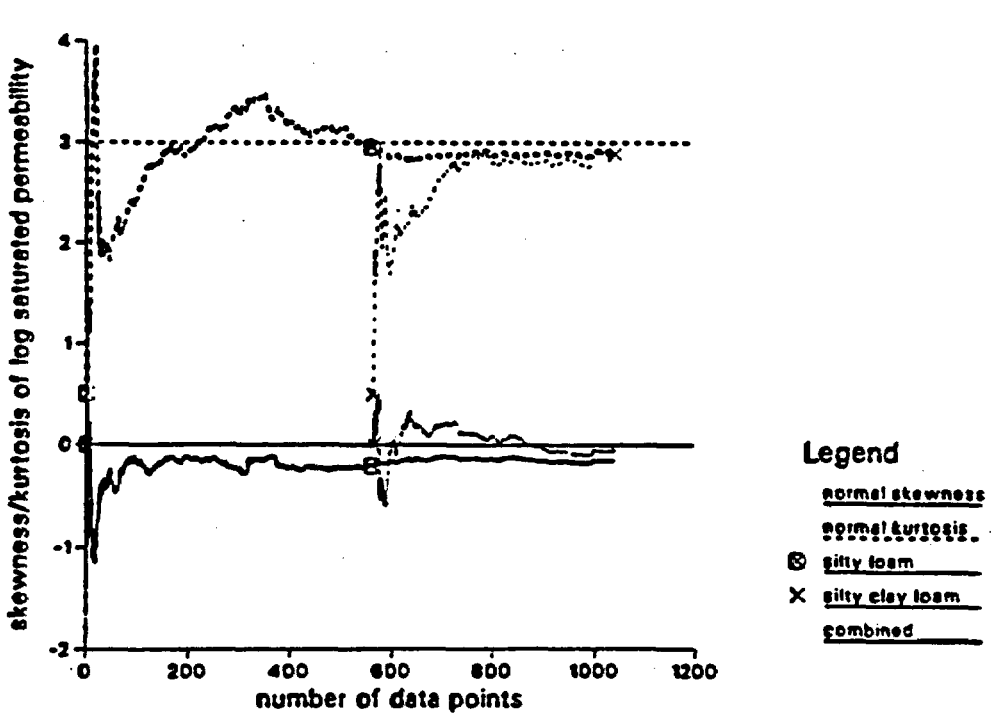

Figure A-15. Distributions of Silty Watershed Soil Log Saturated Permeability (concluded).

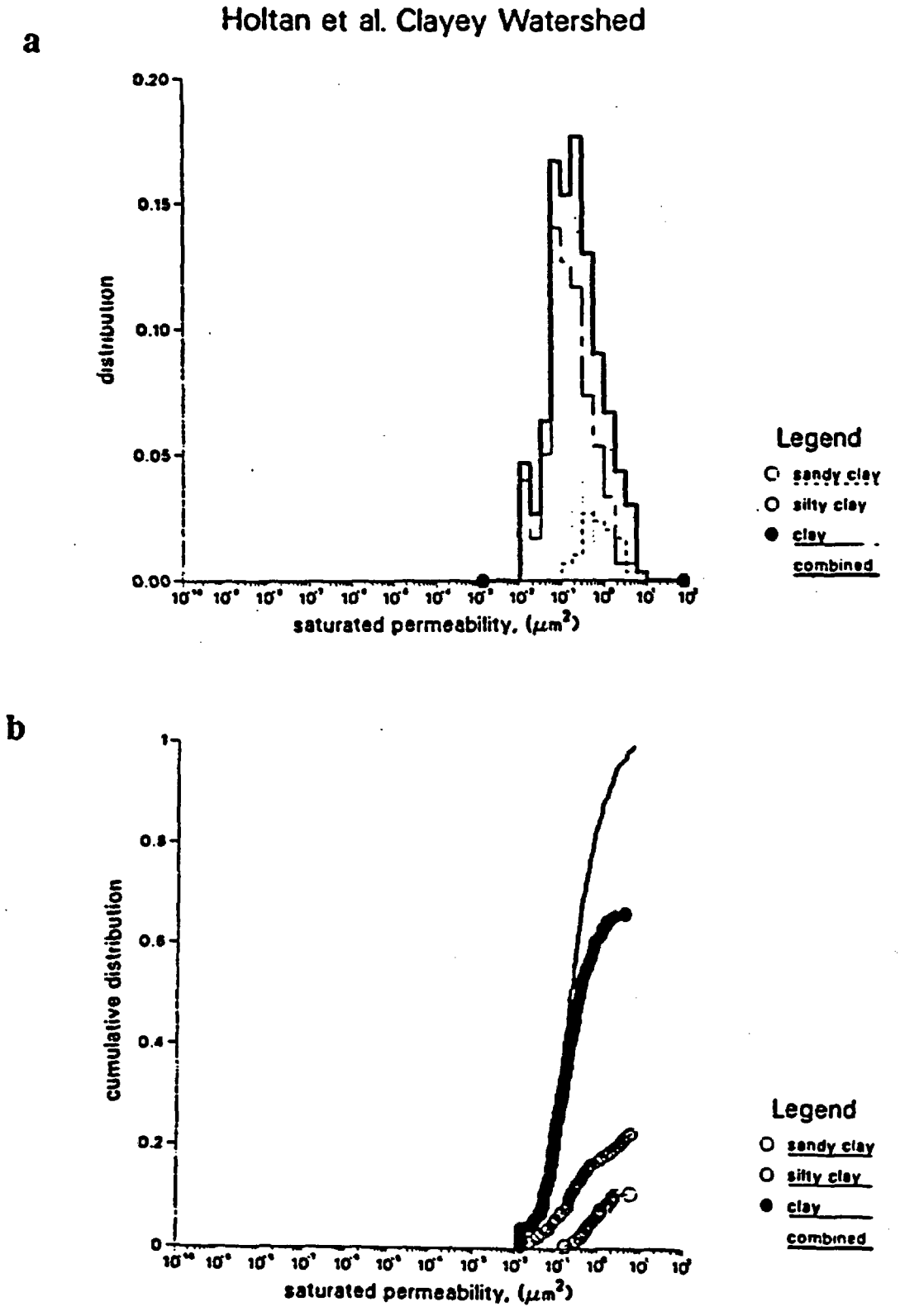

Figure A-16. Distributions of Clayey Watershed Soil Log Saturated Permeability.

c

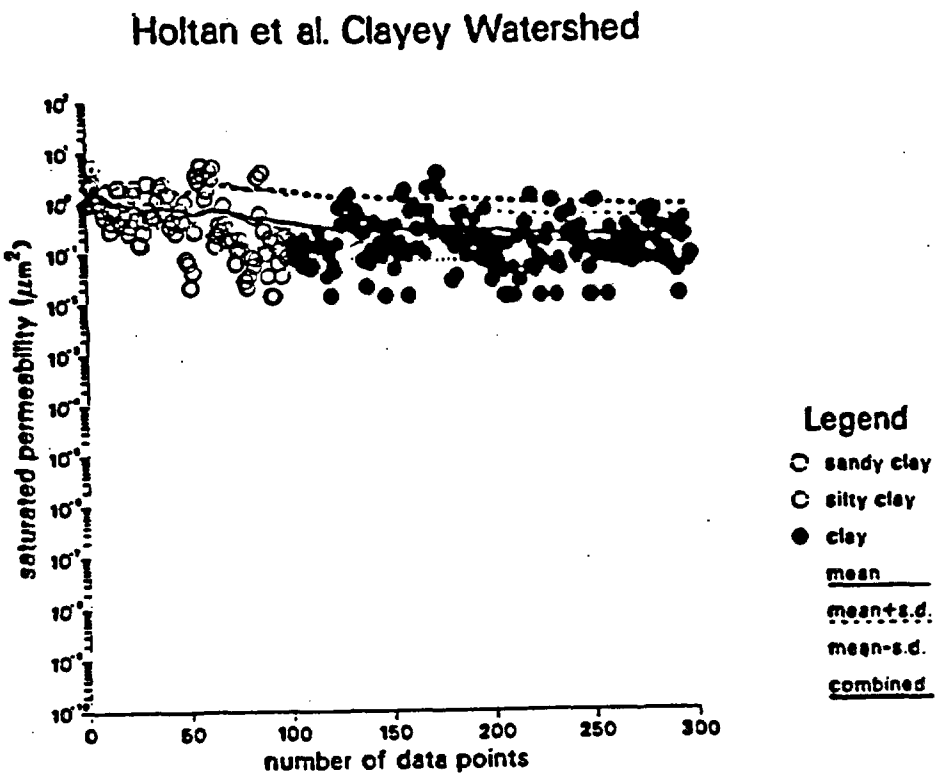

d

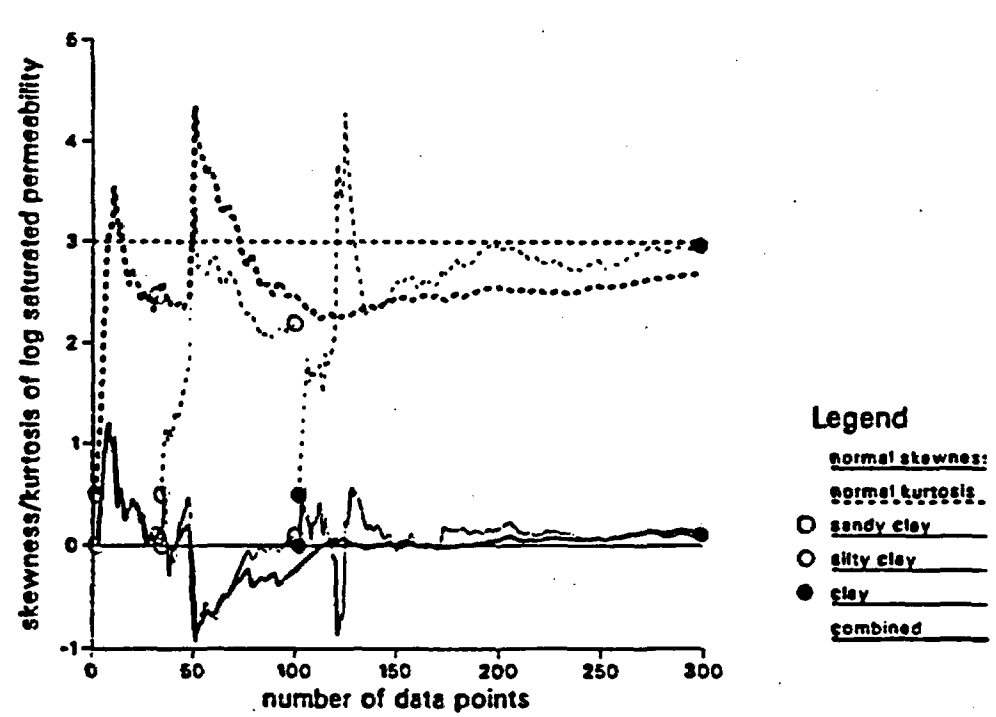

Figure A-16. Distributions of Clayey Watershed Soil Log Saturated Permeability (concluded).

a

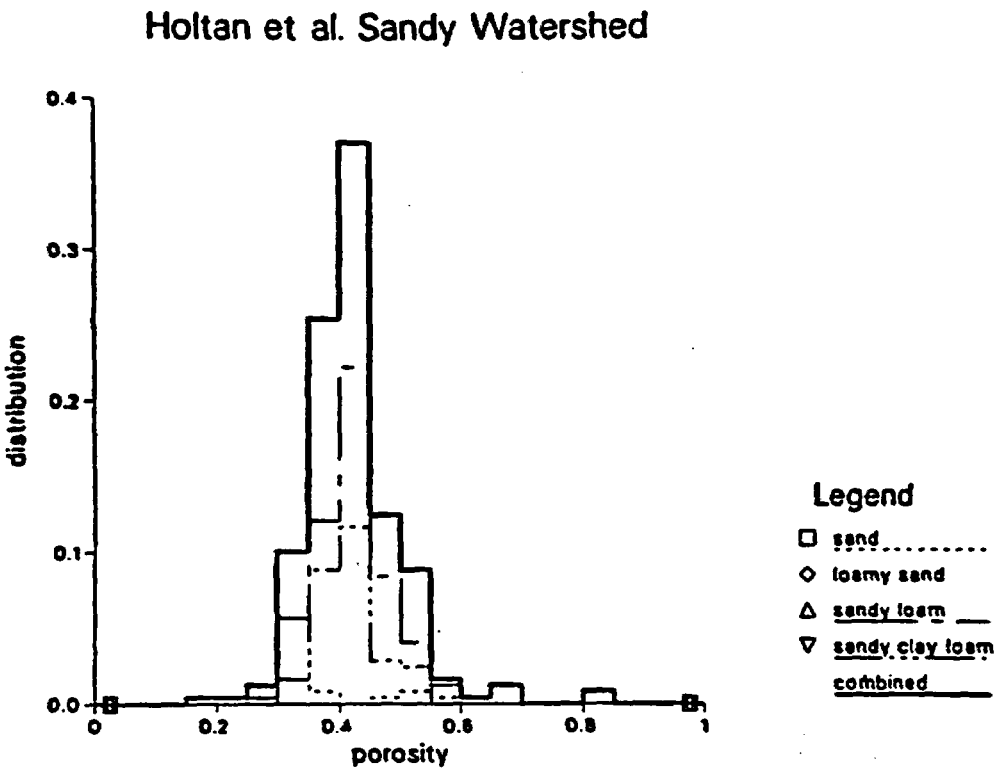

b

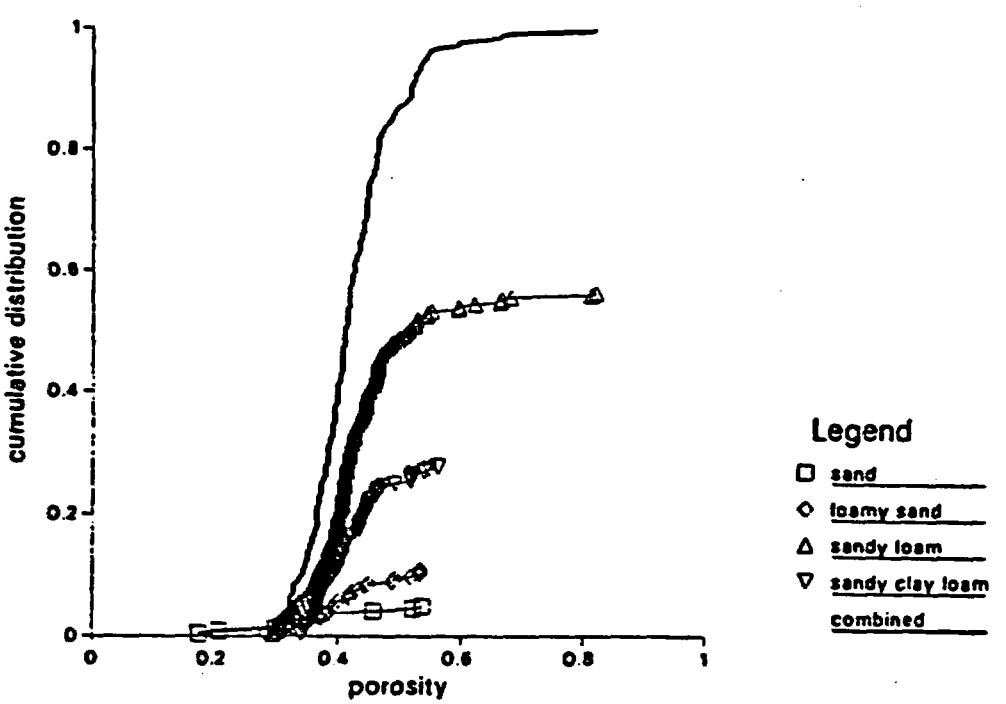

Figure A-17. Distributions of Sandy Watershed Soil Porosity.

c

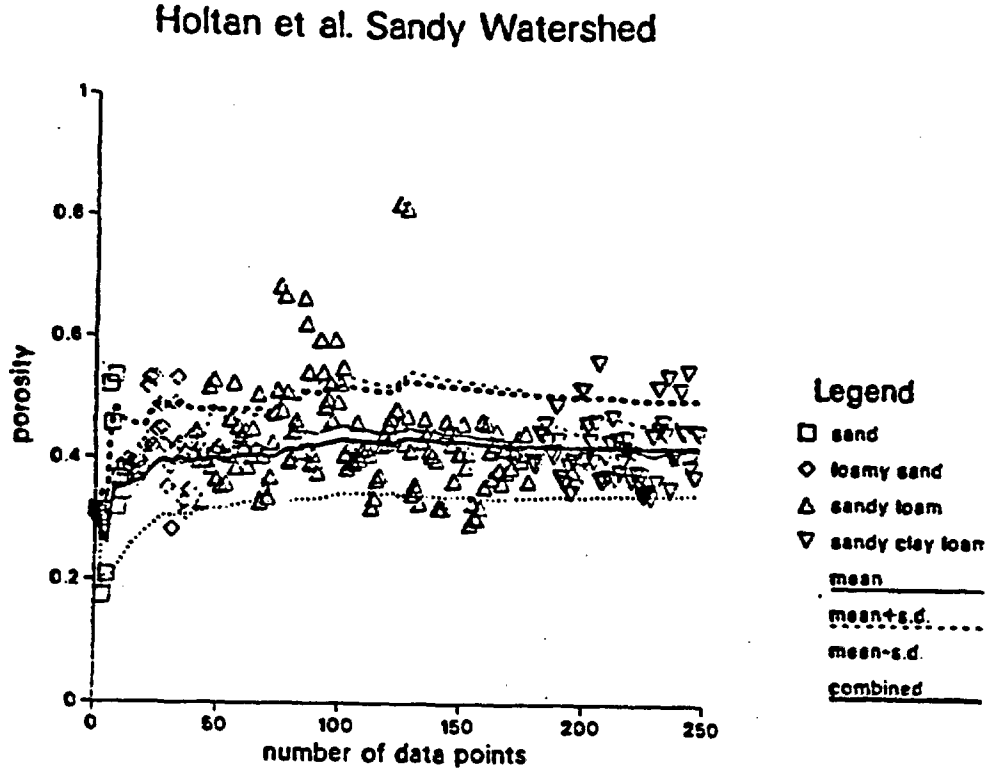

d

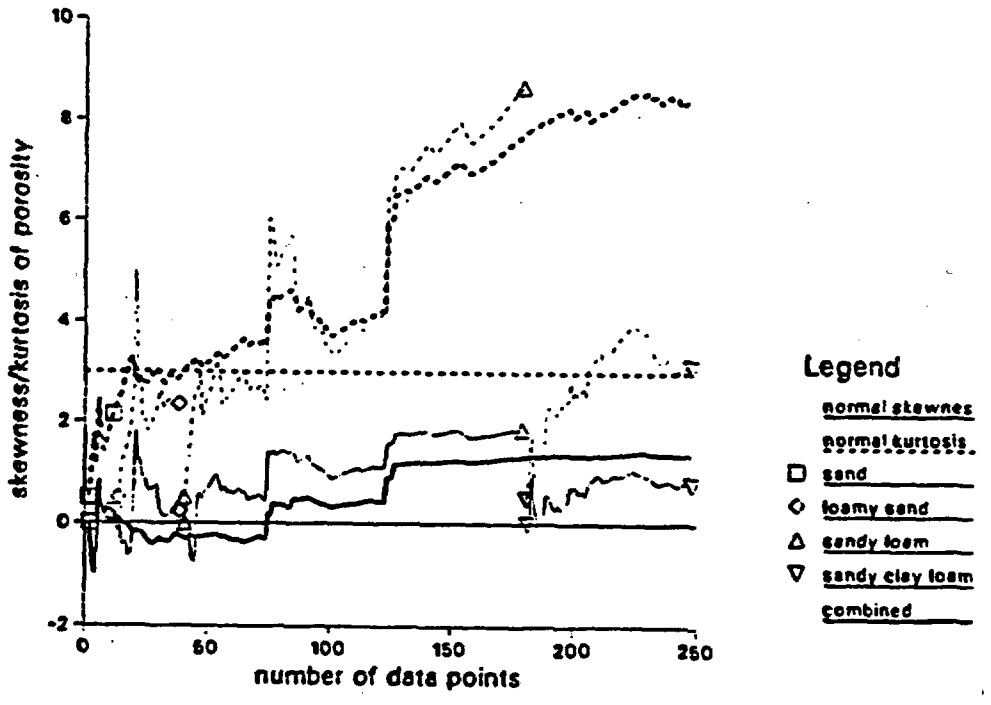

Figure A-17. Distributions of Sandy Watershed Soil Porosity (concluded).

a

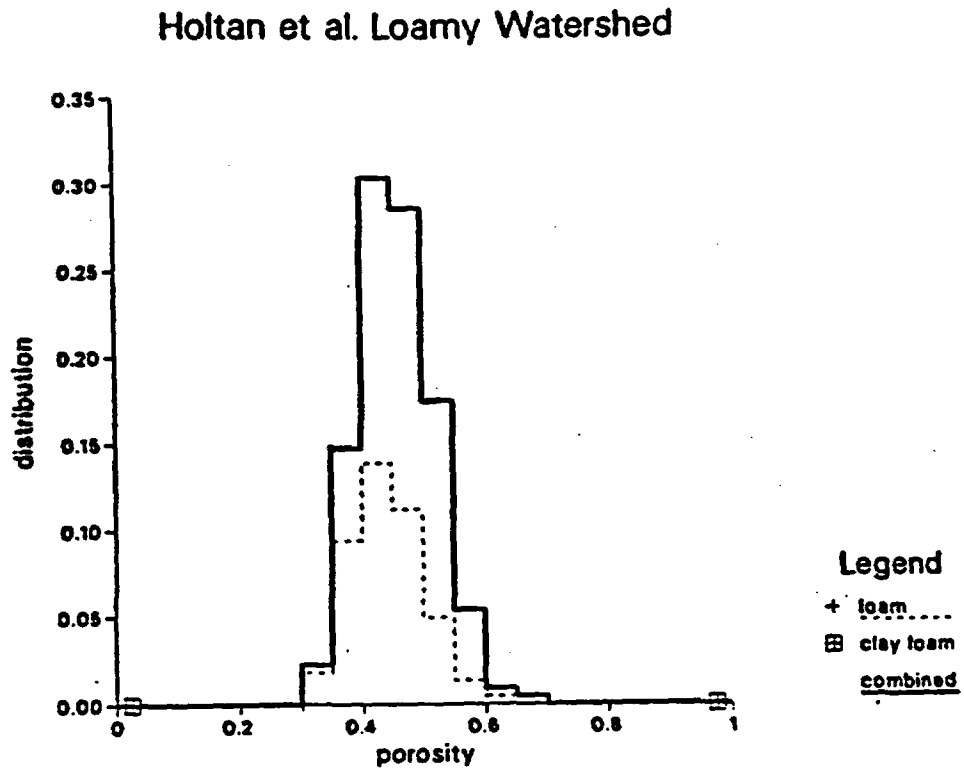

b

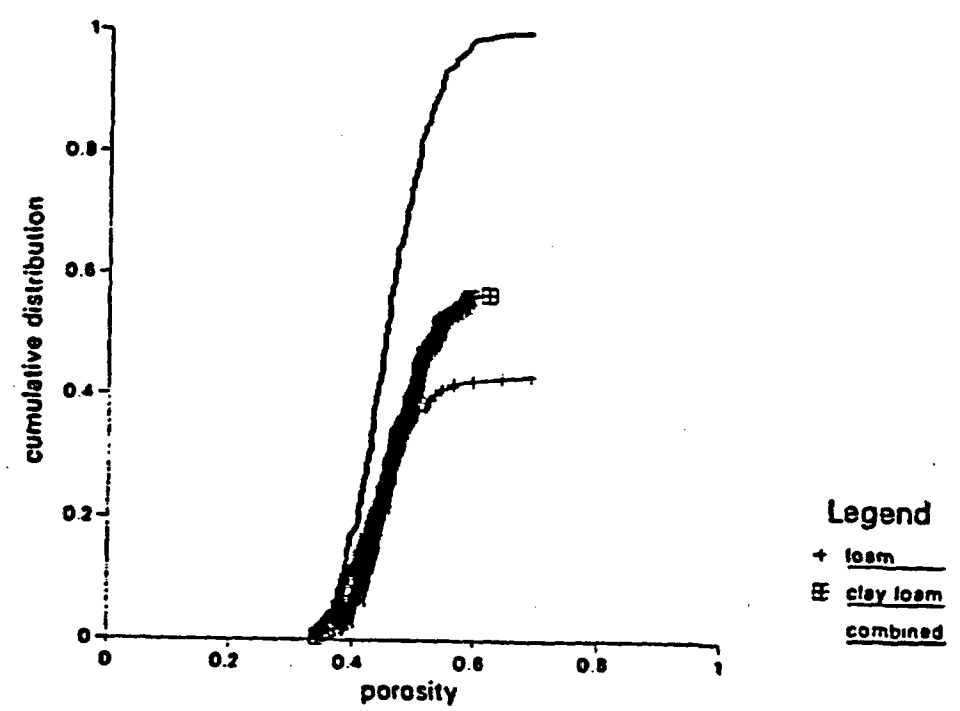

Figure A-18. Distributions of Loamy Watershed Soil Porosity.

c

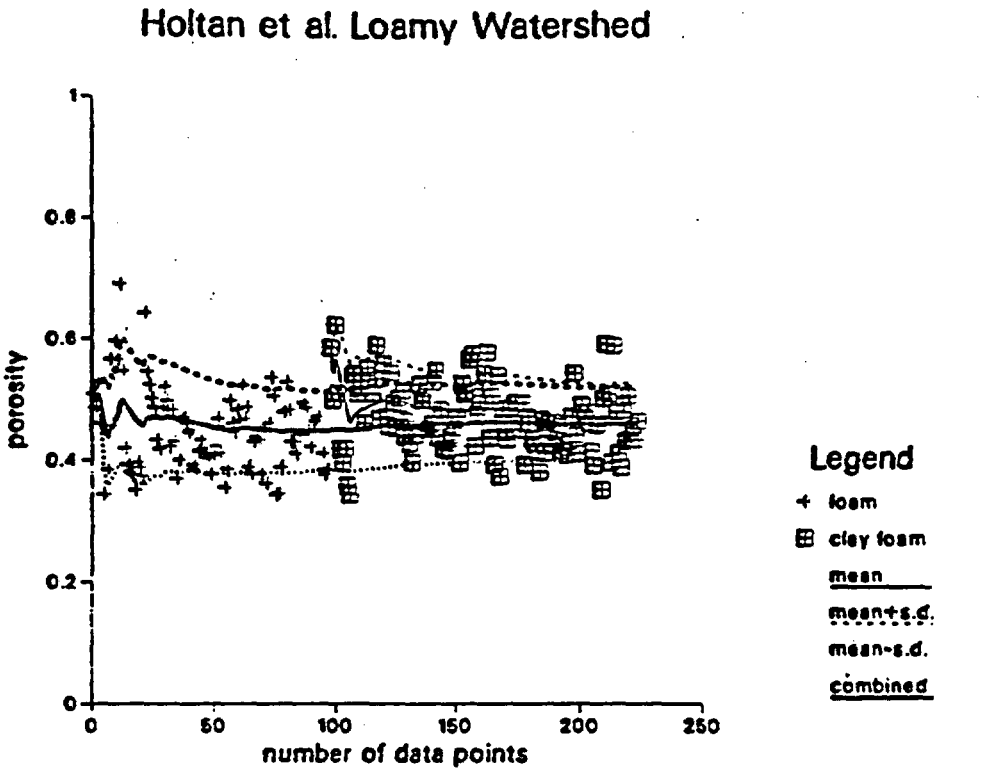

d

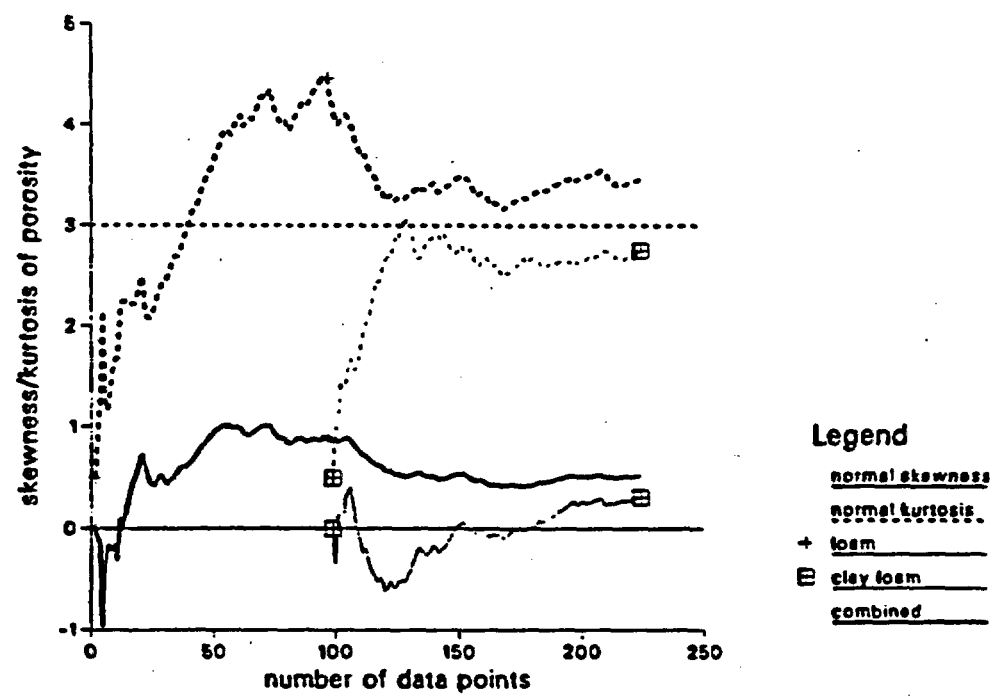

Figure A-18. Distributions of Loamy Watershed Soil Porosity (concluded).

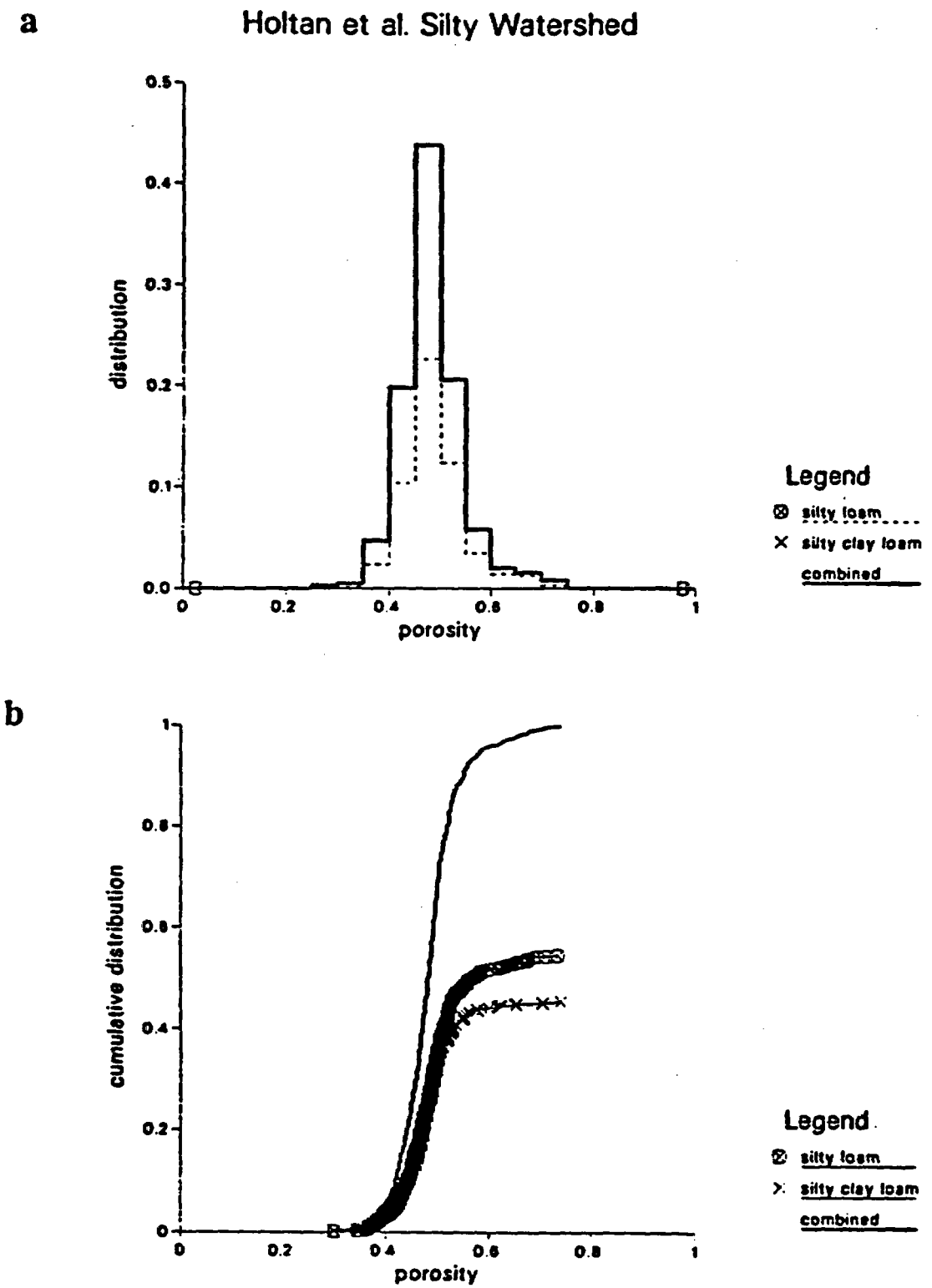

Figure A-19. Distributions of Silty Watershed Soil Porosity.

c

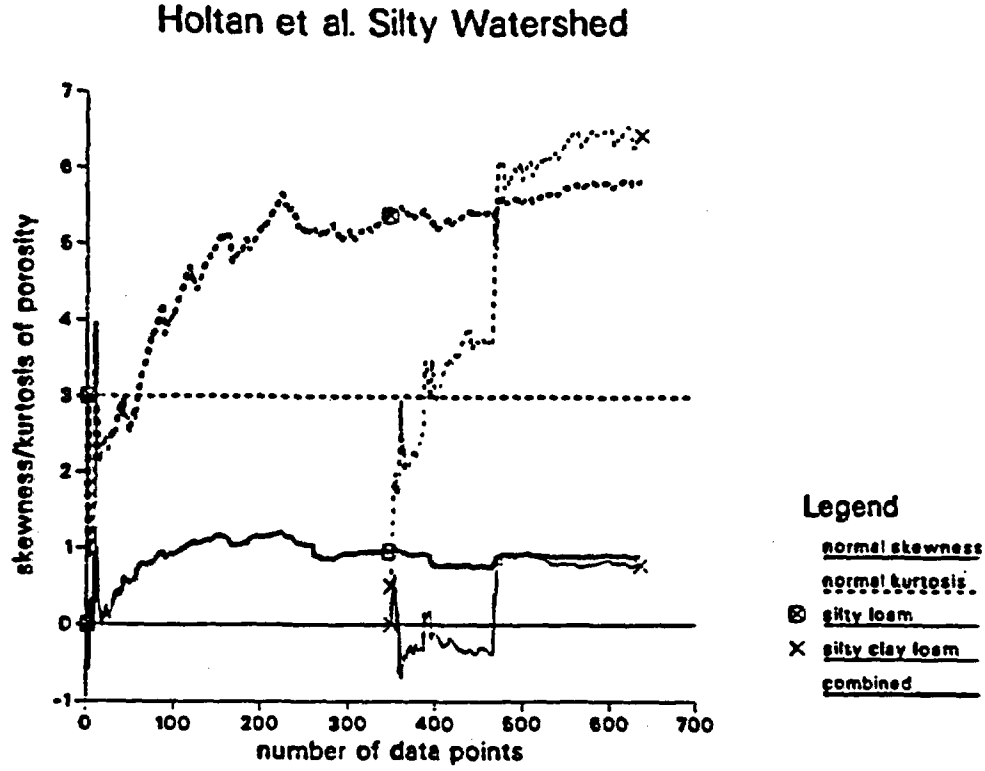

d

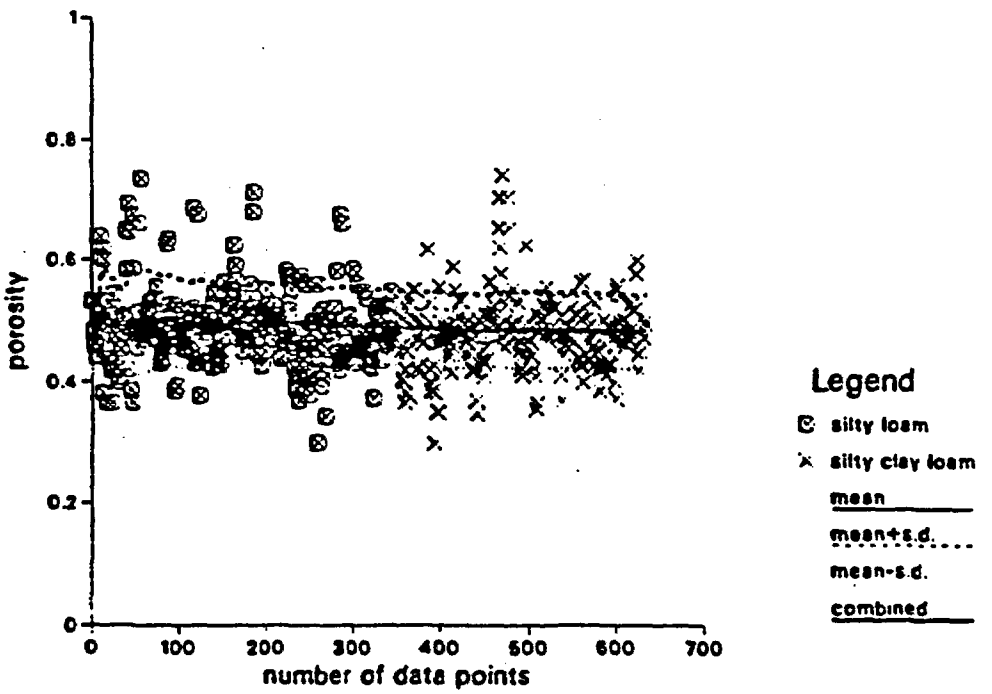

Figure A-19. Distributions of Silty Watershed Soil Porosity (concluded).

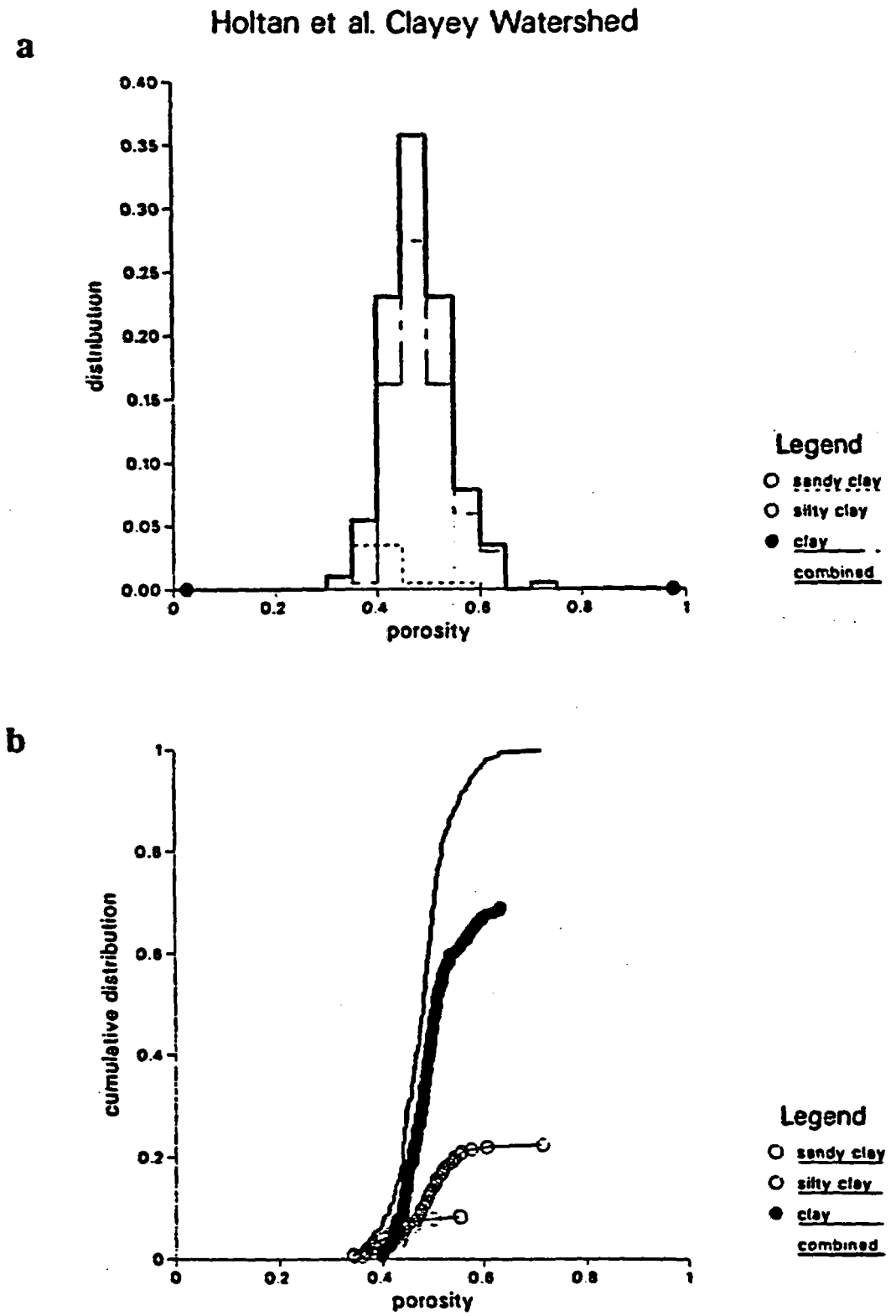

Figure A-20. Distributions of Clayey Watershed Soil Porosity.

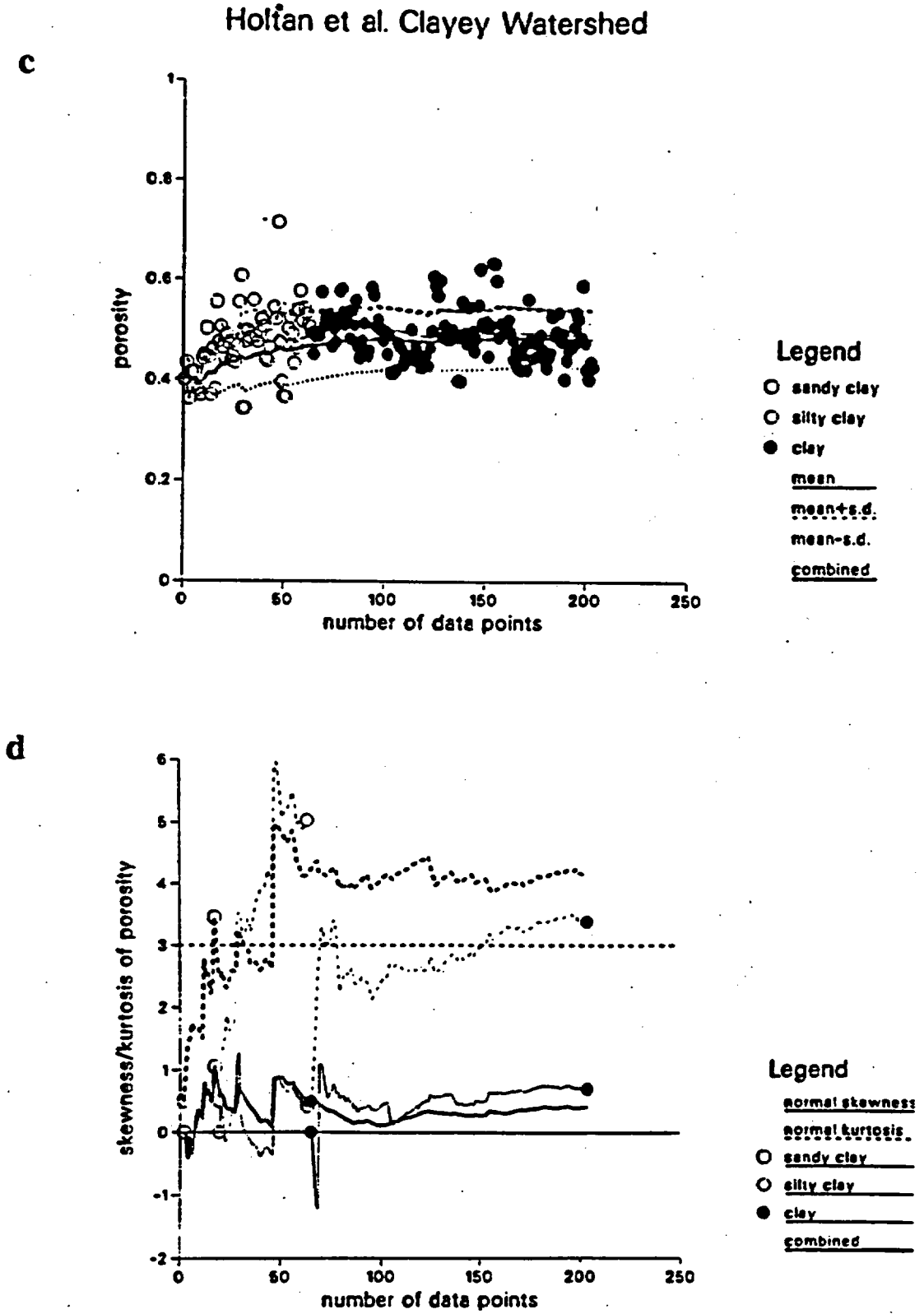

Figure A-20. Distributions of Clayey Watershed Soil Porosity (concluded).

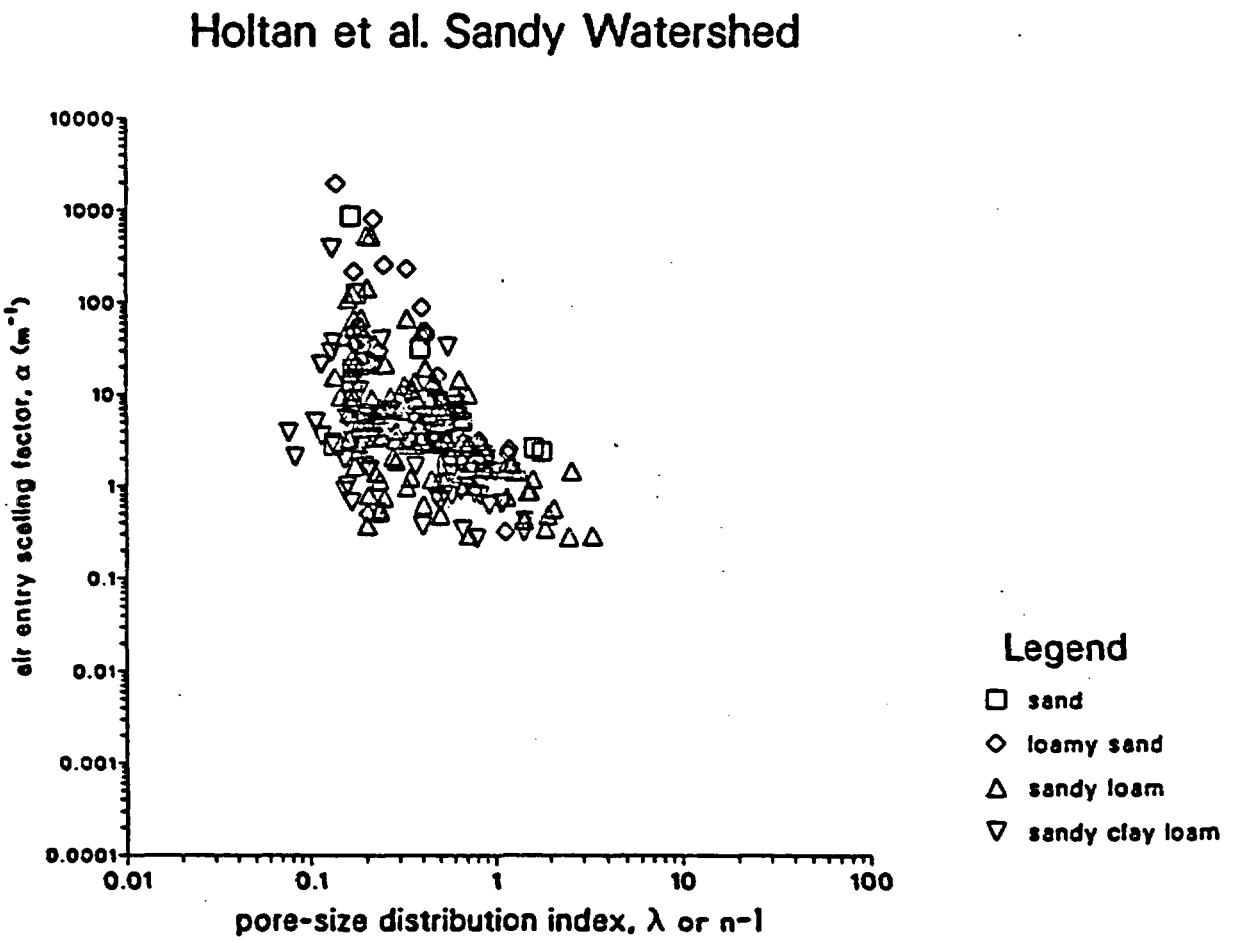

Figure A-21. Correlation Between Air Entry Scaling Factor and Pore-Size Distribution Index for Sandy Watershed Soil.

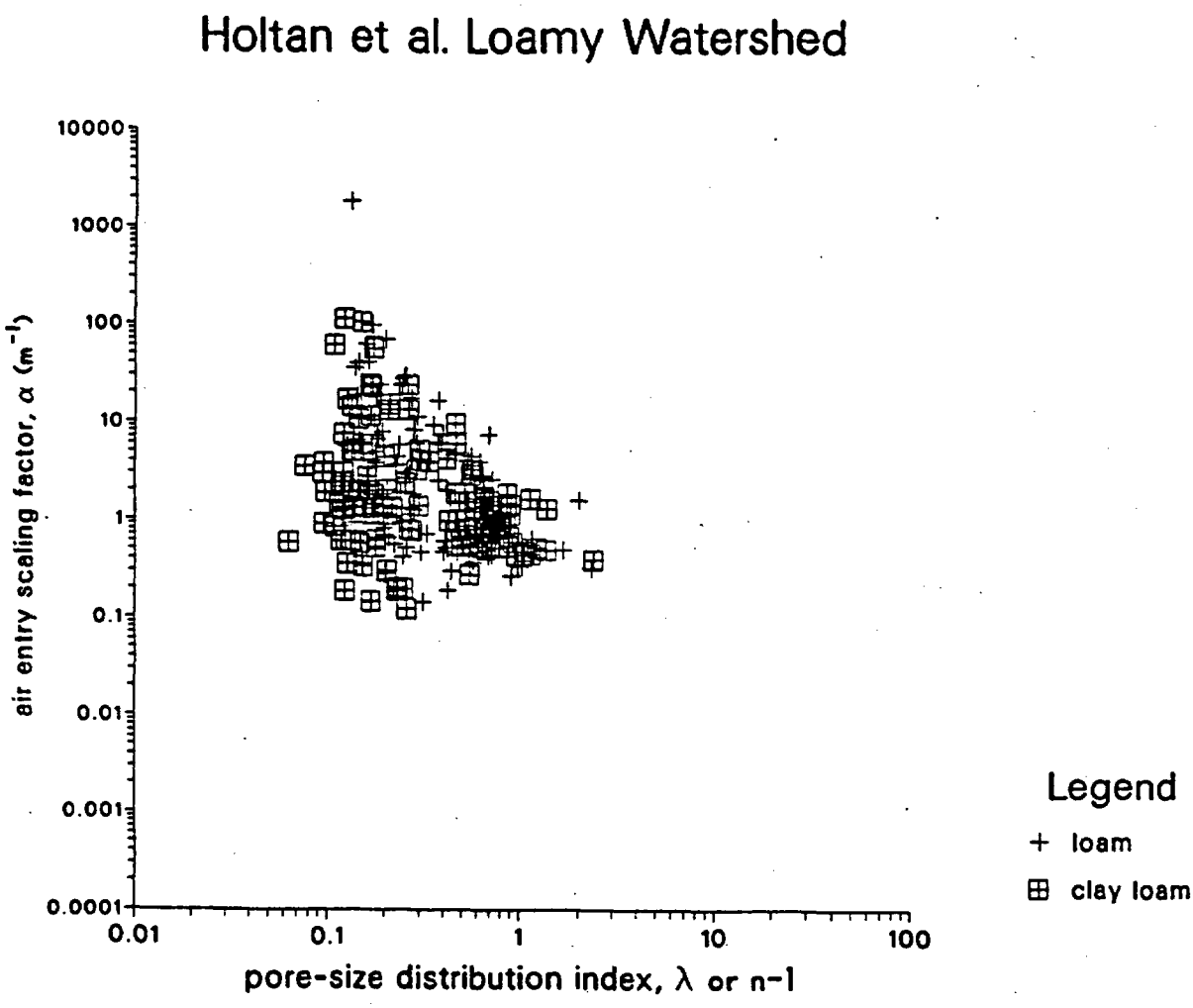

Figure A-22. Correlation Between Air Entry Scaling Factor and Pore-Size Distribution Index for Loamy Watershed Soil.

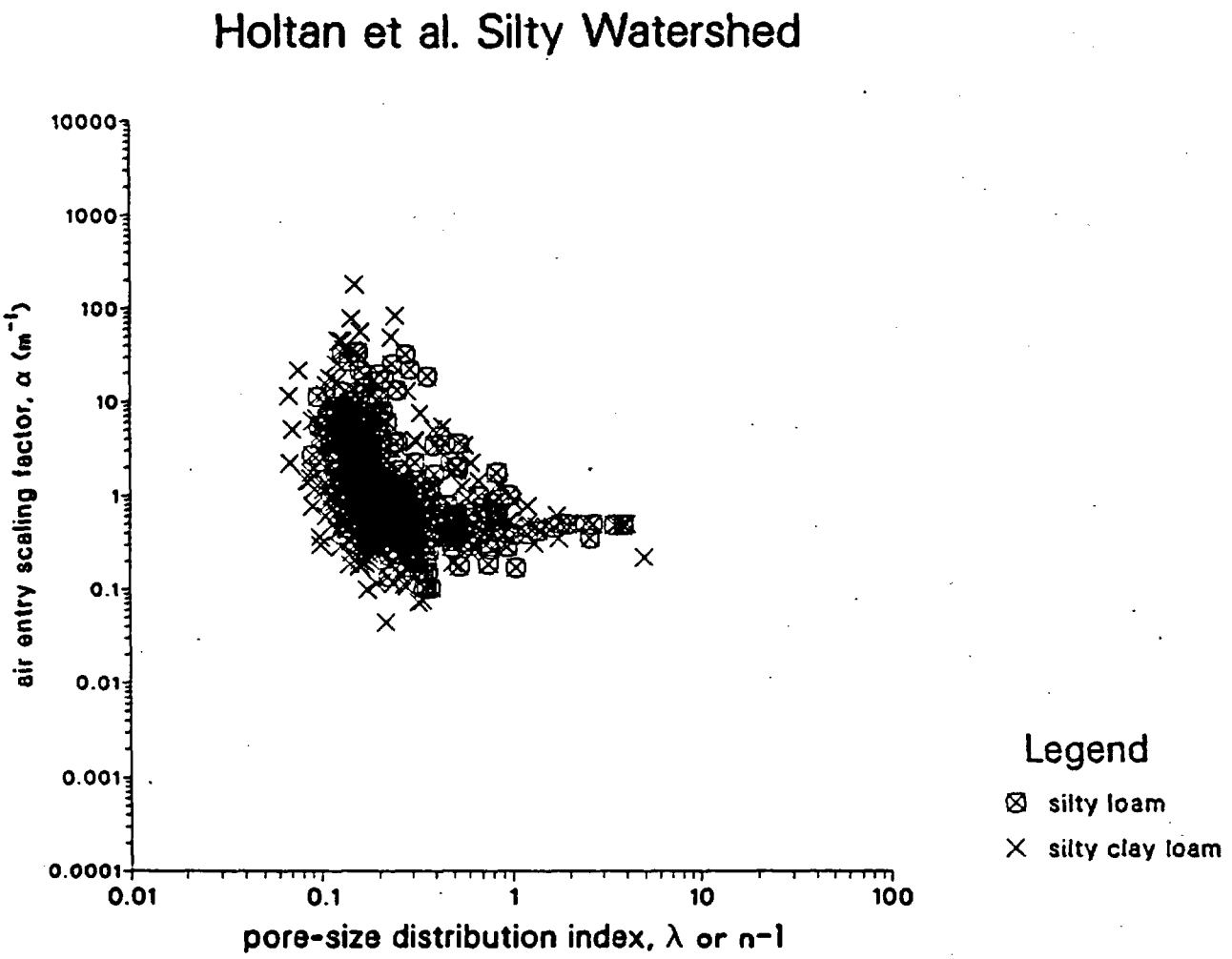

Figure A-23. Correlation Between Air Entry Scaling Factor and Pore-Size Distribution Index for Silty Watershed Soil.

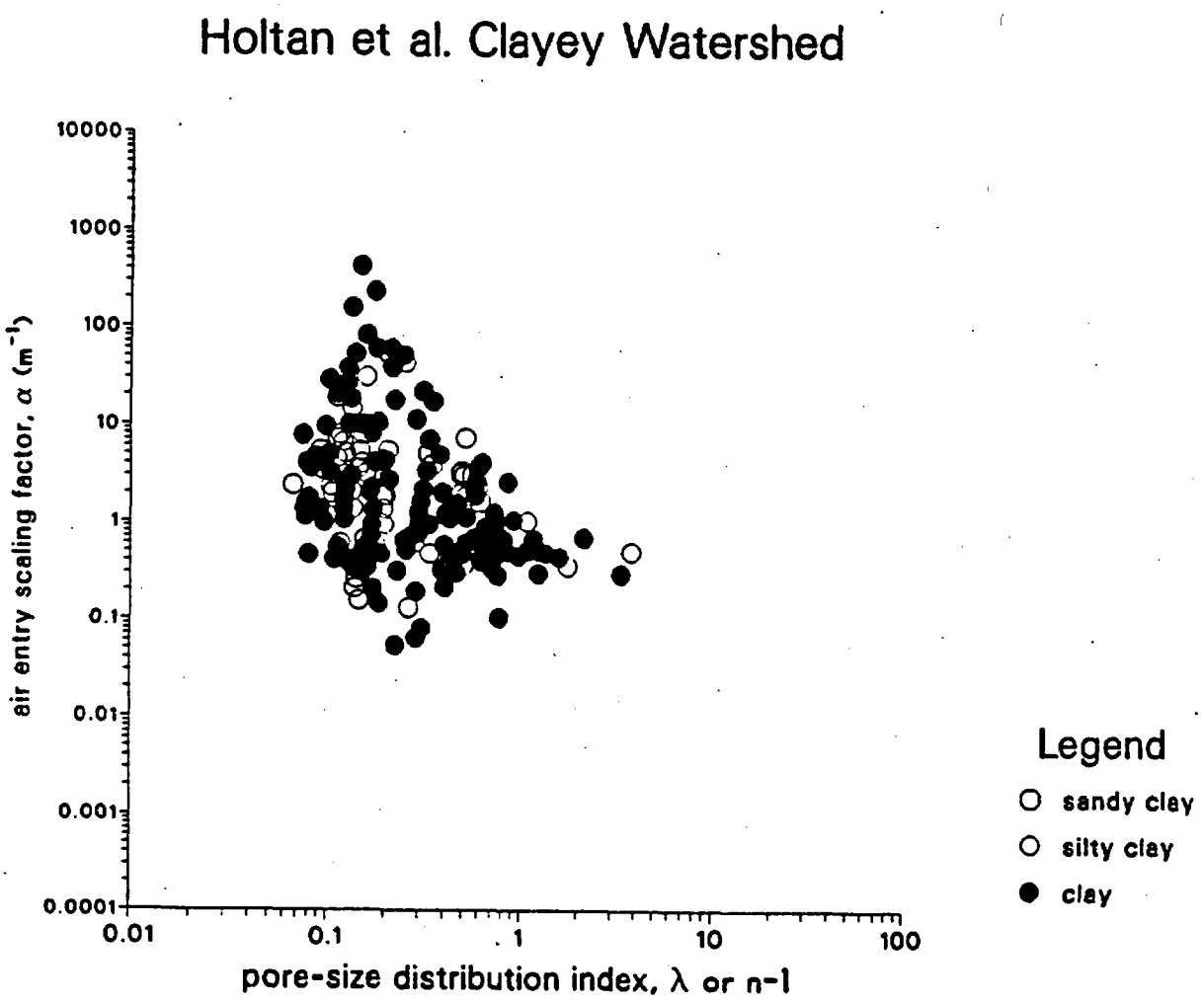

Figure A-24. Correlation Between Air Entry Scaling Factor and Pore-Size Distribution Index for Clayey Watershed Soil.

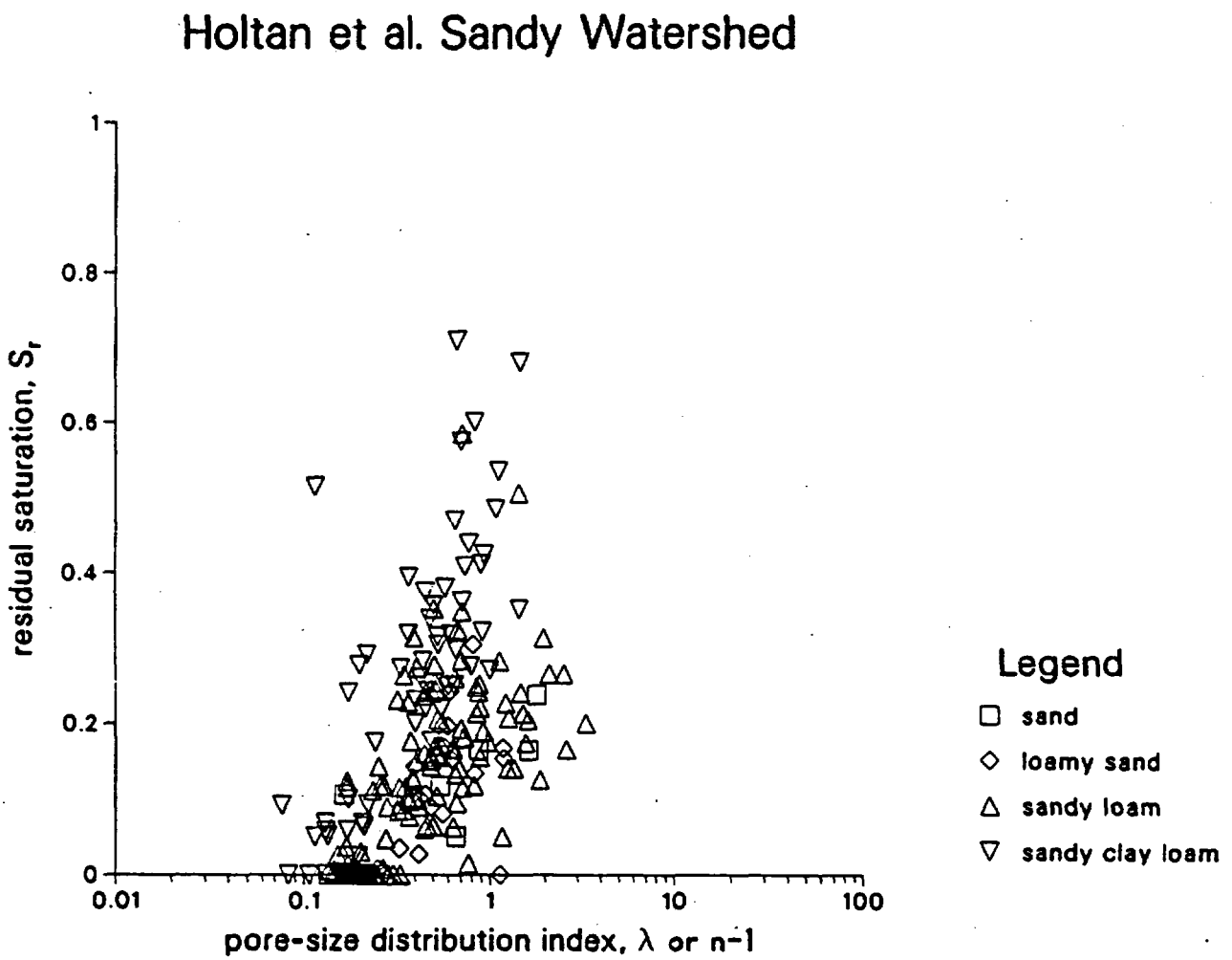

Figure A-25. Correlation Between Residual Saturation and Pore-Size Distribution Index for Sandy Watershed Soil.

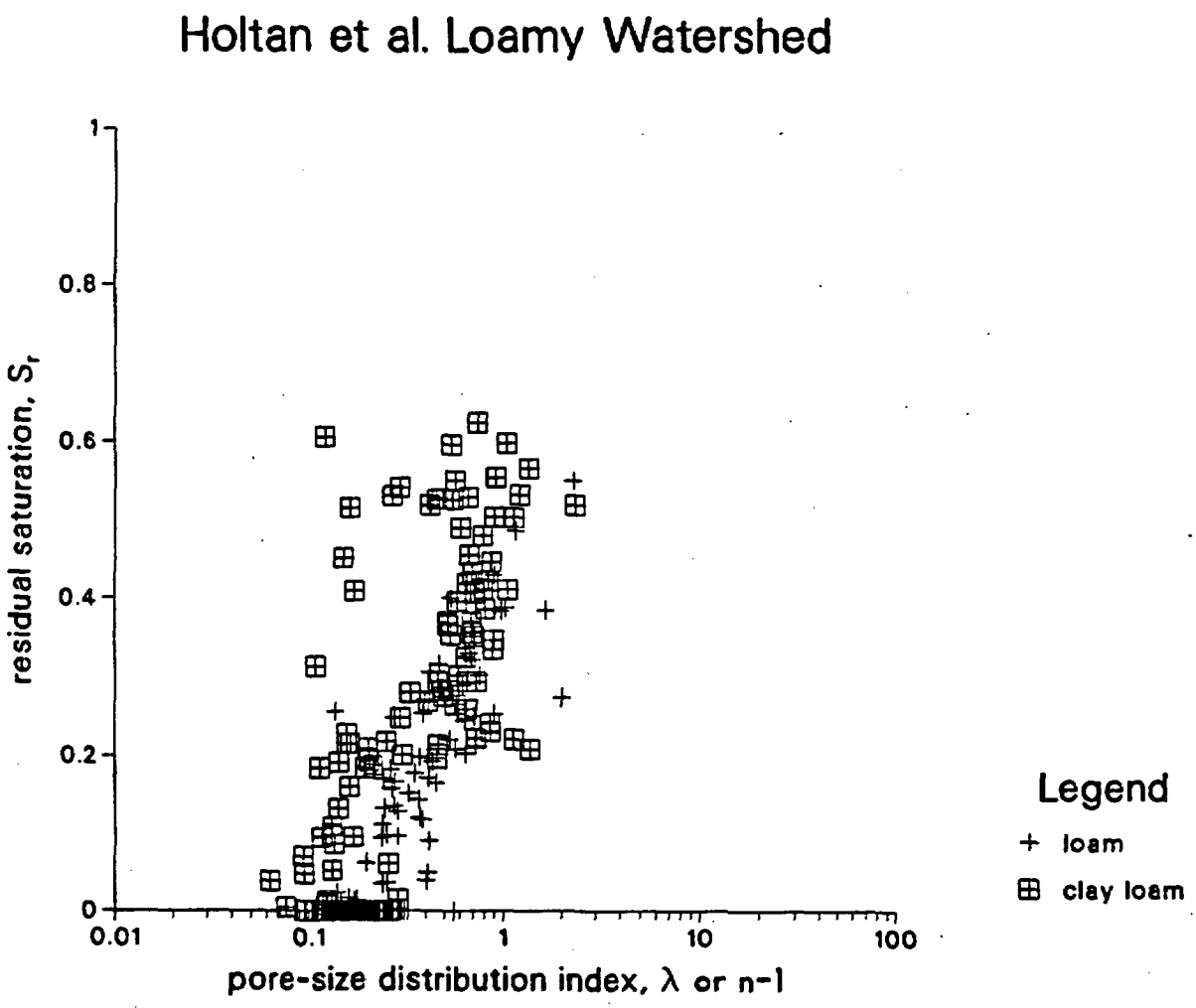

Figure A-26. Correlation Between Residual Saturation and Pore-Size Distribution Index for Loamy Watershed Soil.

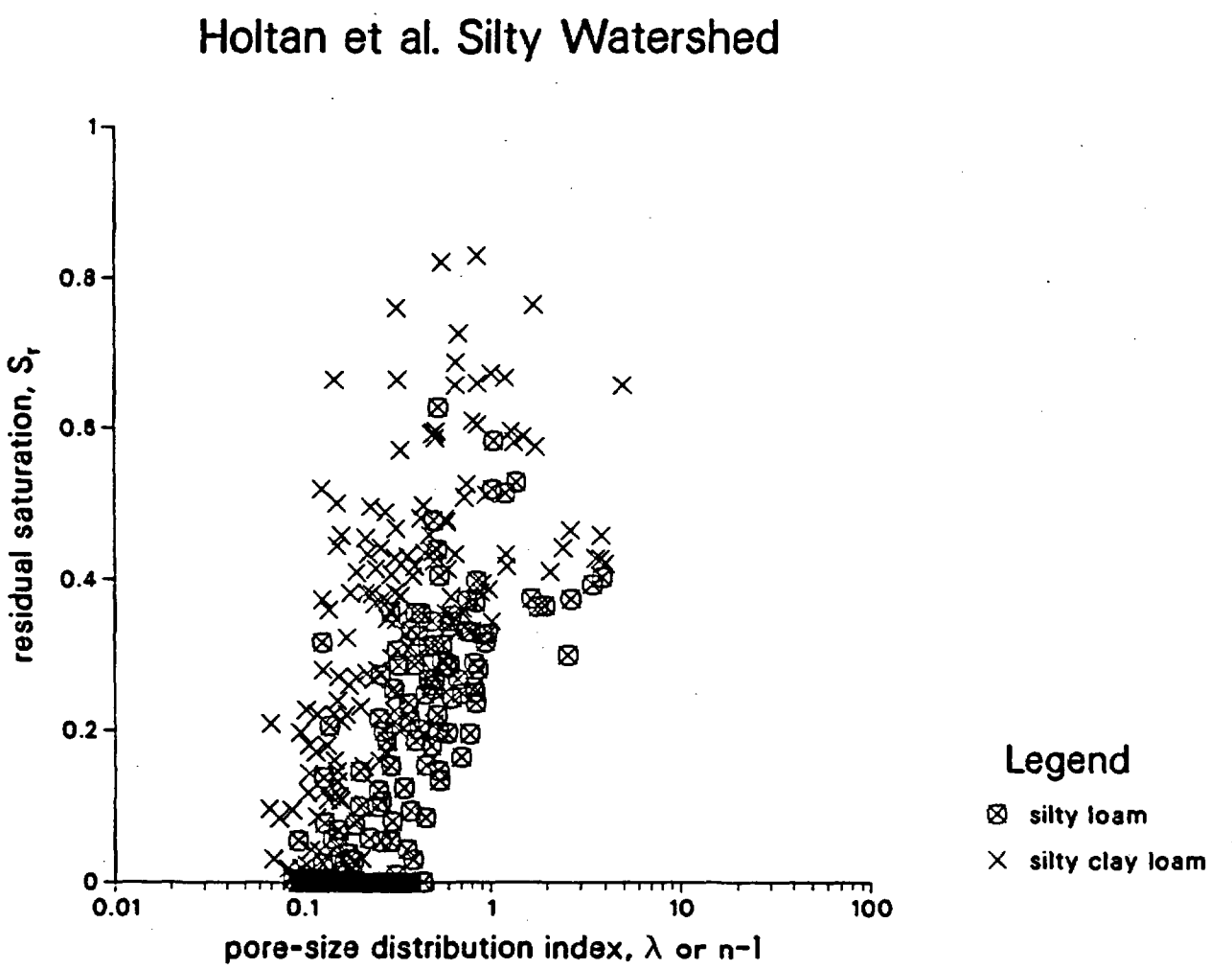

Figure A-27. Correlation Between Residual Saturation and Pore-Size Distribution Index for Silty Watershed Soil.

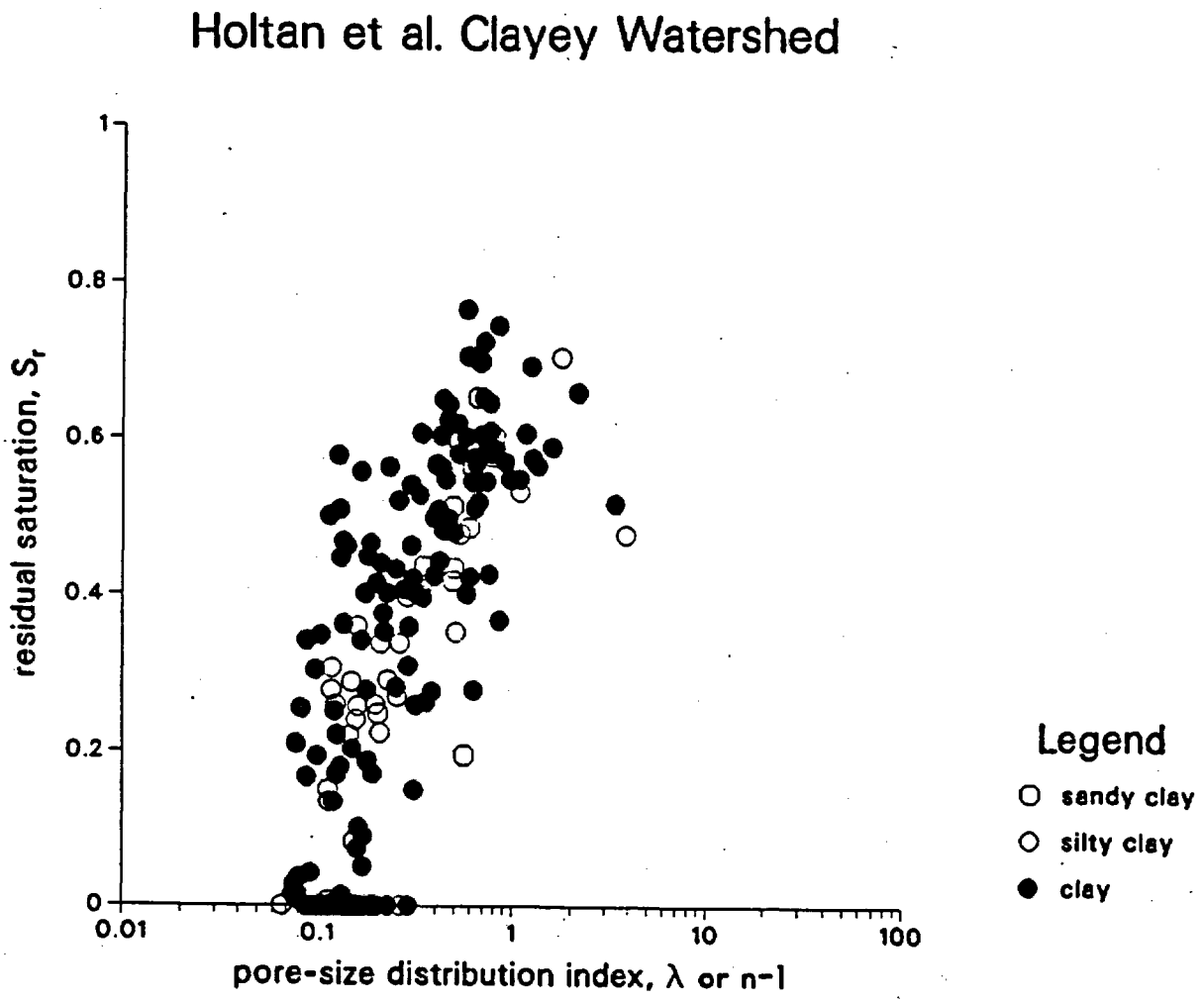

Figure A-28. Correlation Between Residual Saturation and Pore-Size Distribution Index for Clayey Watershed Soil.

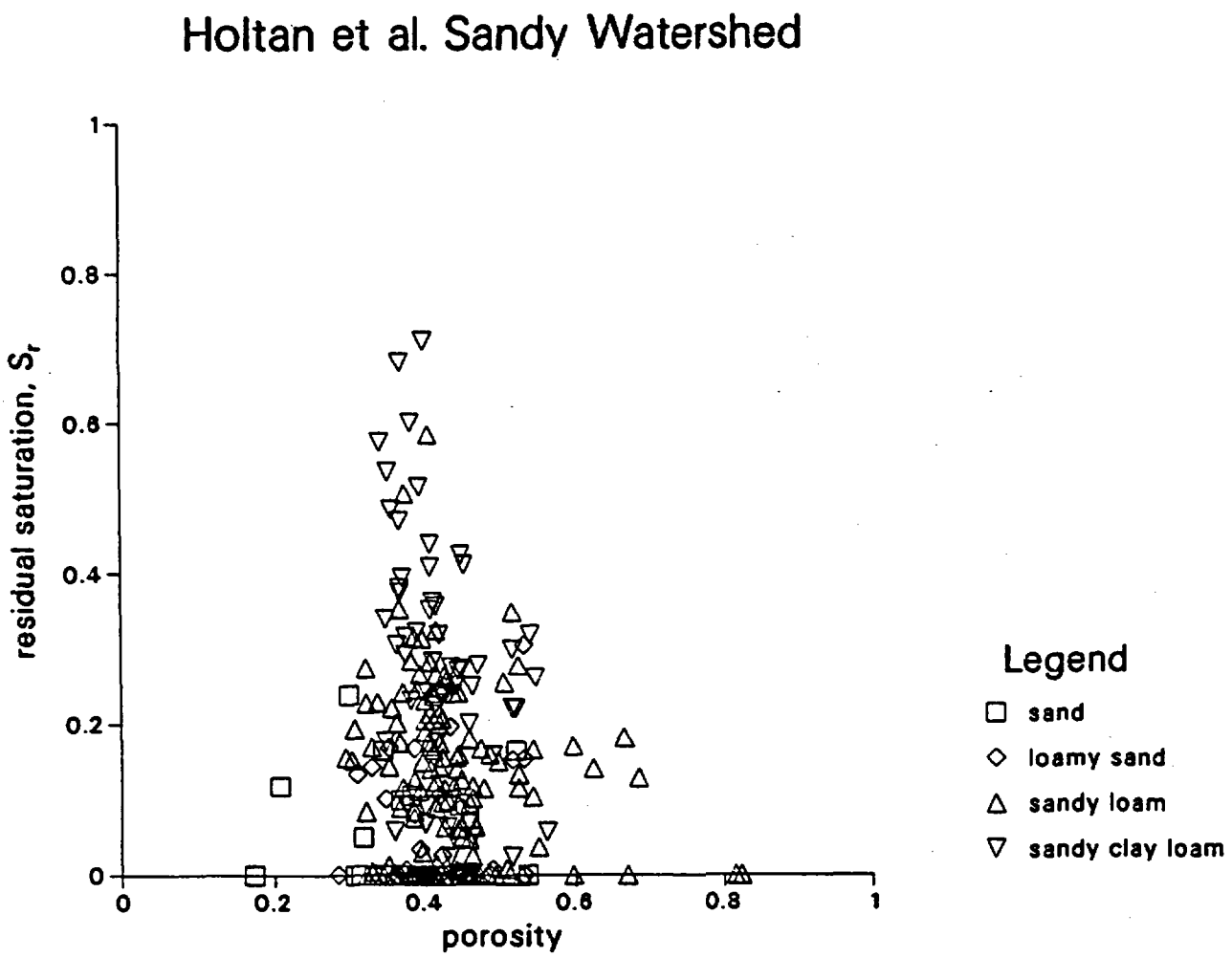

Figure A-29. Correlation Between Residual Saturation and Porosity for Sandy Watershed Soil.

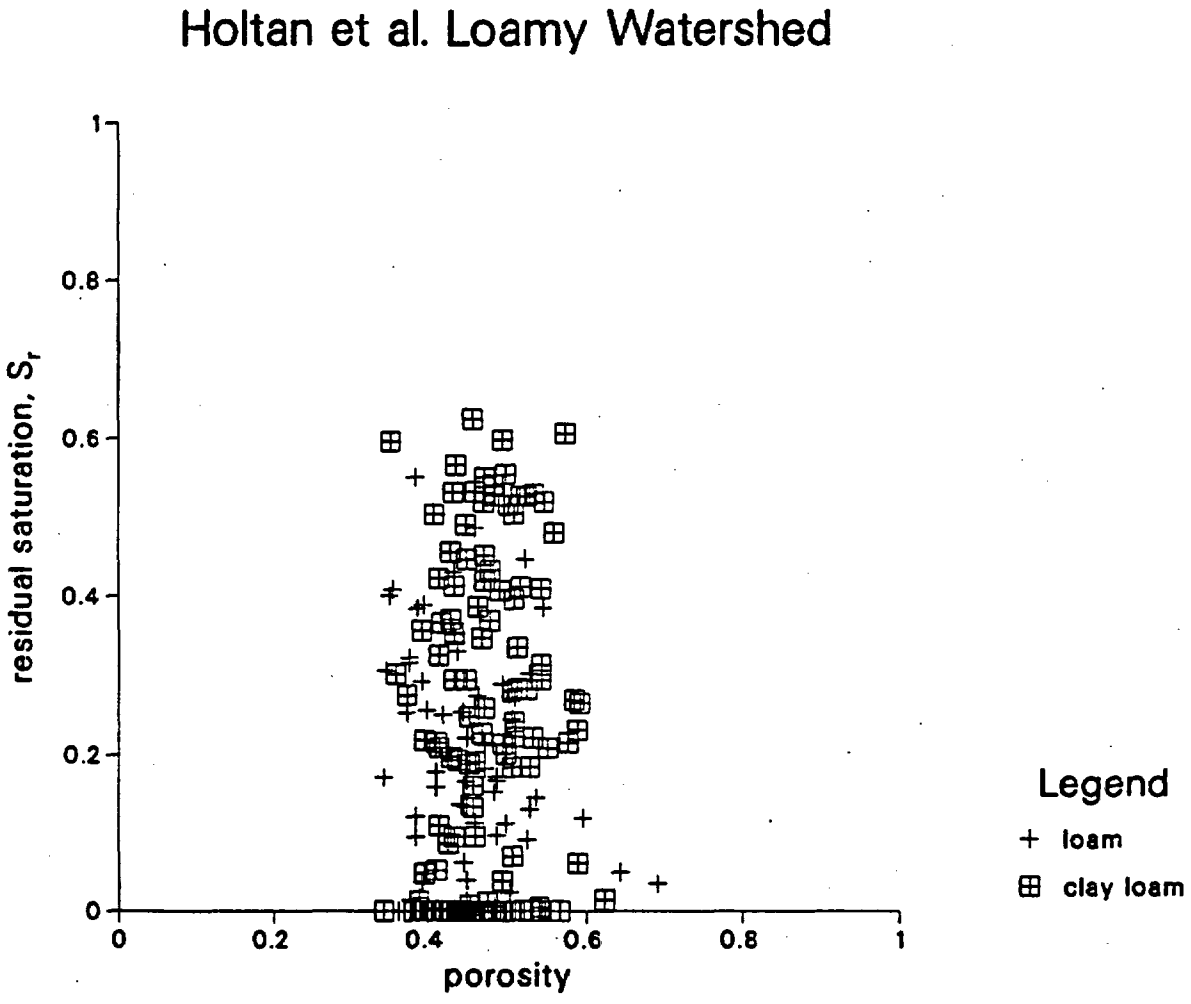

Figure A-30. Correlation Between Residual Saturation and Porosity for Loamy Watershed Soil.

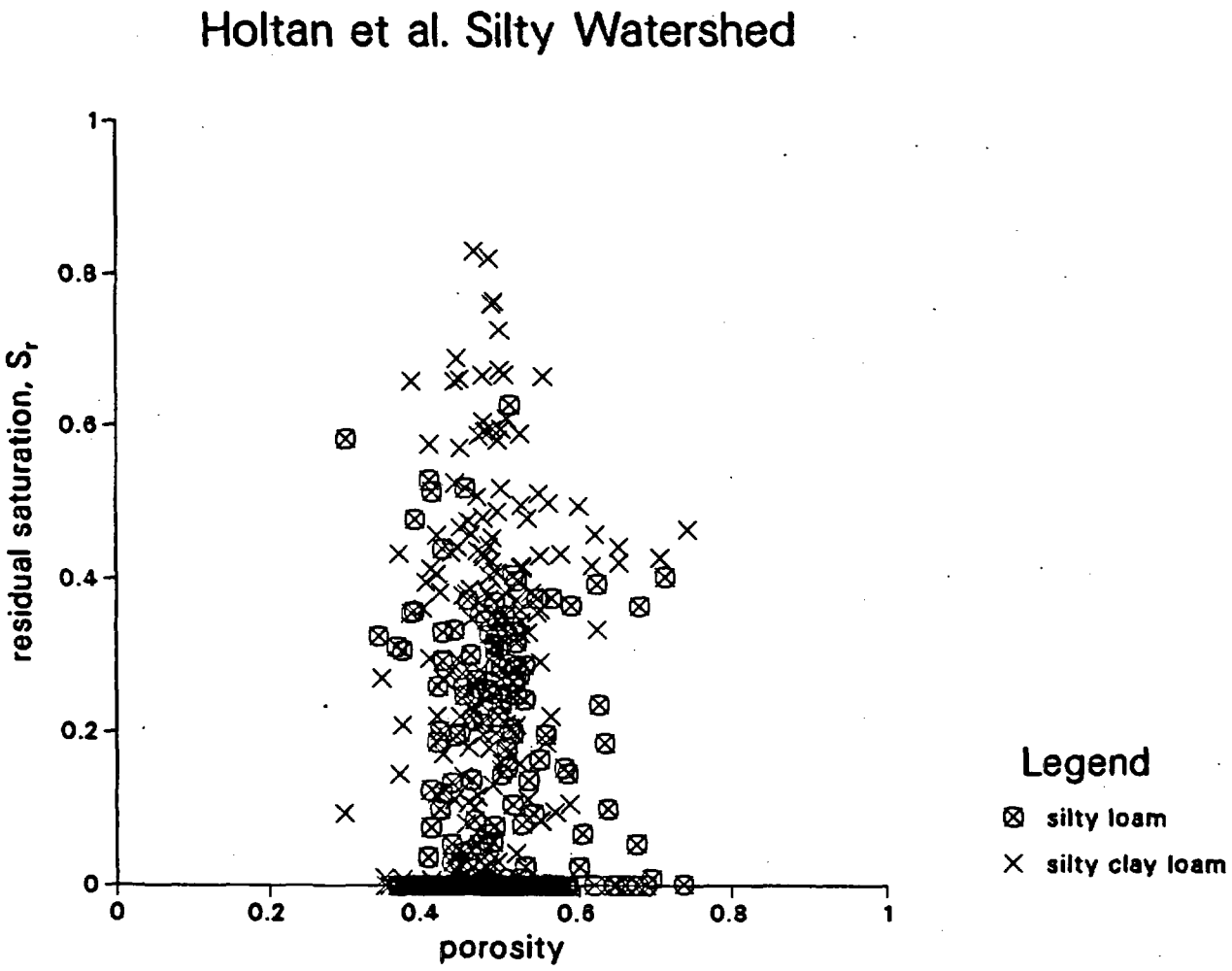

Figure A-31. Correlation Between Residual Saturation and Porosity for Silty Watershed Soil.

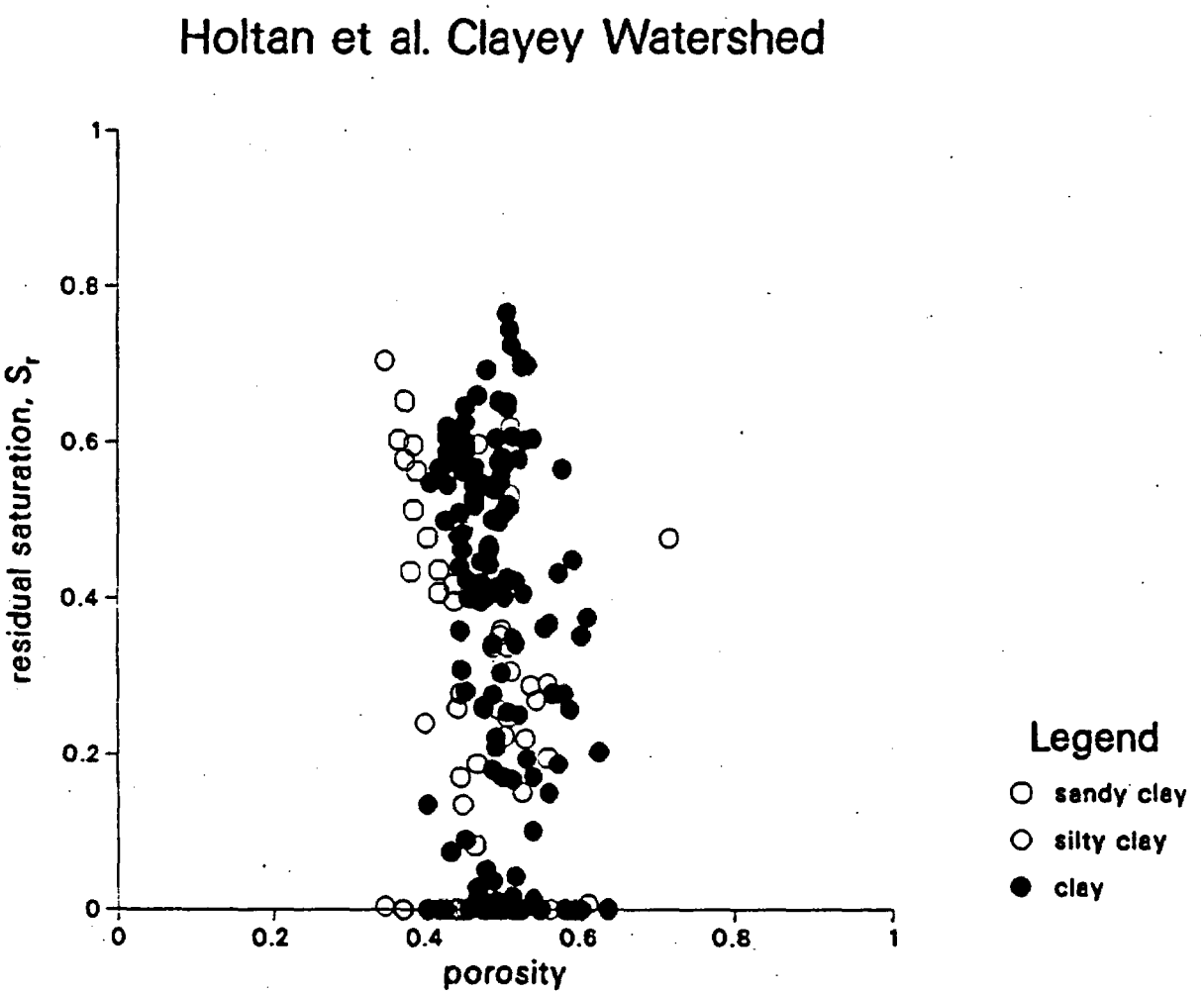

Figure A-32. Correlation Between Residual Saturation and Porosity for Clayey Watershed Soil.

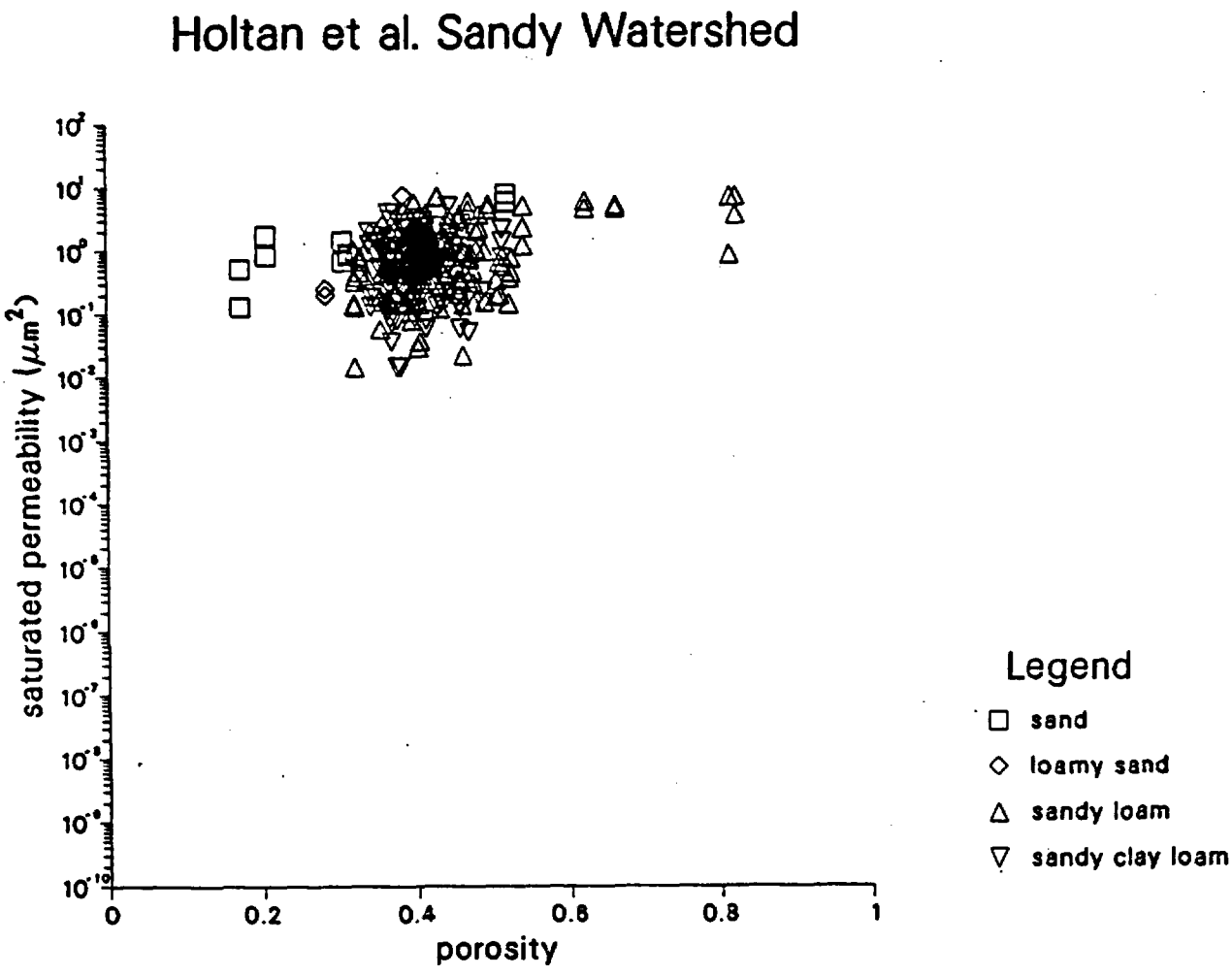

Figure A-33. Correlation Between Saturated Permeability and Porosity for Sandy Watershed Soil.

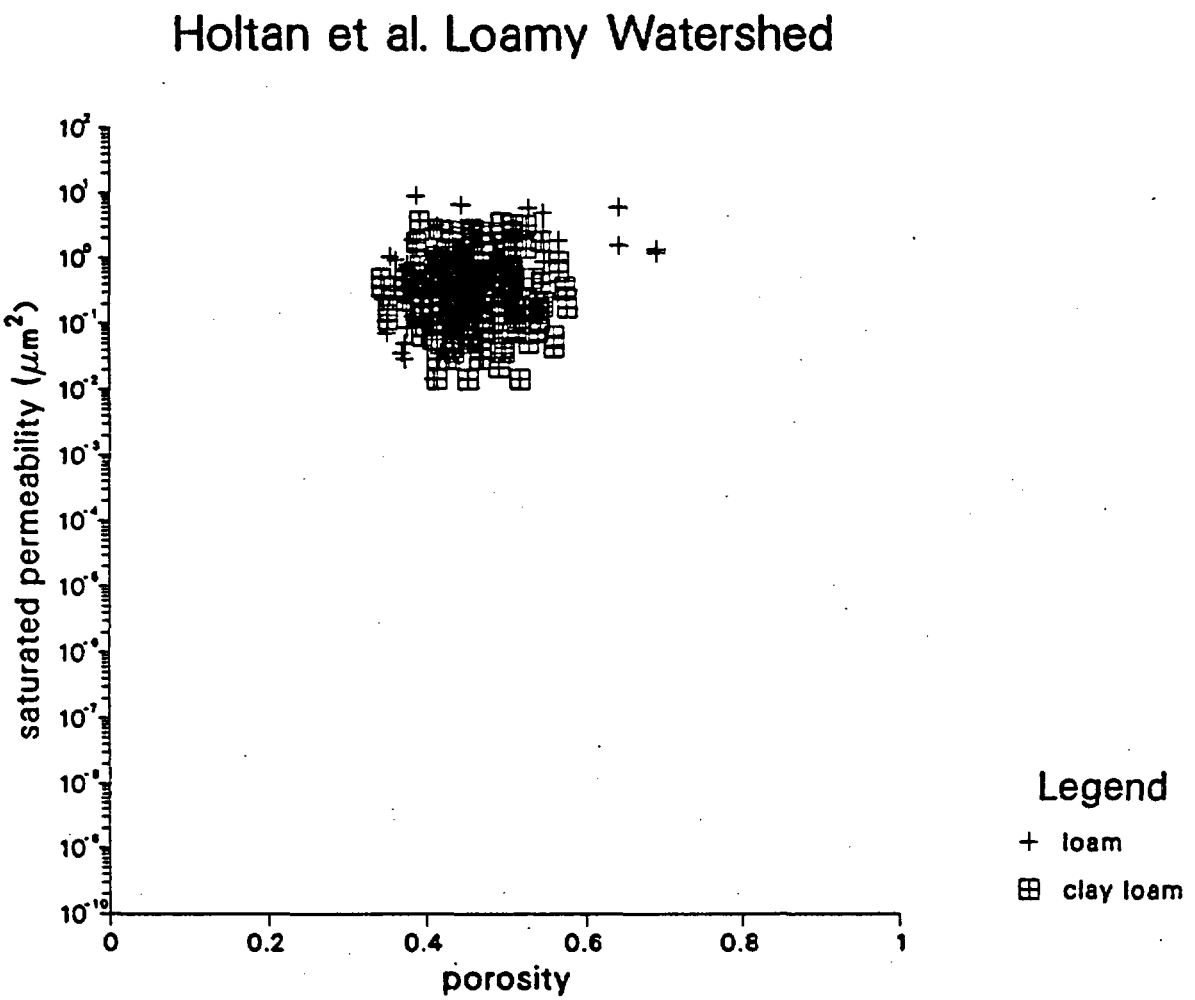

Figure A-34. Correlation Between Saturated Permeability and Porosity for Loamy Watershed Soil.

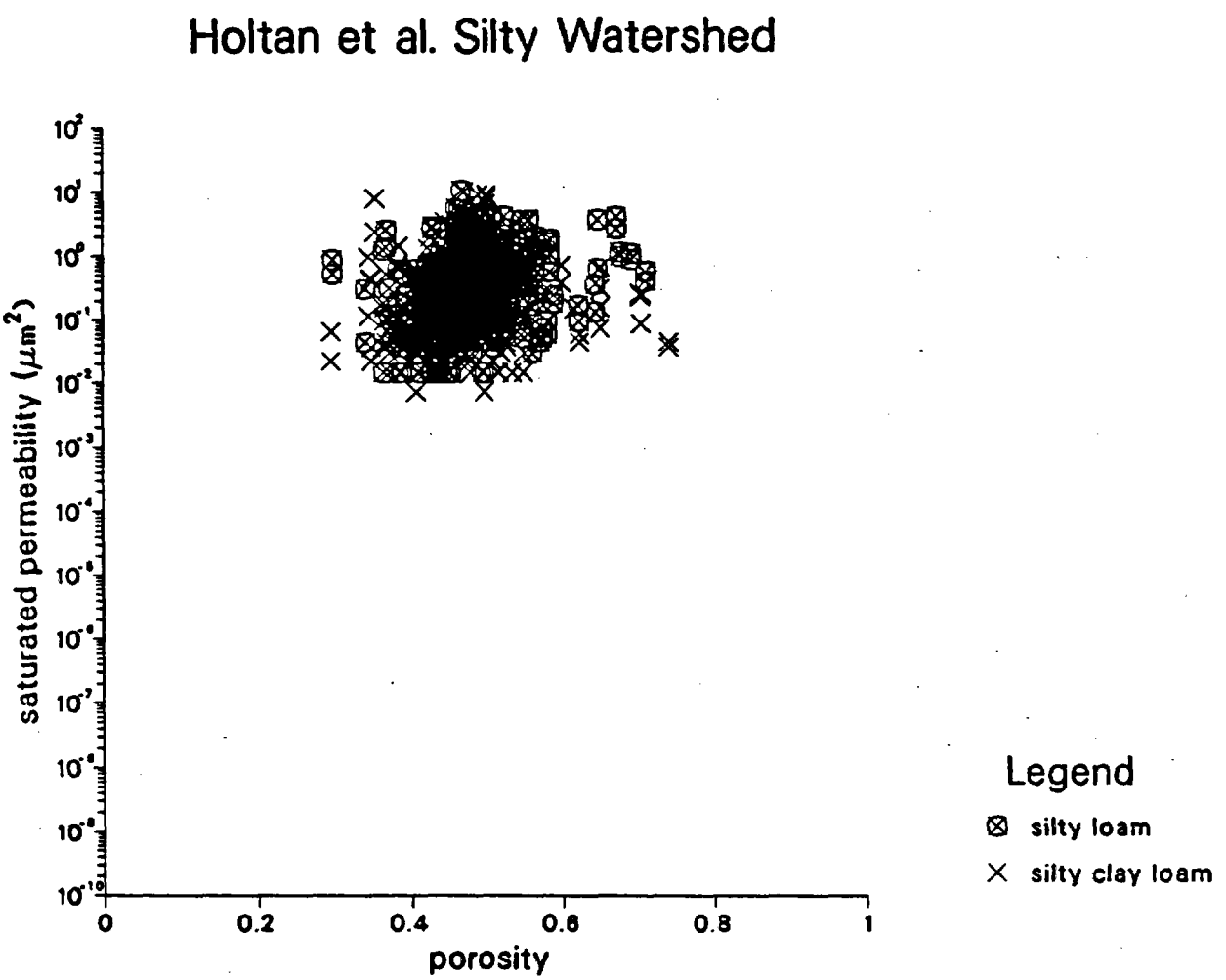

Figure A-35. Correlation Between Saturated Permeability and Porosity for Silty Watershed Soil.

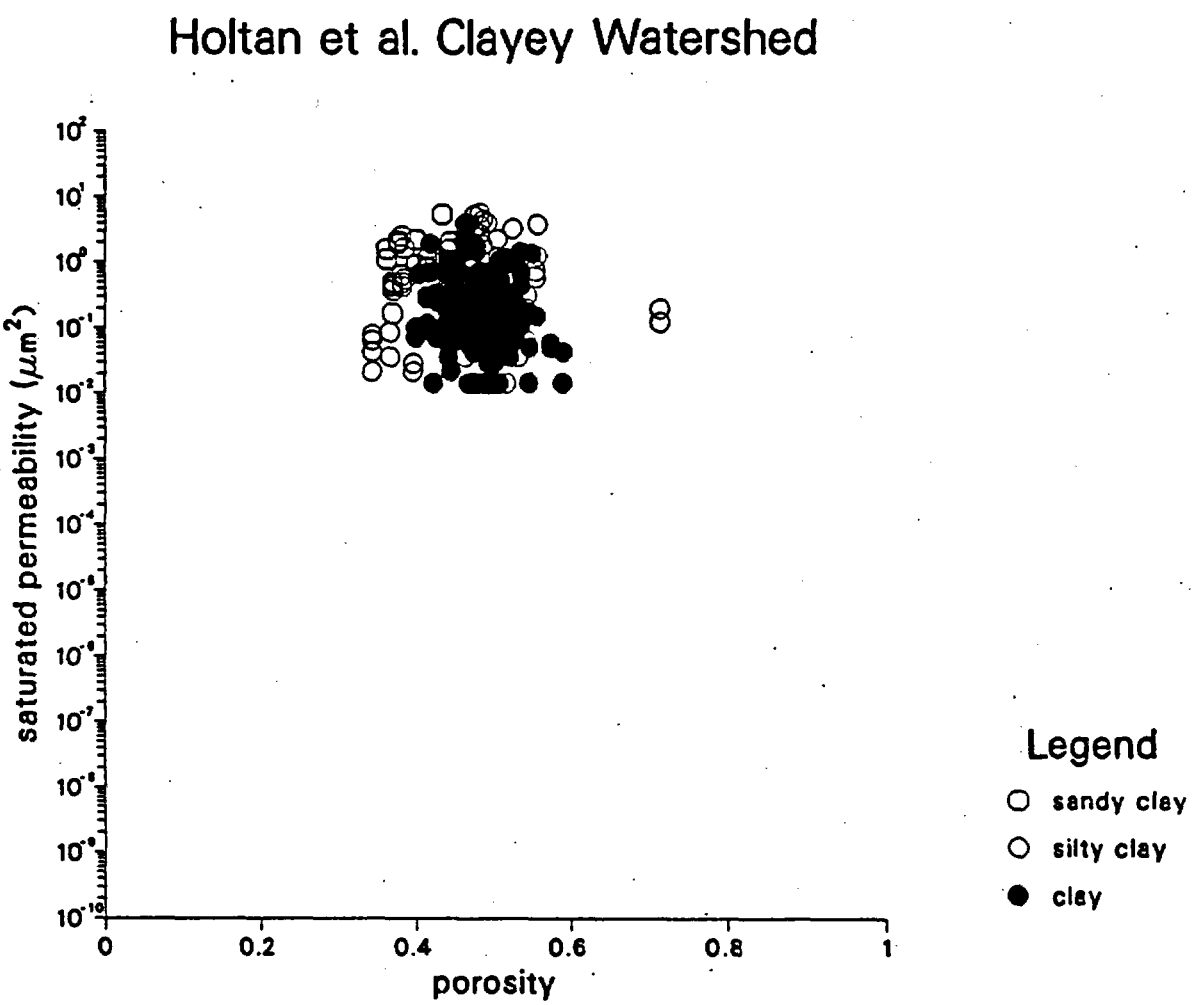

Figure A-36. Correlation Between Saturated Permeability and Porosity for Clayey Watershed Soil.

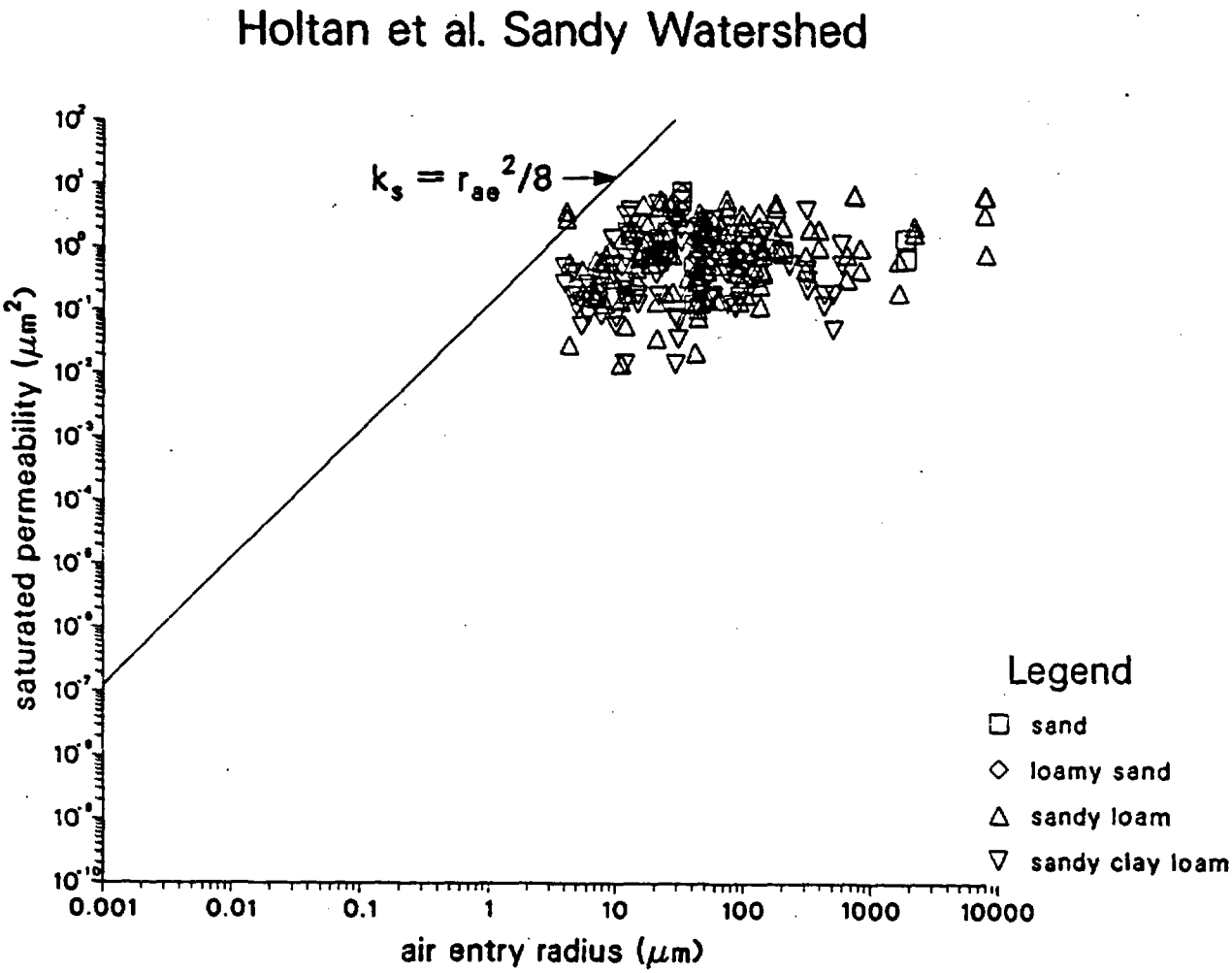

Figure A-37. Correlation Between Saturated Permeability and Air Entry Radius for Sandy Watershed Soil.

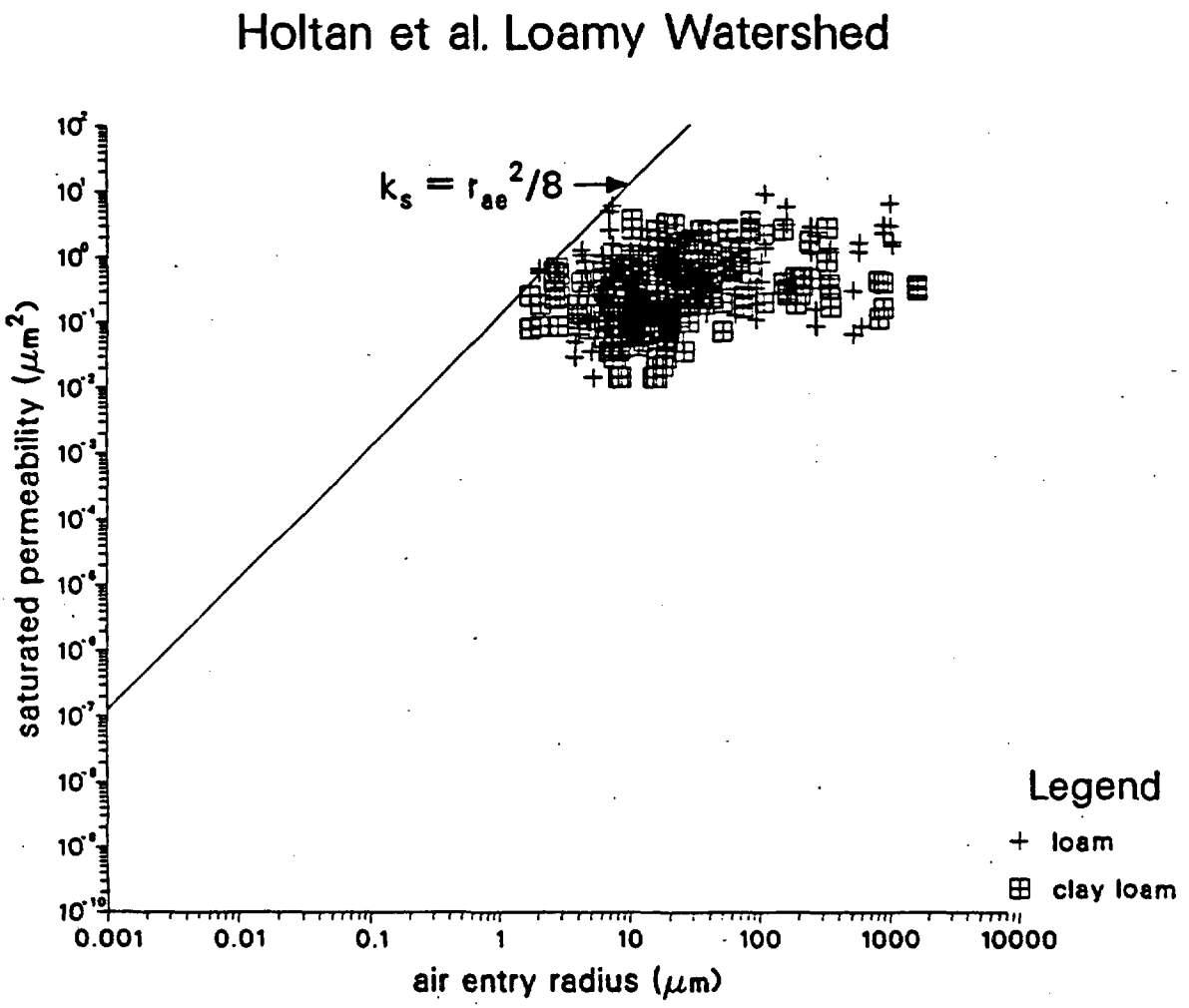

Figure A-38. Correlation Between Saturated Permeability and Air Entry Radius for Loamy Watershed Soil.

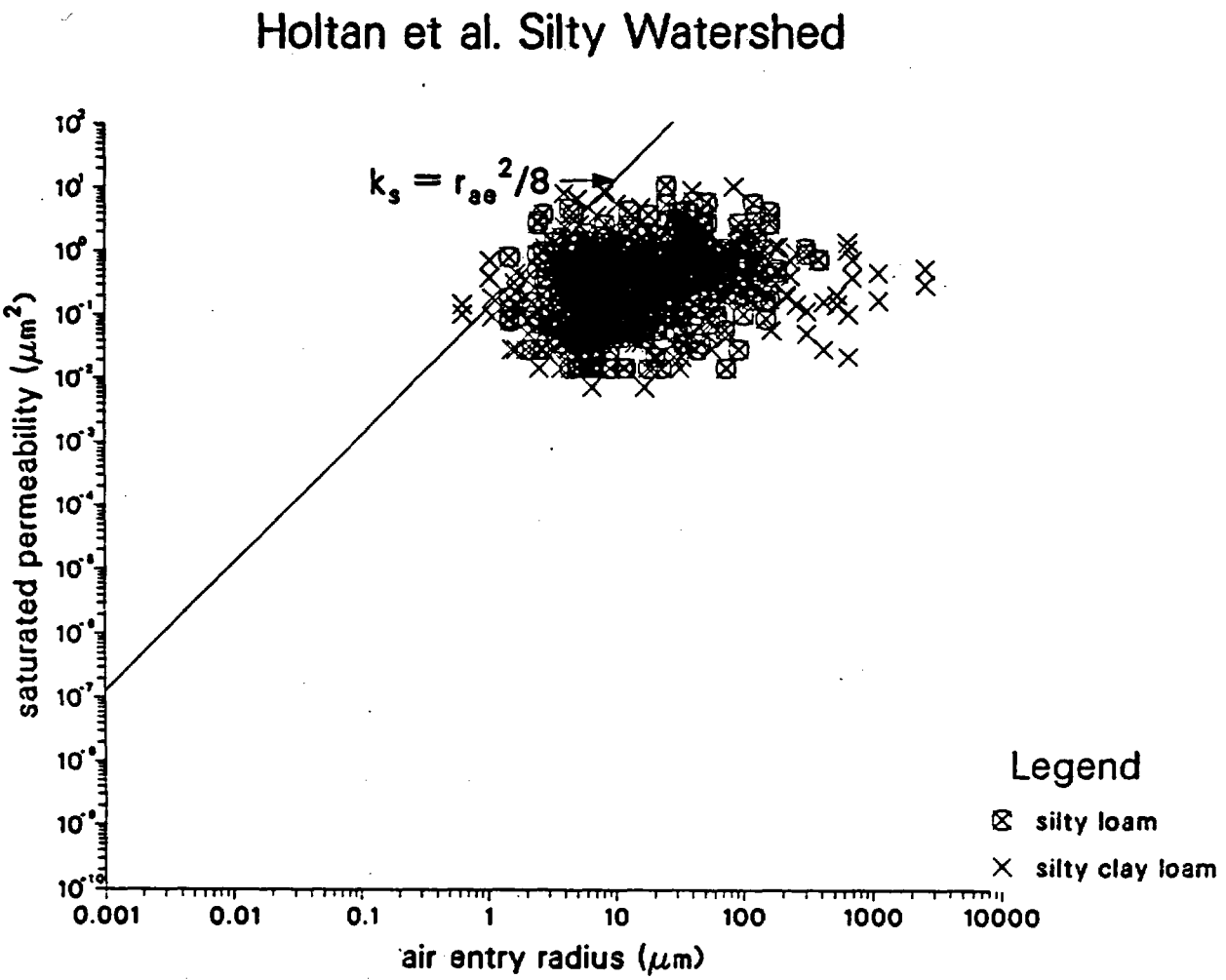

Figure A-39. Correlation Between Saturated Permeability and Air Entry Radius for Silty Watershed Soil.

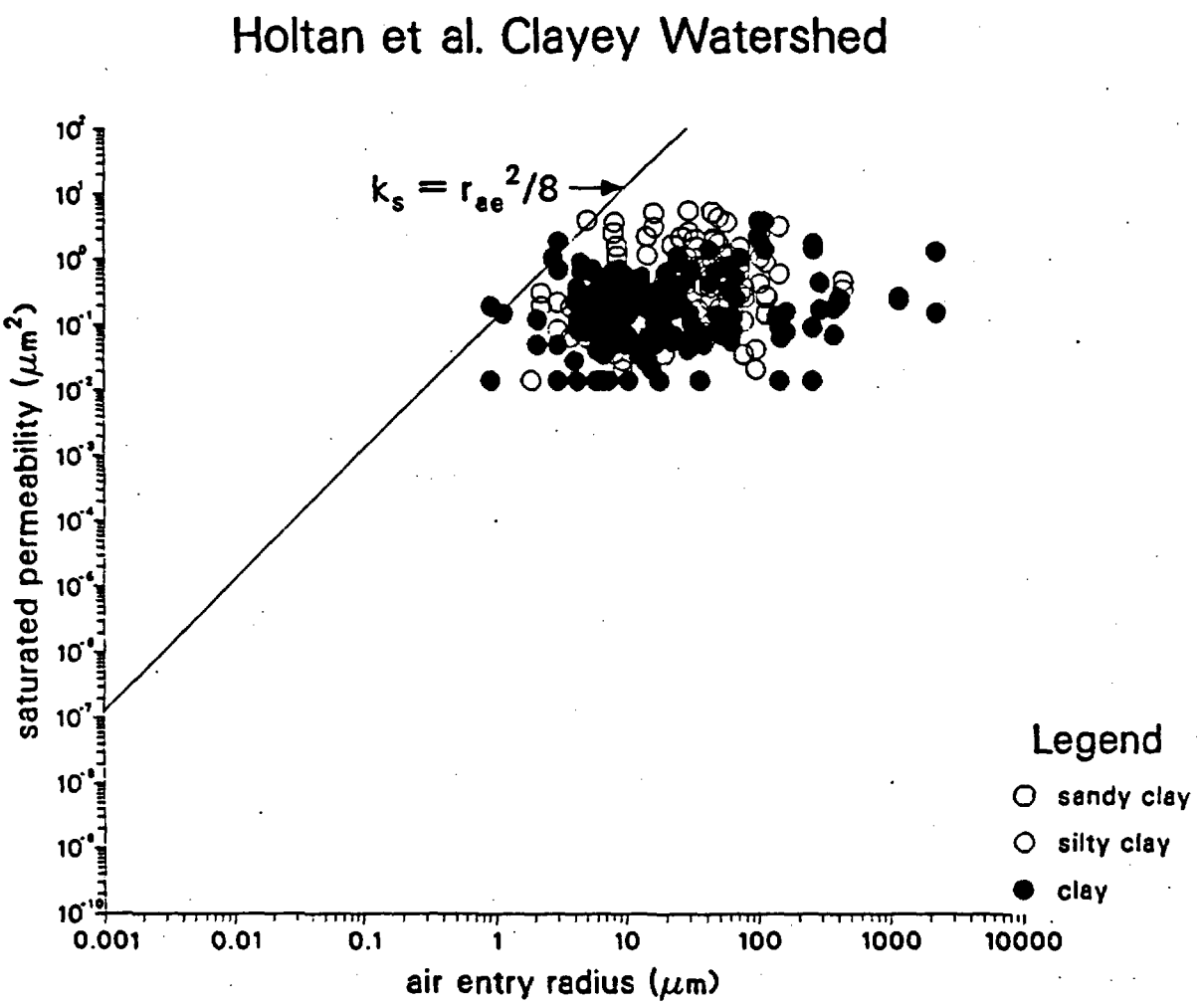

Figure A-40. Correlation Between Saturated Permeability and Air Entry Radius for Clayey Watershed Soil.

- The mean values of air entry scaling factor are fairly constant in the range of 1-10 m^{-1} for all soils, with sandy and loamy soils having slightly larger values than silty and clayey soils (Figures A-5c to A-8c).

- Approximate 60% of silty soil samples have zero residual saturation (Figure A-11a). Other watershed soils also have a significant percentage of samples with zero residual saturation (Figures A-9a, A-10a, A-12a).

- The mean values of saturated permeability are in the range of 0.1-1. μm^2 for all soils, with clayey soils having slightly lower values than other soils (Figures A-13c to A-16c).

- All soils have large porosity values (Figures A-17c to A-20c).

- Skewness and kurtosis coefficients are usually very sensitive to the number of data points in statistical analyses.

- This watershed soil data set supports the presence of correlation between air entry scaling factor and pore-size distribution index (Figures A-21 to A-24), and between residual saturation and pore-size distribution index (Figures A-25 to A-28). The residual saturation is not correlated with porosity (Figures A-29 to A-32). The data set is too scattered within limited range to evaluate the correlation between saturated permeability and porosity (Figures A-33 to A-36), and between saturated permeability and air entry radius (Figures A-37 to A-40).

APPENDIX B
REFERENCE INFORMATION BASE

Information from the Reference Information Base Used in this Report

This report contains no information from the Reference Information Base.

Candidate Information for the Reference Information Base

This report contains no candidate information for the Reference Information Base.

Candidate Information for the Site and Engineering Properties Data Base

This report contains no candidate information for the Site and Engineering Properties Data Base.

YUCCA MOUNTAIN SITE CHARACTERIZATION PROJECT

DISTRIBUTION LIST

1 Director (RW-1)
OCRWM
US Department of Energy
1000 Independence Avenue SW
Washington, DC 20585

1 F. G. Peters (RW-2)
Deputy Director
OCRWM
US Department of Energy
1000 Independence Avenue SW
Washington, DC 20585

1 T. H. Isaacs (RW-4)
Office of Strategic Planning and International Programs
OCRWM
US Department of Energy
1000 Independence Avenue SW
Washington, DC 20585

1 J. D. Saltzman (RW-5)
Office of External Relations
OCRWM
US Department of Energy
1000 Independence Avenue SW
Washington, DC 20585

1 Samuel Rousso (RW-10)
Office of Program and Resource Mgt.
OCRWM
US Department of Energy
1000 Independence Avenue SW
Washington, DC 20585

1 J. C. Bresee (RW-10)
OCRWM
US Department of Energy
1000 Independence Avenue SW
Washington, DC 20585

1 C. P. Gertz (RW-20)
Office of Geologic Disposal
OCRWM
US Department of Energy
1000 Independence Avenue, SW
Washington, DC 20585

1 S. J. Brocoum (RW-22)
Analysis and Verification Division
OCRWM
US Department of Energy
1000 Independence Avenue SW
Washington, DC 2585

1 J. Roberts, Acting Associate Director (RW-30)
Office of Systems and Compliance
OCRWM
US Department of Energy
1000 Independence Avenue, SW
Washington, DC 20585

1 J. Roberts (RW-33)
Director, Regulatory Compliance Division
OCRWM
US Department of Energy
1000 Independence Avenue, SW
Washington, DC 20585

1 G. J. Parker (RW-332)
OCRWM
US Department of Energy
1000 Independence Avenue, SW
Washington, DC 20585

1 R. A. Milner (RW-40)
Office of Storage and Transporation
OCRWM
US Department of Energy
1000 Independence Avenue, SW
Washington, DC 20585

1 S. Rousso, Associate Director
(RW-50)
Office of Contract Business
Management
OCRWM
US Department of Energy
1000 Independence Avenue, SW
Washington, DC 20585

1 T. Wood (RW-52)
Director, M&O Management Division
OCRWM
US Department of Energy
1000 Independence Avenue, SW
Washington, DC 20585

4 Victoria F. Reich, Librarian
Nuclear Waste Technical Review Board
1100 Wilson Blvd, Suite 910
Arlington, VA 22209

5 C. P. Gertz, Project Manager
Yucca Mountain Site
Characterization Project Office
US Department of Energy
P.O. Box 98608--MS 523
Las Vegas, NV 89193-8608

1 C. L. West, Director
Office of External Affairs
DOE Nevada Field Office
US Department of Energy
P.O. Box 98518
Las Vegas, NV 89193-8518

12 Technical Information Officer
DOE Nevada Field Office
US Department of Energy
P.O. Box 98518
Las Vegas, NV 89193-8518

1 P. K. Fitzsimmons, Technical Advisor
Office of Assistant Manager for
Environmental Safety and
Health
DOE Nevada Field Office
US Department of Energy
P.O. Box 98518
Las Vegas, NV 89193-8518

1 D. R. Elle, Director
Environmental Protection and Division
DOE Nevada Field Office
US Department of Energy
P.O. Box 98518
Las Vegas, NV 89193-8518

1 Repository Licensing & Quality
Assurance
Project Directorate
Division of Waste Management
US NRC
Washington, DC 20555

1 Senior Project Manager for Yucca
Mountain
Repository Project Branch
Division of Waste Management
US NRC
Washington, DC 20555

1 NRC Document Control Desk
Division of Waste Management
US NRC
Washington, DC 20555

1 Philip S. Justus
NRC Site Representive
301 E Stewart Avenue, Room 203
Las Vegas, NV 89101

1 E. P. Binnall
Field Systems Group Leader
Building 50B/4235
Lawrence Berkeley Laboratory
Berkeley, CA 94720

1 Center for Nuclear Waste
Regulatory Analyses
6220 Culebra Road
Drawer 28510
San Antonio, TX 78284

3 W. L. Clarke
Technical Project Officer - YMP
Attn: YMP/LRC
Lawrence Livermore National
Laboratory
P.O. Box 5514
Livermore, CA 94551

1 J. A. Blink
Deputy Project Leader
Lawrence Livermore National Laboratory
101 Convention Center Drive
Suite 820, MS 527
Las Vegas, NV 89109

4 J. A. Canepa
Technical Project Officer - YMP
N-5, Mail Stop J521
Los Alamos National Laboratory
P.O. Box 1663
Los Alamos, NM 87545

1 H. N. Kalia
Exploratory Shaft Test Manager
Los Alamos National Laboratory
Mail Stop 527
101 Convention Center Dr., #820
Las Vegas, NV 89101

1 N. Z. Elkins
Deputy Technical Project Officer
Los Alamos National Laboratory
Mail Stop 527
101 Convention Center Dr., #820
Las Vegas, NV 89101

5 L. E. Shephard
Technical Project Officer - YMP
Sandia National Laboratories
Organization 6302
P.O. Box 5800
Albuquerque, NM 87185

1 J. F. Devine
Asst Director of Engineering Geology
US Geological Survey
106 National Center
12201 Sunrise Valley Drive
Reston, VA 22092

1 L. R. Hayes
Technical Project Officer
Yucca Mountain Project Branch
MS 425
US Geological Survey
P.O. Box 25046
Denver, CO 80225

1 V. R. Schneider
Asst. Chief Hydrologist--MS 414
Office of Program Coordination and Technical Support
US Geological Survey
12201 Sunrise Valley Drive
Reston, VA 22092

1 J. S. Stuckless
Geologic Division Coordinator
MS 913
Yucca Mountain Project
US Geological Survey
P.O. Box 25046
Denver, CO 80225

1 D. H. Appel, Chief
Hydrologic Investigations Program
MS 421
US Geological Survey
P.O. Box 25046
Denver, CO 80225

1 E. J. Helley
Branch of Western Regional Geology
MS 427
US Geological Survey
345 Middlefield Road
Menlo Park, CA 94025

1 R. W. Craig, Chief
Nevada Operations Office
US Geological Survey
101 Convention Center Drive
Suite 860, MS 509
Las Vegas, NV 89109

1 D. Zesiger
US Geological Survey
101 Conventional Center Drive
Suite 860, MS 509
Las Vegas, NV 89109

1 G. L. Ducret, Associate Chief
Yucca Mountain Project Division
US Geological Survey
P.O. Box 25046
421 Federal Center
Denver, CO 80225

1 A. L. Flint
US Geological Survey
MS 721
P.O. Box 327
Mercury, NV 89023

1 D. A. Beck
Water Resources Division, USGS
6770 S Paradise Road
Las Vegas, NV 89119

1 P. A. Glancy
US Geological Survey
Federal Building, Room 224
Carson City, NV 89701

1 Sherman S.C. Wu
Branch of Astrogeology
US Geological Survey
2255 N Gemini Drive
Flagstaff, AZ 86001

1 J. H. Sass - USGS
Branch of Tectonophysics
2255 N Gemini Drive
Flagstaff, AZ 86001

1 DeWayne Campbell
Technical Project Officer - YMP
US Bureau of Reclamation
Code D-3790
P.O. Box 25007
Denver, CO 80225

1 J. M. LaMonaca
Records Specialist
US Geological Survey
421 Federal Center
P.O. Box 25046
Denver, CO .80225

1 W. R. Keefer - USGS
913 Federal Center
P.O. Box 25046
Denver, CO 80225

1 M. D. Voegele
Technical Project Officer - YMP
SAIC
101 Convention Center Drive
Suite 407
Las Vegas, NV 89109

2 L. D. Foust
Nevada Site Manager
TRW Environmental Safety Systems
101 Convention Center Drive
Suite 540, MS 423
Las Vegas, NV 89109

1 C. E. Ezra
YMP Support Office Manager
EG&G Energy Measurements Inc
MS V-02
P.O. Box 1912
Las Vegas, NV 89125

1 E. L. Snow, Program Manager
Roy F. Weston Inc
955 L'Enfant Plaza SW
Washington, DC 20024

1 Technical Information Center
Roy F. Weston Inc
955 L'Enfant Plaza SW
Washington, DC 20024

1 D. Hedges, Vice President, QA
Roy F. Weston Inc
4425 Spring Mountain Road
Suite 300
Las Vegas, NV 89102

1 D. L. Fraser, General Manager
Reynolds Electrical & Engineering Co, Inc
MS 408
P.O. Box 98521
Las Vegas, NV 89193-8521

1 B. W. Colston, President and General Manager
Las Vegas Branch
Raytheon Services Nevada
MS 416
P.O. Box 95487
Las Vegas, NV 89193-5487

1 R. L. Bullock
Technical Project Officer - YMP
Raytheon Services Nevada
Suite P-250, MS 403
101 Convention Center Drive
Las Vegas, NV 89109

1 Paul Eslinger, Manager
PASS Program
Pacific Northwest Laboratories
P.O. Box 999
Richland, WA 99352

1 A. T. Tamura
Science and Technology Division
OSTI
US Department of Energy
P.O. Box 62
Oak Ridge, TN 37831

1 Carlos G. Bell Jr
Professor of Civil Engineering
Civil and Mechanical Engineering Dept.
University of Nevada, Las Vegas
4505 S Maryland Parkway
Las Vegas, NV 89154

1 P. J. Weeden, Acting Director
Nuclear Radiation Assessment Div.
US EPA
Environmental Monitoring
Systems Lab
P.O. Box 93478
Las Vegas, NV 89193-3478

1 ONWI Library
Battelle Columbus Laboratory
Office of Nuclear Waste Isolation
505 King Avenue
Columbus, OH 43201

1 T. Hay, Executive Assistant
Office of the Governor
State of Nevada
Capitol Complex
Carson City, NV 89710

3 R. R. Loux
Executive Director
Agency for Nuclear Projects
State of Nevada
Evergreen Center, Suite 252
1802 N. Carson Street
Carson City, NV 89710

1 C. H. Johnson
Technical Program Manager
Agency for Nuclear Projects
State of Nevada
Evergreen Center, Suite 252
1802 N. Carson Street
Carson City, NV 89710

1 John Fordham
Water Resources Center
Desert Research Institute
P.O. Box 60220
Reno, NV 89506

1 David Rhode
Desert Research Institute
P.O. Box 60220
Reno, NV 89506

1 Eric Anderson
Mountain West Research-
Southwest Inc
2901 N Central Avenue #1000
Phoenix, AZ 85012-2730

1 The Honorable Cyril Schank
Chairman
Churchill County Board of
Commissioners
190 W First Street
Fallon, NV 89406

1 Dennis Bechtel, Coordinator
Nuclear Waste Division
Clark County Department of
Comprehensive Planning
301 E Clark Avenue, Suite 570
Las Vegas, NV 89101

1 Juanita D. Hayes
Nuclear Waste Repository
Oversight Program
Esmeralda County
P.O. Box 490
Goldfield, NV 89013

1 Yucca Mountain Information
Office
Eureka County
P.O. Box 714
Eureka, NV 89316

1 Brad Mettam
Inyo County Yucca Mountain
Repository Assessment Office
Drawer L
Independence, CA 93526

1 The Honorable Gloria Derby
Chairman
Lander County Board of
Commissioners
315 South Humbolt
Battle Mountain, NV 89820

1 The Honorable Edward E. Wright
Chairman
Lincoln County Board of
Commissioners
P.O. Box 90
Pioche, NV 89043

1 Vernon E. Poe
Office of Nuclear Projects
Mineral County
P.O. Box 1026
Hawthorne, NV 89415

1 The Honorable Barbara J. Raper
Chairman
Nye County Board of
Commissioners
P.O. Box 1240
Pahrump, NV 89041

1 Planning Department
Nye County
P.O. Box 153
Tonopah, NV 89049

1 Florindo Mariani
White Pine County Nuclear
Waste Project Office
457 Fifth Street
Ely, NV 89301

5 Judy Foremaster
City of Caliente Nuclear Waste
Project Office
P.O. Box 158
Caliente, NV 89008

1 Jason Pitts
Lincoln County Nuclear Waste
Project Office
Lincoln County Courthouse
Pioche, NV 89043

1 Economic Development Dept.
City of Las Vegas
400 E. Stewart Avenue
Las Vegas, NV 89101

1 Commmunity Planning and
Development
City of North Las Vegas
P.O. Box 4086
North Las Vegas, NV 89030

1 Community Development and
Planning
City of Boulder City
P.O. Box 61350
Boulder City, NV 89006

1 Commission of the European
Communities
200 Rue de la Loi
B-1049 Brussells
BELGIUM

6 M. J. Dorsey, Librarian
YMP Research and Study Center
Reynolds Electrical &
Engineering Co Inc
MS 407
P.O. Box 98521
Las Vegas, NV 89193-8521

1 Amy Anderson
Argonne National Laboratory
Building 362
9700 S Cass Avenue
Argonne, IL 60439

1 Steve Bradhurst
P.O. Box 1510
Reno, NV 89505

1 Michael L. Baughman
35 Clark Road
Fiskdale, MA 01518

1	Glenn Van Roekel Director of Community Development City of Caliente P.O. Box 158 Caliente, NV 89008
1	Ray Williams, Jr P.O. Box 10 Austin, NV 89310
1	R. F. Pritchett Technical Project Officer - YMP Reynolds Electrical & Engineering Co Inc MS 408 P.O. Box 98521 Las Vegas, NV 89193-8521
1	Charles Thistlethwaite, AICP Associate Planner Inyo County Planning Department Drawer L Independence, CA 93526
1	Les Bradshaw Nye County District Attorney P.O. Box 593 Tonopah, NV 89049
1	Dr. Moses Karakouzian 1751 E Reno #125 Las Vegas, NV 89119
20	J.S.Y. Wang Lawrence Berkeley Laboratory 1 Cyclotron Road Berkely, CA 94720
20	T. N. Narasimhan Lawrence Berkely Laboratory 1 Cyclotron Road Berkely, CA 94720

1	6300	D.E. Ellis
1	6302	L.E. Shephard
1	6312	H.A. Dockery
1	6313	L.S. Costin
2	6352	G.M. Gerstner-Miller for 100/1215/SAND88-7054/QA
2	6352	G.M. Gerstner-Miller for DRMS files
20	6352	WMT Library
1	6319	R.R. Richards
1	6115	P.B. Davies
1	1502	P.J. Hommert
1	6410	D.A. Dahlgren
5	7141	Technical Library
1	7151	Technical Publications
10	7613-2	Document Processing for DOE/OSTI
1	8523-2	Central Technical Files
1	6312	R.W. Barnard
1	6312	J.H. Gauthier
1	6312	P.G. Kaplan
1	6312	M.L. Wilson

*U.S. GOVERNMENT PRINTING OFFICE 1993-0-774-038/80002

SAND88-7054

The number in the lower right-hand corner is an accession number used for Office of Civilian Radioactive Waste Management purposes only. It should not be used when ordering this publication.

NNA.930623.0026